NASA-TM
84412 Advances in Planetary Geology
1981

Advances in Planetary Geology

November 1981

NASA

NASA TM-84412

Advances in Planetary Geology

NASA Scientific and Technical Information Branch 1981
National Aeronautics and Space Administration
Washington, DC

Page intentionally left blank

Page intentionally left blank

FOREWORD

This document is a compilation of reports from Principal Investigators and their Associates of NASA's Office of Space Science, Solar System Exploration Division, Planetary Geology Program. The reports present research that adds to our knowledge of the origin and evaluation of the solar system and to our understanding of the earth as a planet. Advances in Planetary Geology was established as a complement to the abstract document "Reports of Planetary Geology Program" and to professional journals. This document provides a method of publishing research results which are in a form that would not normally be published elsewhere. The research reports may be in the form of lengthy research reports, progress reports, Ph.D. dissertations, or master's theses.

Joseph M. Boyce
Discipline Scientist
Planetary Geology Program
Office of Space Science

To Contributors:

A wider variety of manuscripts can be accommodated by Advances in Planetary Geology than by most journals. Particularly appropriate are complete theses, dissertations, and research reliant on extensive presentations of data. All contributions must be of direct interest to planetary geologists and must be of high quality. Manuscripts must be typed single spaced in a camera-ready format and sent to:

Alex Woronow
Lunar and Planetary Laboratory
University of Arizona
Tucson, AZ 85721

Page intentionally left blank

Page intentionally left blank

CONTENTS

SECTION I: 1
THE STOCHASTIC EVOLUTION OF ASTEROIDAL REGOLITHS AND THE ORIGIN OF BRECCIATED AND GAS-RICH METEORITES.
Kevin Housen

SECTION II: 219
RIDGE SYSTEMS ON MARS.
Ann Gifford

SECTION III: 365
THE MORPHOLOGY AND EVOLUTION OF GANYMEDE AND CALLISTO.
Steven Squyres

SECTION I

Page intentionally left blank

Page intentionally left blank

THE STOCHASTIC EVOLUTION OF ASTEROIDAL REGOLITHS AND THE ORIGIN OF BRECCIATED AND GAS-RICH METEORITES

by

Kevin Richard Housen

A Dissertation Submitted to the Faculty of the

DEPARTMENT OF PLANETARY SCIENCES

In Partial Fulfillment of the Requirements
For the Degree of

DOCTOR OF PHILOSOPHY

In the Graduate College

THE UNIVERSITY OF ARIZONA

1 9 8 1

Acknowledgements

I wish to thank L. Wilkening, A. Woronow, J. Blum, C. Chapman, R. Greenberg, and R. Jokipii for useful discussions and criticisms; and B. Wilkening, M. C. Holloway, C. Hostetler, A. Hostetler, and B. Housen for support and encouragement.

TABLE OF CONTENTS

		Page
	LIST OF TABLES	7
	LIST OF ILLUSTRATIONS	8
	ABSTRACT	11
1.	INTRODUCTION	13
2.	THE CRATERING, COLLISIONAL, AND CHARGED-PARTICLE ENVIRONMENT OF ASTEROIDS	24
	Crater Size-Frequency Distribution	25
	Relative Velocities	25
	Mass-Frequency Distribution	26
	Crater Size	30
	The Size-Frequency Distribution	38
	Crater Shape	40
	Ejecta Blanket Shape	41
	The Flux of Charged Particles at 3 AU	48
	Catastrophic Impact Events	55
3.	PREVIOUS MODELING	58
	Early Models	58
	The Housen et al. Model	63
	Model for Small Asteroids	64
	Model for Large Asteroids	70
	Comparison of Regolith Evolution on Asteroids and the Moon	73
	Some Critical Remarks	74
	The Orsay Models	76
	The Duraud et al. Model	77
	The Dran et al. Model	78
	The Model of Langevin and Maurette	79
	Comparison of the Two Recent Models	81
	Definitions of Saturation	82
	Crater Flux	86
	Velocity of Crater Ejecta	87
	Summary	88

TABLE OF CONTENTS--Continued

Page

4. THE STOCHASTIC EVOLUTION OF ASTEROIDAL REGOLITHS 90

The Depth of an Asteroidal Regolith 92
A Note on the Forward Equation 94
A Diffusion Approximation 96
An Improved Approximation 106
Physical Interpretation of
the Regolith Depth Equations 114
The Amount of Brecciated Material Liberated from Asteroids 117
Debris Liberated in Cratering Events 118
Debris Liberated in Catastrophic Events 125
A Monte Carlo Algorithm for
the Irradiation of Regolith Grains 130

5. RESULTS 133

Regolith Depth 133
The Depth as a Function of Time 133
The Time Required to Reach Equilibrium 136
The Depth at Fragmentation 141
The Variance of Regolith Depth 142
The Amount of Brecciated Material Released to Space . . . 145
The Irradiation Histories of Regolith Grains 151

6. IMPLICATIONS FOR RECENT MODELS AND THE ORIGIN OF METEORITES 171

Regolith Depth 171
Relationship with Recent Studies 171
Implications for the Brecciated Meteorites 178
The Exposure Histories of Gas-Rich Meteorites 186

7. SUMMARY AND FUTURE WORK 192

APPENDIX 1: THE MOMENTS OF A JUMP IN SURFACE ELEVATION . . . 197

APPENDIX 2: DETAILS OF SOME DERIVATIONS 204

REFERENCES 207

LIST OF TABLES

Table		Page
1.	Parameters Involved in the Projectile Mass Flux	29
2.	Values of K_D	39
3.	Radiation Affecting Meteorites	49
4.	Particle-Track Production Rate	53
5.	Regolith Depth at Fragmentation and at Equilibrium	138
6.	The Number of Fragmentation Events and the Time Required to Disperse an Asteroid	150
7.	Some Results from the Simulated Exposure Histories of Regolith Grains	161

LIST OF ILLUSTRATIONS

Figure		Page
1.	Estimates of the number density of projectiles in the asteroid belt	27
2.	Crater diameter vs. impact energy for weak targets	34
3.	Crater diameter vs. impact energy for strong targets	36
4.	The velocity distribution of crater ejecta	43
5.	An example of the trajectories of ejected material	45
6.	The production rate of charged-particle tracks	51
7.	The effects of various sizes of craters on regolith evolution in a "typical region" on an asteroid's surface	66
8.	The surface elevation in a typical region on a 300 km diameter rocky asteroid	67
9.	The relationship between elevation and regolith depth	95
10.	A test of the diffusion approximation	105
11.	Depth of regolith vs. time for rocky asteroids	134
12.	Depth of regolith vs. time for weak asteroids	137
13.	The approach of the mean depth to an equilibrium value	140
14.	Regolith depth as a function of position on an asteroid's surface	144
15.	The amount of brecciated material which escapes rocky asteroids during cratering events	146
16.	The amount of brecciated material released upon fragmentation or dispersal of rocky asteroids	149

LIST OF ILLUSTRATIONS--Continued

Figure		Page
17.	The amount of brecciated material released upon dispersal of weak asteroids	152
18.	Particle-track distributions using various starting depths for regolith grains	155
19.	Track densities for grains on a 300 km diameter rocky body	160
20.	Track densities for grains on a 100 km rocky asteroid	163
21.	Track densities for grains on a 500 km rocky asteroid	164
22.	Track densities for grains on a 1000 km rocky asteroid . . .	165
23.	Track densities for grains on a 2 km weak asteroid	166
24.	Track densities for grains on a 10 km weak asteroid	167
25.	An illustration of how gravitational settling of debris might affect the variability of regolith depth	177

Page intentionally left blank

Page intentionally left blank

ABSTRACT

A model is constructed which views regolith evolution on asteroids as a stochastic process. Average values are shown to be poor descriptors of regolith depth. Large deviations from the average are expected to occur due both to variations in the depth over the surface of a body and to stochastic fluctuations in the variables which determine regolith depth, e.g. the number of craters produced on an asteroid. The utility of the average depth is not significantly increased by avoiding large craters or thick ejecta deposits; a procedure adopted in previous regolith studies. The statistical uncertainty associated with regolith depth severely limits the power of regolith models in predicting parent-body size for brecciated meteorites. Virtually any rocky asteroid larger than 100-200 km in diameter could have produced the abundance of brecciated material observed in the achondritic meteorites. Bodies which are composed of weaker materials and which have diameters greater than 20 km could have produced the abundance of breccias observed in the chondrites.

A Monte Carlo algorithm is used to simulate the random walks and corresponding charged-particle irradiation histories of grains in regoliths. On rocky asteroids, only about 20% of the grains are exposed to solar cosmic ray ions. These grains typically spend a few thousand years in the upper 100 microns of the regolith and acquire

particle track densities of 10^7-10^9/cm^2 at their surfaces. Only about 5% of the grains acquire track densities greater than 10^8/cm^2. Grains which reach the surface are exposed to galactic cosmic rays for roughly 10^6y. Weak asteroids with diameters less than a few tens of kilometers have very immature regoliths because of short collisional lifetimes and the ejection of heavily irradiated grains to space. Only a few percent of the grains are exposed at the surface and these acquire track densities of 10^7-10^8/cm^2. Exposure times and the fraction of grains irradiated should increase for larger weak bodies due to longer collisional lifetimes. These results, which are based on present-day conditions in the asteroid belt, agree well with irradiation features observed in gas-rich meteorites; an origin during epochs of early solar system evolution is not required.

CHAPTER 1

INTRODUCTION

Modern theories of solar system evolution, although varied and still speculative, typically begin with a nebular cloud of gas and dust which ultimately collapses into a disk (Safronov, 1972; Goldreich and Ward, 1973; Cameron, 1979). The mechanism which initiated collapse, for instance a nearby supernova, probably gave rise to turbulence. Dissipation of the gas occurred with time because of mass inflow into the growing Sun and also, at some point, hydrodynamic expansion of the upper layers of the disk. As the gas dissipated, turbulence died out allowing the dust to settle into a thin disk at the central plane of the nebula. The disk became gravitationally unstable, and broke into localized dust concentrations which formed planetesimals of roughly kilometer dimensions. There is some dispute as to whether these planetesimals directly accreted to form the planets or whether they merely added mass to protoplanetary cores created during earlier epochs as the result of ring instabilities in the nebula (Safronov, 1979; Cameron, 1979). But there seems to be general agreement that the planetesimals were the building blocks for asteroids.

In subsequent evolution large-scale geological processes arose on the terrestrial planets and effectively erased chemical and physical records of the early solar system. On the other hand, the asteroids should be more representative of primordial material because they are too small to have supported geological or geomorphological processes. However, they have experienced an extensive impact history. Before we can read the records stored in asteroids (and the meteorites derived from them) we must understand how they have been modified by impact cratering. This dissertation is a study of the impact-driven evolution of asteroidal surfaces.

During accretion material impacting protoasteroid surfaces was fractured and comminuted, although not extensively because the impact velocities had to be low enough to result in net accumulation. Asteroidal embryos grew by building up layers of broken, weakly bonded rocky debris, i.e. layers of regolith. Part of the regolith may have since been "destroyed" by being converted into cohesive material. For example, some asteroids are believed to have experienced at least one heating event (maybe two; Wilkening, 1979), possibly driven by the decay of radioactive nuclides (Urey, 1955; Fish et al., 1960) or by electromagnetic induction (Sonett et al., 1968). The heating effects ranged from slight thermal metamorphism to the differentiation of silicates and metals. Moreover, self gravity may have effectively compacted and bonded together materials in the interiors of large bodies. These mechanisms undoubtedly increased the internal strength of some asteroids. Still, many bodies, perhaps the small ones or

those which escaped thermal metamorphism, should have survived as being composed mostly of regolith. Such massive collections are sometimes referred to as asteroidal "megaregoliths".

The evolution of asteroids changed from relatively gentle accretion to destructive fragmentation when their relative velocities were increased to the presently observed value (5 km/s). The velocities may have been pumped up by gravitational perturbations from Earth-size planetesimals which Jupiter scattered through the asteroid belt. The population of asteroids was probably depleted by catastrophic mutual collisions (Davis et al., 1979) or by collisions with Jupiter-scattered planetesimals (Safronov, 1979).

The onset of high relative velocities also changed the evolution of regoliths. High velocity debris striking an asteroid's surface produce craters which comminute and eject surface material. The impact velocities are high enough to launch part of the crater ejecta to escape velocity. In fact, most asteroids are presently experiencing net erosion rather than accretion. Even so, if an asteroid is large enough to retain a non-negligible fraction of its ejected debris, then the continual bombardment of its surface results in the formation of a regolith layer. Of course, for those bodies which accreted and retained a primordial regolith-like surface by escaping thermal metamorphism or differentiation, the bombardment merely serves to further comminute the extant regolith. On bodies with consolidated surfaces, regolith is created when large craters penetrate the existing debris layer and excavate "pristine" material.

One can therefore picture a modern-day asteroidal regolith as a surficial layer containing a size spectrum of debris ranging from small grains to possibly large coherent blocks. These debris are further comminuted, transported through the regolith and possibly ejected from the asteroid by subsequent impacts.

The evolution of a regolith ends if a collision occurs which fragments and disperses the asteroid. This may occur rather quickly for a small body. On the other hand, a large asteroid may repeatedly experience collisional events which are sufficiently energetic to cause major internal fracturing but not dispersal of the fragments against their mutual gravitational field. During such events, surficial layers of regolith may be mixed into the asteroid's interior. Thus, prior to dispersal, large bodies should evolve into gravitationally-bound balls of regolith, which Housen et al. (1979a) have referred to as asteroidal "megaregoliths". As mentioned earlier, this terminology has also been applied to the accumulations of regolith formed during accretionary epochs. In order to avoid confusion we will refer to the ancient accumulations as "accretionary megaregoliths".

The story ends when fragments of asteroids find their way to Earth as meteorites. At some point in an asteroid's evolution, a large impact occurs which either scoops out and ejects a sample of surface material or fragments the asteroid and disperses the newly formed meteoroids. Theories have been constructed regarding the mechanisms that transport material into Earth-crossing orbits and thus

possibly transform meteoroid into meteorite. These transfer mechanisms generally rely on gravitational effects (e.g. close planetary encounters or resonances) because the shock effects resulting from collisional transfer alone would exceed those observed in meteorites and might even cause destruction of the meteoroid. These mechanisms now appear to be able to account for, at least to an order of magnitude, observed galactic cosmic ray exposure ages (which partly measure a meteorite's transit time in space, see below) and the total mass influx observed on the Earth (e.g. Zimmerman and Wetherill, 1973; Williams, 1973; Wetherill, 1974).

Samples of asteroidal regoliths might, therefore, be expected to reach the Earth. Indeed, we have "brecciated" meteorites in our museums. These meteorites are unique in that they are composed of angular rock fragments, or clasts, which are embedded in a finer ground mass. The mixture of fragments and "matrix" material was welded into a coherent assemblege, presumably by impact-generated shock waves. Brecciated meteorites are represented in nearly every class of meteorites. The abundances, which vary from class to class, are discussed in more detail in Chapter 6. Wahl (1952) divided the brecciated meteorites into two types: (1) monomict breccias, where the matrix and clasts are similar in the sense that they could have been derived from the same material, and (2) polymict breccias, where the matrix and clasts do not appear to be genetically related. Wasson (1974) proposed a third type, genomict breccias, for intermediate cases where the clasts and matrix are chemically related but differ in

the details of petrography and mineralogy. The structure of most brecciated meteorites suggests a regolith origin, where clasts and matrix might be derived from the crushing and fragmentation of pre-existing rocks. However, we cannot eliminate the possibility that some monomict breccias were derived from a substrate which underlies a regolith layer. The brecciation textures could have been produced by impact-generated shock waves. On the other hand, many polymict and genomict breccias exhibit other regolithic traits, which we now discuss.

A subset of the polymict and genomict meteorites, the so-called gas-rich meteorites, exhibit high concentrations of noble gases. The fact that the gases have the same isotopic composition as the solar wind and that they are confined to regions very near the surfaces of mineral grains in the meteorites indicates that the gases were implanted by low energy ions in the solar wind. The solar origin was confirmed by the discovery of charged-particle tracks in the same grains which contain noble gases. Particle tracks are latent, roughly tubular, areas of solid state damage which can be chemically enlarged so as to become visible in optical microscopes. Tracks are caused by the ionizing effects of energetic particles with atomic number greater than about 20 (Fleisher et al., 1975). Actually most tracks are due to iron-group nuclei because heavier species are rather rare. The number density of tracks was observed to decrease rapidly in the first 100 microns beneath a grain's surface. The steep gradient reflects the steep energy distribution of ions emitted by the Sun, which are

referred to as solar cosmic rays. The coexistence of these particle tracks and the implanted noble gases strongly suggests a solar origin. Tracks are also produced by galactic cosmic rays, which originate outside the solar system. (Chapter 2 contains a more-detailed description of the track producing particles.) Because these ions are much more energetic than the solar cosmic rays the gradient in their track density is quite small, the density varying little over distances of centimeters. These tracks essentially form a low background which is superposed on the more abundant solar cosmic ray tracks.

The presence of the irradiation features in gas-rich meteorites is consistent with a regolith origin. Because solar gases and tracks are due to low energy ions, they can only be acquired when a mineral grain is exposed to space with little or no shielding. This will happen periodically during a grain's travels through a regolith. We would expect some grains to be exposed more than others, and some not at all. This expectation concurs qualitatively with the observation that only a fraction (typically 10%-30%, see Chapter 6) of the grains in gas-rich meteorites have been irradiated. Galactic cosmic ray tracks are acquired when a grain resides within a meter or so of the surface. These tracks should also be accumulated during a meteorite's transit from its parent body to the Earth. Of course, whether or not a regolith origin can quantitatively account for the observed irradiation features can only be determined from detailed calculations.

An alternative to the regolith origin has been suggested. Subsequent to the observation of particle tracks some meteoritic grains were reported to be evenly irradiated around their borders. This prompted the suggestion that the grains were irradiated while they floated freely in space, prior to accretion onto asteroidal embryos (Lal and Rajan, 1969; Pellas et al., 1969). However, comparative studies with samples of the lunar regolith (Wilkening, 1971) and improved spatial resolution in track counting, which showed that grains were not always isotropically irradiated (Macdougall et al., 1974), supported the hypothesis of a regolith origin. Additional observations showed the existence of microcraters, glasses, agglutinates and foreign fragments in gas-rich meteorites (Brownlee and Rajan, 1973; Wilkening, 1973; Rajan et al., 1974). These features are all found in samples of the lunar regolith, so a regolith origin seems likely for most gas-rich meteorites and certain for at least some (see e.g. Anders, 1978; Wasson and Wetherill, 1979).

The conclusion that meteorites are fragments of asteroids was first arrived at by a process of elimination (Anders, 1964). The Apollo-program lunar samples demonstrated that meteorites are not from the Moon. In general, planetary surfaces are not good candidates because the ejection velocity needed to escape is so large that the material would experience extreme shock, fragmentation and even vaporization. (However, the possibility remains open that a few meteorites may have been derived from the surface of Mars; Wasson and Wetherill, 1979.) Research and experimentation in the past decade have

provided several reasons for favoring an origin in the asteroid belt: (a) The continual collisions in the asteroid belt generate a large quantity of debris which would be a good source for meteorites. Furthermore, as mentioned above, some major problems of transporting material from the asteroid belt to the Earth have been solved. (b) Matches between the reflection spectra of most asteroids and meteorite types can be made (Chapman, 1976), although there appears to be a dearth of asteroids with spectra corresponding to the most abundant type of meteorites; the ordinary chondrites. (c) The measured surface exposure ages and the content of implanted noble gases in gas rich meteorites and lunar soils imply a formation location, for the meteorites, between 1 and 8 AU in a region where the cratering rate is two to three orders of magnitude higher than at 1 AU (Anders, 1975). These requirements point to the asteroid belt. (d) The rates at which parent bodies cooled subsequent to heating episodes have been deduced from the metal alloy compositions in meteorites. These cooling rates imply parent bodies of asteroidal size (Wood, 1964; 1979). (e) In the past, the preconception of some was that because asteroids are small bodies experiencing net erosive collisions their regoliths must be mere coatings of dust (see e.g. Hapke, 1971) and therefore incapable of producing any significant quantity of meteorites. Recent modeling (Housen et al., 1971a,b) and the work presented here show this idea to be incorrect, i.e. asteroidal regoliths may be common and quite deep.

Although the view that asteroids are parent bodies for most meteorites seems well founded, some fundamental questions still need to be answered. For example, which asteroids produced the brecciated and gas-rich meteorites? In the following chapters we construct a model for the depth of an asteroidal regolith in order to calculate the relative amounts of regolith and freshly excavated pristine material that a given size of body liberates to space. Results are compared to observed abundances of brecciated meteorites with the hope of eliminating certain sizes of objects from the list of possible parent bodies. Similar calculations and comparisons are performed for the exposure of regolith grains to charged-particle irradiation. The fraction of grains that are irradiated and the track densities in these grains are computed for various sizes of asteroids. Another fundamental question which we will address is, did the brecciated and gas-rich meteorites evolve in modern-day asteroidal regoliths or, as some have suggested (e.g. Wasson, 1972; Poupeau et al., 1974; Chapman, 1976), were the meteorites necessarily formed during early, accretional epochs? We find that the permissible size range of parent bodies for the meteorites is rather broad. Furthermore, we conclude that the observed properties of the meteorites could have arisen from an evolution in modern-day regoliths.

In the next chapter we consider the various "input parameters" required by regolith models. Chapter 3 is a review of previous regolith studies. A new approach, which is a statistical one as opposed to existing determinate models, is given in Chapter 4. We

find that stochastic fluctuations, which are inherent in regolith evolution, limit the power of of regolith models in predicting meteorite parent-body size. Numerical results from the statistical model are described in Chapter 5. The results are discussed and compared with observations in Chapter 6.

CHAPTER 2

THE CRATERING, COLLISIONAL AND CHARGED PARTICLE ENVIRONMENT OF ASTEROIDS

Before the mechanics of regolith evolution can be understood in any detail, the physical quantities which form the "input" to regolith models must be described. These input parameters are the subject of this chapter.

Both the macroscopic properties (e.g. the depth) and the microscopic properties (e.g. the duration of exposure to space irradiation) of a regolith are controlled by the cratering process. The depth of regolith is largely determined by the frequency with which various sizes of craters form on an asteroid. The irradiation histories of regolith grains are additionally dependent on both the geometry of crater bowls and ejecta deposits, which either expose or shield the grains from irradiation and on the flux of charged particles which are responsible for the irradiation. Moreover, all properties of a regolith are dependent on how long an asteroid can survive without experiencing a catastrophic collisional event. This chapter is divided into five sections which cover the size-frequency distribution of craters, the shape of crater bowls, the shape of ejecta blankets, the flux of charged particles in space and the fragmentation and dispersal of asteroids.

All of the above-mentioned quantities depend on the compositional strength assumed for an asteroid. Two hypothetical kinds of asteroids are considered here: (a) relatively "strong" cohesive objects whose strength is akin to rocky materials and (b) "weak" objects whose strength is equivalent to that of loosely bound regolith. Although actual internal strengths of asteroids are poorly known, the properties of both types of hypothetical bodies are derived from experiments with materials whose parameters probably bracket the real asteroids. In general, values for strong and weak bodies are obtained from impacts into basalt and quartz sand or regolith, respectively.

Crater Size-Frequency Distribution

Unlike the lunar case, there are no direct observations or measurements of the size distribution of craters on asteroids. However, the distribution can be derived indirectly from knowledge of the impact velocity of debris which strike an asteroid's surface, the mass distribution of debris and the size of crater produced by an impact of given energy. The quantities involved in the construction of the crater flux are now discussed.

Relative Velocities

The debris complex in the asteroid belt is characterized by two components: (1) material formed during cratering and fragmentation of asteroids themselves, and (2) a so-called cometary component. The distinction relevant to this study between these components lies in

the relative velocities. Because cometary orbits tend to be rather eccentric the velocity of cometary debris tends to be higher, on the average, than that of asteroidal material. In this study we adopt 5 km/s as the mean impact velocity for collisions among asteroids (Dohnanyi, 1969) and 14 km/s for impacts of cometary debris (Dohnanyi, 1976).

Mass-Frequency Distribution

Observations of near-Earth debris span the entire range of masses from micrometeoroids to kilometer-size objects (Dohnanyi, 1972; Hughes, 1978), but the flux further out in interplanetary space is much more uncertian. At present, information regarding the flux in the asteroid belt is derived from satellite cell-penetration data, telescopic observations of large asteroids and the zodiacal light, and theoretical modeling (Figure 1). The Pioneer 10 and 11 spacecraft observed a nearly constant spatial density of dust between 1 and 5 AU (Humes et al., 1974). This indicates a negligible asteroidal contribution at small masses in agreement with Pioneer observations of the zodiacal light (Hanner et al., 1976). Therefore, the small-particle flux in the asteroid belt can be approximated by the known flux of presumably cometary particles at 1 AU. A similar approximation at large masses is not used here because for large objects the flux of cometary and asteroidal components vary with heliocentric distance and the variation is not known to better than an order of magnitude (Kessler, 1970). Moreover, the dependence of mass distribution shape on radial distance is unknown. Soberman et al.

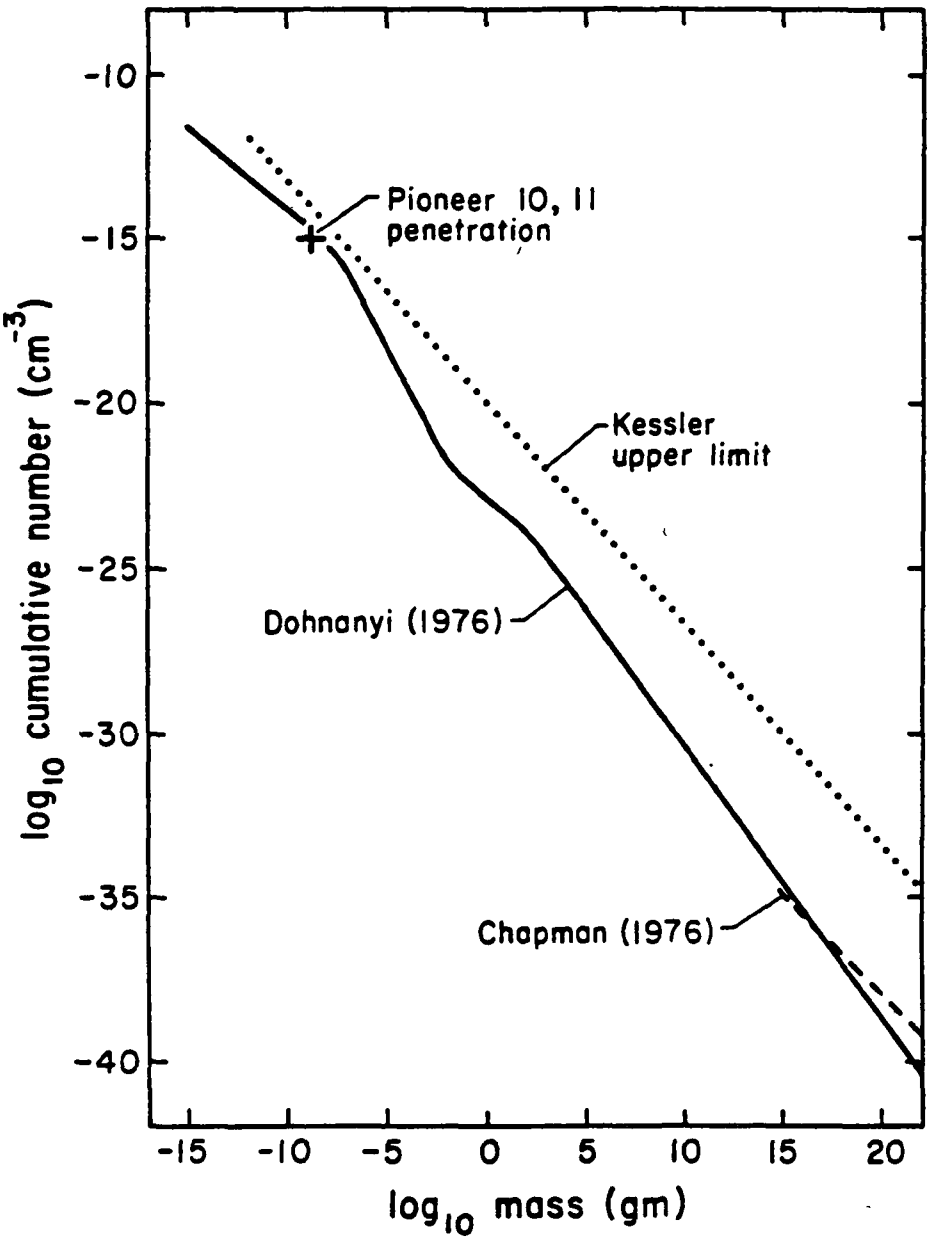


Figure 1. Estimates of the number density of projectiles the asteroid belt. -- All estimates represent the cumulative number of projectiles with mass greater than m. The solid curve (Dohnanyi, 1976) is used here when modeling the exposure of regolith grains to space irradiation. When computing regolith depth, a straight line is fit to the large-mass (i.e. mass > 1 kg) portion of Dohnanyi's curve.

(1974) tried to measure the spatial density of particles smaller than 10 centimeters with the asteroid/meteoroid detector on board Pioneer 10 but calibration difficulties have plagued these observations (Auer, 1974) so they are not used here. For the upper end of the mass spectrum, telescopic observations of asteroids were summarized by Chapman (1976) and are shown in Figure 1. Also shown is an upper limit for the flux which Kessler (1968) established using the observed intensity of the gegenschein.

Observations in the range 1 g to 10^{15} g are rare. In this region we rely on modeling of the collisional evolution of particle populations (Dohnanyi, 1976). Briefly, Dohnanyi's model implies that the number (per cm^3) of objects with mass between m and m+dm should be

$$dN(m) = K_m a_m m^{a_m - 1} dm \qquad (2.1)$$

where K_m and a_m are constant over a given mass range. For large masses, a value of a_m is derived for a theoretical steady-state collisional evolution of asteroids. K_m is determined from observations of the number of large asteroids. At m=1 kg, the flux given by Dohnanyi bends over because collisions with high velocity cometary debris begin to deplete asteroidal material. For even smaller masses, the cometary component dominates by orders of magnitude. For $m<4x10^{-2}$ g, the flux plotted is the observed (cometary) flux at 1 AU, which should reasonably approximate the small-particle environment in the asteroid belt, as discussed above. Dohnanyi's model is summarized in Table 1.

Table 1

Parameters Involved in the

Projectile Mass Flux (cgs units)

mass	K_m	a_m	v_i
$m<10^{-7}$	8.6×10^{-20}	-1/2	1.4×10^{6}
$10^{-7}\leq m<4\times10^{-2}$	8.0×10^{-25}	-7/6	1.4×10^{6}
$4\times10^{-2}\leq m<10^{3}$	1.6×10^{-23}	-1/2	5.0×10^{5}
$10^{3}\leq m$	9.4×10^{-23}	-5/6	5.0×10^{5}

When computing regolith depth it will be convenient to approximate the entire mass distribution by a straight line fit to Dohnanyi's curve for masses greater than a kilogram. This is done because, as discussed at the end of this section, small projectiles are relatively ineffective in generating new regolith, compared to large objects. The "segmented" flux model is used in exposure-time calculations, where small impacts are important.

Crater Size

Hypervelocity impact cratering is now a rather well studied phenomenon, both experimentally and theoretically. As a result, quantitative predictions can be made of the crater sizes produced by impacts under a variety of physical conditions. The cratering physics and sources of information relevant to this study are now briefly reviewed.

Upon impact, a roughly hemispherical shock wave is generated which transfers energy, from projectile to target, both in the form of kinetic energy and heat. The pressures generated in hypervelocity impact are sufficiently large to exceed the strengths of most materials, so the early phases of cratering are characterized by fluid flow. As the shock wave travels out across the target face, rarefaction waves are generated because a free surface cannot maintain a state of stress. The rarefaction waves propagate back into the target and deflect material motions from a more or less radial direction up toward the target surface (see e.g. Gault et al., 1968). This represents the onset of the ejection phase. The upward-deflected

material flows out tangent to the upper wall of the expanding crater bowl and is ejected as an inverted conical-shaped curtain. The angle between the curtain and the target surface is observed to remain constant during much of the excavation stage. The energy density of the shock wave decreases as the wave propagates into the target. Moreover, some energy is transferred into heat. Thus, the kinetic energy transferred to the target decreases and results in a corresponding decrease in ejection velocity. That is, ejection velocities diminish with increasing distance from the impact point.

The fracture and comminution of target material, and hence the formation of the crater bowl, ends when shock-generated stresses decrease to values comparable to target material strength. At this point, flow velocitites are so low that surface material, rather than being ballistically launched, is merely pushed upward to form a structural uplift. If local gravitational forces are small compared to material strength, then the crater bowl assumes its final dimensions at the point on the surface where comminution and ejection of target material cease, because all ejected material is ballistically launched to locations beyond this point. This case is usually referred to as "strength scaling" for craters. On the other hand, when gravitational forces are large, some of the low velocity material is ejected to points inside the edge of the equivalent strength-scaled crater and thus serve to decrease the apparent crater radius (see e.g. Ivanov, 1976). This is referred to as "gravity scaling" for craters.

The two most important variables in determining crater size, therefore, appear to be material strength and gravitational acceleration. This was recognized and quantified through a dimensional analysis by Gault and Wedekind (1977). They demonstrated that the transition between strength scaling and gravity scaling occurs when $s/\rho gD = 1$ where s and ρ are the target's material strength and density, g is the local gravitational acceleration and D is crater diameter. They also derived functional relationships between crater diameter, impact energy, material strength and gravity for the two limiting cases of $s/\rho gD$ being either very large or small. A general expression for crater diameter, which will be referred to as a "cratering law" is

$$D = K_D \left(\tfrac{1}{2} m v_i^2 \right)^{a_D} h(g) \qquad (2.2)$$

where K_D is a constant for a given target material (i.e. strong or weak), v_i is the impact velocity and h(g) is a function of gravity. In the strength-scaling regime, with the ratio $s/\rho gD$ being much larger than unity (e.g. for strong targets, low gravity or small craters) $a_D=1/3$ and $h(g)=1$. For gravity scaling, with $s/\rho gD$ approaching zero, $a_D=1/4$ and $h(g)=g^{-1/4}$. Because the limiting case of zero strength is never attained in practice (except possibly for a liquid target), more appropriate values for gravity scaling are $a_D=0.29$ and $h(g)=g^{-1/6}$ as suggested by many cratering experiments (cf. Nordyke, 1962; Gault, 1974; Gault and Wedekind, 1977).

K_D is determined from cratering experiments. The sources of information used to evaluate K_D for the four combinations of target strengths (weak or strong) and cratering laws (gravity or strength) are now discussed. The estimates for K_D are given in Table 2 at the end of this section.

Weak Target and Gravity Scaling. Cratering data, for weak target materials, spanning twenty orders of magnitude in energy and six in diameter are shown in Figure 2. Vedder (1972) impacted micron-size particles, with velocities from 2.5 km/s to 12 km/s, into weakly cohesive mineral dust targets. The results are plotted as a rectangular region because Vedder presented only average values for a number of experiments involving a range of crater diameters and impact velocities. Gault and Wedekind (1977) and Stoffler et al. (1975) performed impact experiments into unbonded quartz sand and obtained craters of centimeter dimensions. Crater diameters produced by "inert" missile impacts into dry, weakly cohesive, sand are given by Moore (1976). These oblique impacts were adjusted to normal incidence by using the expressions found in Gault (1974). Observations of spacecraft impacts into the lunar regolith (Whitaker, 1972) are scaled down to terrestrial conditions by using $g^{-1/6}$ scaling. The correction for non-normal incidence is also applied. At larger diameters, results of two explosion craters formed in alluvium are plotted. These events are used because their depth to diameter ratios (0.2 and 0.23) are close to the value used here (0.2, discussed below) for impact craters. In order to obtain a value of K_D for a weak target

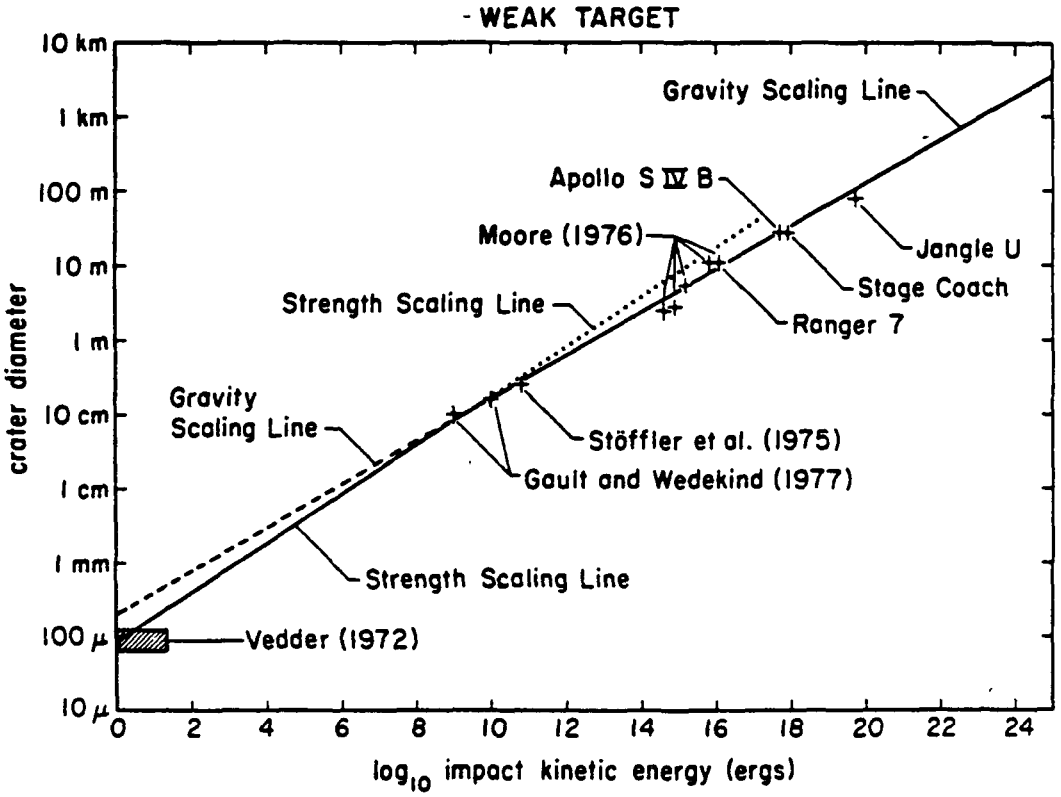


Figure 2. Crater diameter vs. impact energy for weak targets. -- As discussed in the text, the relationship between diameter and energy (for a given target material) is expected to depend on gravity and crater size. At large diameters a gravity scaling law applies whereas strength scaling applies to small craters. This figure pertains to terrestrial gravity conditions. As gravity decreases, the point of transition between strength scaling and gravity scaling moves upward and to the right along the gravity scaling line.

with gravity scaling, a line of slope 0.29 was regressed to the data shown in Figure 2. The data from Vedder (1972) were excluded from the regression because, as we now discuss, they lie in the strength scaling regime.

Weak Target and Strength Scaling. For terrestrial gravity, a transition is made from gravity scaling to strength scaling at a crater diameter of roughly 10 cm (for a reasonable weak-material strength of 5×10^4 d/cm^2), so the data of Vedder (1972) lie in the strength scaling regime. The uncertianties in Vedder's data preclude determination of an exact value for K_D in this case. The value is chosen to make the two cratering laws agree at D=10 cm, i.e. K_D is found from $10 = E_{10}^{1/3}$, where E_{10} is the energy corresponding to a diameter of 10 cm (computed from the gravity scaling law).

Strong Target and Gravity Scaling. This case is rather unconstrained due to a lack of data (Figure 3). There are no man-made craters (in cohesive media) which are large enough to be gravity scaled and for which formation energies are known. As a first approximation we use the gravity scaling law derived for the weak-target case because, by definition, gravity scaling laws are independent of target strength. This is only an approximation because, as mentioned earlier, pure gravity scaling is probably never attained. If this is true then the weak-target law should give upper limits for crater diameters because crater size decreases as target strength increases.

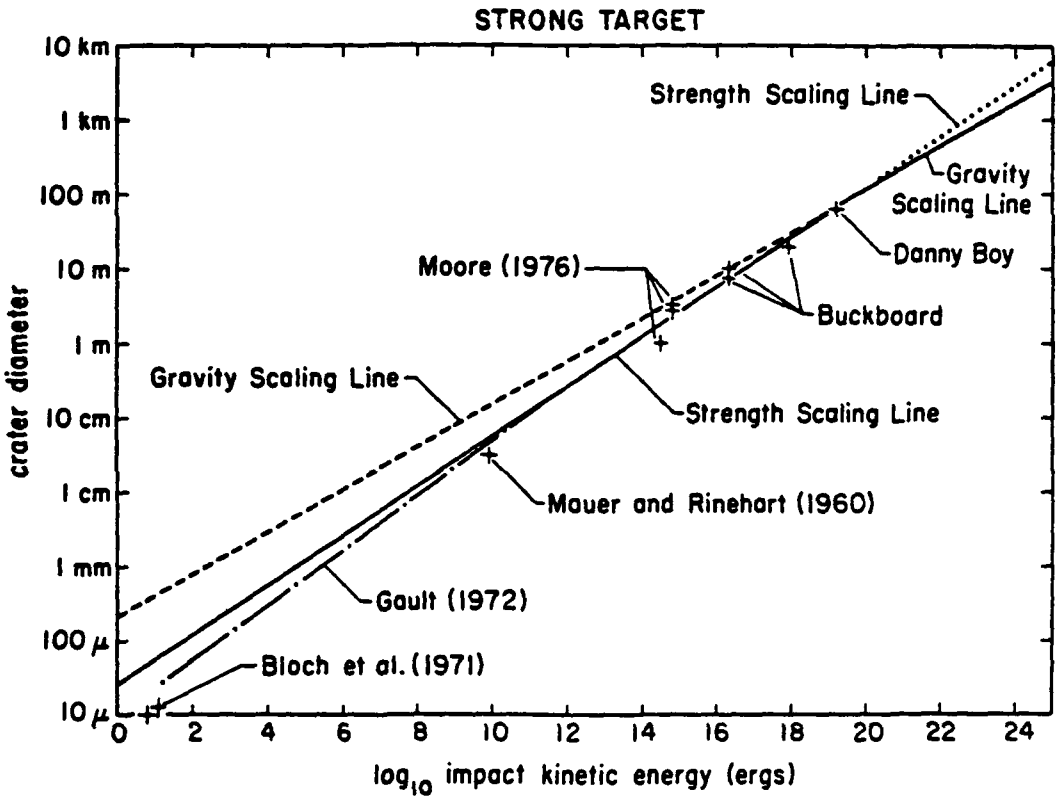


Figure 3. Crater diameter vs. impact energy for strong targets.

Strong Target and Strength Scaling. Bloch et al. (1971) simulated microcraters found on lunar rocks by impacting small particles into glass targets (Figure 3). Results of impact cratering in basalt and granite targets over an energy range of 10 - 10^{12} ergs are given by Gault (1972). Maurer and Rinehart (1960) fired small steel spheres into sandstone and granite resulting in centimeter-size craters. However, these data may not be directly comparable to say, Gault's results, because impact velocities were not high enough to cause hydrodynamic flow or disruption of the projectile. That is, these events may be near the velocity threshold that divides cratering from simple rebound. Missile impacts in sandstone targets are shown in the figure although these results may also be near the cratering threshold (Moore, 1976). The four explosion events shown were formed in dry basalt and should serve as reasonable analogs for impact craters (all have depth to diameter ratios near 0.2 except Danny Boy which has a ratio of 0.29).

Of all the data plotted in Figure 3, except Gault's (1972), the explosion craters are probably the most reliable, hence K_D is determined for this case by fitting a line, of slope 1/3, to the explosion data. Gault's data are not used because they strictly apply only to small craters. The value a_D=1/3 is suggested both theoretically (Gault and Wedekind, 1977) and experimentally (Dence et al., 1977) for large craters, which dominate regolith growth.

The adopted parameter values for the cratering laws are summarized in Table 2.

The Size-Frequency Distribution

The number of craters (per area per time) in a diameter interval dD is found from equations (2.1) and (2.2) as

$$dN(D) = K\, a\, D^{a-1}\, dD \tag{2.3}$$

where

$$K = \tfrac{1}{4} K_m v_i \left(v_i^2/2 \right)^{-a_m} \left(K_D h(g) \right)^{-a}$$

and

$$a = a_m/a_D .$$

The factor of 1/4 is included in K because impacts on an asteroid's surface are spread over an area which is four times the collisional cross-sectional area.

Using the parameter values specified in Tables 1 and 2 for large impacts one can show that the total volume excavated by craters in a diameter interval, centered on an arbitrary diameter, is smaller than the total volume for craters in an equal interval centered on a larger diameter. Large craters are therefore more important than small ones when modeling regolith growth, a fact which is important to remember in subsequent discussions.

Table 2

Values of K_D

	strength scaling	gravity scaling
weak target	8.0×10^{-3}	6.36×10^{-2}
strong target	2.75×10^{-3}	6.36×10^{-2}

Before leaving the subject of crater distributions, an alternate method for finding the distribution should be mentioned. In an attempt to characterize the asteroidal cratering environment without having to rely on estimates of the projectile mass distribution at 3 AU, Langevin and Maurette (1980) used crater scaling laws to "invert" the lunar crater distribution to find the mass distribution of projectiles at 1 AU. They assumed this mass distribution to have the same shape as that at 3 AU (although the rate of impacts was taken to be 30 times higher at 3 AU) and again used scaling laws to find the crater distribution in the asteroid belt, taking into account differences in impact velocity and target strength between the Moon and the asteroids. While this method does not rely on a specific estimate of the projectile distribution at 3 AU, there may be significant uncertainties introduced by the assumption of similar mass distributions for impactors of the Moon and asteroids. The distribution of asteroidal debris is the result of a mutual collisional evolution over a period of time. Conversely, much of the debris delivered to the Moon may have originated in single catastrophic events (Wetherill, 1976). The mass distributions resulting from discrete fragmentation events and from multiple events (i.e. fragmentation of fragments) may not be the same.

Crater Shape

The geometry of crater bowls has been studied over a wide range of sizes. Lunar craters with diameter < 1 mm are typically bowl-shaped pits with depth to diameter ratio, μ, ranging from 0.2 to

1.3 but concentrated near 0.6 (Brownlee et al., 1975). Centimeter to meter-size craters in basalt are rougly conical in shape with μ near 0.24 (Gault, 1972), while craters in unconsolidated sand under a variety of gravitational accelerations exhibit a ratio of 0.2 (Stoffler et al, 1975; Gault and Wedekind, 1977). Fresh craters in the diameter range 0.2 km to 10 km on Phobos, Deimos, and the Moon are bowl shaped with μ about 0.2 (Pike, 1977; Thomas, 1978).

For our calculations, craters are assumed to have the shape of spherical-caps with μ=0.2. The volume of such a crater is

$$\text{Volume} = \pi\mu(3 + 4\mu^2)\ r^3/3 \equiv c\ r^3 \qquad (2.4)$$

where r is the crater radius.

Ejecta Blanket Shape

During a cratering event, material is launched along roughly ballistic trajectories. The launch speed decreases with increasing distance from the impact point while the angle between the initial velocity vector and the surface remains nearly constant. We now determine the thickness of ejecta at a point outside a crater by specifying the inital conditions for ejected material. The ejecta velocity distribution is considered first.

Langevin and Maurette (1980) assumed that the fraction $f_e(v)$ of ejecta with initial launch speed > v is equal to $(v_r/v)^2$ where v_r is the velocity of material at the crater rim. We adopt a more general form of this expression,

$$f_e(v) = (v_r/v)^{a_e} \qquad (2.5)$$

where a_e is a constant. The Langevin and Maurette expressions for v_r are used here. For strength scaled craters,

$$v_r = 0.18\ s_t^{0.55} \qquad (2.6)$$

where s_t is the target strength (d/cm^2). For gravity scaled craters,

$$v_r = \sqrt{gr/6}\ . \qquad (2.7)$$

The exponent a_e is considered as a variable here because the experimentally determined ejecta velocity distributions, upon which Langevin and Maurette based their value of $a_e=2$, are somewhat uncertain. Measurements of $f_e(v)$ are very difficult to make, especially at low ejecta velocities. The only available experimental results are summarized by Greenberg et al. (1978) and are shown in Figure 4 as solid curves. The "strong target" curve was constructed from a single impact into basalt (Gault et al., 1963). The "weak target" curve was derived from an impact into unbonded sand (Stoffler et al., 1975). For the strong target case, where strength scaling applies, a reasonable fit to the high-velocity tail of the distribution is obtained using equations (2.5) and (2.6) with $a_e=2$ and $s_t=1.4\times10^8$ d/cm^2 (see the dashed line labeled $a_e=2$). These parameter values appear to be inadequate to describe the slowest 70% of the ejecta. However, examination of the original data shown in Gault et

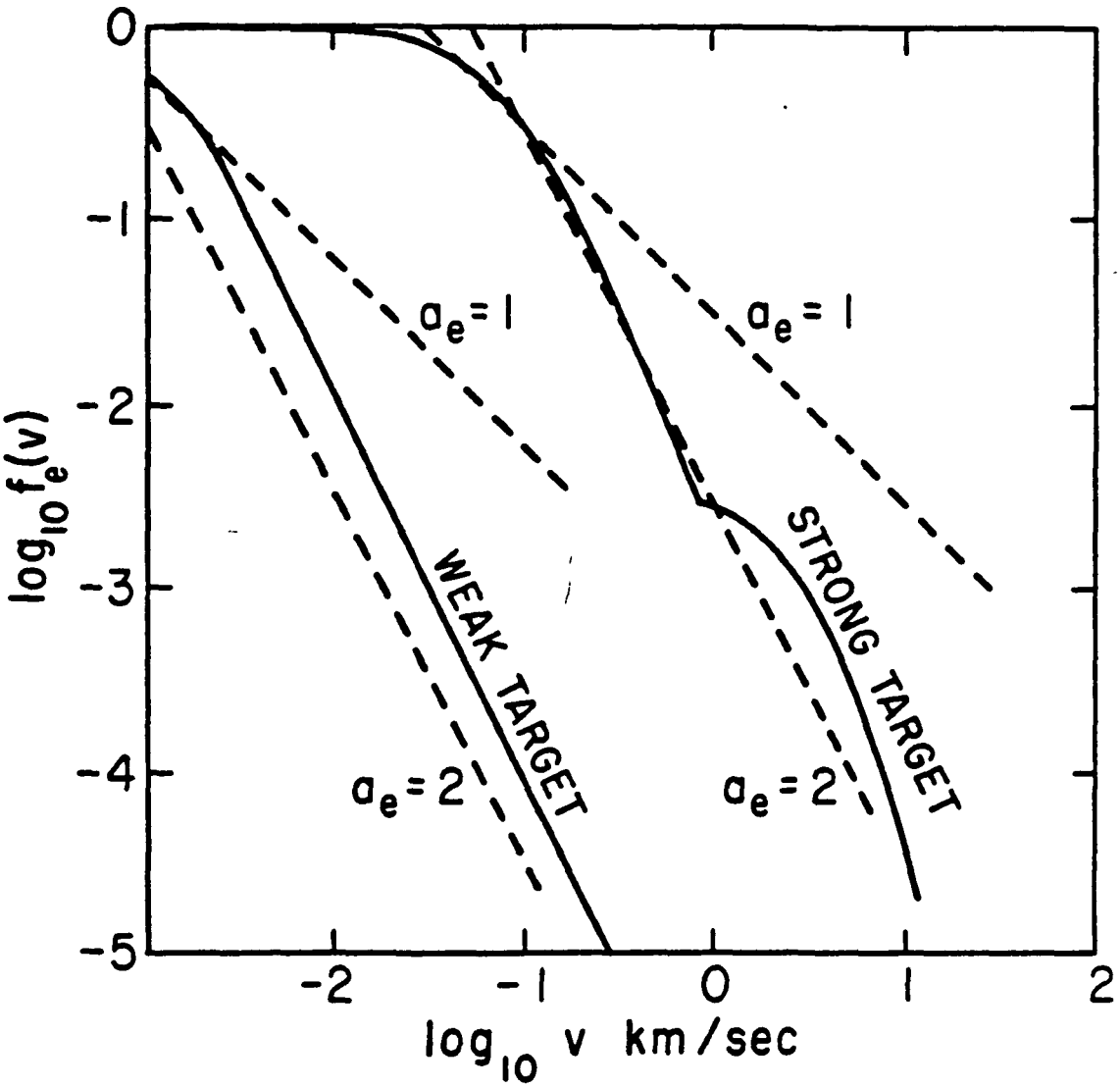


Figure 4. The velocity distribution of crater ejecta. -- The vertical axis shows the fraction, $f_e(v)$, of material with ejection speed greater than v. The solid lines are derived from cratering experiments (Gault et al., 1963; Stoffler et al., 1975). The dashed lines are fits of a theoretical relationship, discussed in the text, with two different parameter values.

al. (1963) shows that the portion of the curve pertaining to slow ejecta is rather uncertain. If the turnover in the curve at low velocities is real then the slow ejecta could be described better by the values a_e=1 and s_t=5x10^7 (shown as the dashed line labeled a_e=1). Similar results are found for the weak-target case using the gravity scaling model, i.e. equations (2.5) and (2.7). (Note that the weak-target data are on the borderline between strength and gravity scaling and so could also be fit with the strength scaling equations.) It is interesting to note that other studies (Ivanov, 1976; Maxwell, 1977; Austin et al., 1980; Croft, 1980) suggest values of a_e which vary between 1 and 2. A nominal value of a_e=2 is adopted here but, due to the uncertainties involved, the effects of assuming a_e=1 are also investigated. We now consider how $f_e(v)$ can be used to find the ejection velocity as a function of distance from the impact point.

Theoretical studies (e.g. Maxwell, 1977; Austin et al., 1980) imply that material motions in a cratering event are characterized by fluid flow along streamlines, one of which is depicted in Figure 5. At a distance x_0 from the impact point, the launch velocity is $v(x_0)$. The ejecta with $v>v(x_0)$ is just the material inside the shaded region in the figure because velocity decreases as x_0 increases. If we make the reasonable assumption that the streamlines are geometrically similar to one another in shape then the volume of the shaded region is proportional to the total volume of ejected material. If the total volume is equated to the crater volume (this is not strictly correct because some material is "compacted", i.e. driven down into the crater

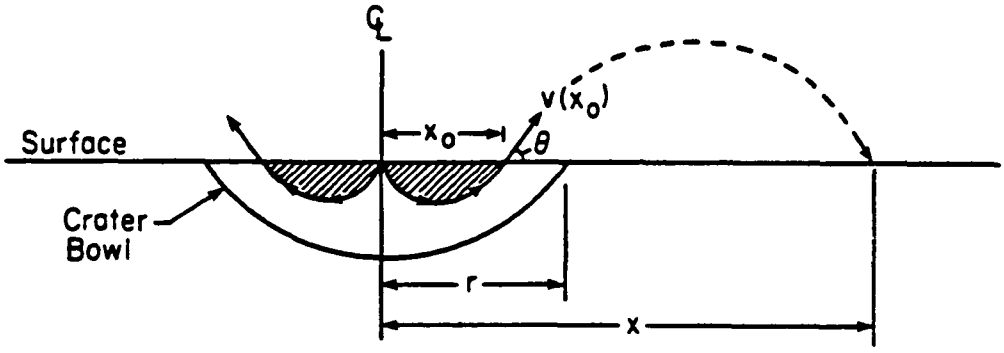


Figure 5. An example of the trajectories of ejected material. -- At launch point x_0 the launch speed is $v(x_0)$. All debris inside the shaded region have ejection speeds greater than $v(x_0)$.

bowl rather than being ejected), then the fraction of ejecta with $v>v(x_0)$ is just $(x_0/r)^3$. Using equation (2.5), the launch velocity can be written as

$$v(x_o) = v_r \left(x_o/r \right)^{-3/a_e}. \qquad (2.8)$$

Letting the (constant) ejection angle be 45 degrees (Stoffler et al., 1975), then equation (2.8) can be used to find the ballistic range, x, as a function of x_0,

$$x = x_o + \left(x_o/r \right)^{-6/a_e} v_r^2/g. \qquad (2.9)$$

Equation (2.9) implies that the range assumes a minimum value, x_m,

$$x_m = (a_e+6)(6\ v_r^2/a_e gr)^{a_e/(a_e+6)}\ r/6. \qquad (2.10)$$

For gravity scaled craters, the minimum range is just beyond the rim (x_m=1.1r to 1.2r for a_e=1 to 2). Actually this expression only applies to gravity scaled craters. One can show that for crater diameters appropriate to the strength scaling regime the launch point corresponding to the value of x_m in equation (2.10) lies outside the crater rim. Thus, for these craters the minimum range is instead given by

$$x_m = r + v_r^2/g. \qquad (2.11)$$

Let us now consider the shape of an ejecta blanket at points far from the rim, i.e. $x>>r$ or equivalently $x_0<<r$. In this case, the first term on the r.h.s. of equation (2.9) is small. If we let V be the total volume of material ejected beyond range x, then V is proportional to x_0^3. Equation (2.9) now implies that V is proportional to $x^{-a_e/2}$. The thickness of an ejecta blanket, B(x), at range x can be obtained by noting that

$$x\,B(x) \propto dV(x)/dx$$

so

$$B(x) \propto x^{-a_e/2 - 2}$$

That is, for large x, the thickness of ejecta decreases as the -2.5 power for $a_e=1$ and as the -3 power for $a_e=2$.

The behavior of B(x) near the crater rim is harder to determine because the first term in equation (2.9) is no longer negligible. This means equation (2.9) cannot be inverted analytically to find V(x) as before. Of course the inversion could be done numerically but this would greatly complicate subsequent calculations. Instead we adopt a simplified model for ejecta blankets. For gravity scaled craters, B(x) is assumed proportional to the $-a_e/2-2$ power of x for all $x>r$. Actually equation (2.10) implies that B(x) should be zero for $x_m>x>r$ but ejecta are observed to extend all the way up to the rims of gravity scaled craters. This means the model is not quite correct at low velocities for this case. The same shape is used for strength scaling except now $B(x)=0$ for $x_m>x>r$. The region of zero

thickness is expected to exist for this case because v_r for strength scaled craters is usually much larger than for gravity scaled craters.

The proportionality constants can be evaluated by equating the volume of an ejecta blanket to the volume of nonescaping ejecta. The resulting expression for B(x) is

$$B(x) = (a_e c/4\pi)\ (1-\gamma)\ r^3\ x_m^{a_e/2}\ x^{-a_e/2\ -\ 2} \qquad x > x_m$$
$$= 0 \qquad x < x_m \tag{2.12}$$

where x_m is given by equation (2.11) for strength scaling and $x_m = r$ for gravity scaling. The fraction, γ, of ejecta which escapes an asteroid of radius R_A is given by

$$\gamma = \left(v_r/\sqrt{2gR_A} \right)^{a_e}$$

where v_r is found from equation (2.6) or (2.7) for strength scaling or for gravity scaling, respectively.

The Flux of Charged Particles at 3 AU

Interplanetary space is inhabited by a wide spectrum of energetic ions. The ones which are particularly relevant to studies of regolith evolution and the origin of meteorites can be broadly classified into three groups (Table 3). (1) Solar wind (SW) ions are continuously emitted by the Sun. Their energies are usually only a few keV/nucleon so they are just deposited on the surfaces of material

Table 3

Radiation Affecting Meteorites

Name	Energy (MeV/nucleon)	Range (cm)
Galactic cosmic rays	Peaks near 100 extends to $>10^{15}$	$1\text{-}2 \times 10^{2}$
Solar cosmic rays (heavy nuclei)	1-10 sharply decreasing for higher energy	10^{-2}
Solar wind	10^{-3}	10^{-6}

exposed directly to space. Some of these ions are responsible for the high abundance of noble gases observed in gas-rich meteorites. (2) Solar cosmic rays (SCR) are more energetic than SW ions, having energies on the order 1-10 MeV/nucleon. Particles with atomic number greater than about 20 penetrate silicate materials to depths of less than roughly 100 microns and leave paths of solid state damage. These damaged areas, or particle tracks, can be chemically etched so as to become visible in optical microscopes. (3) Galactic cosmic rays (GCR) are energetic ions which enter from outside the solar system. Their energies peak near 100 MeV but can be much larger than 1 GeV. These ions produce radioactive nuclides in spallation reactions and also form particle tracks. The energies involved allow penetration to depths of a few meters.

The production rate of particle tracks (both SCR and GCR) as a function of depth in a target has been measured at 1 AU by counting the number of tracks at a given depth in lunar rocks having known exposure ages (Bhandari et al., 1973; Hutcheon et al., 1974; Blanford et al., 1975). The estimated track production rates (Figure 6) are quite discordant, differing by two orders of magnitude at depths below 1 mm. The differences are in part due to nonstandardized track counting techniques and to differences in the degree of surface erosion in the samples used (Lal, 1977). Various supporting evidence and arguments can be cited for each production rate (Morrison and Zinner, 1977; Lal, 1977; Zinner, 1980) but there seems to be no compelling reason for choosing one over the others. We will use the

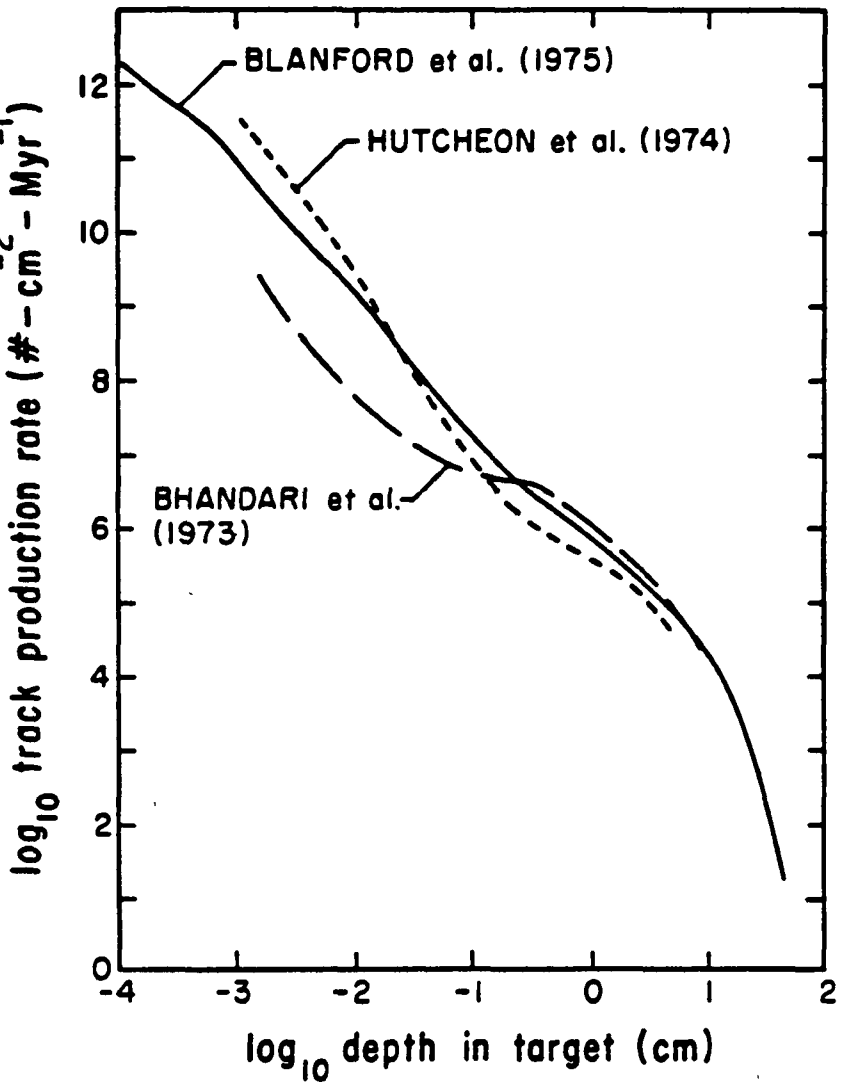


Figure 6. The production rate of charged-particle tracks. -- All estimates pertain to 1 AU. In this dissertation the Blanford et al. (1975) estimate is used and is approximated by the function shown in Table 4.

Blanford et al. (1975) estimate in our calculations, if for no other reason than because it represents an intermediate case. We must remember, however, that the track production rate may be uncertain by as much as an order of magnitude at small depths. For computational convenience the Blanford et al. profile is approximated by straight line segments over three depth intervals. The adopted function in given in Table 4. We must now consider how this production rate varies between 1 and 3 AU.

Because the GCR particles (which become the dominant source of tracks below about 1 cm depth) are of such high energy their spatial density does not change drastically between 1 and 3 AU. The cosmic ray telescopes on board Pioneer 10 and 11 showed that the GCR flux increases by only a few percent per AU between the Earth and Jupiter. Thus we will assume that the 1 AU flux is also pertinent for the asteroid belt. The variation of SCR flux with heliocentric distance is more complex. This flux can be broken into two components. Solar flares produce SCR ions in bursts which can vary greatly in intensity from flare to flare. The fluence of flare-produced protons is observed to decrease by roughly a factor of 10-20 between 1 and 3 AU (Zwickl and Webber, 1977) in reasonable agreement with analytical treatments based on standard diffusion-convection-adiabatic deceleration theory (Lee, 1976; Hamilton, 1977). The second component of the SCR flux arises from long lived streams of low energy (<5 MeV) particles which corotate with the interplanetary magnetic field. These streams are apparently uncorrelated with optical flares or radio

Table 4

Particle-Track Production Rate ($\#\text{-cm}^{-2}\text{-Myr}^{-1}$)

Adapted from Blanford et al. (1975)

depth, d, in target (cm)	type of radiation	production rate at 1 AU	production rate at 3 AU
$d<0.22$	SCR	$2.7\text{x}10^{5}d^{-1.8}$	$2.7\text{x}10^{4}d^{-1.8}$
$0.22\leq d<10$	primarily GCR	$9.1\text{x}10^{5}d^{-1.3}$	$9.1\text{x}10^{5}d^{-1.3}$
$10\leq d$	GCR	$6.0\text{x}10^{9}d^{-5.1}$	$6.0\text{x}10^{9}d^{-5.1}$

emissions and are emitted more or less continuously. Contrary to expectations the intensity of these streams was observed to increase with heliocentric distance out to 4 AU (McDonald et al., 1975). The reason for this behavior is not well understood although interplanetary acceleration appears to be a viable explanation. In any event we are primarily interested in the magnitude of the increase between 1 and 3 AU, which is roughly a factor of ten for 1-5 MeV protons (Van Hollebeke et al., 1978).

Before we can estimate the SCR track production rate at 3 AU we must determine the relative magnitudes of the contributions from flares and from corotating streams. The time averaged flux of flare-produced protons at 1 AU can be obtained from Lanzerotti and Maclennan (1973) while the flux due to corotating streams is given in McDonald et al. (1975). Comparison of these data reveals that the flare produced particles dominate by two orders of magnitude. A similar conclusion can be reached by noting that the average particle flux (for energies > 10 MeV) due to flares is about 100 particles/cm^2-s (Lanzerotti and Maclennan, 1973). This is comparable to the SCR particle flux, averaged over time periods ranging from a few years to 10^6 years, obtained from studies of the glass in the Surveyor 3 spacecraft camera (Crozaz and Walker, 1971), from balloon and satellite measurements and radiochemical studies of lunar rocks (Damon, 1977; Reedy, 1980). Note that we have used the proton flux here whereas particle tracks are formed by heavier nuclei, e.g. Fe. This is a reasonable procedure because all of the ions have roughly

the same charge to mass ratio, so the radial dependence of the flux should be insensitive to the ionic species. Thus at 1 AU solar flares are the major source of SCR tracks. Consequently we will assume that the SCR track production rate is a factor of ten smaller at 3 AU than at 1 AU. Actually the rate may be somewhat larger than this because, while the fluence of flare associated ions decreases by a factor of ten, the component from corotating streams increases by a factor of ten at 3 AU. Hence the two components there should be roughly equal. But in light of the uncertainties involved in the measured rate at 1 AU and in the radial dependence of the flux, a factor of 2 seems worthy of little consternation. The adopted flux model is shown in Table 4.

Catastrophic Impact Events

An asteroid is fractured into a multitude of smaller objects, which may or may not remain mutually gravitationally bound, when an impact occurs with energy exceeding a critical value. We will distinguish between two types of catastrophic events: fragmentation (or rupture), and dispersal. In the former case an asteroid is highly fractured but remains at least gravitationally bound. In the latter case a body is impacted with sufficient energy to cause fragmentation and dispersal of the fragments against their mutual gravitational field. For the moment we discuss only the energy required to fragment a body. The subject of dispersal is taken up in Chapter 4.

The critical projectile energy per unit target volume, s_i, required to cause fragmentation has been determined experimentally for various target materials. Moore and Gault (1965) fired small (0.5 cm diameter) spherical basalt projectiles into basalt spheres of diameter 5 cm at impact velocities of 1.4, 2 and 2.5 km/s. The lower velocity impacts resulted only in cratering of the targets with some spall fragments ejected in the later stages. The more energetic events (2.5 km/s) fragmented the target, the largest fragment being somewhat bigger than half the diameter of the original sphere. The ratio of projectile energy to target volume for the 1.4 km/s events was roughly 2×10^7 erg/cm^3 while the catastrophic events corresponded to a ratio of 6×10^7 erg/cm^3; hence the critical ratio for fragmentation must lie between these two values.

Gault and Wedekind (1969) simulated the destruction of tektites by firing projectiles into glass spheres of diameter 4.5 to 10 cm at velocities up to 7.5 km/s. Events with energy per unit volume less than 3×10^6 produced craters while higher energies caused spallation at the antipodal point of impact. Complete fragmentation occurred when the ratio reached 3×10^7 erg/cm^3.

Fujiwara et al. (1977) performed similar experiments using cubic blocks of basalt. Cratering occurred for ratios less than 10^7 erg/cm^3. Slightly more energetic impacts chipped off surfaces or

broke the targets into a few pieces. For ratios in the range $3x10^7$ - $3x10^8$ spallation of the target surface was observed while an intact core remained. The targets were completely shattered when the energy per volume exceeded 10^8.

Hartmann (1978) performed experiments with various materials in a low-velocity regime (0.5 to 50 m/s). Basalt balls and igneous rocks were found to catastrophically fragment (defined to occur when the mass of the largest fragment is half of the original mass) when the energy per volume exceeded roughly 10^7 - $3x10^7$. Water ice was disrupted for ratios of $3x10^5$ -10^6 while "dirt clods", used to represent weakly cohesive carbonaceous-chondrite-like material, fragmented with ratios of 10^4 - 10^5 erg/cm^3.

The two types of materials used here, i.e strong and weak, are meant to simulate very strong and very weak asteroids, thus bracketing the real range of asteroidal material strengths. As such, we adopt a value of $s_i=3x10^7$ for strong targets and $s_i=10^4$ for weak targets. Note that s_i is used here to determine only collisional lifetimes, so any uncertianties in impact strength will appear as uncertianties only in asteroid fragmentation lifetimes.

Having described the sources of input for regolith models we now review previous studies of asteroidal regolith evolution.

CHAPTER 3

PREVIOUS MODELING

To date, models of asteroidal regoliths have been concerned largely with two aspects of regolith evolution: the thickness of a debris layer as a function of time and the accumulation of charged-particle irradiation effects. The main thrust has been to understand the origin of gas-rich meteorites, although some effort has been devoted to the interpretation of optical and radar observations of asteroids. The methodologies, computational results and conclusions reached in each of the modeling efforts are now reviewed. First we consider a collection of theories which provided early, preliminary estimates of regolith properties and then we examine two more recent, refined models.

Early Models

The earliest model of asteroidal regoliths was developed by Chapman (1971) in order to understand the texture of the uppermost microns of asteroid surfaces as inferred from astronomical observations and was later used (Chapman, 1976) in speculations on the origin of brecciated meteorites. Chapman emphasized the erosive effects of numerous small impacts on the wide-spread ejecta deposits of large craters. He concluded that asteroidal regoliths are very

thin, except for those on the largest bodies and that even large bodies must have regoliths only "skin deep" (< 100 m). This conclusion, in conjunction with (1) the fact that a significant fraction (tens of percent) of all meteorites are brecciated and (2) the assumption that most meteorites are derived from large cratering events which sample parent bodies to kilometer depths, led Chapman to believe that the formation and irradiation of meteorites must have occurred during very early epochs. Only the accretionary mmegaregoliths were believed to be thick enough to produce the observed ratio of brecciated to nonbrecciated meteorites. In the following chapters we will find that regoliths are probably thicker than indicated by Chapman's model. Hence an early irradiation is not a necessity.

In order to deduce the formation location of gas-rich meteorites, Anders (1975, 1978) constructed a simple model using the observation that these meteorites have shorter cosmic ray exposure ages and lower gas contents than do lunar soils. He argued that the amount of implanted solar gases should be inversely proportional to the square of the distance from the Sun and directly proportional to the mean residence time of a grain at the surface. Anders ascribed the differences between the gas contents and exposure ages of meteorites and lunar soils to differences in cratering rates. In fact, he argued that mean residence times are inversely proportional to mean cratering rates. Thus the data implied to Anders that the meteorites have come from an environment in which the cratering rate

is 1 to 3 orders of magnitude greater than in the vicinity of the Moon and at a location a few times farther from the Sun, i.e. the meteorites have come from the asteroid belt. Anders isolated the critical parameters which differentiate between the lunar and asteroidal environment but his model did not show how the irradiation process may vary between asteroids. A Monte Carlo algorithm which simulates the exposure histories of regolith grains is described in the next chapter.

Borg et al. (1975) modified a Monte Carlo program, designed to simulate the charged-particle irradiation of the lunar regolith, and applied it to an asteroidal case, the first statistical consideration of the irradiation of regoliths on asteroids. Simulations of the irradiation of grains contained in the Kapoeta meteorite suggested an origin on a small body (diameter=50 km) with a regolith stirring rate roughly 15 times greater than that on the Moon. The details of this model have not been published so it is difficult to comment on it, but it is clear that more work is needed in this area. Borg et al. considered only a single size of asteroid and did not comment on the sensitivity of their results to uncertainties in input parameters.

In a preliminary model, Housen (1976) determined regolith depth at a given time by computing the average distance below an asteroid's surface such that only one excavation had occurred. Rocky bodies 200 km in diameter were found to accumulate debris layers roughly 100 m thick over a period of 1 Gyr. Although these calculations gave regolith thicknesses a factor of ten below those

required by Anders (1975, 1978) to explain the observed prevalence of gas-rich meteorites, they did show that regoliths on bodies much smaller than the Moon are considerably more than the thin coatings of dust Chapman (1971, 1976) had assumed. Refined modeling techniques and improved input parameters have since revised estimates of regolith thicknesses upward, as discussed later.

Matson et al. (1977) took a unique approach to the consideration of asteroidal regoliths. They addressed the question of whether lunar-regolith-like processes occur on asteroids by examining asteroid spectral data for the tell-tale signs of optical "maturation", which produces an anticorrelation between redness and albedo of surface materials. Finding no such evidence, Matson et al. considered several possible explanations for the differences between asteroids and the Moon. They concluded that asteroidal regoliths are thinner and coarser than the lunar regolith and that they are created by impacts at velocities too low to produce much glass. However, neither the evidence cited by Matson et al. nor the other remote-sensing data about asteroid surfaces is really capable of addressing the all-important question of how deep asteroidal regoliths may be.

Cintala et al. (1978, 1979) considered the effects of impact cratering on small bodies. They pointed out that the small radii of curvature and weak gravity fields will result in widely spread ejecta deposits. Also, because the coarsest debris ejected from a crater are those with the lowest velocity, regoliths on small asteroids, where

escape velocities are low, should be quite blocky whereas larger bodies will retain the high velocity fine grained material. Cintala et al. (1979) suggest that impact generated seismic waves may loft surface debris over a large part of an asteroid. On small bodies this mechanism may contribute to regolith erosion. Seismic shaking may enhance regolith gardening on larger bodies. Higher energy events are expected to cause spallation of asteroids.

Horz and Schaal (work in preparation) considered the formation of agglutinates in asteroidal regoliths. They noted that 5 km/s impacts into porous, fine grained, targets result in the formation of agglutinates, which are ubiquitous in lunar soils but are rare in brecciated meteorites. They then addressed mechanisms which might prevent asteroidal regoliths from becoming fine grained. Based on cratering theory and experiments Horz and Schaal propsed that energetic impacts on asteroids should generate seismic waves of sufficient intensity to cause spallation at free surfaces. The spallation products were expected to be very blocky and slow moving, with speeds of the order of meters per second. Moreover, it was suggested that the volume of spalled ejecta may be an order of magnitude larger than the crater volume. This mechanism was expected to make asteroidal regoliths more coarse-grained than the lunar regolith, thus reducing the agglutinate content of meteoritic breccias. This may also increase the burial rate of surface debris beyond that computed in existing regolith models.

Although Cintala et al. (1978, 1979) and Horz and Schaal (work in preparation) pointed out some processes which might play a role in regolith evolution, their work was extremely qualitative. Just how important seismic waves are can only be assessed through quantitative calculations. Seismic effects are not considered in this dissertation but may be an important area for future research.

The Housen et al. Model

Although regolith depths vary over the surface of an asteroid, all models to date have attempted to characterize this distribution by the mean, or average, regolith depth. Early studies (e.g. Housen, 1976) computed the average by considering all sizes of impact craters. Housen et al. (1979a,b) realized that the impacting debris population in the present-day asteroid belt is dominated in number and cross-section by small objects and dominated in mass by larger bodies. These large bodies produce a few big craters whose effects are not typical of the more uniform terrain resulting from saturation of a surface by numerous small craters. An average value based on all sizes of craters probably would represent neither the uniform terrain nor the "atypical" regions (created by large impacts) very well. Therefore, in order to compute a meaningful average, only the portions of the surface saturated with small craters were considered in the averaging by Housen et al. The relatively uniform terrain was called the "typical region".

The model of Housen et al. (1979a) applies only to asteroids sufficiently small such that crater ejecta are very widely spread over the surface. Although the large sparsely scattered craters themselves are not part of the typical region, their highly dispersed ejecta contribute to regolith buildup and so should be included when computing the average regolith depth. This contrasts to the case of large asteroids (or small weak bodies with correspondingly lower ejecta velocities) where ejecta are retained in the local vicinity of a crater. On these bodies, crater ejecta deposits may produce nonuniform (atypical) terrain, hence they are not included as part of the typical region until a time when the ejecta blankets saturate the surface. A model for large asteroids (Housen et al., 1979b) is summarized later.

Model for Small Asteroids

In order to determine which craters were to be included in the typical region Housen et al. devised a criterion for crater saturation and defined $D_s(t)$ to be the diameter of the largest craters which had saturated the surface by time t. The crater population was thus divided into two parts.

1. Craters smaller than $D_s(t)$ comprise the typical region because they saturate the surface. The fraction of their ejecta which escapes the asteroid depletes the regolith.
2. The craters larger than $D_s(t)$, up to a diameter D_r of a crater that catastrophically ruptures the asteroid, are widely dispersed and are excluded from the typical region. However they do

generate a substantial amount of ejecta. The portion of ejecta which is not lost to space is spread widely over the surface and onto the typical region. The effects of all craters are summarized in Figure 7a.

The expression for $D_s(t)$ was used to compute the surface elevation of the typical region as a function of time. Early in an asteroid's evolution, only the very smallest craters are sufficiently numerous to saturate the surface. These small craters remove very little regolith. Most sizes of craters, being larger than D_s, deposit a lot of material onto the typical region, causing the elevation to initially increase. With passing time, D_s increases (i.e. moves to the right in Figure 7a) so that larger craters are incorporated into the typical region, resulting in more erosion. Simultaneously, the rate of deposition decreases because the diameter range, D_s to D_r, shrinks. These two effects cause the elevation to level off and to eventually decrease. Finally, at some point in time a crater of diameter D_r or larger forms and ruptures the asteroid. At this point, regolith evolution suffers a large discontinuity, so the analytical treatment is stopped.

After computing the surface elevation the actual regolith depth was found in the following manner. For asteroids where the surface elevation continues to increase until catastrophic fragmentation (Figure 8 shows an example), the regolith depth was approximated by the surface elevation. This was deemed reasonable because in such cases, impacts which penetrate the debris layer and

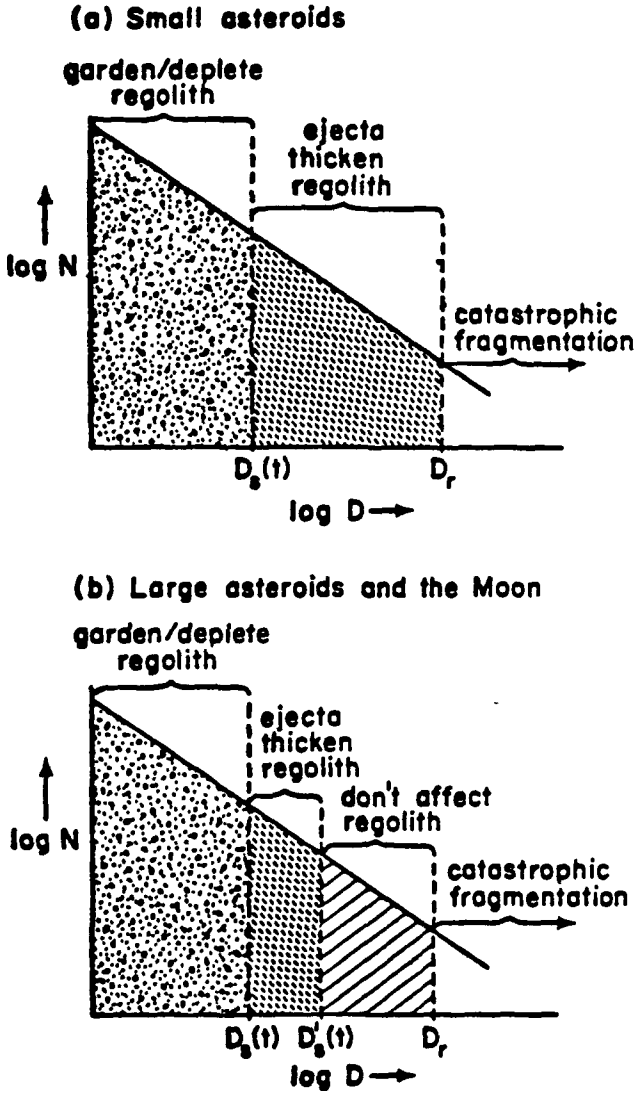


Figure 7. The effects of various sizes of craters on regolith evolution in a "typical region" on an asteroid's surface. -- N is the number (per area and time) of craters of diameter D or larger. At time t only craters smaller than some diameter $D_s(t)$ saturate the surface and so compose a "typical region". These craters garden and deplete (i.e. eject to space) regolith in the typical region. In Figure 7a, which applies to small asteroids where ejecta are globally distributed, the regolith is thickened by all craters outside the typical region (i.e. $D_s<D<D_r$, where D_r represents the smallest crater that can catastrophically rupture the asteroid). Figure 7b applies to large bodies, where ejecta are not widespread. Only those craters whose ejecta blankets saturate the surface [$D>D'_s(t)$] add regolith to the typical region. This figure is from the work of Housen et al. (1979b).

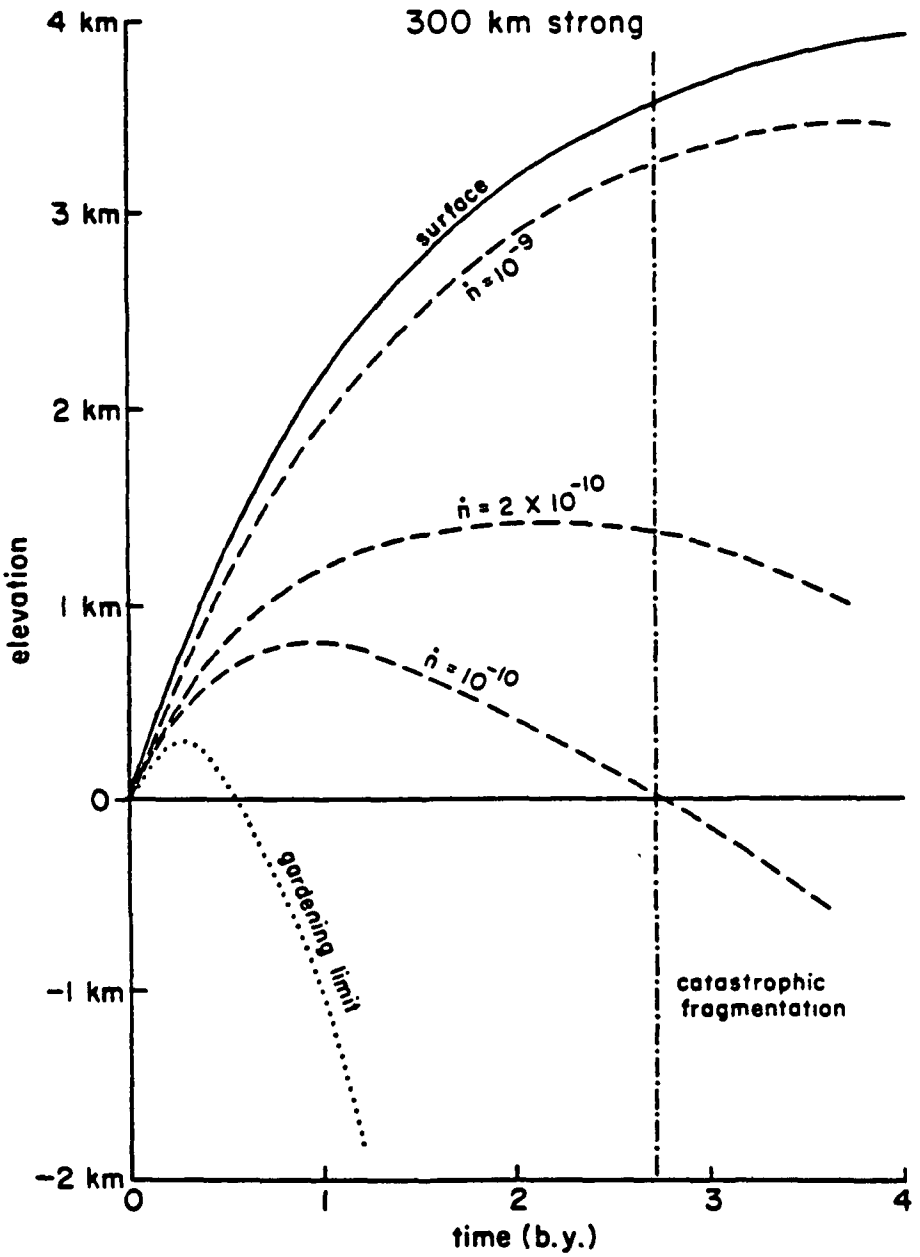


Figure 8. The surface elevation in a typical region on a 300 km diameter rocky asteroid. -- The dashed lines are contours of constant excavation rate (1/yr). A regolith depth of roughly 3.5 km is developed before the asteroid is catastrophically fragmented by a large impact. After fragmentation, the asteroid may continue on as gravitationally bound debris. This figure is from the work of Housen et al. (1979b).

comminute underlying bedrock are very rare. For smaller bodies, which lose more ejecta, the surface elevation may reach a maximum and then decrease below the initial (t=0) value. For these bodies the regolith thickness was determined by computing the depth below the surface where one excavation is expected to have occurred.

The calculations of Housen et al. (1979a) pertain to the two asteroid types, i.e. strong and weak, described in Chapter 2. Rocky (i.e. strong) bodies with diameter < 10 km maintain only thin dusty coatings because of their very small gravity fields. Regolith depth increases with asteroid size because more impact ejecta are retained. Thus, a 300 km body accumulates 3.5 km of regolith (Figure 8). Larger bodies, where ejecta are not globally distributed, were treated using the methods discussed in the next section. Ejecta are not widespread on weak bodies larger than about 10 km. Weak asteroids of diameter 1 km to 10 km develop centimeters to meters of regolith.

Housen et al. also considered the charged-particle irradiation of regolith material. Because typical penetration depths (in silicate materials) of SCR and GCR particles are roughly 100 microns and 1 m respectively (Table 3), the radiation effects acquired are dependent on how long regolith grains are exposed at or near the surface of an asteroid. Thus, one needs to know how extensively the regolith is churned or "gardened" by craters. This was characterized by comparing the formation rate of ejecta blankets of a specific depth to the formation rate of craters which excavate to the same depth. For all the asteroids modeled, regolith gardening was found to be minimal

because ejecta blankets occur faster than excavations. Grains in the regolith are excavated very few times, if at all. This is in sharp contrast to the lunar regolith where reworking of material is the dominant process. The relative immaturity (e.g. lower agglutinate and glass content, lower exposure ages, etc.) of gas-rich meteorites compared with lunar breccias was explained by the high rate of blanketing compared with excavation. Housen et al. (1979a) concluded that moderate-size asteroids 100-300 km in diameter would provide a suitable environment in which gas-rich meteorites could be formed. In this environment, blanketing by widespread ejecta occurred at a rate sufficient to provide 1 m of shielding of buried surface materials from GCR irradiation within 2 Myr and also permitted adequate exposure durations of 10^3-10^4 yr for lower energy SCR particles and solar wind gases. In order to account for the relatively large fraction of meteorites that are gas-rich, Housen et al. required that several generations of surficial regolith be incorporated into the interior of a parent body prior to catastrophic dispersal and delivery of meteorite fragments to Earth. These conclusions differ markedly from those of earlier investigators (e.g. Borg et al., 1975 or Matson et al., 1977) who assumed that the immaturity of asteroidal regoliths, compared to the lunar regolith, is due to a higher stirring rate for asteroids and the escape of shocked and glassy materials from small-body regoliths.

Model for Large Asteroids

On a large asteroid ejected debris are restricted more to the proximity of a crater so it is no longer reasonable to consider a uniform layer of ejecta surrounding the body. The formation and superposition of these ejecta blankets results in a spectrum of surface elevations just as the superposition of crater bowls produced a distribution of elevations in the small-body model. In order for the average regolith depth to be meaningful, Housen et al. retained the concept of a typical region over which most of the ejecta was considered to be approximately of uniform depth. A roughly uniform surface elevation was "assured" by requiring that ejecta blankets had overlapped one another extensively, i.e. saturated the surface, before they were included in the typical region. This was analogous to the earlier treatment of small asteroids where craters were not included until saturation had occurred. This method allowed the characterization of regolith depth on large bodies without actually specifying the shape of ejecta blankets. The only requirement was that, when ejecta blankets had saturated, they combined to form a relatively uniform layer of debris.

In order to define ejecta saturation, Housen et al. constructed annuli around craters. Ejecta blankets were said to saturate the surface only if their associated annuli were sufficiently numerous to meet a mathematical criterion. Once this criterion was met, the surface elevation was computed under the assumption that all ejecta were spread in a uniform layer. It is in this sense that the Housen et al. model gave the average surface elevation.

As discussed by Housen et al., the size of an ejecta annulus is difficult to decide upon. The size chosen determines how well the average surface elevation characterizes the true distribution of elevations. Two models for the radial width (i.e. outer radius minus inner radius) of an annulus were adopted: (1) the width is a constant A_1 independent of crater diameter, as implied by some experimental and theoretical studies of ejecta velocity distributions, and (2) the width is a constant, A_2, times the crater diameter, as suggested by some studies of ejecta blanket topographic profiles (see discussion, below). These two models were referred to as Type 1 and Type 2 ejecta blankets respectively. Values for A_1 and A_2 were determined from experimental ejecta velocity distributions.

The largest crater diameter whose ejecta annuli had saturated by time t was defined to be $D'_{s,i}(t)$, where i (i=1,2) indicates the ejecta blanket model used. Notice that together, $D_s(t)$ and $D'_s(t)$ split the crater population into three parts (Figure 7b).

1. Craters smaller than $D_s(t)$ remove regolith from the typical region.

2. The craters larger than $D_s(t)$ but smaller than $D'_s9(t)$ do not saturate the surface and so do not reside in the typical region. However, the ejecta blankets of these craters are saturated and so contribute to regolith buildup.

3. Craters larger than $D'_s(t)$ do not affect regolith evolution in the typical region because neither the craters themselves nor their ejecta annuli saturate the surface.

The expressions for D_s and D_s' were used to find the surface elevation as a function of time. For a 1000-km diameter strong asteroid the surface elevation at fragmentation was found to be 1.2 km. A 25% variation in the size of ejecta annuli caused the surface elevation to change by 15%. Housen et al. found that regolith grains may be excavated a few times over the lifetime of the asteroid. Similar results were found for a 500 km diameter asteroid because, even though more ejecta escape, the ejecta were assumed to be more widespread than on the 1000 km body.

Note that the computed regolith depths for large asteroids are smaller than those for moderate size bodies. This is due primarily to the less widespread ejecta blankets on large asteroids. Thus, much of the ejecta that is widespread (and so builds up the regolith in the typical region) on moderate size bodies is excluded from the typical region on large asteroids. Furthermore, as asteroid size increaes, more craters tend to be gravity scaled as opposed to the predominant strength scaled craters on smaller rocky bodies. Compared to strength scaling, a gravity scaled population of craters has relatively less volume concentrated in large diameters and more in small ones. Thus, gravity scaled craters are less efficient in generating new regolith and more efficient in reworking existing debris. This transition in scaling laws tends to make the regolith in the typical region on large bodies thinner and perhaps more extensively gardened as compared to smaller asteroids.

Comparison of Regolith Evolution on Asteroids and the Moon

In order to check their model and to help delineate the difference between regolith evolution on asteroids and the Moon, Housen et al. used their large-body model to compute the regolith depth expected to develop on lunar maria. Depths of 7-10 m were found to accumulate over 3.5 Gyr depending on the assumed size of ejecta annuli. Although the calculated depths are slightly higher than the observed value (about 5 m), the agreement was thought to be satisfactory given the precision of the input parameters; therefore, Housen et al. concluded that their large-asteroid model worked reasonably well.

The depth of the lunar regolith is of the order of a few meters. Conversely, asteroids, which are smaller than the Moon and so retain less crater ejecta, can have regoliths as deep as a few kilometers. This somewhat paradoxial situation arises for two reasons.

Differences in Crater Flux. Consider for example, a Vesta-size object at 3 AU. Roughly 1.5 km of regolith is developed in 3.5 Gyr. If this body were moved to 1 AU it would accumulate only 30 m of regolith in 3.5 Gyr due soley to the reduced flux at 1 AU. Obviously, for equal evolution times, if the cratering flux is reduced then the amount of regolith is also reduced. The small mass flux and higher impact velocity at 1 AU result in a cratering rate which is a factor of 100 below that at 3 AU. The reason that the regolith depth only decreases by a factor of 50, rather than by a factor of 100, is because regolith growth is not linear in time.

Size of the Body. Comparing the Vesta-size asteroid at 1 AU with the Moon, we see that the Moon develops the lesser amount of regolith. This occurs for the same reasons that the largest asteroids have deeper regoliths than slightly smaller bodies.

Some Critical Remarks

While the model of Housen et al. represents the first major contribution to our understanding of asteroidal regoliths and their connection to gas-rich meteorites, it is lacking in five respects.

1. Regolith evolution was modeled over a portion (roughly 2/3) of an asteroid's surface; the so-called typical region. If meteorites are derived primarily from the catastrophic dispersal of asteroids then the whole regolith, not just the part corresponding to the typical region, is sampled. Also, if some meteorites are derived from large but noncatastrophic events, some or all of the ejecta may be sampled from the part of the surface not described by the model. Information about the entire surface would be helpful.

2. For large bodies Housen et al. defined saturation of craters or ejecta annuli to occur when the craters or annuli had occupied 2/3 of an asteroid's surface. However, the area occupied by craters is not necessarily the same area occupied by ejecta, i.e. atypical ejecta deposits can exist on typical craters and vice-versa. Therefore, on large asteroids the size of the typical region will be less than 2/3. In order to assess the magnitude of this effect, a Monte Carlo computer program was written which generated atypical craters and

ejecta on a square grid (representing the asteroid's surface) according to the saturation criteria of Housen et al. The actual size of the typical region turned out to be < 1/2 rather than 2/3. The "typical" region therefore occupies less than 50% of the surface.

3. Housen et al. actually computed the average surface elevation, not the average regolith depth. As noted earlier in this chapter, equating elevation and depth seems reasonable in cases where the elevation continually increases until fragmentation (e.g. Figure 8) because large impacts which excavate below the debris layer are rare. However, a subtle difference between regolith depth and surface elevation is that regolith depth depends on the order in which cratering and blanketing events occur. This point is discussed further in Chapter 6.

4. The regolith depth in the typical region is characterized by the average value. But the present-day asteroid belt is such that regolith growth is significantly affected by a few large impacts. The size, number, and time of formation of these large events and the evolution time (lifetime) of the asteroid are subject to large stochastic fluctuations. Therefore there may be a large variance associated with the computed regolith depth. The magnitude of this variance should be determined in order to assess the validity of conclusions based soley on average depths.

5. The exposure times, for regolith grains, to solar and galactic cosmic rays were also evaluated as average values. But these exposure times will differ among grains because each grain performs its own

random walk through the regolith. A statistical treatment (as opposed to the determinate model of Housen et al.) of the irradiation processes can be used to determine the distribution of exposure times one might expect to find in the grains comprising a meteorite derived from a particular parent body. This distribution will yield not only mean exposure time but also will give an important quantity which Housen et al. did not obtain: the fraction of regolith grains which are expected to be irradiated. Moreover, the regolith mixing calculations of Housen et al. may contain considerable errors due to incorrect modeling of small-scale impact events. They approximated the entire crater diameter distribution by a single power-law function. The function they used applied to the largest craters, which dominate regolith growth. However, the exposure histories of regolith grains are strongly dependent on the small scale events. Calculations which incorporate variations in the mass distribution of projectiles and changes in the cratering laws at small scales should be be performed in order to correctly determine exposure times.

The Orsay Models

The other major regolith model, which is actually a collection of separate efforts using the same modeling techniques, has been constructed recently by a group of authors in Orsay, France, and differs fundamentally from the work of Housen et al. Unfortunately the details of the model have not been published yet, so in-depth descriptions and critiques are not possible at this time.

The Duraud et al. Model

Duraud et al. (1979) briefly described a model for the equilibrium depth of regolith on small bodies. The erosive and depositional effects of cratering on an existing regolith layer were considered. For a 20 km diameter asteroid, an equilibrium depth of 2 m was computed. For a 200 km body the depth was found to be 200 m.

In order to assess the characteristic time required to reach equilibrium, Duraud et al. assumed the flux of debris in the asteroid belt to be 10 times higher than at 1 AU. Using this flux they found that the 20 km body reached equilibrium in less than 100 Myr and that the regolith subsequently receded in toward the center of the asteorid at a rate of 10 m/Gyr. The rate for a 200 km asteroid is 2 m/Gyr.

Emplacement of crater ejecta is envisioned to occur as a "steady rain" on small bodies, rather than in discrete layers as observed on the Moon. Hence the small-body regoliths should be devoid of layers.

I have two comments on this model: (1) The equilibrium regolith thickness is claimed to be independent of any assumptions concerning the mass distribution of impacting debris. While the equilibrium value should not depend on the impact rate, it is not clear why the shape of the projectile distribution should not affect the equilibrium thickness. Furthermore, in an environment where a few large impacts can cause major changes in regolith thickness, it is not obvious how a state of equilibrium can be reached before the body is catastrophically fragmented. This point is discussed further in

Chapter 6. (2) The factor of ten increase in mass flux between 1 AU and 3AU is very low. A more reasonable assumption for the increase in flux of large bodies is 10^2 or perhaps 10^3 (Kessler, 1970; Dohnanyi, 1972; Chapman, 1976). Note that the rate of small-asteroid surface erosion calculated (10m/Gyr) is roughly 50 times smaller than that computed by Housen et al. (1979a) for a 10 km diameter asteroid. A higher impact rate in the Duraud et al. model would produce agreement between the two models.

The Dran et al. Model

Dran et al. (1979) applied the calculations of Duraud et al. to the irradiation of regolith material. The rate at which the regolith recedes into an asteroid's interior dictates the time of exposure of regolith grains to charged particles. Dran et al. predicted, for the 20 km body, that GCR exposure effects for regolith material should be depleted by a factor of >10 relative to lunar soils. The densities of SCR particle tracks should be roughly 300 times less than those observed for the Moon. They suggested that their predictions fit observations of irradiated grains in the Kapoeta meteorite, i.e. a recent origin on a small body was proposed. Early origins were discarded. Irradiation while the grains floated freely in space prior to parent body accretion was rejected because the exposure times to SCR and GCR particles would be similar, contrary to observations. Irradiation during accretion apparently results in exposure times smaller than those observed, due to the presumably high flux of impacting debris during accretion.

The erosion rate calculated by Duraud et al. for the 20 km asteroid results in an exposure time of 10^8 yr for regolith material to galactic cosmic rays. This is two orders of magnitude greater than the observed exposure ages in meteorites (Anders, 1975). Unless another mechanism is called on to limit the exposure times (e.g. catastrophic rupture), the claim that model results are in accord with observations is clearly unfounded. Note however that, as discussed above, if a more reasonable value for the impact flux in the asteroid belt is assumed, the erosion rate increases (thus the exposure times decrease) by a factor of 10 to 100 relative to those given by Dran et al. Clearly this would improve the calculated exposure times.

The Model of Langevin and Maurette

Langevin and Maurette (1980) (denoted by L-M) developed a regolith model in order to isolate the input parameters which are the most critical in determining regolith thickness. They constructed an estimate of the asteroidal crater size-frequency distribution based on the observed lunar crater distribution, as discussed in Chapter 2. The other important input parameter addressed was the velocity distribution of ejecta. This was also discussed in Chapter 2.

The evolution of regolith depth at a point on the surface was modeled by evaluating the amount of depletion due to local cratering and the buildup due to deposition of crater ejecta, although ejecta from the largest craters were excluded. The radial distance, R_c, such that a given percentage (they did not clearly state whether a value of 50% or 90% was used) of ejecta lie within R_c, was computed. The

ejecta from craters of a given size were not included until a time when at least one crater of the given size or larger formed at a distance less than R_c from the surface-point in question.

Although both the projectile mass distribution and the crater ejecta velocity distribution are poorly known, L-M concluded that the velocity distribution is the most critical parameter in regolith evolution. This distribution governs the extent of localization of ejecta (i.e. determines R_c), which dictates when ejecta are included in the regolith depth computations. For example, large ejecta velocities imply large values of R_c. In this case, ejecta are quickly included, so relatively thick regoliths result.

Regolith depths, at the time of asteroid fragmentation, were computed for various sizes and strengths of bodies. Small (17.5 km diameter) weak bodies accumulated 70 m of regolith during their 700 Myr collisional lifetime. Larger weak bodies built up thinner debris layers due to the higher gravity fields which resulted in more-localized ejecta deposits. Small and moderate-size strong objects (diameter<150 km) developed little regolith because of the escape of most ejecta. Larger bodies, of diameter 300 km, developed roughly 800 m of regolith over a collisional lifetime greater than 4 Gyr. Regolith thickness on the Moon was estimated to be a few to several meters depending on the material strength assumed.

As discussed in the next section, the model of L-M describes the average regolith depth in a "typical region" and is therefore subject to some of the same criticisms as the Housen et al. model. Briefly, a description of the entire surface area is desirable including the statistical uncertainties associated with the average depth computed. The details of any irradiation calculations have not been published and so cannot be critiqued at this time.

Comparison of the Two Recent Models

The results of the two recent models (Housen et al. 1979a,b; Langevin and Maurette, 1980) are somewhat disparate. We now compare these two studies, concentrating on the differences between estimates of regolith depth. As discussed earlier, discrepancies in exposure-time calculations are probably due to discrepancies in the assumed impact fluxes.

In general, Housen et al. predict thicker regoliths than those of L-M. For example, Housen et al. (1979a,b) computed regolith depths, at the time of fragmentation, of 3.5 km, 1.2 km and 1.2 km for 300 km (diameter), 500 km and 1000 km asteroids. L-M found depths of roughly 800 m, 500 m and 250 m.

For the 300 km body, the difference arises because Housen et al. assumed ejecta to be globally distributed while L-M used more localized ejecta deposits. Housen et al. justified global dispersion by computing the radial distance (410 km) which encompassed 90% of the ejecta. Thus 90% of the ejecta was spread over 95% of the surface area. However, the ballistic range for the 50th percentile of ejecta

is 45 km which corresponds to only 2% of the surface area. Although the use of either the 50th or the 90th percentile cannot be rigorously justified, the fact that 50% of the ejecta covers only 2% of the surface implies that the Housen et al. assumption is not correct for this body. If the ejecta is considered to be localized, according to the L-M ejecta velocity model, then the depth decreases to 1.5 km because debris from large craters are now excluded from the typical region. The assumption of globally distributed ejecta should be reasonable for asteroids smaller than 300 km.

For the 500 km and 1000 km bodies both models considered ejecta to be localized. We now address three possible reasons for discrepency in the large-body calculations.

Definitions of Saturation

Housen et al. computed the average regolith depth in a typical region on an asteroid's surface by excluding the effects of craters or ejecta blankets until they had saturated the surface. L-M also excluded the largest craters and so, in a sense, also modeled the evolution in a typical region. Essentially, both models required knowledge of the diameter $D_s(t)$ of the largest craters which saturated the surface by time t and the diameter $D'_s(t)$ of the largest craters whose ejecta had saturated. Because these two diameters dictate the amount of erosion and buildup of regolith (see Figure 7b), we now consider the methods used to find $D_s(t)$ and $D'_s(t)$.

Housen et al. computed D_s' by requiring that the fraction of surface area exterior to the ejecta annuli of craters with unsaturated ejecta (i.e. craters larger than D_s') was f. That is, f represented the size of the typical region. A nominal value of f=0.65 was used. The size of the typical region was related to the actual area taken up by the atypical ejecta annuli (including the statistical effects of overlap) through the expression

$$t \int_{D_s'}^{D_r} A(D)\, dN(D) = -\ln(f) = 0.43 \qquad (3.1)$$

where D_r is the diameter of the smallest crater which can fragment the asteroid, A(D) is the area of an ejecta blanket (i.e. annulus) for a crater of diameter D, t is the time and dN(D) is the number of craters produced per unit area per unit time in the diameter interval dD. Equation (3.1) was used to find $D_s'(t)$. $D_s(t)$ was found in a similar manner by replacing, in equation (3.1), D_s' by D_s and by replacing A(D) by the area of a crater, $\pi D^2/4$.

L-M used a different method to compute $D_s'(t)$. They required

$$t\pi R_c^2(D_s')\, N(D_s') = 1 \qquad (3.2)$$

where N(D) is the cumulative number of craters per area per time larger than D and $R_c(D)$ is the radial distance, from the center of a crater of diameter D, which encompasses a specified percentage of

crater ejecta. This is analagous to the expression used by Housen et al.

The expressions used to compute D_s' differ in two respects. First, note that the l.h.s. of both equations (3.1) and (3.2) represent a total number of impacts in a given area. The fact that Housen et al. require the number to be 0.43 rather than 1 tends to produce a larger value of D_s' than that calculated by L-M. For example, in the L-M model, suppose that at some time only one impact had occurred for a crater of diameter D_s'. Then one would have to consider a crater diameter larger than D_s' in order that only 0.43 impacts had occurred. The larger values of D_s' used by Housen et al. resulted in the inclusion of ejecta from larger craters, which tended to produce thicker regoliths than L-M. Second, note that the l.h.s. of equations (3.1) and (3.2) differ. L-M multiplied the area πR_c^2 (with R_c evaluated for craters of diameter D_s') by the cumulative number of impacts, per area per time, larger than D_s'. This is incorrect because the area over which impacts are collected is obviously a function of crater diameter (i.e. R_c is a function of diameter) so an integral of the type used by Housen et al. should be employed. Moreover, the area used should be that of the ejecta annulus, not the area πR_c^2, because blanketing occurs only when crater centers form in the annular area. The fact that Housen et al. used the integrated area means that they computed larger values of D_s' while their use of the annular area (rather than πR_c^2) results in smaller values of D_s', compared to L-M.

Similar discrepencies seem to exist in the methods used to find the diameter D_s. L-M did not explicitly describe the method used although they did state that "regolith loss through local cratering is computed using the same concepts..." (as those used to find D_s'). Thus $D_s(t)$ was undoubtedly computed from

$$t\pi(D_s^2/4)\ N(D_s) = 1 \tag{3.3}$$

while Housen et al. found D_s from

$$t \int_{D_s}^{D_r} (\pi D^2/4)\ dN(D) = 0.43. \tag{3.4}$$

Therefore, by reasoning analagous to that given above for D_s', the use of 0.43 on the right side of equation (3.4) and an integral on the left side resulted in larger values of D_s for Housen et al.

In short, the methodology used by Housen et al. tends to produce larger values of both D_s' and D_s, relative to L-M. How does this affect regolith growth? Large values of D_s' obviously favor thick debris layers. Large values of D_s result in thin regoliths, due mainly to shrinkage of the range of crater diameters (i.e. $D_s < D < D_s'$) which contribute to regolith buildup (see Figure 7b). In order to determine the magnitude of these effects the regolith depth for a 500 km strong asteroid was computed, using the same input parameters as Housen et al., but with the L-M expressions for D_s' and D_s. At the

time of fragmentation (t = 3.4 Gyr) the regolith depth from the Housen et al. model was 1.2 km while D_s' and D_s were 105 km and 18 km respectively. Using the L-M expressions, D_s' and D_s were found to be 46 km and 2 km while the regolith depth was 2.1 km, due to the larger range of crater diameters contributing to regolith growth. Their methodology for computing D_s' and D_s therefore produces deeper regoliths than that of Housen et al. Obviously this does not explain why L-M predict a regolith depth depth of 500 m rather than the 1.2 km reported by Housen et al. The difference must lie in the input parameters used.

Crater Flux

The crater-size distributions, described earlier in this chapter, are apparently similar in shape except for a relative tenfold depletion in the L-M flux near a crater diameter of 1 km. The exact expression they used is not stated. Their lower flux should produce less regolith than Housen et al. but the magnitude of the effect cannot be determined until a complete description of the flux model is available.

Velocity of Crater Ejecta

The ejecta blanket model of L-M is similar to the Housen et al. annuli. Using their ejecta velocity model (described in Chapter 2) one can show that, for gravity scaled craters, 90% of ejecta lie within a distance R_c=D. This corresponds to the Type 2 model of Housen et al. with A_2=0.5. For strength scaled craters R_c is a weak function of D, but for values of D appropriate to strength scaling, R_c and also the width of a Housen et al. annulus, are roughly constant. Thus, strength scaling corresponds to a Type 1 annulus.

Although the strength and gravity scaling cases of L-M are equivalent to Type 1 and 2 annuli, the assumed sizes for ejecta deposits differ. For example, for the 500 km body, where gravity scaling applies, the L-M model implies A_2=0.5 but Housen et al. used A_2=1.4. The reason for this discrepency is that Housen et al. determined annuli widths from ejecta velocity data that pertained to strength scaling (where velocities are high) rather than gravity scaling. Their regolith depths are larger because the more widespread ejecta is incorporated into the typical region faster than in the L-M model.

The lower ejecta velocities of L-M also mean that more ejecta are retained on asteroids. Moreover, the fraction of escaping ejecta for gravity scaled craters is dependent on crater size (Housen et al. assumed the fraction was constant).

By repeating the Housen et al. calculations, with A_2=0.5 and a diameter-dependent fraction of escaping ejecta for gravity scaled craters, a regolith depth of 900 m was calculated for both a 500 km and a 1000 km asteroid.

Summary

The main difference between the two regolith models is in the assumed velocity distribution of ejecta. Housen et al. somewhat overestimated regolith depths by overestimating ejecta velocities. The Housen et al. saturation criterion results in thinner regoliths than L-M. Neither model is more "correct" than the other because the "degree of saturation" required to produce a nearly uniform debris layer in the typical region (so that the average value meaningfully characterizes the actual distribution of regolith depths) is itself arbitrary. However, the Housen et al. approach is preferable because the exact portion of the surface modeled is clearly defined. The Housen et al. model (with the same ejecta velocities as L-M) still gives deeper regoliths than L-M. This may be due to factors not considered above, e.g. the fragmentation lifetimes of asteroids differ between the two models. The method used by L-M in computing lifetimes has not yet been published, so a comparison cannot yet be made.

The models described above give estimates of the average regolith depth over a portion of an asteroid's surface. Also, Housen et al. attempted to compute exposure times of regolith grains to charged-particle irradiation by assessing the degree to which a regolith is mixed or gardened. In the next chapter we address some of

the criticisms made of these models. A statistical model will be constructed for regolith depth (as opposed to surface elevation) which describes the whole surface of an asteroid. In order to determine how well the average value characterizes regolith depth we compute the variance of the depth. Furthermore, a Monte Carlo computer program is described which simulates exposure of regolith grains to charged-particle irradiation.

CHAPTER 4

THE STOCHASTIC EVOLUTION OF ASTEROIDAL REGOLITHS

In Chapter 3 the properties of regoliths were described from a determinate point of view. In that approach, two asteroids of the same size and strength were considered to be indistinguishable in terms of depth of regolith and irradiation of surface debris. Furthermore, the regolith depth, which varies from point to point on the surface, was characterized by the average value taken over a restricted portion of the surface.

In reality, regolith evolution is dictated by the laws of chance. Consider for example a fictitious population of a large number of bodies of common size and strength. When averaged over the entire population, the number of craters of a given size produced per asteroid will be the same as that given by the average crater flux in the determinate models. However, any one asteroid may experience a flux somewhat different than the mean value. In particular, the number of relatively large (thus rare) craters produced on a body is subject to major statistical fluctuations. Because regolith evolution is dominated by the large impacts, we might expect regoliths to differ considerably among bodies in the population. There are other, probably less important, factors which should be included. For

example, the relative positions of craters and their order of occurrence are random variables which should affect regolith depth.

The actual population of bodies of the given size and strength that exists in the asteroid belt today is envisioned as being a random sample from the larger fictitious population. This is merely a convenient way to conceptualize the fact that each asteroid has been subjected to a unique impact history.

In this chapter a statistical approach is used to model regolith evolution. This allows us to evaluate both the degree of variability among similar-size asteroids and also the amount of variation in regolith depth over an asteroid's surface. If the statistical variability associated with regolith depth is large, then the utility of the determinate models becomes questionable, and the conclusions drawn from such models should be re-evaluated. In any event, a statistical analysis of the problem will indicate how well simple average values characterize regolith evolution.

The stochastic model is broken into three parts. The evolution of regolith depth is considered first. The depth of regolith is then used to determine how much brecciated material a given size of asteroid liberates to space. Finally, a Monte Carlo program is described which simulates the exposure of regolith grains to space irradiation.

The Depth of an Asteroidal Regolith

The evolution of regolith depth, for an asteroid of some given size and strength, is modeled by selecting a body at random from the large (fictitious) population. In order to be precise in our definition, we consider the evolution at a single point selected at random on the surface of the body. As is discussed later in this section, knowledge of the evolution at a random point allows us to make statements regarding the "mean regolith depth on an asteroid". This permits useful comparisons between determinate and stochastic models.

Both the surface elevation and the regolith depth at the randomly selected point change with time: they increase when debris from a nearby impact blankets the point, and they decrease when a crater forms over the point, removing regolith. These blanketing and excavation events are referred to as "jumps". The size of a jump depends on the crater size and its distance from the point. The jump size is, therefore, a random variable because in any given impact event the crater size and position are both random variables. Note also that the total number of events which have occurred up to any particular time is random because the time interval between jump events is random.

For some time t, the surface elevation Z(t) and regolith depth X(t), being the result of a random number of random jumps, are both random variables themselves, i.e. both Z(t) and X(t) random walk in time. One possible realization, and the relationship between Z(t) and

X(t), is shown in Figure 9. The difference between surface elevation and regolith depth is apparent. Although a positive jump increases Z(t) and X(t) by the same amount, a large negative jump may cause only a small decrease in X(t). This occurs when a large crater forms over the point removing all the regolith.

All of the information regarding X(t) is contained in the cumulative distribution function (c.d.f.) F(x,t),

$$F(x,t) = \text{Prob} \{ X(t) < x \}$$

An exact expression for F(x,t) is not obtained here. However, an approximation based on a diffusion process is found to perform well. Before deriving the approximation a brief comment is given on a classical method that sometimes yields exact results.

A Note on the Forward Equation

A standard textbook-method for finding the probability distribution of a random variable defining a stochastic process is to solve the so-called forward equation for the process. However when one strays from the "simple" textbook cases the solutions often become extremely difficult. For the present case the forward equation is an integro-partial-differential equation which seems to elude the methods typically used to obtain analytical solutions. A numerical solution is possible by converting the forward equation into a system of ordinary differential equations; however, the number of equations

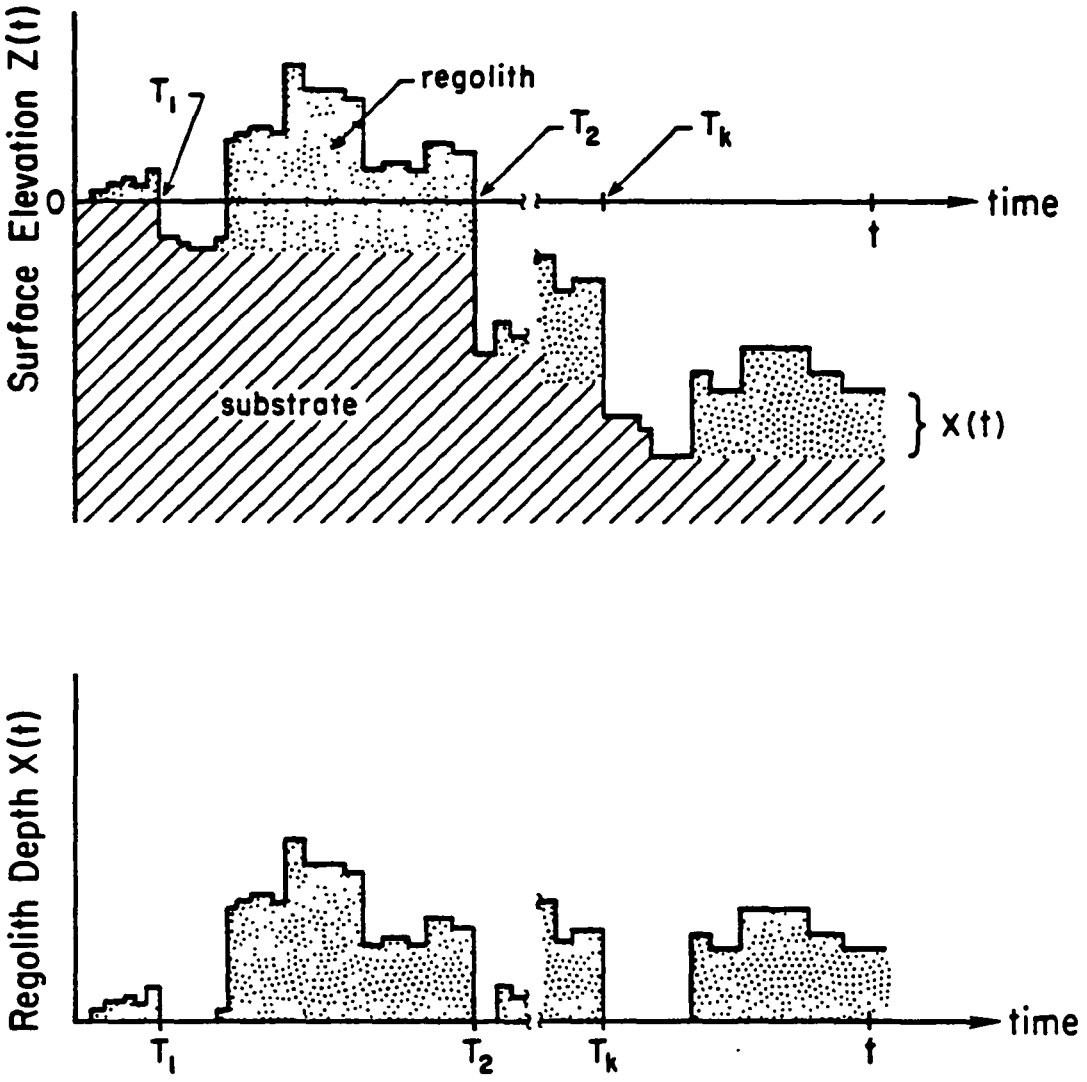


Figure 9. The relationship between elevation and regolith depth. -- The surface elevation, Z(t), at a point on an asteroid's surface, decreases when a crater forms over the point and increases when a nearby crater blankets the point. At any given time the regolith depth, X(t), is the thickness of deposited debris which overlies the undisturbed substrate. Note that a large excavation event may remove all the regolith from the surface point (e.g. at the times indicated).

required to obtain an accurate solution is so large that computer run-time costs are prohibitive. Because an exact solution does not appear possible, we turn our attention to approximate methods.

A Diffusion Approximation

In this section an approximation is derived for the c.d.f. of regolith depth at time t. This expression is used to estimate the time required for a regolith to reach a state of statistical equilibrium. The distribution of depth at the time of catastrophic fragmentation of the asteroid is then derived and is followed by an assessment of the accuracy of the approximation.

The Regolith Depth at a Fixed Time, t. One of the more famous theorems in probability and statistics, the central limit theorem, roughly states that the sum a large number of random variables is approximately normally distributed. Note that for large t the surface elevation Z(t) is the sum of many random jumps. Thus we can expect the distribution of Z(t) to approach the normal distribution if regolith evolution proceeds for a "long" time. The fact that Z(t) tends toward normality allows approximation of the actual random walk shown in Figure 9 by another type of random walk; a diffusion called the Wiener process. At any given time the random variable defining the Wiener process has a normal distribution. Consequently, for large t, Z(t) can be approximated by the Wiener process.

Let us consider how knowledge of the distribution of Z(t) determines the distribution of regolith depth X(t). By referring to Figure 9 it is obvious that X(t) can be written as

$$X(t) = Z(t) - \min[\, Z(\tau):\ 0 < \tau < t \,]. \tag{4.1}$$

That is, the regolith depth at time t is just the current surface elevation minus the lowest value of the surface elevation recorded in the time interval (0,t). We now make use of a rather surprising result from queueing theory (see Feller, 1971 for a short proof)

$$\begin{aligned} F(x,t) &= \text{Prob}\ \{\, Z(t) - \min[\, Z(\tau):\ 0 < \tau < t \,] < x \,\} \\ &= \text{Prob}\ \{\, \max[\, Z(\tau):\ 0 < \tau < t \,] < x \,\}. \end{aligned} \tag{4.2}$$

The basis for a stochastic model of regolith depth is now established, i.e. for large t the probability distribution of regolith depth, X(t), has approximately the same distribution as the maximum value in the Wiener process.

Note that equations (4.1) and (4.2) apply to general random walks, i.e. in principle we could find the distribution of regolith depth resulting from the actual random walk (Figure 9). The reason for approximating the real process by a diffusion is that the distribution of the maximum (or even the distribution of the random walk itself) is very difficult to obtain except in very few cases, the Wiener process being one of them. The paper of Marcus (1970) presents a good example. Marcus attempted to derive the distribution of Z(t) for planetary surfaces (in particular, the Moon). After a lengthy analysis, he found analytic expressions only under rather specific conditions, e.g. the slope of the crater size-frequency distribution was restricted to a set of three specific values and the largest

crater was taken to be infinitely large. Note that the distribution of the maximum, for the case studied by Marcus, would be even harder to find. The central limit theorem is indeed a useful tool.

The distribution of the maximum in the Wiener process (i.e. $F(x,t)$, the distribution of regolith depth, as shown above) with mean β and variance σ^2 is given by Cox and Miller (1972) as

$$F(x,t) = \Phi\left((x-\beta t)/\sigma\sqrt{t} \right) - e^{2\beta x/\sigma^2} \Phi\left(-(x+\beta t)/\sigma\sqrt{t} \right) \qquad (4.3)$$

where $\Phi(\cdot)$ is the standard normal integral. Baxter and Donsker (1957) derived a similar expression for the probability density function (p.d.f.) of $X(t)$ but their result appears to contain a typographical error.

In order to use equation (4.3) we must determine the mean and variance of our random walk. At any time t, $Z(t)$ can be written as

$$Z(t) = Y_1 + Y_2 + \cdots\cdots + Y_{N(t)} \qquad (4.4)$$

where Y_i is the size of the ith jump experienced at the surface point in question and $N(t)$ is the random number of events which occur in time t. The occurrence of jump events is assumed to form a Poisson process with parameter λ, i.e. $N(t)$ is Poisson distributed with mean λt. The parameter λ is just the mean rate of occurrence of excavation or burial events. An expression for λ is given below.

Now, the Y_i's are independent and identically distributed random variables and are independent of N(t). If m_1 denotes the mean size of a jump, then

$$E[Z(t)] = m_1 \lambda t$$

where E denotes the expectation operator. The variance can be easily shown to be (e.g. Feller, 1971)

$$Var[Z(t)] = E[N(t)]\ Var[Y_1] + E^2[Y_1]\ Var[N(t)] .$$

If we let m_2 be the second moment (about the origin) of the jump size and note that the variance of a Poisson random variable is equal to its mean, then

$$Var[Z(t)] = m_2 \lambda t .$$

We now substitute in equation (4.3), $\beta = m_1\lambda$ and $\sigma^2 = m_2\lambda$, and recast it in a slightly different form as

$$F(x,t) = \tfrac{1}{2} \{ \operatorname{erf}[(x-m_1\lambda t)/\sqrt{2m_2\lambda t}\ ] + 1 - e^{2m_1 x/m_2} \operatorname{erfc}[(x+m_1\lambda t)/\sqrt{2m_2\lambda t}\ ] \} \tag{4.4}$$

where, in order to simplify subsequent manipulations, the standard normal integral $\Phi(\cdot)$ has been replaced with the error function erf$(\cdot)$, using the relationships

$$\mathrm{erf}(z) = 2\Phi(\sqrt{2}\,z) - 1$$

$$\mathrm{erfc}(z) = 1 - \mathrm{erf}(z)\,.$$

We now have, in equation (4.4), an approximation for the c.d.f. of regolith depth at time t for a point chosen at random on the surface of an asteroid chosen at random from a population of bodies of a given size and strength. The size and strength of the asteroid in question, the assumed geometry of craters and ejecta blankets and the assumed size-frequency distribution for crater formation determine the values of m_1 and m_2. So as not to disrupt the continuity of this section, the computations of m_1 and m_2 are deferred to Appendix 1.

The mean and variance of X(t), which will be of use in later discussions, can be found from the moment generating function $\Omega(s,t)$,

$$\Omega(s,t) = \int_0^\infty e^{sx}\,\frac{\partial F(x,t)}{\partial x}\,dx \qquad (4.5)$$

$$= \{\,(m_1+m_2 s)\,\exp[(2m_1+m_2 s)\,m_2 s\,\psi^2/m_1^2]\;\mathrm{erfc}[-(m_1+m_2 s)\,\psi/m_1]$$

$$+\; m_1\,\mathrm{erfc}[\psi]\,\}\,/(2m_1+m_2 s)$$

where

$$\psi = m_1\sqrt{\lambda t/2m_2}$$

See Appendix 2 for details of the integration. The mean value of X(t) can be found from

$$E[X(t)] = \frac{\partial \Omega(s,t)}{\partial s}\Big|_{s=0}$$

$$= (m_2/m_1)\left\{ \psi^2 \mathrm{erfc}[-\psi] + \tfrac{1}{2}\mathrm{erf}[\psi] + \psi e^{-\psi^2}/\sqrt{\pi} \right\}. \tag{4.6}$$

The second moment of X(t) is

$$E[X^2(t)] = \frac{\partial^2 \Omega(s,t)}{\partial s^2}\Big|_{s=0}$$

$$= (m_2/m_1)^2 \left\{ 2(\psi^2+1)\psi^2\, \mathrm{erfc}[-\psi] - \tfrac{1}{2}\mathrm{erf}[\psi] \right. \tag{4.7}$$

$$\left. + (2\psi^2+1)\psi e^{-\psi^2}/\sqrt{\pi} \right\}.$$

The variance of X(t) is obtained from equations (4.6) and (4.7).

The Equilibrium State of a Regolith. The approximation given in equation (4.4) allows us to investigate the long term behavior of a regolith. Notice that when the average size of a jump in surface elevation is negative (i.e. $m_1 < 0$), as is the case for most asteroids due to the net loss of material to space, the c.d.f. of regolith depth has the equilibrium distribution,

$$F(x,\infty) = 1 - e^{2m_1 x/m_2}.$$

A characteristic time to reach equilibrium can be estimated by requiring that the argument of erf(·) in equation (4.4) be > 1 and the argument of erfc(·) be < -1. If we construct the dimensionless space and time variables

$$\xi = -2m_1 x/m_2$$

$$\tau = 2m_1^2 \lambda t/m_2$$

then the above condition on the error function is roughly satisfied when $\tau \approx 1$. Thus a characteristic equilibrium time t_e for the process is

$$t_e = m_2/2m_1^2\lambda . \tag{4.8}$$

The Regolith Depth at Fragmentation. The expression for $F(x,t)$ gives the distribution of regolith depth at time t. This is useful in predicting regolith depths for bodies that are large enough to have escaped catastrophic fragmentation. However, for the vast majority of the asteroids there comes a time when an energetic impact causes major fracturing. This introduces a great discontinuity and forces us to end our analytic treatment of the evolution. Furthermore, it is convenient to speak of the depth at fragmentation because this quantity is independent of the (relatively poorly known) rate of impacts. Therefore, for small and moderate-size asteroids, it is more useful to speak of the regolith depth at fragmentation. Notice that the depth at fragmentation cannot be obtained by setting t equal to the fragmentation time in the expressions derived above because the time of fragmentation is a random variable. The c.d.f. and the moments of regolith depth at fragmentation are now derived.

Because the occurrence of craters is assumed to form a Poisson process, the waiting time until the first impact capable of rupturing the asteroid is exponentially distributed with parameter, say, λ_r. If w(t) is the probability density function (p.d.f.) of the fragmentation time then

$$w(t) = \lambda_r e^{-\lambda_r t} . \tag{4.9}$$

The flux of craters of diameter D or larger is assumed to be of the form $N=KD^a$, where K and a are constants (see Chapter 2), thus

$$\lambda_r = 4\pi R_A^2 K D_r^a \tag{4.10}$$

where R_A is the radius of the asteroid and D_r is the smallest crater which can rupture the body.

The c.d.f. of the regolith depth, X_r, at rupture can now be written as

$$\begin{aligned} F_r(x) &= \int_0^\infty F(x,t)\, w(t)\, dt \\ &= 1 - \exp\left[(m_1 x/m_2)\left(1 - \text{sign}(m_1)\sqrt{1 + 2m_2\lambda_r/m_1^2\lambda}\,\right)\right]. \end{aligned} \tag{4.11}$$

See Appendix 2 for details of the integration.

The regolith depth at fragmentation is, therefore, exponentially distributed so the mean depth is just the negative reciprocal of the expression inside the square brackets in equation (4.11),

$$E[X_r] = (m_1\lambda/2\lambda_r)[1 + \text{sign}(m_1)\sqrt{1 + 2m_2\lambda_r/m_1^2\lambda}\,]. \quad (4.12)$$

Note, because X_r has an exponential distribution, the standard deviation of X_r is equal to the mean depth.

How good is the diffusion approximation? The utility of these results is of course dependent on how well the diffusion approximates the true random walk. We now investigate the accuracy of the approximation by comparing the expressions for the regolith depth at fragmentation with Monte Carlo simulations of the actual process.

A Monte Carlo (computer) algorithm was constructed which followed the evolution of regolith depth at a point on the surface of a 300 km diameter strong asteroid unitl the asteroid was catastrophically fragmented by a large impact. Craters were positioned randomly on the surface and the change in regolith depth, at the modeled point, caused by each event was recorded. Figure 10 shows the Monte Carlo results when strength scaling was used for craters and their ejecta blankets (see the ejecta model described in Chapter 2).

Following the evolution at a single point until fragmentation represented one Monte Carlo "trial". The c.d.f. of regolith depth, shown in Figure 10, was constructed by performing 1000 trials. The stippled region in the figure represents a 95% confidence band derived from the Kolmogorov-Smirnov test statistic. The curve labeled "Approximation # 1" is the c.d.f. given by the diffusion approximation (equation 4.4) using the same cratering relationships and diameter

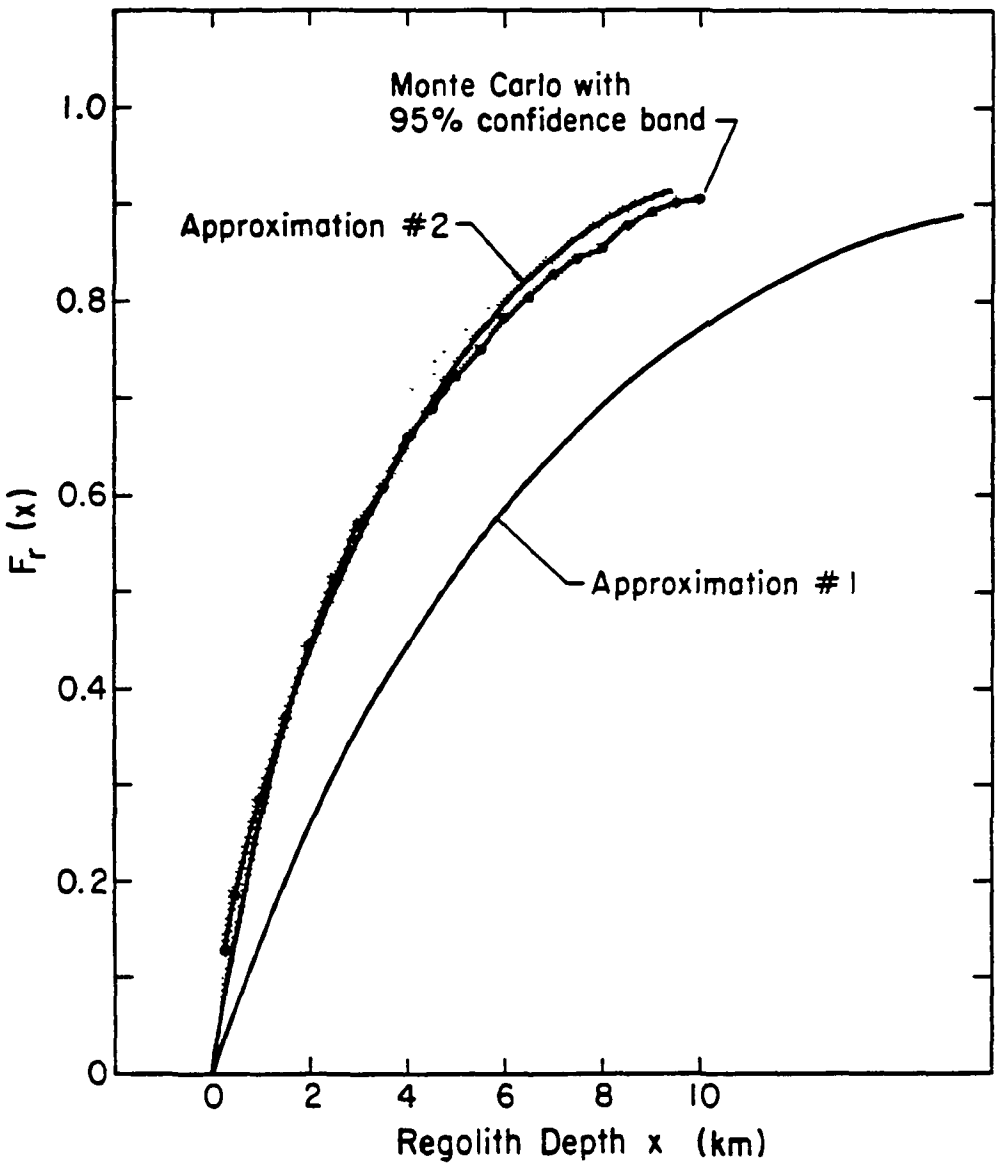


Figure 10. A test of the diffusion approximation. -- $F_r(x)$ is the probability that the regolith depth, at a randomly selected point on an asteroid's surface, is less than x at the time of catastrophic rupture. The series of connected points is the result of a Monte Carlo simulation of regolith growth. A 95 % confidence band is shown as a stippled region. Results from two analytical approximations to $F_r(x)$ are also plotted. The approximations are discussed in the text.

range used in the Monte Carlo calculations. Clearly the approximation is not very good for predicting regolith depth. If the mean depths implied by the respective probability distributions are computed, one finds that the diffusion gives values which are roughly a factor of 2-3 larger than the true (i.e. Monte Carlo) mean. Similar discrepencies are obtained when gravity scaling is used instead of strength scaling.

The reader may wonder why a Monte Carlo approach was not used to find the c.d.f. of regolith depth, rather than the method used to find an analytic expression. The problem is that when gravity scaling must be applied to craters, computing costs become large because a very large number of craters must be generated in each run in order to account for most of the mass in the impacting debris population. The analytic approach is, therefore, a matter of practicality.

An Improved Approximation

The diffusion approximation described above is merely a method by which the surface elevation is approximated by a normally distributed random variable. The elevation represents a sum of a large number of random jumps. But the normal approximation is expected to do best when many random variables are summed. The poor performance of the approximation is due to the fact that blanketing events are much more likely to occur than are excavation events because ejecta blankets cover a much bigger area than do crater bowls. Therefore, because the mean jump size is less than zero, the typical size of a positive jump is rather small compared to that of a negative

jump. That is, the evolution of surface elevation is characterized by many, relatively small, positive jumps and a few, rather large, negative jumps. One might guess that the excavation events are responsible for the bad performance of the normal approximation. A simple procedure is now described in which the largest excavation events can be "removed" from the approximation and treated separately.

The main effect of the occasional large excavation is to reset the regolith depth, at the modeled point, to zero. The depth at any time is just the amount of regolith accumulated since the last occurrence of a large excavation. In order to incorporate this fact into our model we can remove the large excavations from the diffusion and now let the regolith evolution proceed for a duration equal to the elapsed time since the last "large" event. The evolution time is discussed below, but first we define more precisely what is meant by a "large" excavation event.

We will define a crater diameter, D^*, and assume that if a crater of diameter larger than D^* excavates the surface point then the regolith depth is reset to zero. In order to be precise we should let D^* be a function of $X(t)$. However, this would make m_1 and m_2 functions of time and so would greatly complicate the analysis. Thus it seems worthwhile to try, as a first step, a value of D^* that is constant in time. A reasonable procedure is to let

$$D^* = E[X]/\mu \qquad (4.13)$$

where μ is the depth to diameter ratio assumed for craters and $E[X]$ is

the average regolith depth for either the fixed-time case (equation 4.6) or the case of fragmentation (equation 4.12). For the fixed-time case, E[X] is evaluated at the time, t, of interest. This probably makes an upper bound for D^* because the average regolith depth increases with time, so, early in the evolution craters smaller than $E[X]/\mu$ could reset the depth. There is of course nothing wrong with using an upper limit for D^*. In doing so we merely fail to exclude a few large excavations which are capable of zeroing the regolith depth. This is fine, as long as the diffusion approximation can handle these events. The accuracy of the improved approximation is considered below.

There is an obvious problem with equation (4.13): how can E[X] be determined until D^* is known? An iterative procedure could be used, however a much simpler method is to use the estimate of E[X] given by the "first-order" approximation (equation 4.6 or 4.12). Before proceeding to compute the evolution time we briefly consider the rate at which events occur.

Because some of the large excavation events are to be removed from the random walk, the rate of occurrence of events must be adjusted. If the rate of excavation events from craters larger than D^* (and of course smaller than D_r) is λ^*, then

$$\lambda^* = \int_{D^*}^{D_r} (\pi D^2/4)\, KaD^{a-1}\, dD$$

because $KaD^{a-1}dD$ is the number of craters produced (per area per time) in the diameter interval dD (see Chapter 2). The event rate is therefore just the total production rate of craters minus λ^*,

$$\lambda = 4\pi R_A^2 K (D_l^a - D_r^a) - \lambda^* \qquad (4.14)$$

where D_l is the smallest crater which forms on the asteroid.

Note also that the effects of large excavations must be excluded when calculating m_1 and m_2. The procedure for doing this is described in Appendix 1. We now separately consider the case of regolith depth at a fixed time t and the case of depth at the time of fragmentation.

The Regolith Depth at a Fixed Time, t. The large excavation events are excluded from the random walk itself but now, so as not to ignore the effects of these events, a new evolution time for the random walk must be computed. The random variable T_k is used to denote the random time of occurrence of the last event which resets the regolith depth (at the surface-point) to zero. The subscript k indicates that k reset-events occurred in the time interval (0,t). The new evolution time T^* is, therefore, just $t - T_k$ (see Figure 9). The p.d.f. of T^* is now derived. The probability that $t-T_k<s$ is just the probability that $T_k<t<T_{k+1}$, $T_k=y$, and $t-T_k<s$ for some combination of k and the dummy variable y. That is

$$\text{Prob}\{T^* < s\} = \text{Prob}\{t - T_k < s\}$$

$$= \sum_{k=0}^{\infty} \int_{\max(0,t-s)}^{t} \text{Prob}\{T_k \in dy,\ T_{k+1} - T_k > t-y\}. \tag{4.15}$$

The upper limit of integration in equation (4.15) appears because we require $y<t$ otherwise t would not lie between T_k and T_{k+1}. We also require $t-y<s$ because y represents a value for the random variable T_k and we want the probability that $t-T_k<s$. But y must be positive because T_k is always positive, so two cases need to be considered for the lower limit of integration. When $t>s$ then $y=t-s$ is the lower limit. When $t<s$ then $y=0$ is the lower limit. Note also that the $k=0$ term must be treated as a special case. Physically, $k=0$ means that fragmentation occurs before the regolith is ever reset to zero, i.e. $k=0$ is equivalent to $T_k=0$. So again two cases must be considered: when $t>s$ the $k=0$ term is zero because $t-T_k>s$. When $t<s$ the term is just $\exp(-\lambda^* t)$, the probability that the first reset-event occurs after time t.

The random variables T_k and $T_{k+1}-T_k$ are independent, hence their joint distribution given on the r.h.s. of equation (4.15) can be written as the product of their respective marginal distributions. The occurrence of events which reset the depth forms a Poisson process with parameter λ^*, so T_k is gamma distributed and $T_{k+1}-T_k$ is exponentially distributed. Therefore

$$\text{Prob}\{ T_k \in dy \} = \frac{\lambda^*}{(k-1)!} (\lambda^* y)^{k-1} e^{-\lambda^* y} dy$$

$$\text{Prob}\{ T_{k+1} - T_k > t-y \} = e^{-\lambda^*(t-y)}. \tag{4.16}$$

Substitution of equations (4.16) into (4.15) yields

$$\text{Prob}\{ T^* < s \} = \begin{cases} 1 - e^{-\lambda^* s} & s \leq t \\ 1 & s > t \end{cases} . \tag{4.17}$$

The p.d.f., $f^*(s,t)$, of T^* is seen to contain an atom of weight at $s=t$,

$$f^*(s,t) = \begin{cases} \lambda^* e^{-\lambda^* s} & s < t \\ e^{-\lambda^* s} & s = t \\ 0 & s > t \end{cases} . \tag{4.18}$$

Note that $f^*(s,t)ds$ is just the probability that the evolution time, i.e. the elapsed time between the last reset event and time t, is between s and $s + ds$.

The improved approximation for the c.d.f. of regolith depth at time t can now be obtained from

$$F(x,t) = \int_0^t F_0(x,s)\, f^*(s,t)\, ds + F_0(x,t)e^{-\lambda^* t} \qquad (4.19)$$

where, for notational convenience, we have used $F_0(x,t)$ to denote the "first approximation" to $F(x,t)$ given in equation (4.4). Unfortunately, the integral in equation (4.19) must be done numerically.

The mean regolith depth can be found from

$$E[X(t)] = \int_0^t E_0[X(s)]\, f^*(s,t)\, ds + E_0[X(t)]e^{-\lambda^* t} \qquad (4.20)$$

where, again, $E[X(t)]$ represents the first approximation to the mean depth given in equation (4.6). The variance of $X(t)$ is again found from the second moment, which is found from equation (4.7) and an expression analogous to equation (4.20).

The Regolith Depth at Fragmentation. For this case the p.d.f. of T^* differs from that given above because the fragmentation time T_r is a random variable. The c.d.f. can be written as

$$\text{Prob}\{T^* < s\} = \int_0^\infty \text{Prob}\{T^* < s \mid T_r = t\}\, w(t)\, dt . \qquad (4.21)$$

Substituting equations (4.17) and (4.9) into (4.21) yields

$$\text{Prob}\{ T^* < s \} = 1 - e^{-(\lambda^* + \lambda_r)s}.$$

Thus, we now have the remarkable result that the new evolution time, i.e. the time period between fragmentation and the last event to reset the regolith depth, is exponentially distributed with parameter $\lambda^* + \lambda_r$. This is fortunate because the improved approximation for the regolith depth c.d.f.,

$$F_r(x) = \int_0^\infty F_0(x,s)\, f^*(s)\, ds$$

can be obtained from equation (4.11) with no additional work. The functional form of $f^*(s)$ is the same as that of $w(s)$, so we can immediately write down the improved approximation for $F_r(x)$ by replacing λ_r in equation (4.11) by $\lambda^* + \lambda_r$,

$$F_r(x) = 1 - \exp[(m_1 x/m_2)(1 - \text{sign}(m_1)\sqrt{1 + 2m_2(\lambda^*+\lambda_r)/m_1^2\lambda}\,)]. \quad (4.22)$$

Similarly the expected value is

$$E[X_r] = \{m_1\lambda/2(\lambda_r+\lambda^*)\}(1 + \text{sign}(m_1)\sqrt{1 + 2m_2(\lambda^*+\lambda_r)/m_1^2\lambda}\,). \quad (4.23)$$

Again, the standard deviation is equal to the mean and so the variance can be obtained by squaring the r.h.s. of equation (4.23).

The steps followed in implementing the new approximation are: (1) Compute from equation (4.14) and compute m_1 and m_2 (Appendix 1) using a value of $D^*=D_r$ so that λ^*, the rate of formation of reset events, is zero; (2) Compute the first approximation for the mean regolith depth using either equation (4.6) or (4.12) depending on whether the depth at time t or the depth at fragmentation is desired; (3) Compute D^* using the mean depth and equation (4.13); (4) Recompute λ, m_1 and m_2 using the new value of D^*; (5) Find the improved approximations for $F(x,t)$ or $F_r(x)$ by using equation (4.19) or (4.22).

Using this procedure the accuracy of the new approximation was tested. The results can be compared to the Monte Carlo simulations (discussed in the previous section) in Figure 10. Clearly the approximation has been significantly improved. The c.d.f. computed from equation (4.19) lies well within the 95% confidence band. The values of $E[X_r]$ were found to differ by only $\pm 1\%$. Similar results were found when gravity scaling was examined.

Physical Interpretation of the Regolith Depth Equations

In the preceding section, approximations were developed for the c.d.f., the mean and the variance of regolith depth at a single point chosen at random on the surface of an asteroid randomly chosen from a large fictitious population of bodies, all with common size and strength. As discussed earlier, the depth varies over the surface of a given asteroid. Furthermore, each asteroid's regolith is unique, e.g. the mean depth on an asteroid changes depending on which body is chosen. At first glance, modeling the regolith depth at a single

point seems to have little practical application. However, because the asteroid and the surface point were selected at random, information about other points on the surface and about the surfaces of other bodies in the population should be implicit in the regolith depth equations. We now examine the stochastic model for clues concerning the global properties of an asteroid's regolith and how much "interasteroid variation" can be expected.

The C.D.F. of Regolith Depth. Suppose, for the sake of argument, that the surface of an asteroid could be sampled enough times to construct the distribution (i.e. the c.d.f.) of regolith depth on the asteroid. If this is done for a large number of asteroids of common size then the distributions for each body could be combined into an "overall" c.d.f. for the population. Taking a random sample of size one from this overall distribution is precisely equivalent to measuring the regolith depth at a randomly selected point on a randomly selected asteroid. The c.d.f. for regolith depth, derived in the previous section, is therefore the overall distribution of depths for the fictitious population.

The Expected Regolith Depth. Let us now arbitrarily assign an identifying number to each asteroid in the population such that once a number is specified, then the distribution of regolith depth on that asteroid is known. If a body is selected at random from the population and its identifying number is denoted by I, a uniformly distributed random variable, then, for example, the mean regolith depth at fragmentation is given by the conditional expectation

$E(X_r|I)$. The mean depth on a randomly selected asteroid is, therefore, a random variable whose average value is $E[E(X_r|I)] = E[X_r]$, where the expectation outside the square brackets is taken with respect to the distribution of I. The expected regolith depth can now be interpreted as the mean depth on an asteroid, averaged over many bodies of the same size and strength.

The Variance of Regolith Depth. The variance of the depth (for example, at fragmentation) can be written as the sum of two components,

$$\mathrm{Var}[X_r] = E[\mathrm{Var}(X_r|I)] + \mathrm{Var}[E(X_r|I)] \qquad (4.24)$$

where $\mathrm{Var}(X_r|I)$ is a random variable representing the variance of depth on a particular (but unknown) asteroid. The first component is the variation in depth over an arbitrary asteroid's surface, averaged over the bodies in the fictitious population. The second component represents the variation in the mean depth among bodies.

The determinate models, discussed in Chapter 3, attempted to reduce the total variance (in order to make the average a meaningful desciptor of regolith depth) by minimizing the first component only. This was done by excluding areas on an asteroid's surface that were occupied by large craters. The amount by which the determinate models reduce the first component, and the relative magnitude of the two components, is discussed in the next two chapters. In any event, the

total variance of regolith depth can be used as an indicator of how well the average value can characterize the variation of depth over one asteroid's surface and the variation in depth among asteroids.

The Amount of Brecciated Material Liberated from Asteroids

One observable property of the brecciated meteorites, which colud prove useful as an indicator of parent body size, is the volumetric fraction of brecciated material in a given group of meteorites. Assuming that brecciated material was derived from asteroidal regoliths (as opposed to an origin in the zones of fracturing beneath crater bowls), the regolith-depth equations described in the previous section can specify the amount of brecciated material liberated from an asteroid. The computed quantity can be compared to observed values in order to eliminate certain sizes of asteroids from the list of possible parent bodies.

Asteroids release debris to space in essentially two ways. Low-energy impacts produce craters which excavate surface material, part of which is able to escape the asteroid. In this case the fraction of ejecta which is brecciated is determined by the size of the crater and the regolith depth at the impact point. High-energy impacts can fragment and disperse an entire asteroid. Here the fraction of brecciated debris is determined by the volume of an asteroid's regolith. These two cases, i.e. noncatastrophic and catastrophic events, are treated separately.

Debris Liberated in Cratering Events

Consider the case where a group of meteorites is derived from some number, n, of cratering events on the surface of a given size asteroid. (The possibility of deriving meteorites from more than one impact on more than one asteroid is discussed in a later chapter.) The fraction Q(n) of brecciated ejecta resulting from n impacts can be written as

$$Q(n) = \sum_{j=1}^{n} v_j \Big/ \sum_{j=1}^{n} V_j \qquad (4.25)$$

where v_j is the volume of brecciated material which escapes the asteroid during the jth impact event and V_j is the total volume of ejecta escaping the asteroid during the jth impact.

A complete statistical analysis of the problem, e.g. finding the p.d.f. of Q(n), is exceedingly difficult. In order to make calculations tractable we must to make some simplifying assumptions. Even so, expressions can be derived for the mean and variance of Q(n) which are sufficiently accurate for present purposes.

We assume that v_j can be expressed as

$$v_j = \pi D_j^2 X_j q_j / 4 \qquad (4.26)$$

where D_j is the crater diameter for the jth event, X_j is the regolith depth at the point of impact, and q_j is the fraction of ejecta which escapes. Note q_j may depend on crater diameter. Equation (4.26) is not strictly correct, for three reasons. (1) The equation implies

that craters have the shape of flat-bottomed cylinders. In reality craters are roughly bowl-shaped. However, for a bowl-shaped geometry, v_j contains quadratic and cubic terms in X_j. The presence of these terms precludes the derivation of an expression for the variance of Q(n), hence the simple expression is adopted. (2) When the crater depth is less than the regolith depth at the impact point, equation (4.26) no longer applies. The total volume of regolith ejected from a crater is equal to the crater volume, independent of X_j. In order to avoid this problem, craters too small to puncture through the regolith layer, i.e. craters for which equation (4.26) is incorrect, are ignored. This is not a bad approximation because, as discussed in Chapter 2, the largest craters contain more mass than the smaller ones. This tends to make the computed values of Q(n) slightly low. (3) Regolith- and nonregolith-derived ejecta are assumed to have the same chance of escaping. Actually, the regolith is more likely to escape because ejection velocities tend to be highest near the surface. Again, this means Q(n) will be slightly underestimated.

These three circumstances make the expressions for Q(n) approximate. However a more detailed model probably would not drastically change the conclusions reached. We now proceed with the derivation of the mean and variance of Q(n).

The volume of escaping debris, both regolith and nonregolith, can be expressed as

$$V_j = cD_j^3 q_j/8 \tag{4.27}$$

where c is given in equation (2.4). From equations (4.25), (4.26) and (4.27) Q(n) can be written as

$$Q(n) = b \sum_{j=1}^{n} D_j^2 X_j q_j \Big/ \sum_{j=1}^{n} D_j^3 q_j \tag{4.28}$$

where $b=2\pi/c$.

The Expected Value of Q(n). Consider an asteroid of radius R_A selected at random from a large (fictictious) population of such bodies, each labeled by an identifying number. If I is a random variable representing the identifying number of an asteroid under consideration, then the mean value of Q(n) is

$$E[Q(n)] = \int \cdots \int \sum_{I} E[Q(n) | D_1=u_1, \cdots, D_n=u_n, I=i] \cdot \text{Prob}\{ I=i \} \prod_{j=1}^{n} f(u_j)\, du_j \tag{4.29}$$

where $f(u_j)$ is the p.d.f. for the random variable D_j. Equation (4.28) allows us to write

$$E[Q(n)|D_1=u_1, \cdots, D_n=u_n, I=i] = b\, E[X|I=i]\, \phi_2/\phi_3 \qquad (4.30)$$

$$\phi_2 = \sum u_j^2 q_j$$

$$\phi_3 = \sum u_j^3 q_j$$

$$\phi_4 = \sum u_j^4 q_j .$$

Note that $E[X_j|I=i]$ is assumed to be the same for all j, i.e. we have assumed that the formation of one crater doesn't substantially affect the regolith over the rest of the asteroid. Also, because the regolith depth is time dependent, we assume that the n craters are not widely separated in time. If equation (4.30) is substituted back into equation (4.29) and the summation over I is performed, we obtain

$$E[Q(n)] = b\, E[X] \int \cdots \int (\phi_2/\phi_3) \prod f(u_j)\, du_j . \qquad (4.31)$$

The method used to evaluate the n-fold integral in equation (4.31) is described later.

The Variance of Q(n). The second moment of Q(n) is

$$E[Q^2(n)] = \int \cdots \int \sum_I E[Q^2(n)|D_1=u_1, \cdots, D_n=u_n, I=i] \cdot \text{Prob}\{ I=i \} \prod f(u_j)\, du_j . \qquad (4.32)$$

If we square the expression given for Q(n) in equation (4.28) then

$$E[Q^2(n)|D_1=u_1, \cdots, D_n=u_n, I=i] = (b/\phi_3)^2 \left\{ E[X^2|I=i]\phi_4 + E^2[X|I=i] \sum\sum_{j\neq k} u_j^2 u_k^2 q_j q_k \right\} \tag{4.33}$$

$$= (b/\phi_3)^2 \{ \text{Var}[X|I=i]\phi_4 + E^2[X|I=i]\phi_2^2 \}.$$

Substituting this expression into equation (4.32) yields

$$E[Q^2(n)] = b^2 E[\text{Var}(X|I)] \int\cdots\int \left\{ \phi_4/\phi_3^2 + (\phi_2/\phi_3)^2 \sum_I E^2[X|I=i] \text{ Prob } \{ I=i \} \right\} \prod f(u_j)\, du_j. \tag{4.34}$$

If we add and subtract the quantity

$$b^2 \left(\sum_I E[X|I=i] \text{ Prob}\{I=i\} \right)^2 \int\cdots\int (\phi_2/\phi_3)^2 \prod f(u_j)\, du_j$$

on the r.h.s. of equation (4.34) and note that the term which is summed over I in this quantity is just EX, then

$$E[Q^2(n)] = b^2 \int\cdots\int \left\{ \phi_4 E[\text{Var}(X|I)] + \phi_2^2 \text{Var}[E(X|I)] + \phi_2^2 E^2[X] \right\} \phi_3^{-2} \prod f(u_j)\, du_j. \tag{4.35}$$

In order to simplify the expressions let us write

$$\mathrm{Var}[X] = k_1 E^2[X] \qquad (4.36)$$

and

$$\mathrm{Var}[E(X|I)] = k_2 E[\mathrm{Var}(X|I)]$$

where k_1 and k_2 are constants for a given size of asteroid. We can now substitute equations (4.36) into equations (4.35), subtract $E^2[Q(n)]$ from equation (4.35), and simplify to obtain

$$\mathrm{Var}[Q(n)] = \{(bE[X])^2/(1+k_2)\}\int\cdots\int\left\{[1 + k_2(1+k_1)]\,\phi_2^2 + k_1\phi_4\right\}\phi_3^{-2}\prod f(u_j)\,du_j - E^2[Q(n)]. \qquad (4.37)$$

The values of the constants k_1 and k_2 are estimated from Monte Carlo experiments described in Chapter 5.

In order to use equations (4.31) and (4.37) the n-fold integrals must be evaluated. The functional form of $f(u_j)$ precludes an analytic evaluation. Numerical methods can be used but become extremely expensive for $n>3$. However there is a very simple way to perform the integrals. Note that the integrals always appear as a function of the n crater diameters multiplied by the joint p.d.f. of the diameters. That is, the integrals are really just expected values of the functions. For example, the integral in equation (4.31) is the expected value of the function ϕ_2/ϕ_3. These expectations can easily be evaluated by Monte Carlo methods. The integral in equation (4.31)

can be evaluated if we generate n crater diameters at random (following the joint p.d.f.), evaluate the function shown above and then repeat this process many times to get an average value. A similar method can be applied to the integral in equation (4.37).

The Monte Carlo calculations were performed as follows. The formation rate of craters of diameter D or larger was assumed to be proportional to D^a where a is a constant (see Chapter 2 for details). The probability of getting a crater in a given size range was taken as proportional to the formation rate weighted by the volume of material the craters liberate to space. This weighting was used because the chance that a meteorite was liberated from its parent body by a crater of some specified diameter depends on the volume of debris contributed by all of the craters of the given size. The smallest crater generated was one whose depth was equal to the mean regolith depth because, as mentioned earlier, the expressions for Q(n) are valid only for those craters which puncture through the regolith layer.

The fraction of ejecta which escapes an asteroid was taken to be a constant (for a given size of asteroid) when strength scaling was applicable to craters. When gravity scaling was appropriate q_j was taken to be proportional to D_j in accord with the ejecta velocity distributions discussed in Chapter 2.

The results of calculations are given in Chapter 5. We now consider the volumetric fraction of brecciated debris liberated when an asteroid is catastrophically fragmented.

Debris Liberated in Catastrophic Events

When an asteroid is finally ruptured and dispersed by an energetic impact, the fraction of debris which is brecciated is the total volume of regolith divided by volume of the asteroid. The volume of regolith on an asteroid of radius R_A chosen at random from a large (fictitious) population of such bodies is

$$\begin{aligned} \text{vol. of regolith} &= \int_0^\infty (\text{surface area with depth} \in dx) \cdot x \\ &= \int_0^\infty 4\pi R_A^2 \, \text{Prob}\{ X_r \in dx \mid I \} \, x \\ &= 4\pi R_A^2 \, E[X_r \mid I] \end{aligned} \tag{4.38}$$

where X_rr is the regolith depth at fragmentation and I is the (random) identifying number of the asteroid chosen. The fraction Q_r of brecciated material is

$$Q_r = 4\pi R_A^2 \, E[X_r \mid I]/(4\pi R_A^3/3) = (3/R_A) \, E[X_r \mid I]. \tag{4.39}$$

Q_r is, therefore, a random variable whose expectation is

$$E[Q_r] = (3/R_A) \, E[X_r] \tag{4.40}$$

and whose variance is

$$\text{Var}[Q_r] = (9/R_A^2) \, \text{Var}(E[X_r \mid I]). \tag{4.41}$$

If we use equations (4.36) and note that, as shown earlier in this

chapter, the mean regolith depth at fragmentation is equal to the standard deviation (i.e. $k_1 = 1$ in equation 4.36), then the standard deviation of Q_r is

$$\sigma_{Q_r} = \sqrt{k_2/(1+k_2)}\ E[Q_r] \qquad (4.42)$$

Equations (4.40) and (4.42) give the mean and standard deviation of Q_r at the time when an asteroid is catastrophically fragmented. But, as mentioned in the Introduction and in Chapter 2, fragmentation does not necessarily imply that the fragments are dispersed. Therefore, an asteroid may undergo a number of fragmentation events before complete dispersal occurs. This effect could increase Q_r significantly.

The manner in which a large impact affects regolith evolution is poorly known. Impacts which are energetic enough to cause fragmentation (but not dispersal) may still eject a large quantity of material from an asteroid. Perhaps the uncohesive regolith is preferentially lost in such impacts; that regolith which is retained may be mixed into the asteroid's interior.

Keeping in mind the uncertianties involved, let us make a crude estimate of the mean and standard deviation of Q upon dispersal of an asteroid. We will estimate the number of times an asteroid experiences fragmentation before dispersal and assume that regolith evolution proceeds as "usual", i.e. as described in the first section of this chapter, in the time intervals between fragmentation events.

Fragmentation occurs when a mass larger than m_r strikes an asteroid, thus forming a crater of diameter $>D_r$. Dispersal is defined to occur when a mass larger than say, m_d, occurs. The value of m_r is determined by setting the kinetic energy of a projectile of mass m_r equal to the product of an asteroid's volume and the impact strength, s_i, for the asteroid. The parameter s_i was described in Chapter 2. We will estimate m_d by equating the projectile kinetic energy to the sum of the energy required for fragmentation and the energy required to disperse the fragments, which is taken to be the gravitational binding energy of the asteroid. Note that some of the impact energy should be partitioned into heating of the target and the angular momentum of the fragments. Thus our estimate of both m_d and the number of fragmentation events before dispersal will be lower limits. We now have

$$m_r = (2/v_i^2)\ 4\pi R_A^3 s_i/3$$

and (4.43)

$$m_d = (2/v_i^2)\ [4\pi R_A^3 s_i/3 + 16G\pi^2\rho^2 R_A^5/15].$$

The second term in the expression for m_d is the gravitational binding energy for an asteroid of radius R_A and density ρ. G is the gravitational constant.

Recall that λ_r is the rate at which an asteroid is impacted by masses larger than m_r. We denote by λ_d the rate of impacts of masses larger than m_d. In any catastrophic event, i.e. in any impact of mass larger than m_r, the probability that the impact is a dispersal event is λ_d/λ_r. The number, N_r, of fragmentation events that occur before dispersal can be viewed as a geometrically distributed random variable with parameter λ_d/λ_r. Thus the mean and variance of N_r are

$$E[N_r] = \lambda_r/\lambda_d - 1$$

and (4.44)

$$Var[N_r] = (\lambda_r/\lambda_d)\ (\lambda_r-\lambda_d)/\lambda_d .$$

Now if S_j is the volume of regolith developed between the j-1th and the jth fragmentation events then the total volume of regolith, S, at dispersal is

$$S = S_1 + \cdots + S_{N_r+1} \qquad (4.45)$$

To make the problem tractable, the random variables S_j are assumed independent of one another and of N_r. This assumption will break down when N_r becomes large, i.e. when an asteroid is fragmented so many times that it is composed mostly of regolith. Taken to the extreme, S will become larger than the volume of the asteroid.

The value of Q at dispersal, denoted by Q_d, is obtained by dividing both sides of equation (4.45) by the volume of the asteroid. In doing so we find the mean and variance of Q_d to be

$$E[Q_d] = E[N_r + 1]\ E[Q_r]$$

and (4.46)

$$Var[Q_d] = E[N_r + 1]\ Var[Q_r] + E^2[Q_r]\ Var[N_r + 1].$$

Using the expressions for the mean and variance of Q_r (equations 4.40 and 4.41) and the constant k_1 introduced earlier, the mean and standard deviation of Q_d are found to be

$$E[Q_d] = (\lambda_r/\lambda_d)\ E[Q_r]$$

and (4.47)

$$\sigma_Q = E[Q_d] \sqrt{\{ k_2/(1+k_2) + (\lambda_r-\lambda_d)/\lambda_d \}\ \lambda_d/\lambda_r}\ .$$

Finally we note that, because the flux of projectiles of mass larger than m is proportional to m^{a_m}, the ratio λ_r/λ_d is just $(m_r/m_d)^{a_m}$.

A Monte Carlo Algorithm for the Irradiation of Regolith Grains

As discussed in the previous chapter, the charged particle irradiation of regolith grains has not yet been simulated in detail. Borg et al. (1975) gave a brief account of a Monte Carlo simulation of regolith grains but their simulation was far from comprehensive. Housen et al. (1979a) considered the extent to which a regolith grain is gardened by impacts and, by using mean excavation and burial rates, estimated the amount of time a regolith grain might spend near the surface. But they used the projectile flux and cratering laws applicable to large craters. While large craters dominate regolith growth, the small impacts play a very important role in determining the exposure history of regolith grains. In this section a Monte Carlo computer program is described which simulates the random walks and irradiation histories of regolith grains.

In the program a regolith grains starts out at a specified initial (time=0) depth below the surface. At exponentially weighted time intervals the grain experiences random jump events. The size of a jump is determined by randomly generating a crater diameter and the distance between the grain and the crater center. In order to account for the "kinks" in the projectile mass distribution, the differing impact velocities for cometary and asteroidal debris, and changes in scaling laws with crater size, the crater diameter distribution is divided into a number of bins. Within each bin the diameter distribution is a power law which is determined by the projectile mass

distribution, the impact velocity and the scaling law appropriate to the particular bin (equation 2.3).

Depending on the the crater diameter and location, the grain can either (a) move further beneath the surface if it is buried by ejecta, (b) move toward the surface if the crater removes some material above the grain, or (c) excavate the grain from the regolith. When an excavation occurs the grain is either randomly emplaced in an ejecta blanket or ejected from the asteroid.

The type (a) events deserve a little more explanation. For gravity scaled craters or large strength scaled scraters the magnitude of a burial event is determined from the ejecta blanket model described in Chapter 2. For small strength scaled craters a slightly different procedure is used because these craters are not expected to have continuous ejecta blankets. For example, according to the ejecta model described in Chapter 2, a 1 cm crater on a 300 km diameter asteroid should have a continuous ejecta deposit with a maximum thickness of 0.3 microns. In order to model small scale ejecta deposits in a more realistic manner the debris from small strength scaled craters are assumed to occur as discrete fragments. The number of fragments with mass in a small interval dm is taken to be proportional to $m^{a_{f-1}}$. The proportionality constant and the mass, m_L, of the largest fragment generated are determined by setting the total mass of fragments equal to the nonescaping mass of ejecta and by setting the number of fragments of mass$>m_L$ equal to 1. The value of a_f and the smallest size of fragment are free parameters. A nominal

value of a_f=0.-67 is adopted as suggested by various impact experiments (e.g. Hartmann, 1969). The smallest size of fragment considered is 1 micron. Variations from the nominal values are also investigated.

Note that, in reality, a grain will experience a great may jumps due mainly to the large number of small cratering events. Lest the Monte Carlo program run slower than the actual process, only a part of the jumps are handled on an individual basis. Impact events which change the grain depth by less than a specified percentage, p, are assumed to form a continuous process. In the time intervals between large discrete jumps the effects of the small events are added in. The choice of p is somewhat arbitrary. A nominal value of 1% is used and the effects of variation from this value are investigated.

Using this procedure a grain undergoes random walk either until it is ejected from the asteroid or until a specified time limit is exceeded. The program keeps track of the total time spent at various depths beneath the surface so that an exposure age can be computed for the grain. By using the charged-particle flux described in Chapter 2 and by using many trial grains, a distribution of particle-track densities can be determined.

The results from this Monte Carlo program and from the expressions derived earlier are presented in the next chapter.

CHAPTER 5

RESULTS

The expressions derived in Chapter 4 have been evaluated for various sizes of both strong and weak asteroids. The results pertaining to regolith depth are presented first. The calculation of Q and the results from the Monte Carlo irradiation program are given in the second and third sections.

Regolith Depth

The Depth as a Function of Time

Equation (4.20) was used to find the mean regolith depth as a function of time for several sizes of asteroids. The cratering laws and ejecta model described in Chapter 2 were adopted as nominal parameters and the effects of variations from these values were tested. Figure 11 shows the mean depth for four sizes of strong asteroids. The dashed lines in the figure represent plus and minus one standard deviation from the mean value. The collisional fragmentation lifetime of each asteroid is indicated by a vertical line.

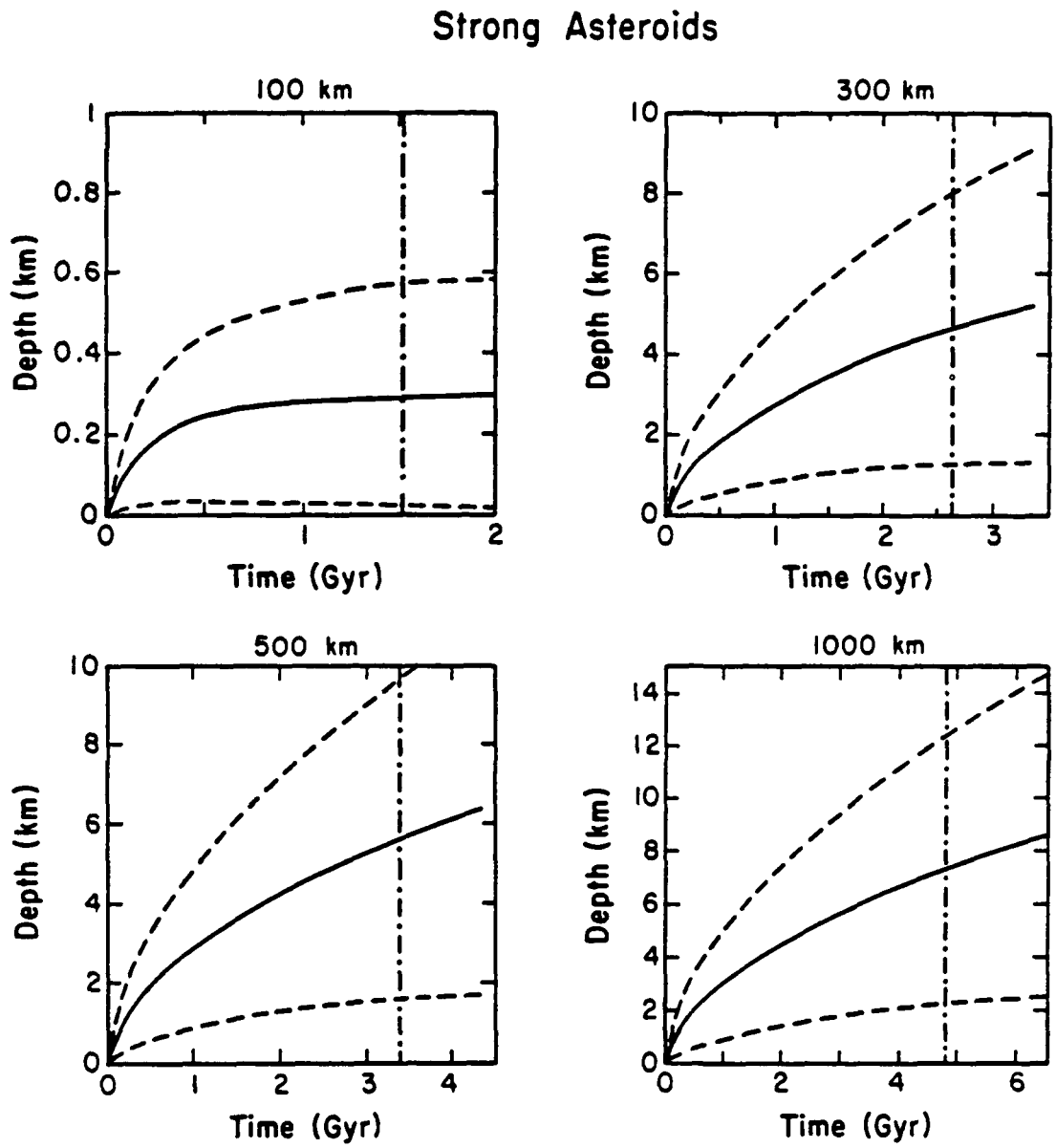


Figure 11. Depth of regolith vs. time for rocky asteroids. -- The solid line in each plot represents the mean regolith depth. The dashed lines indicate plus and minus one standard deviation from the mean. The time of catastrophic fragmentation is shown as a vertical line (dash-dot).

A 1000 km diameter asteroid acquires a mean depth of roughly 7 km over its 5 Gyr collisional lifetime. Note that the regolith depth is highly variable, as indicated by the large standard deviation. The source of the large variance is discussed below. Smaller asteroids develop less regolith because less crater ejecta are retained and because of shorter lifetimes. Bodies smaller than 100 km-diameter are not shown in the figure because they lose nearly all crater ejecta and therefore develop negligible regoliths.

Gravity scaling was used for cratering on the 500 km and 1000 km asteroids because the largest craters, i.e. the ones most important for regolith growth, are gravity scaled (see discussion in Chapter 2). Both gravity and strength scaling were applied to the 300 km asteroid, however the results were nearly identical. Strength scaling was used for the 100 km body.

The computed depths were examined for sensitivity to changes in the cratering laws and the ejecta velocity distribution. For example if a_e, the exponent in the ejecta velocity distribution, is varied from the nominal value of 2 to a value of 1, then the depth decreases by a factor of 1.5, primarily because a_e=1 means more crater ejecta is able to escape (see equation 2.5). If the proportionality constants in the cratering laws are varied by 25% then the depth changes by roughly a factor of 2 in the same direction as the change in the cratering constants. Thus the depth is fairly sensitive to uncertainties in the cratering laws.

Calculations for two weak asteroids are shown in Figure 12. Meter-scale and centimeter-scale regoltihs are developed on asteroids of diameter 10 km and 2 km. Smaller bodies lose nearly all crater ejecta. Strength scaling was used for both sizes of bodies. Gravity scaling is marginally applicable for the 10 km body; it produces regoliths roughly twice as thick as strength scaling. For these weak bodies, the sensitivity of the results to variations in a_e and the cratering constants are the same as those for strong asteroids.

Results for larger weak asteroids are not shown because the adopted impact strength for weak targets produces unrealistically low fragmentation lifetimes and regoliths depths (see Table 5, discussed below). For large weak bodies, high internal lithostatic pressures will probably produce impact strengths much larger than those adopted. If, as a limiting case, the strength is assumed to be approximately equal to that adopted for strong targets, then the regolith depths computed for large weak asteroids would be comparable to those for large strong ones because, when in the gravity scaling regime, cratering laws are relatively independent of target strength.

The Time Required to Reach Equilibrium

The characteristic time required for a regolith to reach an equilibrium state (equation 4.8) is shown in Table 5. The equilibrium times and depths, which were computed from the first approximation derived in Chapter 4, are meant only to be rough estimates. Judging by the accuracy of the first approximation, these depths (and times?) may be a factor of 2-3 too high. In order to test the accuracy of

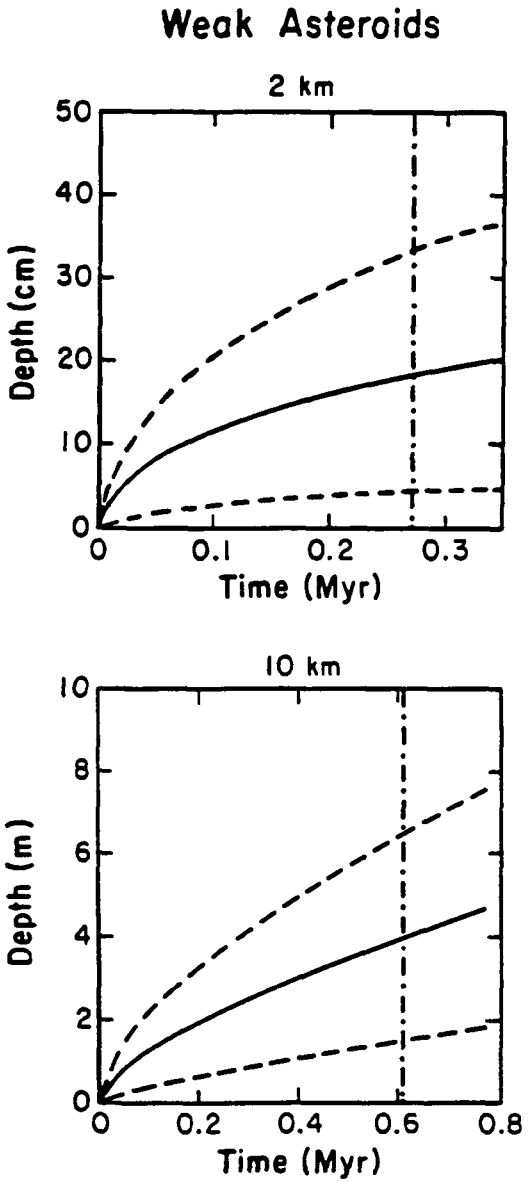


Figure 12. Depth of regolith vs. time for weak asteroids.

Table 5

Regolith Depth at Fragmentation and at Equilibrium

strong asteroids

asteroid diam.	crater scaling law	equil. time	equil. depth	mean frag time	mean depth at frag.
100 km	strength	0.88Gyr	2km	1.5Gyr	0.23km
300	strength	22	23	2.6	3.6
300	gravity	100	39	2.6	3.7
500	gravity	240	65	3.4	4.6
1000	gravity	780	130	4.8	6.1

weak asteroids

asteroid diam.	crater scaling law	equil. time	equil. depth	mean frag time	mean depth at frag
2 km	strength	3.4Myr	7.4m	0.27Myr	15cm
10	strength	1.1Gyr	0.47km	0.61	3.5m
10	gravity	4.5	1.3	0.61	7.6
100	gravity	220	13.2	1.9	16
300	gravity	1500	40	3.3	24
500	gravity	3500	67	4.3	28
1000	gravity	12000	136	6.2	36

these estimates, a Monte Carlo simulation of a 300 km strong asteroid was performed. The results are shown in Figure 13. The asteroid was allowed to evolve, without the occurrence of catastrophic fragmentation events, for a period of 50 Gyr. The regolith depth at a surface point was measured every 1 Gyr. This experiment was repeated 100 times so that an average depth as a function of time could be constructed. The predicted equilibrium time for this asteroid is 22 Gyr (Table 5) which appears to be in reasonable agreement with Figure 13. As suggested above, the actual equilibrium depth is roughly a factor of 2-3 lower than that given in Table 5.

Small bodies have shorter equilibrium times than do large asteroids, for two reasons. First, small bodies do not retain much ejecta so large craters cannot cause large fluctuations in regolith depth which might slow down the approach to equilibrium. Secondly, on large asteroids, the equilibrium time is highly dependent on the time interval between the occurrence of the biggest allowable craters, which increases with increasing asteroid size.

Weak asteroids take longer to reach equilibrium than do strong bodies of equal size. Because ejecta velocities are quite low in uncohesive targets, weak asteroids retain more crater ejecta than strong asteroids. Thus the value of m_1, i.e. the mean size of a jump in surface elevation, approaches zero, so t_e gets large (see equation 4.8). Physically this means the surface elevation (and regolith depth) may take very large positive excursions. Thus a long time is required for the random walk to settle into equilibrium.

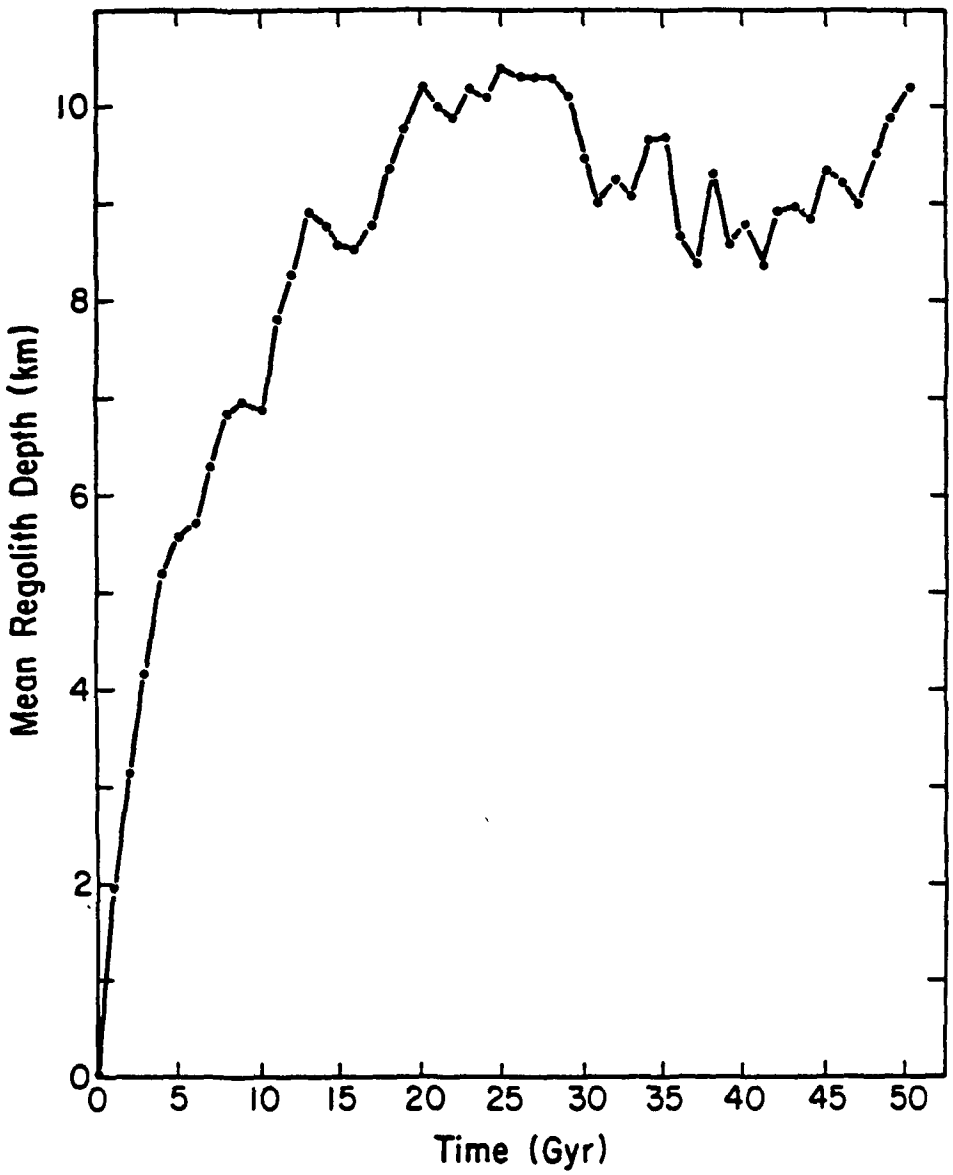


Figure 13. The approach of the mean depth to an equilibrium value. -- The mean depth was computed from Monte Carlo simulations of regolith growth on a 300 km rocky asteroid. The time required to reach equilibrium is several times larger than both the asteroid's fragmentation lifetime and the age of the solar system. As discussed in the text, this conclusion applies to most sizes of asteroids.

For nearly all the asteroids shown in the table, equilibrium times are at least as large as fragmentation lifetimes and, in general, excéed the age of the solar system. In fact for all bodies, except the 100 km strong one, fragmentation occurs at a factor of ten more quickly than does equilibrium.

The Depth at Fragmentation

The mean regolith depth at the time when an asteroid is catastrophiclly fragmented was computed from equation (4.23). Results are given in Table 5. Note, from the expressions derived in Chapter 4, the standard deviation of regolith depth at fragmentation is equal to the mean value.

The regolith depth on large strong asteroids is generally in the kilometer range. The depths computed for weak bodies are much smaller due to the short collisional lifetimes. For the larger weak bodies, the actual lifetimes are undoubtedly larger that those shown and therefore serve as extreme lower limits. If the impact strength for these bodies is similar to that of the strong asteroids, then the computed depths would be approximately equal to those expected for the strong asteroids, as discussed above.

Not surprisingly, the mean depth at fragmentation is not equal to the mean depth evaluated at the mean fragmentation time (cf. Table 5 and Figures 11 and 12). Differences as large as 30% occur. This fact is generally not considered in other current models of regolith depth at fragmentation.

The Variance of Regolith Depth

Both the regolith depth at fixed time and at fragmentation exhibit a large variance. As shown in Chapter 4, the variance can be broken into two components: (1) the average variation in depth over any one asteroid's surface and (2) the variation in the average depth among bodies of equal size. We now consider the relative magnitude of these two components in order to see if one or the other is primarily responsible for the large total variance.

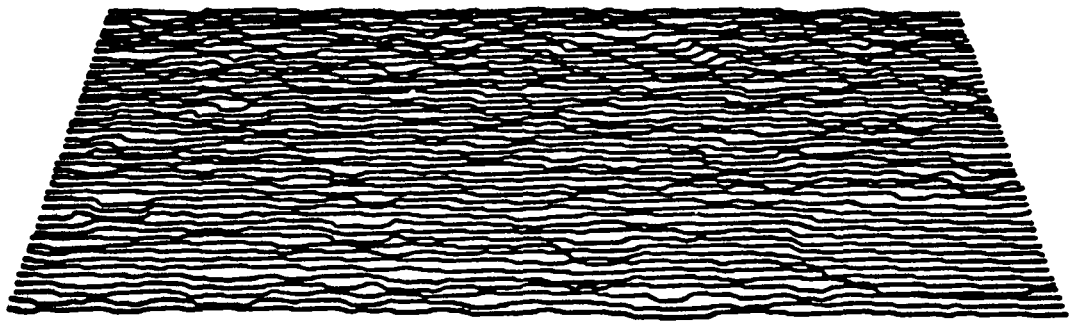
A Monte Carlo computer program was written in order to simulate regolith evolution. In the program the surface of an asteroid was represented by a square grid. Craters were generated on the grid until a large impact resulted in catastrophic fragmentation. The regolith depth at each grid point was followed throughout the evolution. For each asteroid, the mean and standard deviation of regolith depth was computed. This experiment was repeated many times so that the average variation in depth over a surface and the interasteroid variation in the average depth could be found.

Simulations were performed for two generic types of bodies: "small" asteroids, on which low gravity fields result in widespread ejecta deposits, and "large" asteroids, on which ejecta are constrained to lie near craters. The actual diameter division between small and large asteroids, i.e. the division between global and nonglobal ejecta deposits, depends on the material strength of an asteroid because ejecta velocities depend on material strength (see discussion in Chapter 2). Thus, as noted by Housen et al. (1979a),

ejecta should be widespread on rocky bodies of diameter less than a couple of hundred kilometers. On weak bodies, where ejecta velocities are lower, global ejecta deposits should occur for diameters less than a few kilometers. In the simulations of small asteroids, ejecta were spread in a uniform layer over the surface. For large bodies the ejecta blanket profile described in Chapter 2 was adopted as a nominal model and two additional models were examined, i.e. (1) the thickness was constant out to a distance of one crater radius beyond the crater rim, and zero beyond, and (2) the thickness decreased linearly from a maximum at the rim to zero at a distance of one radius from the rim. The results for large bodies were found to be relatively insensitive to the ejecta model used.

The output for a "typical" small asteroid is shown in Figure 14a. In the figure, the regolith depth, i.e. the thickness of the debris layer, is plotted as a function of position on the surface grid. The Monte Carlo experiments showed that, for small asteroids, the average variation in depth over a surface was roughly equal to the variation in mean depth between bodies. That is, the two components of variance in equation (4.24) were about equal. A similar plot for a large asteroid is shown in Fig. 2b. (Note, in order to graphically illustrate the effects of differing eject morphologies on large and small bodies, the same sequence of crater sizes and positions, used in part a of the figure, were used in part b.) The experiments for large bodies showed that the average surficial variation in depth (i.e. the first component in equation 4.24) was 1.5 to 2 times larger than the

(a)



(b)

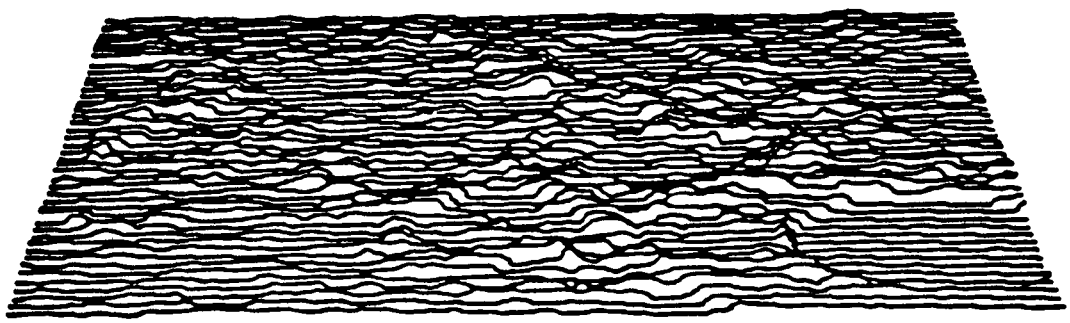


Figure 14. Regolith depth as a function of position on an asteroid's surface. -- Part (a) applies to an asteroid which is sufficiently small such that crater ejecta are globally spread over the surface. Part (b) represents a larger body, where ejecta are constrained to lie near craters. The increased variability in depth is due to the localization of ejected debris.

variance of the mean depths (the second component in equation 4.24). This is due to the increased roughness caused by the localization of ejecta. Thus, it would appear that neither component vastly dominates the other.

The Amount of Brecciated Material Released to Space

Recall that, for n impacts on an asteroid, Q(n) is the volume fraction of escaping ejecta that is brecciated, i.e. derived from the regolith. Q_r is the volume fraction at the time when an asteroid is catastrophically ruptured and Q_d is the fraction resulting from dispersal of a body. Results for strong asteroids and weak asteroids are shown in Figures 15, 16 and 17. The open circles in the figures represent the mean value of Q(n), Q_r or Q_d when gravity scaling is applied to craters. The solid dots indicate strength scaling. Plus and minus one standard deviation from the mean are indicated by the vertical "error bars". In Figures 16 and 17 these appear as dashed lines when the mean time for fragmentation or dispersal exceeds 4.5 Gyr.

Results for the case of a single impact (n=1) on strong asteroids are shown at the top of Figure 15. The n-fold integrals required when calculating Q(n) (see equation 4.31) were evaluated using the Monte Carlo technique described in Chapter 4. The required mean and standard deviation of regolith depth were found from the expressions for depth as a function of time, evaluated at a time of 3.5 Gyr. The mean and standard deviation were used to evaluate the constant, k_1, introduced in Chapter 4. The constant, k_2, which

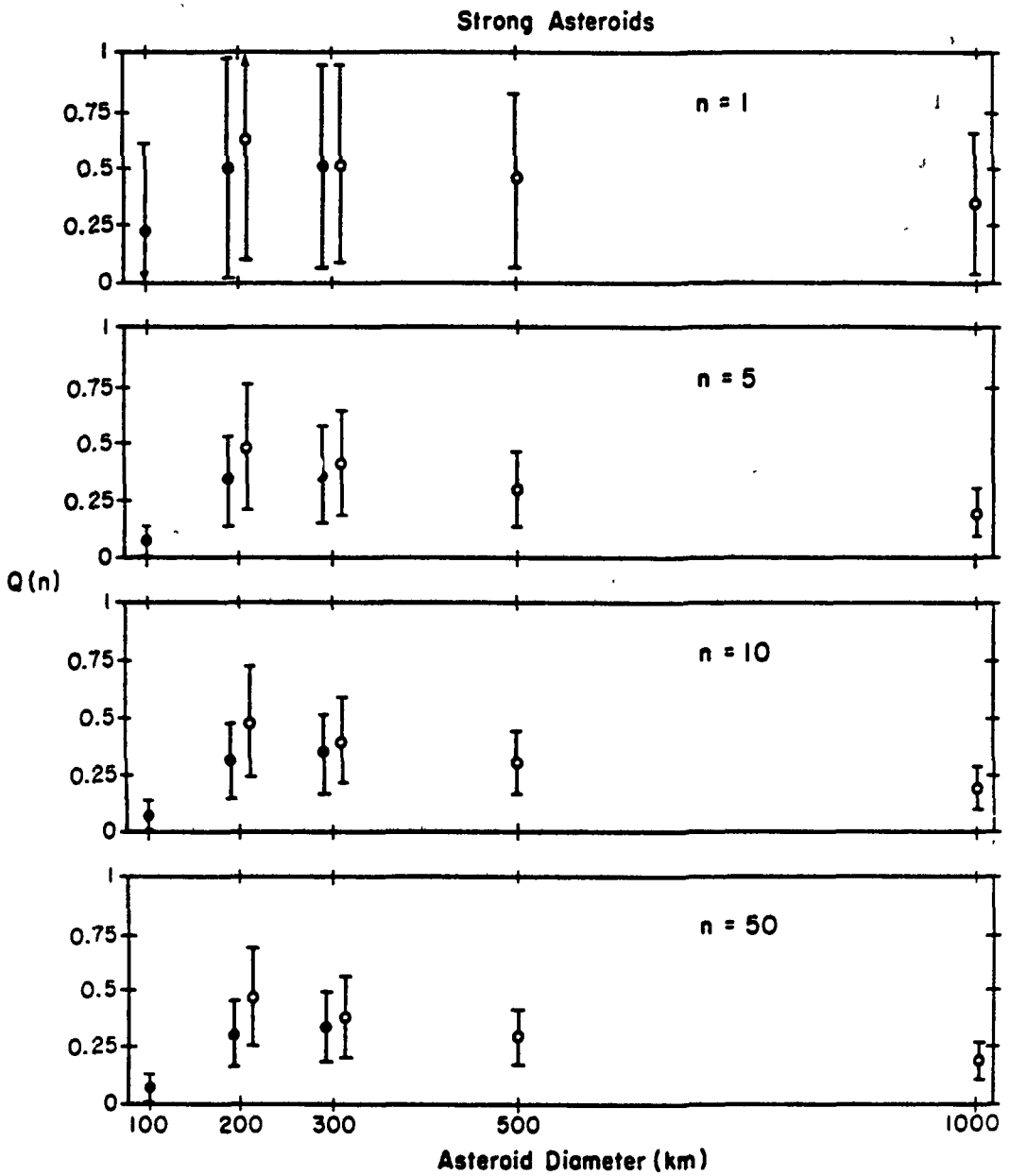


Figure 15. The amount of brecciated material with escapes rocky asteroids during cratering events. -- Q(n) is the fraction of regolith-derived debris amongst the total volume of material which escapes a rocky asteroid during n cratering events. Q(n) is a random variable because both the regolith depth at the impact sites and the diameters of the n craters are random. The open circles represent the mean value of Q(n) when gravity scaling applies to craters. The filled circles represent strength scaling. The vertical "error bars" indicate plus and minus one standard deviation from the mean. In the text the computed values of Q(n) are compared to the observed abundances of brecciated meteorites.

describes the relative magnitudes of the two components of variance of regolith depth, was estimated from the Monte Carlo experiments described in the previous section. A value of k_2=1 was used for strength scaling, which typically applies to smaller asteroids on which ejecta are widespread. A value of k_2=0.5 was adopted for gravity scaling, which applies to large asteroids on which ejecta are fairly localized. The results were found to be only weakly dependent on k_2. For the smaller bodies in Figure 15 the average value of Q increases with asteroid size because regolith depth increases. For larger bodies (diameter > 200-300 km) the mean value decreases. Note that, in the gravity scaling regime, large craters launch more ejecta beyond escape velocity than do small craters because ejection velocities increase with crater size. For the small, strength scaled, bodies ejecta velocity is independent of crater size. Thus on large asteroids, where gravity scaling applies, the mean value of Q is more heavily weighted by large craters, which tend to lower Q because they tend to excavate mainly bedrock.

For larger values of n both the mean and standard deviation of Q decrease. Note that if we generate a sequence of n craters then the size of the largest craters in the sequence should grow as n increases. The largest craters, which are important because they represent most of the volume of the impacting population, tend to make Q small because they excavate a lot of bedrock. Thus, the mean value of Q decreases with increasing n. The standard deviation decreases because the more times a particular asteroid is sampled, the

better-known its surficial distribution of regolith becomes. That is, as n gets large, the first component of variance in equation (4.24) becomes less important. Only the interasteroidal variation in regolith depth contributes to the standard deviation.

The values of Q_r for strong asteroids are shown in Figure 16a. The mean values here are smaller than those in Figure 15 because now the brecciated material is diluted by a much larger volume of unbrecciated "substrate". Note that, as discussed in the previous chapter, an asteroid may experience many fragmentation events before it is finally impacted with enough energy to disperse the fragments against their mutual gravitational field. A rough estimate of Q at dispersal, i.e. Q_d, is given in Figure 16b, following the procedure outlined in Chapter 4. The mean number of fragmentation events before dispersal and the lifetimes against dispersal are shown in Table 6. As is obvious from the figure, the mean value of Q at dispersal is significantly higher than that at fragmentation, especially for big asteroids whose large gravitational binding energies allow many fragmentation events prior to dispersal. Note that as Q_d approaches unity the assumptions used to derive equations (4.31) and (4.37) break down. Thus, unrealistically high values of Q_d are obtained for large bodies. Even so, the calculations indicate that large bodies should be composed largely of regolith before they are dispersed by an energetic impact. Of course the large bodies have dispersal lifetimes which are significantly greater than the age of the solar system. Hence the values of Q_d for these large asteroids are irrelevant,

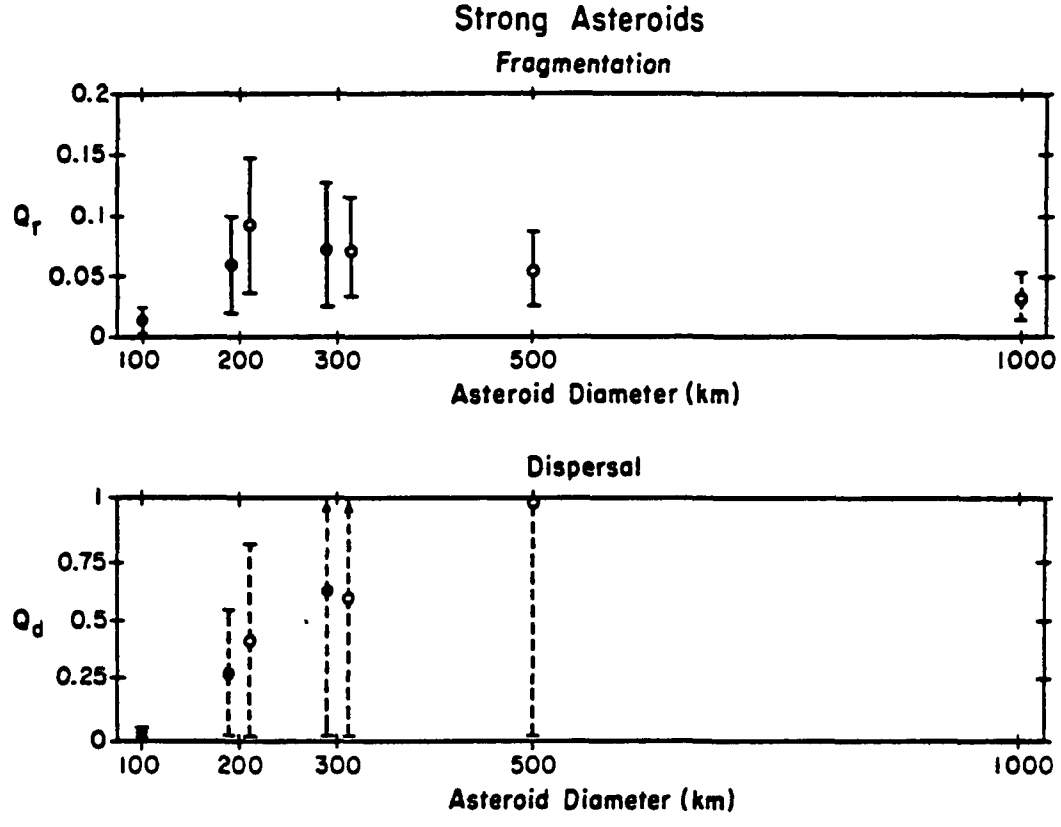


Figure 16. The amount of brecciated material released upon fragmentation or dispersal of rocky asteroids. -- Q is the ratio of the volume of regolith to the volume of the asteroid. The mean values are represented by circles, as in Figure 15. The vertical lines, which represent plus and minus one standard deviation, are dashed when the lifetimes against fragmentation or dispersal exceed the age of the solar system. Bodies larger than a few hundred kilometers in diameter are expected to be composed mostly of regolith when they are finally dispersed.

Table 6

The Number of Fragmentation Events and the Time Required to Disperse an Asteroid

strong asteroids

asteroid diameter	mean number of frag. events before dispersal	mean time until dispersal
100km	2	3Gyr
300	8	21
500	18	61
1000	57	270

weak asteroids

asteroid diameter	mean number of frag. events before dispersal	mean time until dispersal
2km	2	0.54Myr
10	21	13
100	960	1.8Gyr
300	6000	20
500	14000	60
1000	44000	270

assuming that the flux of projectiles was not significantly higher in the past. A higher impact rate would decrease the fragmentation and dispersal lifetimes (but would not change the value of Q_d).

The values of Q_d for weak asteroids are shown in Figure 17. Results for Q(n) are not presented because weak asteroids are expected to be fragmented rather frequently. The fragmentation events tend to mix surficial layers of regolith into the interiors of these bodies. Thus the concept of the regolith existing as a surficial layer, i.e. the concept upon which the expressions for Q(n) were founded, is not valid in this case. Results for Q_r are not presented because they are not needed in subsequent discussions. Inspection of Figure 17 shows that weak asteroids as small as 10 km can produce a significant quantity of brecciated material when they are dispersed. As can be seen from Table 6, weak asteroids are expected to undergo may fragmentation events before dispersal. Note that the impact strength of the large asteroids shown in the table may be higher than that used in the calculations because of high lithostatic pressures. Thus the number of fragmentation events experienced by these bodies is probably lower than those listed in the table. In any event, bodies larger than a few tens of kilometers should be composed mostly of regolith when they are finally dispersed.

The Irradiation Histories of Regolith Grains

Results from the Monte Carlo irradiation program are presented in Figures 18-24. The main result of the program is the prediction of particle-track densities due to irradiation by solar cosmic ray (SCR)

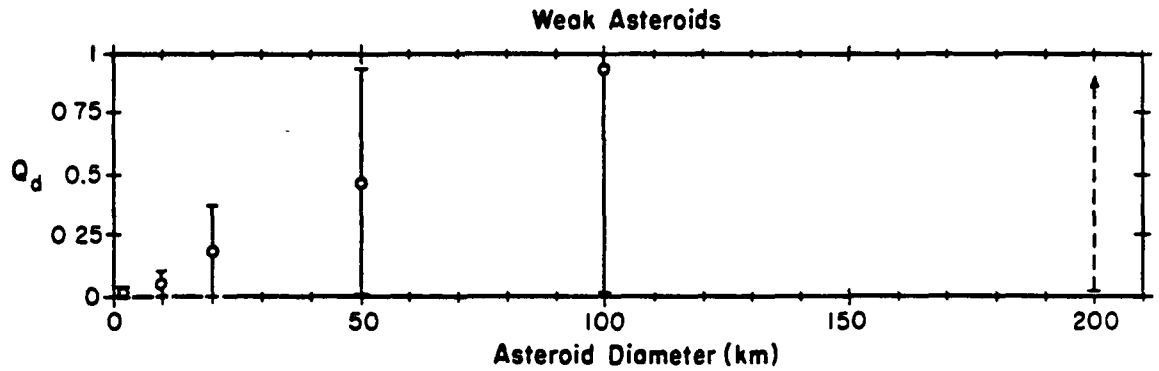
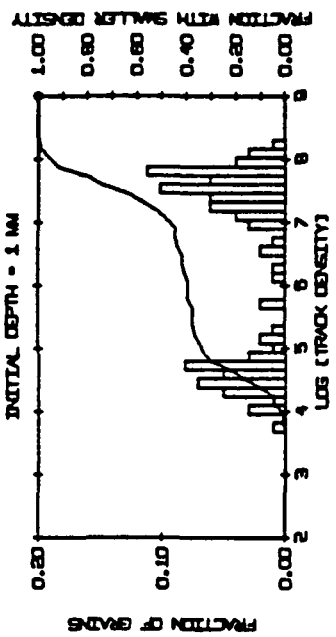
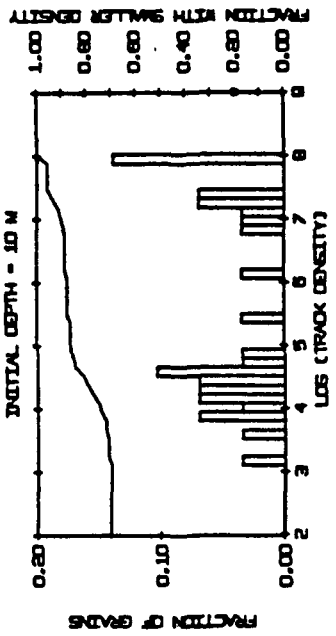


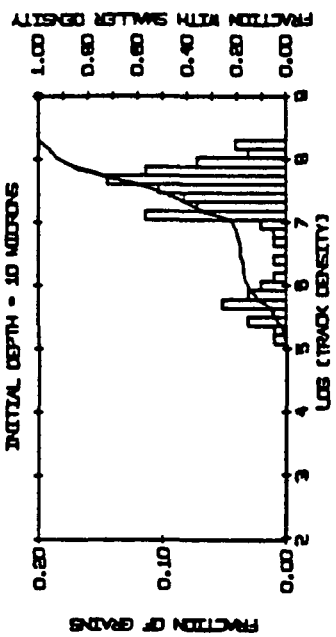
Figure 17. The amount of brecciated material released upon dispersal of weak asteroids.

and galactic cosmic ray (GCR) ions. In the Monte Carlo simulations, we essentially random walk a "point" through a regolith. The track density is computed from the total time spent at various depths below the surface and from the track production rate described in Chapter 2. This track density is assumed to be equivalent to the track density at the surface of a finite-size grain. This would not be a good procedure if grains were constantly impacted, eroded or reoriented as grains are in the lunar regolith. However, grains in asteroidal regoliths tend to be buried, i.e. protected from impacts, rather quickly so erosion and reorientation should not be a problem here. We will also find it convenient to discuss the track density at the center of a grain of given size. Note that the penetration depth of SCR ions is so low that the track production rate can change drastically with depth below a grain's surface. The additional shielding at the center of a grain is accounted for when central track densities are computed. Much of the data presented in the literature on meteorites pertain to 100 micron diameter grains. Therefore, when central track densities are presented here they will apply to a grain size of 100 microns.

Figure 18 shows the particle track densities accumulated at the surfaces of grains which reside in the regolith of a 300 km strong asteroid. Results are given for four different starting (i.e. time=0) depths in order to illustrate how a grain's initial depth below the surface affects its exposure history. For each starting depth 100-200 random walks were performed so that a distribution of track densities


INITIAL DEPTH = 1 MM
FRACTION WITH SMALLER DENSITY
FRACTION OF GRAINS
LOG (TRACK DENSITY)


INITIAL DEPTH = 10 M
FRACTION WITH SMALLER DENSITY
FRACTION OF GRAINS
LOG (TRACK DENSITY)


INITIAL DEPTH = 10 MICRONS
FRACTION WITH SMALLER DENSITY
FRACTION OF GRAINS
LOG (TRACK DENSITY)

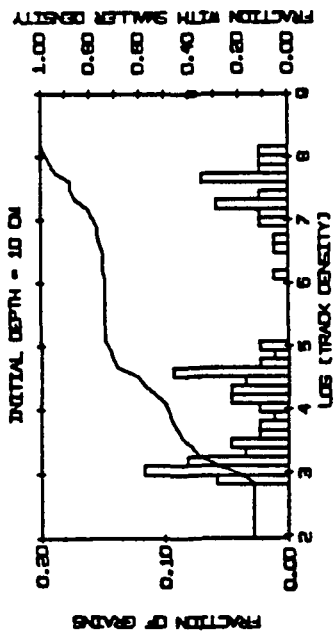

INITIAL DEPTH = 10 CM
FRACTION WITH SMALLER DENSITY
FRACTION OF GRAINS
LOG (TRACK DENSITY)

Figure 18. Particle-track distributions using various starting depths for regolith grains. -- The track densities are those produced at the surfaces of grains in the regolith of a 300 km diameter rocky asteroid. In each plot the histogram (read on the left ordinate) gives the distribution for grains which acquired track densities above $10^3/cm^2$. Grains with lower densities are considered to be unirradiated. The smooth curve (read on the right ordinate) shows the fraction of all grains which acquired a given track density or less. The solid square on the right ordinate indicates the fraction of grains which were exposed to solar cosmic ray irradiation. The peak in a histogram at low track densities is generally due to galactic cosmic ray ions. The higher density peak is the result of solar cosmic rays.

could be constructed. In general, the starting depth was varied from 10 microns to 100m or 1 km in logarithmic steps. The grains were allowed to random walk for a period equal to the mean fragmentation lifetime of the asteroid. Each distribution shown in Figure 18 contains three pieces of information. (1) The histogram gives the fraction of grains (read on the left vertical axis) which accumulated a given density of tracks. Actually, only the grains with densities greater than $10^3/cm^2$ are shown in the histogram. Grains with smaller densities spent a negligible part of their time in the upper meter of the regolith and, therefore, were for all practical purposes unirradiated. These unirradiated grains were excluded from the histogram in order to facilitate comparisons with observed track-density data given in the literature. (2) The "smooth" curve in each figure represents the fraction of grains (read on the vertical axis on the right) with a given track density or less. This curve applies to all grains, even those with densities less than 10^3. (3) The fraction of grains which approached close enough to the surface to be irradiated by SCR particles is indicated by the solid square on the right vertical axis.

As an example, consider Figure 18a which applies to grains starting out 10 microns below the surface. The track density histogram exhibits two peaks. The peak centered near $3x10^7$ is primarily due to the high flux of SCR particles. Even though all of these grains begin their evolution quite close to the surface, some of them are quickly buried to depths below a millimeter or so, thus

shielding them from SCR particles. However, they may spend a considerable amount of time in the upper meter of the regolith and thus acquire a significant number of tracks from GCR ions. The GCR irradiation is largely responsible for the second peak in the histogram, near $5x10^5$. Because all of these grains started out near the surface they all received some SCR irradiation, as indicated by the solid square at the top of the vertical axis on the right side of the figure.

Figure 18b shows the distribution of tracks for grains which started out 1mm beneath the surface. The SCR peak is less pronounced here, compard to Figure 18a, because the larger starting depths prohibit some grains from reaching the uppermost surface regions.

Figures 18c and 18d apply to starting depths of 10cm and 10m and further illustrate the effect of increasing the initial depth of a grain. Roughly 10-15% of the grains starting at 10cm are essentially unirradiated (track density$<10^3$) by either SCR or GCR ions and only 40% are SCR irradiated. Note also that the average density of GCR tracks decreases with increasing starting depth. This is to be expected because, the deeper a grain starts, the less time it will spend in the upper meters of the regolith. Conversely, the average density of SCR tracks is seen to be rather insensitive to starting depth. This is a result of the low penetration depths of SCR ions compared to GCR ions. In order to acrue SCR tracks a grain must be exposed essentially at the surface; "close approaches" to the surface do not contribute much. On the other hand, GCR ions penetrate to

meter depths. Thus grains originating from great depths can still acquire GCR effects by making close approaches to the surface, but the density of tracks in such grains will be low.

One of the problems involved in modeling the irradiation histories of grains in meteorites is that we have no idea where the grains originated within their parent body. While the SCR track density is insensitive to initial depth, the fraction of grains which are irradiated depends quite heavily on the depth. One possible remedy is to combine all of the results, for the various initial depths, into a single track distribution, thereby "averaging out" the dependence on initial grain depth. In order to implement such a procedure we must find a method for combining the distributions. Note that most meteorites are probably derived in large cratering events, which scoop out massive sections of regolith and bedrock, or perhaps in catastrophic impact events, in which all parts of the regolith might be sampled with equal probability. In both cases the entire vertical extent of the regolith is sampled. Hence it seems reasonble to assume that all starting depths, from zero down to the thickness of the regolith layer, contribute equally to the distribution of track densities for grains. Actually, on bodies which lose most of their ejecta, grains in the regolith may originate from depths much larger than the thickness of the regolith because as the asteroid is eroded its surface (and regolith) recede in toward the center of the body. But this should not be too important because most of the bodies which we will consider retain most of their crater ejecta. Besides, the

Monte Carlo simulations show that the exposure histories are not very sensitive to the initial depth for depths below 100m or so. Therefore, we will construct a single track distribution by averaging together the distributions, for the various initial depths, and weighting them by the volume of debris they are responsible for. Note that the distributions for small starting depths will contribute very little in the averaging because very little debris originates from such shallow depths.

Figure 19 shows the depth-averaged distributions for a 300 km strong asteroid. As seen in part (a) of the figure, which applies to the surfaces of grains, some 70% of the grains are never irradiated and only about 15% are SCR-irradiated. Part (b) shows the distribution of track densities at the center of 100 micron grains. Note the GCR peak does not change between the two figures, as we would expect. The SCR track densities are all lowered due to the extra distance the ions must penetrate while a grain is exposed at the surface. Table 7 lists some additional information regarding the depth-averaged distributions. The mean ($\pm$ one standard deviation) exposure times to SCR and GCR irradiation are roughly indicated by the total time the "point" in the Monte Carlo program spent at depths less than 100 microns and at depths less than 1 meter. The table also gives the number of times that the point entered these two depth regimes and the number of times it was excavated. The numbers in parentheses apply only to those points that received SCR irradiation.

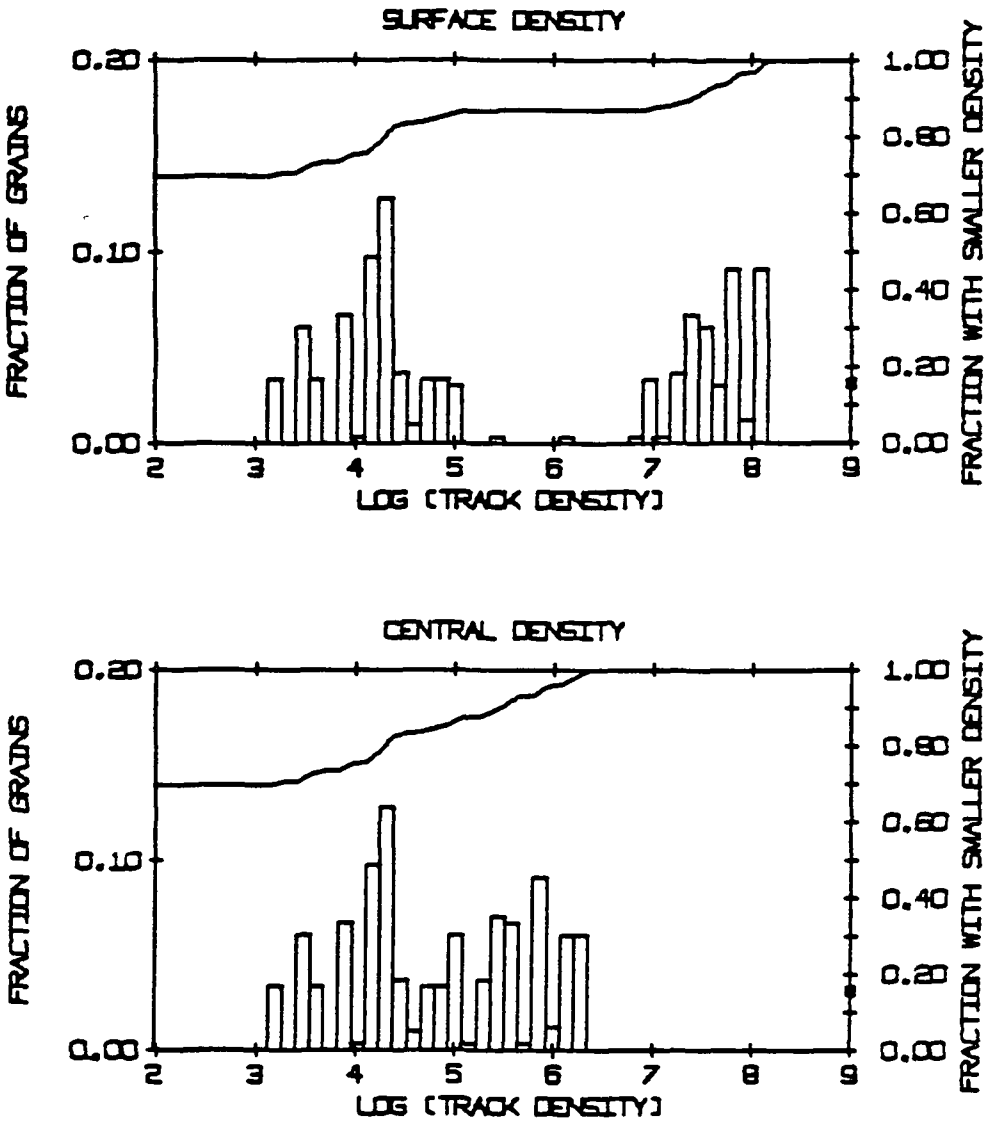


Figure 19. Track densities for grains on a 300 km diameter rocky body. -- The distributions were obtained by averaging together the distributions for various starting depths. The method used in the averaging is discussed in the text. Results are shown for the density of tracks both at the surfaces of grains and at the centers of 100 micron diameter grains.

Table 7

Some Results from the Simulated Exposure Histories of Regolith Grains*

	region defined by 0 < grain depth < 100μ			region defined by 0 < grain depth < 1m		
case	total time (yr) spent in region	no. times entered region	no. times excavated	total time (Myr) spent in region	no. times entered region	total no. of times excavated
300 km strong	350±1200 (2700±2400)	0.67±2.20	0.39±1.50	0.41±0.78 (1.10±0.94)	1.40±2.50	3.20±5.40
100 km strong	260±1100 (3100±2500)	0.54±2.30	0.40±1.70	0.23±0.65 (1.30±1.00)	1.30±1.00	1.50±5.00
500 km strong	230±880 (2200±1900)	0.39±1.40	0.12±0.64	0.44±0.84 (1.20±1.00)	0.97±1.50	2.80±3.80
1000 km strong	540±1700 (2600±2900)	0.95±2.70	0.61±2.20	0.89±1.60 (1.90±1.90)	1.60±2.70	5.10±7.10
2 km weak	11±72 (300±280)	0.06±0.40	0	0.30±0.05 (0.30±0.05)	0	0.05±0.26
10 km weak	33±172 (54±502)	0.14±0.65	0.04±0.28	0.03±0.08 (0.18±0.14)	0.16±0.39	0.21±1.00

*entries not in parentheses are average values ± 1 standard deviation for all grains

entries in parentheses pertain only to SCR irradiated grains

Figure 20 shows the results for a 100 km diameter strong asteroid. The track distributions for this case are strikingly similar to those in Figure 19. The only difference is that the SCR track densities are slightly higher, on the average, for this asteroid. This is probably due to the fact that grains at the surface of a 100 km asteroid are not buried quite as heavily as they are on larger bodies, where more ejecta are retained.

The track distributions for a 500 km and a 1000 km body are shown in Figures 21 and 22 (note the change of scale on the vertical axes in some plots). Again the results are very similar to the ones discussed earlier, except for the fact that a slightly higher percentage of grains were exposed to SCR irradiation on the 1000 km body compared to the smaller ones.

Figures 23 and 24 are plots of the density distributions for weak asteroids of diameter 2km and 10km. Because the fragmentation lifetimes of these bodies are typically only a million years (see Table 5), grains starting at centimeter to meter depths essentially are never irradiated. This is consistent with the fact that these bodies buildup very little regolith (on the order of 10cm and 1m for the 2km and 10km bodies, respectively) over their collisional lifetime. Grains starting below 10cm-1m are rarely excavated and brought to the surface before catastrophic fragmentation occurs. Thus, the track distributions shown in Figures 23 and 24 were obtained by averaging over depths ranging from zero to 10cm, for the 2 km body, and to 1m for the 10 km asteroid. Figure 23 implies that roughly 2/3

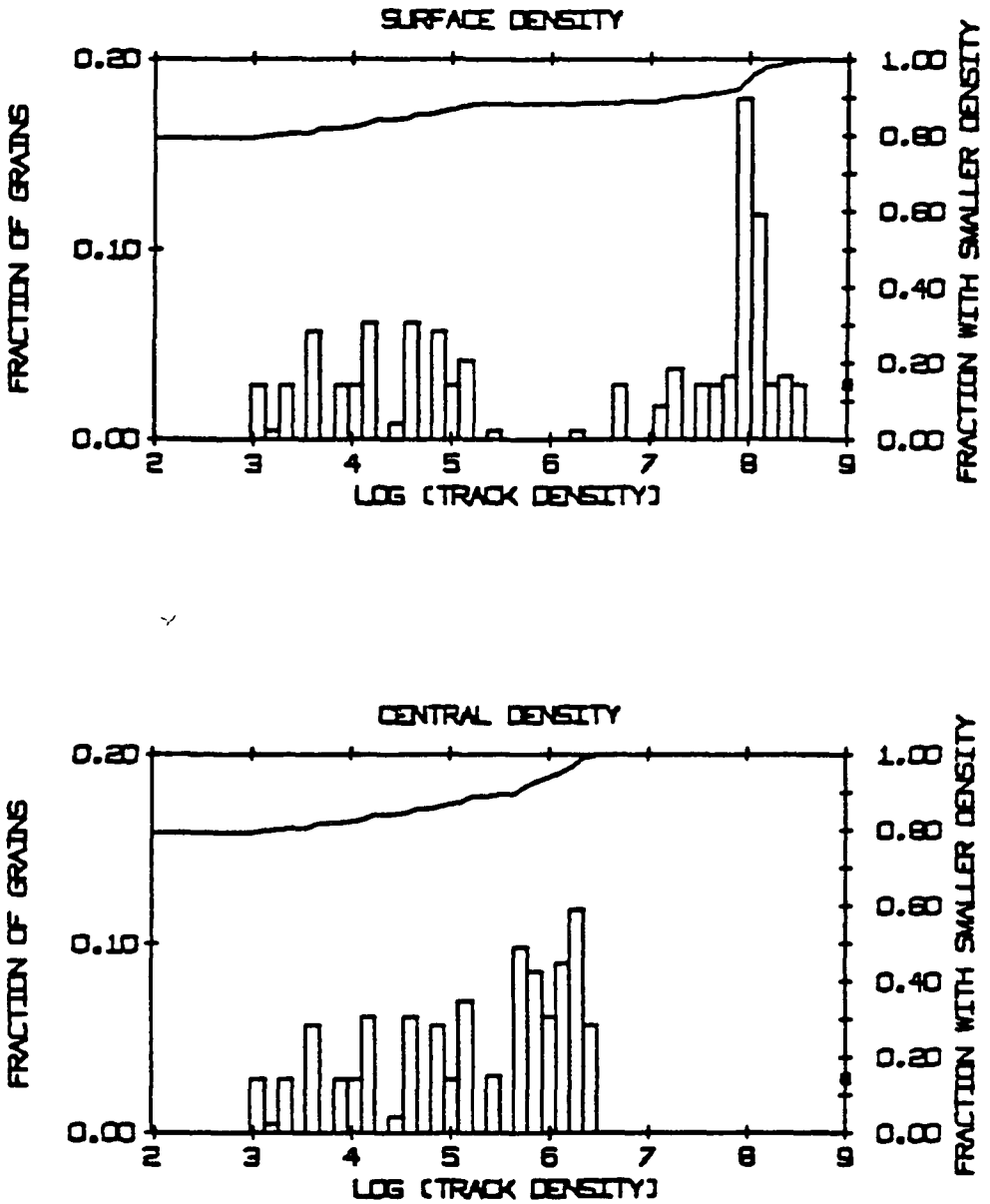


Figure 20. Track densities for grains on a 100 km rocky asteroid.

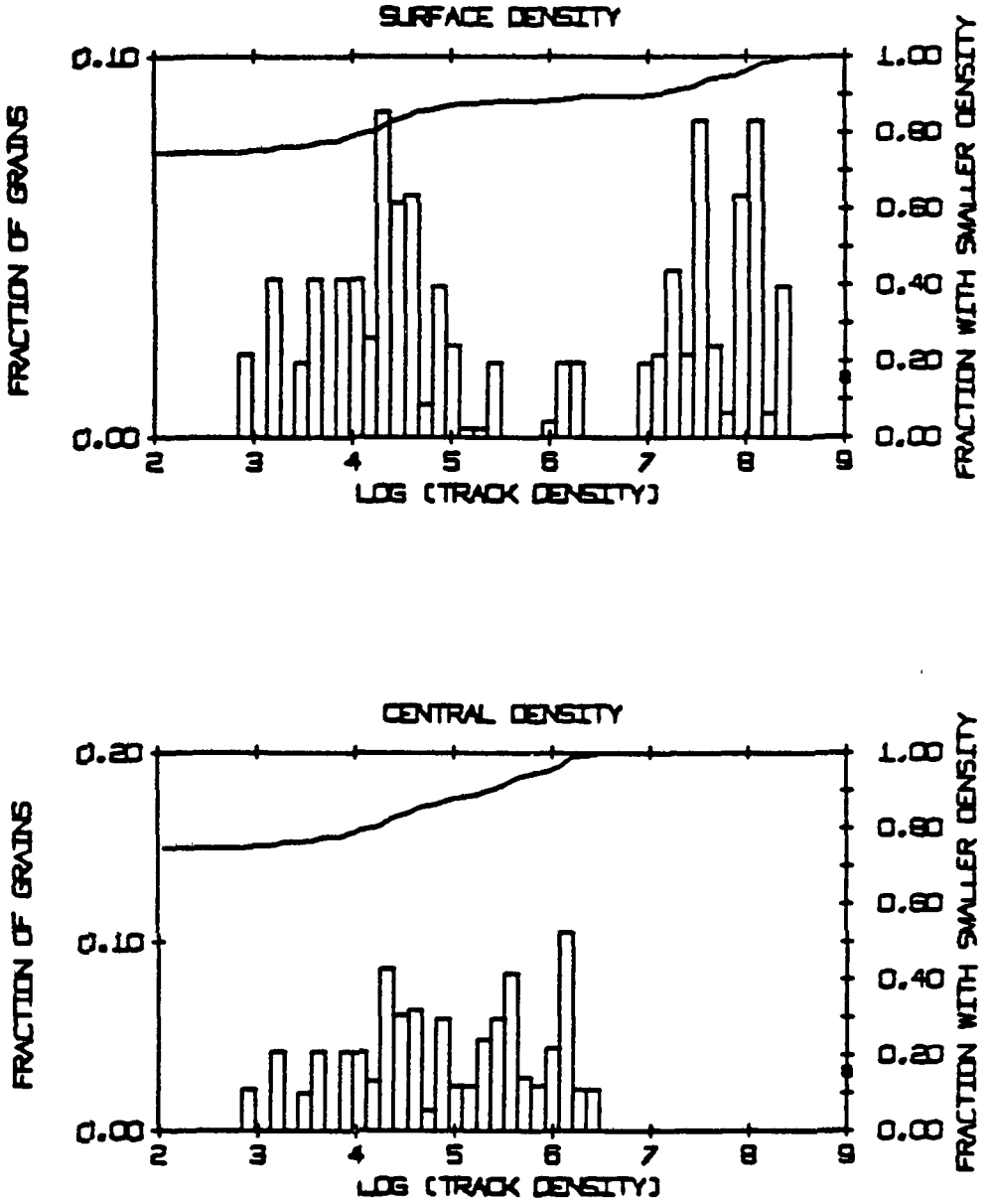


Figure 21. Track densities for grains on a 500 km rocky asteroid.

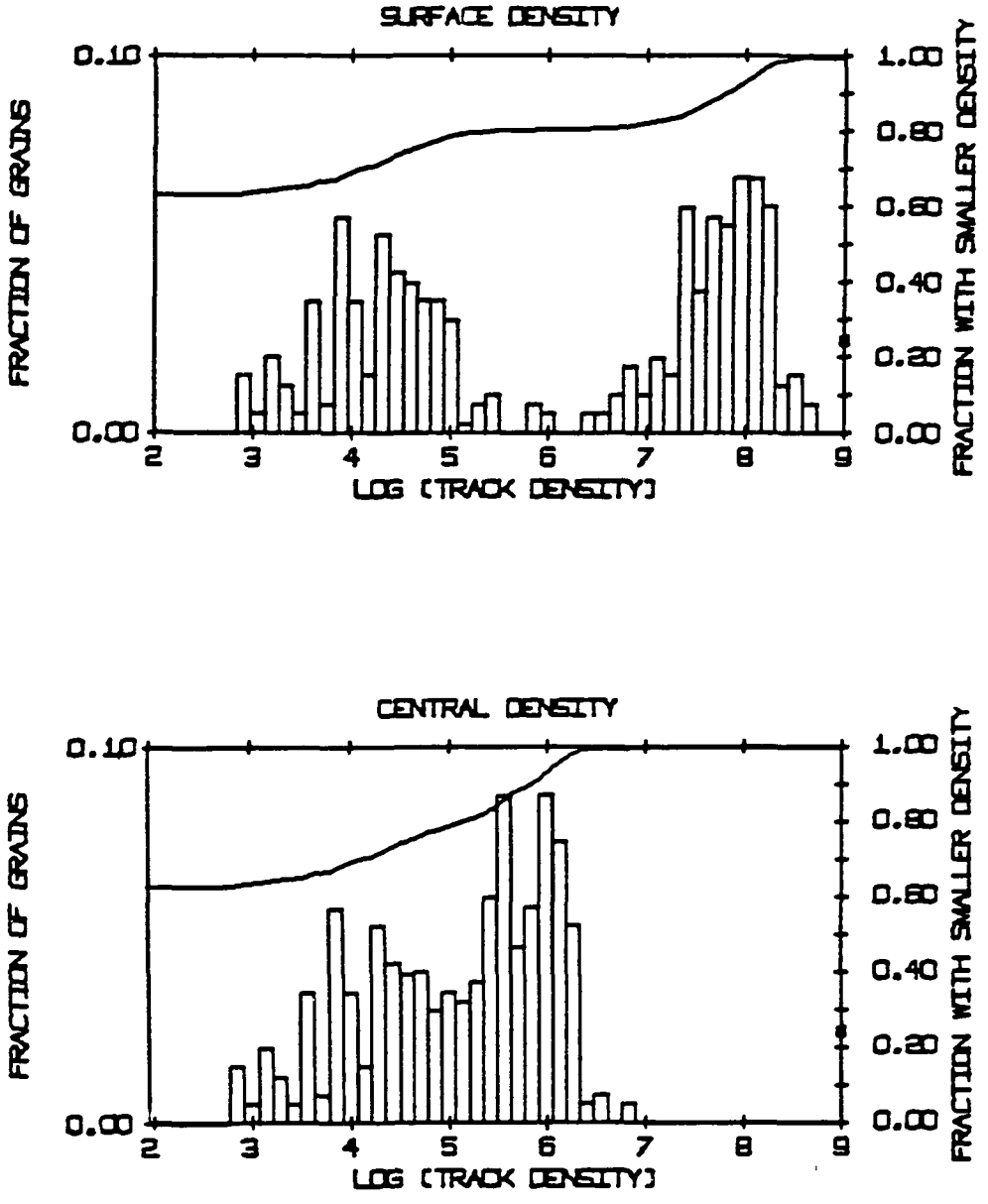


Figure 22. Track densities for grains on a 1000 km rocky asteroid.

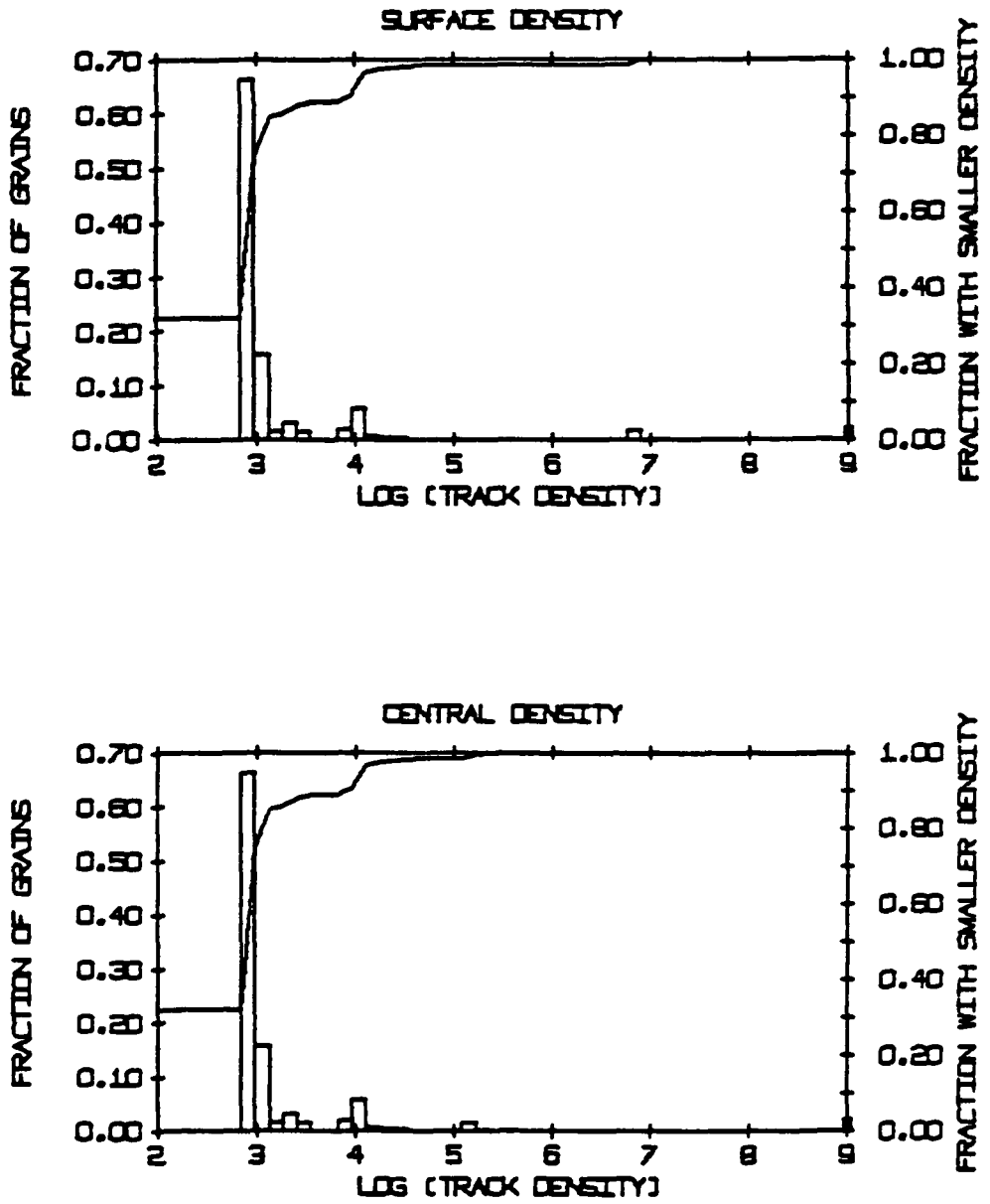


Figure 23. Track densities for grains on a 2 km weak asteroid.

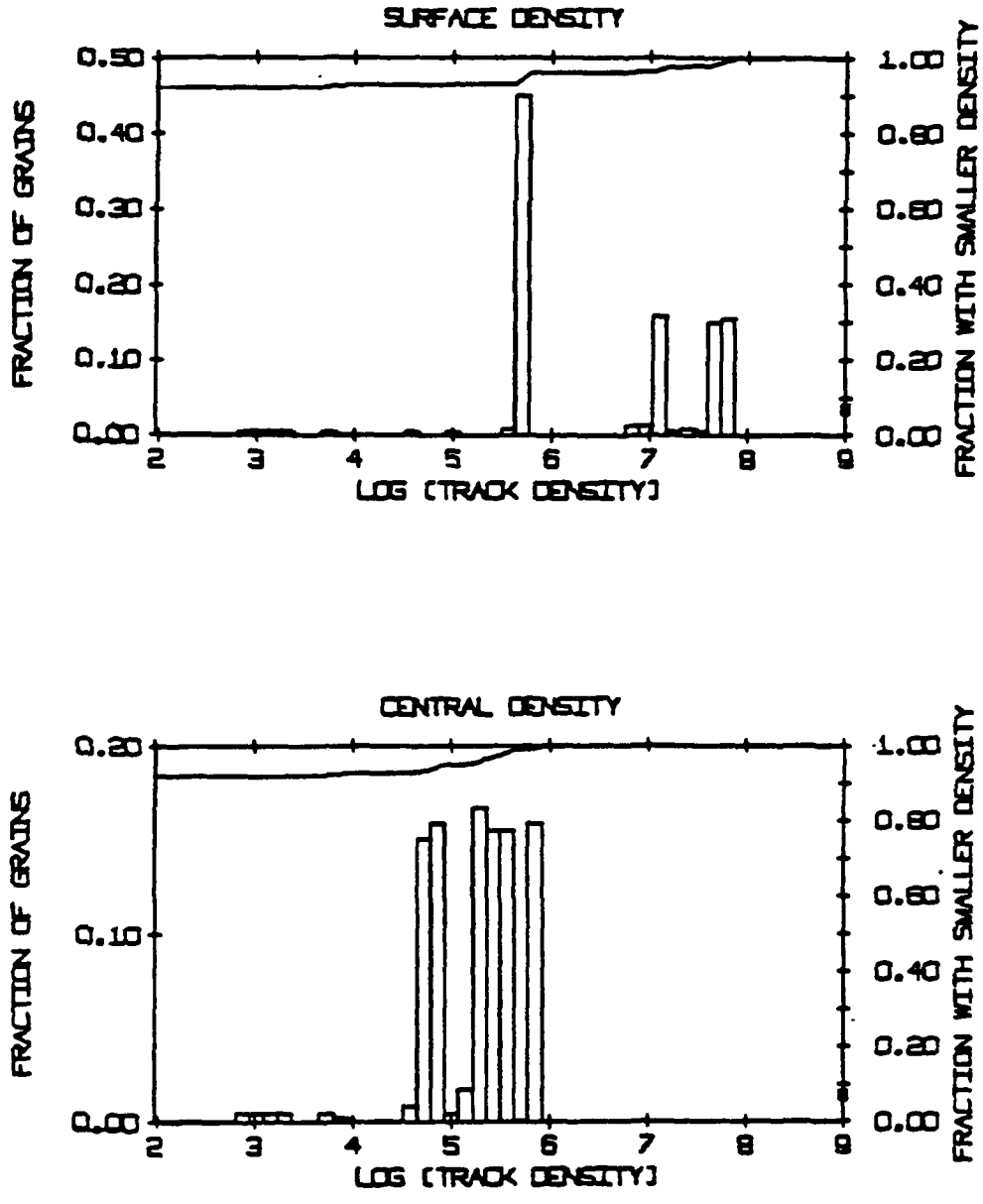


Figure 24. Track densities for grains on a 10 km weak asteroid.

of the grains on kilometer-size weak bodies are irradiated by GCR ions. The reason that such a large percentage of grains are irradiated is that they all started at depths of 10cm or less. Only a few percent acquire SCR tracks. Furthermore, the grains that are irradiated have very low track densities. High densities of SCR tracks are absent because grains that make it to the surface are easily ejected from the asteroid's weak gravity field. The story is quite different for a 10 km weak asteroid (Figure 24). Whereas the majority of GCR irradiated grains on the 2 km body have track densities near 10^3, most grains on the 10 km asteroid have densities less than 10^3 (because they started out further beneath the surface), so these grains are not shown in the histogram in Figure 24. Thus the distribution is made up mostly of SCR irradiated grains. Note that the comparitively high gravity field of this asteroid allows it to retain the grains which were heavily irradiated by SCR ions.

Additional Monte Carlo experiments were performed in order to examine the sensitivity of the computed track distributions to variations in uncertain parameters. For the most part, only the parameters which pertain to small-scale impacts were varied because the small impacts are primarily responsible for determining exposure histories. A series of six experiments, each involving a 300 km strong asteroid, was performed.

1. The flux of low-mass (cometary) debris was lowered by a factor of three below that shown in Table 1. A factor of three was chosen because this is the level of uncertainty involved in

the Pioneer-spacecraft observations of interplanetary dust (Humes et al., 1974).

2. The track distributions shown in Figures 18-24 were based on the assumption that small craters (diameters less than about 1 cm) formed in regolith. However, blocks of rocks should be present, so small craters may often form in a "strong" target rather than in a "weak one". As an extreme case, a distribution of track densities was generated under the assumption that the small craters formed in rock.

3. As discussed in Chapter 2, the size of craters produced in weak targets, when strength scaling is appropriate, is not well known. For the asteroids this regime includes craters with diameters less than 1-10m. A test case was run using a value of K_D which was twice as large as the value shown in Table 2 for strength scaling in a weak target.

4. The slope of the mass distribution of ejecta fragments produced in an impact event (see the discussion of the Monte Carlo irradiation algorithm in Chapter 4) was varied from the nominal value of a_f=-0.67 to -0.9. Note that the nominal value really only applies to the ejecta from a single impact event. Craters which excavate previously fragmented debris might produce a relatively "steeper" mass distribution of fragments, i.e. a distribution with a higher proportion of small fragments compared to the nominal distribution. Thus, a value of a_f=-0.9 was also tried.

5. The size of the smallest fragment produced was varied from the nominal value of 1 micron to 10 microns.

6. The parameter, p, that determined which impact events were to be handled individually and which were to be considered as a continuous process, was lowered, by a factor of ten, from the nominal value of 0.01.

All of these experiments produced track distributions which were essentially identical to those shown in Figure 19. However, there were some small differences. By lowering the flux of small projectiles (experiment number 1), the fraction of SCR-irradiated grains decresed to roughly a few percent because grains near the surface were not excavated as often as those in Figure 19. On the other hand, increasing the sizes of craters produced in small impacts (experiment number 3) allowed roughly 25% of the grains to be irradiated by SCR ions. Also, the maximum track density observed increased by a factor of 5. Overall, the results were found to be relatively insensitive to the parameters which were varied.

This concludes the discussion of the numerical results from our regolith model. We now consider some of the implications of these results.

CHAPTER 6

IMPLICATIONS FOR RECENT MODELS AND THE ORIGIN OF METEORITES

Having described the results of the stochastic model for regolith evolution, we now discuss the implications of these results in connection with previous regolith models and the origins of brecciated and gas-rich meteorites.

Regolith Depth

Relationship with Recent Studies

We begin with a brief comment on how the calculations of the time required for a regolith to reach equilibrium bear on the model of Duraud et al. (1979). The equilibrium times shown in Table 5 imply that most asteroids are not able to reach an equilibrium state before they are catastrophically fragmented. This seems quite obvious in light of the fact that large craters tend to dominate regolith growth. Equilibrium cannot be expected to be reached until formation of "several" large impacts, by which time fragmentation is likely to have occurred. The equilibrium model of Duraud et al. therefore appears exceedingly suspect. In general, asteroidal regoliths are not able to attain equilibrium before being fragmented.

The mean depth of regolith at the time of fragmentation was computed and described in Chapters 4 and 5. Housen et al. (1979a,b) also computed the mean depth, but by a different method. We now take a moment to compare these two results. Using the same set of input parameters and ejecta blanket model as adopted by Housen et al., the mean depths were again computed. For 100 and 300 km strong asteroids the depths found from equation (4.23) were roughly a factor of 3 and 1.15 larger than those computed by Housen et al. This seems rather perplexing because while the present calculations are based on all sizes of craters on the surface, the Housen et al. calculations excluded the areas occupied by large crater bowls, where the depth should be small. This should make their depths the larger of the two. Note, however, that Housen et al. actually computed the surface elevation and argued that it should closely approximate regolith depth. There is a subtle and interesting facet of regolith evolution which makes regolith depth distinct from surface elevation: elevation is independent of the order in which cratering events occur whereas regolith depth is not. As a simple illustration, suppose we are sitting at a point on a surface (where the initial elevation is zero) and four impact events occur. Further suppose that the four events all cause equal changes in the surface elevation, although two increase it and the other two decrease it. The elevation at the point does not depend on the order of the events; it is always zero. But the regolith depth at the point will be larger if the negative changes occur preferentially early rather than if they occur late. The fact

that regolith depth should exceed elevation is supported by equation (4.1) because the minimum surface elevation is always negative.

For asteroids of diameter 500 and 1000 km the Housen et al. depths are smaller than those computed from the present model by a factor of 2. The difference between elevation and depth again applies but there is an additional effect. In modeling a "typical region" on large bodies Housen et al. excluded the ejecta of large craters whereas equation (4.23) includes the effects of all craters. The exclusion of large-crater ejecta tends to make the Housen et al. depths lower.

Which method is the correct one for computing regolith depth? Clearly the present model has the advantage of actually computing the depth, not the surface elevation. But the Housen et al. model has the apparent advantage of modeling a "typical region". Recall that the typical region avoids the parts of the surface occupied by large craters or their ejecta. This procedure was adopted in order to make the average value a meaningful descriptor of regolith depth. Housen et al. conjectured that the average would misrepresent most of the surface if the large crater bowls, where the regolith was thought to be "atypically" thin, and the large-crater ejecta, where the regolith was atypically deep, were included in the averaging.

Housen et al. were right in their contention that the regolith is highly variable in depth when all parts of the surface are considered. This was demonstrated in Chapter 4 where the standard deviation of depth was shown to be equal to the mean. However, we

also showed in that chapter that the variance of depth consists of two components, one due to the variation in depth over an asteroid's surface and a second component which arises from statistical fluctuations in the quantities which determine regolith depth (i.e. the number of craters on an asteroid, their order of occurrence, etc.). In Chapter 5 these two components were found to be of comparable magnitude. The Housen et al. procedure should reduce the first component of variance. It may also reduce the second component because part of the interasteroidal variability arises from the statistical uncertianty in the number of large craters on a body. Thus avoiding the areas occupied by large craters may reduce the interasteroidal component.

Let us now consider the effectiveness of modeling a typical region by seeing how much this reduces the variance of regolith depth. Using the same regoliths that were generated by the Monte Carlo program described in the previous chapter (see section on the variance of regolith depth) the mean and variance of the depth were recomputed. However, this time the mean and variance were computed over the same parts of the surface considered by Housen et al. For small asteroids the bowls of large craters were avoided, where "large" was determined from the saturation criterion of Housen et al. (1979a) described in Chapter 3. This caused the mean depth, and standard deviation, to increase. The coefficient of variation (standard deviation divided by the mean) decreased slightly but was still found to be 1. Thus, avoiding the parts of the surface occupied by large crater bowls does

not significantly decrease the uncertainty associated with regolith depth. For large asteroids, the ejecta deposits of big craters were also avoided according to the Housen et al. (1979b) definition of ejecta saturation. This caused the mean depth to decrease, however, the coefficient of variation was still roughly unity. In both cases the two components of variation were again observed to be of equal magnitude.

It would appear that modeling a typical region does not significantly improve the utility of the average value in describing regolith depth on asteroids. That is, the Housen et al. model describes the regolith depth in the typical region no better than does a model which computes the mean depth by averaging over the entire surface of an asteroid. Note that these comments apply equally well to the model of Langevin and Maurette (1980).

While on the subject of of the variablilty of regolith depths, we might reasonably ask if there are any processes which might tend to reduce the the variablility below that calculated. For example, if an asteroid does not conform to a shape of hydrostatic equilibrium then components of the gravity field which are tangent to the local surface may redistribute the regolith, thus smoothing the debris layer to conform to the geoid (see discussion in Cintala et al., 1979). This mechanism may have played a role in forming the smooth appearance of Deimos' surface (Thomas, 1979).

It is, however, worthwhile to note that a smooth surface does not guarantee a regolith of uniform depth; variability also arises from the topography at the bottom of a regolith. To illustrate this we can consider the extreme case where the regolith is sufficiently mobile to redistribute itself into gravitationally "low" spots. In order to estimate how smoothing affects the variance of depth, the computer-generated regoliths, referred to earlier, were allowed to "relax" so as to produce a smooth, planar, surface.

After the surfaces were smoothed, the standard deviation of the surficial depth distribution (i.e. the square root of the first component of variance in equation 4.24) was observed to increase by roughly a factor of 1.7. Figure 25 shows an example. Parts a and b of the figure are plots of the surface elevation before and after smoothing. Parts c and d show the regolith depth before and after. The reason for the increased variance is clear; by removing the regolith from the high surface elevations and accumulating it in the low spots we tend to add more weight to the tail of the regolith-depth distribution.

The above simulation was meant to be a simple example of the effects of smoothing an asteroid's surface. The actual process is difficult to simulate because in reality the extent to which a regolith is redistributed depends on how far the asteroid deviates from an equilibrium figure, on the cohesive properties of its regolith and on how frequently impacts "shake" the regolith (Cintala et al., 1979; Langevin and Maurette, 1981). However, the simulations do

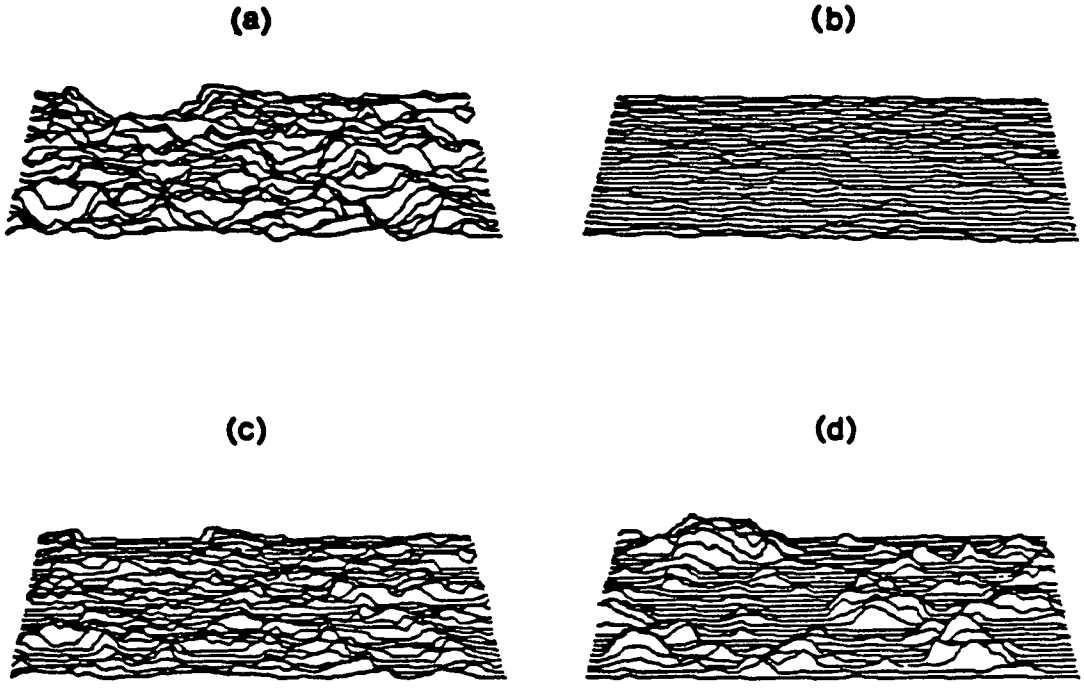


Figure 25. An illustration of how gravitational settling of debris might affect the variability of regolith depth. -- In order to illustrate the effects of debris settling, the regoliths generated by a Monte Carlo program were allowed to "relax" so as to produce a smooth top surface. Part (a) shows the elevation of the top surface of a regolith before smoothing. The surface elevation on the same asteroid, after the regolith has been redistributed, is plotted in part (b). Part (c) shows the regolith depth, i.e. the thickness of the debris layer, corresponding to the surface in part (a). The regolith depth, after the surface was smoothed, is shown in part (d). Smoothing an asteroid's surface can actually increase the variance of the regolith depth distribution because, by removing regolith from the high surface elevations and accumulating it in the gravitationally low spots (e.g. the bottoms of large craters), more weight is added to the tail of the regolith depth distribution.

indicate that, while an asteroid (or planetary satellite) may have a smooth surface, its regolith may be quite variable in depth.

Implications for the Brecciated Meteorites

As discussed in the Introduction, many of the meteorites now in our museums are composed of angular fragments of rock embedded in a finer ground mass. The structure of these brecciated meteorites is indicative of a regolith origin. The observed abundance of brecciated meteorites is determined largely by the prevalence of regolith-derived material in the total volume of debris that is ejected from an asteroid. The volume fraction, Q, of escaping debris that is derived from a regolith was shown in the previous chapters to be a function of asteroid size. We now compare the calculated values of Q with the values observed in meteorite collections in order to determine the extent to which regolith models can constrain parent body size for the brecciated meteorites. The basaltic achondrites are considered first and are followed by a discussion of the chondritic meteorites.

Of the basaltic achondrites we will concentrate primarily on the eucrites, howardites, diogenites and aubrites. The other subclasses, e.g. the chassignites, ureilites, nakhlites, shergottites and angrites are not considered because they are rare. Nearly all of the basaltic achondrites are brecciated. For example, the eucrites, howardites, diogenites and aubrites are, by volume, roughly >98%, 100%, 80% and 100% brecciated (Mason, 1962; Heymann et al., 1968; Wasson, 1974; Hutchison et al., 1977). Based on a variety of cosmochemical and petrological arguments, the eucrites, howardites and

diogenites appear to be genetically related and are often suggested as having originated on one, or perhaps a few, parent bodies (e.g. Duke and Silver, 1967; Mason, 1967; Ganapathy and Anders, 1969; Jerome and Goles, 1971; McCarthy et al., 1972; Stolper, 1975; Dreibus et al., 1977; Takeda, 1979). Consolmagno and Drake (1977) modeled the evolution of rare earth element abundances in eucrites and concluded that these meteorites were likely the result of 5%-15% partial melting of an essentially chondritic parent body. Based on the observed meteoritic abundances and asteroid reflection spectra they further concluded that the eucrite parent body is still intact and that the most likely source body is asteroid 4 Vesta. (The Vesta scenario has been embellished by Hostetler and Drake, 1978 and has been disputed by Wasson and Wetherill, 1979.) Furthermore, Ganapathy and Anders (1969) suggest that the eucrites and howardites were liberated from their parent body in a few impacts.

With the above considerations in mind let us now compare the observed values of Q for the eucrites, howardites, and diogenites with the calculated values of Q given in Figure 15. If the meteorites were liberated in a single impact then, because of the large standard deviation associated with the calculated values of Q, virtually any size of asteroid larger than 100 km could have produced the fraction of brecciated material observed in the basaltic achondrites. If a few impacts ($n<5$?) were responsible then the most probable size of parent body is 200-300 km. Note however that the values shown in Figure 15 may be somewhat low because of the assumptions made in deriving Q (see

Chapter 4). Thus, for the case of a few impacts, even a Vesta-size asteroid is probably capable of producing the values of Q observed for the basaltic achondrites. In short, it would appear that the eucrites, howardites and diogenites were derived from a body whose diameter is > 100-200 km.

The Consolmagno and Drake (1977) conclusion that the eucrite parent body is still intact was based on the observation that no meteorites have been found with the expected composition of the parent body mantle. The calculated 5%-15% melting would imply a 4-13 km-thick crust of eucritic basalts (for a uniform layer on a 500 km body). We can check to see if our regolith depth calculations are consistent with the Consolmagno and Drake model by determining the extent to which the mantle material might be mixed into the regolith. This can be roughly estimated by computing the volume of material excavated from beneath a crust of specified thickness. If we divide this volume by the total volume of regolith, obtained from the calculations described in Chapter 5, then the fraction of regolith material which is derived from the mantle can be calculated. For crustal thicknesses of 5, 10, 15 and 20 km the calculated abundances of mantle material are roughly 60%, 30%, 15% and 7%. Taken at face value these numbers would suggest that the eucrite parent body crust should have been at least 15 or 20 km thick. A thinner crust would likely result in meteorites composed largely of mantle material, contrary to observation. We can obtain another estimate of the thickness of the crust by computing the amount of material which is

excavated from the mantle and ejected from the asteroid (along with debris excavated from the crust) in meteorite-producing impact events. This is easily found from the expressions derived for Q(n) in Chapter 4. If the crustal thickness is substituted for the mean regolith depth in equation (4.31) then the fraction of meteoritic material derived from the parent body mantle (this is analagous to the fraction of material derived from the beneath the regolith) can be found. For a 500 km asteroid we find that, unless the crust is thicker than about 15 km, a significant fraction (more than a few tens of percent) of the debris liberated from the asteroid will be derived from the mantle. Hence, the crust on the eucrite parent body must have been thicker than roughly 15 km. This is a bit larger than the thickness computed by Consolmagno and Drake. In this regard it is interesting to note that Fukouka et al. (1977), using a slightly different rare earth element abundance for the eucrite parent body than that used by Consolmagno and Drake, estimated that the eucrites may have been formed by 8-24% partial melting. This would imply a crust of thickness 7-22 km.

In the above discussion of parent body size as inferred from the observed values of Q we assumed that the eucrites, howardites and diogenites were derived from a common parent body. This assumption is often a convenient one but cannot be rigorously justified. In fact, geochemical arguments can be made for the case of several parent bodies (Delaney et al., 1981). However, even if several parent bodies were involved, our conclusions regarding parent body size are

unchanged. The virtual ubiquity of brecciated material among the basaltic achondrites argues for parent bodies larger than 100-200 km in diameter. This conclusion also applies to the aubrites, for which Q is observed to be very nearly unity.

So far our discussion has been based on the assumption that the basaltic achondrites were liberated in a few, nondestructive, cratering events. Although this is supported by geochemical arguments (Consolmagno and Drake, 1977), there is another point to consider. That is, volumetrically speaking, should we expect cratering events to generate more debris than catastrophic dispersal events? For the moment let's assume that only bodies smaller than 200 km in diameter have dispersal lifetimes less than 4.5 Gyr (Table 6). If we compute the total volume of material liberated during cratering events on all sizes of asteroids and the total volume liberated during dispersal of bodies smaller than 200 km, then we find that the dispersal events dominate by about an order of magnitude. But figure 16b implies that the bodies which are disrupted (diameters less than 200 km) are expected to produce very little brecciated material. This would seem hard to reconcile with the observed prevalence of brecciated material among the achondrites. Of course there are caveats. First, the dispersal lifetimes shown in Table 6 are lower limits because, as mentioned in Chapter 4, some of the impact energy which was assumed to be partitioned into the dispersal of the fragments is actually taken up in heating of the target, etc. Davis et al. (1979) have computed dispersal lifetimes in some detail and find that only asteroids

smaller than about 10 km are dispersed over the age of the solar system. This will considerably reduce the contribution of debris from dispersal events. Secondly, Horz and Schaal (1981, work in preparation) have suggested that impact-generated shock waves may spall off the regolith-laden outer layers of rocky asteroids. The volume of debris produced by spallation may exceed the volume produced by craters. If, in the future, this mechanism is shown to be quanitatively important then the quantity of material derived from dispersal events will be judged as even less significant. If we are willing to accept these somewhat circumstantial arguments then the assumption that the achondrites were derived in nondestructive cratering events is reasonable. We now turn our attention to the undifferentiated meteorites, i.e. the chondrites.

As a group, the chondritic meteorites are much more abundant than the achondrites. The literature on these meteorites is quite voluminous but tends for the most part to avoid the question of whether or not a particular chondrite is brecciated. However, there are a few sources of information pertinent to the values of Q. Wahl (1952) described the brecciated structure of many stony meteorites but his survey, now quite old, is rather incomplete. In a more recent work, Binns (1967) conducted a petrological study of many noncarbonaceous chondritic meteorites and found that roughly 15%, 33%, 20% and 60% of the enstatite chondrites, H chondrites, L chondrites and LL chondrites are brecciated. While these represent percentages by number of meteorites, rather than the percentages by volume, they

do indicate that brecciated material is less common among the chondrites than among the basaltic achondrites. Actually, as we shall see, these qualitative estimates of Q are sufficiently accurate for the purposes at hand.

We will compare these observations with the values of Q estimated for the dispersal of weak asteroids. As mentioned in the previous chapter, it is difficult to compute Q(n) for these asteroids. Besides, catastrophic events may actually contribute more debris than cratering events. Because of low ejection velocities less debris escapes a weak asteroid than from a strong body. Furthermore, the spallation mechanism which was called upon to augment the quantity of debris liberated in noncatastrophic events for strong asteroids, should be less effective in weak materials. Thus, dispersal may be the dominant source of meteorites from weak asteroids. Inspection of Figure 17 shows that virtually any asteroid larger than 20 km in diameter could have produced enough brecciated material to be a parent body for the enstatite, H, L, or LL chondrites. This is a good example of why it is important to consider the stochastic nature of regolith evolution. If only the average values of Q are considered one might conclude that a 20 km body is unable to develop enough regolith to produce the LL chondrites or that bodies larger than 100 km produce more breccias than observed for the enstatite chondrites. The large variance of Q renders such conclusions invalid.

Descriptions of the textures of carbonaceous chondrites are even more scarce than for the other chondrites. All of the C1 chondrites are observed to be gas-rich (Anders, 1978) and, therefore, are also brecciated. Several C3V chondrites are brecciated (McSween, 1977), the most notable member being Allende. The large mass of Allende (2000 kg) results in a value of Q near unity for these meteorites. The C3O chondrites are described by Methot et al. (1975) as being typically brecciated. Thus it would appear that Q for the carbonaceous chondrites, both as a group and within each subgroup, approaches one. Figure 17 would suggest a parent body whose diameter is greater than a few tens of kilometers. Again, the statistical uncertainties inherent in the calculated values of Q preclude a more precise estimate of parent body size.

To summarize, the ubiquity of brecciated material among the basaltic achondrites suggests a parent body (or bodies) with diameter greater than 200-300 km. If Consolmagno and Drake (1977) are correct in their identification of Vesta as the eucrite parent body then basaltic flows on Vesta should be thicker than about 15 km. The observed proportion of brecciated material among the enstatite and ordinary chondrites is consistent with an origin on bodies of diameter greater than 10-20 km. The high value of Q observed for the carbonaceous chondrites suggests a parent body of diameter greater than a few tens of kilometers.

The Exposure Histories of Gas-Rich Meteorites

We saw in Chapter 5 that the predicted charged-particle track distributions for regolith grains on rocky asteroids are quite different from those expected on weak bodies. However, we also found that the distributions do not vary much from one size of rocky asteroid to another. Thus, it would appear that we cannot use these track data to precisely pinpoint the size of meteorite parent bodies. Taking a somewhat more optimistic view, perhaps there is no unique size of parent body that can be associated with a given class of meteorites, i.e. mateorites may indeed originate from a wide size range of asteroids. We now compare the Monte Carlo irradiation results described in Chapter 5 with the observed irradiation features in gas-rich meteorites to see what we can infer about the origins of these meteorites.

Measurements of the particle-track density distributions in meteorites are not overly abundant in the literature. One group of stony meteorites, the aubrites, has been studied in some detail. Roughly 1/3 of the aubrites are gas-rich (Anders, 1978). Typically, in the gas-rich members, 20% of the grains have surface densities of SCR tracks of $>10^8/cm^2$, but this fraction can vary from 3% to nearly 50% (Poupeau and Berdot, 1972; Poupeau et al., 1974). Thus, of all the grains in the aubrites, about 6% (varying from 1% to 15%) have SCR track densities greater than 10^8. This is consistent with the track density distributions shown in Chapter 5. For rocky asteroids between 100 and 1000 km diameter the fraction of grains with track densities

greater than 10^8 is about 3-5% (cf. Figures 18-22). There is a slight discrepency in that Poupeau and Berdot (1972) observed maximum track densities of 10^9 whereas the maximum densities resulting from the Monte Carlo simulations was about $5x10^8$. However, this maximum density would probably increase if a larger number of grains were tested in the simulations. Poupeau and Berdot also observed a peak in the GCR track density at about $5x10^5$, which they attributed to irradiation while the meteorites were in transit to the Earth. This peak is rather large and undoubtedly envelopes the GCR peak near 10^4 produced in the Monte Carlo model. The number of tracks with densities between 10^6 and 10^8 was observed to be comparable to the number above 10^8, whereas the predicted distributions show a somewhat smaller fraction of grains above 10^8. This could easily be explained by the uncertainties in the assumed track production rate discussed in Chapter 2. Poupeau et al. (1974) estimated that the SCR irradiated crystals spent no more than 10^3-10^4 years in the upper 10-100 microns of the regolith. From the density of GCR tracks, the time spent in the upper 10cm-1m was estimated to be less than 10^6 yr. These estimates agree very well with the data presented in Table 7. Poupeau et al. suggested that the exposure times of the aubritic grains, which are very short compared to lunar soils, could only result from evolution in a regolith where the stirring rate was high compared to that in the lunar regolith. The assumption that such a high mixing rate existed only long ago in the asteroid belt led Poupeau et al. to the conclusion that the aubrites must have formed 3.8-4 Gyr ago. The

Monte Carlo simulations, which employ present-day estimates of input parameters, clearly demonstrate that the aubrites could be the result of a more recent regolith origin.

Numerous studies of another group of stony meteorites, the howardites, have been made (Lal and Rajan, 1969; Pellas et al., 1969; Wilkening et al., 1971; Wilkening, 1971; Barber et al., 1971; Macdougall et al., 1974; Rajan, 1974; Price et al., 1975; Anders, 1978). Some of the basic observations, which are pertinent to our discussions, are (a) SCR tracks are most often observed to be 10^8 at grain surfaces and 10^7 in the central regions; (b) 50-90% of the track-rich grains (defined as those grains with central track densities $>10^8$) exhibit nonuniform densities of tracks around their borders; (c) roughly 1/3 of the howardites are gas-rich; and (d) typically 5-20% of the grains are track-rich. The observation that many grains have surface densities near 10^8 agrees roughly with the computed track distributions. The observation that most irradiated grains have higher track densities on one side than on another is also consistent with our calculations. Table 7 indicates that regolith grains should be reoriented only a few times during their exposure histories. Observations (c) and (d) imply that about 1-6% of the regolith grains should have central densities greater than 10^8. On the other hand, Figures 18b-22b exhibit central densities which rarely exceed $5x10^6$ to 10^7. This discrepency might be explained by uncertainties in the assumed production rate of tracks. For example, the production rate of Hutcheon et al. (1975) is about a factor of ten

higher than the adopted rate (see Chapter 2). We could also explain the discrepency in track densities if the howardites were irradiated during a period of solar system evolution when the ion flux was higher than at present. This, however, is purely speculative because there is no conclusive evidence for a higher SCR flux in the past (Crozaz, 1980). Alternatively, the heavily irradiated grains may have acquired their tracks prior to being chipped off of larger "parent rocks", as suggested by Borg et al. (1975).

A few studies of the irradiation histories of ordinary chondrites have been made (Shultz et al., 1972; Lorin and Pellas, 1979) but details of the track density distributions are not available. We will just note that the observed abundances of gas-rich members among the ordinary chondrites (about 10%; Anders, 1978) is in rough agreement with our results.

Because of their peculiar nature, the carbonaceous chondrites have been fairly well scrutinized. They stand out among the meteorites in that they exhibit very low track densities. For example, most grains have surface track densities of roughly 10^7 and only rarely exceed 10^8 (Goswami et al., 1976; Macdougall and Phinney, 1977; Korotkova et al., 1979). Around 60-80% of the carbonaceous chondrites are gas-rich (Anders, 1978) but only a few percent (ranging from 1-20%) of the grains have central track densities greater than 10^5 (Goswami et al., 1976), and only about 30% of these irradiated grains have densities exceeding 10^8 (Goswami and Lal, 1979). Additionally, only a few percent of the heavily irradiated grains show

evidence of irradiation on more than one side (Macdougall, 1976; Goswami and Lal, 1979). By comparing these observations to our results for small weak asteroids (Figures 23-24) we see that, first of all, these small bodies should produce rather immature meteorites. The primary reason is, of course, that catastrophic fragmentation occurs rather quickly. Such impacts cause major internal fracturing and undoubtedly will mix much of the surficial material into the interior, thus shielding it from further irradiation. Indeed only a few percent of the regolith grains acquire central track densities higher than 10^5 (Figures 23b and 24b), in agreement with the observed values. Furthermore, Table 7 implies that grains emplaced on the surface hardly ever change their orientation and thus should develop very anisotropic track distributions. There is, however, a marked disparity between the Monte Carlo results and the observations: roughly 0.5-3% of the grains should have central densities higher than 10^8 but none are observed in the computed track distributions. This might be written off as a result of the statistics of small numbers (only 100 test grains were used) but the lack of any grains with densities greater than 10^6 makes this an unlikely possibility. Goswami and Lal (1979) noted this problem and suggested that the grains in carbonaceous chondrites were irradiated while they resided in centimeter-size clumps prior to accretion onto their parent bodies. The Monte Carlo results seem to indicate that a regolith scenario is

incapable of producing the carbonaceous chondrites. However, we should again note that a higher charged-particle flux could remove the discrepency.

Overall, the Monte Carlo simulations of the exposure histories of regolith grains agree quite well with observations of irradiated grains in gas-rich meteorites. The calculations presented remove the necessity to invoke an early irradiation of meteorites as some have suggested in the past (Lal and Rajan, 1969; Poupeau et al., 1974). The near constancy of the model distributions for different sizes of asteroids suggests that any given group of meteorites may originate from a rather wide size range of parent bodies. This contrasts with the conclusions of Housen et al. (1979a,b) who suggested that large asteroids should have better-mixed and rather mature regoliths compared to smaller bodies. The predicted central track densities are somewhat lower than those observed, but this discrepency can be accounted for by uncertainties in the assumed track production rate. Determining whether regolith models can account for the details of the observed irradiation features cannot be done until better estimates of the various input parameters, especially the production rate of tracks, become available.

CHAPTER 7

SUMMARY AND FUTURE WORK

Models of asteroidal regoliths are important tools in the study of the origins of brecciated and gas-rich meteorites. Previous investigations in this area were reviewed in Chapter 3. The two most detailed models are those of Housen et al. (1979a,b) and Langevin and Maurette (1980). Both of these models concentrated primarily on the depth of an asteroid's regolith and attempted to characterize the depth by an average taken over a restricted part of the surface. In order that the average might reasonably describe at least part of the surface, only the areas over which the regolith was thought to be relatively uniform in depth, i.e. the areas "saturated" by numerous small impacts, were modeled. Housen et al. (1979 a,b) collectively referred to these areas as the "typical region". Note that modeling a typical region implies that some parts of an asteroid's surface were ignored. For example, in the Housen et al. model, roughly 1/3 of the surface area of small bodies and at least 1/2 of the area on large bodies were ignored. Of course, there is no reason to expect meteorites to be derived only from the typical regions on asteroids. Furthermore, Housen et al. and Langevin and Maurette could not estimate the effectiveness of modeling a typical region, i.e. they

could not determine the degree to which the average value characterized the distribution of regolith depths over the modeled parts of the surface.

Another drawback of previous studies is that regolith evolution was considered from a determinate point of view, i.e. asteroids of identical size were assumed to have identical regoliths. Actually, every similar-size asteroid should develop a unique regolith because of the stochastic nature of the cratering process. For instance, even though we might precisely specify the average formation rate of craters, we cannot predict with certainty the number of craters that will form on any given body. These stochastic effects are important when regolith models are used in speculations on the origin of meteorites.

A third drawback of earlier studies is that none have considered, in detail, the exposure histories of regolith grains to space irradiation. A few calculations of exposure times have been performed but the investigations were far from exhaustive.

The stochastic evolution of asteroidal regoliths and the connections with brecciated and gas-rich meteorites were considered in Chapters 4,5 and 6. A model of regolith growth was constructed which has an advantage over previous models in that it describes the entire surface of an asteroid. Furthermore, the distribution of regolith depths, not just the mean value, was obtained. A Monte Carlo algorithm was constructed and used to simulate the charged-particle irradiation histories of regolith grains. The main results from the statistical modeling are now summarized.

1. The computed distribution of regolith depths was found to have a rather large standard deviation (approximately equal to the mean depth) because of variations in depth over the surface of any given asteroid and because of stochastic fluctuations in the average regolith depth among similar-size bodies. Avoiding the parts of a surface that were occupied by large craters or thick ejecta deposits did not change the magnitude of the standard deviation relative to the mean. Thus, modeling a typical region, as opposed to modeling the entire surface, does not significantly improve the utility of the average value in describing asteroidal regolith depths.

2. The large statistical uncertianty associated with regolith depth limits the power of regolith models in predicting the sizes of meteorite parent bodies. For example, virtually and rocky asteroid of diameter larger than 100-200 km could have produced the quantity of brecciated material observed in the achodritic meteorites. Smaller bodies can be ruled out because they do not retain enough ejecta to develop regoliths of the required depth. Weak asteroids larger than about 20 km could have produced the observed abundance of brecciated material in the chondrites.

3. Most asteroids are collisionally fragmented before their regoliths can attain a state of statistical equilibrium. Moreover, the equilibrium times are generally greater than the age of the solar system. Thus, equilibrium models of regolith evolution (e.g. Duraud et al., 1979) are not valid.

4. Monte Carlo simulations showed that the irradiation history of a regolith is quite independent of asteroid size, for those bodies large enough to generate regoliths. Thus, Housen et al. (1979a,b) were wrong in their conclusion that large asteroids should have highl-gardened and rather mature regoliths compared to smaller bodies. The irradiation of grains is much more extensive on rocky asteroids than on weaker bodies, primarily because of the short fragmentation lifetimes of weak asteorids. This is in qualitative agreement with the observed differences between the irradiation features in the achondrites and the chondrites. The computed fraction of grains which were exposed to space irradiation agrees well with the fraction observed in gas-rich meteorites. The range of densities of charged-particle tracks in regolith grains is comparable to that observed in meteorites, although the computed fraction of heavily irradiated grains is significantly smaller that that observed. This discrepency could be explained by uncertainties in the assumed production rate of tracks. Alternatively, the heavily irradiated grains might be due to irradiation while the grains were part of larger "parent rocks", as suggested by Borg et al. (1975). In general, the irradiation features observed in gas-rich meteorites do not require an origin during early epochs of solar system evolution, as previously suggested.

Modeling asteroidal regolith evolution is currently hampered by inadequate knowledge of some of the necessary input parameters and certain aspects of the cratering process. The most critical gaps in our knowledge are the mass-frequency distribution of matter and the flux of track-producing ions in the asteroid belt, now and in the past, and the physics of the impact process in low gravity environments. These deficiencies are amenable to some improvement by possible, albeit difficult, observations or experiments.

In short, regolith models have reached a level of detail which is roughly similar to the precision of the required input parameters. Further advances in our understanding of regoliths on asteroids must come from further experimentation.

APPENDIX 1

THE MOMENTS OF A JUMP IN SURFACE ELEVATION

We now derive expressions for m_1 and m_2, the first two moments of the size of a jump in surface elevation. The methodology involved in the "improved approximation" described in Chapter 4 is used. That is, excavations by craters larger than a diameter, D^*, are excluded from the calculations. The moments for the "first approximation" can be found by setting $D^*=D_1$, where D_1 is the diameter of the smallest crater assumed to form on the asteroid. In doing so the excavation effects of all sizes of craters are included.

If Y is the (random) size of a jump in the surface elevation at a randomly selected point on an asteroid's surface then the nth absolute moment of Y can be written as

$$E[Y^n] = \int_{D_1}^{D_r} G_n^-(u)\, C^-(u)\, H(u)\, du + \int_{D_1}^{D_r} G_n^+(u)\, C^+(u)\, H(u)\, du \qquad \text{(A1.1)}$$

$$\equiv E[Y^n]_{excavation} + E[Y^n]_{burial}.$$

Note that m_1 and m_2 are obtained from equation (A1.1) by setting n=1 or n=2 respectively. $G_n^-(u)$ is defined as the conditional expectation of Y^n given that a crater of diameter u has formed over the surface

point. $C^-(u)$ is the probability that the crater forms over the point given that the crater diameter is equal to u. H(u)du is the probability that the crater diameter is in the interval du. The symbols with + superscripts are defined similarly for burial events. The excavation and burial terms in equation (A1.1) are now considered separately.

Excavation

If a crater of diameter D forms on the surface and the distance between the crater center and a surface point is R then the change, Y, in the surface elevation at the point is

$$Y = -c_1 D - \sqrt{c_2 D^2 - R^2} \qquad \text{(A1.2)}$$

for R<D/2. The constants c_1 and c_2 are given by

$$c_1 = (4\mu^2 - 1)/8\mu$$
$$c_2 = [(4\mu^2 + 1)/8\mu]^2$$

where μ is the depth to diameter ratio for craters.

In computing $G_n^-(u)$ we are given that D has the value u. Thus, Y is a function of the single random variable R. $G_n^-(u)$ can be evaluated by noting that the probability that R is in the interval dx is

$$\text{prob}\{ R \in dx \} = 2\pi x\, dx/(\pi u^2/4) = 8x/u^2 \qquad 0 \le x \le u/2.$$

Thus, we can write

$$G_n^-(u) = \int_0^{u/2} [-c_1 u - \sqrt{c_2 u^2 - x^2}]^n \, (8x/u^2) \, dx. \qquad (A1.3)$$

This integral can be easily evaluated by substituting a new variable for the expression in brackets on the r.h.s. of equation (A1.3). After some algebra we obtain

$$G_n^-(u) = (-\mu)^n \, \frac{[n(4\mu^2 + 1) + 2]}{(n+1)(n+2)} \, u^n . \qquad (A1.4)$$

Recall that $C^-(u)$ is the probability that an excavation occurs given the formation of a crater of diameter u. Thus

$$\begin{aligned} C^-(u) &= (\pi u^2/4)/4\pi R_A^2 && u < D^* \\ &= 0 && u > D^* \end{aligned} \qquad (A1.5)$$

$C^-(u)$ is zero when $u>D^*$ because craters larger than D^* are not allowed to excavate (see Chapter 4).

The crater size-frequency distribution which was adopted in Chapter 2 allows us to to express the p.d.f. of crater diameter as

$$H(u) = a u^{a-1} \, / \, (D_r^a - D_l^a) \qquad D_l < u < D_r. \qquad (A1.6)$$

Substituting equations (A1.4), (A1.5) and (A1.6) into the expression for $E[Y^n]_{excavation}$ given in equation (A1.1) we find

$$E[Y^n]_{excavation} = \frac{(-\mu)^n \, [n(4\mu^2+1) + 2] \, a \, (D^{*n+2+a} - D_l^{n+2+a})}{(n+1)(n+2) \, 16R_A^2 \, (D_r^a - D_l^a) \, (n+2+a)} \qquad (A1.7)$$

Burial

The burial term in equation (A1.1) is now evaluated. Because ejecta blanket morphology for gravity scaling differs from that of strength scaling (see Chapter 2), these two cases are considered separately.

Gravity Scaling

Let us now compute $G_n^+(u)$, the nth moment of the size of a jump given that a crater of diameter u has buried a surface point. $G_n^+(u)$ can be found by multiplying the nth power of the expression for the thickness, B(x), of ejecta at a distance x from a crater (equation 2.12) times the probability that the crater forms at a distance x from the surface point and then integrating over all x. The p.d.f. of the distance is

$$2\pi x/(4\pi R_A^2 - \pi u^2/4) = x/(2R_A^2 - u^2/8).$$

Thus, we can write

$$G_n^+(u) = \int_{u/2}^{2R_A} \left\{(a_e c/4\pi)[1- (u/24R_A)^{a_e/2}](u/2x)^{a_e/2 + 3} x \right\}^n \frac{x}{2R_A^2 - u^2/8}\, dx$$

$$= \left\{(a_e c/4\pi)[1-(u/24R_A)^{a_e/2}]\ (u/2)^{a_e/2 + 3}\right\}^n \frac{(2R_A)^{e_1} - (u/2)^{e_1}}{(2R_A^2 - u^2/8)\ e_1} \qquad \text{(A1.8)}$$

where $e_1 = -n(a_e/2+2)+2$. The probability, $C^+(u)$, of getting a burial event, given the formation of a crater of diameter u, is

$$C^{+}(u) = (4\pi R_A^2 - \pi u^2/4)/4\pi R_A^2 \ . \qquad \text{(A1.9)}$$

Now, $E[Y^n]_{burial}$ is found from

$$E[Y^n]_{burial} = \int_{D_l}^{D_r} G_n^{+}(u)\ C^{+}(u)\ H(u)\ du. \qquad \text{(A1.10)}$$

Equations (A1.8), (A1.9) and (A1.6) are substituted into equation (A1.10). By expanding the expression $\{\cdots\}$, given in equation (A1.8), in a binomial series, substituting in the expression for c given in equation (2.4), and performing some straightforward algebra we find

$$E[Y^n]_{burial} = [a_e \mu(3+4\mu^2)/24]^n\ a/[e_1(D_r^a - D_l^a)\ 8R_A^2]$$
$$\cdot \sum_{i=0}^{n} \binom{n}{i} (-1)^i\ (24R_A)^{-ia_e/2} \left\{ (4R_A)^{e_1} (D_r^{e_2} - D_l^{e_2})/e_2 \right.$$
$$\left. - (D_r^{e_3} - D_l^{e_3})/e_3 \right\} \qquad \text{(A1.11)}$$

where

$$e_2 = ia_e/2 + n(a_e/2 + 3) + a$$

and

$$e_3 = ia_e/2 + n + 2 + a.$$

Strength Scaling

We can evaluate $G_n^+(u)$ in the same way that we found equation (A1.8). But note that, for strength scaling, the p.d.f. for the distance between the surface point and the crater center is

$$2\pi x/(4\pi R_A^2 - \pi x_m^2).$$

Using the expression for B(x) in equation (2.13) we find

$$G_n^+(u) = \int_{x_m}^{2R_A} [B(x)]^n \, [2x/(4R_A^2 - x_m^2)] \, dx$$

$$= \left\{(a_e c/4\pi)\ (1-\gamma)\ (u/2)^3\ x_m^{a_e/2}\right\}^n \ \frac{(2R_A)^{e_1} - x_m^{e_1}}{(2R_A^2 - x_m^2/2)\ e_1} \ . \quad \text{(A1.12)}$$

For strength scaling the fraction, γ, of escaping ejecta is independent of crater diameter. An expression for γ is given in Chapter 2. The minimum ballistic range, x_m, is a function of u.

For strength scaling a burial event only occurs when a crater forms at a distance greater than x_m from the surface point. Thus, we can write $C^+(u)$ as

$$C^+(u) = (4\pi R_A^2 - x_m^2)/4\pi R_A^2 \ . \quad \text{(A1.13)}$$

Substituting equations (A1.12), (A1.13) and (A1.6) into equation (A1.10) yields

$$E[Y^n]_{burial} = [a_e \mu(3+4\mu^2)\ (1-\gamma)/12]^n\ a/[(D_r^a - D_l^a)2R_A^2 e_1]$$

$$\cdot \int_{D_l}^{D_r} (u/2)^{3n}\ x_m^{nae/2}\ [(2R_A)^{e_1} - x_m^{e_1}]\ u^{a-1}\ du. \qquad \text{(A1.14)}$$

The integral in equation (A1.14) is evaluated numerically.

We now have all the expressions required to find the moments of the jump size. For gravity scaling, $E[Y^n]$ is found by summing equations (A1.7) and (A1.11). For strength scaling we sum equations (A1.7) and (A1.14). The moments m_1 or m_2 can be found by setting n=1 or n=2 in the expressions for $E[Y^n]$.

APPENDIX 2

DETAILS OF SOME DERIVATIONS

We now outline the derivations of the expressions for the moment generating function, $\Omega(s,t)$, of regolith depth at time t (equation 4.5)' and the c.d.f., $F_r(x)$, of regolith depth at catastrophic rupture (equation 4.11).

The Moment Generating Function of Regolith Depth at Time t

Equation (4.5) involves the p.d.f. of regolith depth at time t. The p.d.f. is obtained by differentiating equation (4.4) with respect to x. By substituting the resulting expression into the integral in equation (4.5) we can write

$$\Omega(s,t) = \sqrt{2/\pi m_2 \lambda t} \int_0^\infty \exp[-(x-m_1\lambda t)^2/2m_2\lambda t + sx]\, dx \qquad \text{(A2.1)}$$

$$- (m_1/m_2) \int_0^\infty \exp[2m_1 x/m_2 + sx]\, \operatorname{erfc}[(x+m_1\lambda t)/\sqrt{2m_2\lambda t}]\, dx$$

The first integral in equation (A2.1) can be found in the table of integrals by Gradshteyn and Ryzhik (1980). We will find that an integral of this kind is also useful in evaluating the second term in equation (A2.1). The integral can be written in general form as

$$\int_0^\infty \exp[-a(x+b)^2 + cx]\,dx = \sqrt{\pi/4a}\,\exp[(c/4a - b)c] \cdot \operatorname{erfc}[(2ab-c)/2\sqrt{a}] \tag{A2.2}$$

where a,b and c are constants and a>0. Thus, the first term in equation (A2.1) can be written as

$$\exp[(2m_1 + m_2 s)s\lambda t/2]\,\operatorname{erfc}[-(m_1 + m_2 s)\sqrt{\lambda t/2m_2}] \tag{A2.3}$$

The second integral in equation (A2.1) can be integrated by parts to yield

$$\begin{aligned} -(m_1/m_2)\int_0^\infty \exp[2m_1 x/m_2 + sx]\,\operatorname{erfc}[(x+m_1\lambda t)/\sqrt{2m_2\lambda t}]\,dx \\ = [m_1/(2m_1+m_2 s)]\Big\{ \operatorname{erfc}[m_1\lambda t/\sqrt{2m_2\lambda t}] \\ - (2/\sqrt{2\pi m_2\lambda t})\int_0^\infty \exp[-(x+m_1\lambda t)^2/2m_2\lambda t + (2m_1/m_2 + s)x]\,dx\Big\} \end{aligned} \tag{A2.4}$$

The integral on the r.h.s. of equation (A2.4) can be evaluated by using equation (A2.2). Combining the resulting expression with expression (A2.3) we find

$$\begin{aligned} \Omega(s,t) = \{\ (m_1+m_2 s)\ \exp[(2m_1+m_2 s)s\lambda t/2]\ \operatorname{erfc}[-(m_1+m_2 s)\sqrt{\lambda t/2m_2}] \\ + m_1\ \operatorname{erfc}[m_1\sqrt{\lambda t/2m_2}]\ \}/(2m_1+m_2 s) \end{aligned}$$

which is equivalent to equation (4.5) presented in Chapter 4.

The C.D.F. of Regolith Depth at Fragmentation

According to equations (4.9) and (4.11) the c.d.f., $F_r(x)$, can be written as

$$F_r(x) = \int_0^\infty F(x,t)\ \lambda_r e^{-\lambda_r t}\ dt \tag{A2.5}$$

If we substitute equation (4.4) into equation (A2.5) and express the function erf(·) in terms of erfc(·) then we find

$$F_r(x) = 1 + (\lambda_r/2) \int_0^\infty \mathrm{erfc}[(x-m_1\lambda t)/\sqrt{2m_2\lambda t}]\ e^{-\lambda_r t}\ dt$$

$$- e^{2m_1 x/m_2}\ (\lambda_r/2) \int_0^\infty \mathrm{erfc}[(x+m_1\lambda t)/\sqrt{2m_2\lambda t}]\ e^{-\lambda_r t}\ dt \tag{A2.6}$$

If we now make the simple transformation $s^2=t$ then the two integrals in equation (A2.6) can be expressed in a form which can be found in Gradshteyn and Ryzhik (1980), i.e.

$$\int_0^\infty \mathrm{erfc}[as + b/s]\ e^{(a^2-c)s^2}\ s\ ds = \exp[-2b(a+\sqrt{c})]/2\sqrt{c}(\sqrt{c} + a) \tag{A2.7}$$

where a,b, and c are constants and b,c>0. The two integrals in equation (A2.6) can be evaluated, using equation (A2.7), combined and simplified to yield

$$F_r(x) = 1 - \exp[(m_1 x/m_2)\ (1 - \mathrm{sign}(m_1)\ \sqrt{1 + 2m_2\lambda_r/m_1^2\lambda})]$$

which is the desired result.

LIST OF REFERENCES

Anders, E. (1964). Origin, age and composition of meteorites. Space Sci. Rev. 3, 583-714.

Anders, E. (1975). Do stony meteorites come from comets? Icarus 24, 363-371.

Anders, E. (1978). Most stony meteorites come from the asteroid belt. In Asteroids: An Exploration Assessment (D. Morrison and W.C. Wells, eds.), NASA Conf. Publ. 2053, 57-76.

Auer, S. (1974). The asteroid belt: Doubts about the particle concentrations measured with the Asteroid/Meteoroid detector on Pioneer 10. Science 186, 650-652.

Austin, M.G., Thomsen, J.M., Ruhl, S.F., Orphal, D.L. and Shultz, P.H. (1980). Calculational investigation of impact cratering dynamics: Material motions during the crater growth period. Proc. Lunar Planet. Sci. Conf. 11th, 2325-2345.

Barber, D.J., Cowsik, R., Hutchison, I.D., Price, P.B. and Rajan, R.S. (1971). Solar flares, the lunar surface, and gas-rich meteorites. Proc. Second Lunar Sci. Conf., 2705-2714.

Baxter, G. and Donsker, M.D. (1957). On the distribution of the supremum functional for processes with stationary independent increments. Trans. Am. Math. Soc. 85, 73-87.

Bhandari, N., Goswami, J.N., and Lal, D. (1973). Kinetic energy spectra of 5-1500 Mev/n VH nuclei-long term averaged flux at 1-3 a.u. Proc. 13th International Cosmic Ray Conference 1, 281-286.

Binns, R.A. (1967). Structure and evolution of the non-carbonaceous chondritic meteorites. Earth Planet. Sci. Lett. 2, 23-28.

Blanford, G.E., Fruland, R.M. and Morrison, D.A. (1975). Long-term differential energy spectrum for solar flare iron-group particles. Proc. Lunar Sci. Conf. 6th, 3557-3576.

Bloch, M.R., Fechtig, H., Gentner, W., Neukum, G., and Schneider, E. (1971). Meteorite impact craters, crater simulations, and the meteoroid flux in the early solar system. Proc. Second Lunar Sci. Conf., 2639-2652.

Borg, J., Durand, J.P., Langevin, Y. and Maurette, M. (1975). A Monte-Carlo model for the accumulation of solar flare tracks and spallation products in extraterrestrial regoliths. Meteoritics 10, 365-368.

Brownlee, D.E., and Rajan, R.S. (1973). Micrometeorite craters discovered on chondrule-like objects from Kapoeta meteorite. Science 182, 1341-1344.

Brownlee, D.E., Horz, F., Hartung, J.B., and Gault, D.E. (1975). Density, chemistry, and size distribution of interplanetary dust. Proc. Lunar Sci. Conf. 6th, 3409-3416.

Cameron, A.G.W. (1979). On the origin of asteroids. In Asteroids (T. Gehrels, ed.). Univ. of Arizona Press, 992-1007.

Chapman, C.R. (1971). Surface properties of asteroids. Ph.D. dissertation, Mass. Inst. Tech.

Chapman, C.R. (1976). Asteroids as meteorite parent bodies: The astronomical perspective. Geochim. Cosmochim. Acta 40, 701-719.

Cintala, M.J., Head, J.W. and Veverka, J. (1978). Characteristics of the cratering process on small satellites and asteroids. Proc. Lunar Planet. Sci. Conf. 9th, 3803-3830.

Cintala, M.J., Head, J.W. and Wilson, L. (1979). The nature and effects of impact cratering on small bodies. In Asteroids (T. Gehrels., ed.). Univ of Arizona Press, 579-600.

Consolmagno G.J. and Drake M.J. (1977). Composition and evolution of the eucrite parent body: evidence from rare earth elements. Geochim. Cosmochim. Acta 41, 1271-1282.

Cox, D.R. and Miller H.D. (1972). The Theory of Stochastic Processes. Chapman and Hall Ltd., 398 pp.

Croft, S.K. (1980). Cratering flow fields: Implications for the excavation and transient expansion stages of crater formation. Proc. Lunar Planet. Sci. Conf. 11th, 2347-2378.

Crozaz, G. (1980). Solar flare and galactic cosmic ray tracks in lunar samples and meteorites: What they tell us about the ancient sun. Proc. Conf. Ancient Sun, 331-346.

Crozaz, G. and Walker, R.M. (1971). Solar particle tracks in glass from the Surveyor III Spacecraft. Science 171, 1237-1239.

Damon, P.E. (1977). Solar induced variations of energetic particles at one AU. In The Solar Output and Its Variation. (O.R. White, ed.) Colorado Assoc. Univ. Press, Boulder, Colorado, 429-445.

Davis, D.R., Chapman, C.R., Greenberg, R., Weidenschilling, S.J., and Harris, A.W. (1979). Collisional evolution of asteroids: Populations, rotations, and velocities. In Asteroids (T. Gehrels, Ed.). Univ. of Arizona Press, 528-557.

Delaney, J.S., Prinz, M., Nehru C.E. and Harlow, G.E. (1981). A new basalt group from howardites: mineral chemistry and relationships with basaltic achondrites. Lunar Planet. Sci. Conf. XII, 211-213.

Dence, M.R., Grieve, R.A.F., and Robertson, P.B. (1977). Terrestrial impact craters: Principal characteristics and energy considerations. In Impact and Explosion Cratering, Proc. of Symposium on Planetary Cratering Mechanics. (D.J. Roddy, R.O. Pepin, and R.B. Merrill, Eds.). Pergamon, New York, 247-275.

Dohnanyi, J.S. (1969). Collisional model of asteroids and their debris. J. Geophys. Res. 74, 2531-2554.

Dohnanyi, J.S. (1972). Interplanetary objects in review: Statistics of their masses and dynamics. Icarus 17, 1-48.

Dohnanyi, J.S. (1976). Sources of interplanetary dust: Asteroids. In Interplanetary Dust and Zodiacal Light, Proc. of IAU Colloq. No. 31, (H. Elsasser and H. Fechtig, Eds.). Springer-Verlag, 187-205.

Dran, J.C., Duraud, J.P., Langevin, Y. and Maurette, M. (1979). The predicted irradiation record of asteroidal regoliths and the origin of gas-rich meteorites. Lunar Planet. Sci. Conf. X, 309-311.

Dreibus, G., Kruse, H., Spettel, B. and Wanke, H. (1977). The bulk composition of the moon and the eucrite parent body. Proc. Lunar Sci. Conf. 8th, 211-227.

Duke, M.B. and Silver, L.T. (1967). Petrology of eucrites, howardites and mesosiderites. Geochim. Cosmochim. Acta 31, 1637-1665.

Duraud, J.P., Langevin, Y. and Maurette, M. (1979). An analytical model for the regolith evolution on small bodies in the solar system. Lunar Planet. Sci. Conf. X, 323-325.

Feller W. (1971). An Introduction to Probability Theory and Its Applications, Vol. II. Wiley and Sons, 669 pp.

Fish, R.A., Goles G.G., and Anders E. (1960). The record in meteorites III. On the development of meteorites in asteroidal bodies. Astrophys. J. 132, 243-258.

Fleischer, R.L., Price, P.B. and Walker, R.M. (1975). Nuclear Tracks in Solids. Univ. of Calif. Press, Berkeley, 605 pp.

Fujiwara, A., Kamimoto, G., and Tsukamato, A. (1977). Destruction of basaltic bodies by high-velocity impact. Icarus 31, 277-288.

Fukuoka, T., Boynton, W.V., Ma, M.-S. and Schmitt, R.A. (1977). Genesis of howardites, diogenites, and eucrites. Proc. Lunar Sci. Conf. 8th, 187-210.

Ganapathy, R. and Anders, E. (1969). Ages of calcium-rich achondrites-II. Howardites, nukhlites, and the Angra dos Reis angrite. Geochim. Cosmochim. Acta 33, 775-787.

Gault, D.E., Shoemaker, E.M., and Moore, H.J. (1963). Spray ejected from the lunar surface by meteoroid impact. NASA TN D-1767.

Gault, D.E., Quaide, W.L., and Oberbeck, V.R. (1968). Impact cratering mechanics and structures. In Shock Metamorphism of Natural Materials (B.M. Short and N.M. Short, Eds.). Mono Book Corp., Baltimore, 87-99.

Gault, D.E., and Wedekind, J.A. (1969). The destruction of tektites by micrometeoroid impact. J. Geophys. Res. 74, 6780-6794.

Gault, D.E. (1972). Displaced mass, depth, diameter, and effects of oblique trajectories for impact craters formed in dense crystalline rocks. The Moon 6, 32-44.

Gault, D.E. (1974). Impact Cratering. In A Primer in Lunar Geology (R. Greeley and P. Shultz, Eds.). Collection of papers from a short course in lunar geology, NASA Ames Research Center.

Gault, D.E., and Wedekind, J.A. (1977). Experimental hypervelocity impact into quartz sand-II, Effects of gravitational acceleration. In Impact and Explosion Cratering, Proc. of Symposium on Planetary Cratering Mechanics. (D. J. Roddy, R. O. Pepin, and R. B. Merrill, Eds.). Pergamon, New York, 1231-1244.

Goldreich, P., and Ward, W.R. (1973). The formation of planetesimals. Astrophys. J. 183, 1051-1061.

Goswami, J.N., Hutcheon, I.D. and Macdougall, J.D. (1976). Microcraters and solar flare tracks in crystals from carbonaceous chondrites and lunar breccias. Proc. Lunar Sci. Conf. 7th, 543-562.

Goswami, J.N., and Lal, D. (1979). Formation of the parent bodies of the carbonaceous chondrites. Icarus 40, 510-521.

Gradshteyn, I.S. and Ryshik, I.M. (1980). Table of Integrals, Series and Products. Academic Press, 1160 pp.

Greenberg, R., Wacker, J., Hartmann, W.K. and Chapman, C.R. (1978). Planetesimals to planets: Numerical simulation of collisional evolution. Icarus 35, 1-26.

Hamilton, D.C. (1977). The radial transport of energetic solar flare particles from 1 to 6 AU. J. Geophys. Res. 82, 2157-2169.

Hanner M.S., Sparrow, J.G., Weinberg, J.L., and Beeson, D.E. (1976). Pioneer 10 observations of zodiacla light brightness near the ecliptic: Changes with heliocentric distance. In Interplanetary Dust and Zodiacal Light, Proc. of IAU Colloq. No. 31 (H. Elsasser and H. Fechtig, Eds.). Springer-Verlag, 29-35.

Hapke, B. (1971). Inferences from optical properties concerning the surface texture and composition of asteroids. In Physical Studies of the Minor Planets (T. Gehrels, ed.), Univ. of Ariz. Press, 67-77.

Hartmann, W.K. (1969). Terrestrial, lunar and interplanetary rock fragmentation. Icarus 10, 201-213.

Hartmann, W.K. (1978). Planet formation: Mechanism of early growth. Icarus 33, 50-61.

Heymann, D., Mazor, E. and Anders E. (1968). Ages of calcium-rich achondrites-I. Eucrites. Geochim. Cosmochim. Acta 32, 1241-1268.

Hostetler, C.J. and Drake M.J. (1978). Quench temperatures of Moore County and other eucrites: residence time on the eucrite parent body. Geochim. Cosmochim. Acta 42, 517-522.

Housen, K.R. (1976). A model of regolith formation on asteroids. Meteoritics 11, 300-301.

Housen, K.R., Wilkening, L.L., Chapman, C.R., and Greenberg, R. (1979a). Asteroidal Regoliths. Icarus 39, 317-351.

Housen, K.R., Wilkening, L.L., Chapman, C.R., and Greenberg, R. (1979b). Regolith development and evolution on asteroids and the moon. In Asteroids, (T. Gehrels, Ed.). Univ. of Arizona Press, 601-627.

Hughes, D.W. (1978). Meteors. In Cosmic Dust (J.A.M. McDonnell, ed.). Wiley and Sons, 123-185.

Humes, D.H., Alvarez, J.M., O'Neal, R.L., and Kinard, W.H. (1974). The interplanetary and near-Jupiter meteoroid environments. J. Geophys. Res. 79, 3677-3684.

Hutcheon, I.D., Macdougall, D. and Price, P.B. (1974). Improved determination of the long term Fe spectrum from 1 to 460 Mev/amu. Proc. Fifth Lunar Sci. Conf., 2561-2576.

Hutchison, R., Bevan, A.W.R. and Hall J.M. (1977). Appendix to the Catalog of Meteorites. British Museum (Natural History), 297 pp.

Ivanov, B.A. (1976). The effect of gravity on crater formation: Thickness of ejecta and concentric basins. Proc. Lunar Sci. Conf. 7th, 2947-2965.

Jerome, D.J. and Goles, G.G. (1971). A re-examination of relationships among pyroxene-plagioclase achondrites. In Activation Analysis in Geochemistry and Cosmochemistry (A.O. Brunfelt and E. Steinnes, eds.), Universitetsforlarget, Oslo, 261-266.

Kessler, D.J. (1968). Upper limit on the spatial density of asteroidal debris. AIAA Journ. 6, 2450.

Kessler, D.J. (1970). Meteoroid environment model-1970 (Interplanetary and planetary). NASA SP-8038.

Korotkova, N.N., Lavrukhina, A.K. and Perelygin, V.P. (1979). Iron group cosmic-ray tracks in the Allende olivine: Evidence of a complex exposure history. Proc. Lunar Planet. Sci. Conf. 10th, 907-920.

Lal, D. (1977). Irradiation and accretion of solids in space based on observations of lunar rocks and grains. Phil. Trans. R. Soc. Lond. A. 285, 69-95.

Lal, D. and Rajan, R.S. (1969). Observations on spave irradiation of individual crystals of gas-rich meteorites. Nature 223, 269-271.

Langevin, Y. and Maurette, M. (1980). A model for small body regolith evolution: The critical parameters. Lunar Planet. Sci. XI, 602-604.

Langevin, Y. and Maurette, M. (1981). Grain size and maturity in lunar and asteroidal regoliths. Lunar Planet. Sci. XII, 595-597.

Lanzerotti, L.J. and Maclennan, C.G. (1973). Abundances of solar cosmic ray alpha particles. J. Geophys. Res. 78, 3935-3941.

Lee, M.A. (1976). Modulation of solar flare particles and track density profiles in gas-rich meteorite grains. J. Geophys. Res. 81, 3207-3213.

Lorin, J.C. and Pellas, P. (1979). Preirradiation history of Djermaia (H) chondritic breccia. Icarus 40, 502-509.

Macdougall, D., Rajan, R.S. and Price, P.B. (1974). Gas-rich meteorites: Possible evidence for origin on a regolith. Science 183, 73-74.

Macdougall, J.D. (1976). Particle track distributions in Murchison (C2) inclusions. Meteoritics 11, 325-326.

Macdougall, J.D. and Phinney D. (1977). Olivine separates from Murchison and Cold Bokkeveld: Particle tracks and noble gases. Proc. Lunar Sci. Conf. 8th, 293-311.

Marcus, A.H. (1970). Distribution and covariance function of elevations on a cratered planetary surface. The Moon 1, 297-337.

Mason, B. (1962). Meteorites. Wiley and Sons, 274 pp.

Mason, B. (1967). The Bununu meteorite, and a discussion of the pyroxene-plagioclase achondrites. Geochim. Cosmochim. Acta 31, 107-115.

Matson, D.L., Johnson, T.V. and Veeder, G.J. (1977). Soil maturity and planetary regoliths: the Moon , Mercury, and the asteroids. Proc. Lunar Sci. Conf. 8th, 1001-1011.

Maurer, W.C., and Rinehart, J.S. (1960). Impact crater formation in rock. J. Appl. Physics 31, 1247-1252.

Maxwell, D.E. (1977). Simple Z-model of cratering, ejection and the overturned flap. Impact and Explosion Cratering, Proc. of Symposium on Planetary Cratering Mechanics. (D.J. Roddy, R.O. Pepin, and R. B. Merrill, Eds.). Pergamon, New York, 1003-1008.

McCarthy, T.S., Ahrens, L.H. and Erlank A.J. (1972). Further evidence in support of the mixing model for howardite origin. Earth Planet. Sci. Lett. 15, 86-93.

McDonald, F.B., Teegarden, B.J., Trainor, J.H., von Rosenvinge, T.T. and Weber, W.R. (1975). The interplanetary acceleration of energetic nucleons. Astrophys. J. 203, L149-L154.

McSween, H.Y. (1977). Petrographic variations among carbonaceous chondrites of the Vigarano type. Geochim. Cosmochim. Acta 41, 1777-1790.

Methot, R.L., Noonan, A.F., Jarosewich, E., deGasparis, A.A. and Al-Far, D.M. (1975). Mineralogy, petrology and chemistry of the Isna (C3) meteorite. Meteoritics 10, 121-131.

Moore, H.J., and Gault, D.E. (1965). The fragmentation of spheres by micrometeoroid impact. USGS Annual Report, 127-150.

Moore, H.J. (1976). Missile impact craters (White Sands Missle Range, New Mexico) and applications to lunar research. USGS Professional Paper 812-B.

Morrison, D.A. and Zinner, E. (1977). 12054 and 76215: New measurements of interplanetary dust and solar flare fluxes. Proc. Lunar Sci. Conf. 8th, 841-863.

Nordyke, M.D. (1962). An analysis of cratering data from desert alluvium. J. Geophys. Res. 67, 1965-1974.

Pellas, P, Poupeau, G., Lorin, J.C., Reeves, H. and Audouze, J. (1969). Primitive low-energy particle irradiation of meteoritic crystals. Nature 223, 272-274.

Pike, R.J. (1977). Apparent depth/apparent diameter relation for lunar craters. Proc. Lunar Sci. Conf. 8th, 3427-3436.

Price, P.B., Hutcheon, I.D., Braddy, D. and Macdougall, D. (1975). Track studies bearing on solar-system regoliths. Proc. Lunar Sci. Conf. 6th, 3449-3469.

Poupeau, G. and Berdot, J.L. (1972). Irradiations ancienne et recente des aubrites. Earth Planet. Sci. Lett. 14, 381-396.

Poupeau, G., Kirsten, T., Steinbrunn, F. and Storzer, D. (1974). The records of solar wind and solar flares in aubrites. Earth Planet. Sci. Lett. 24, 229-241.

Rajan, R.S. (1974). On the irradiation history and origin of gas-rich meteorites. Geochim. Cosmochim. Acta 38, 777-788.

Rajan, R.S., Brownlee, D.E., Heiken, G.H. and McKay, D.S. (1974). Glassy agglutinate-like objects in the Bununu howardite. Meteoritics 9, 394-397.

Reedy, R.C. (1980). Lunar radionuclide records of average solar-cosmic-ray fluxes over the last ten million years. Proc. Conf. Ancient Sun, 365-386.

Safronov, V.S. (1972). The evolution of the protoplanetary cloud and the formation of the earth and planets. (Nauka Press, Moscow), transl. from Russian, NASA TT F-677.

Safronov, V.S. (1979). On the origin of asteroids. In Asteroids (T. Gehrels, Ed.). Univ. of Arizona Press, 975-991.

Shultz, L., Signer, P., Lorin, J.C. and Pellas, P. (1972). Complex irradiation history of the Weston chondrite. Earth Planet. Sci. Lett. 15, 403-410.

Soberman, R.K., Neste, S.L., and Lichtenfeld, K. (1974). Optical measurement of interplanetary particulates from Pioneer 10. J. Geophys. Res. 79, 3685-3694.

Sonett, C.P., Colburn, D.S. and Schwartz, K. (1968). Electrical heating of meteorite parent bodies and planetesimals by dynamo induction from a premain sequence T Tauri "solar wind". Nature 219, 924-926.

Stoffler, D., Gault, D.E., Wedekind, J., and Polkowski, G. (1975). Experimantal hypervelocity impact into quartz sand: Distribution and shock metamorphism of ejecta. J. Geophys. Res. 10, 4062-4077.

Stolper, E. (1975). Petrogenesis of eucrite, howardite and diogenite meteorites. Nature 258, 220-222.

Takeda H. (1979). A layered-crust model of a howardite parent body. Icarus 40, 455-470.

Thomas P.C. (1978). The morphology of Phobos and Deimos. Ph.D. Dissertation, Cornell Univ. CRSR 693.

Thomas, P.C. (1979). Surface features of Phobos and Deimos. Icarus 40, 223-243.

Urey H.C. (1955). The cosmic abundances of potassium, uranium, and thorium, and the heat balances of the Earth, Moon and Mars. Proc. Natl. Acad. Sci. U.S. 41, 127-144.

Van Hollebeke, M.A.I., McDonald, F.B., Trainor, J.H. and von Rosenvinge, T.T. (1978). The radial variation of corotating energetic particle streams in the inner and outer solar system. J. Geophys. Res. 83, 4723-4731.

Vedder J.F. (1972). Craters formed in mineral dust by hypervelocity microparticles. J. Geophys. Res. 77, 4304-4309.

Wahl, W. (1952). The brecciated stony meteorites and meteorites containing foreign fragments. Geochim. Cosmochim. Acta 2, 91-117.

Wasson, J.T. (1972). Formation of ordinary chondrites. Rev. Geophys. Space Phys. 10, 711-759.

Wasson, J.T. (1974). Meteorites. Springer-Verlag, 316 pp.

Wasson J.T., and Wetherill, G.W. (1979). Dynamical, chemical and isotopic evidence regarding the formation locations of asteroids and meteorites. In Asteroids (T. Gehrels, Ed.). Univ. of Arizona Press, 926-974.

Wetherill, G.W. (1974). Solar system sources of meteorites and large meteoroids. Ann. Rev. Earth Planet. Sci. 2, 303-331.

Wetherill, G.W. (1976). Where do meteorites come from? A re-evaluation of Earth-crossing Apollo objects as sources of chondritic meteorites. Geochim. Cosmochim. Acta 40, 1297-1317.

Whitaker, E.A. (1972). Artificial lunar impact craters: Four new identifications. Apollo 16 Preliminary Science Report, Part 1. NASA SP-315, 29:39-29:45.

Wilkening, L.L. (1971). Particle track studies and the origin of gas-rich meteorites. Center for Meteorite Studies (monograph), Tempe, Ariz., Arizona State Univ.

Wilkening, L.L., Lal, D. and Reid, A.M. (1971). The evolution of the Kapoeta howardite based on fossil track studies. Earth Planet. Sci. Lett. 10, 334-340.

Wilkening, L.L. (1973). Foreign inclusions in stony meteorites. I. Carbonaceous chondritic xenoliths in the Kapoeta howardite. Geochim. Cosmochim. Acta 37, 1985-1989.

Wilkening, L.L. (1979). The asteroids: Accretion, differentiation, fragmentation, and irradiation. In Asteroids (T. Gehrels, Ed.). Univ. of Arizona Press, 61-74.

Williams, J.G. (1973). Meteorites from the asteroid belt? (abstract) EOS 54, 233.

Wood, J.A. (1964). The cooling rates and parent planets of several iron meteorites. Icarus 3, 429-459.

Wood, J.A. (1979). Review of the metallographic cooling rates of meteorites and a new model for the planetesimals in which they formed. In Asteroids (T. Gehrels, Ed.). Univ. of Arizona Press, 849-891.

Zimmerman, P.D. and Wetherill, G.W. (1973). Asteroidal sources of meteorites. Science 182, 51-53.

Zinner, E. (1980). On the constancy of solar particle fluxes from track, thermoluminescence and solar wind measurements in lunar rocks. Proc. Conf. Ancient Sun, 201-226.

Zwickl, R.D. and Webber, W.R. (1977). Solar particle propagation from 1 to 5 AU. Solar Physics 54, 457-504.

Page intentionally left blank

Page intentionally left blank

SECTION II

Page intentionally left blank

Page intentionally left blank

RIDGE SYSTEMS OF MARS

By

Ann Winslow Gifford

A Thesis submitted to

The Faculty of

The Graduate School of Arts and Sciences

of The George Washington University in partial satisfaction
of the requirements for the degree of Master of Science

May 3, 1981

Thesis directed by

Farouk El-Baz

Research Director

Center for Earth and Planetary Studies

Smithsonian Institution

ACKNOWLEDGEMENTS

I would like to thank the Center for Earth and Planetary Studies at the Smithsonian Institution for the use of facilities, Ted A. Maxwell for invaluable discussion and many good suggestions, and the National Space Science Data Center for photographic enlargements of some of the Viking images. This work was performed while working at the Center for Earth and Planetary Studies, a part of the National Air and Space Museum at the Smithsonian Institution, under a National Aeronautics and Space Administration Planetary Geology grant.

TABLE OF CONTENTS

ACKNOWLEDGEMENTS 222

LIST OF FIGURES 224

LIST OF TABLES 226

ABSTRACT 227

INTRODUCTION 229

LUNAR MARE RIDGES 231

Morphology 231

Modes of Origin 236

MARTIAN RIDGES 246

Previous Studies 246

General Background 248

A Note on Terrain Types 249

Method 250

DISTRIBUTION OF RIDGES ON MARS 252

Ridges on Plains Units 252

Ridges in Basins and Craters 290

Ridges in Calderas 304

Ridge-Rings 309

DISCUSSION 313

CONCLUSIONS 322

APPENDIX I: Maps of Ridge Distribution on Mars by MC 324

APPENDIX II: Rose Diagrams of Ridges on Mars by MC 354

REFERENCES 359

LIST OF FIGURES

1. Location Map of the Moon 232

2. Examples of Lunar Mare Ridges 233

3. Details of Lunar Mare Ridge Morphology 234

4. Lunar Mare Ridge Associations 237

5. Models for Mare-type Ridge Formation 240

6. Location and Generalized Geologic Map of Mars 247

7. Examples of Martian Ridges 255

8. Orientations of Ridges by Mars Chart (MC) Region 256

9. Rose Diagram of Total Ridge Trends for Mars 257

10. Mosaic of Viking Images of the Hesperia Planum Region of Mars 260

11. Rose Diagram of Ridge Trends in Hesperia Planum 262

12. Ridge Trends in Hesperia Planum Divided by Sector 263

13. Mosaic of Viking Images of Sinai Planum 265

14. a) Sketch Map of the Coprates Quadrangle Showing Ridge Locations 267

    b) Sketch Map of the Coprates Quadrangle Showing Rose Diagrams of Ridge Trends 268

15. Sketch Map of the Lunae Palus Quadrangle Showing Ridge Locations 270

16. Sketch Map of Lunae Planum Showing Locations of Figures 17 and 18 273

17. Details of Ridge Morphology in Lunae Planum 274

18. Intersecting Ridges and Fossae North of Lunae Planum 277

19. Ridges Intersecting Nirgal Vallis 280

20. Polygonal Ridge Patterns on the Moon and Mars 281

21. Mosaic of Viking Images of Ridges in the Amazonis Planitia Area of Mars 283

22. Mosaic of Viking Images of Ridges and Scarps in Acidalia Planitia 284

23. Rose Diagrams of Ridge Trends South of -30° and North of 30° 286

24. Examples of Ridges Near Volcano Flanks 288

25. Ridge on Large Flow Lobe 289

26. Rose Diagrams Showing Trends of Ridges in Craters and Basins on Mars 294

27. Mosaics and Sketch Maps of Four Basins on Mars 295

28. Ridges in Calderas on Mars 306

29. Rose Diagrams of Trends of Ridges in Martian Calderas 308

30. Sketch Map of Mars Showing Locations of Ridge-Rings 311

31. Examples of Ridge-Rings on Mars 312

LIST OF TABLES

1. Ridges on Mars by Mars Chart Region 253

2. Martian Basins that Contain Ridges 293

ABSTRACT

Mare ridges, which were first observed on the Moon have been the subject of much discussion with proposed models of their origin ranging from volcanic to structural. In this study mare-type ridges on the planet Mars have been systematically mapped and described based on Viking images. The ridges mapped range from 5 to 400 km long and 1 to 8 km wide. Most ridges on Mars are on plains and plateau units; 4321 ridges with a total length of 153,835 km were mapped on these unit types.

There are three main areas of ridged plains on Mars. Hesperia Planum, an irregularly shaped plains region surrounding the ancient volcanic construct, Tyrrhena Patera, is characterized by a polygonal arrangement of ridges with a major northwest trend. Western Sinai Planum contains parallel curvilinear ridges and, farther east, a more reticulate arrangement. The curvilinear trends are concentric to the Tharsis uplift, an elevated volcanic plateau that dominates much of the tectonic patterns on Mars. Lunae Planum is an area of extremely long, parallel, north and northwest trending ridges. Numerous smaller, intercrater plains areas also contain ridges; these generally display polygonal patterns.

Ridges which resemble lunar mare ridges are also mapped in craters, basins, and several volcanic calderas on Mars. Ridges in the large (> 100 km diameter) craters and basins tend to mirror the north and northwest trends of regional structures, rather than displaying radial and concentric basin-related trends as in lunar mare basins. Ridges are present in the summit calderas of several of the large volcanic constructs on Mars, including Olympus Mons. Ridges also locally take the form of rings. These are either

complete circular ridges, which range in diameter from 10 to 40 km, or they are partial arcs that follow the trend of buried crater rims.

Mapping of ridges on a global scale reveals that they are preferentially developed in older, thinner plains units which are probably of flood basalt origin. Measuring the trends of ridges in plains units on Mars shows that there is a planetwide predominance of north, northwest and northeast trends.

It is proposed that ridges are compressional tectonic features which have formed in response to changes in the planet's rotational equilibrium figure early in its history. In addition, the Tharsis uplift has created a regional stress system which accounts for the trends of ridges in areas nearby. Ridges in craters and basins are similarly caused by shortening across the basin in response to regional stresses.

INTRODUCTION

When the Mariner 4 spacecraft flew by Mars in 1965, its imaging system revealed a planetary surface which closely resembled the cratered surface of the Earth's moon. Extensive imaging of the surface of Mars during the Mariner 9 mission in 1971 produced a much more complex picture, with some surface features resembling lunar landforms, and some features like nothing else then known in the solar system. One type of Martian surface features with striking lunar analogs are extensive systems of elongate, raised structures. On the Moon they are referred to as mare ridges, because of their ubiquitous occurrence in lunar mare (basaltic) units, or "wrinkle" ridges. In the official Latin designation for named ridge systems the term used is dorsa (singular dorsum), meaning ridge or backbone (International Astronomical Union, 1977). The informal term ridge is used in this study for positive Martian topographic features having morphologic affinities with the lunar mare-type ridges.

The origin of lunar mare ridges is highly controversial. The similar morphology of ridges in various settings, associations with different terrain types and structural features, complex cross-cutting relationships, and varying trends and patterns in plan view have led to the proposal of numerous models for their origin. Consequently, detailed mapping and analysis of ridge morphology and distribution place strong constraints on any hypothesis for their origin.

The purpose of the present study is to systematically map and describe the distribution of ridges for the planet Mars, including morphology and occurrence on various terrain types, and to measure planet wide ridge

orientations. Based on this information, a comparison with lunar ridges, and a review of criteria used to support proposed modes of formation, the various mechanisms hypothesized for ridge origins can be evaluated. This study provides additional information about the origin of ridges on both planetary bodies.

LUNAR MARE RIDGES

Morphology

Study of the ridges on the Moon is an essential beginning to a study of similar Martian features. The type morphology of lunar mare ridges has been described by Strom (1972) as a broad, low, gently sloping elongate arch or swell associated with a narrower, steeper, crenulate ridge or spine (Fig. 2). This sharper portion may either cap the arch at its highest point, lie alongside the arch, or meander from side to side. Individual ridges (including the arch portion) are between 1 and 20 km wide, several hundred meters high, and may be up to several hundred kilometers long.

In detail, the crestal ridge displays ropy, braided morphology, and the edges of the arch are generally lobate. Contacts between a ridge or arch and the surrounding terrain may be scarplike or more gently sloping. In a few instances the edge of a ridge overlaps a small crater, where it occurs as a lobe part way down the crater wall (Fig. 3a).

In cross section, mare ridges are commonly asymmetrical, with one side steeper than the other (Lucchitta, 1976). Also in cross section the levels of the mare units on opposite sides of some ridges are at different elevations (Lucchitta, 1976).

Individual ridges are either straight, curvilinear or sinuous in plan view. Straight ridge segments are either continuous over extended lengths, shorter parallel segments, short segments arranged en echelon, or at large angles to each other (Figs. 3b and 3c). In plan view, ridges in the circular maria follow one of three trends; either they are radial or concentric with respect to the basin center, or they follow north-south

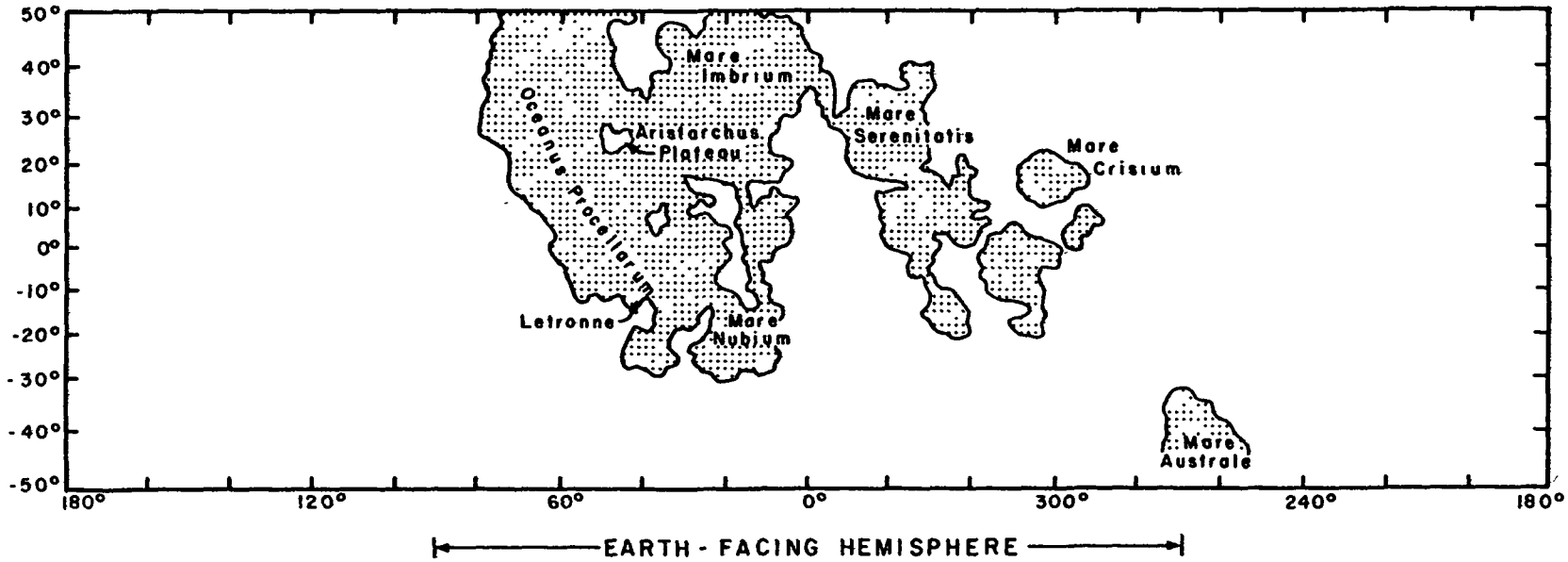


Figure 1. Sketch map of the Moon showing locations of features mentioned in the text. The stipled area shows the extent of major mare units, and the white area consists of upland materials.

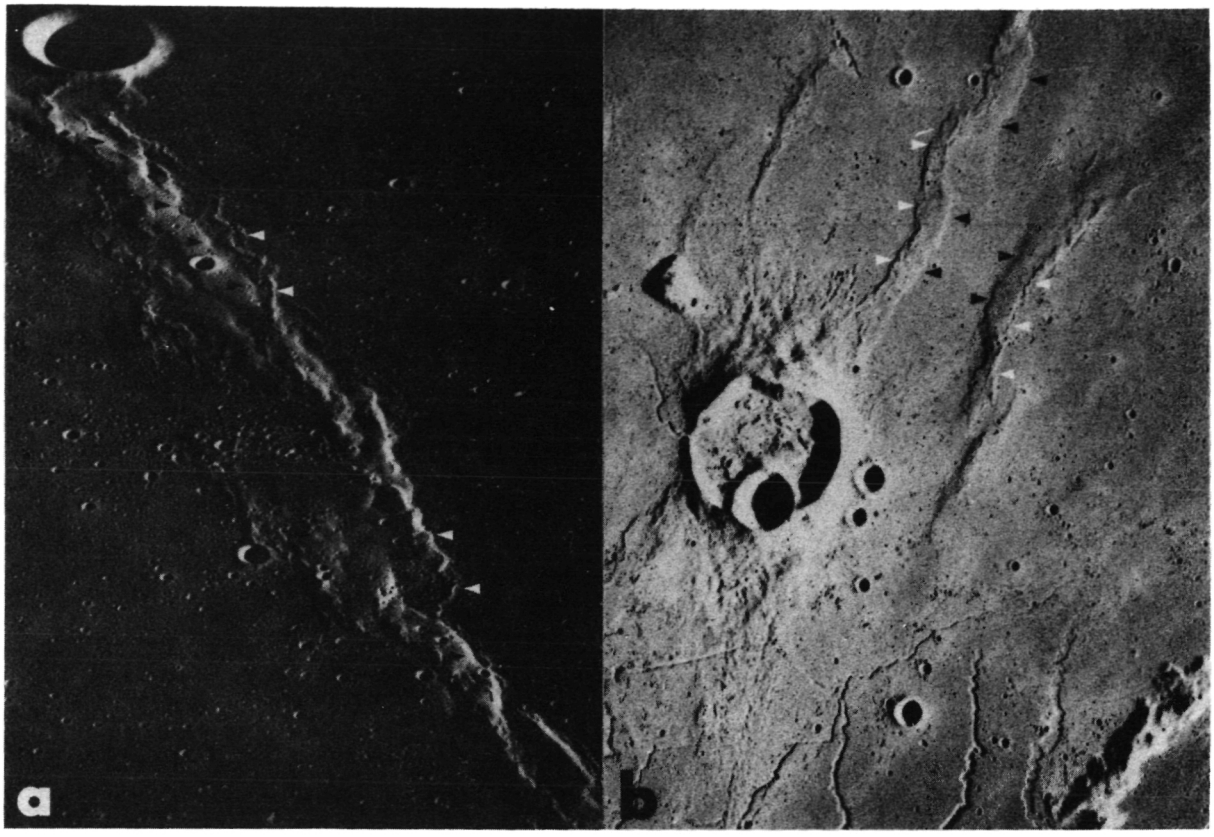


Figure 2. Examples of lunar mare ridges. Note broad, gently sloping arches (black arrows) and crenulated ridges (white arrows). The ridge portion is located either to the side or directly on top of the arch. (a) Part of a mare ridge in Oceanus Procellarum northwest of the Aristarchus Plateau. The portion of the ridge shown is approximately 40 km long. Oblique view looking north (Apollo pan frame AS15-0361). (b) Mare ridges northeast of the Aristarchus Plateau, near the border between Oceanus Procellarum and Mare Imbrium. The frame is about 100 km wide. (Apollo metric frame AS15-M3-2339).

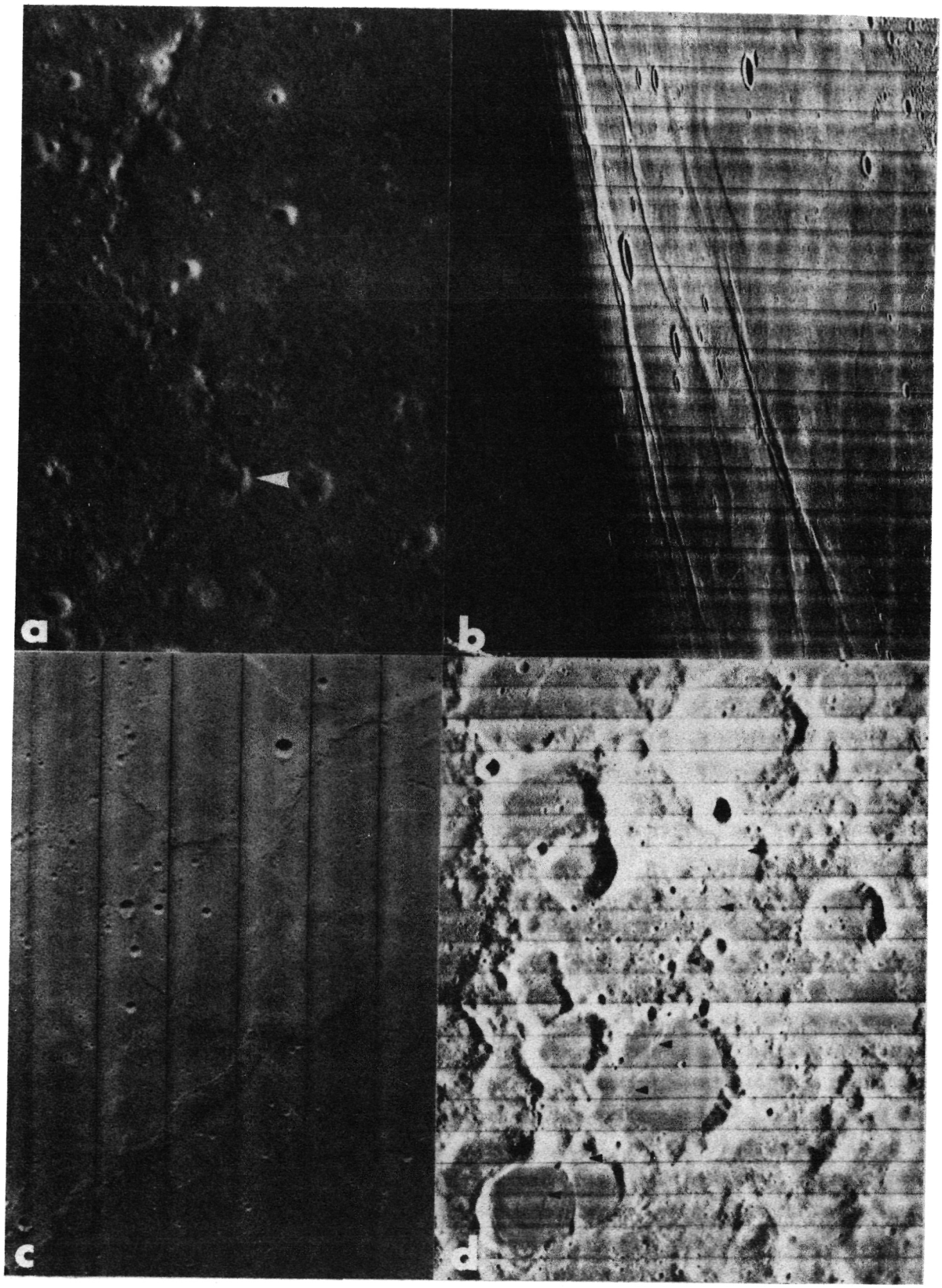

a
b
c
d

Figure 3. (a) Detail of lobe formed where the edge of a mare ridge intersects a crater (arrow). Crater is 1 km in diameter (Apollo pan frame AS16-5428). (b) Oblique view of linear ridges in Oceanus Procellarum. Frame is 150 km high (Lunar Orbiter frame LOIII-M-161). (c) Intersecting ridges in northwestern Oceanus Procellarum. Frame is 85 km wide (Lunar Orbiter frame LOIV-H-170). (d) Trend of mare ridges in crater expressed as a scarp in surrounding highlands east of Mare Australe. The ridge is striking N30°E. The frame is approximately 200 km wide (Lunar Orbiter frame LOIV-H-10).

trends. The latter trend is generally seen in ridges near the basin center, and the former trends more often occur nearer to the basin rim (Fig. 4a, 4b, and 4c). Concentric trends either form complete rings or partial arcs around the basin center. In addition, lunar mare ridges locally take the form of rings as smaller circles of ridges not necessarily centered on a basin, ranging from 1 to more than 80 km in diameter. The smaller ridge-rings are generally continuous; larger ring complexes are often broken into segments or interrupted by superposed craters or peaks of bright pre-mare highlands protruding through the mare surface (Fig. 4d). These latter ridges seem to follow trends of partially buried crater rims.

Mare ridge morphology is expressed exclusively in the maria. However, some ridges cross the mare-highland contact and continue into the highlands. In these cases, the ridge trends can still be clearly followed in the highland unit by their expression as scarps (Fig. 3d) (Lucchitta, 1976). Some ridges are confined to a single mare unit; others cross the contact between two units. In Mare Imbrium, mare ridges are closely associated with extensive lava flows.

Modes of Origin

Mare-ridgelike landforms are unknown on Earth. When first discovered, lunar mare ridges were thought by many to be of certain volcanic origin. In detail, the lobe-like edges and ropy braided appearance suggest flow morphology as known on the Earth although the scale is greatly different. In addition, ridges are commonly found in association with landforms suggestive of volcanic activity, such as sinuous rilles, dark-haloed craters, small cones, domes, and rimless pits. The first sample returns from an Apollo mission proved conclusively that the maria are, in fact, "seas" of basalt,

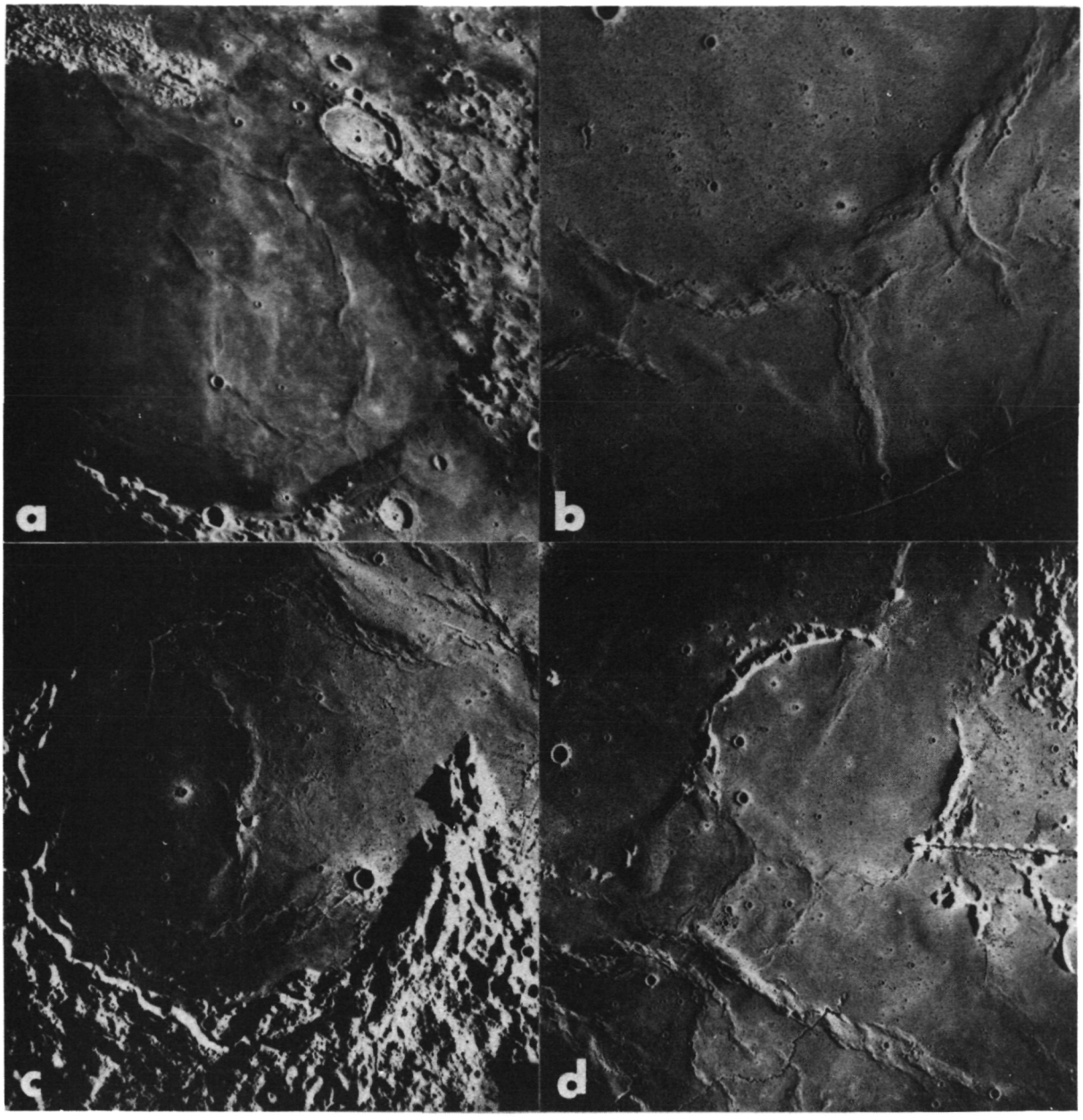


Figure 4. Lunar mare ridge associations.
(a) Mare Serenitatis, occupying a circular basin on the Moon's near side. Three main ridge systems are present: a circular arrangement concentric with the basin rim, ridges near the basin rim oriented radially to the basin center, and north and northwest trending ridges in the central portions of the basin. The Serenitatis basin is 680 km in diameter. Earth-based telescopic view from Kuiper and others (1967).

(b) Close-up of Mare Serenitatis showing part of the concentric ring and several radially trending ridges. Frame is 220 km across (Apollo metric frame AS17-M-602). (c) Letronne, a 120-km crater in southern Oceanus Procellarum. The crater rim is incomplete, and several mare ridges trace the position of the missing portion. In the southern part of the crater, ridges are concentric with the rim. A well-developed north trending ridge strikes through the center (Apollo metric frame AS16-M-2994). (d) An unnamed, breached, mare-filled crater in southern Oceanus Procellarum. The crater is 120 km in diameter. Ridges form part of the crater outline. In addition, there are radial ridges trending northeast to the north and south of the crater (Apollo metric frame AS16-M-2837).

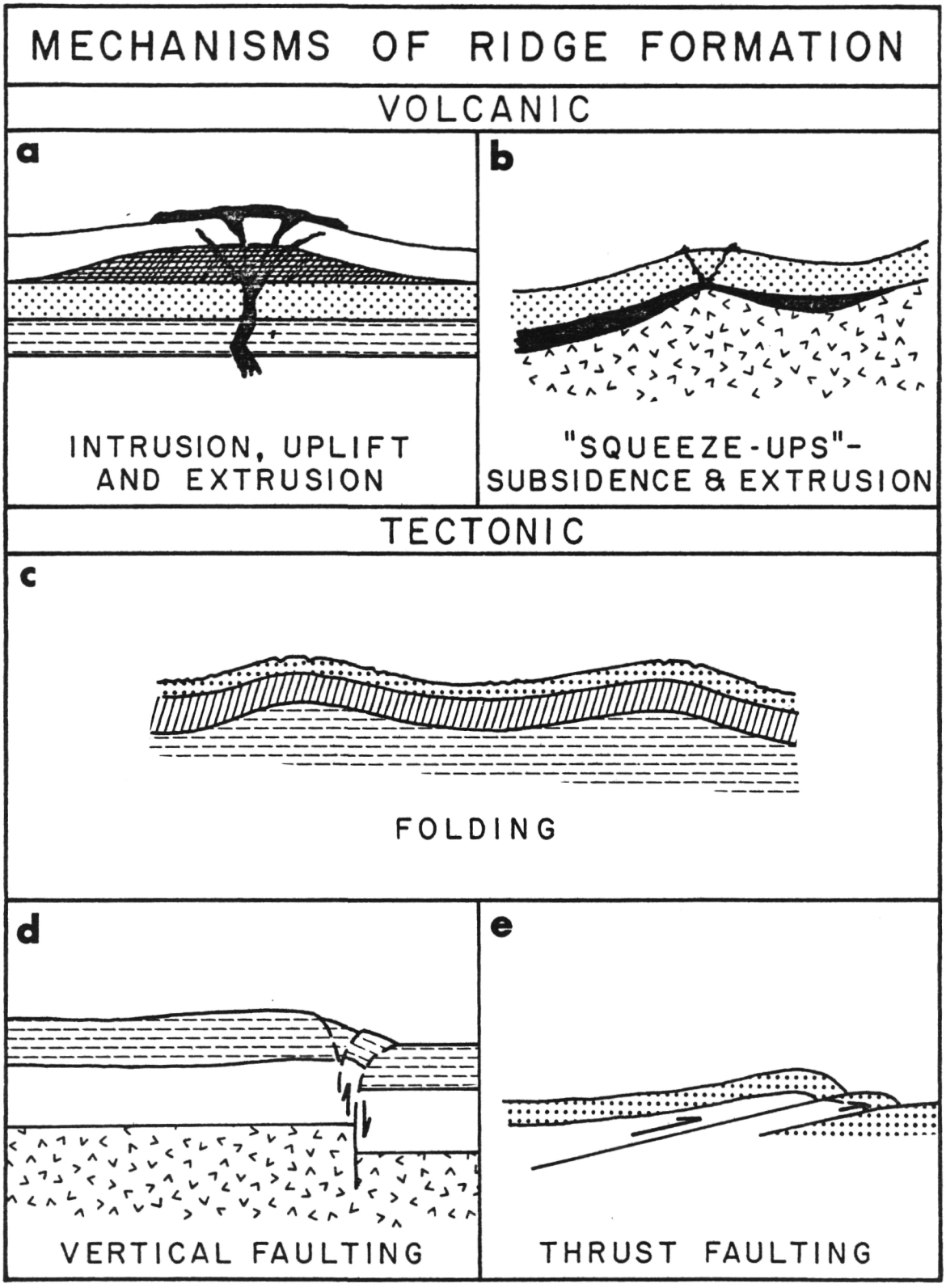
providing certain evidence for extrusive igneous activity on the Moon.

Both intrusive and extrusive activity have been suggested as origins for wrinkle ridge landforms. Whitaker (1966) believes that morphologic evidence indicates an origin by intrusions spreading horizontally at some depth forcing the surface into the observed forms. Strom (1972) advocated a combination of laccolithlike intrusion causing doming of overlying strata to form the arch portion of a ridge system, with extrusion along tension gashes at the crest responsible for the crenulated wrinkle (Fig. 5a).

Mare ridges have also been explained as the surface expression of intrusions in the form of dikes. Quaide (1965) argues that they are volcanic ridges which grew above feeder dikes during mare filling. Mare ridges which comprise ring structures have been explained as the products of magmatic activity associated with ring fractures as observed in ring dike complexes on Earth (Strom, 1972). Positive Bouguer gravity anomalies discernible over mare ridges suggest that they are buildups of high density mare basalts, or expressions of dense intrusions into less dense crustal rock. In particular, a long, narrow gravity high in Oceanus Procellarum coincides with a northwest-southeast trending system of ridges (Scott, 1974).

A few lobate margins of ridges overlap small craters. In these cases, the ridges greatly resemble fissure eruptions. Lava flowing outward from the elongate vent seems to have overflowed and partially buried the small craters. The most distinct lava flows on the Moon have been mapped as emanating from ridges in Mare Imbrium (Kuiper, 1965). In several cases, the rim of a pre-existing mare crater is seen to have deflected the edge of a ridge. Schultz (1976) suggests that these are instances of a topographic obstacle (the crater rim) blocking the outward flow of lava. An extrusive origin is also consistent with the association of ridges with other features interpreted as volcanic, for example ventlike craters with sinuous rilles

Figure 5. Models for mare-type ridge formation. (a) Laccolith or sill intrusion resulting in uplift, extensional fracturing at the surface, and extrusion; redrawn from Strom (1972). (b) Subsidence of a surface layer over buried topography resulting in surface fracturing and 'squeeze-up' of underlying magma; redrawn from Hodges (1973). (c) Folding of a thick sequence of basalt flows, accompanied by disharmonic folding of the uppermost layer to form tight, narrow wrinkles; after Muehlberger (1974). (d) Vertical faulting as proposed by Lucchitta (1976,1977). (e) Thrust faulting, proposed for some mare ridge-type features by Howard and Muehlberger (1973).


MECHANISMS OF RIDGE FORMATION
VOLCANIC
a
INTRUSION, UPLIFT AND EXTRUSION
b
"SQUEEZE-UPS"- SUBSIDENCE & EXTRUSION
TECTONIC
c
FOLDING
d
VERTICAL FAULTING
e
THRUST FAULTING

(probable lava channels) emanating from them (Colton et al., 1972).

The braided ridges with steep flanks have been compared to lava squeeze-ups or pressure ridges on Earth. Squeeze-ups occur where molten lava emerges from cracks in a solidified lava crust (Colton et al., 1972). The cracks could be tension fractures formed by downwarping of a solidified crust over buried topography, and magma could be derived from the still-molten lower portion of the ponded lava and moved upward because of density differences between the melt and the crust, and as a result of the lithostatic pressure of the sinking crust (Fig. 5b; Hodges, 1973). Possible terrestrial analogs for this mode of formation are the squeeze-ups of lava at the boundaries of solidified crust on the surface of lava ponds in Hawaii (Hodges, 1973). Such an autointrusive mechanism could explain the close association of the ridges with small fissures seen in several places on the Moon. Pressure ridges are elongate uplifts of lava, generally caused by molten lava flowing under an already-cooled crust, causing it to warp and buckle. Pressure ridges are common at the distal ends of lava flows.

Downwarping of the mare surface over buried subsurface topography has been suggested in several other contexts as well. One of the first suggestions for the origin of mare ridges, made on the basis of telescopic observations, was differential settling and compaction of sediments over buried basement topographic structures, as is sometimes observed on Earth (Arthur, 1962). Baldwin (1963) suggested that mare ridges are formed by a thin lava veneer over elongate swells in the pre-mare surface. The occurrence of ridges in ring complexes has been similarly explained as surface expressions of the trends of buried crater rims on both the Moon and Mars (Strom, 1972; Gifford, 1980). Maxwell and others (1975) mapped several large ridge rings in Mare Serenitatis and proposed that they overlie large

buried craters. The continuation of crater rims as wrinkle ridges provides strong support for this mechanism (e.g. Fig. 4d).

Structural models for the origin of ridges have also been proposed. Among these are diverse folding and faulting mechanisms; their proper interpretation is very important not only for the understanding of the structural history of specific regions but also for the entire planet.

Folding due to cooling and contraction of an initially molten Moon (Kuiper, 1954) was one of the most dramatic and imaginative ideas. This hypothesis is untenable because of the youth of the maria relative to the age of the Moon. Distinct north-south trends of some major ridge systems in the central portion of Maria Imbrium, Serenitatis, and Crisium, and Oceanus Procellarum have been attributed to global east-west compression caused by a reduction in the angular velocity of the Moon (Fagin et al., 1978).

Compressional folding due to subsidence of the solid surface crust of ponded mare lavas better explains the restriction of ridges to mare areas and the relative scarcity of compressional features in the highlands. Such compression could be caused by sinking of the denser, cooler upper layer of a lava ocean, by magma withdrawal from below, or by downwarping due to increasing weight of thickening mare fill (Baldwin, 1963). Localized compressional deformation of a thin crust uncoupled from underlying topography and structure has been invoked to account for the apparent randomness of some ridge systems (Bryan, 1973). A two layer folding model was outlined by Muehlberger (1974), who proposed that the arch portion of a ridge system formed by folding of a thick, coherent mare layer, and the crenulated and sometimes fractured ridges are produced by disharmonic folding of a thin upper layer (Fig. 5c).

A host of models based on various faulting mechanisms has also been devised. The continuation of some ridges as rilles or scarps, the truncation

or shortening of craters, and en echelon trends of ridge axes all seem to call for a tectonic mode of formation. Strike-slip (Tjia, 1970), normal or reverse (Lucchitta, 1976) and thrust faulting (Howard and Muehlberger, 1973) have all been proposed. Tjia (1970) suggests that the en echelon trends within ridge systems which are oriented in similar directions throughout the maria reflect fracture control. He interprets the actual ridges as drag folds or dikes occupying tension gashes that have been formed by strike slip movements along faults in the submare basin floor.

Lucchitta (1976) has studied mare ridges which continue as highland scarps, and has found evidence for both reverse faulting (compressional regime) and normal faulting (extensional regime) (Fig. 5d). Thus, the stresses responsible must be the result of local adjustments (Moody and Hill, 1956). In a mare basin these may be due to vertical structural adjustments in the mare load caused by differential gravitational movement, possibly following pre-existing structural or topographic irregularities.

One-sided scarps on the Moon with appearances similar to lunar mare ridges have been explained as anticlines and thrust faults, the result of sliding on a décollement surface (Howard and Muehlberger, 1973) (Fig. 5e). Evidence for a thrust fault origin includes the shortening of craters, apparently by low angle faulting, and the climbing of "thrust lobes" over higher elevations. However, thrusting does not account for the crenulated wrinkles that occur on top of typical two-sided ridges.

Conel (1969) suggests that ridges represent surface disturbances caused by shallow subsurface faulting. He has calculated vertical displacements of 70 m for a ridge truncating a crater in Mare Nubium. Cross sectional profiles from 1:250,000 scale topographic maps of Mare Imbrium which show variations in mare elevations on opposite sides of ridges of 100 to 200 m (Lucchitta, 1977) also support a fault origin.

Finally, fault controlled intrusion or extrusion could account for both the morphologic details of ridges as well as the surface patterns of ridge trends. In recent years, because of the many contradictory clues to their origin, combinations of tectonic and volcanic mechanisms have been the most widely favored (e.g., Sharpton and Head, 1980; Lucchitta and Klockenbrink, 1979; Raitala, 1980).

MARTIAN RIDGES

Previous Studies

Because most previous research on ridges has been with reference to the Moon, literature on the subject of Martian ridges is relatively scarce. With the exception of regional overviews in the Chryse Planitia region (Greeley et al., 1977; see Fig. 6 for locations of sites named in text) and the equatorial belt (Lucchitta and Klockenbrink, 1979) there has been no systematic effort to classify or describe mare-type ridges on Mars. Mention has been made of ridges in studies outlining volcanic features on Mars (Carr et al., 1977) and basin tectonics with regard to the Schiaparelli basin (Mouginis-Mark et al., 1980). A study of plains units which contain wrinkle ridges has shown that these units span a narrow range of ages (Gregory et al., 1979), possible evidence for a global episode of plains formation.

Phillips and Lambeck (1980) have modeled the global surface pattern of the principle deviatoric stresses associated with the Tharsis uplift, a raised volcanic area on Mars. This study was based on an evaluation of the stress state of the Martian lithosphere due to the gravitational anomaly over the Tharsis area as measured by the Viking spacecraft. The directions of the horizontal compressive stresses show a striking degree of orthogonality to the trends of ridges near Tharsis, suggesting that these ridges are of structural origin and are a tectonic expression of crustal failure due to the extremely large volcanic load (Phillips et al., 1981; Arvidson et al., 1980).

An origin by folding is also supported by Saunders and Gregory (1980) who found that the ratio of ridge spacing to plains thickness for the ridged plains units is approximately constant over widely separated units. They conclude that ridge spacing is related to the dominant wavelengths of folding of the surface materials in response to the load centered on Tharsis.

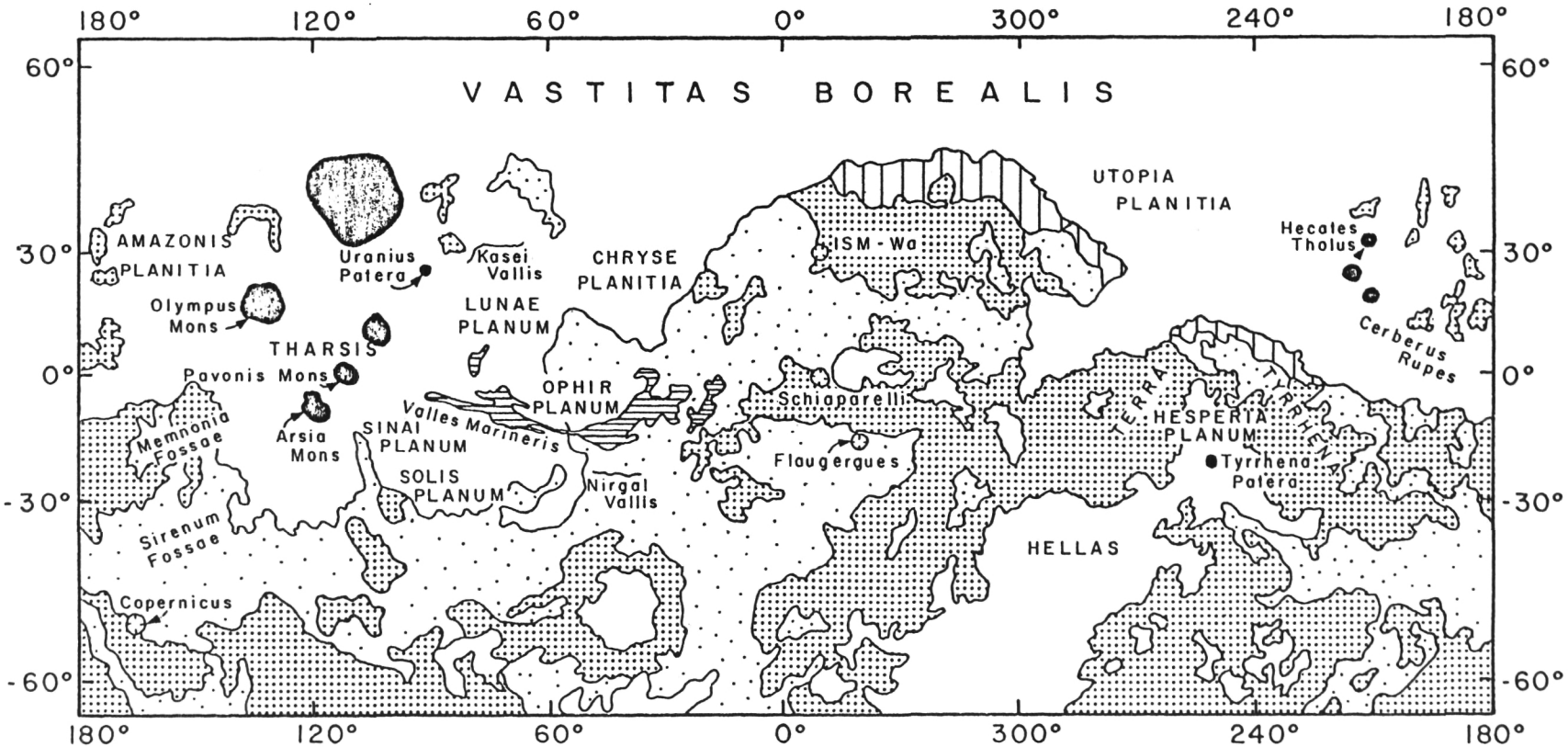


Figure 6. Sketch map of Mars showing locations of features mentioned in text and generalized geologic terrain units. These units include plains regions (open areas), cratered plateau material (widely spaced dots), old cratered, hilly and basin terrain (closely spaced dots), canyon systems (horizontal lines), fretted terrain (vertical lines) and volcanic edifices (solid areas). Terrain units are based on Scott and Carr (1978).

General Background

A general overview of the planet Mars and Martian geology is important for understanding the processes that may be responsible for ridge formation and modification. Mars is 227.9 million km from the Sun, 78.3 million km from Earth. Its equatorial diameter is 6787 km, compared to 12,756 km for Earth and 3,476 km for the Moon. Mars takes 24.5 hours to rotate once on its axis, and 687 days to make one complete revolution around the Sun. Mars does have an atmosphere, although the average atmospheric pressure at the surface is only 6 mbars (compared with 1000 mbars for Earth), and the surface gravity is 0.38 times that of the Earth (all information from Mutch et al., 1976).

Modifications of the Martian surface by impact cratering, volcanism, and tectonic processes are widespread. That Mars has an atmosphere means, most importantly, that surface winds will be available for surface modification. In fact, wind is a very important force on Mars as evidenced by large dune fields and numerous wind streaks associated with topographic obstacles. Evidence of running water, ground water, and probably ice, as surface modifiers in the geologic past is also present (Mutch et al., 1976).

An imaginary plane dipping at approximately 35° to the equator would divide Mars into two hemispheres of markedly different surface character (Fig. 6). The southern half of this division includes the most ancient, densely cratered terrain, whereas the northern half consists mostly of lightly cratered, smoother plains. Most of the volcanic edifices on Mars are situated in the northern hemisphere. The boundary between these two regions is often expressed as a scarp, with the northern lightly cratered plains averaging 2-3 km lower in elevation than the southern cratered terrain. Whereas the northern plains consist almost entirely of smooth, hummocky, or knobby plains, the southern cratered terrain contains inter-

spersed areas of smooth plains, and it is tectonically more complex. The cause of the hemispheric dichotomy is the subject of controversy. Plausible explanations include: an unequal distribution of low density crustal materials (Carr, 1980); resurfacing related to subcrustal erosion and isostatic foundering leading to convective overturn (Wise et al., 1979); destruction of surface features due to some modifying agent (Head et al., 1977); and intense erosion coupled with lessening of the impact flux (Soderblom et al., 1974).

There is no evidence for plate tectonics on Mars. A stable crust, sustained internal activity, and relatively little destruction of surface features by running water has resulted in enormous surface relief and the preservation of relatively ancient features (Carr, 1980). Very little is known about the internal structure of Mars; however, density and rotational characteristics suggest the presence of an iron-sulfide core, and the abundant volcanic features indicate the presence of molten material at least until the fairly recent geologic past. Gravimetric and altimetric data indicate that Mars' mean crustal thickness is at least 50 km, more than three times the mean for Earth (Phillips et al., 1973).

A Note on Terrain Types

Because "geologic" maps of Mars are made on the basis of photogeologic observations rather than by traditional terrestrial methods, the various definable units are called terrain units rather than true geologic units. Surface features such as channels, volcanoes, craters, dunes, and fractures can be readily observed and mapped, but often larger areas are consigned to general units with conflicting opinions on the origin. For example, when there are no constraining criteria, large expanses of smooth plains material

could be either volcanic flows or eolian deposits.

For this reason the study of ridges may be helpful in providing another diagnostic characteristic. Lunar mare ridges occur on basaltic regolith; therefore examining the morphology of ridges for each terrain type on Mars and the frequency of distribution for each terrain should help to ascertain whether certain terrain types are responsible for the morphologic expression and occurrence of the ridges contained in them.

The various criteria used to support volcanic versus tectonic modes of formation have already been reviewed. Unfortunately, sufficiently high resolution images of many of the Martian ridges are not available to determine fine scale structures. Another problem is in using already published geologic maps of Mars to compare mapped units with ridge distribution; often plains units containing ridges are interpreted as volcanic because of the existence of ridges in them. Also, most of the U.S. Geological Survey 1:5,000,000 scale geologic maps of Mars are based on Mariner 9 images, which are of lower resolution than the Viking images used in this study. Nevertheless, published descriptions of terrain units and their distribution will be included here for completeness.

Method

The morphologic classification of the ridges in this study is based on the arch/ridge definition of lunar mare ridges: a broad, gently sloping arch with a sharper crestal ridge on top or to one side of the arch. Two sides must be visible in order to classify features as ridges. Suitable low-sun angle Viking images are available to achieve this. The definition omits sharp ridges such as crater rim remnants and other steeper, higher massifs; linear one-sided scarps and low swells which are seen in plains units are

also excluded.

A survey of Viking images of the entire Martian surface was carried out in search of these mare-type ridges. Ridges were plotted on U.S. Geological Survey shaded relief maps of Mars. The planet has been divided by the U.S. Geological Survey into thirty quadrangles, and each quadrangle has a 1:5,000,000 scale shaded relief map. Seventeen of the quadrangles have generalized (1 km contour interval) topographic maps, and 27 have corresponding geologic maps. This series of maps is based on Mariner 9 data which are of lower resolution than Viking data, but the shaded relief maps provide a good base for plotting ridges. The ridge maps are reproduced in Appendix I, and will be referred to in the following sections by Mars Chart (MC) numbers 1 through 30. Positions of features are based on latitude designations of -90° (south pole) to 90° (north pole) and longitude designations of 0° to 359° (west longitude).

More than 10,000 Viking images were examined to produce the ridge maps in this study. The length of each ridge segment was measured to the nearest five kilometers, and the orientation was measured to the nearest degree. This information was used to construct regional and global rose diagrams in order to study the relationships of local and global stresses to ridge trends. Ridges within craters and basins are not included in rose diagrams for a region because of the possibility that they are an expression of basin-related trends rather than global or regional features. Ridges within summit calderas of volcanic constructs are also treated separately, as are ridge-rings that cannot be separated into straight segments. A Tectronix 4051 Cathode Ray Tube terminal was used to plot orientation data.

DISTRIBUTION OF RIDGES ON MARS

The search for mare-type ridges on Mars was carried out on a quadrangle (MC chart) basis. The MC format provides a standard area of the planet's surface. In addition, most major concentrations of ridges are confined to one or two MC regions. Tabulations of total ridges and lengths are shown in Table 1.

The ridges on Mars are divided into four groups for purposes of description and discussion. These are: Ridges on Plains Units; Ridges in Basins and Craters; Ridges in Calderas; and Ridge-Rings.

Ridges on Plains Units

The "type" Martian ridges are found on smooth plains units (Fig. 7). These ridges closely resemble their lunar counterparts (compare with Fig. 2). The Martian ridges studied here are between 1 and 10 km wide; the shortest ridge segment measured was 5 km long, and the longest continuous ridge is over 400 km. Most of the ridges on Mars are on plains and plateau units; 4321 ridges and ridge segments with a total length of 153,835 km were measured on these units. Rose diagrams showing ridge trends and lengths for each MC are presented in Figure 8 and Appendix II. The rose diagrams show predominant trends of north (N10°W to N10°E) (Fig. 9) and northwest (N20°W), with substantial minor trends of N60°W and N20°E. Areas with predominantly north and north-northwest trends do not have as highly developed secondary trends as areas where the predominant trend is northwest, which tend to have secondary northeast trends 70° to 100° removed. The north and northwest trends of ridges reflect a global-scale predominance of these trends in other

Table 1. Ridges on Mars by Mars Chart Region

Mars Chart	No. of Ridge Segments Measured	Total Length (km)	Ridges in Craters			No. of Ridge-Rings
			No. of Craters	No. of Ridges	Total Length (km)	
1. Mare Boreum	0	0	0	0	0	0
2. Diacria	8	340	0	0	0	0
3. Arcadia	53	1725	0	0	0	0
4. Mare Acidalium	28	1180	0	0	0	0
5. Ismenius Lacus	139	4815	1	9	310	0
6. Casius	27	1210	0	0	0	0
7. Cebrenia	68	2930	0	0	0	0
8. Amazonis	98	3700	0	0	0	0
9. Tharsis	3	130	0	0	0	0
10. Lunae Palus	775	27185	0	0	0	5
11. Oxia Palus	50	2015	0	0	0	0
12. Arabia	106	3275	0	0	0	6
13. Syrtis Major	164	5650	1	2	30	3
14. Amenthes	39	1725	0	0	0	0
15. Elysium	163	6110	0	0	0	0
16. Memnonia	141	4635	7	14	435	3
17. Phoenicis Lacus	2	65	0	0	0	0
18. Coprates	525	22645	0	0	0	2
19. Margaritifer Sinus	52	1750	1	1	60	0
20. Sinus Sabaeus	108	3285	5	40	1395	11
21. Iapygia	97	3385	2	22	1035	1

Table 1. (cont). Ridges on Mars by MC.

22. Mare Tyrrhenum	553	18535	0	0	0	25
23. Aeolis	280	7795	13	25	710	8
24. Phaethontis	90	3550	2	15	920	7
25. Thaumasia	10	440	0	0	0	1
26. Argyre	30	1410	0	0	0	0
27. Noachis	102	4305	0	0	0	2
28. Hellas	334	10415	0	0	0	17
29. Eridania	221	7015	0	0	0	6
30. Mare Australe	55	2615	0	0	0	2

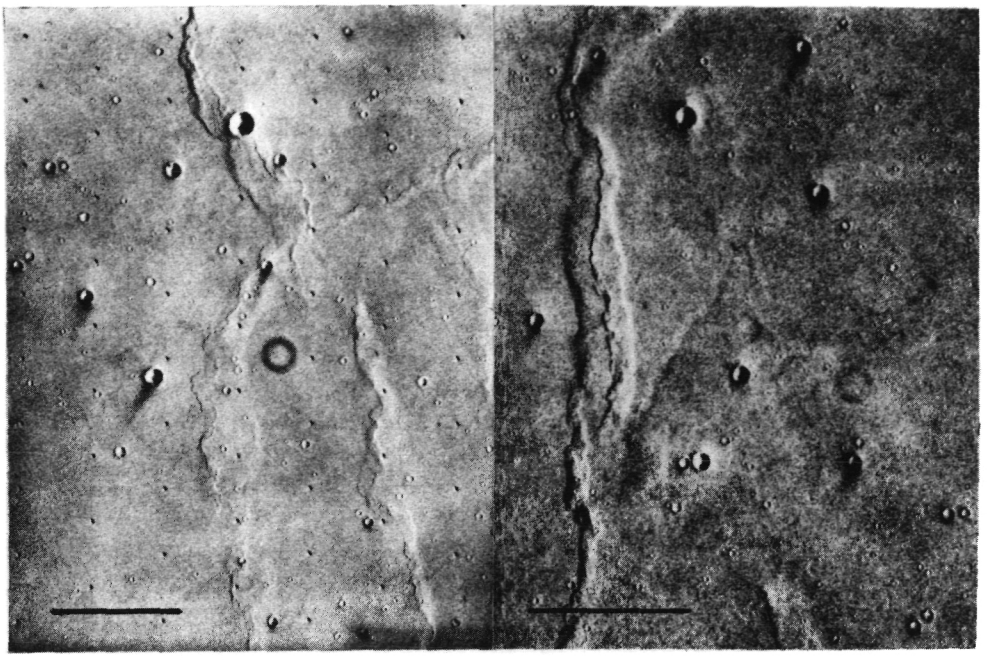


Figure 7. Examples of mare-type ridges on Mars. These ridges are located in the Chryse Planitia region. Scale bars are 10 km long. Viking Orbiter 1 frames 41A91 (left) and 27A34 (right).

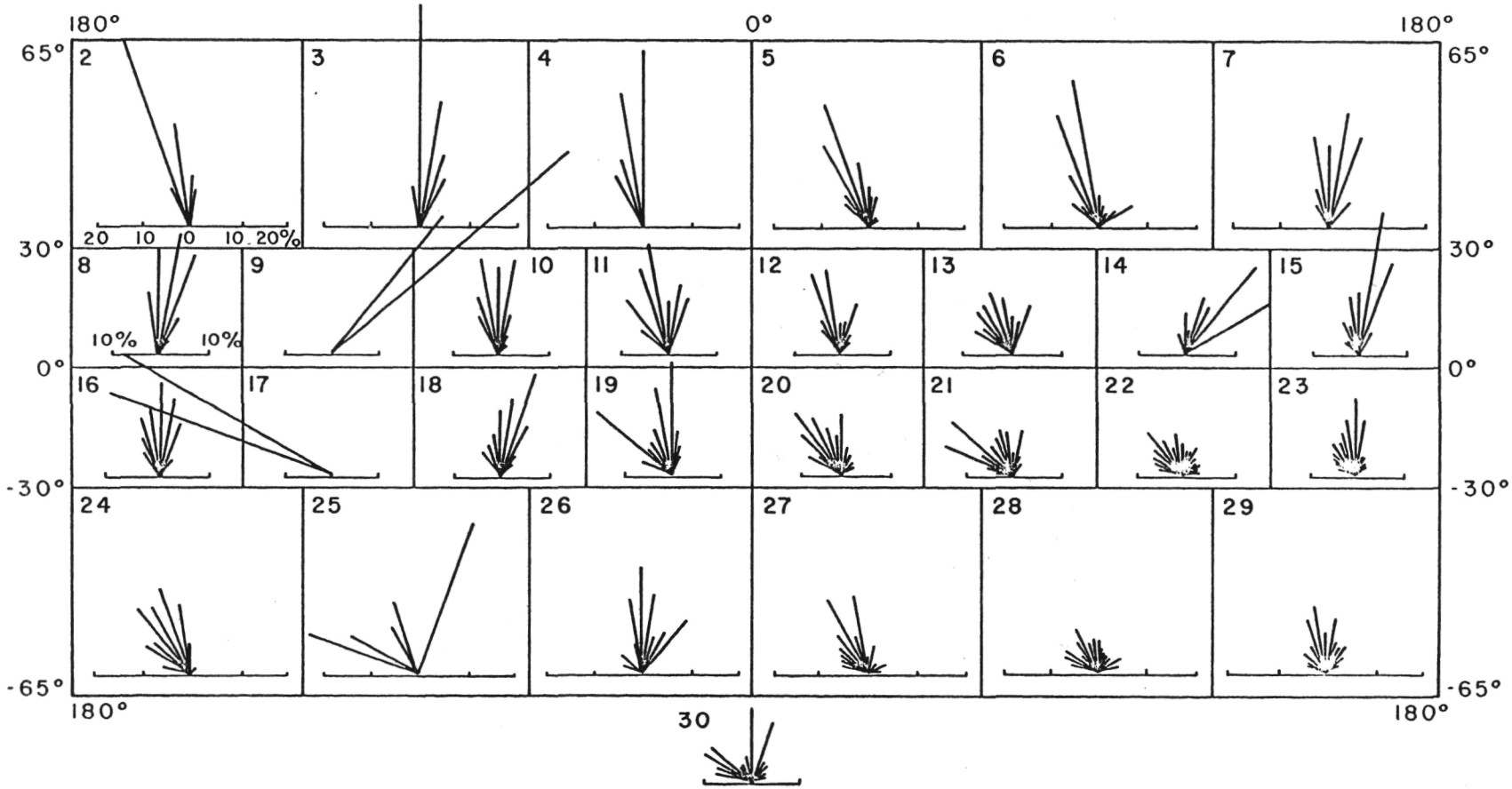


Figure 8. Orientations of ridges for each Martian quadrangle. Rose diagrams are plotted in percentages.

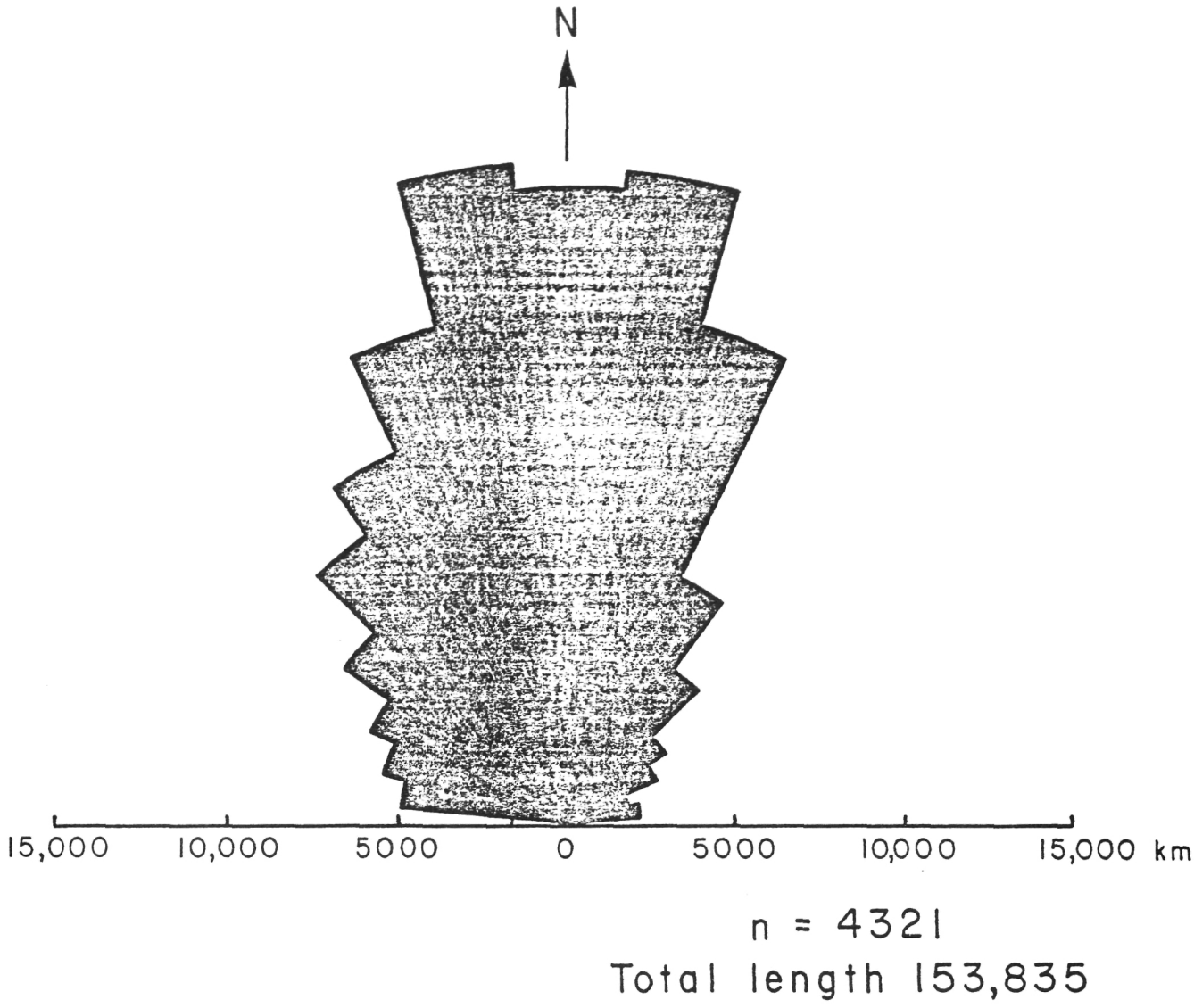


Figure 9. Rose diagram showing trends of all ridges mapped on Martian plains units.

classes of features on Mars as well (e.g. massifs, crater rim segments, central peaks; Masursky et al., 1980; Hamdan and El-Baz, 1980). The major exceptions to this generalization are the fracture or fossa (non-genetic term for narrow linear trench; International Astronomical Union, 1977) systems of Mars, which have predominant west-northwest and east-northeast trends (Harp, 1976). The implications of these trends will be discussed in another section.

The largest numbers of ridges are concentrated in the eastern hemisphere of Mars. Major exceptions are MC's 10 and 18, isolated in the western, sparsely ridged hemisphere. MC's 10 and 18 contain 29% of the ridges on Mars; the rest of the western hemisphere contains 12%, while 59% of all ridges are in the eastern half of the planet.

The plains and plateau materials on Mars have been subdivided based on relative age, morphology, and associated features. Large plains units on Mars are interpreted variously as volcanic flows, either flood-type lavas or ash, or eolian or other sedimentary fill. Most probably the uppermost surface layer is mantled by eolian materials in many areas. Thus, although mare ridges on the Moon are developed in basaltic surface units, the original material of ridge-containing plains on Mars is debatable, except when other supporting evidence is available such as visible lava flow morphology or proximity to a volcano. Therefore, although many vast plains areas on Mars are at least partially made of flood-type lavas (Scott and Carr, 1978) with a thin mantling of eolian and other debris, this cannot be taken as a certainty in all areas.

Major ridge systems are present in three large plains regions, Hesperia Planum, Sinai and Solis Plana, and Lunae Planum (planum, pl. plana, refers to a high plain or plateau; planitia, pl. planitiae, is a low plain or large level expanse of lowlands; International Astronomical Union, 1977). Apart

from these three areas, ridges are found on small intercrater plains units with various degrees of relief, on smooth plateaus, and a few on obvious lava flow units.

Hesperia Planum is a 1.3 x 10^6 sq km expanse of plains (-35° to -5°N, 240° to 260°W) bounded by the heavily cratered terrain of Terra Tyrrhena (MC-22). Near the center of the plains area is Tyrrhena Patera, an old volcanic structure. Radial and concentric grooves (lava channels and graben) have deeply dissected the structure. The dissected flanks of this feature are embayed by the plains material, which has been interpreted as basaltic lava flow material based on the presence of a volcanic construct (King, 1978). The plains material is relatively smooth and uncratered, reminiscent of the lunar maria; also the albedo is lower than many of the other plains units on Mars.

The ridges of Hesperia Planum have an exceedingly complex geometry. There are ridges concentric and radial to the volcanic center, several sets of parallel ridges, several prominent northwest and northeast trending sets displaying an orthogonal pattern, and numerous ridge-rings (Fig. 10). Cross-cutting relationships between ridges, and between ridges and scarps, are complicated. Several of the trends of negative relief features which are radial to Tyrrhena Patera are expressed as ridges farther away from the volcano. Several of the ridge-ring structures in this area also have radially oriented ridges surrounding them.

Hesperia Planum provides a general analog to an irregularly-shaped lunar mare, being a vast expanse of lava bounded by cratered terra (highlands). The main difference between the two is the presence of a central volcanic edifice in the Martian example. Ridge orientations for Hesperia Planum have been treated both as a whole and in segments centered on Tyrrhena Patera. This latter method was developed by Maxwell and Gifford (1980) to depict the

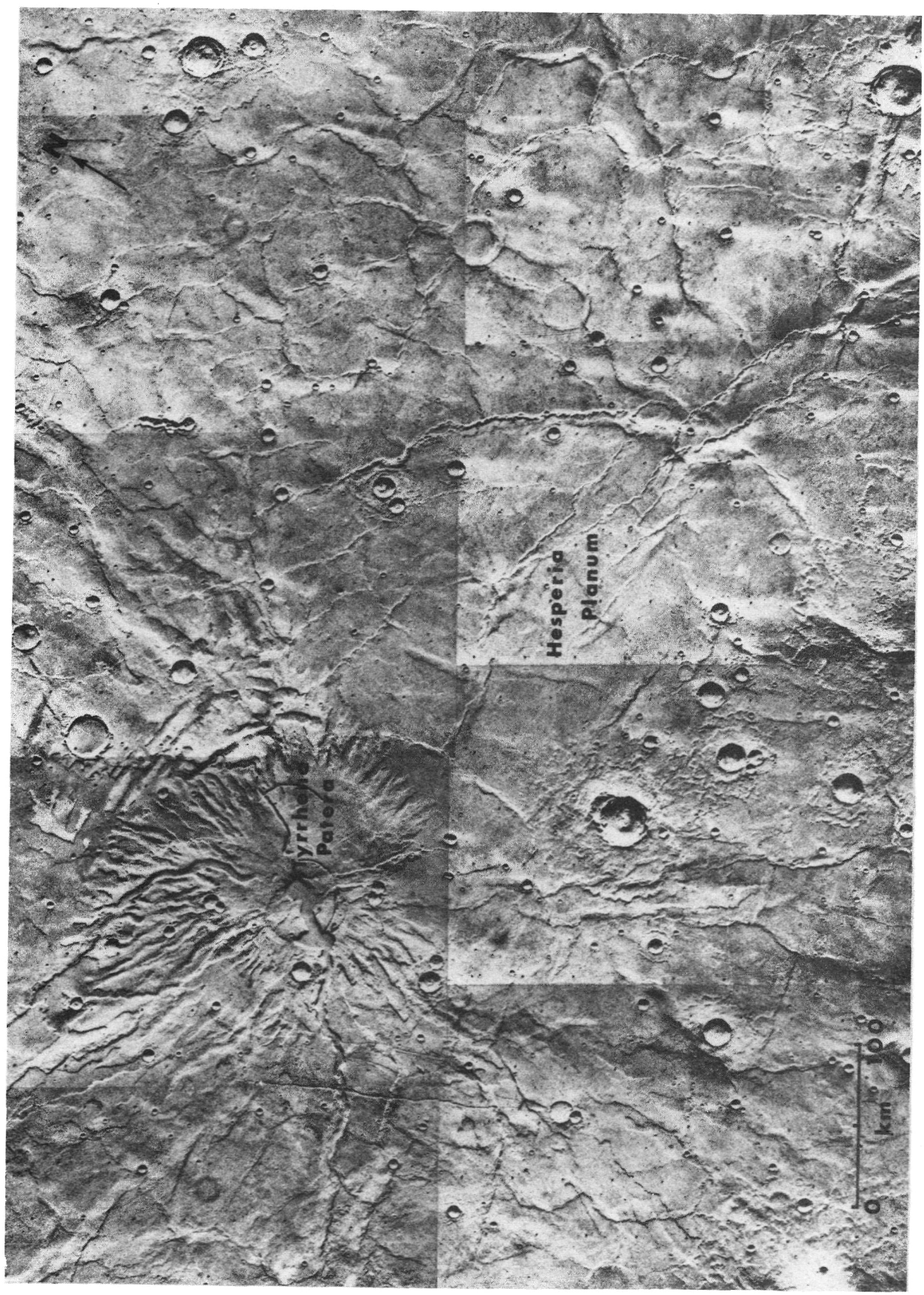

Hesperia
Planum
0
100
km

Figure 10. Mosaic of Viking images of part of the Hesperia Planum region of Mars. The mosaic covers the area from -15° to -26° latitude, 243° to 257° longitude. Tyrrhena Patera is a highly dissected volcanic construct.

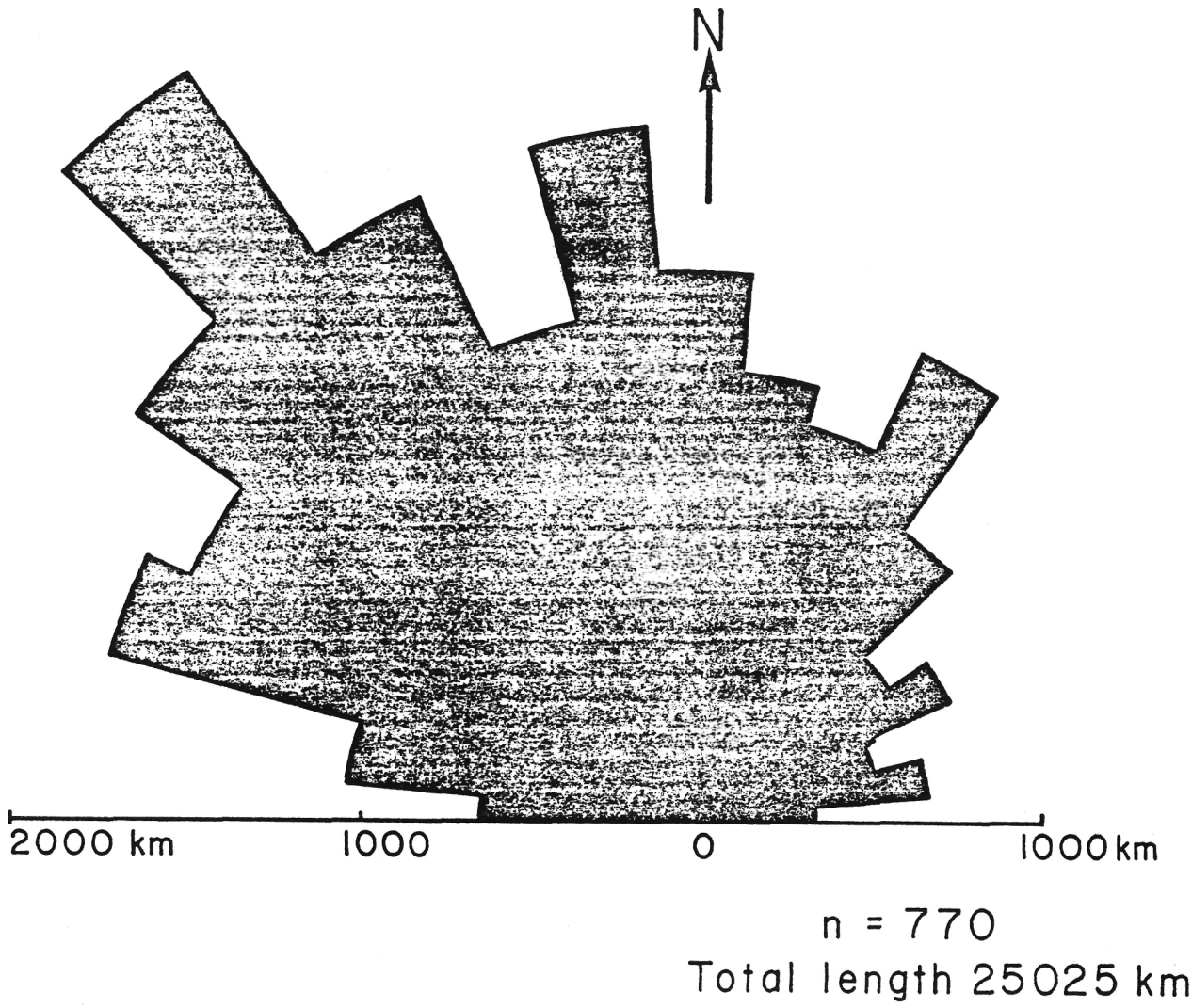
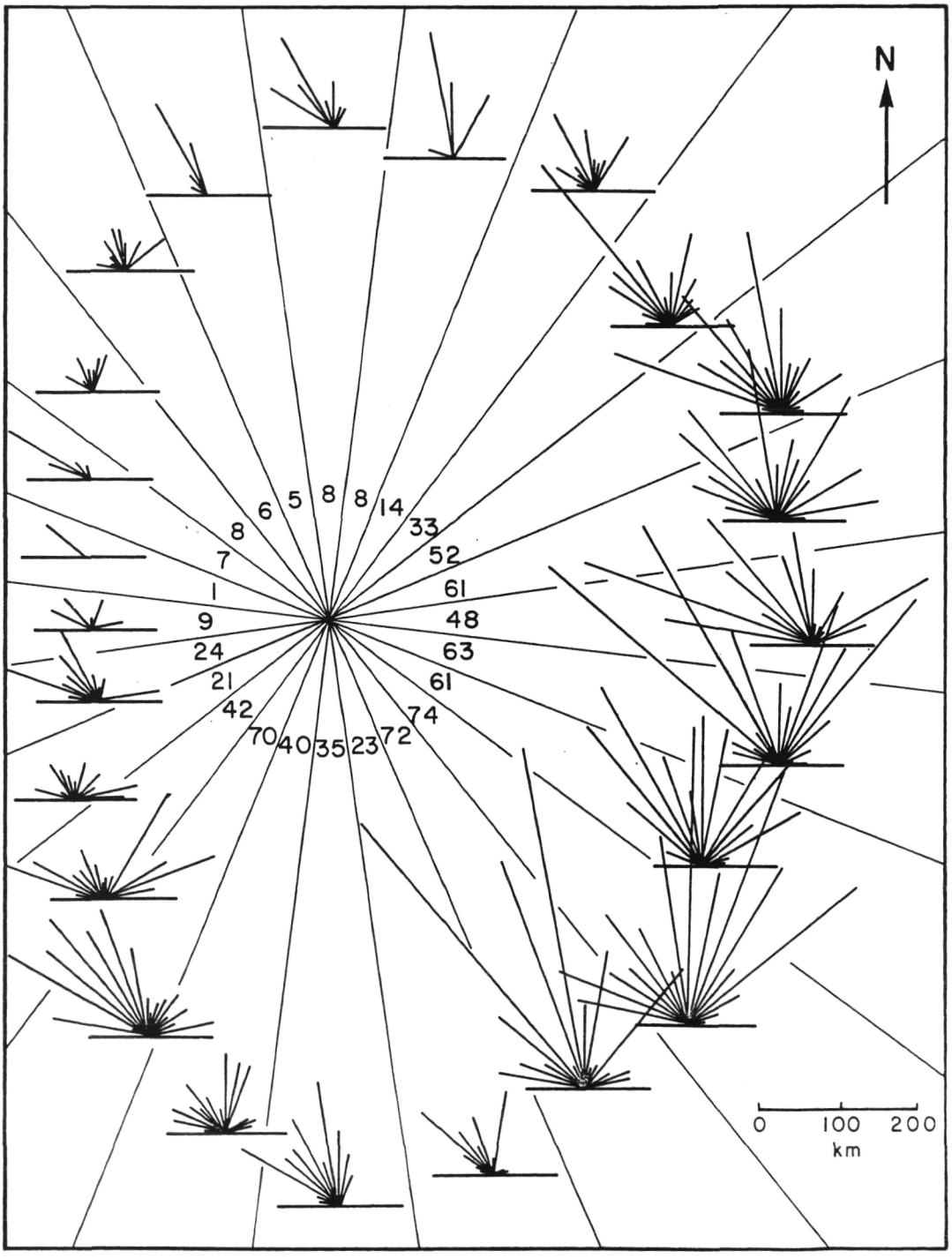


Figure 11. Rose diagram of all ridge trends in Hesperia Planum.

Figure 12. This figure shows rose diagrams of ridge trends in 15° segments radiating from Tyrrhena Patera (-22°, 254°) near the middle of Hesperia Planum. The ridges included are in an area that extends from -5° to -40° latitude, 240° to 260° longitude. Numbers in each segment refer to the total number of ridges in that area. All rose diagrams are drawn to the scale shown in the lower right. The ridge data are broken down in this manner to ascertain whether or not there are any predominant ridge trends which are radial or concentric with respect to the volcanic center.



relative contributions of concentric and radial trends to the overall pattern of ridges within basins on the Moon and Mercury. The extremely complex pattern of ridges in Hesperia Planum lends itself well to this type of analysis. The central volcanic structure was used as the center point for examining ridge trends in the surrounding plains to see if the volcanic load itself is in any way responsible for ridge orientation.

A rose diagram of all ridges in Hesperia Planum (bounded by -40° to -5° N, 240° to 260°W) shows a substantial overall background (averaging about 900 km on the figure) with peaks at N30°E, N10°W, N70°W and a substantial peak centered on N40°W (Fig. 11). Subdivided in the manner shown in Figure 12, the segments with the most ridges, and ridges which contribute most to these peaks can be ascertained. A pattern of well-developed concentric and radial trends is not observed, nor is any one direction consistently emphasized except for a northwest trend. Thus the ridges of Hesperia Planum are among the most complex on Mars, neither being dominated by a global lineament direction nor expressing an orientation related to the central volcanic complex.

Sinai and Solis Plana are two areas of smooth plains in western MC-18 and eastern MC-17. The portions of these plains units containing ridges are confined to MC-18. The ridges in Sinai Planum form a long parallel curvilinear arrangement (Fig. 13). Individual ridges are between 1 and 5 km wide, and several continuous curvilinear ridges are up to 400 km long. Locally, the ridges are interrupted by small areas of furrowed or grooved material, and several ridges are truncated by craters or E-W trending fractures. To the east of Sinai and Solis Plana are two areas (50° to 57°W and 62° to 70°W) where the ridge arrangement is more polygonal or reticulate; short ridge segments are arranged in intersecting trends and partial orthogonal patterns. These two areas are relatively smooth plains units; they are separated by

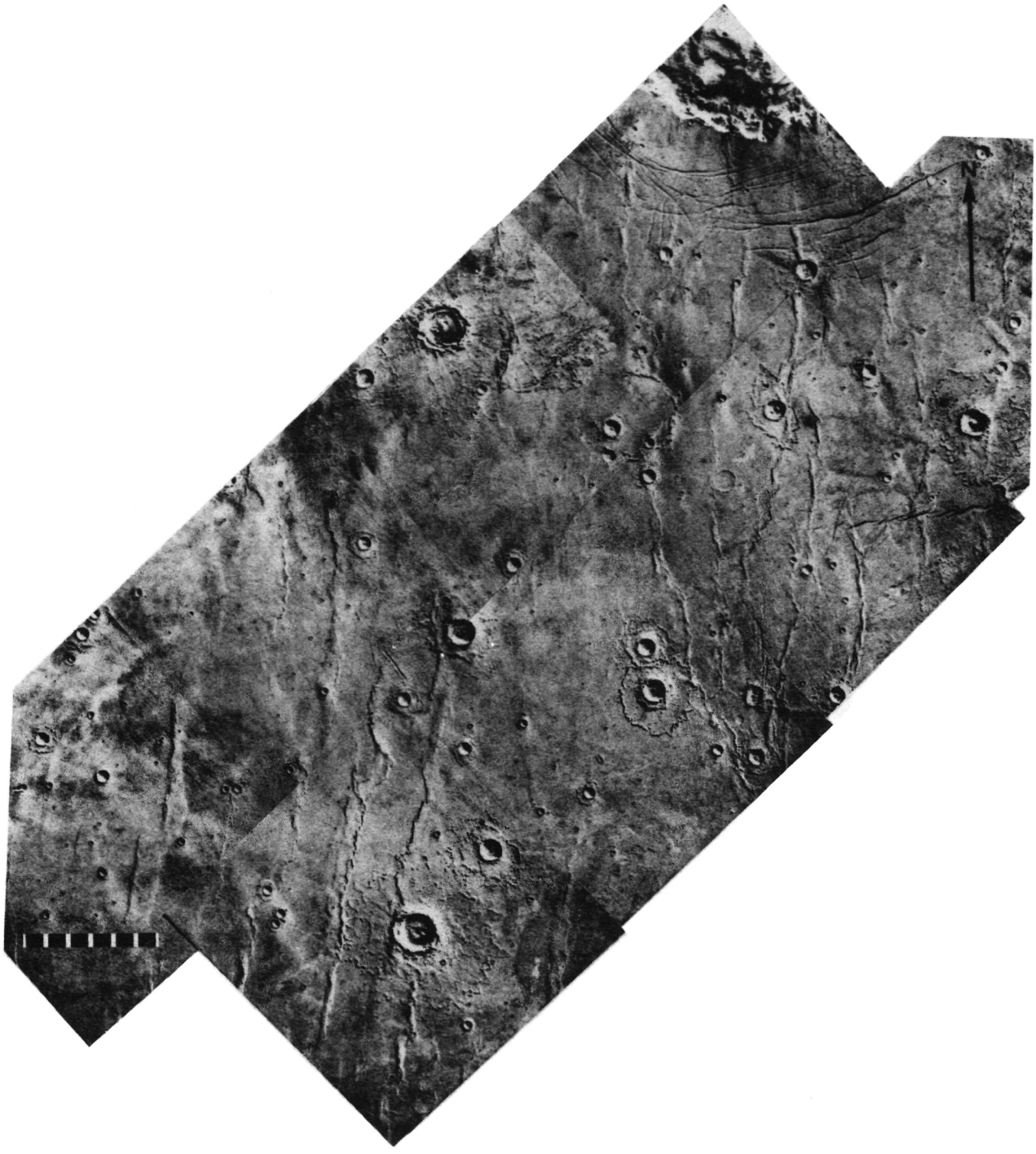
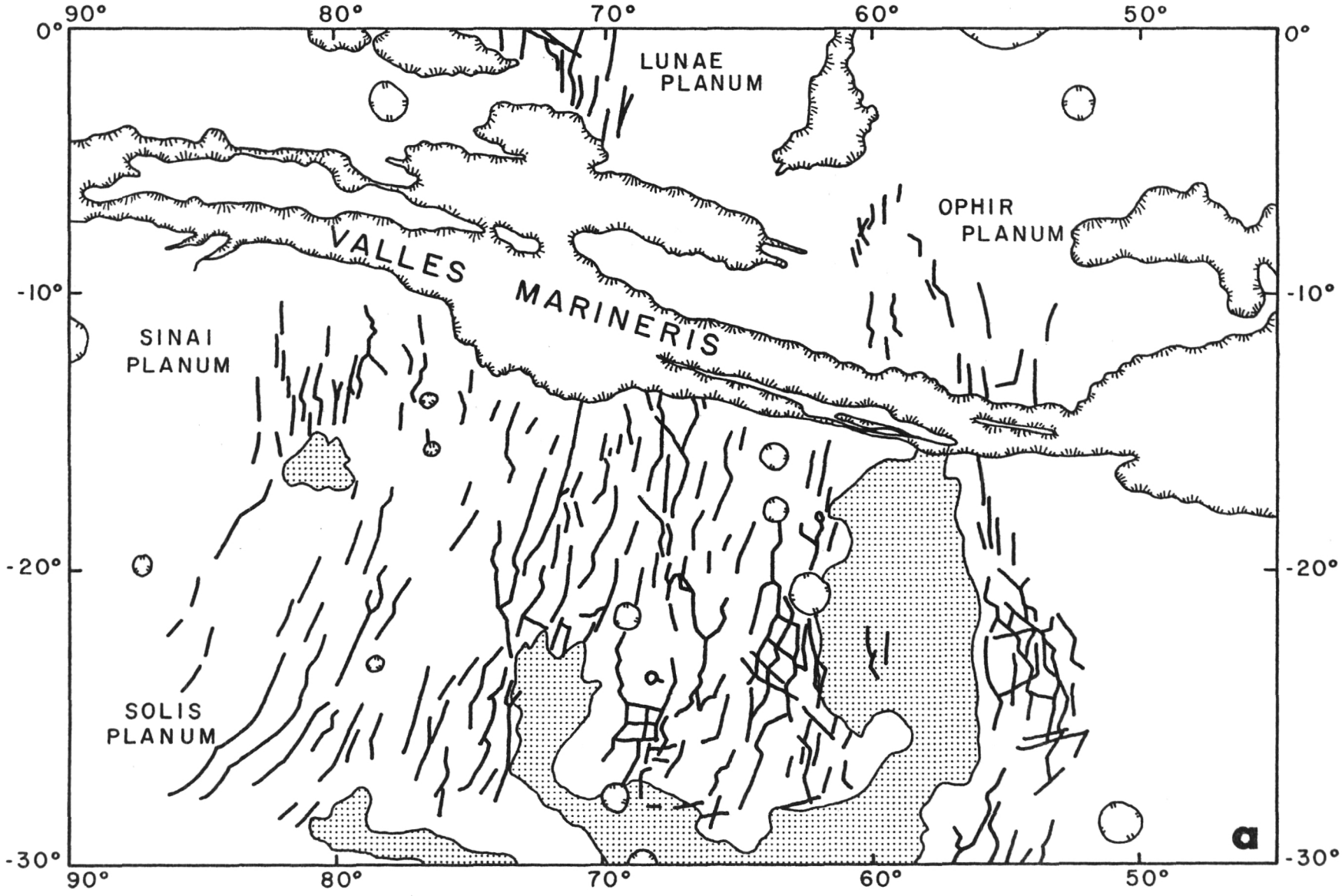
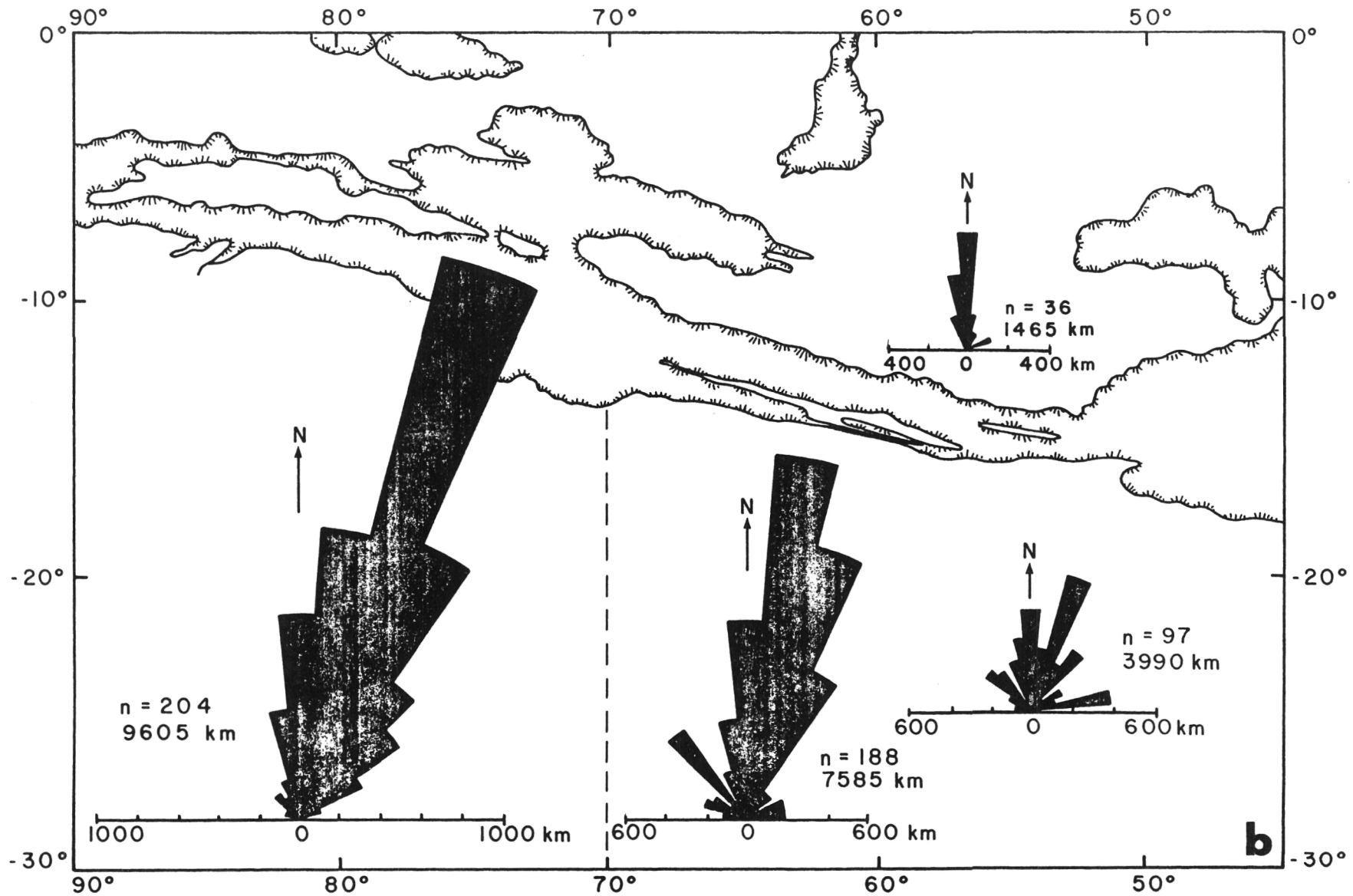


Figure 13. Mosaic of Viking images of northern Sinai Planum, showing linear ridges trending nearly due north. Sinai Planum is south of Valles Marineris, the southern rim of which can be seen at the top of the mosaic. The scale bar is 100 km long.

Figure 14. (a) Sketch map of MC-18, the Coprates quadrangle on Mars, including the ridged plains units Sinai, Solis, and Ophir Plana. Valles Marineris, a system of interconnecting canyons, stretches across the quadrangle in an east-west direction. Ridges are shown by heavy lines. Shaded area is trough-and-furrow material mapped by McCauley (1978); this is moderately undulating terrain characterised by numerous subdued troughs and furrows. It is higher than the surrounding ridged plains materials, and it contains very few ridges relative to the smoother, lower plains. (b) Rose diagrams showing trends of ridges in Sinai and Solis Plana between 70° and 90°W, between 62° and 70°W, between 50° and 57°W east of the trough-and-furrow material, and in Ophir Planum north of Valles Marineris. The major trend of ridges shifts from northeast in the western part of the quadrangle to north-northwest in Ophir Planum to the west, with the most scatter in the ridges toward the southeast. The main structural trends in the trough-and-furrow material are northwest and northeast.


0°
90°
80°
70°
60°
50°
LUNAE
PLANUM
OPHIR
PLANUM
VALLES
MARINERIS
-10°
SINAI
PLANUM
-20°
SOLIS
PLANUM
-30°
a


0°
90°
80°
70°
60°
50°
-10°
-20°
-30°
N
n = 36
1465 km
400 0 400 km
n = 204
9605 km
1000 0 1000 km
n = 188
7585 km
600 0 600 km
n = 97
3990 km
600 0 600 km
b

rougher terrain called "trough-and-furrow" material which has been interpreted as tectonically modified cratered plateau material (McCauley, 1978).

Sinai and Solis Plana are just south of the giant Valles Marineris, a 5000-km long network of canyons (chasmata) stretching from MC-17 to MC-19. The major trend of Valles Marineris is N70°W. The ridges of Sinai Planum begin at the scarp marking the southern edge of the canyons. These ridges trend nearly north-south near the canyon rim and curve around to trend northeast-southwest farther to the south (Fig. 14). Farther east, near the center of MC-18 (60°-70°W), the ridges also abut the southern edge of the canyon. These ridges form a more reticulate pattern than the parallel trending ridges farther west. Although a rose diagram of trends shows the scatter inherent in the more reticulate pattern, the main trend is northeast. The easternmost ridges south of Valles Marineris in MC-18 also form a polygonal arrangement, with a dominant northern trend. Thus from west to east across Sinai and Solis Plana the main trend gradually shifts from north-northeast to north.

Just north of Valles Marineris between 57°W and 61°W is another small area of ridged plains, Ophir Planum. These ridges are truncated by the northern scarp of the canyon; several of them seem to continue the trend of ridges that are south of the canyon (Fig. 14).

The third main area of ridged plains on Mars is Lunae Planum (-5° to 23°N; 57° to 77°W; MC-10). The ridges in the northern part of Lunae Planum are truncated by a large channel system, Kasei Vallis, which trends generally east-west. The western edge of Lunae Planum is marked by an extensive scarp and several intersecting fractures or fossae; to the east, the plains abut ancient cratered terrain, and in the south Lunae Planum is bounded by Valles Marineris.

The ridges in Lunae Planum are generally parallel with major north and north-northwest trends (Fig. 15). These ridges are significant because of

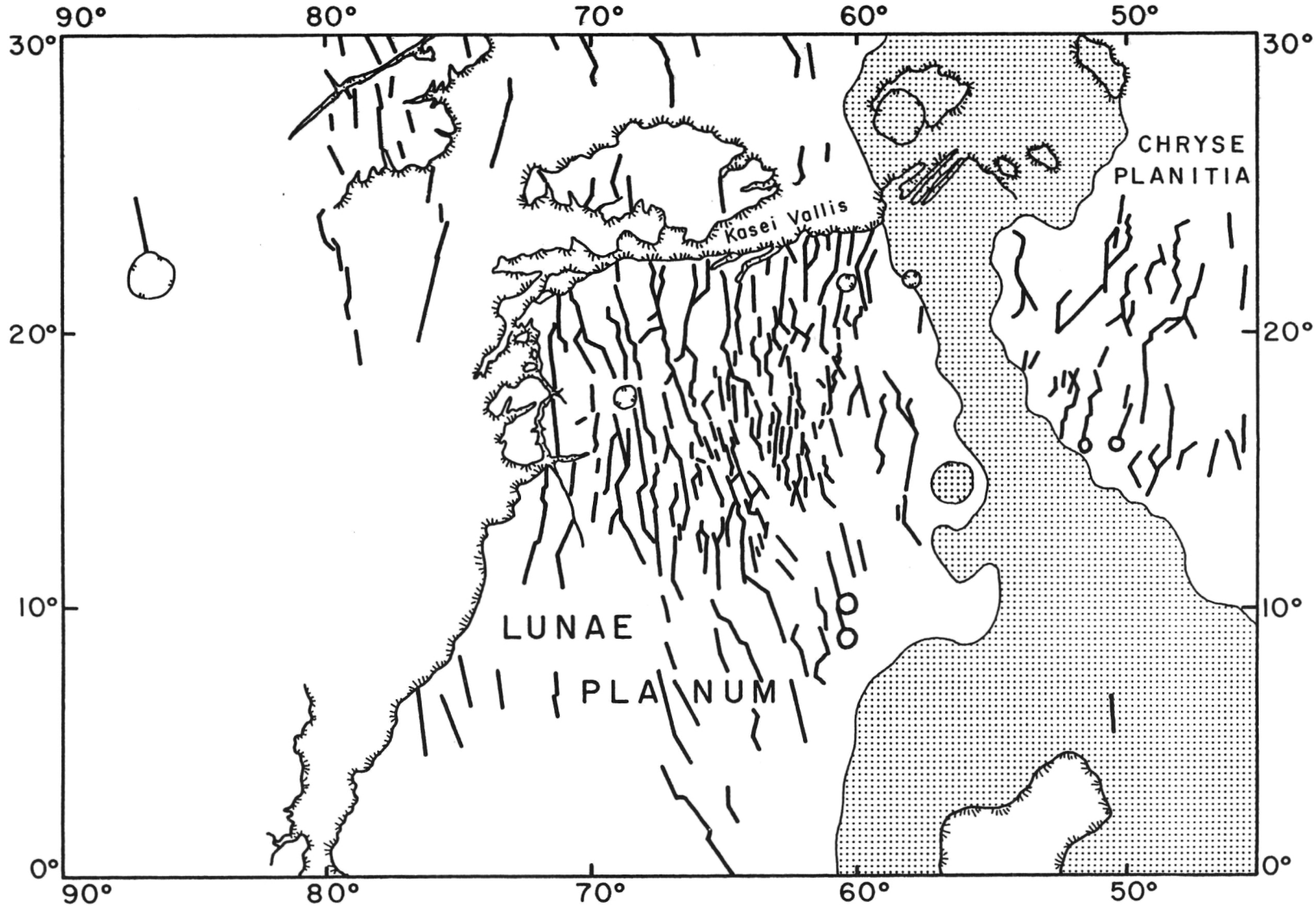

90°
80°
70°
60°
50°
30°
20°
10°
0°
CHRYSE
PLANITIA
Kasei Vallis
LUNAE
PLANUM

Figure 15. Sketch map of MC-10, the Lunae Palus quadrangle on Mars. Ridges in Lunae Planum and Chryse Planitia are shown by heavy lines. Shaded area is cratered terrain separating the two plains areas.

their extreme length, and relative lack of the polygonal and reticulate arrangements which abound in other plains units, although several ridges display anastomosing or branching trends. There are several examples where ridges have been deflected or interrupted by craters, and several ridge-rings are present.

The scarps bounding Lunae Planum show a change in slope partway up, being steeper near the top than towards the base. This has been interpreted as showing the presence of a well-consolidated upper layer of Lunae Planum, and a less consolidated lower layer (probably lava flows and sediments respectively; Milton, 1974), although the lower slopes could be composed of material formed by mass wasting from the steep wall. In either case it is apparent from the steep upper slopes that the ridges are developed in a well-consolidated layer of Lunae Planum material.

The intersections of ridges with the bounding scarps are diverse. In many cases the scarp has apparently been eroded preferentially along the ridge trend, forming tributary valleys (Fig. 17a). Other ridges abut the scarp with no apparent effect on the wall erosion. In one case the ridge stops abruptly 4 km from the scarp (Fig. 17a). Where the ridges cross the smaller fossae at the western edge of Lunae Planum, they are either continuous across the trench, apparently offset by it, or they end abruptly and are not continued on the other side. Examples of all three are shown for the same ridge in Figure 17b. Where erosion has exposed ridges on the valley walls, a few details can be seen. Figure 17c shows a segment of scarp bounding Kasei Vallis and a tributary fossa. One end of the ridge appears to form a resistant prong, while at the other end a dark streak can be seen on the valley wall; this may be a shadow caused by a protruding vertical structure under the ridge, or else it represents a material difference in the erosional products along the wall.

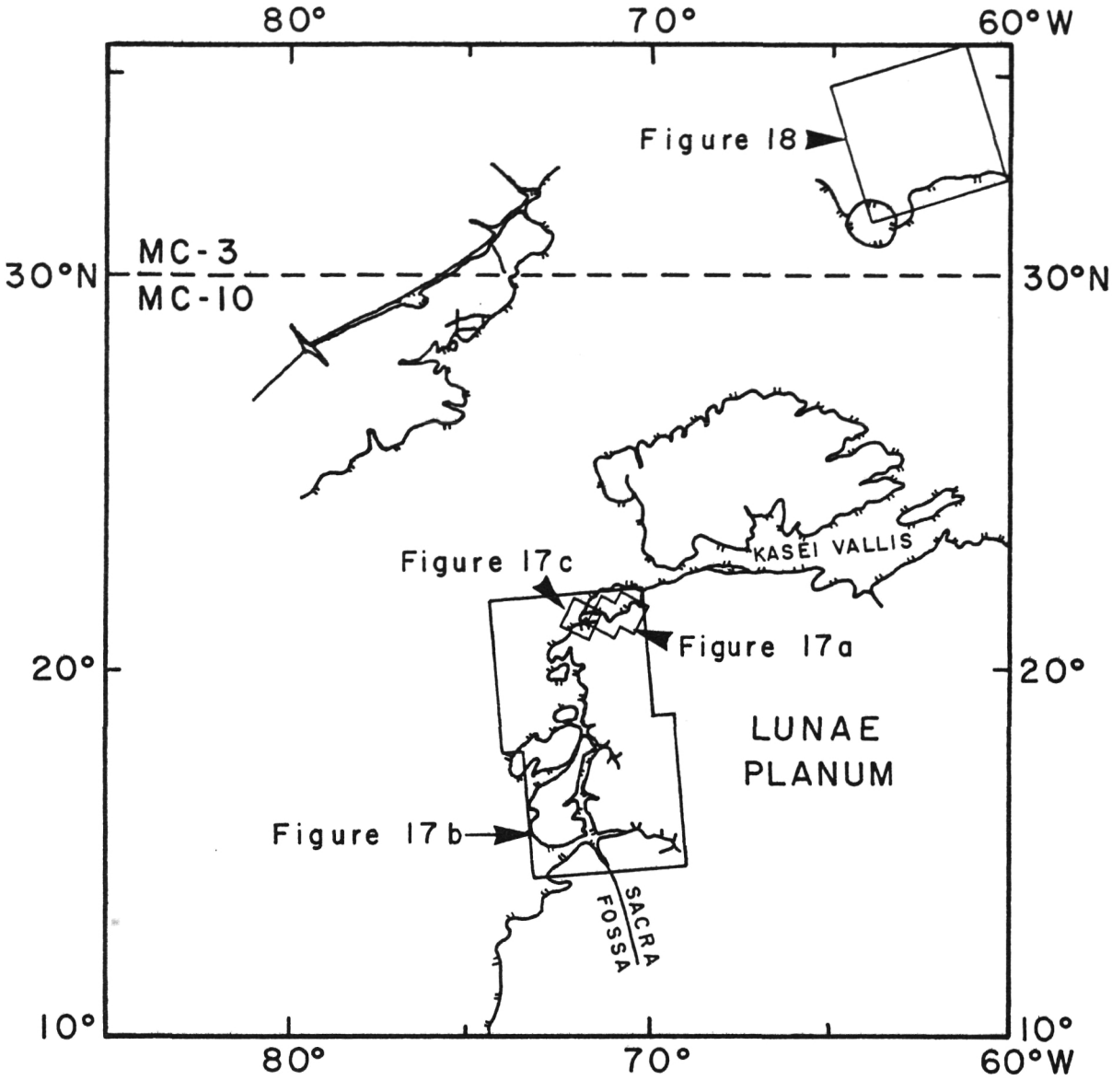


Figure 16. Sketch map of northwestern corner of Lunae Planum showing positions of the frames in Figures 17 and 18.

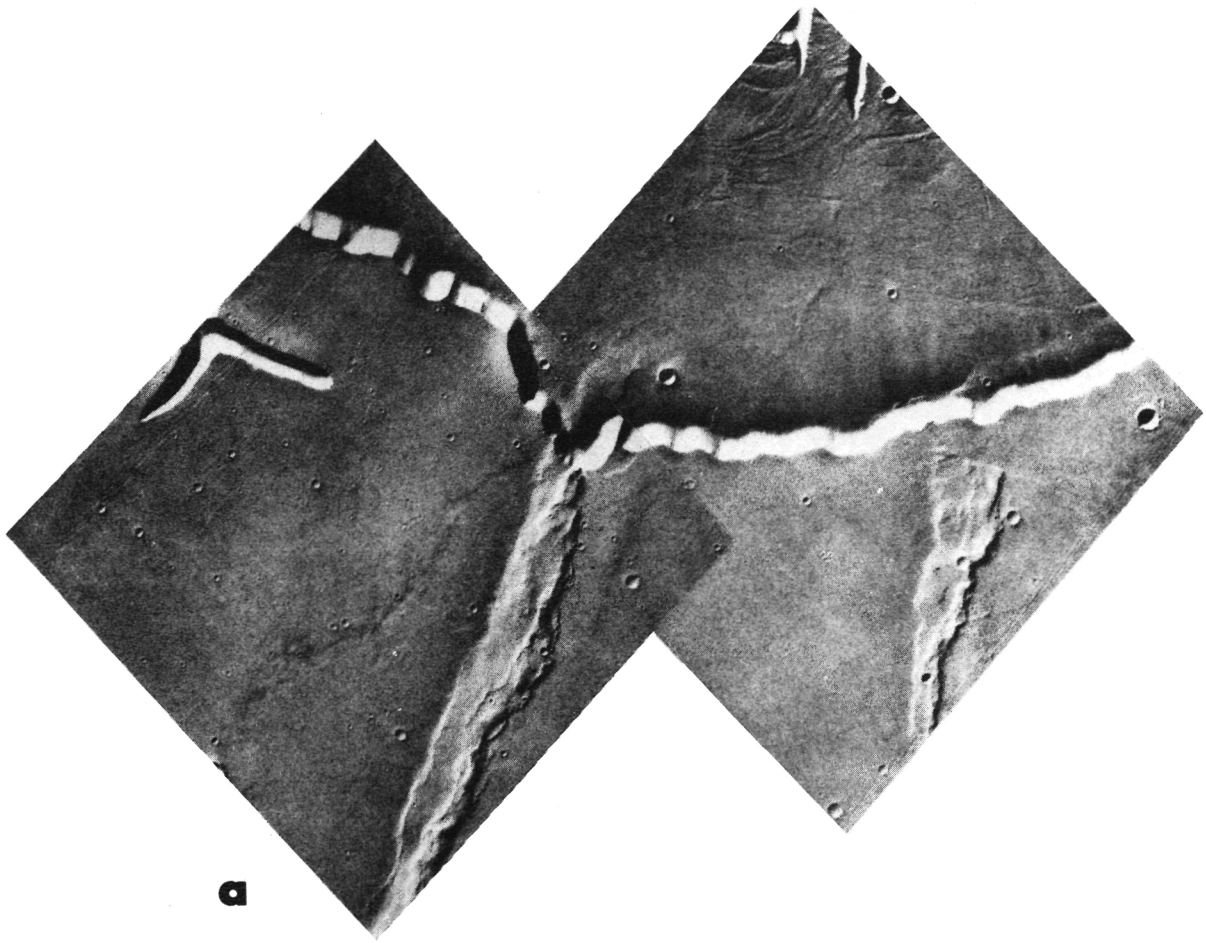
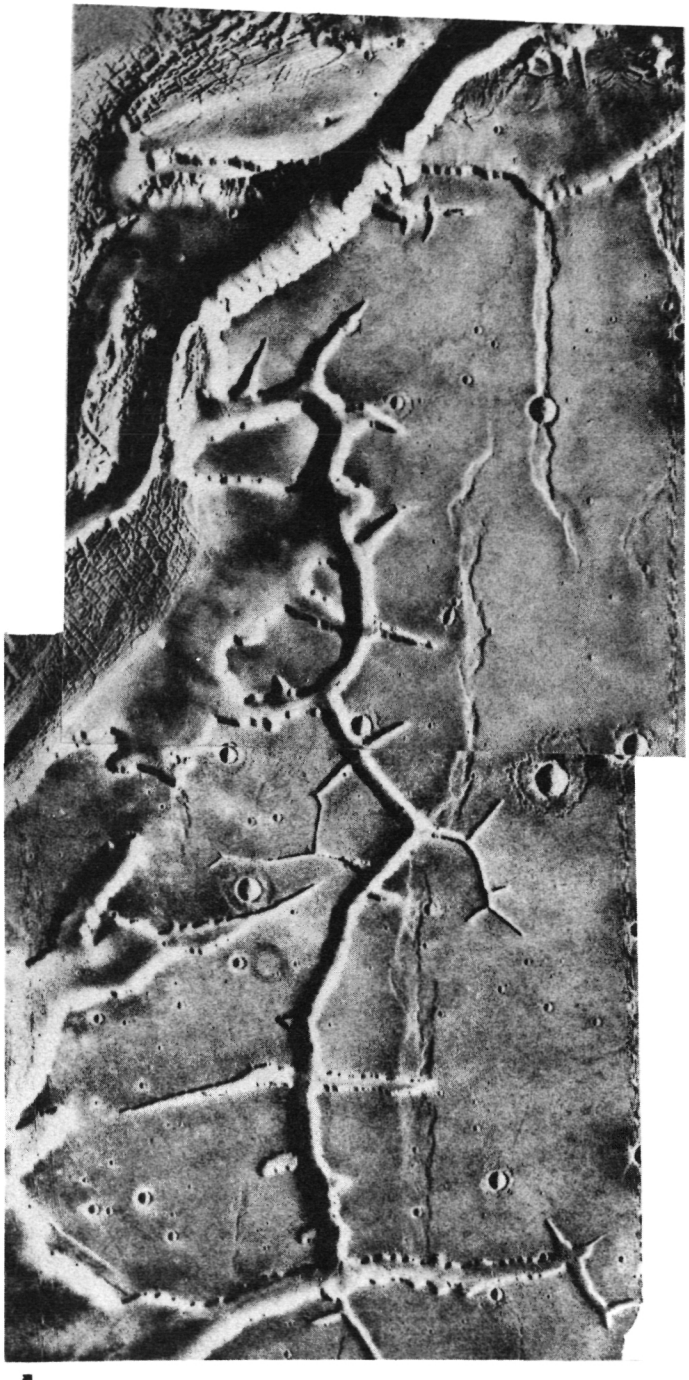


Figure 17. Details of ridge morphology in Lunae Planum.
(a) High resolution view of terminations of two ridges. The one on the left intersects the scarp bounding Kasei Vallis, which has been eroded along the trend of the ridge. The ridge on the right stops abtuptly 4 km from the scarp. Both ridges are 8 km wide at their widest point (Viking Orbiter 1 frames 664A16, 664A17).
(b) Details of ridge and fossae intersections (Viking Orbiter 1 frames 519A04, 519A06).
(c) High resolution view of intersection of ridge and scarp. A dark streak (arrow) can be seen under the ridge on the scarp wall (Viking Orbiter 1 frame 664A64).



b

Figure 17, continued.



c

Figure 17, end.



Figure 18. North trending ridges and northeast trending fossae or fractures north of Lunae Planum. See Figure 16 for location. Frame is 170 km wide (Viking Orbiter 1 frame 520A33).

West of the scarp bounding Lunae Planum proper there is a vast expanse of lowlands which have been divided into two units based on cratering ages and terrain roughness (Milton, 1974). A 320-km long ridge is present at the contact of these two units (19° to 24°N, 79°W). The contact probably represents the easternmost extent of some of the lava flows from the volcanoes in MC-9.

North of MC-10, there are ridges which continue the northerly trend of ridges in Lunae Planum and are intersected by northeast trending fossae (Fig. 18). This pattern of fracture/ridge associations is seen in several areas on Mars. The most obvious examples have already been described; the intersection of north trending ridges with generally east trending channels or canyons in MC-18 (Solis and Sinai Plana and Valles Marineris) and MC-10 (Lunae Planum and Kasei Vallis).

Other areas where ridges and fossae, canyons, or scarps intersect are in MC's-3, 5, 15, 16, 19, 24, 25, and 29. The ridges in most of these are north or northwest trending while the fossae are east-northeast (e.g. Memnonia Fossae, MC-16; Sirenum Fossae, MC-16, 24 and 29); in MC-15, northeast trending ridges cross west-northwest trending Cerberus Rupes (scarp). In these cases the ridges are generally short segments between parallel fossae; some of them continue across the trenches, others appear to be offset. Details of these particular intersections are unknown due to the relatively poor image resolution of these areas.

Another ridge/scarp association occurs in the southwestern corner of MC-19 where several ridges intersect a meandering rille-type feature called Nirgal Vallis. The sinuous, meandering course, dendritic tributaries, and steep walls of Nirgal Vallis have led to much interest in it from a channel geomorphologist's view; as a result, some very high resolution images were obtained of the valley, a few of which show the intersecting mare-type ridges

in some detail. Fifteen of 19 observed intersections have involved headward erosion of tributary valleys along the ridge trends (Fig. 19). High resolution images show dark streaks on the valley walls where the ridges intersect them (Baker, 1980) similar to the one seen in Lunae Planum (see Fig. 17).

In addition to the three main ridged plains regions (Hesperia Planum, Sinai and Solis Plana, and Lunae Planum), there are numerous smaller ridged plains units and lesser concentrations of ridges. In the southern, generally cratered hemisphere there are patches of smooth intercrater ridge bearing plains. The ridges are either parallel to the bounding structures (generally crater rims) or they form polygonal patterns. Some of these areas are smooth and dark, resembling the lunar maria (Fig. 20). Others are lighter and rougher; they may have an origin similar to the lunar light plains or, more probably, they are mantled by eolian material.

Other ridges occur on rougher terrain termed "knobby", "rolling", or "hummocky" on generalized geologic maps (e.g. Scott and Carr, 1978), and generally interpreted as eolian mantling of lava plains or old cratered terrain. In areas of several distinct plains units, the ridges are generally included within the older, thinner deposits. Ridges are rarely found in areas of thick volcanic fill, interpreted as such by the absence of surface features such as craters and proximity to a volcanic construct. An illustrative example of this is the distribution of ridges in MC-8, Amazonis Planitia, which is just west of Olympus Mons. In the central part of this quadrangle many large flows are observed extending from Olympus Mons to 1700 km from the volcano. At the western edge of Amazonis Planitia the volcanic fill is thinner; increasing numbers of peaks and craters become visible further from the volcano and with the appearance of these protruding features, ridges also become more numerous. The ridges in this area generally trend



Figure 19. Ridges intersecting Nirgal Vallis, a dendritic channel south of Valles Marineris. Several of the tributary channels have been eroded preferentially along the trends of ridges. The portion of Nirgal Vallis shown is 100 km long.

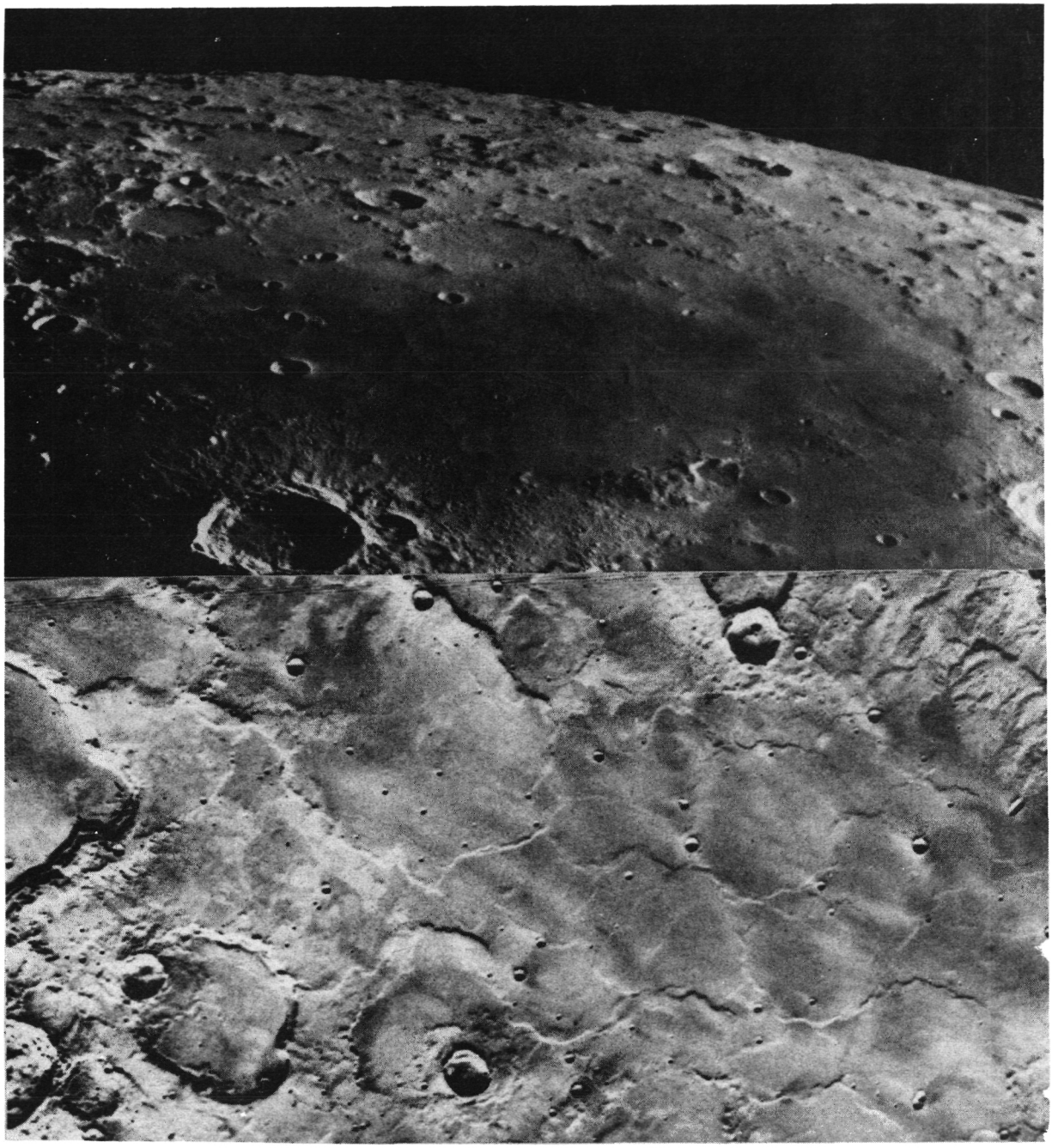


Figure 20. Polygonal ridge patterns in an irregular mare unit on the Moon (top) and in a similarly-shaped plains unit on Mars (bottom). (Earth-based telescopic view of the Moon from Kuiper et al., 1978; Viking Orbiter 1 frame 595A74).

north-south, stretching between the knobs, peaks, and craters (Fig. 21).

The relationship of thinner fill with more numerous ridges also applies to Chryse Planitia (MC's-10, 11 and 4). The Chryse region is a large depression north of the cratered terrain boundary. Ridges are numerous in western Chryse but are absent to the east and north. In this case the fill is probably thicker in these directions because of infilling by fluvial or eolian sediments (Greeley et al., 1977; Theilig and Greeley, 1979). Ridges also occur on plains and plateau deposits that are relatively thinner in MC's-5 and 6.

South of -30°, most ridges are on ridged or rolling plains localized in the cratered terrain. These units have been interpreted as old lava or ash flow units in MC-24 (Howard, 1979), MC-26, MC-28 (Potter, 1976) and MC-29 (De Hon, 1977). The generally light color of these suggests that they are either eolian deposits (MC-25; McGill, 1978) or eolian mantled. In MC-27 ridges are located on the eroded plains surrounding an ancient shield-volcano complex (Peterson, 1977). These ridges are more rugged than most other mare-type ridges on Mars.

North of about 30°, ridges are found on plateau materials as well as on the lower smooth plains. In MC-5 ridges occur on two plateau units which have been interpreted as volcanic flows similar to flood basalts and which have an eolian mantle (Lucchitta, 1978). Ridges are more numerous on the less cratered (younger?) plateau unit, and they are truncated at the scarp edges of the plateau by a subsequent system of broad, steep valleys. The plateau dissection has destroyed portions of the ridges, and the age relationships are fairly straightforward. By contrast, in MC-4, a similar plateau unit of apparently similar age (Underwood and Trask, 1978) is crossed by ridges which continue across the bounding scarps and continue into the surrounding low plains of Acidalia Planitia (Fig. 22). The ridges in the lower plains are

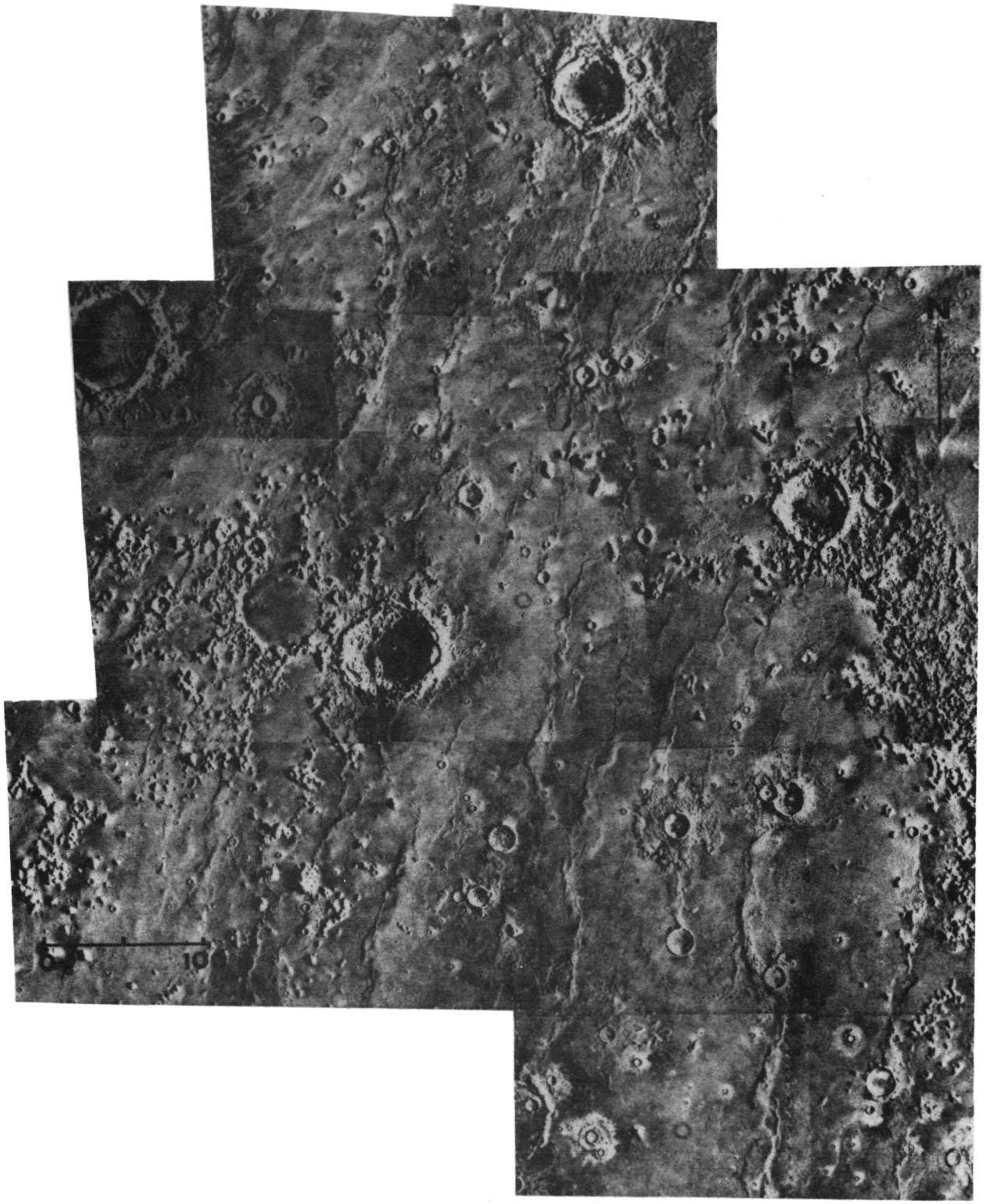


Figure 21. Mosaic of Viking images of Amazonis Planitia, centered at 24°,178°. Ridges are seen in the relatively smooth plains between craters and knobby terrain. The scale bar is 100 km long.

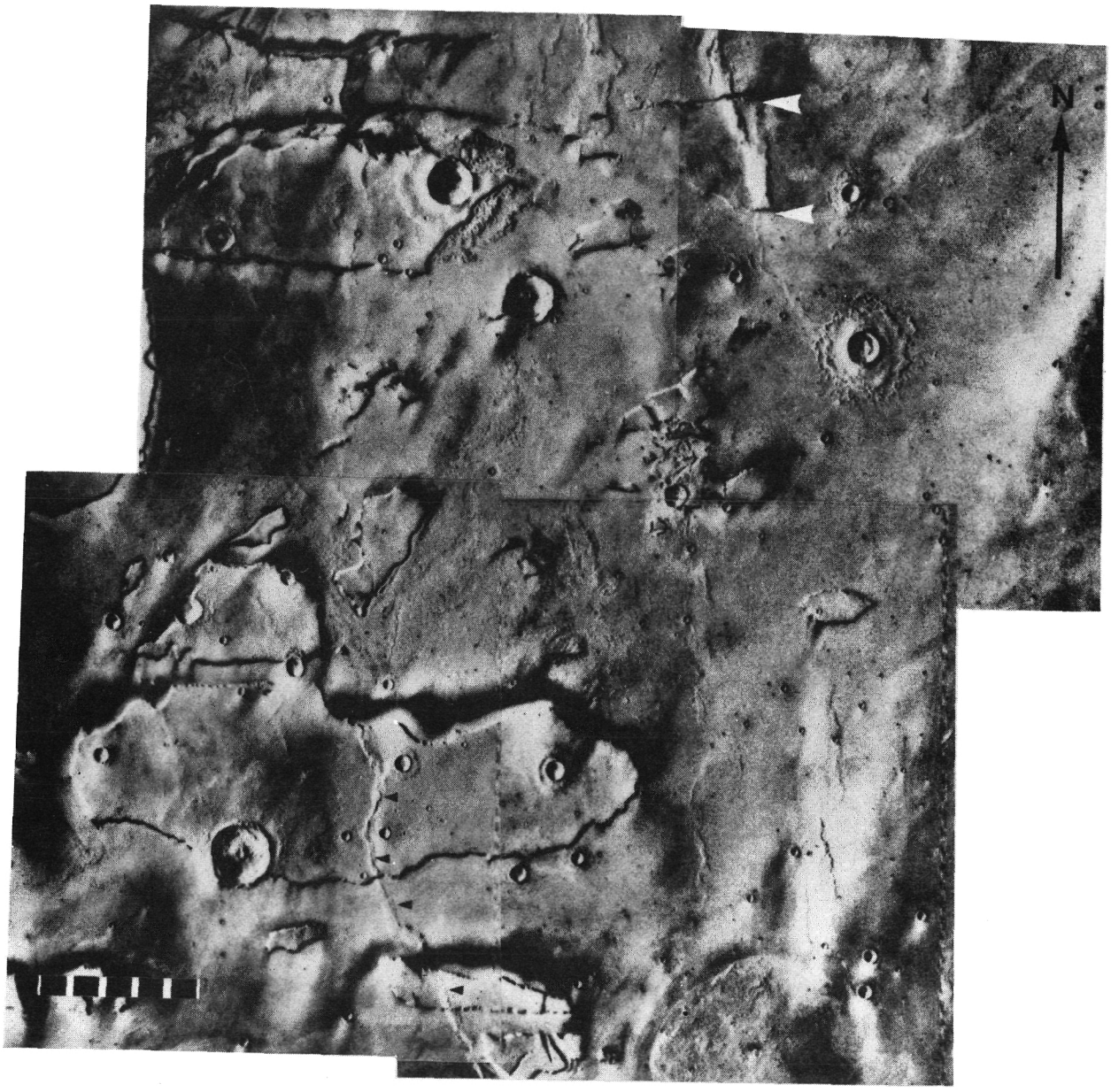


Figure 22. Mosaic of Viking images of southwestern Acidalia Planitia centered at 36°,52°. A mare-type ridge can be traced across the raised plateau units and intervening troughs (black arrows). In the north, an upraised portion of a ridge is bounded by two scarps (white arrows). Scale bar is 50 km long.

not as morphologically distinct as on the plateau remnants; this is also true of ridges completely contained in the plains east of the dissected area. The same effect is seen in the ejecta blanket of a crater which is situated at the edge of the plateau; radial flow features in the ejecta are clearly visible on the higher ground, but past the scarp which bounds the plateau the extent and any morphologic details of the ejecta are absent. This effect may be due to eolian filling of the scarp-bounded canyon, covering and muting the features. A ridge to the northeast of this location gives a further clue. A broad, rugged, linear massif is bounded on the north and south by scarps; south of the scarp the massif trend continues as a smaller ridge (Fig. 22). Normal faulting and subsequent eolian modification would account for this configuration.

The predominant trends of ridges north of 30° are between north and N20°W (Fig. 23). This rose diagram actually includes ridges in a latitude band between 30°N and 45°N.; there are very few ridges north of 45° in the Vastitas Borealis (northern wasteland) and no true mare-type ridges were observed in MC-1, the north polar region.

In contrast to the Moon, most ridges on Mars are not found in association with proven volcanic features, although this does not rule out the possibility that they are developed in flood-type lava units. Most regions on Mars which are unquestionably volcanic flows or are probably thick volcanic units lack ridges (e.g. see MC-9, and eastern MC-8, the major surface units of which are composed almost entirely of flows from Olympus Mons and the other Tharsis volcanoes). The major exceptions are the occurrence of mare-type ridges within actual volcanic calderas, several examples of ridges very near volcano flanks, and one on a large flow lobe.

Southeast of Olympus Mons, a 130-km long ridge in several sections is parallel to the bounding scarp of the volcano's slope, or concentric to the

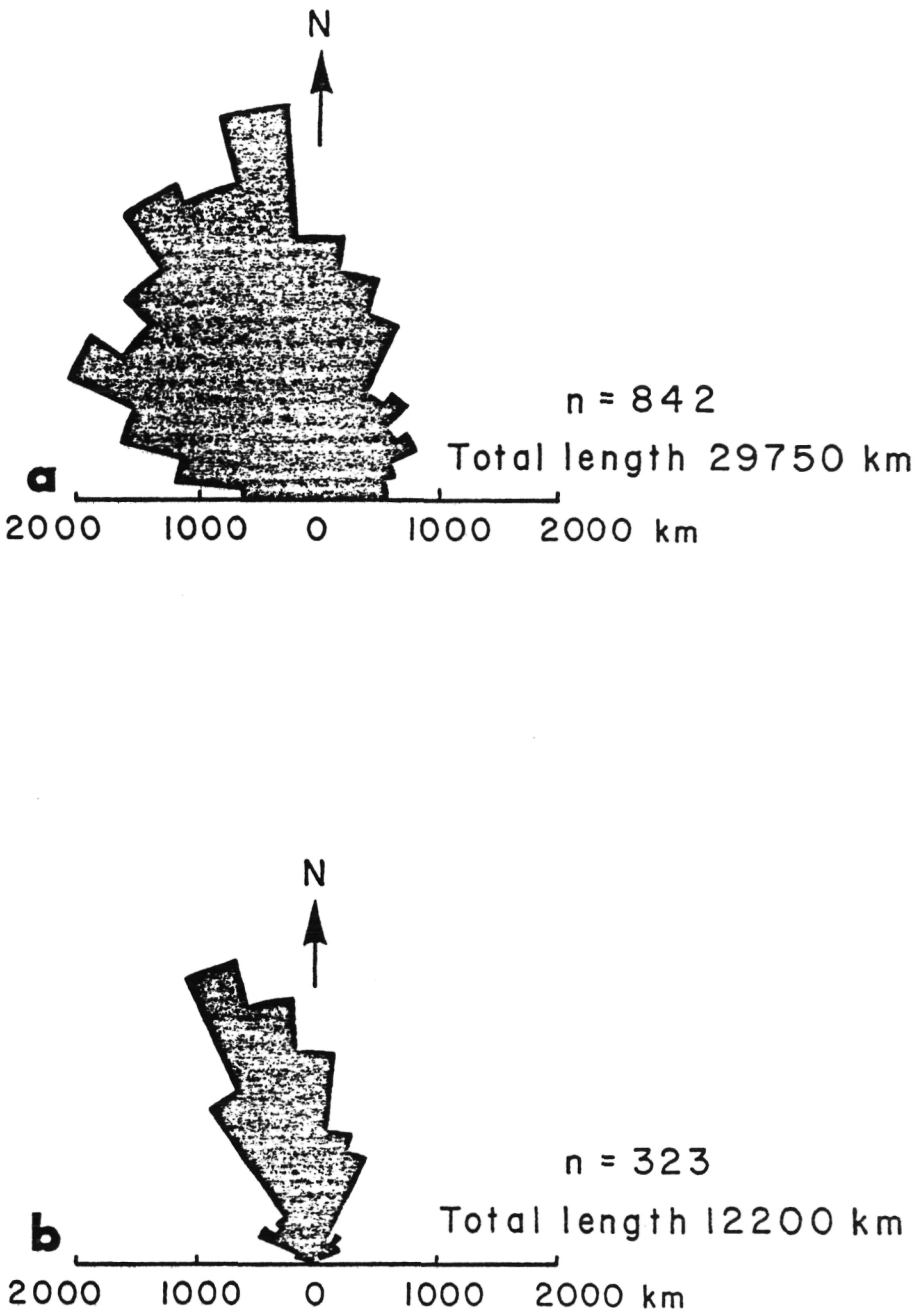


Figure 23. Rose diagrams of trends of ridges (a) south of -30° and (b) north of 30°.

center (Fig. 24). At the southern end of this ridge a gentle swell can be seen, topped by a bifurcating fracture. This suggests that the trend of the ridge is the site of a concentric line of weakness or fracture with accompanying extrusion, or of a pressure ridge.

A similar ridge adjoins the edge of Hecates Tholus in Utopia Planitia (MC-7) and extends 80 km southward (Fig. 24). This ridge displays true mare-type ridge morphology for only a portion of its length; elsewhere it lacks the underlying arch section and consists only of a sharp ridge. The surface to the west of this ridge appears smoother, less cratered, and of slightly higher albedo than the area east of the ridge; this may indicate that the position of the ridge marks the boundary between two flow units, and that it may have an origin similar to pressure ridges on the Earth.

The only ridges definitely associated with a flow feature are several ridges near the edge of an extremely long, thick flow, probably from Arsia Mons in MC-17 (Fig. 25). These ridges generally parallel the direction of flow. The best-developed ridge is nearest to the edge of the flow, once again suggesting a pressure ridge origin.

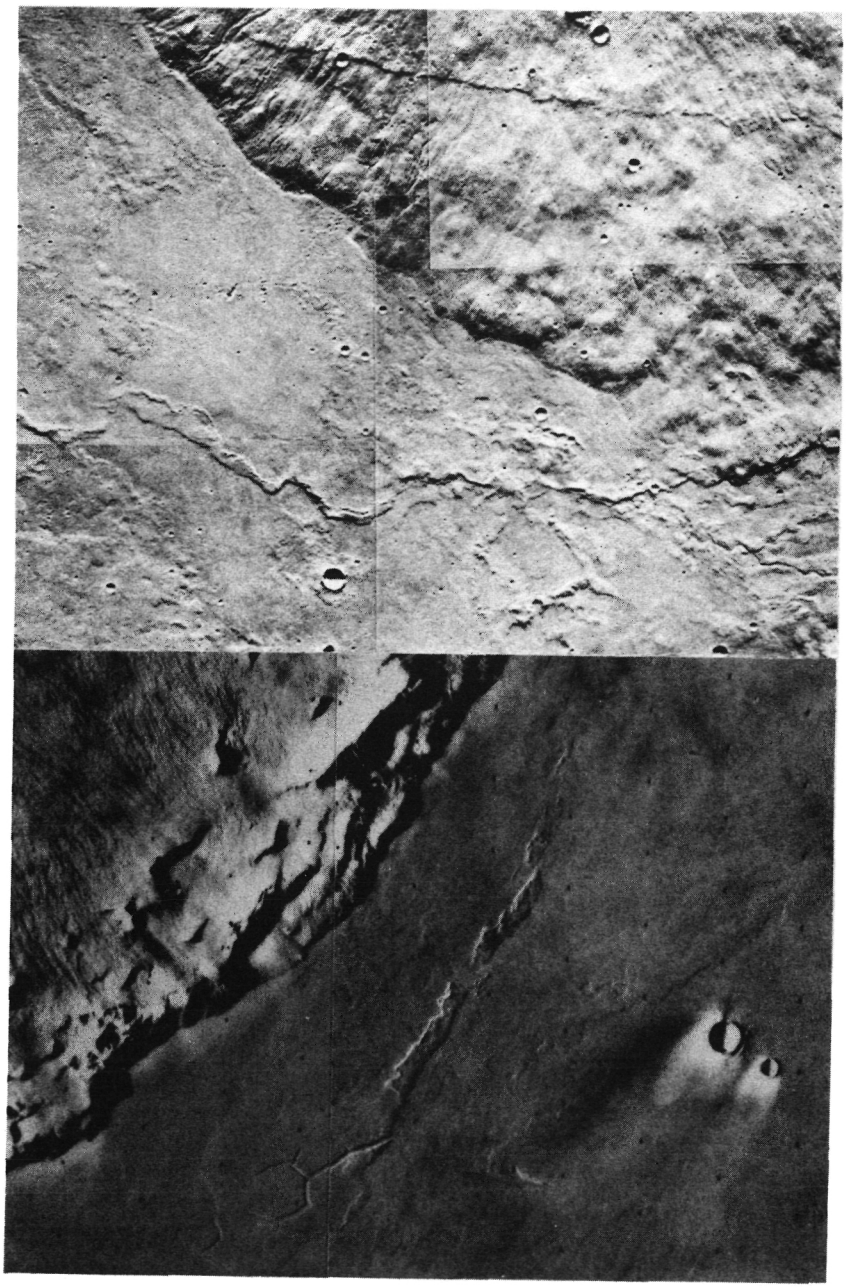


Figure 24. Examples of ridges near volcanoes.
(a) Ridge abutting the flank of Hecates Tholus, a large shield-type volcanic structure in Utopia Planitia. The ridge is 80 km long.
(b) Ridge near the bounding scarp of the Olympus Mons flank. This ridge is 130 km long.

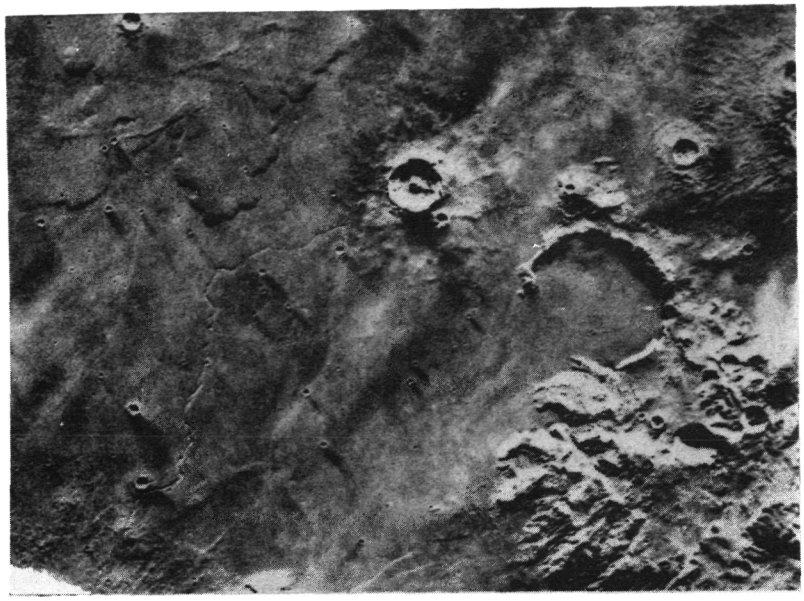


Figure 25. Ridge-type structure
on large flow lobe (upper left) south of Arsia Mons.

Ridges in Basins and Craters

In contrast to the occurrence of mare ridges in lunar basins, relatively few large craters and basins on Mars display basin related (concentric and radial) ridge patterns. Ridges were found in 32 craters and basins which range in size from 30 to 470 km. Ridges also occur in the 1600-km basin Hellas; however, because of the degraded basin structure, large size, and probable complex history these ridges are included in the section on plains rather than here. In most of the smaller craters (30 to 90 km) there are very few ridges; those present tend to be very close to the crater rim. They are generally straight segments forming a chord between two points of the crater interior rim wall (several examples can be seen in MC-23). In other small craters ridges parallel regional trends and create a preponderance of ridges striking northwest in accordance with a major global trend (Fig. 26).

Likewise, the major trends of ridges in larger craters and basins also do not appear to be basin-related but instead reflect the dominant global north and northwest trends. This is apparent from the rose diagram showing weighted trends of ridges in large craters (> 100 km) and basins on Mars (Fig. 26). A more nearly random distribution would be expected from a pattern of concentric and radial ridges such as is found near the outer edges of lunar basins (Fagin et al., 1978).

A few circumferential or arcuate patterns of ridges are present surrounding the basin edge of seven Martian basins. These are listed in Table 2. The largest of these, the Schiaparelli basin, displays a dichotomy of floor material with smooth, darker material to the north and east and lighter, rougher material to the south and west; these have been interpreted as volcanic infill and eolian mantling, respectively (Mouginis-Mark et al., 1980).

Ridges in the Schiaparelli basin show a lunarlike circumferential

pattern in the eastern part of the basin; some of these ridges are located over the inferred subsurface position of buried parts of a peak ring which is visible in the western part of the basin (Fig. 27a). However, detailed mapping and measuring of ridge orientations reveal a strong northwest trend and an absence of a prominent basin-concentric system (Mouginis-Mark et al., 1980). Mouginis-Mark and others (1980) also observed a more uniform spacing of ridges within Schiaparelli relative to lunar basins. They believe this expresses the influence of subsurface topography, due to the observation of a concentration of ridge elements over the buried peak ring. Thus while overall ridge trends within the basin are consistent with the regional stress field, the morphologic expression is also partly due to the material of the floor unit and to subsurface topography.

The most lunarlike ridge patterns are in a 150-km unnamed basin (ISM-Wa) at 29°N, 350°W (Fig. 27b). A major concentric ridge system in this basin is situated 0.6 times the rim-crest diameter, similar to the position of circumferential ridges in lunar basins (Maxwell, 1978). In the northern part of ISM-Wa the ridge system is not present, and the circumferential trend is continued as two closely spaced arcuate rilles. These probable graben are developed in rugged crater floor material rather than the smooth plains which contain the ridges. In the middle of the basin floor there are several north and northwest trending ridges similar to those of some lunar mare basins (e.g. Serenitatis, Fig. 4a). In the south and west of the basin the segments are arranged en echelon.

Other ridge systems within Martian basins display less of a similarity to those within lunar basins. Flaugergues, a 220-km basin at 17°N, 341°W, exhibits a strong northwest trend of ridges, similar to a regional system of scarps in the same area (Fig. 27c). The ridges are well defined in the northern half of the basin, where the floor consists of a smooth dark

material. The southern half of the floor is a rougher unit, and the structural patterns are expressed in this as scarp-bounded ridges or at least in one case as a rille. Ridges closest to the basin rim form arcuate sections parallel to the rim near the west and east walls of this basin.

In Copernicus (260 km diameter, -49°N 69°W), semi-concentric ridges are present near the east and west edges of the basin floor (Fig. 27d). However, elsewhere in the basin the similarity to lunar ridge systems is lacking. Four major ridge sets strike almost due north through the middle of the basin. This trend can be traced northward through the basin rim into the surrounding plains. South of Copernicus the regional structural trend is defined by several large, steep-sided ridges of non-mare ridge morphology.

Table 2. Martian basins that contain ridges.

NAME	LOCATION	DIAMETER (KM)	RIDGE SYSTEM CHARACTERISTICS
ISM-Wa	29°, 350° (MC-5)	150	Prominent northwest trend; Circumferential system; Northwest system in basin center.
Ptolemaeus	-46°, 157° (MC-24)	160	One northwest trending ridge through center part of basin extending beyond peak ring.
Flaugergues	-17°, 341° (MC-20)	220	Arcuate circumferential trends near east and west walls; numerous north and northwest trending ridges.
Copernicus	-49°, 169° (MC-24)	260	North-trending ridge system in central part of basin similar to regional trend of scarps and ridges; Partial circumferential system near east and west basin walls.
Cassini	24°, 328° (MC-12)	400	Northwest trending ridges in northeast and central part of basin.
Huygens	-14°, 304° (MC-21)	460	Random arrangement of ridges throughout basin.
Schiaparelli	-5°, 345° (MC-20)	470	Ridges in eastern part of basin with prominent northwest trend; some appear to overlie position of buried peak ring.

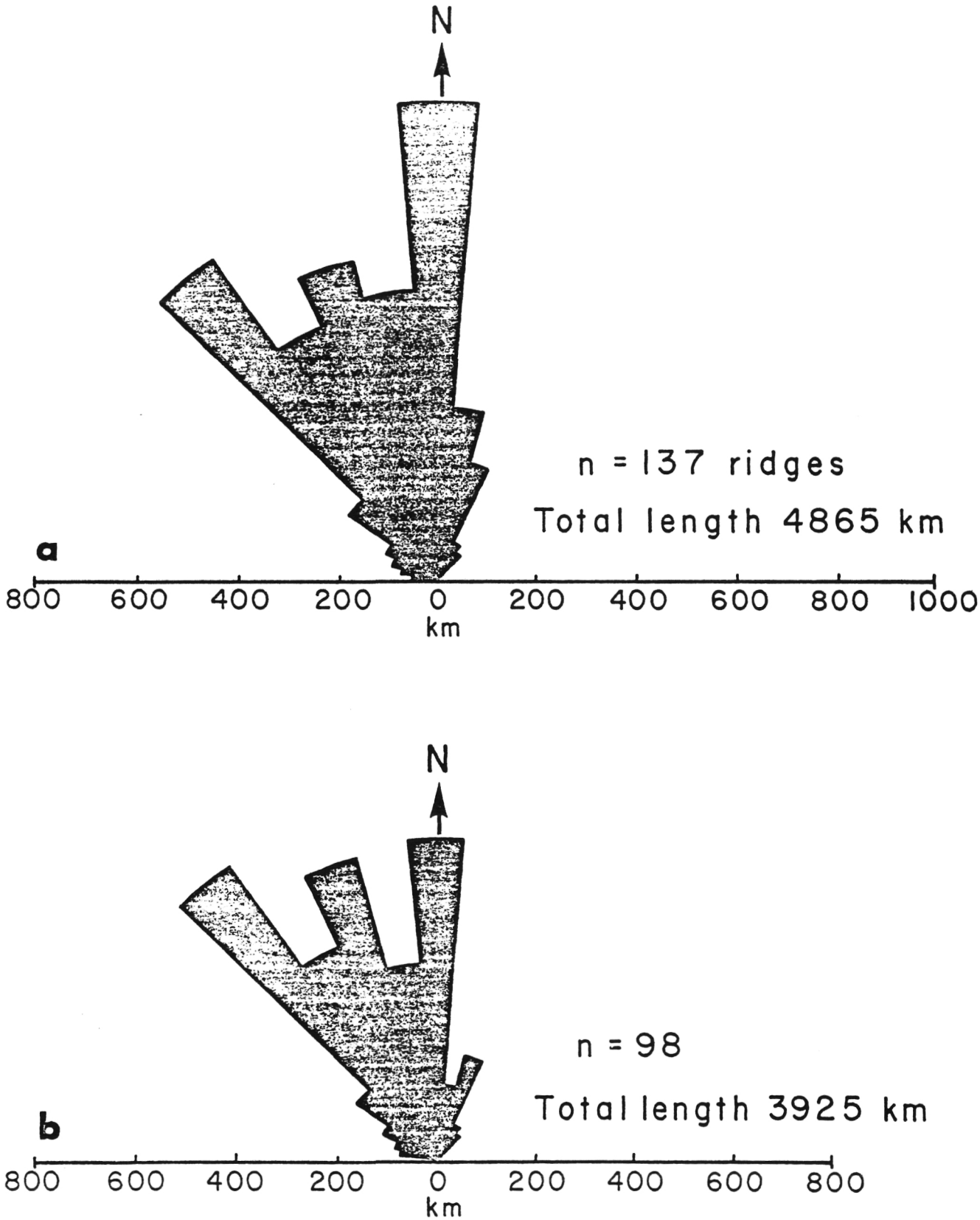
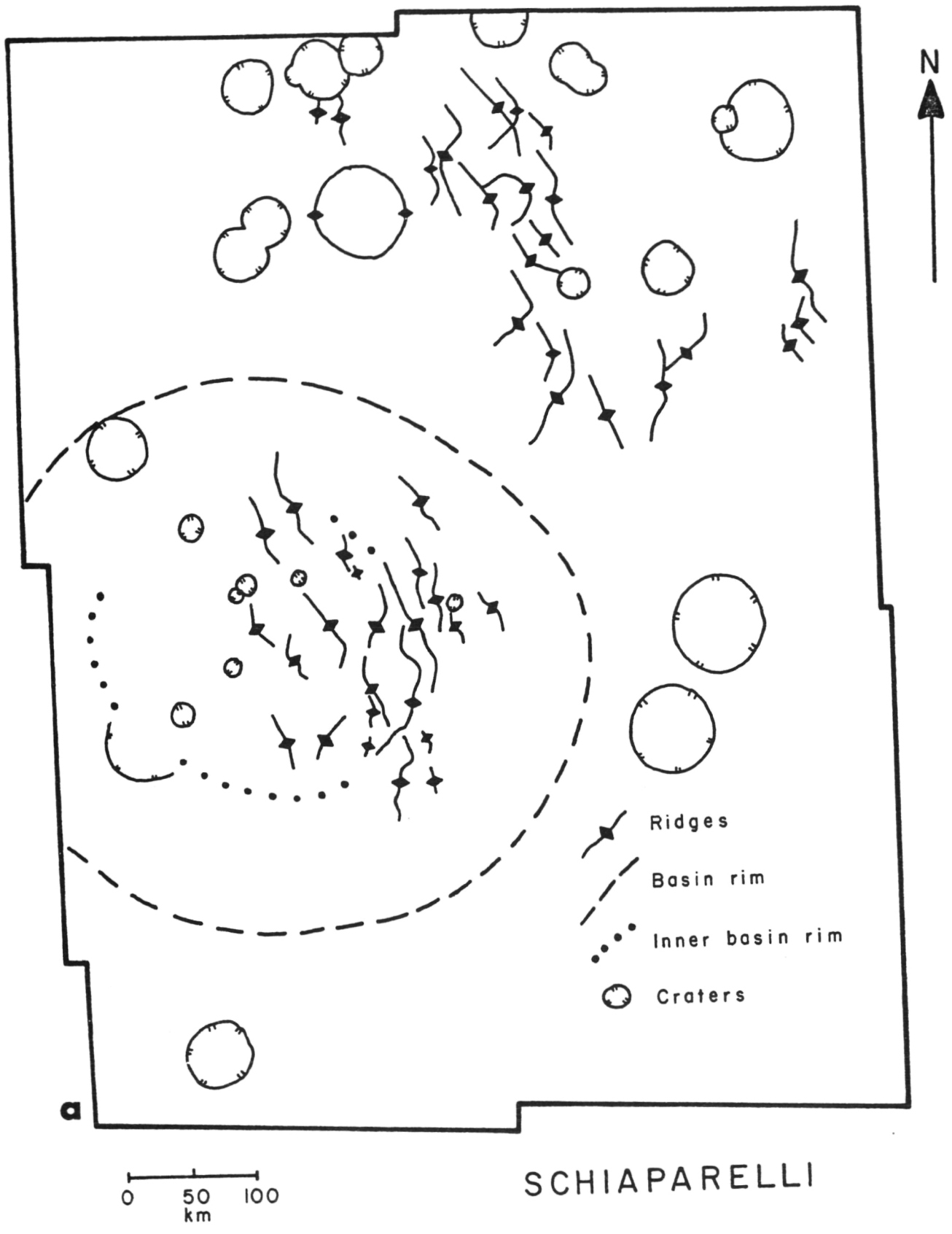


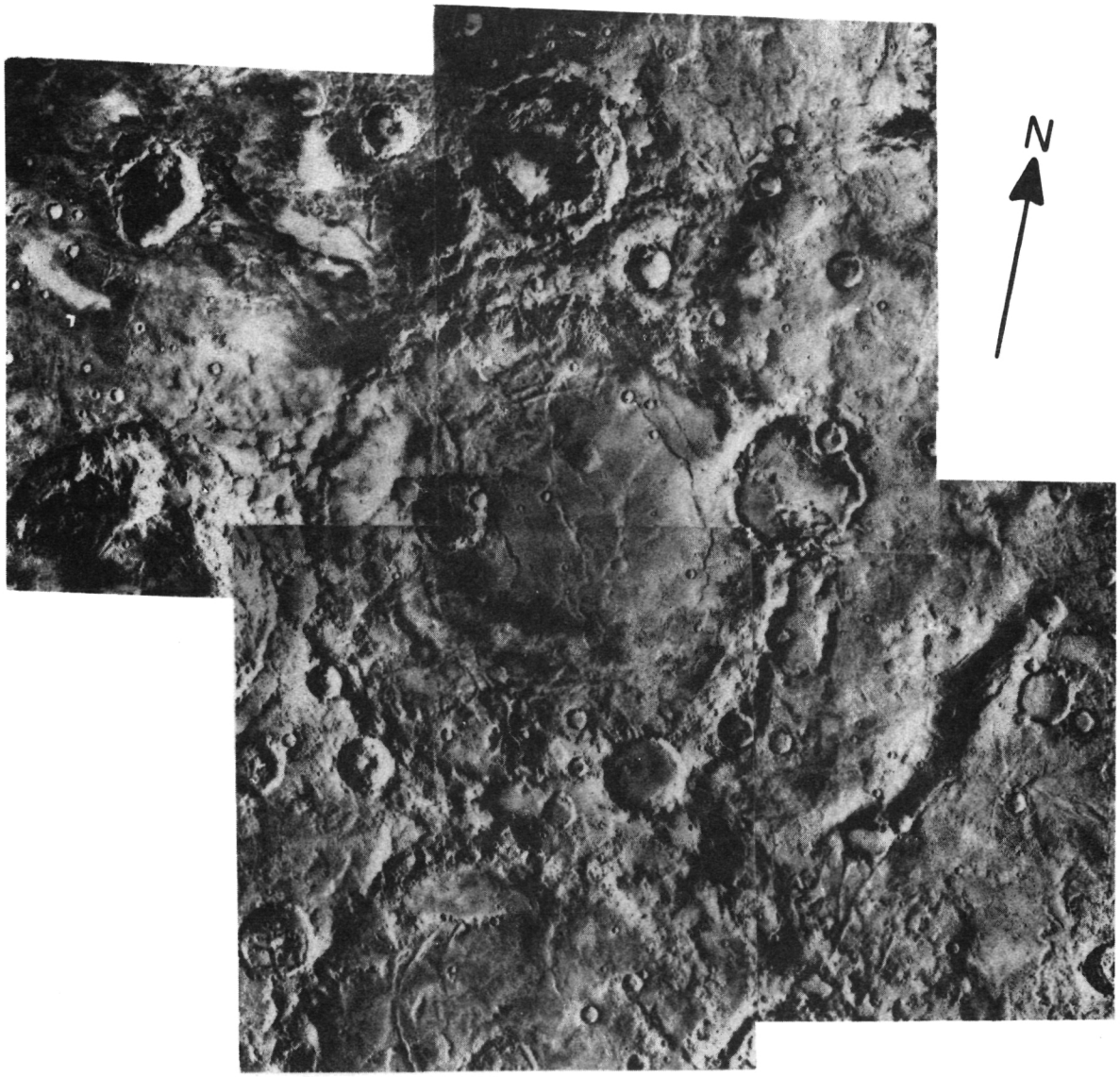
Figure 26. Rose diagrams showing trends of ridges in craters and basins on Mars. (a) Ridges in all craters and basins on Mars; size range 30 to 470 km. (b) Ridges in large craters and basins (100 to 470 km).

Figure 27 (following 8 pages). Examples of basins on Mars with associated ridge systems; each mosaic is accompanied by a sketch map delineating ridges and other features which can be seen.
(a) Schiaparelli, a 470-km basin located at -5°, 345°.
(b) An unnamed 150-km basin at 29°,350°. The designation ISM-Wa refers to the Mars chart on which the feature appears (MC-5, Ismenius Lacus) and the postition on the map.
(c) Flaugergues, 220 km in diameter, at -17°,341°.
(d) The basin Copernicus, 260 km in diameter, located at 49°, 169°.

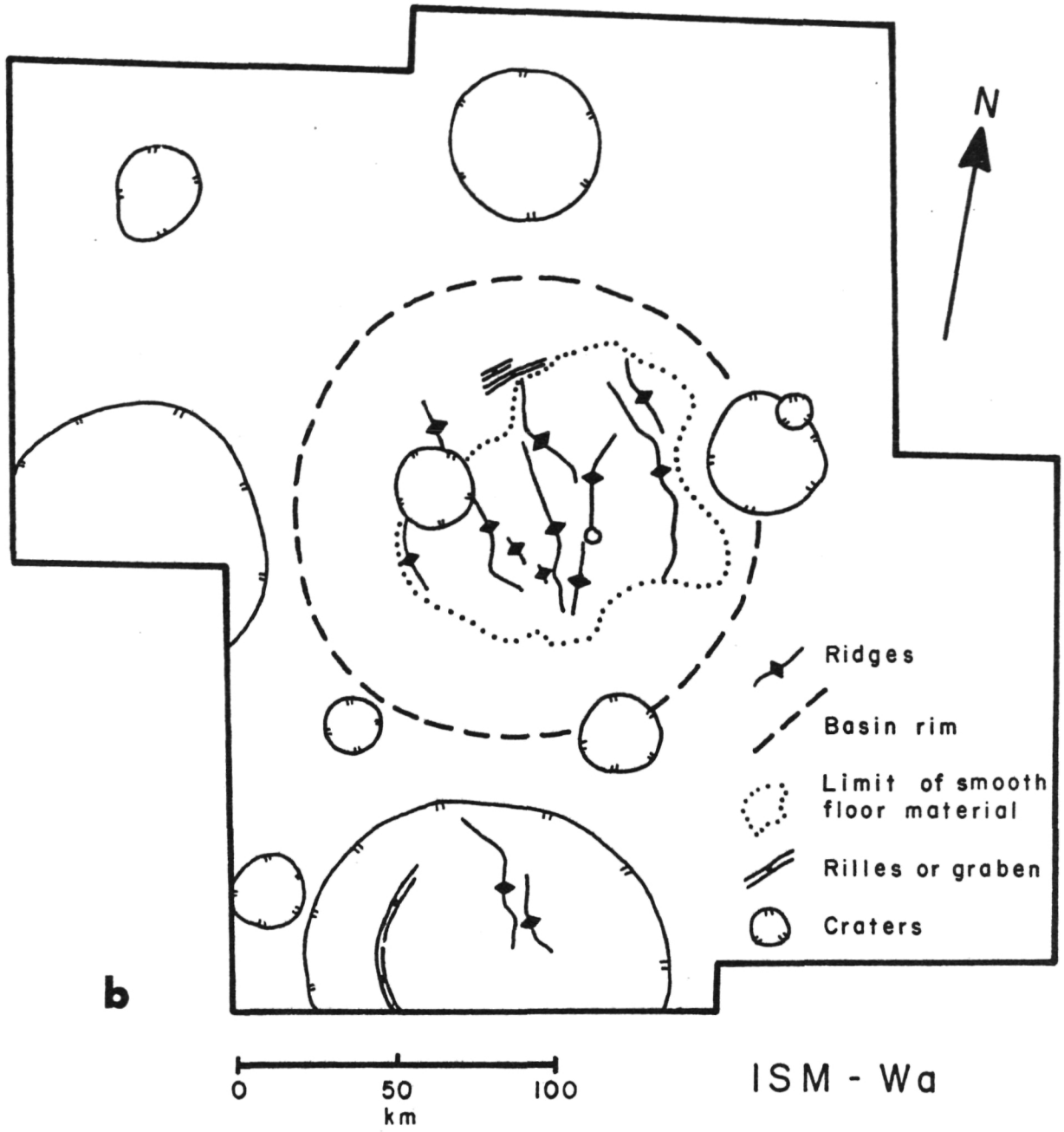


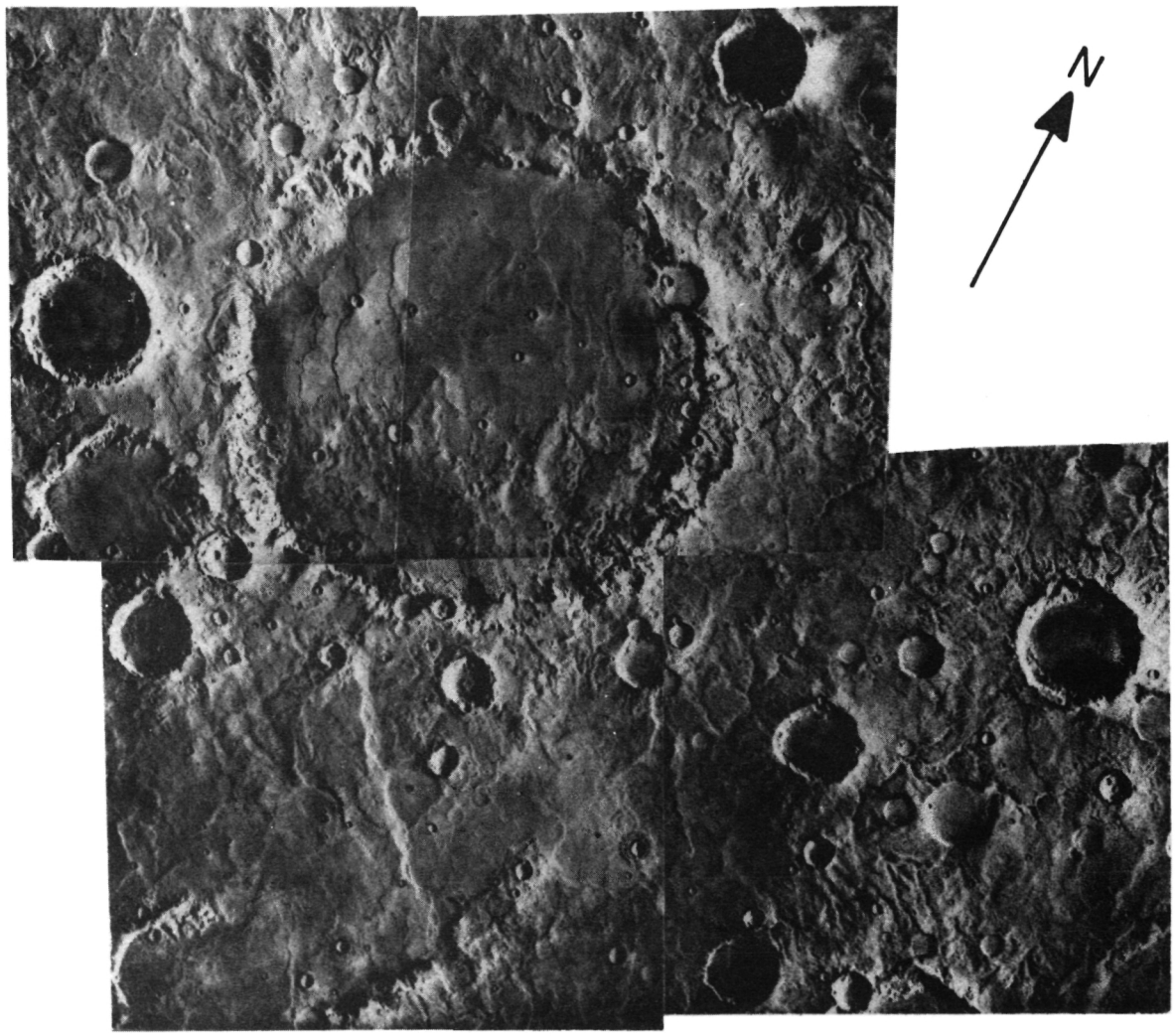
SCHIAPARELLI


N
Ridges
Basin rim
Inner basin rim
Craters
a
0
50
100
km
SCHIAPARELLI



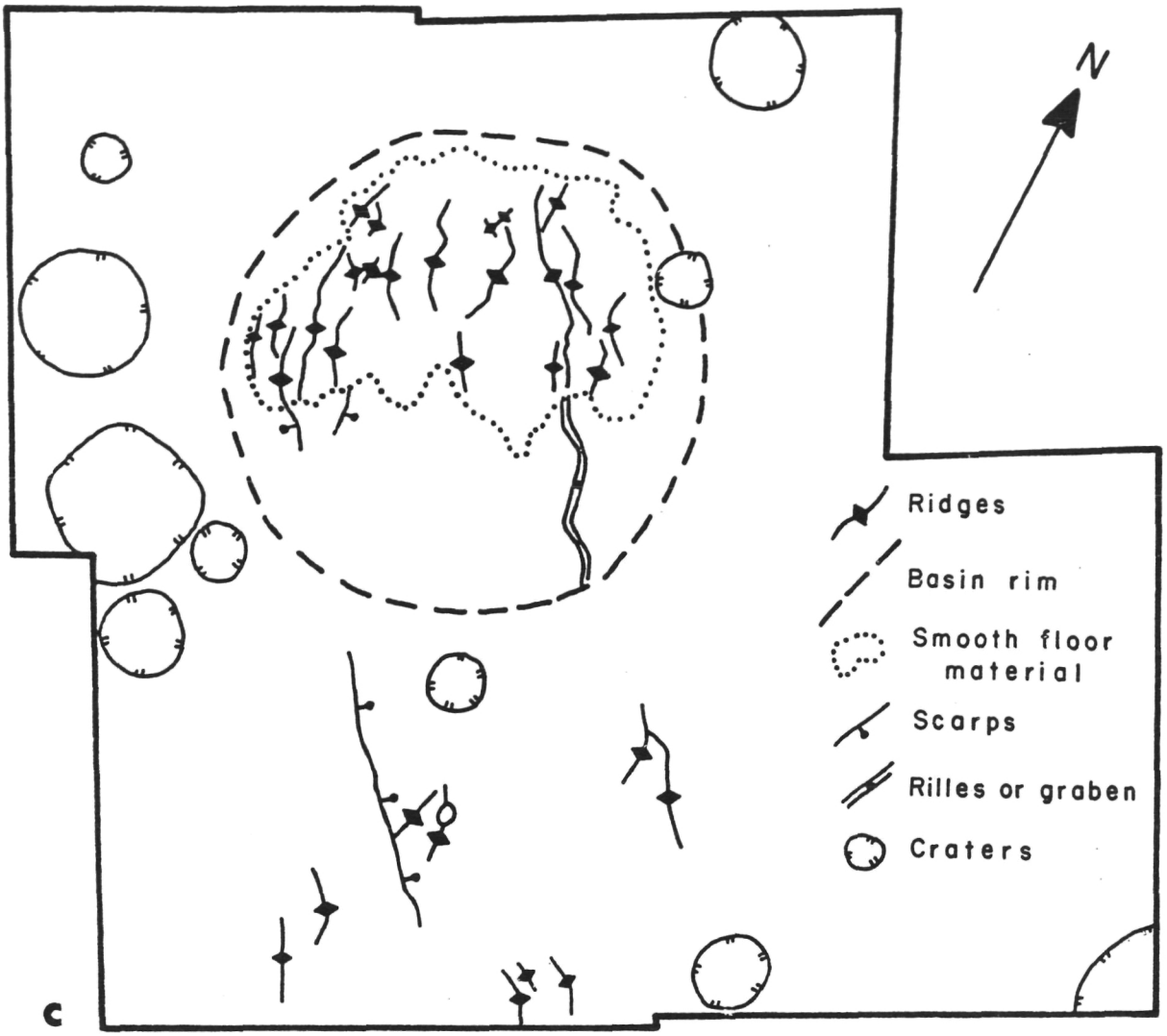
ISM - Wa

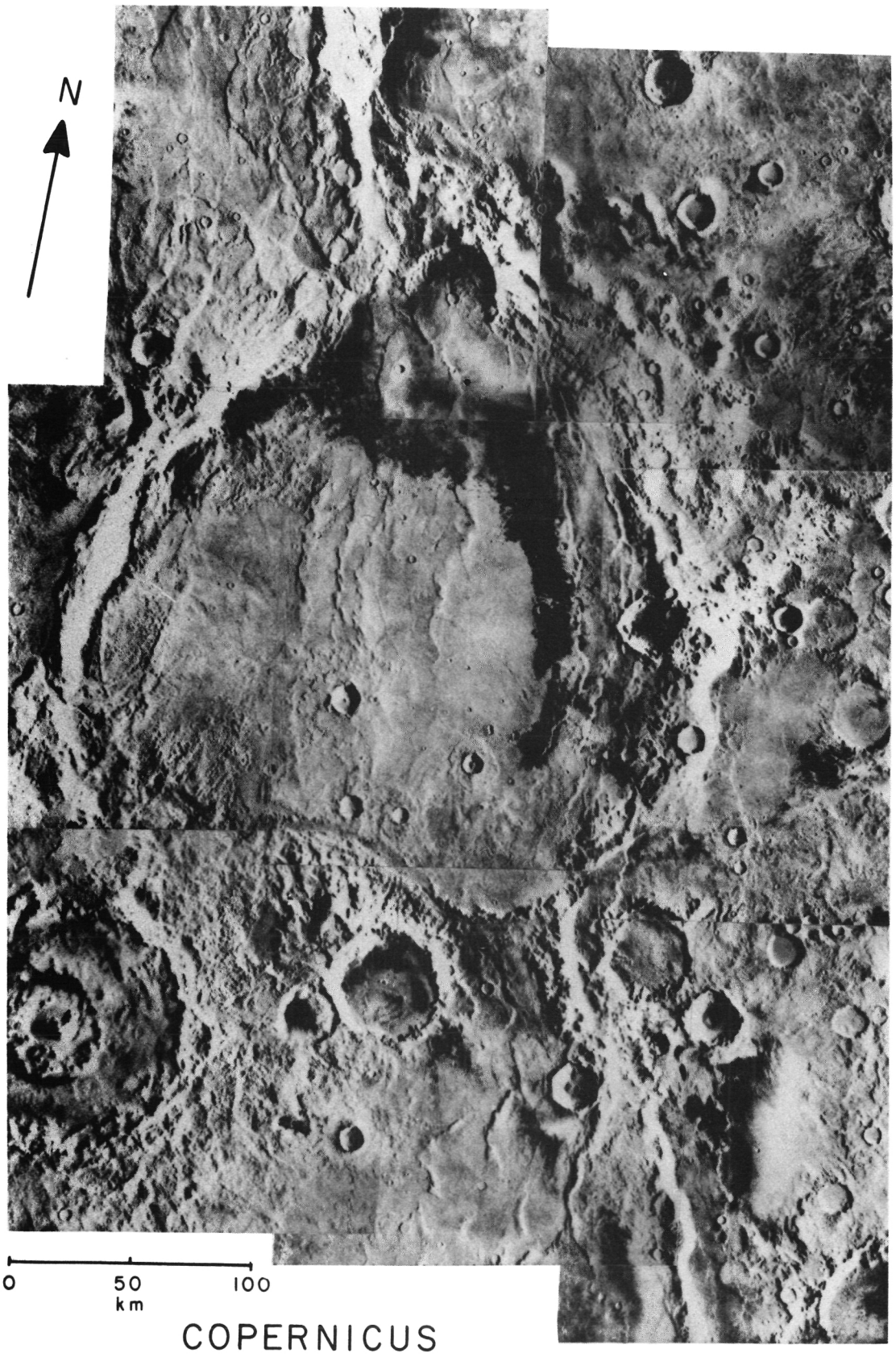

N
Ridges
Basin rim
Limit of smooth floor material
Rilles or graben
Craters
b
0
50
100
km
ISM - Wa



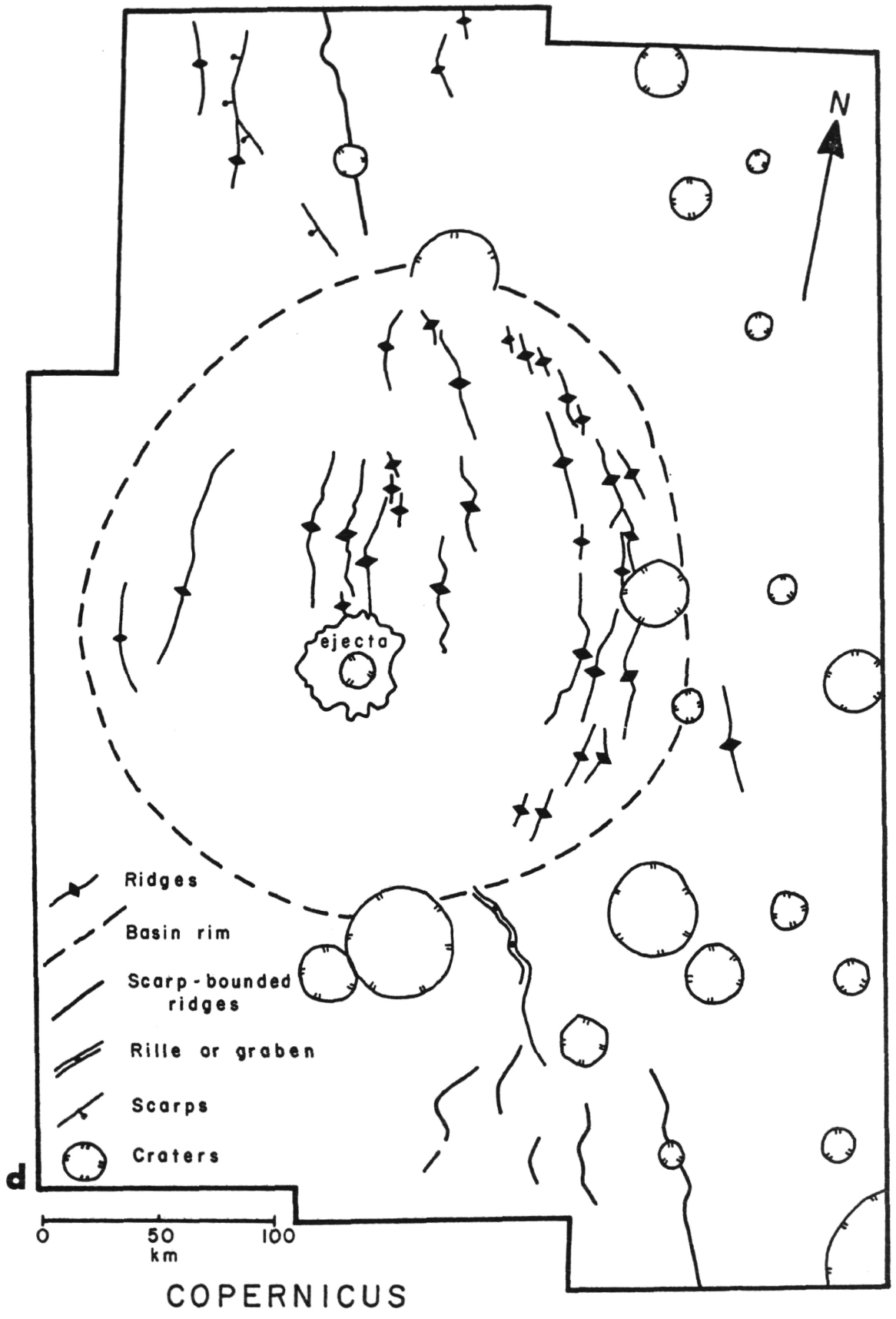
0 50 100
km

FLAUGERGUES


N
Ridges
Basin rim
Smooth floor material
Scarps
Rilles or graben
Craters
c
0
50
100
km
FLAUGERGUES



COPERNICUS


N
ejecta
Ridges
Basin rim
Scarp-bounded ridges
Rille or graben
Scarps
Craters
d
0
50
km
100
COPERNICUS

Ridges in Calderas

Mare-type ridges were observed in the summit calderas of three major volcanic constructs on Mars: Olympus Mons, Pavonis Mons, and Uranius Patera. All three are located in MC-9. These edifices are interpreted as volcanic, based on their geomorphologic resemblance to terrestrial shield volcanoes and the observation of numerous flow lobes, channels, fissures, and small vents on the flanks and in the surrounding plains (Mutch et al., 1976).

Olympus Mons (18°, 133°), the largest volcano yet found in the solar system, is over 700 km across at the base, and its summit is 24 km above the surrounding plains (27 km above Martian zero datum). The 70-km diameter summit caldera is a complex of overlapping circular structures, the largest being approximately 60 km in diameter (Fig. 28a). The caldera floor elevations average 4 km below the rim. Ridges are present on the floor of the oldest (largest) circular part of the caldera and in at least three other distinct circular sections. The floors of these are at different elevations, and ridges are truncated at the boundaries between them, indicating several cycles of ridge formation accompanying caldera collapse.

A system of circular fractures lies just inside the remaining rim of the largest portion of the caldera. The existence of both fractures and ridges within the caldera suggests cyclical swelling by magma filling and emptying (Carr et al., 1977). Sequential uplift and subsidence is also observed in the larger terrestrial basaltic shields such as Kilauea and Mauna Loa (Eaton and Murata, 1960).

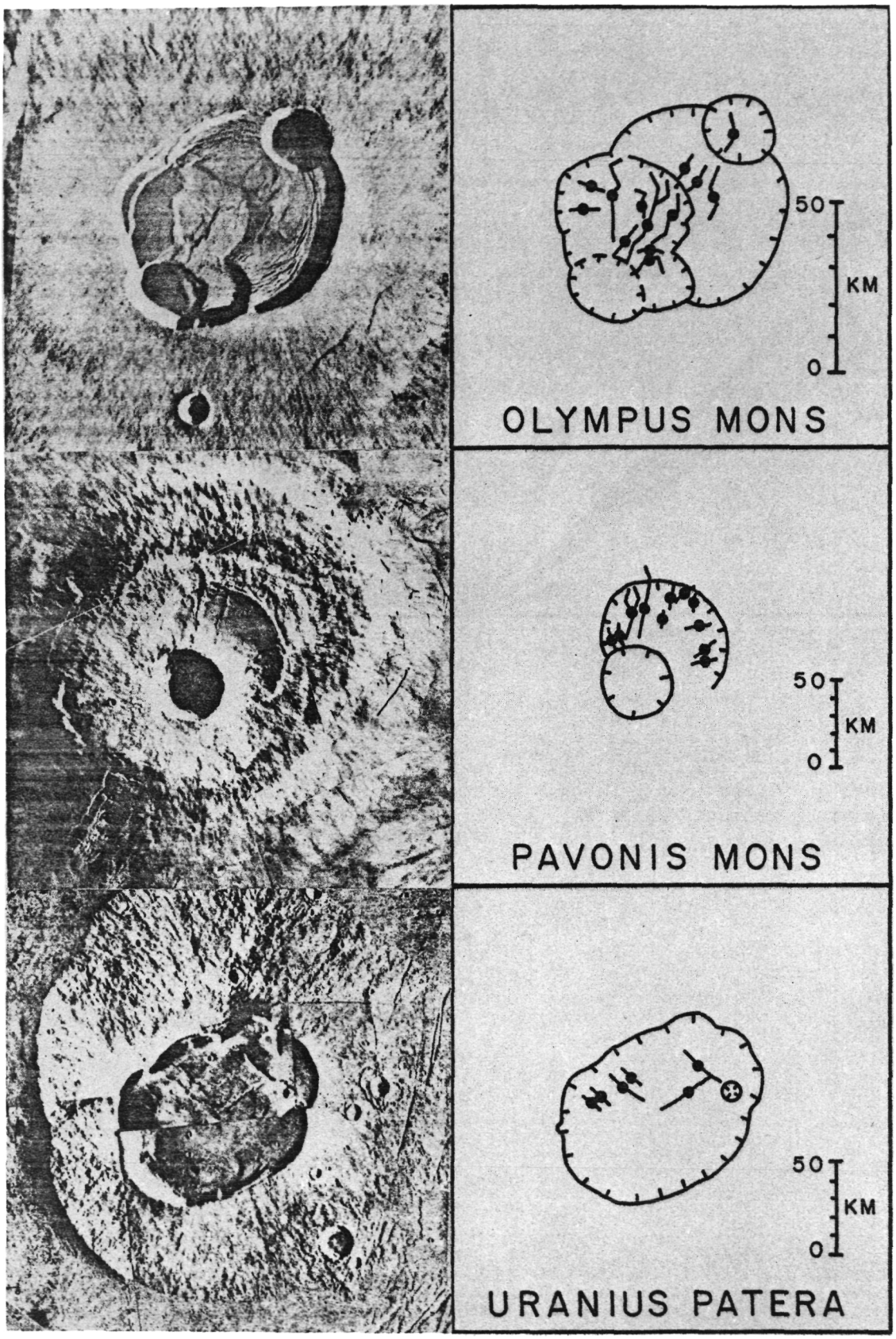
The summit caldera of Pavonis Mons (0°, 113°) is simple, consisting of two main craters. The underlying one (approximately 70 km diameter) displays a system of ridges which are approximately radial to the younger one (Fig.

28b). The floor of the larger circular structure does not appear to have subsided as far below the rim as the Olympus Mons caldera. The summit of Pavonis Mons is approximately 17 km above the surrounding plains; the base of the shield is about 400 km across.

The third edifice, Uranius Patera (27°, 93°) is of a different form from the two montes. A patera (Latin for saucer) is lower and less steep than a mons. The caldera of Uranius Patera (100 km) is much larger in relation to the size of the entire structure (430 km) than the montes discussed above. Only a few ridges are present in the caldera; these are located in the northeast and northwest sections of the caldera floor (Fig. 28c). The summit of Uranius Patera is only about 1 km above its base.

Because the volcano summits are so high above the surrounding plains, ridges in the calderas might not be expected to display evidence of regional or global stress regimes; rather, features within the caldera are likely to be a result of the volcano growth and localized activity within the crater. Therefore, the ridges within the three calderas have been plotted separately (Fig. 29). The strong northwest trend is entirely due to the ridges within Uranius Patera (compare with sketch map of Fig. 28c). The north-northeast trend is caused by the longest ridges in Olympus and Pavonis Montes. Apart from these strong trends, the distribution of ridge orientations is more random than other ridge associations seen on Mars (e.g. ridges in craters and basins).

Figure 28. Ridges in calderas of volcanic constructs on Mars. Sketch maps show caldera rims and location of ridges. North is toward the top in each example. (a) The complex summit caldera of Olympus Mons. Several coalescing crater forms contain ridges. (b) Pavonis Mons, showing the major portion of the volcano's flanks as well as the summit caldera. (c) Uranius Patera; although the caldera is larger than (a) and (b), it contains fewer ridges.


50
KM
0
OLYMPUS MONS
50
KM
0
PAVONIS MONS
50
KM
0
URANIUS PATERA

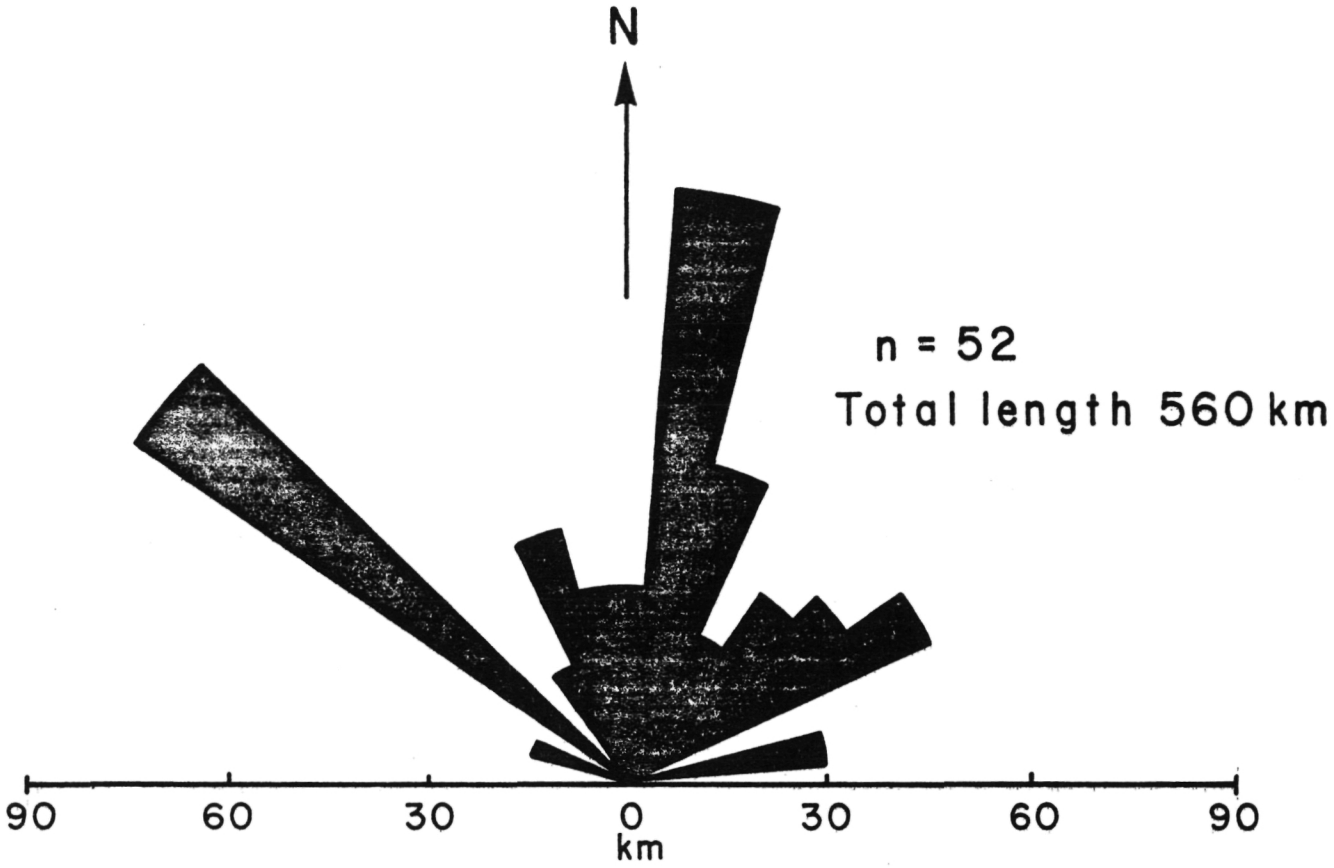


Figure 29. Rose diagram showing orientations of ridges in Olympus Mons, Pavonis Mons, and Uranius Patera, three volcanic constructs on Mars.

Ridge-Rings

The occurrence of ridges in ring structures contrasts with the linear style of most mare-type ridges on Mars. Ridges which form circular rings are here informally termed ridge-rings. These include entire circles and partial arcs; they do not include polygonal arrangements which can be broken down into linear segments.

Ninety-nine ridge-rings were identified on Mars, all between latitude -65° and 30°. (Fig. 30). Almost all of them are in small smooth plains units within the cratered uplands. The rest are on more extensive plains. They range from 10 to 70 km in diameter, and can be divided into several types based on morphology and associations.

One type consists of an incomplete ridge-ring that follows the trace of a crater rim which has been partially buried or destroyed (Fig. 31). The remaining parts of the crater rims are either continuous or have been degraded into numerous distinct knobs or peaks. Examples of this type of ridge-ring seen on Mars are between 40 and 70 km in diameter. The ridges of these rings almost everywhere display the arch/ridge morphology described for lunar ridges by Strom (1972). In plan view, the ridge segments generally lie slightly outside a circle drawn through the remaining rim sections. As is true of all the ring types, the ridge-rings associated with crater rims are found in volcanic plains as well as undifferentiated plains units in cratered terrain.

Ridge-rings interrupted by only scattered protruding peaks are transitional between circular structures composed of both rim and ridge segments and rings composed only of ridges. These features form the second major type of ridge-rings on Mars. Rings of ridges, either complete or segmented, range in diameter from 10 to 40 km. They are common in areas which have numerous

other ridges, and often interrupt otherwise linear ridge systems (Fig. 31). Morphologically, the ridges in ring structures usually consist of an arch with a crenulated ridge on top meandering from side to side of the arch. Sometimes the crenulated ridge on top is absent and the ring is formed by steep-sided arches.

A third ridge-ring type is an association of rounded portions of ridge patterns with otherwise polygonal trends. These rings are circular or sub-circular in plan view, some with one or more flattened sides which parallel the trend of other polygonal ridge forms in the same area. This pattern occurs primarily in plains units of limited extent bounded by cratered terrain.

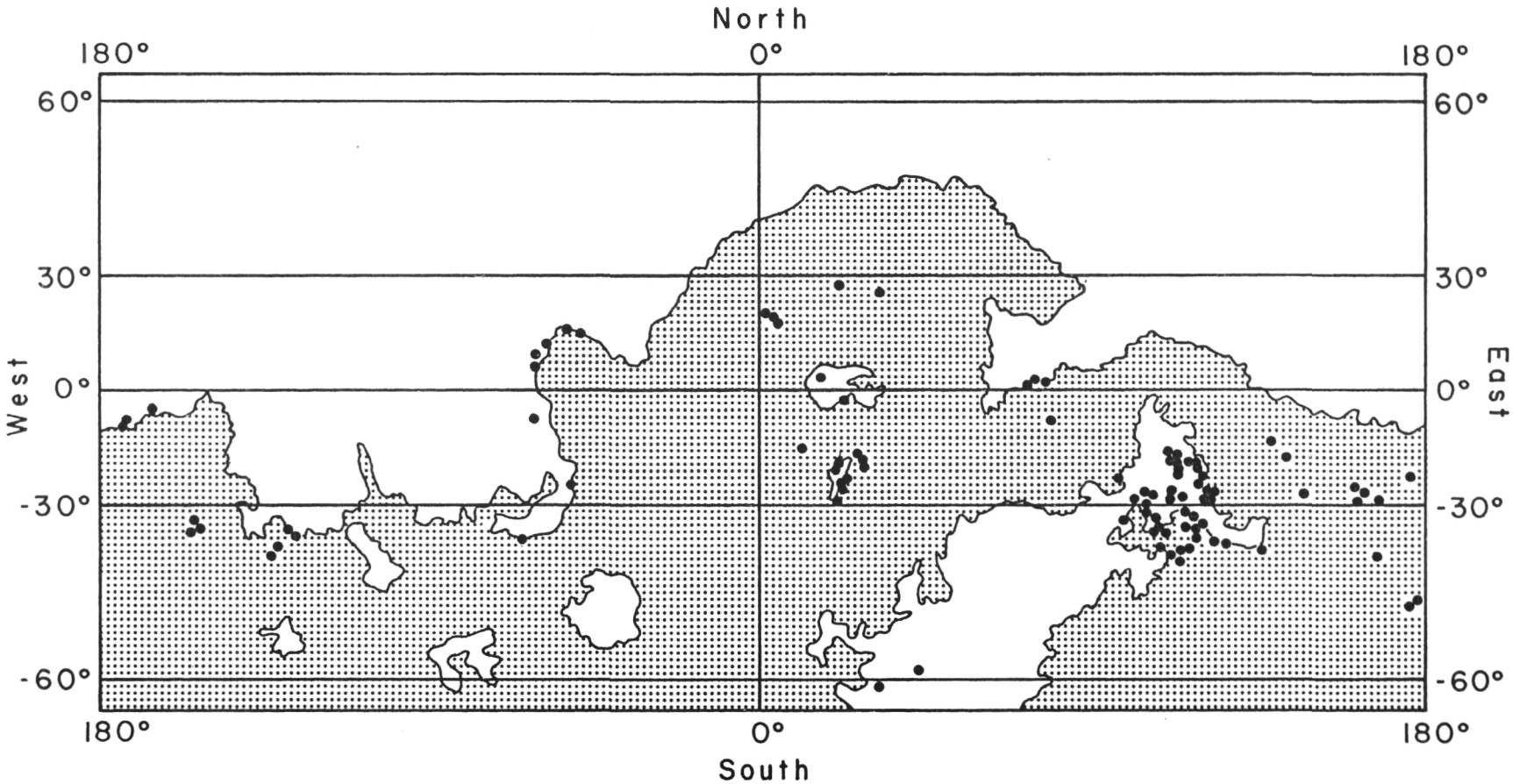


Figure 30. Distribution of ridge-rings (dark circles) on Mars. Shaded area is old cratered, hilly and plateau terrain; open area marks relatively smooth, low plains regions.

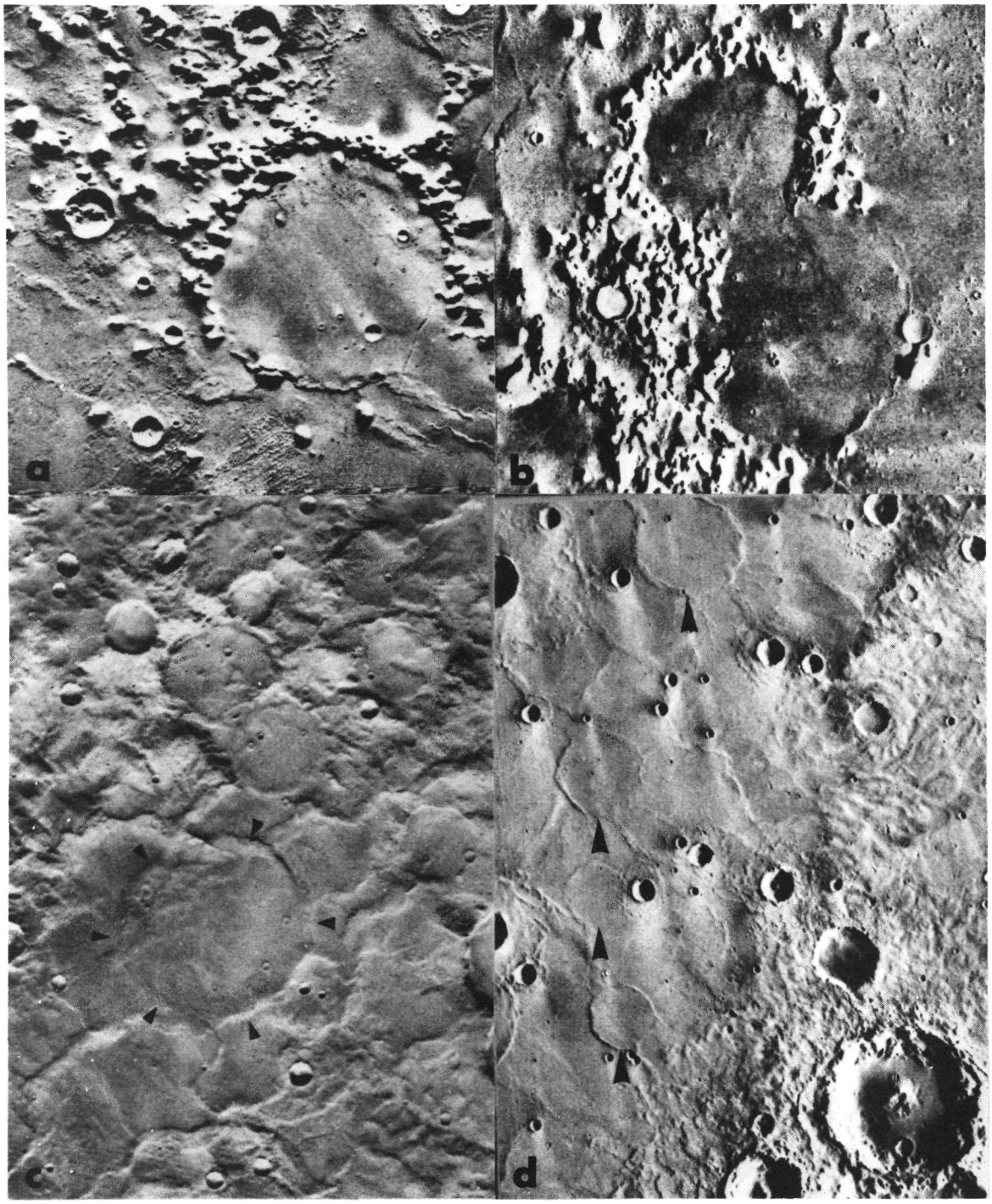


Figure 31. Examples of ridge-rings on Mars.
(a) and (b) Ridges following outline of a crater rim, a portion of which has been buried or destroyed. Both craters are 50 km in diameter.
(c) 60-km ridge-ring and other ridges associated with degraded crater remnants (Viking Orbiter 1 frame 655A71).
(d) Ridge-rings in relatively smooth intercrater plains units. Straight ridge segments are found in association with the ridge-rings. (Viking Orbiter 1 frame 629A07).

DISCUSSION

The presence of a global distribution of a geologic feature on any planet is an indicator of the evolution of the planetary body and the tectonic processes that shape its surface. The ridges on Mars are one such class of feature. Their global distribution and regional patterns suggest that their morphologic expression is an important aspect of Martian geomorphology.

The planetary hemispheric dichotomy of cratered/uncratered terrain is reflected in the numbers of ridges present. There are 323 ridges (7% of the ridges on Mars) in MC's-1 through 7 (all the planet north of 30°) and 824 ridges (19% of all ridges) in MC's-24 through 30 (south of -30°). Thus whatever process shaped the northern uncratered plains has also affected ridge distribution, either by destroying pre-existing ridges or by creating a terrain in which ridges are not formed.

The ridges which are present north of 30° generally occur in the vicinity of, or adjacent to, other topographic relief. This means that most of the ridges are close to the cratered/uncratered terrain boundary with very few ridges farther north in the relatively featureless Vastitas Borealis. In detail, the cratered/uncratered terrain boundary is commonly expressed as a scarp, with dissected plateaus to the south and lower plains to the north. Ridges on the plateaus are truncated by these scarps; the ridges were developed in these older plateau units which were subsequently eroded by the process responsible for the development of the Vastitas Borealis.

The association of ridges with other topographic features is seen elsewhere on the planet. The relationships of ridges with knobs and crater rims in Amazonis Planitia (western MC-8 and eastern MC-15) and the

concentration of ridges in Chryse Planitia nearer to the edge of the plains have been described above. In addition the occurrence of ridges on generally older units and their relative scarcity on the younger units is seen, for example, in MC-6 where all the ridges are on the older "variegated" plains and none are on the younger plains units. In cases such as this where there is a correlation between terrain units and ridge distribution, the ridges gradually die out near the contact; no sharp breaks were observed. Even where flows from volcanoes can be seen embaying fractured, fretted and grooved terrain producing distinct contacts, the ridges are not truncated at the edge of an obvious flow or at an otherwise definable contact between two plains units.

Therefore, in almost all cases ridges are developed on older plains units. Although in many cases these are thinner than some younger units, there are still numerous ridges on many plateau areas which are probably composed of thick, flood-type lava units. Thus photogeologic evidence presented here supports the conclusion that ridges were formed by a process which had its major effect prior to the formation of the northern hemisphere plains and the emplacement of the youngest lavas of the Tharsis volcanoes.

This conclusion is supported by a study of crater populations of various ridged plains regions of Mars which have crater densities similar to Lunae Planum, implying similar ages (Gregory et al., 1979). The Lunae Planum surface has been estimated to be 3.9 billion years (Neukum and Wise, 1976), making it and the other plains of similar age among the oldest plains units on Mars. The similarity of plains ages also implies a period of enhanced ridge formation early in the planet's history.

The predominance of north and northwest trending ridges on Mars is well documented (see Appendix II). Dominant north and northwest trends are present in 25 out of 30 MC quadrangles. Global scale lineament patterns

(often referred to as "grid systems") have been proposed for most of the terrestrial planets. Northwest and northeast lineaments are the most predominant on the Moon (Fielder, 1963; Strom, 1964) and Mars (Binder and McCarthy, 1972; Wilson et al., 1973; Harp, 1976) although Mercury has an additional significant north trend (Strom et al., 1975; Dzurisin, 1978). Planetwide lineament systems such as this are generally thought to be caused by crustal stresses produced by changes in the planet's rotational equilibrium figure. Because of interactions of a spinning planet with two stationary poles, north-south and east-west lineaments would represent tensional and compressional features with northwest-southeast and northeast-southwest lineaments representing the complementary shear directions. I propose that ridges are compressional tectonic features which reflect global and regional stresses. The existence of potential ridge-forming stresses is explored in the following paragraphs.

In a rigorous study of the effects of flattening and polar axis shifts on stresses in the Earth's crust, Vening-Meinesz (1974) described shear patterns on Earth as well as those expected as a result of various other changes in planetary rotational figures. However, the predictions by Vening-Meinesz which are relevant to the present study are incorrect due to his use of an obsolete rupture criterion (Melosh, 1977). In a series of studies with applications to the planet Mercury, Melosh (1977), Melosh and Dzurisin (1978) and Pechmann and Melosh (1979) examined the effects of tidal despinning on a planet with a thin crust (less than 1/20 the planet's radius) and predicted the presence of two distinct fault provinces: an equatorial belt of dominantly strike-slip faulting and a polar province of mainly normal faulting. With a thicker lithospheric shell or some planetary contraction coincident with loss of angular momentum, the model predicts an equatorial belt of thrust faulting and moving of the strike-slip fault province boundary to

high latitudes.

Although Melosh and Dzurisin (1978) presume that Mars has not been significantly despun, there is evidence for planetary contraction in models of thermal evolution of the planet and core formation (Thurber and Toksoz, 1978; Arvidson et al., 1980). In addition, several aspects of the fracture pattern predicted by Melosh (1977) are present in the Martian crust. In an analysis of fracture systems of Mars on approximately the same scale as this study, Harp (1976) mapped conjugate sets of shear fractures throughout most of the cratered terrain oriented N40°-50°W and N40°-50°E. Equatorial (east-west) compression (σ_3 horizontal) invoked to account for this fracture pattern could also account for complementary compressional ridges normal to σ_3 (parallel to σ_1), in other words dominantly north trending ridges. This pattern of fracture/ridge associations is documented here for Mars.

Intersections of ridges with fossae on Mars are of several types; either ridges are truncated at the fracture edges, continuing the same trend on the other side or offset, or in a few instances they may be traced across the fossa floor. This is evidence that the development of the planetary tectonic fabric as outlined above was taking place over a finite span of time, that the complementary stresses are consistent, and that a mechanism does exist for the development of such a pattern on a planet with a suitable lithosphere.

The major aspects of the pattern of ridges and fractures on Mars on a global scale are outlined above. This pattern is supported by the mapping in 16 quadrangles. Variations in these patterns with latitude is an important factor for both the Vening-Meinesz (1974) and Melosh (1977) models. Several fracture analyses have supported the pattern that Vening-Meinesz (1947) predicted would result from despinning. Melosh (1977) predicts the appearance of normal faulting at upper latitudes as a result of despinning, and a

concurrent decrease in features of compressional origin. The relatively low frequency of ridges at higher latitudes certainly supports this. Unfortunately, we only have one polar hemisphere to consider because of the relative lack of surface features on the northern hemisphere uncratered terrain.

Not all ridges on Mars conform to a planetwide pattern; regional and local tectonics have also had an effect on ridge distribution. The major expression of a regional feature, and indeed probably the most important indicator of the tectonic evolution of Mars (Wise et al., 1979) is the Tharsis uplift, the largest volcanic field on the planet.

The Tharsis province, centered at 0°N, 110°W (MC-9), is a plateaulike feature approximately 4000 km in diameter, averaging 8-10 km above the planet's zero datum. The domelike shape (often called the Tharsis uplift or bulge) is topped by four of the largest volcanoes on Mars. Morphologically, the relative contributions of uplift or doming and the formation of the shield volcanoes to the province are unclear.

Gravity data indicate that while most of Mars is apparently in isostatic equilibrium, there is a large free-air anomaly implying a mass excess over Tharsis (Sjogren, 1979). In a detailed analysis of models which could account for the support of such a mass excess, Phillips and Lambeck (1980) have calculated the magnitude and direction of horizontal tensile and compressive (principal) deviatoric stresses at the surface of Mars. In the areas to the east of the Tharsis uplift the tensile fractures and wrinkle ridges have orientations which are approximately consistent with these modeled stress trajectories (Arvidson et al., 1980; Eppink and Saunders, 1980). There is a prominent fracture system radial to Tharsis. The main component of this fracture system is Valles Marineris, the largest canyon system on Mars. The canyons separate Sinai and Solis Plana on the south

(MC-18) from Lunae Planum on the north (MC-10). These plains represent the same surface unit which was originally continuous for over 70° of latitude, and is cross-cut by Valles Marineris and, further north, Kasei Vallis. The ridges in these areas show orientations orthogonal to the modeled compressive stress trajectories of Phillips and Lambeck (1980).

In a related study, Saunders and Gregory (1980) interpreted the correlation of compressional stresses related to the Tharsis load with the existence of parallel ridges as being due to the long-term viscous response of crustal rocks. By measuring ridge spacing for several of the main areas of parallel ridges and estimating plains thickness by crater rim heights and diameters, they found that the ratio of ridge spacing to plains thickness is approximately constant over widely separated plains regions and a range of ridge spacings. Using a theory that this ratio is related to the viscosity of the ridge and underlying layers (Biot, 1961) the viscosity ratio (plains to substrate) must also be constant over different plains units. This finding confirms the hypothesis that the ridge spacing in areas near Tharsis is related to the dominant wavelengths of folding of surface materials in response to the Tharsis load.

In general, within an area extending approximately 2500-3000 km from the center of the Tharsis uplift, there is a close relationship of structural features to those predicted by a model of failure due to Tharsis loading. However, the correspondence is not complete even for the case of the more prominent fracture system, and the correlation diminishes with increasing distance from the uplift. Thus crustal loading by the Tharsis bulge overprints the global pattern in areas close to Tharsis, but other stress regimes are obviously present on the planet as well, even in areas affected by the Tharsis uplift.

A compressional origin for ridges is also consistent with the polygonal

ridge patterns seen in several small plains areas. The predominant northwest trends in these areas are complicated by orthogonal and polygonal patterns. It is proposed that these are the result of interactions between the material filling a slightly depressed region, the confining higher cratered terrain which surrounds it, and underlying cratered terrain remnants. The interaction between fill and underlying craters produces the polygonal patterns which roughly trace underlying cratered remnants. I suggest that this is the explanation for the complicated ridge systems in the Hesperia Planum area. In the case of lunar mare basins, the impact events have destroyed pre-existing cratered terrain. Hesperia Planum is not a basin but a lower portion of the cratered uplands, possibly depressed as a result of isostatic adjustments to the volcanic load from Tyrrhena Patera. Therefore, the underlying cratered terrain remnants interact with the sinking load to create the polygonal ridge forms so prevalent in the region.

In the calculations of plains thicknesses based on crater rim heights and diameters, Saunders and Gregory (1980) estimate a thickness of .866 km for the Hesperia plains, whereas eastern Solis Planum and Lunae Planum are estimated to be 1.5 km thick. These latter two areas are characterized by parallel ridges. Furthermore, the Lunae and Solis plains thin to the east; estimates of thickness at the eastern edges are 1.05 and .8 respectively (Saunders and Gregory, 1980). Ridges to the east in Solis Planum display an increasingly reticulate or polygonal pattern. Ridges are observed which have been deflected by post-mare or plains craters as well; these surface disturbances have similarly affected the trends of ridges. The many polygonal offsets of predominant global trends are due to the deflection of ridges around subsurface topographic irregularities.

The greater numbers of ridge-rings in plains regions which display

reticulate ridge arrangements are further evidence for this idea. Ridge-rings in the lunar maria have been interpreted as pre-mare crater rims which have been draped by mare lavas (Schultz, 1976), and a similar mechanism is proposed here. In the case of volcanic fill burying crater rims the expression of ridge-rings could be caused by differential settling due to cooling and degassing of the material.

This brings us to the problem of ridges in craters and basins on Mars. Whereas on the Moon ridges are probably formed by compression due to sinking of the mare load confined by the basin structure (Maxwell, 1978), ridges in Martian basins generally reflect regional north and northwest trends instead of basin concentric and radial structure. It therefore must be possible for the basin load to "feel" the regionally imposed stresses.

An estimate of the strain involved can be made as follows: although it is difficult to measure ridge heights accurately due to the lack of sufficient low-sun angle images, measurements may be estimated from a few suitable examples and also from comparable lunar mare ridges for which detailed topographic data are available. Using these height estimates and width measurements the amount of shortening across a particular surface can be approximated. In Flaugergues (Fig. 27c), for example, an east-west line through the basin center crosses 13 ridges, with a resulting estimation of 0.6% shortening. Interactions between a regional stress system and the basin fill can therefore easily account for these trends.

Material properties are another important consideration. It is hypothesized here that a coherent material similar to the lunar mare basalt is essential for formation of wrinkle ridge morphology. On Mars, all occurrences of ridges are consistent with a hypothesized substrate of lava-like material. The ridges in several of the larger basins, notably Flaugergues, Schiaparelli,

and ISM-Wa, are only present in portions of the basins with smooth floor material and are absent in the rough or hummocky terrain units. In many examples on Mars the material is higher in albedo than the lunar mare basaltic units, and in fact resembles the lunar light plains more than the maria. On windswept Mars, however, this can be due to a thin covering of eolian or some other sedimentary material.

Ridges in calderas represent another variation. This is an obvious volcanic situation with a known lava substrate. There are two ways in which the ridges within the volcanic calderas may be formed. One is by sinking of a portion of the caldera floor material after cooling of the crustal layer has taken place. The other is by updoming of a portion of the central caldera floor, fracturing of the cooled crust and subsequent extrusion of molten material through the fractures. Because of the proposed compressional nature of other ridges in this study, the first hypothesis is preferred. Ridges in Pavonis Mons are radial to a point, which could be suggestive of either hypothesis, however, the lower crater of Olympus Mons consists of concentric fractures outlining the rim and long ridge segments toward the center. This suggests sinking of the caldera center after the crust had already cooled sufficiently so that no lava was extruded through the fractures, thus compressing the more central part of the caldera floor.

This study provides a global scale framework for understanding one type of geologic feature on Mars. Details of particular ridges and ridge systems are no doubt complicated by other geologic processes which operate on the planet, some of which are still beyond our understanding. The lack of terrestrial analogs for mare-type ridges contrasted with the abundance of such features on Mars, the Moon, and Mercury creates an intriguing problem in planetary geology. The geologist who first has a ridge in her field area will be lucky indeed.

CONCLUSIONS

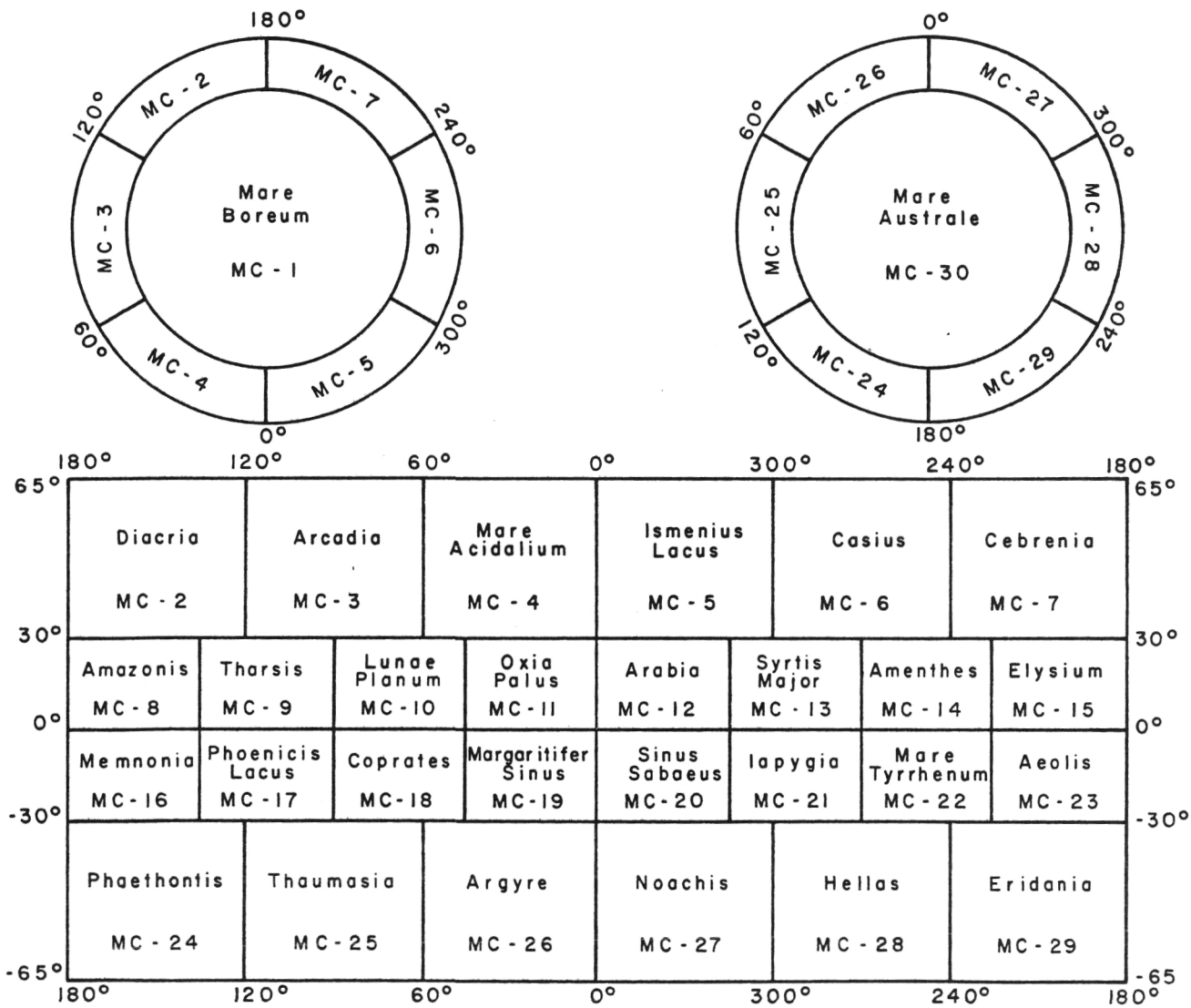
This global study of mare-type ridges on Mars has shown that:

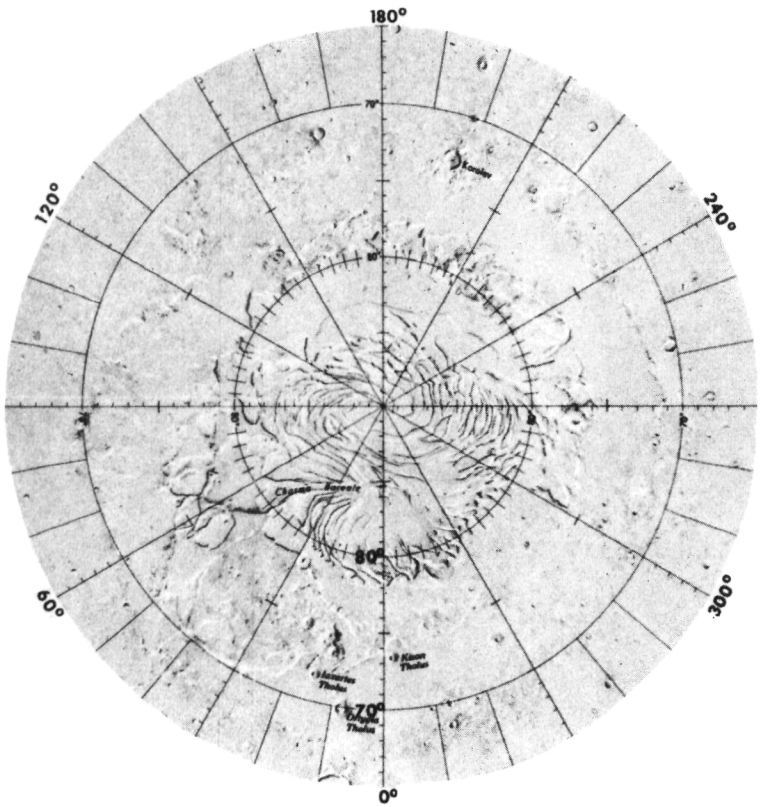
1. Ridges are preferentially developed in older, thinner plains and plateau units. In areas of younger, thicker fill, especially in volcanic flows, older ridges may have been buried, or they were not developed.
2. In areas where the fill is thin enough, the effect of irregular underlying topography is seen at the surface in polygonal or reticulate ridge patterns.
3. Ridges are present in some basins and craters which have smooth floors. Several large basins have two distinct floor materials, a smooth dark unit, and a more hummocky, rougher unit. Ridges are developed exclusively on the smooth areas. This material is probably volcanic fill.
4. Ridges are present in three major ridged plains areas, Hesperia Planum, Sinai and Solis Plana, and Lunae Planum, and numerous smaller plains areas. Ridges in plains are either long, linear or curvilinear, and parallel, or they display irregular or polygonal trends.
5. Ridges are also present in several volcanic calderas, and in the form of partial or complete rings.
6. Measuring planetwide ridge orientations in the ridged plains shows a dominant north trend with strong northwest and northeast trends. These trends are orthogonal to an extensive system of east-northeast and west-northwest trending fractures.
7. Ridges are interpreted as compressional tectonic features which reflect global and regional stresses. Global ridge trends are related to changes in the planet's rotational equilibrium figure. The ridges are concurrent

with a planetwide fracture system which formed in response to the same stresses. Regional ridge patterns are modified by local tectonic regimes (e.g. in the area near Tharsis), fill thickness, and underlying topography, and local confining topography (e.g. within a crater, basin, or small lowland area).

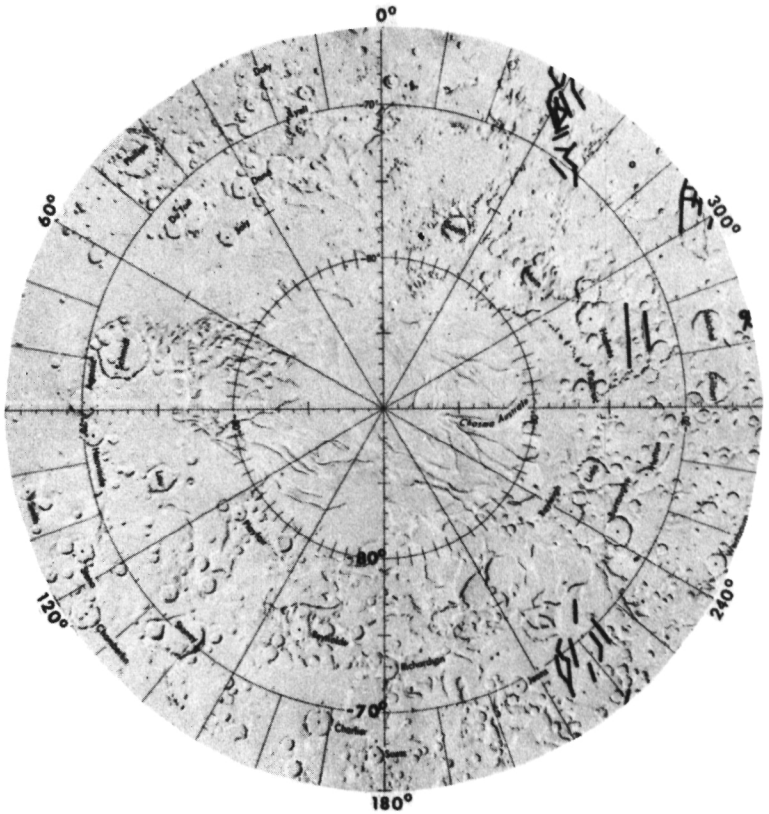
APPENDIX I

Maps for each Martian quadrangle (MC area) showing ridges mapped in this study. U.S. Geological Survey shaded relief maps (original scale 1:5,000,000) were used as the base for plotting ridges. A key to MC areas is reproduced below. Ridges are designated by heavy lines.

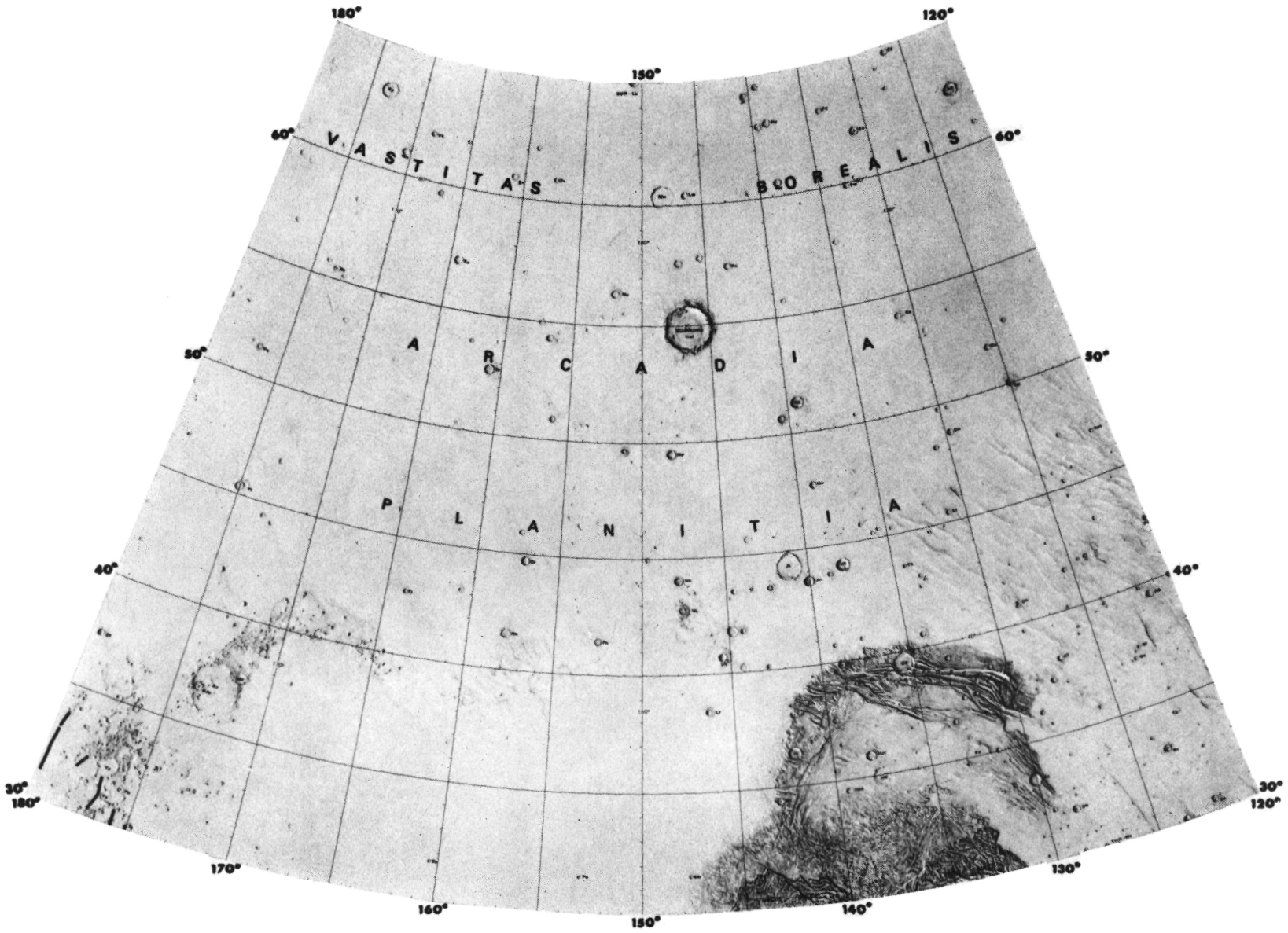




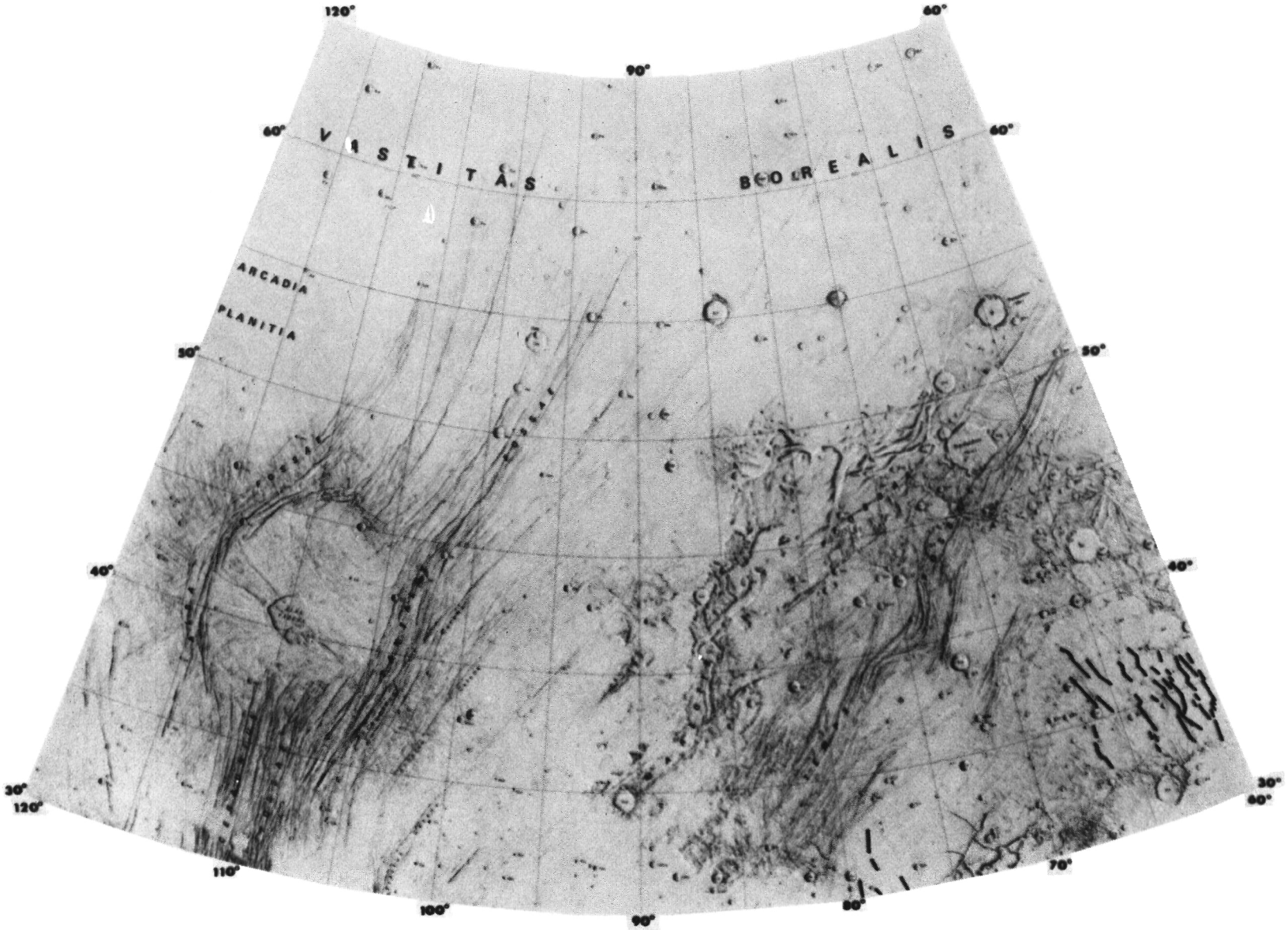
MC·1 MARE BOREUM



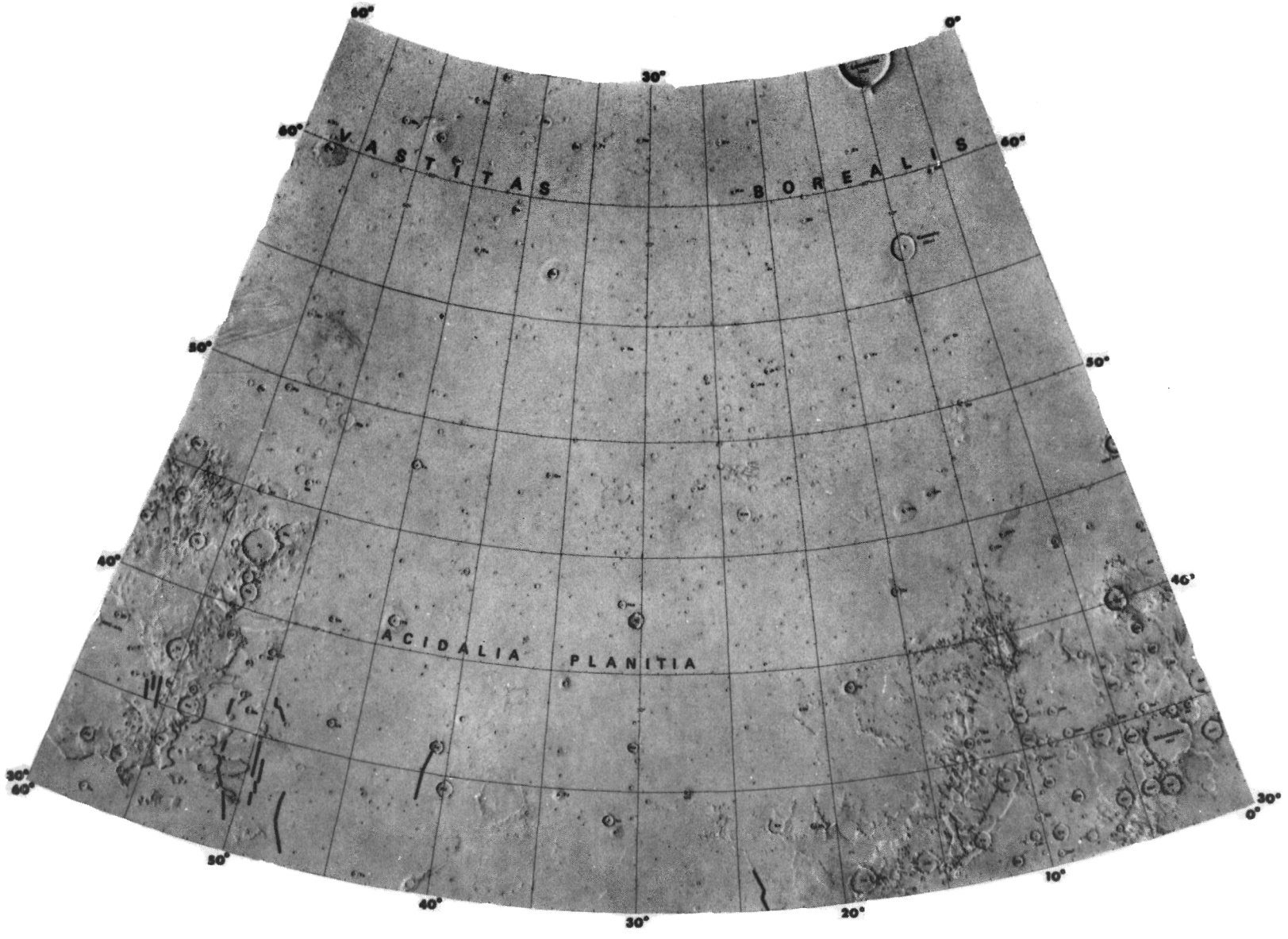
MC·30 MARE AUSTRALE


180°
120°
150°
60°
VASTITAS BOREALIS
60°
50°
ARCADIA
50°
PLANITIA
40°
40°
30°
180°
30°
120°
170°
130°
160°
140°
150°

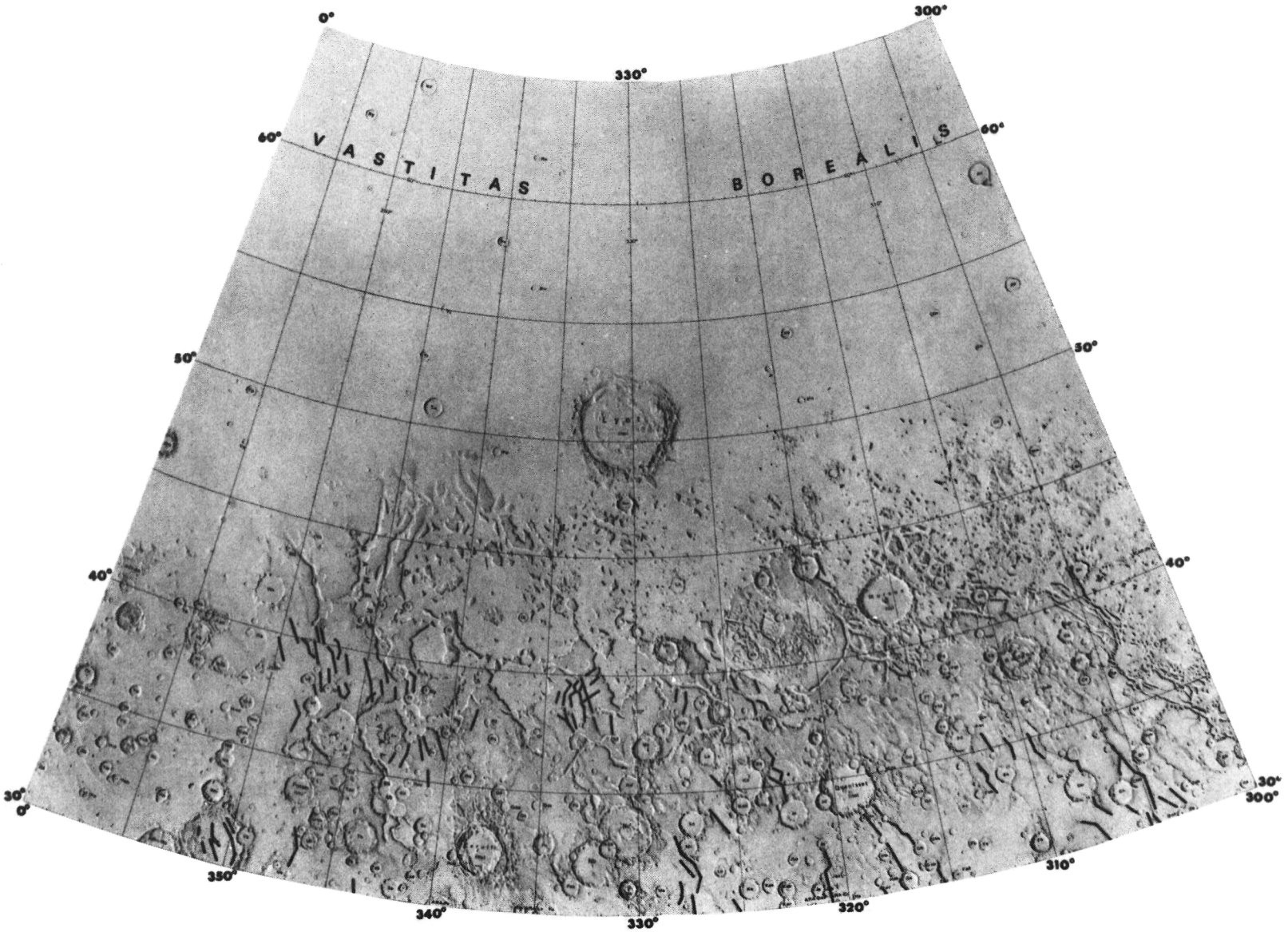
MC-2 DIACRIA


120°
90°
60°
60°
V E S T I T A S
B O R E A L I S
60°
ARCADIA
PLANITIA
50°
50°
40°
40°
30°
120°
30°
60°
110°
70°
100°
80°
90°

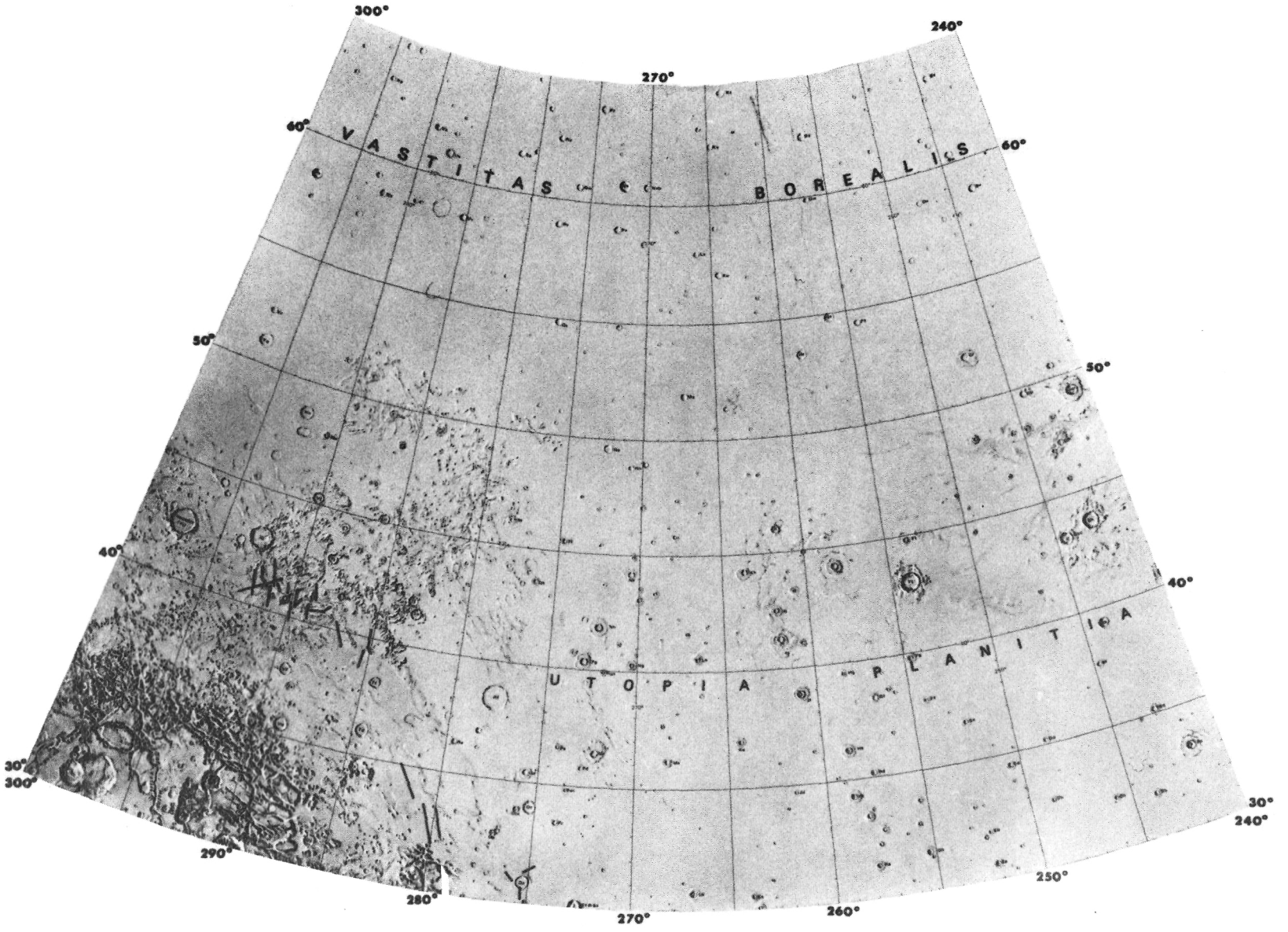
MC-3 ARCADIA



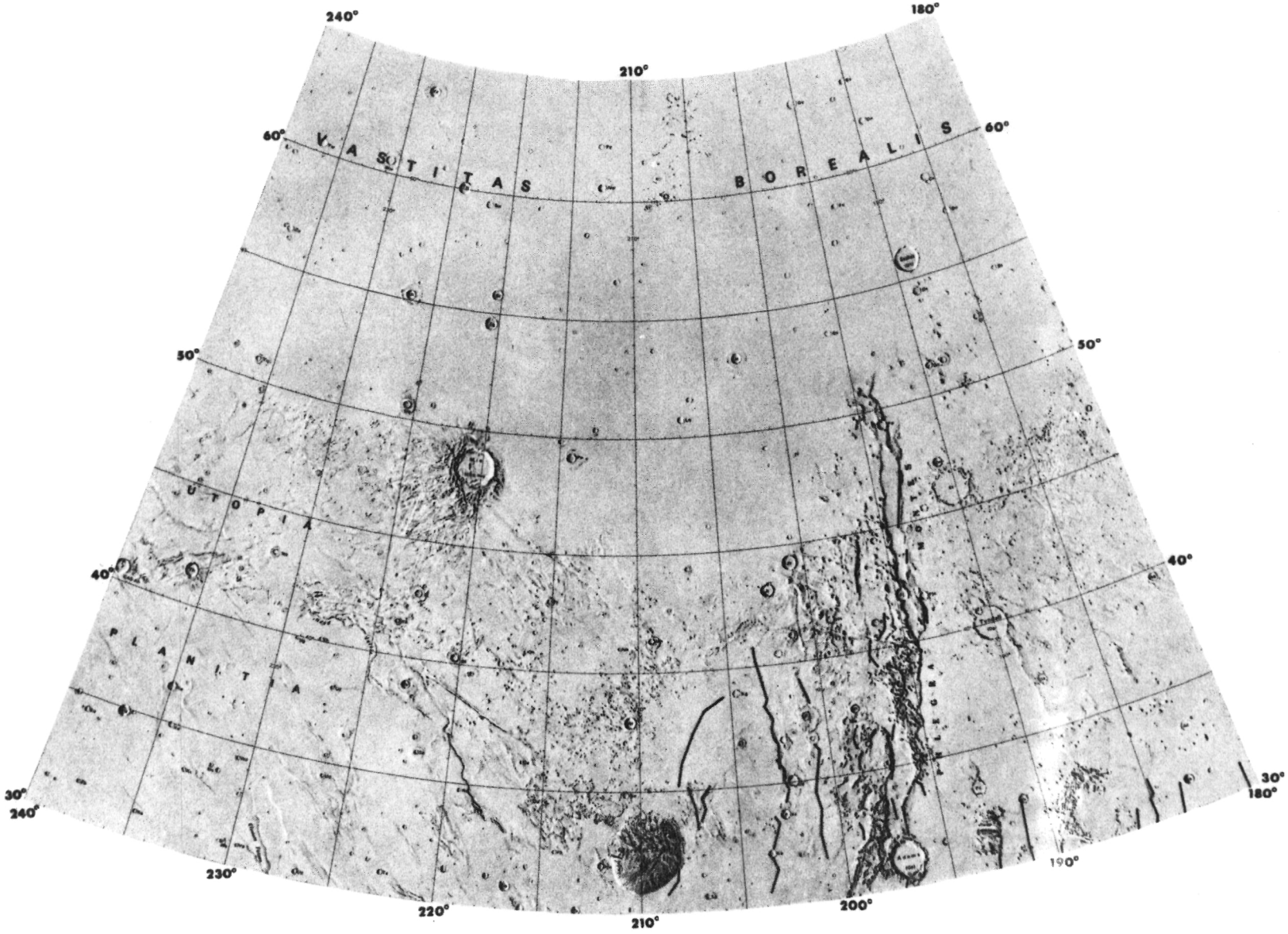
MC-4 MARE ACIDALIUM



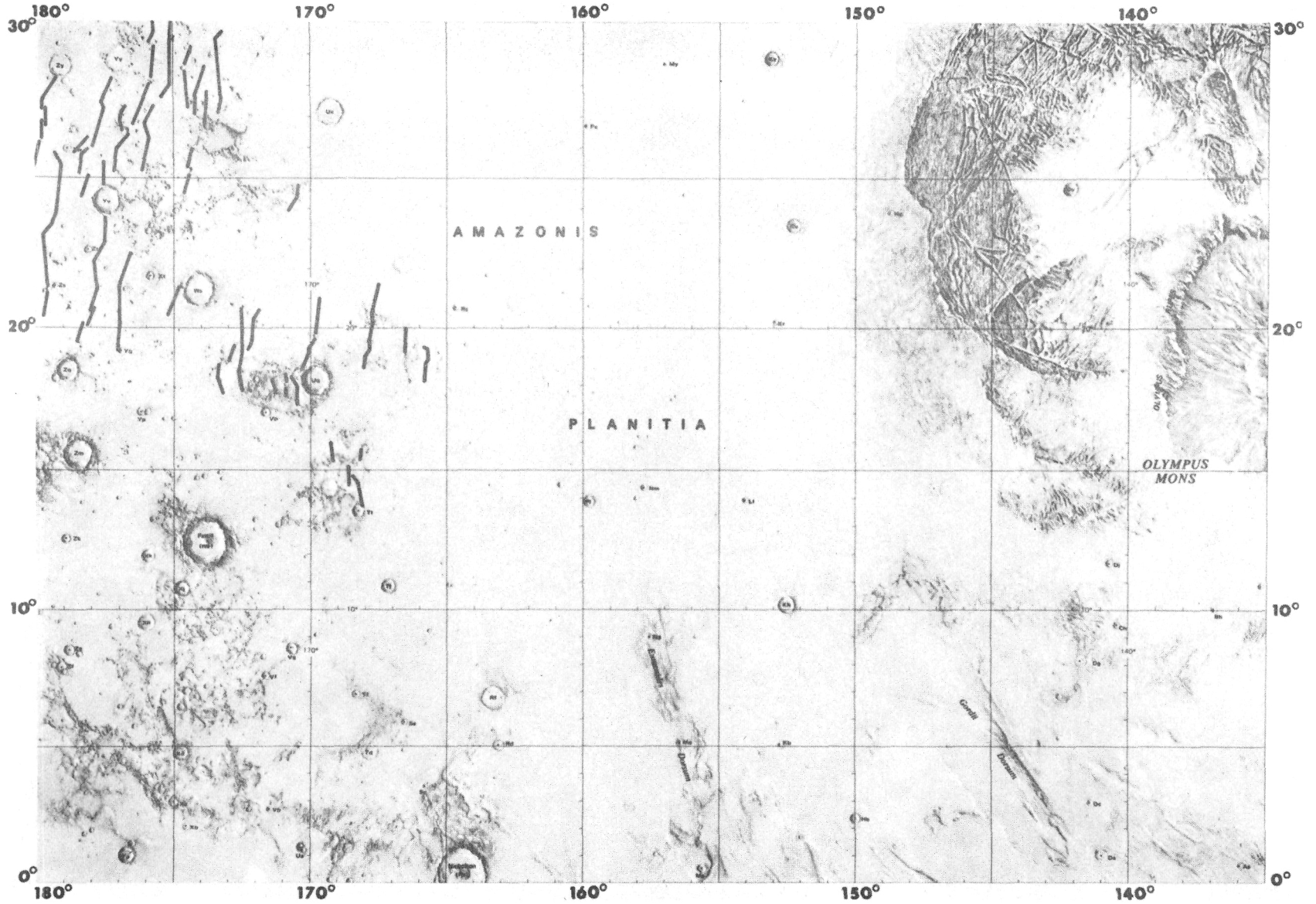
MC-5 ISMENIUS LACUS


300°
240°
270°
60°
VASTITAS BOREALIS
60°
50°
50°
40°
40°
UTOPIA PLANITIA
30°
300°
30°
240°
290°
280°
270°
260°
250°

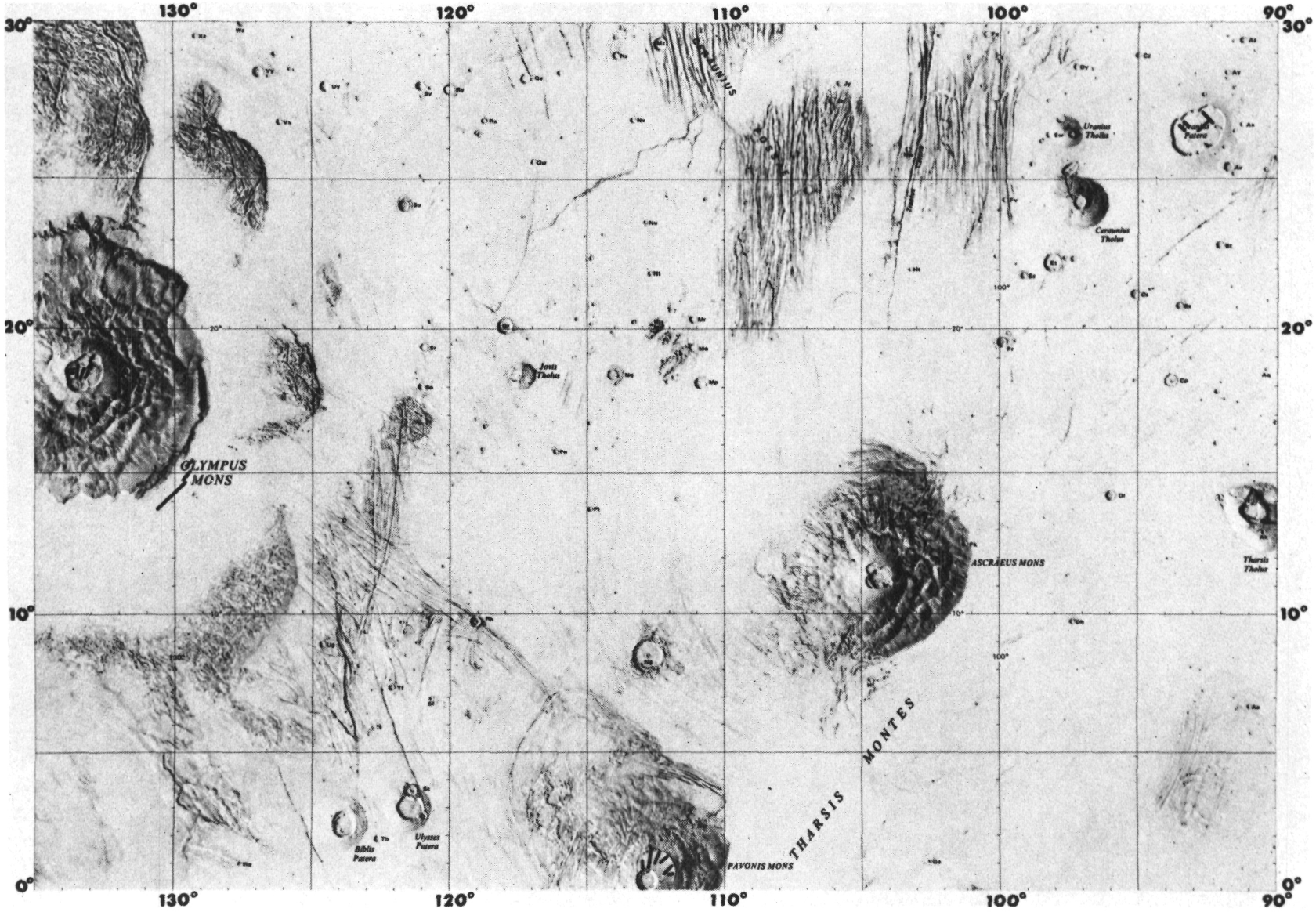
MC-6 CASIUS



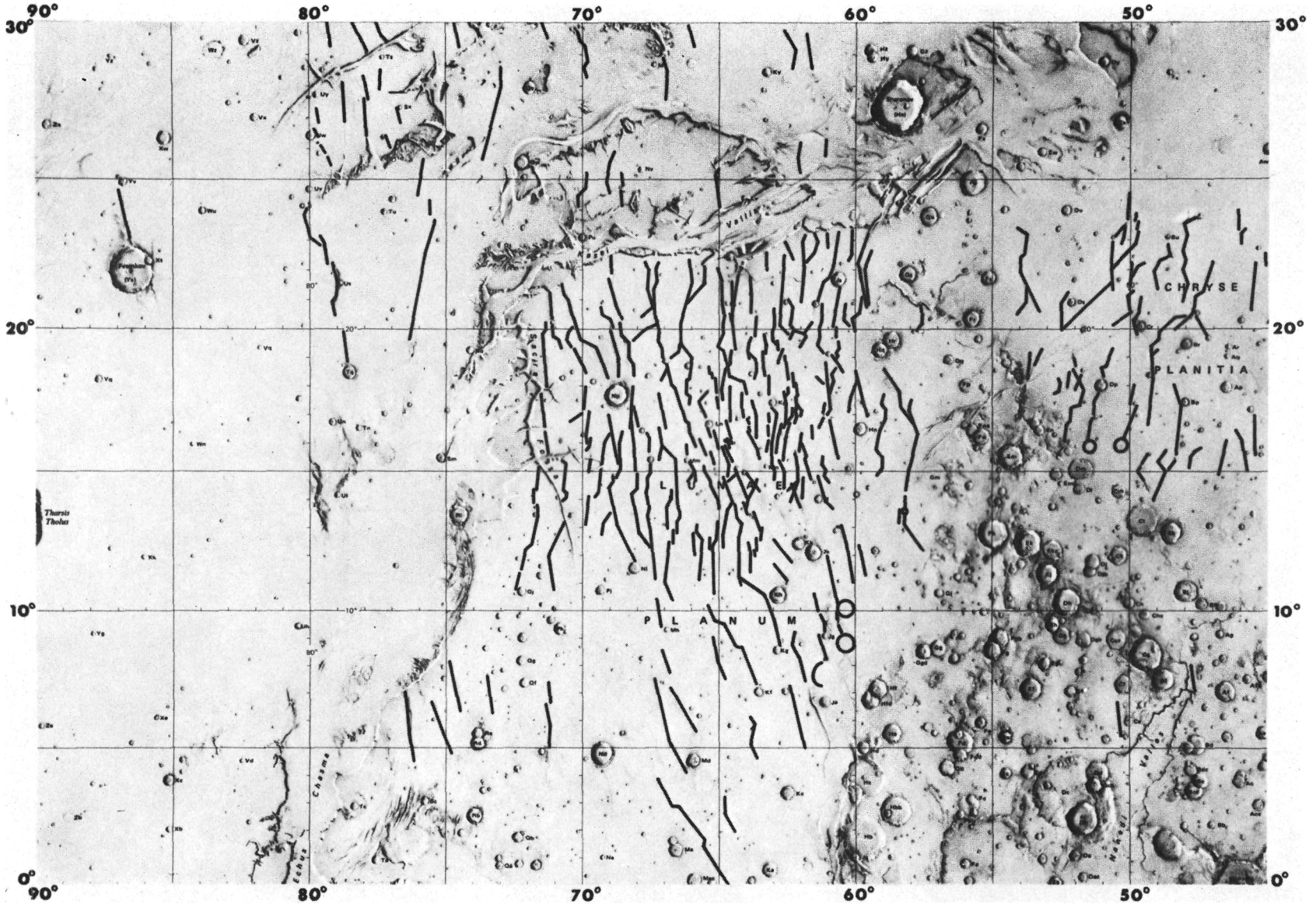
MC-7 CEBRENIA



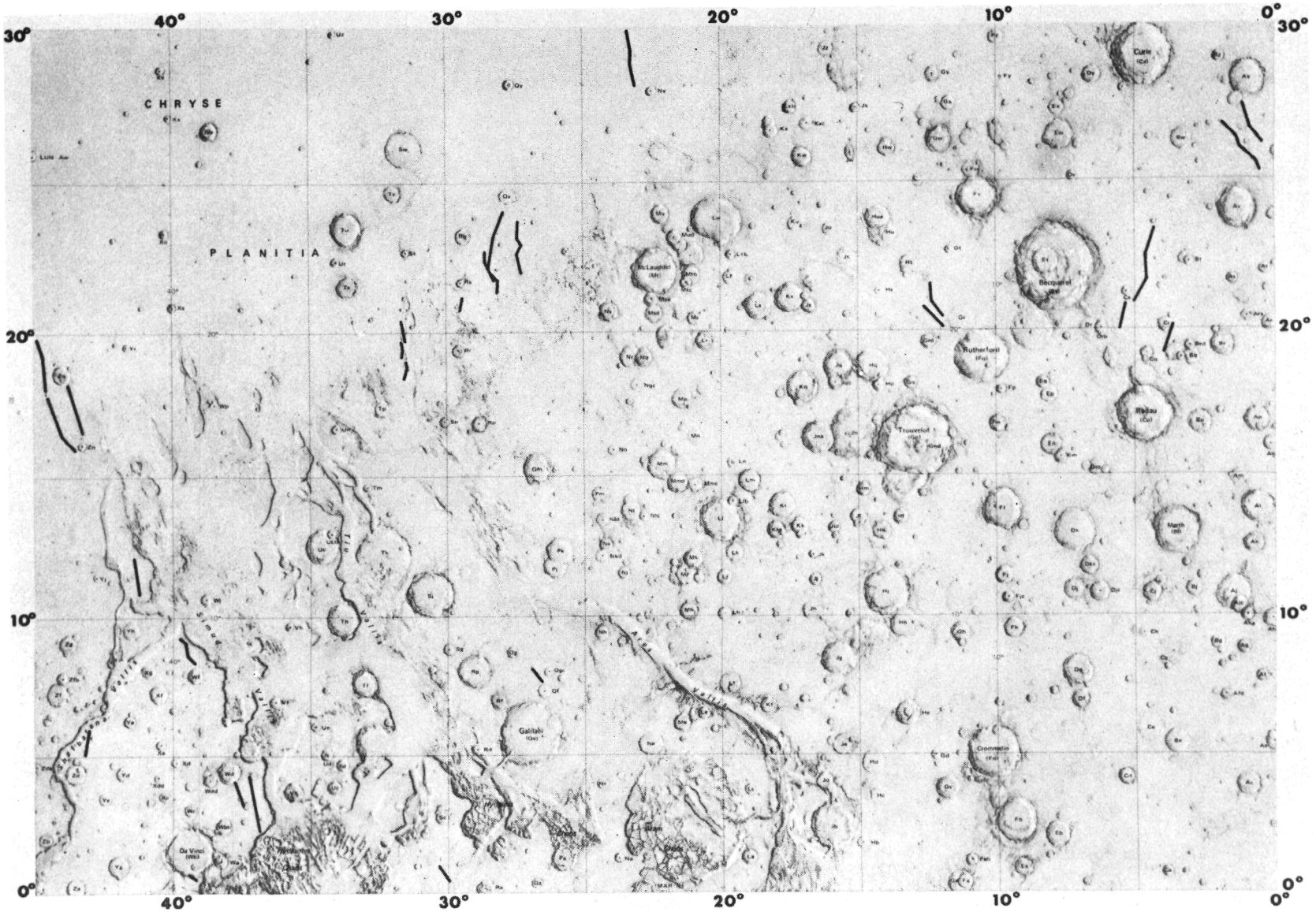
MC-8 AMAZONIS


130°
120°
110°
100°
90°
30°
20°
10°
0°
OLYMPUS MONS
Jovis Tholus
Uranius Tholus
Ceraunius Tholus
Tharsis Tholus
ASCRAEUS MONS
PAVONIS MONS
THARSIS MONTES
Biblis Patera
Ulysses Patera

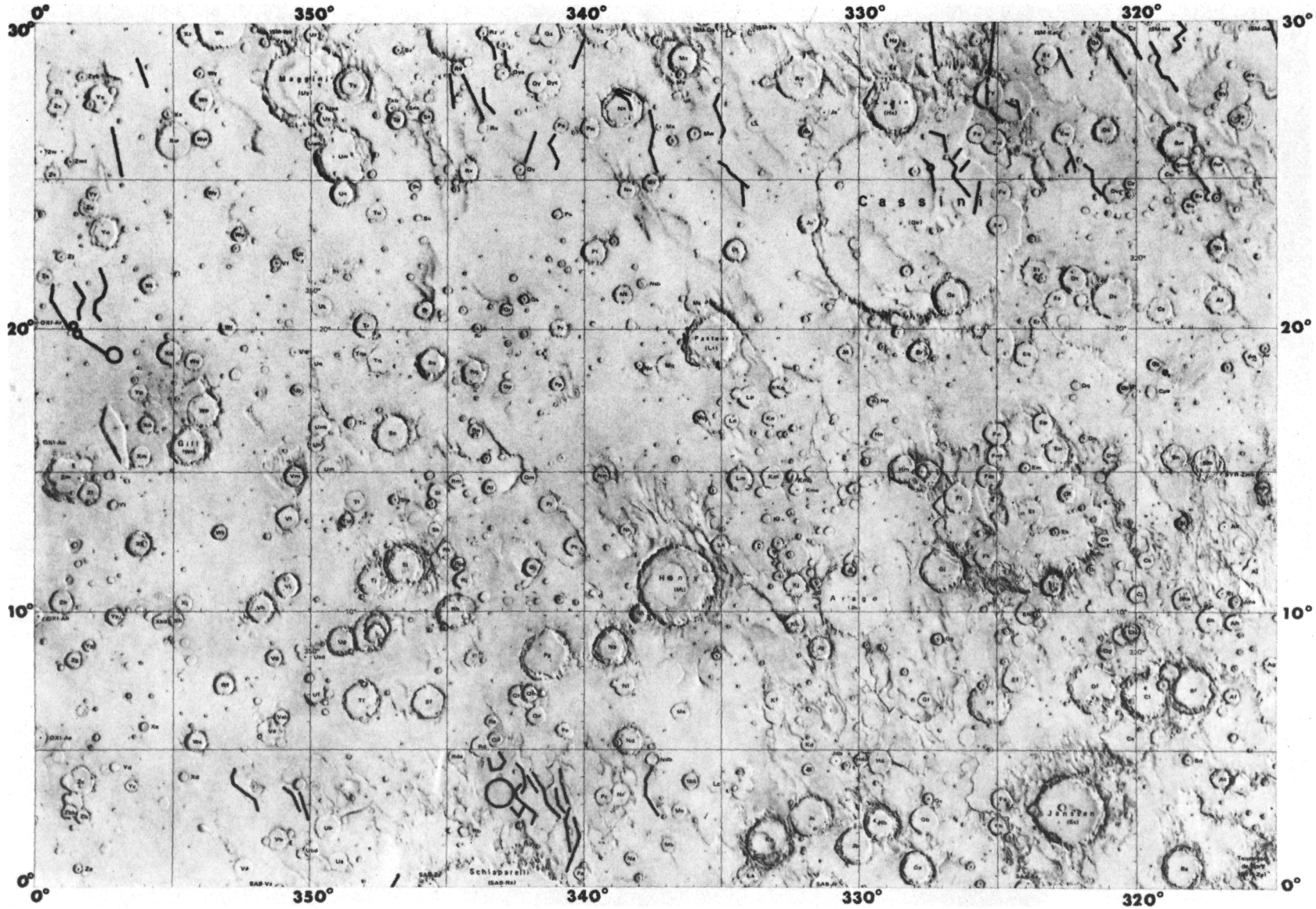
MC-9 THARSIS



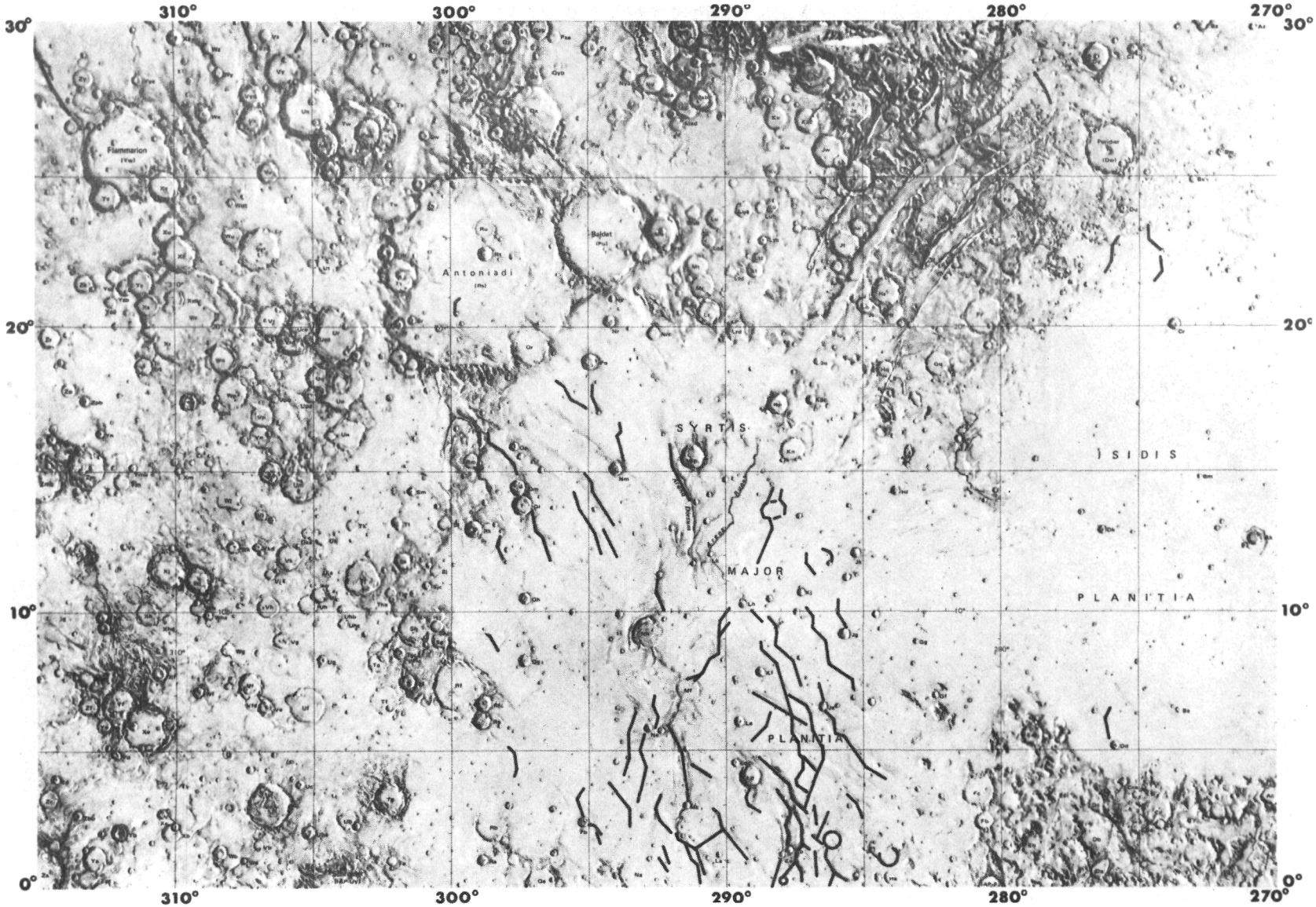
MC-10 LUNAE PALUS



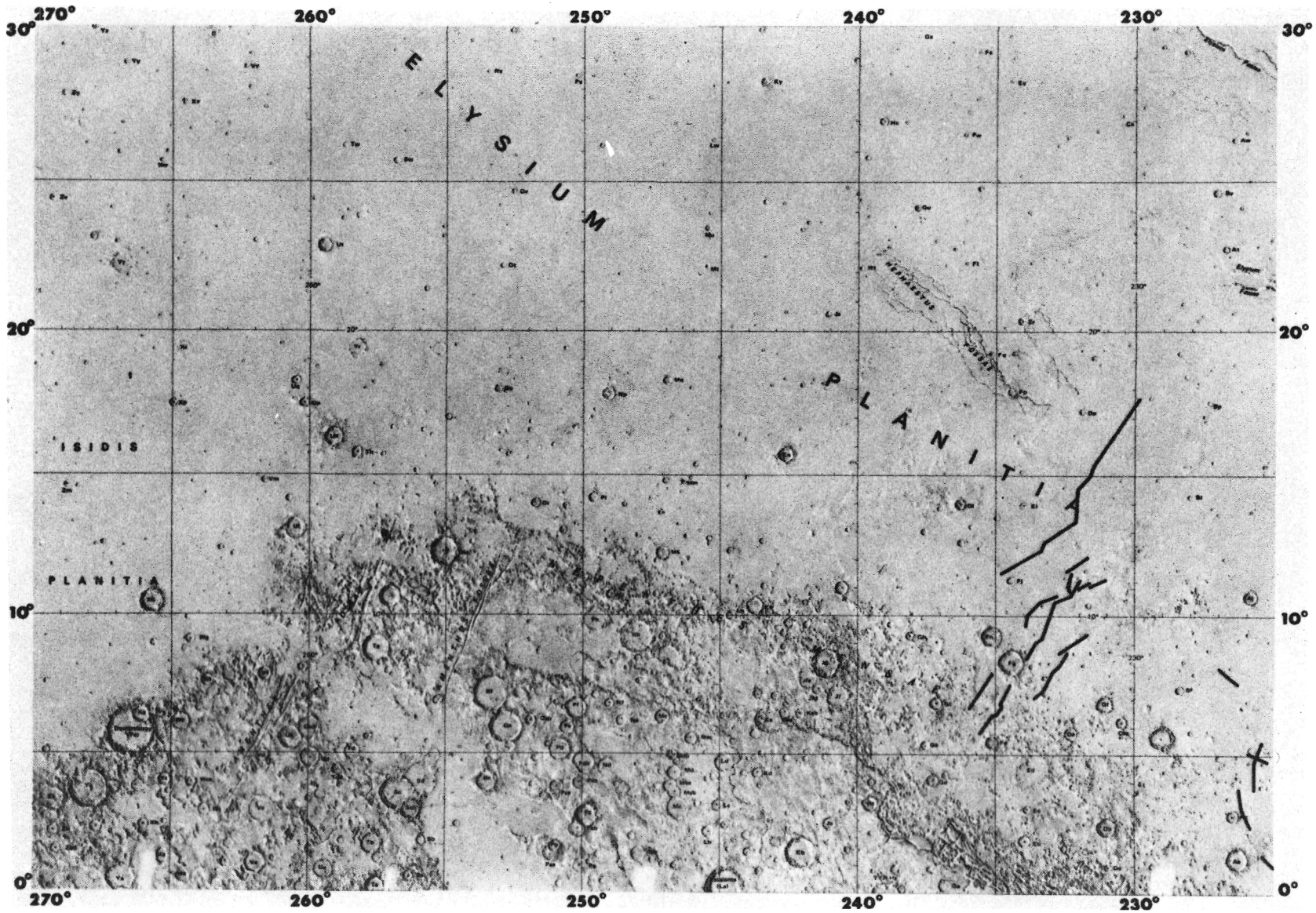
MC-11 OXIA PALUS



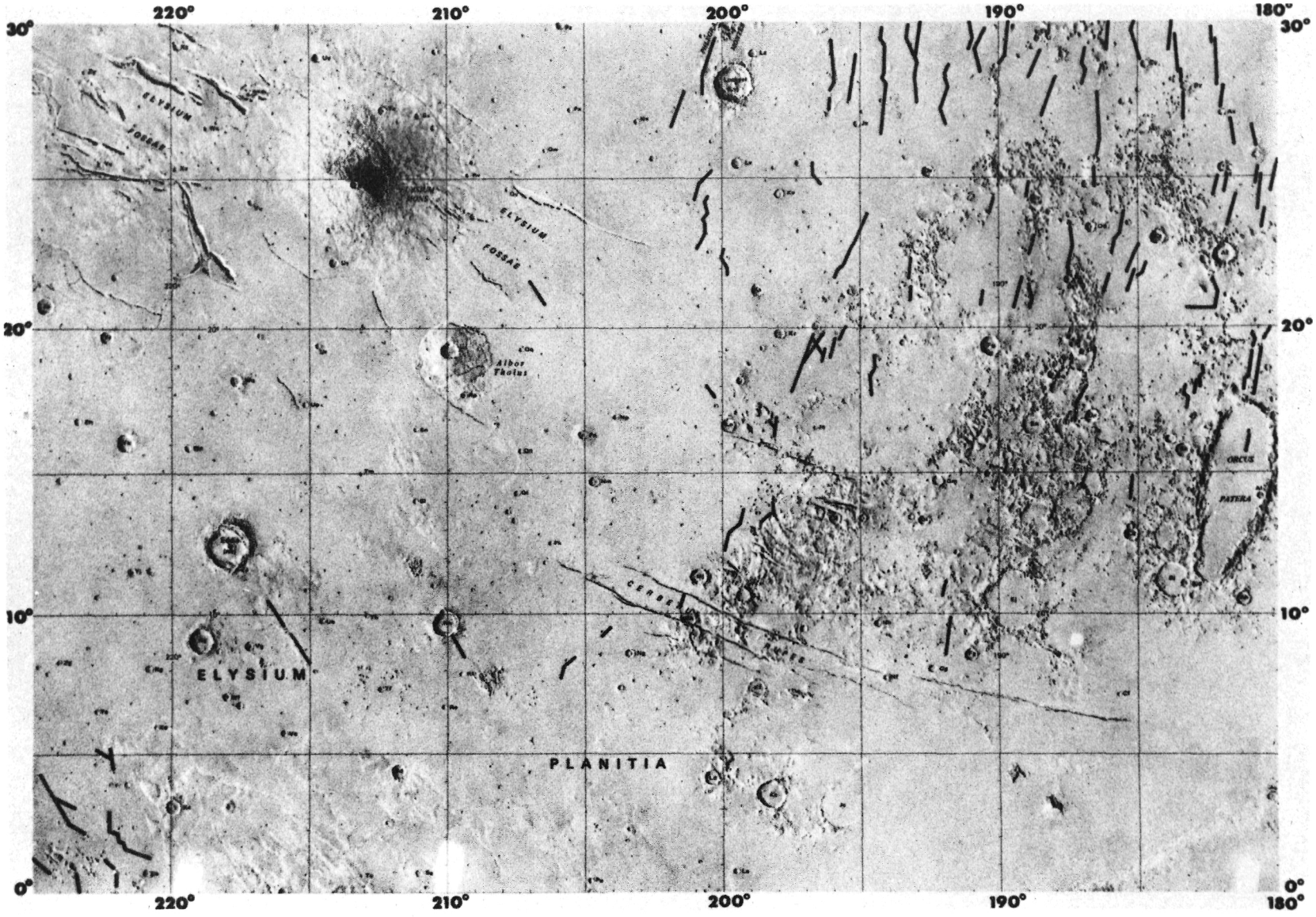
MC-12 ARABIA



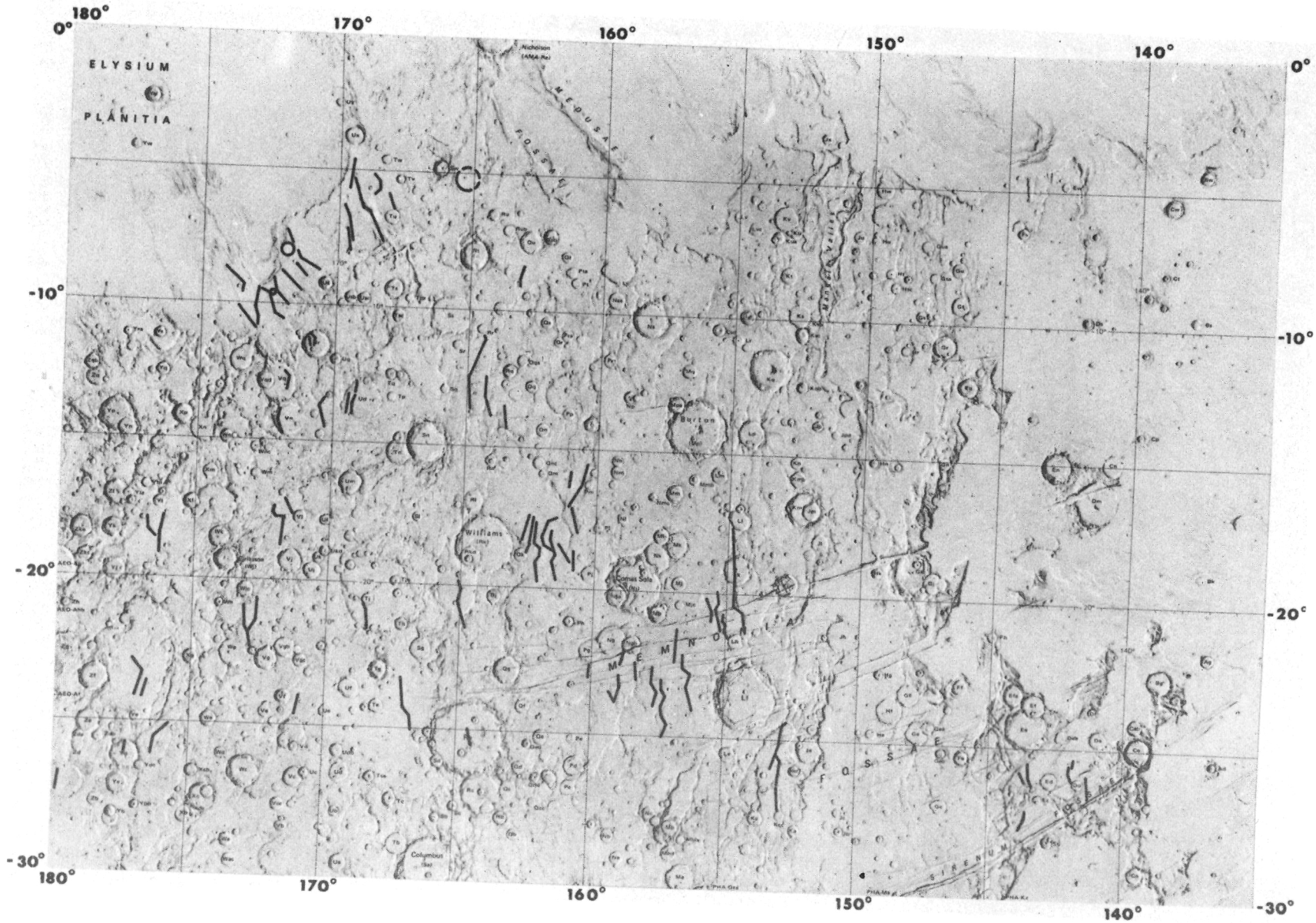
MC-13 SYRTIS MAJOR



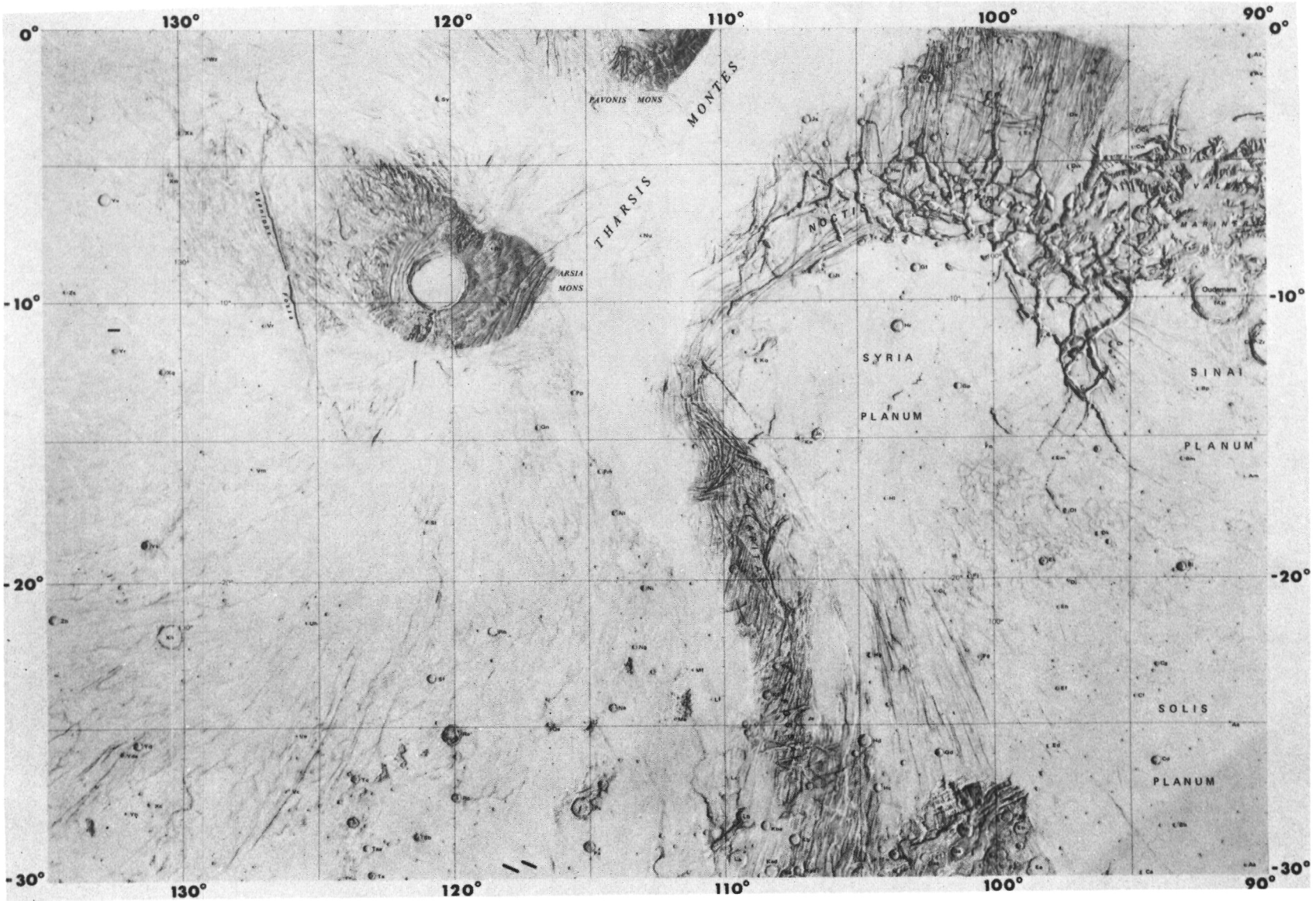
MC-14 AMENTHES



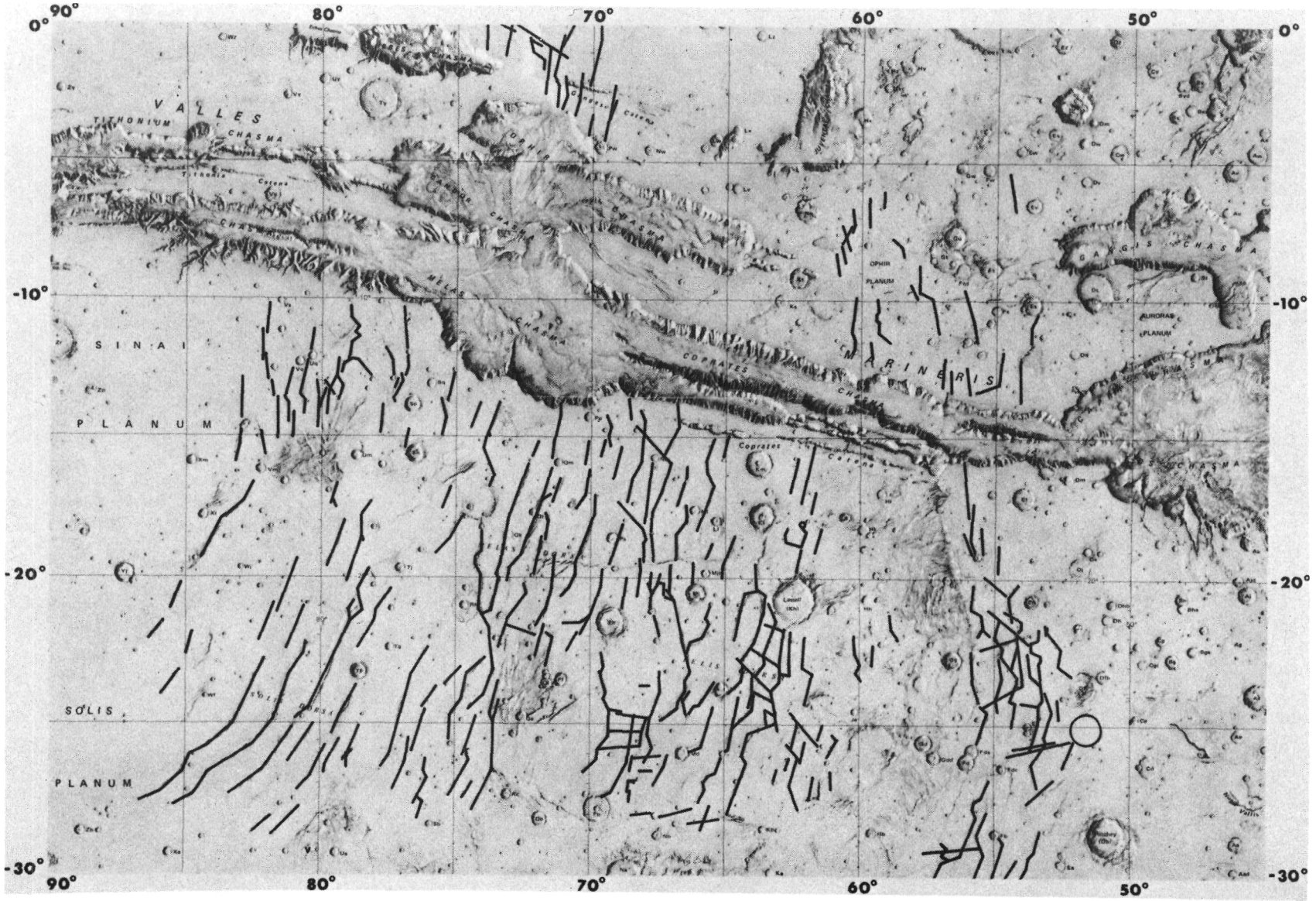
MC-15 ELYSIUM



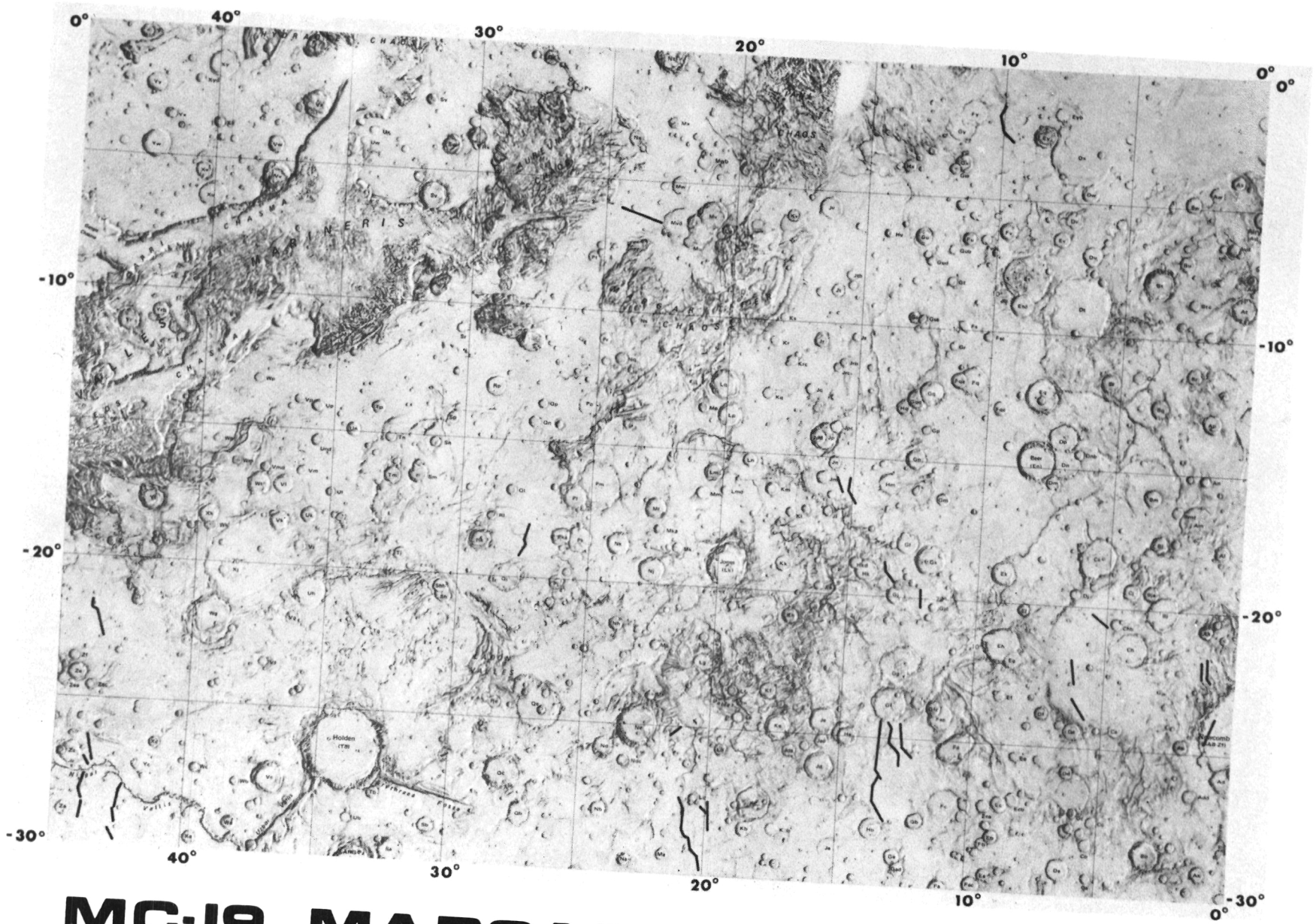
MC-16 MEMNONIA



MC-17 PHOENICIS LACUS



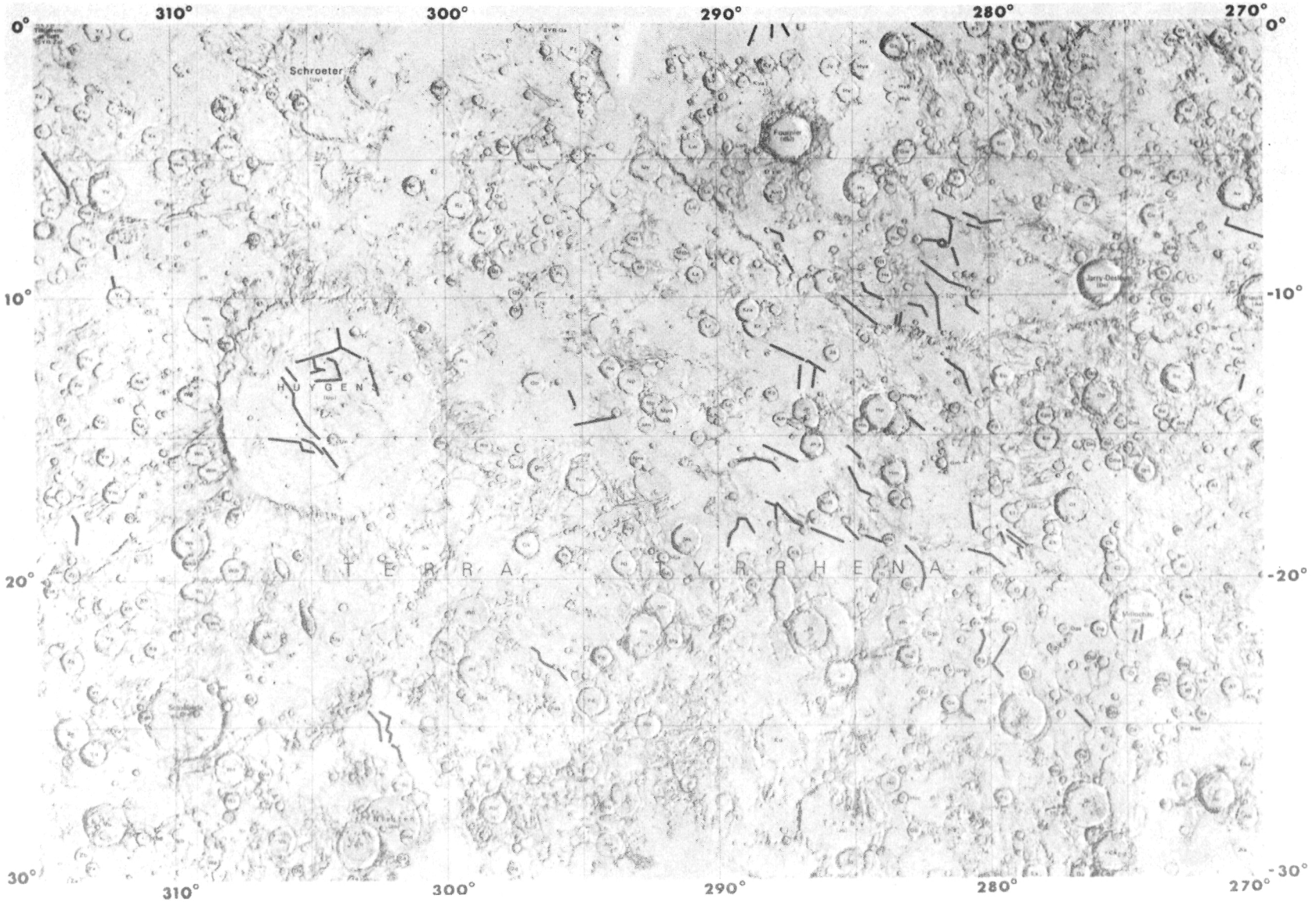
MC-18 COPRATES



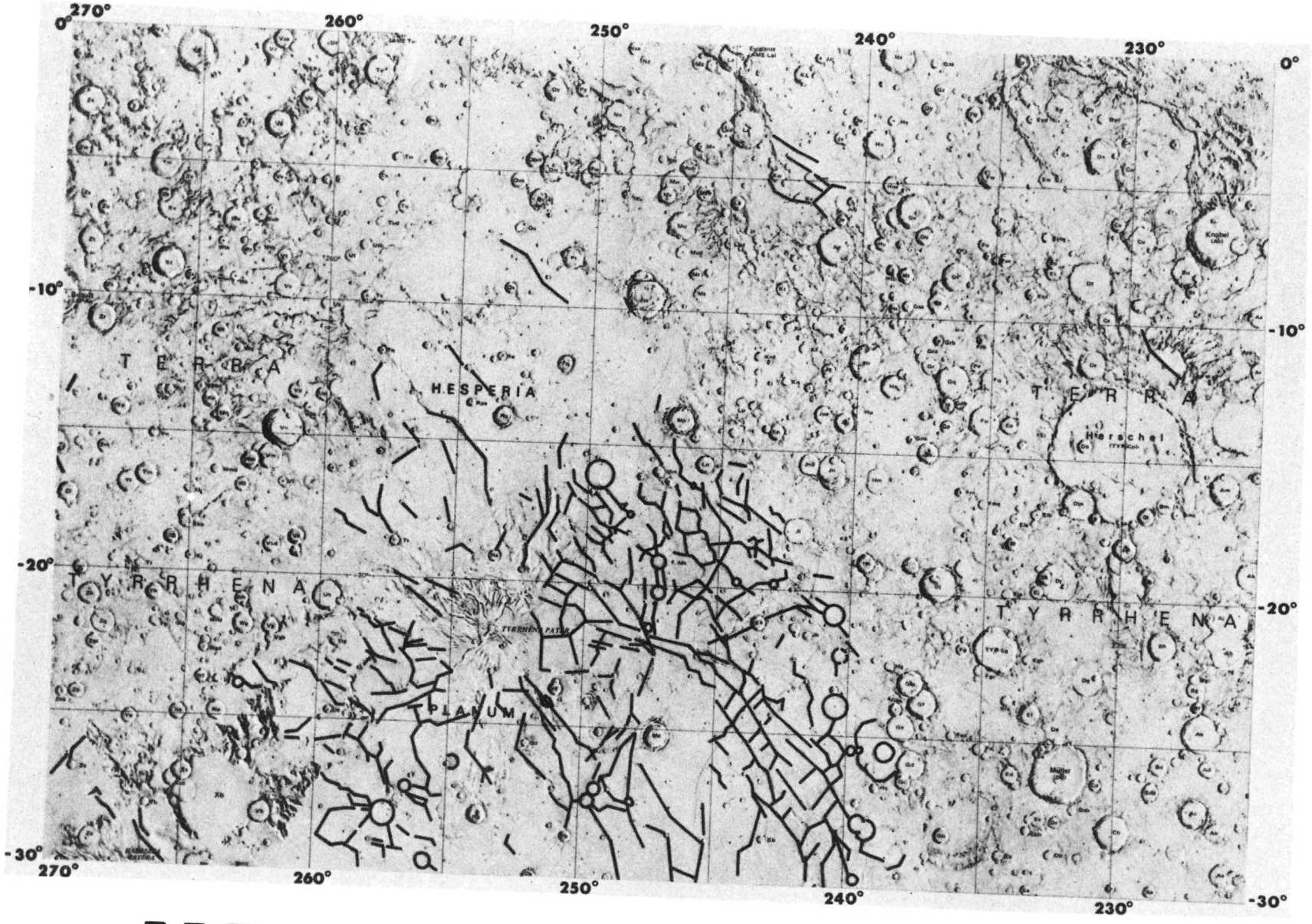
MC-19 MARGARITIFER SINUS



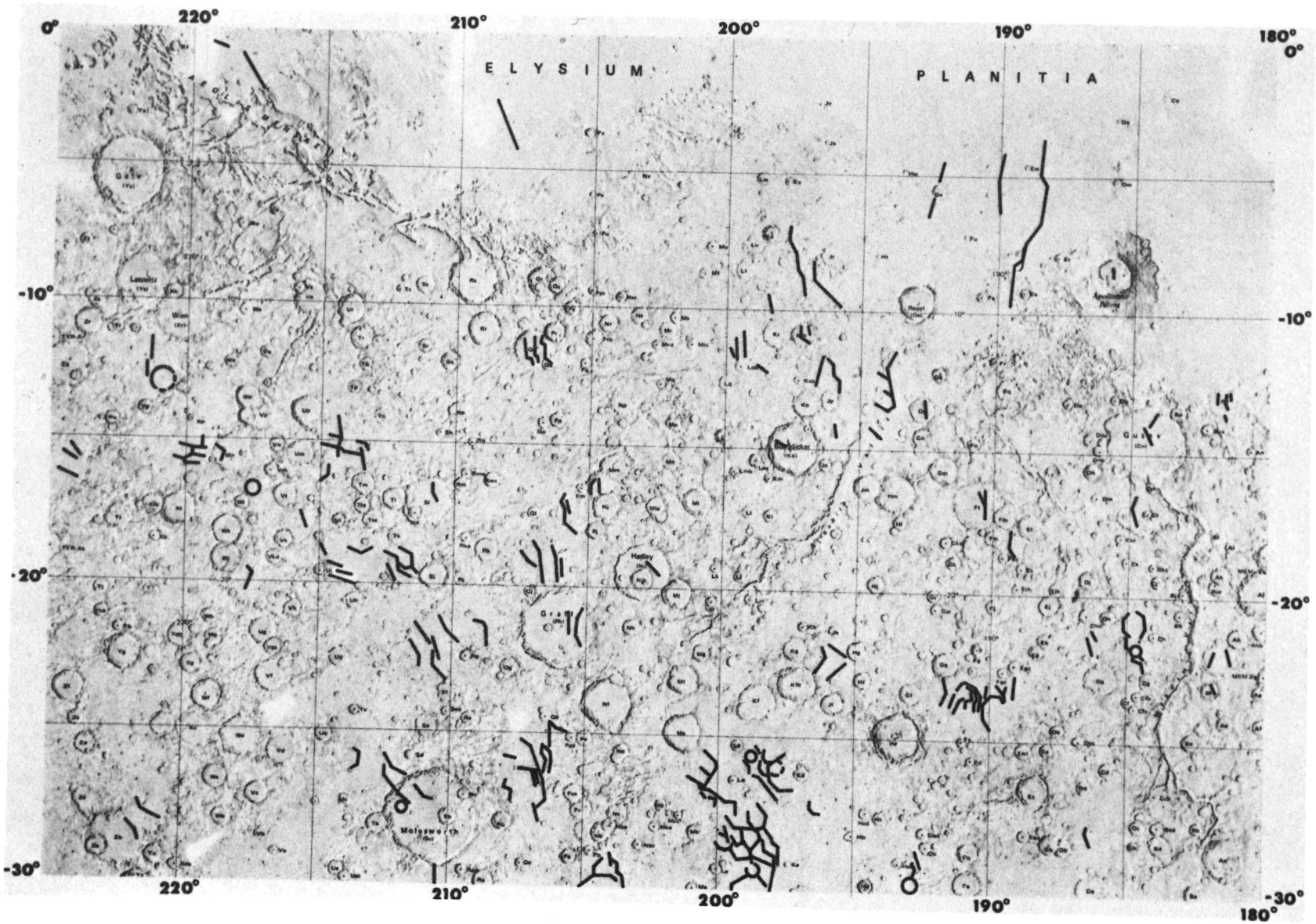
MC-20 SINUS SABAEUS



MC-21 IAPYGIA



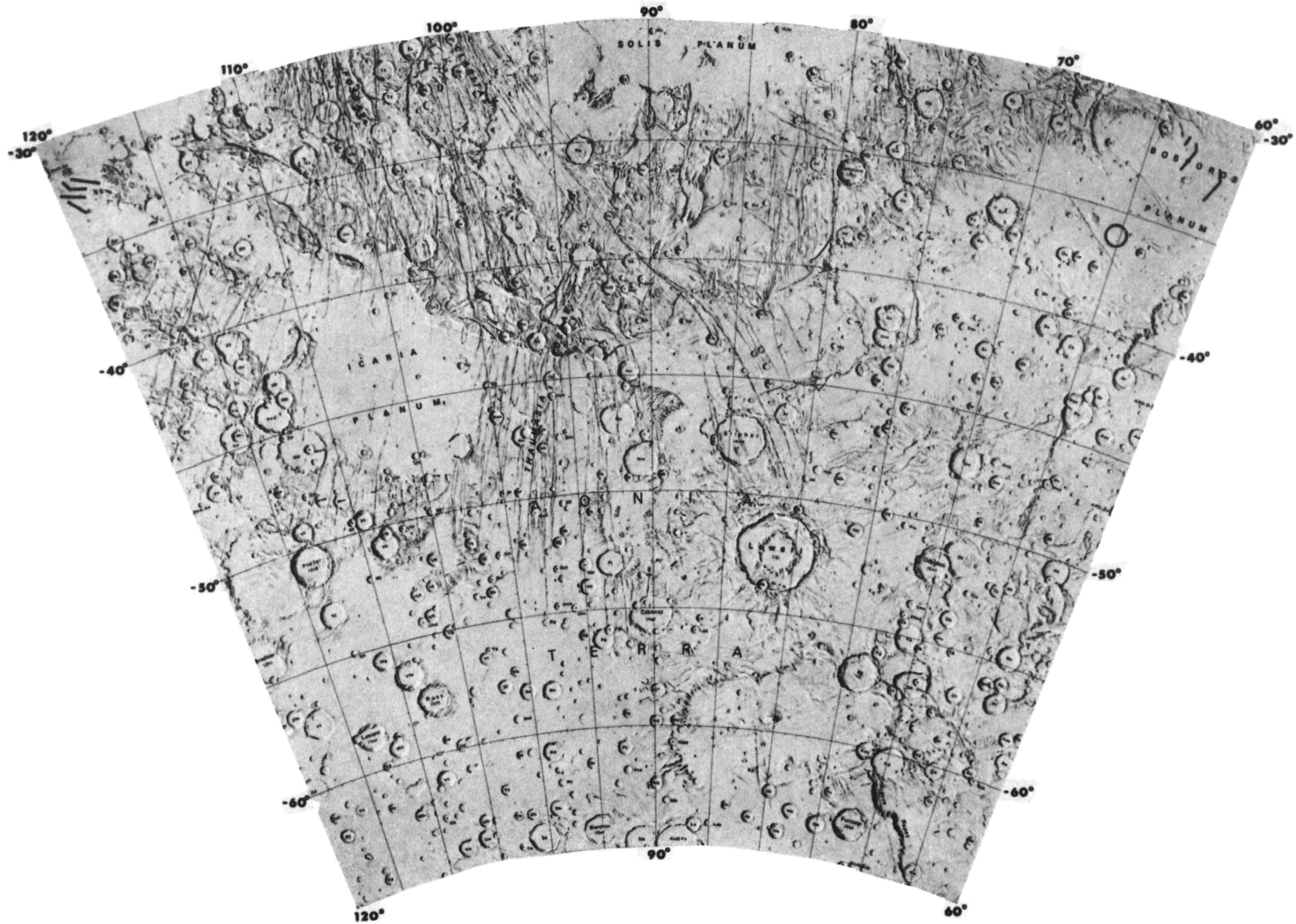
MC-22 MARE TYRRHENUM


0°
220°
210°
200°
190°
180°
0°
ELYSIUM
PLANITIA
-10°
-20°
-30°
Lassell
Wien
Bürg
Hadley
Moiseyev
Apollinaris Mons

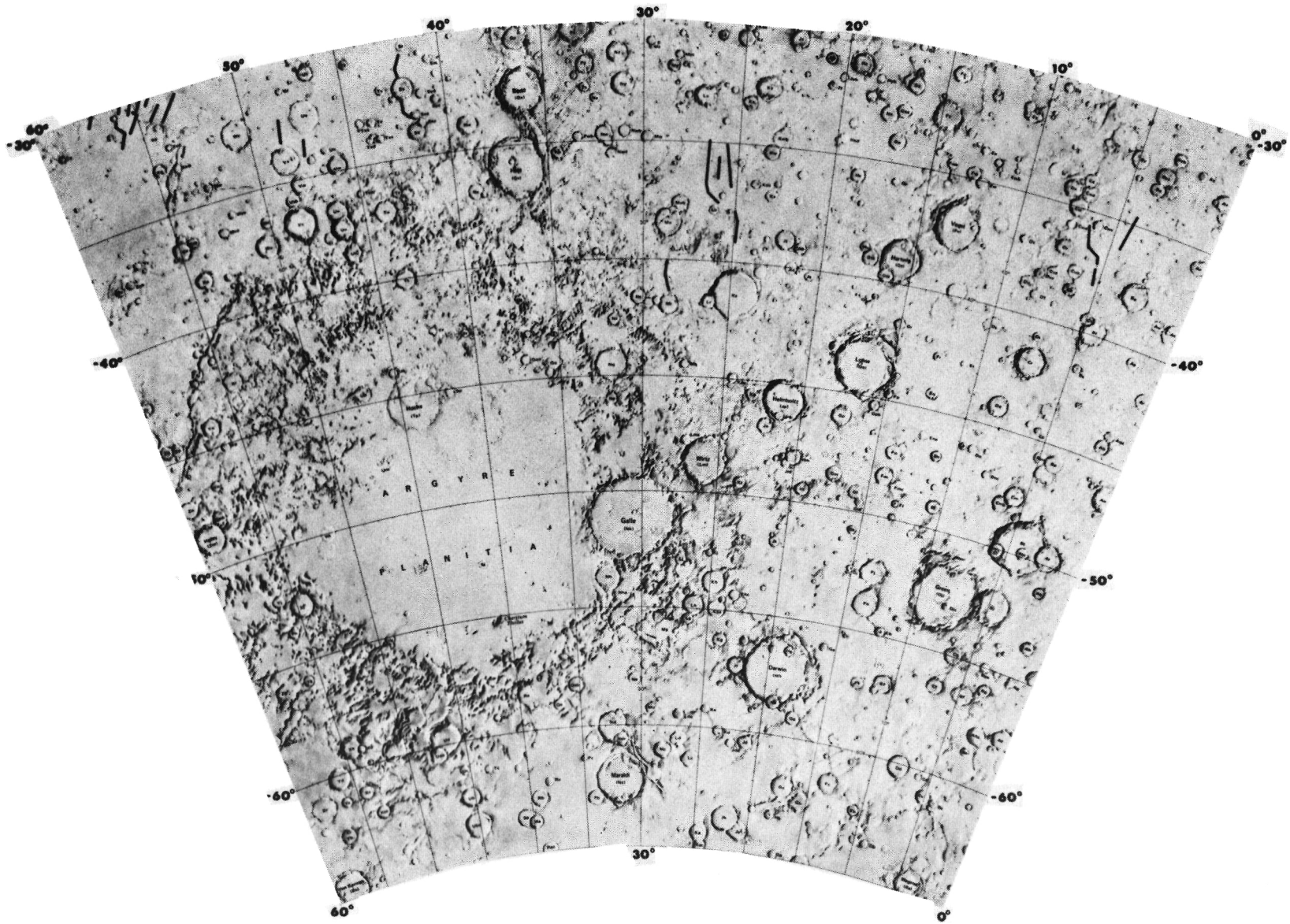
MC-23 AEOLIS



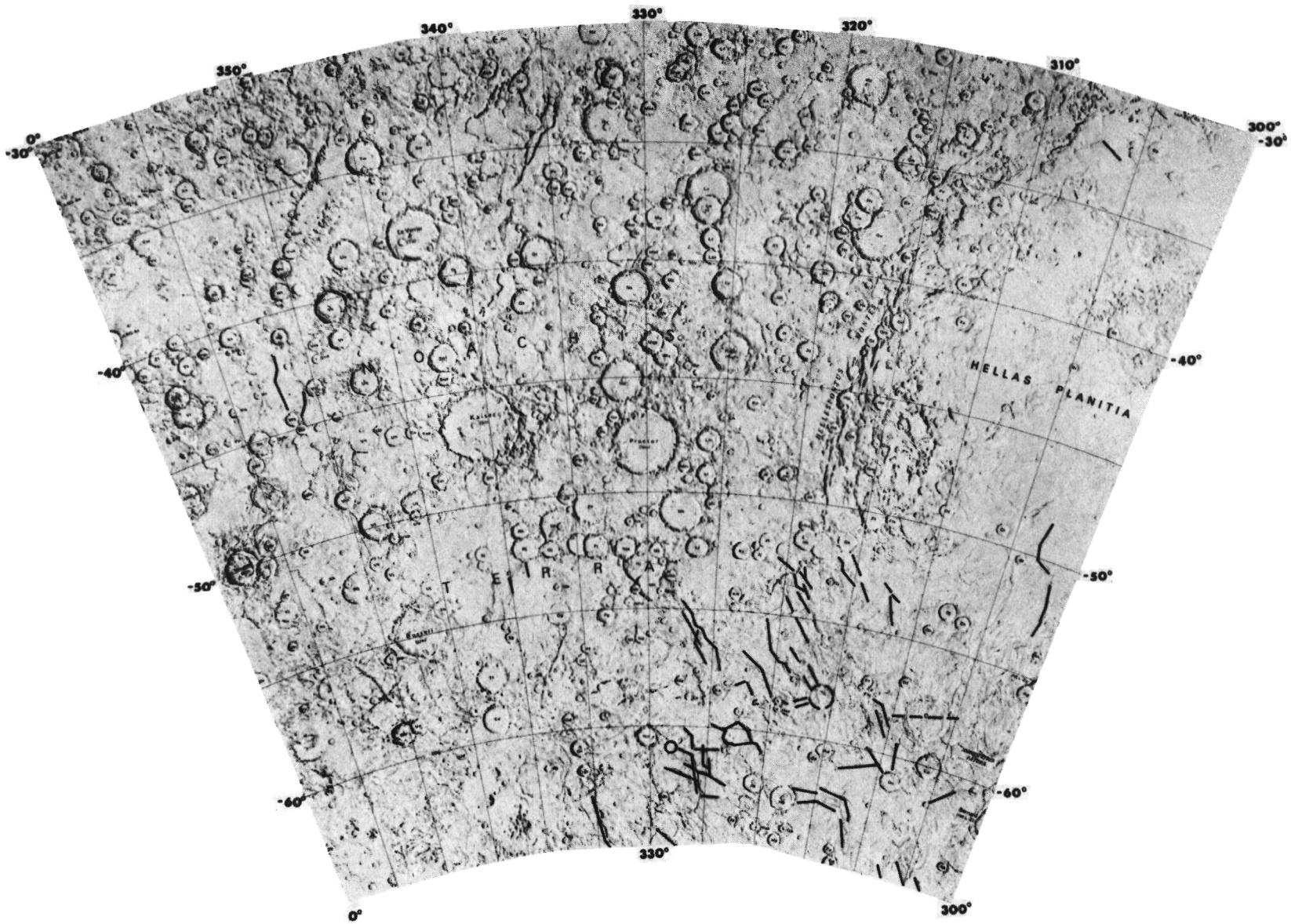
MC-24 PHAETHONTIS



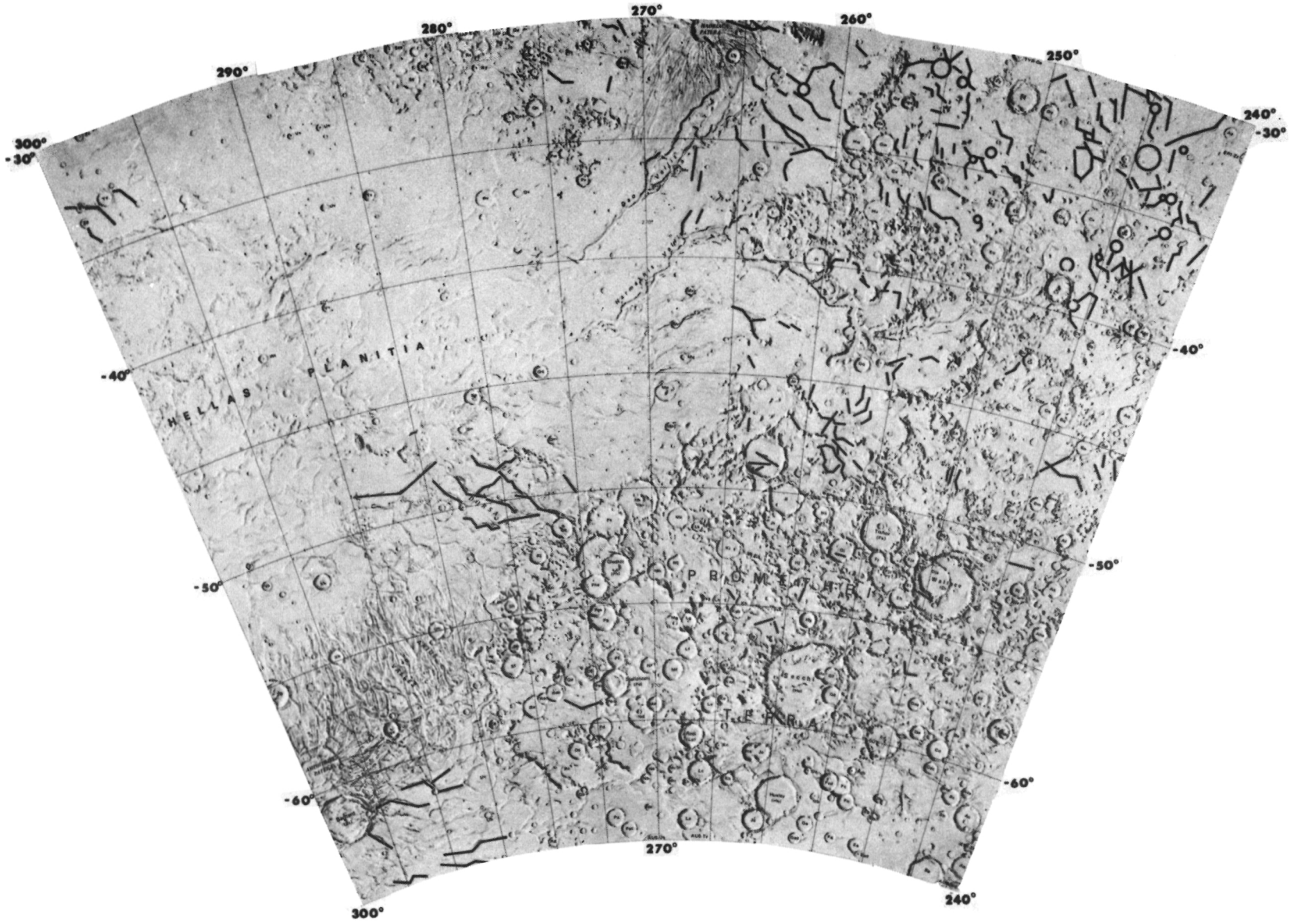
MC-25 THAUMASIA



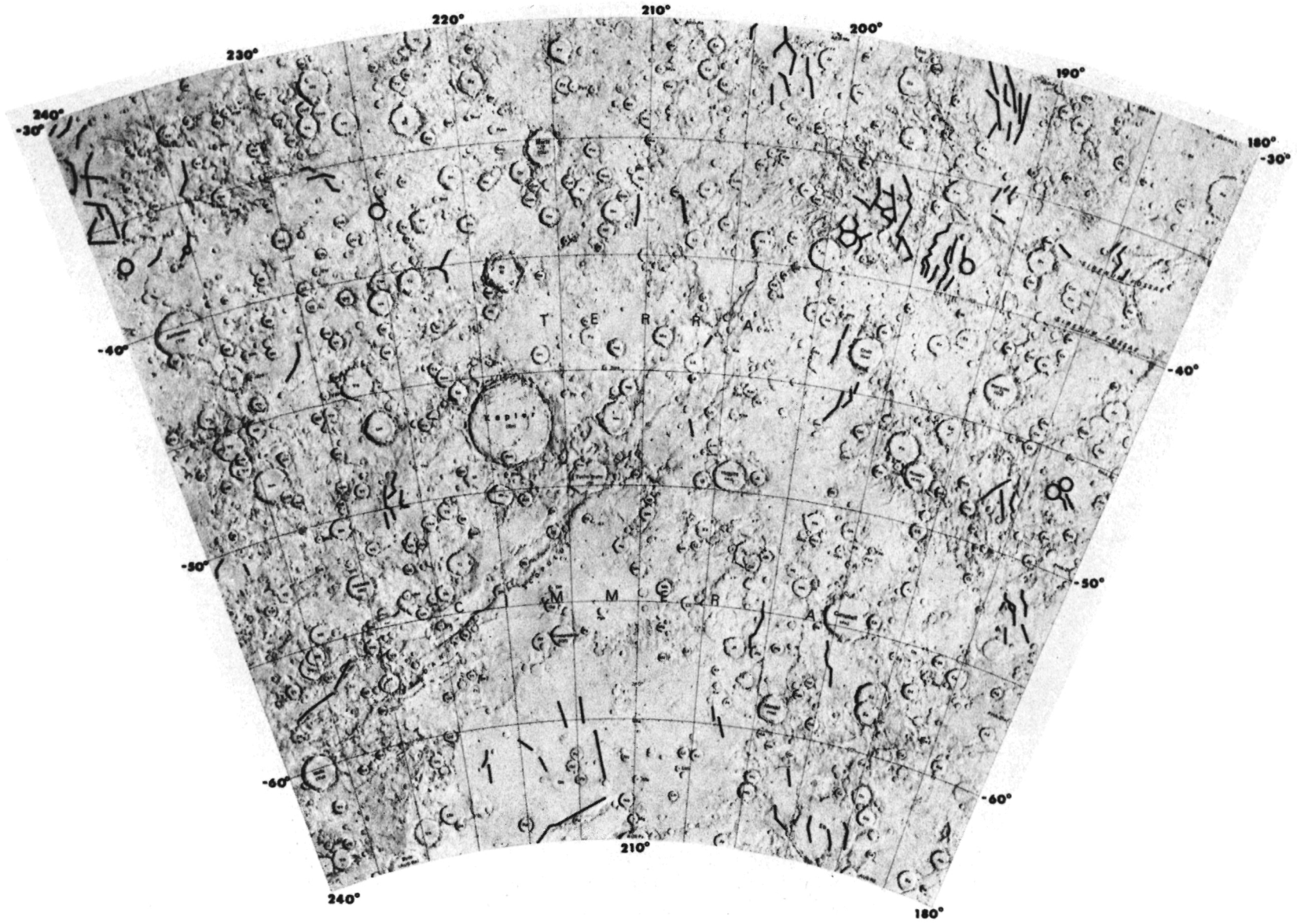
MC-26 ARGYRE



MC-27 NOACHIS


270°
280°
260°
290°
250°
300°
-30°
240°
-30°
HELLAS
PLANITIA
-40°
-40°
-50°
-50°
-60°
-60°
270°
300°
240°

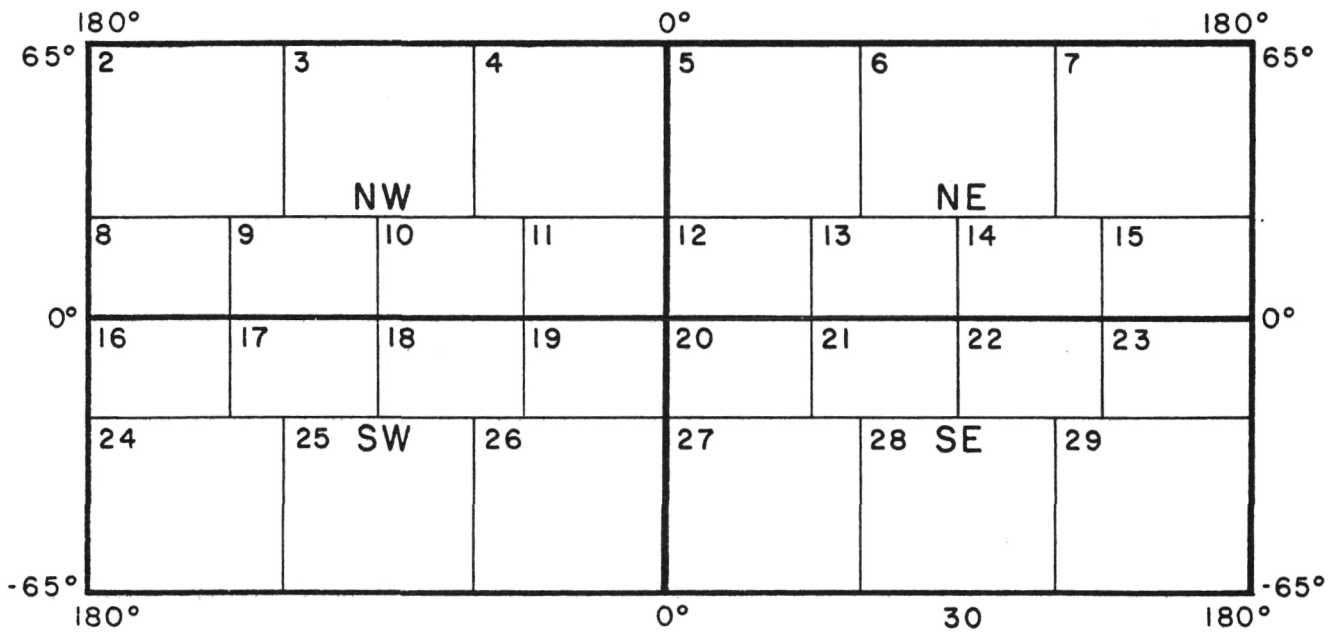
MC-28 HELLAS

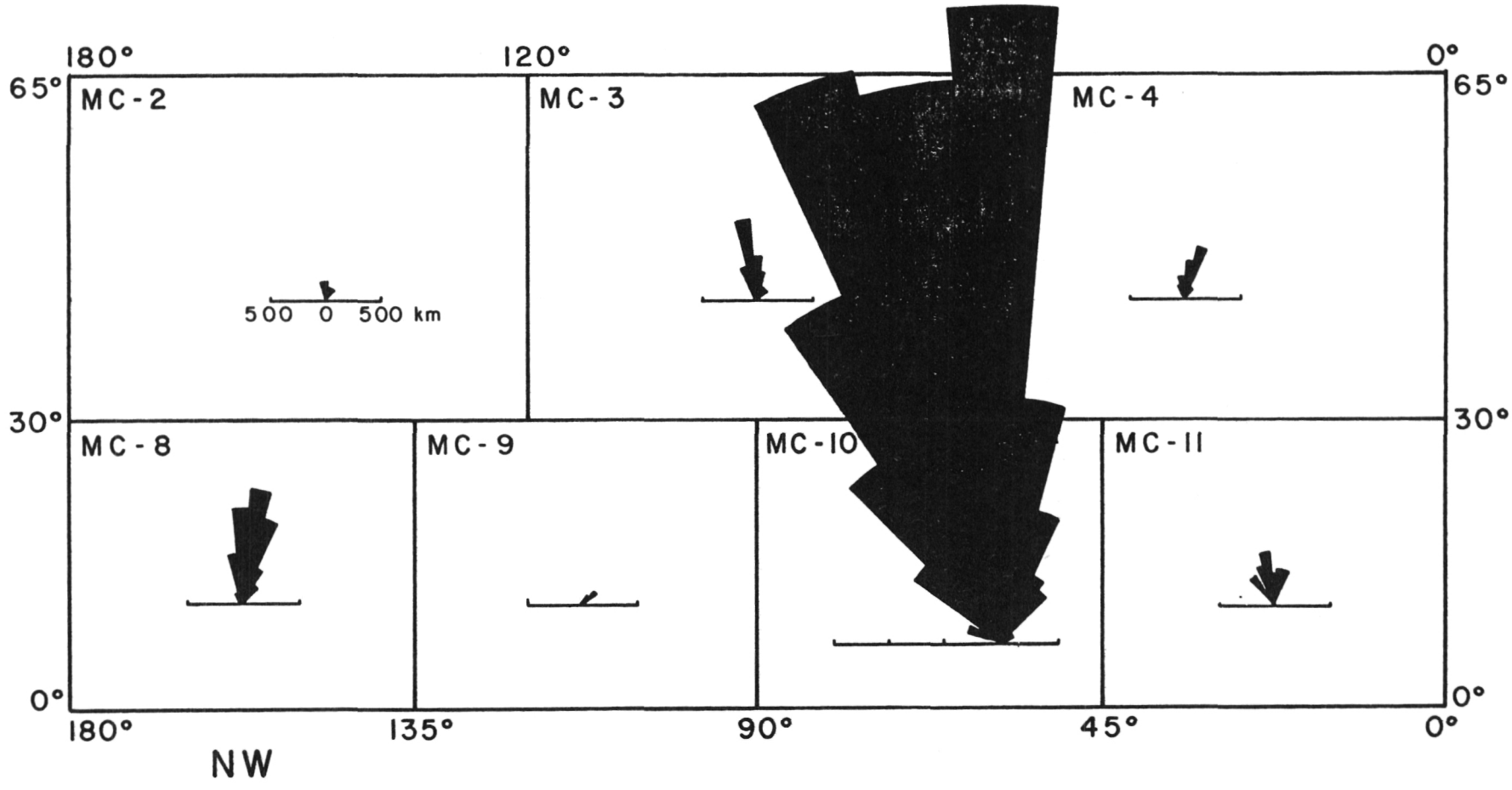


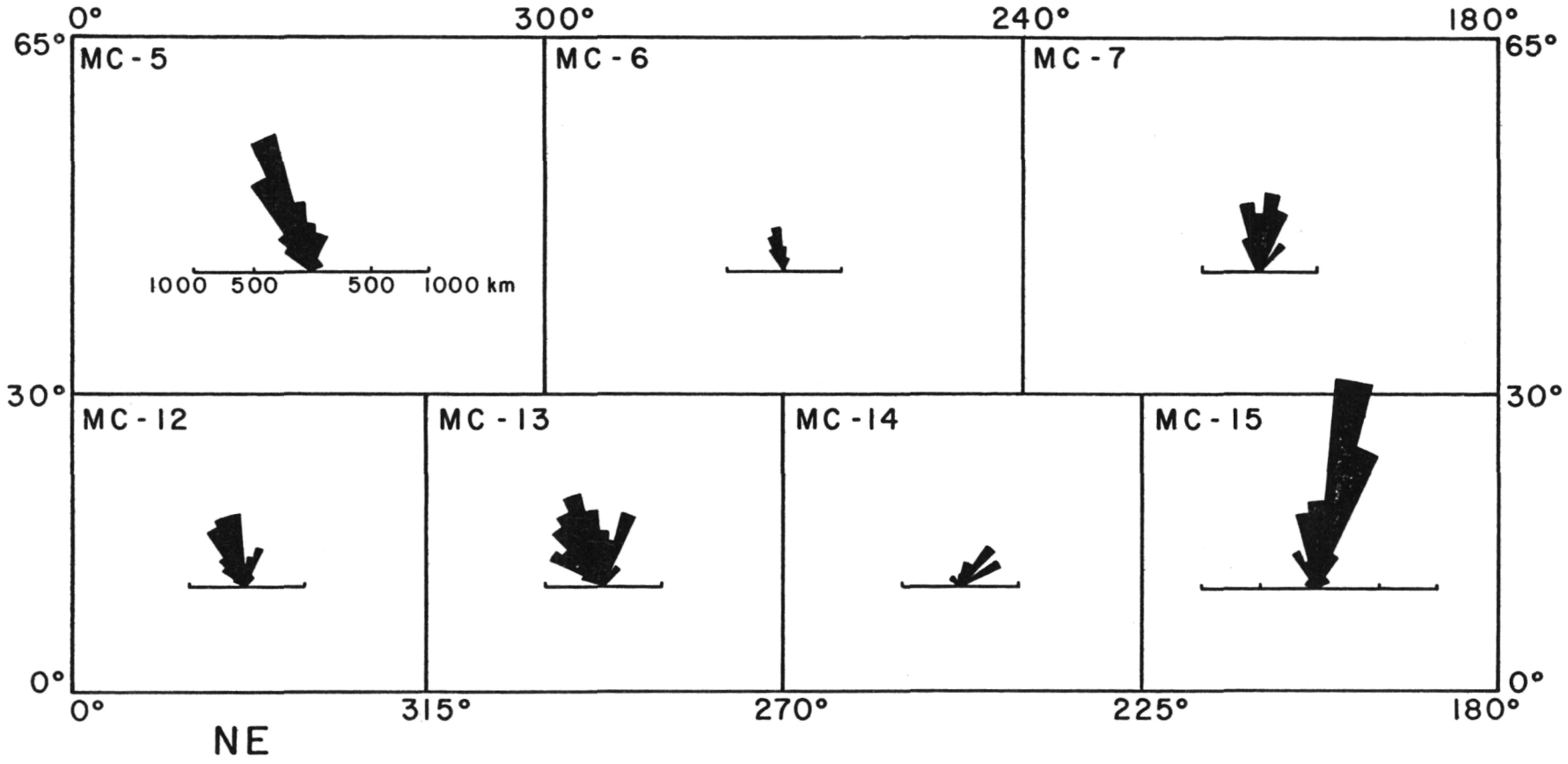
MC-29 ERIDANIA

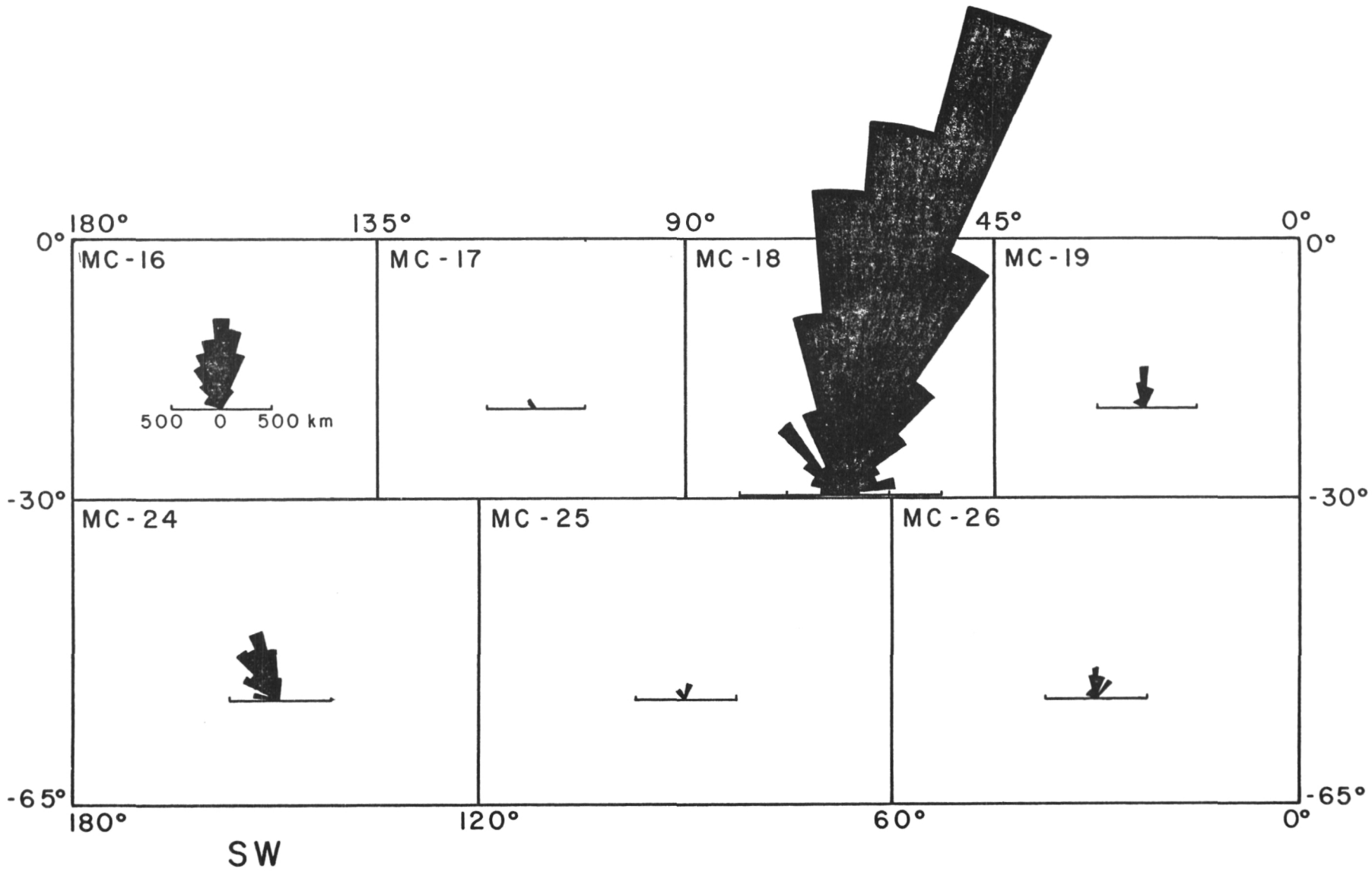
APPENDIX II

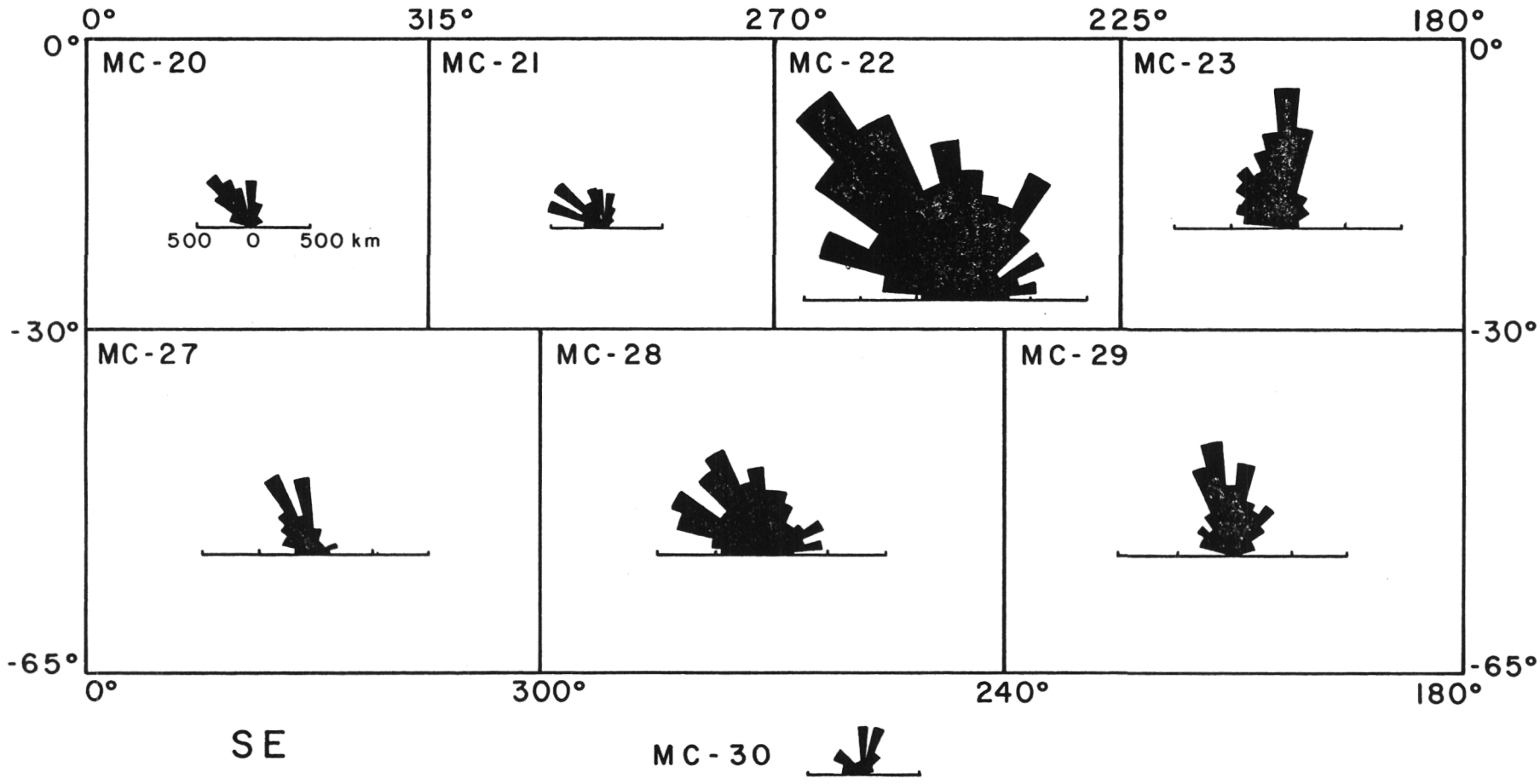
The following four pages show rose diagrams for each of the martian quadrangles. Mars has been divided into four quadrants for purposes of presenting the diagrams, as shown in the sketch below. The MC numbers are shown in the upper left-hand corner of each quadrangle area. In each rose diagram, the orientation data is weighted according to length, and all are plotted at the same scale.




180°
120°
0°
65°
MC-2
MC-3
MC-4
65°
500 0 500 km
30°
MC-8
MC-9
MC-10
MC-11
30°
0°
0°
180°
135°
90°
45°
0°
NW


0°
300°
240°
180°
65°
MC - 5
MC - 6
MC - 7
1000 500 500 1000 km
30°
MC - 12
MC - 13
MC - 14
MC - 15
0°
0°
315°
270°
225°
180°
NE


0°
180°
135°
90°
45°
0°
MC - 16
MC - 17
MC - 18
MC - 19
500 0 500 km
-30°
MC - 24
MC - 25
MC - 26
-65°
180°
120°
60°
0°
SW


0°
315°
270°
225°
180°
0°
-30°
-65°
MC-20
MC-21
MC-22
MC-23
MC-27
MC-28
MC-29
500 0 500 km
0°
300°
240°
180°
SE
MC-30

REFERENCES

Arvidson, R.E., Goettal, K.A., and Hohenberg, C.M., 1980, A Post-Viking View of Martian Geologic Evolution, Rev. Geophys. Space Phys., 18, 565-603.

Arthur, D.W.G., 1962, Some Systematic Visual Lunar Observations, in: The Moon, Kopal, Z. and Milchailov, Z.K., eds., Academic Press, New York, 317-344.

Baker, V.R., 1980, Nirgal Vallis, Repts. Planet. Geol. Prog.-1980, NASA Tech. Mem. 82385, 345-347.

Baldwin, R.B., 1963, The Measure of the Moon, University of Chicago Press, Chicago, Ill., 488pp.

Binder, A.B. and McCarthy, D.W., 1972, Mars: The Lineament Systems, Science, 176, 279-281.

Biot, M.A., 1961, Theory of Folding of Stratified Viscoelastic Media and Its Implications in Tectonics and Orogenesis, Geol. Soc. Am. Bull., 72 1595-1620.

Bryan, W.B., 1973, Wrinkle-Ridges as Deformed Surface Crust on Ponded Mare Lava, Proc. Lunar Sci. Conf. 4th, 93-106.

Carr, M.H., 1980, The Geology of Mars, American Scientist, 68, 626-635.

Carr, M.H., Greeley, R., Blasius, K.R., Guest, J.E., and Murray, J.B., 1977, Some Martian Volcanic Features as Viewed from the Viking Orbiters, J. Geophys. Res., 82, 3985-4015.

Colton, G.W., Howard, K.A., and Moore, H.J., 1972, Mare Ridges and Arches in Southern Oceanus Procellarum, Apollo 16 Prelimary Science Report, NASA SP-315, 29-90 to 29-93.

Conel, J.E., 1969, Structural Features Relating to the Origin of Lunar Wrinkle Ridges, JPL Space Programs Summary 37-56, III, 58-63.

De Hon, R.A., 1977, Geologic Map of the Eridania Quadrangle of Mars, U.S. Geol. Surv. Map I-1008.

Dzurisin, D., 1978, The Tectonic and Volcanic History of Mercury as Inferred from Studies of Scarps, Ridges, Troughs, and Other Lineaments, J. Geophys. Res., 83, 4883-4906.

Eaton, J.P. and Murata, K.J., 1960, How Volcanoes Grow, Science, 132, 925-938.

Eppink, J.F. and Saunders, R.S., 1980, Patterns of Ridges and Scarps on Mars, Repts. Planet. Geol. Prog., 1979-1980, NASA Tech. Mem. 81776, 66-67.

Fagin, S.W., Worrall, D.M., and Muehlberger, W.R., 1978, Lunar Mare Ridge Orientations: Implications for Lunar Tectonic Models, Proc. Lunar Planet. Sci. Conf. 9th, 3473-3479.

Fielder, G., 1963, Lunar Tectonics, Quart. J. Geol. Soc. Lond., 119, 65-94.

Gifford, A.W., 1980, Ridge-Rings on Mars, Repts. Planet. Geol. Prog.-1980, NASA Tech. Mem. 82385, 90-92.

Greeley, R., Theilig, E., Guest, J.E., Carr, M.H., Masursky, H., and Cutts, J.A., 1977, Geology of Chryse Planitia, J. Geophys. Res., 82, 4093-4109.

Gregory, T., Saunders, R.S., and Plescia, J.B., 1979, A Martian Global Plains System Represented by Lunae Planum Surface Units, Repts. Planet. Geol. Prog., 1978-1979, NASA Tech. Mem. 80339, 75-77.

Hamdan, A. and El-Baz, F., 1980, Statistical Analysis of Central-Peaked Craters on Mars, Repts. Planet. Geol. Prog.-1980, NASA Tech. Mem. 82385, 161-163.

Harp, E.L., 1976, Fracture Systems of Mars, Proc. First International Conf. on the New Basement Tectonics, June 3-7, 1974, Utah Geol. Assoc., 389-408.

Head, J.W., Wood, C.A. and Mutch, T.A., 1977, Geologic Evolution of the Terrestrial Planets, American Scientist, 65, 21-29.

Hodges, C.A., 1973, Mare Ridges and Lava Lakes, Apollo 17 Preliminary Science Report, NASA SP-330, 31-12 to 31-21.

Howard, J.H., 1979, Geologic Map of the Phaethontis Quadrangle of Mars, U.S. Geol. Surv. Map I-1145.

Howard, K.A. and Muehlberger, W.R., 1973, Lunar Thrust Faults in the Taurus-Littrow Region, Apollo 17 Preliminary Science Report, NASA SP-330, 31-22 to 31-25.

International Astronomical Union, 1977, Report of the Working Group for Planetary System Nomenclature, Proc. 16th General Assembly, Grenoble, Trans. I.A.U., XVIB, 321-369.

King, E.A., 1978, Geologic Map of the Mare Tyrrhenum Quadrangle of Mars, U.S. Geol. Surv. Map I-1073.

Kuiper, G.P., 1954, On the Origin of the Lunar Surface Features, Proc. Nat. Acad. Sci., 40, 1096-1112.

Kuiper, G.P., 1965, Interpretation of Range VII Records, Range VII Experimenters Analyses and Interpretations, Part II, JPL Tech. Rept. 32-700, 9-73.

Kuiper, G.P., Whitaker, E.A., Strom, R.G., Fountain, J.W., and Larsen, S.M., 1967, Consolidated Lunar Atlas, Lunar Planet. Lab., Univ. Arizona, Tucson, Arizona.

Lucchitta, B.K., 1976, Mare Ridges and Related Highland Scarps-Result of Vertical Tectonism?, Proc. Lunar Sci. Conf. 7th, 2761-2782.

Lucchitta, B.K., 1977, Topography, Structure, and Mare Ridges in Southern Mare Imbrium and Northern Oceanus Procellarum, Proc. Lunar Sci. Conf. 8th, 2691-2703.

Lucchitta, B.K., 1978, Geologic Map of the Ismenius Lacus Quadrangle of Mars, U.S. Geol. Surv. Map I-1065.

Lucchitta, B.K. and Klockenbrink, J.L., 1979, Ridges and Scarps in the Equatorial Belt of Mars, Lunar and Planetary Science X, Lunar and Planetary Institute, 750-752.

Masursky, H., Eliason, E., Ford, P.G., McGill, G.E., Pettengill, G.H., Schaber, G.G., and Schubert, G., 1980, Pioneer Venus Radar Results: Geology from Images and Altimetry, J. Geophys. Res., 85, 8232-8260.

Maxwell, T.A., 1978, Origin of Multi-Ring Basin Ridge Systems: An Upper Limit to Elastic Deformation Based on a Finite-Element Model, Proc. Lunar Planet. Sci. Conf. 9th, 3541-3559.

Maxwell, T.A., El-Baz, F., and Ward, S.H., 1975, Distribution, Morphology, and Origin of Ridges and Arches in Mare Serenitatis, Geol. Soc. Am. Bull., 86, 1273-1287.

Maxwell, T.A. and Gifford, A.W., 1980, Ridge Systems of Caloris: Comparison with Lunar Basins, Proc. Lunar Planet. Sci. Conf. 11th, 2447-2462.

McCauley, J.F., 1978, Geologic Map of the Coprates Quadrangle of Mars, U.S. Geol. Surv. Map I-897.

McGill, G.E., 1978, Geologic Map of the Thaumasia Quadrangle of Mars, U.S. Geol. Surv. Map I-1077.

Melosh, H.J., 1977, Global Tectonics of a Despun Planet, Icarus, 31, 221-243.

Melosh, H.J. and Dzurisin, D., 1978, Mercurian Global Tectonics: A Consequence of Tidal Despinning?, Icarus, 35, 227-236.

Milton, D.J., 1974, Geologic Map of the Lunae Palus Quadrangle of Mars, U.S. Geol. Surv. Map I-894.

Moody, J.D. and Hill, M.J., 1956, Wrench Fault Tectonics, Geol. Soc. Am. Bull., 67, 261-263.

Mouginis-Mark, P.J., Sharpton, V.L., and Hawke, B.R., 1980, Schiaparelli Basin, Mars: Morphology, Tectonics, and Infilling History, in: Papers Presented to the Conference on Multi-Ring Basins, Nov. 10-12, 1980, Lunar and Planetary Institute, Houston, Texas, 65-67.

Muehlberger, W.R., 1974, Structural History of Southeastern Mare Serenitatis and Adjacent Highlands, Proc. Lunar Sci. Conf. 5th, 101-110.

Mutch, T.A., Arvidson, R.E., Head, J.W., Jones, K.L., and Saunders, R.S., 1976, The Geology of Mars, Princeton University Press, Princeton, N.J., 400pp.

Neukum, G. and Wise, D.U., 1976, Mars: A Standard Crater Curve and Possible New Time Scale, Science, 194, 1381-1387.

Pechmann, J.B. and Melosh, H.J., 1979, Global Fracture Patterns of a Despun Planet: Application to Mercury, Icarus, 38, 243-250.

Peterson, J.E., 1977, Geologic Map of the Noachis Quadrangle of Mars, U.S. Geol. Surv. Map I-910.

Phillips, R.J., Saunders, R.S., and Conel, J.E., 1973, Mars: Crustal Structure Inferred from Bouguer Gravity Anomalies, J. Geophys. Res., 78, 4815-4820.

Phillips, R.J. and Lambeck, K., 1980, Gravity Fields of the Terrestrial Planets: Long-Wavelength Anomalies and Tectonics, Rev. Geophys. Space Phys., 18, 27-76.

Phillips, R.J., Banerdt, W.B., Sleep, N.L., and Saunders, R.S., 1981, Martian Stress Distributions: Arguments About Finite Strength Support of Tharsis, J. Geophys. Res., in press.

Potter, D.B., 1976, Geologic Map of the Hellas Quadrangle of Mars, U.S. Geol. Surv. Map I-941.

Quaide, W., 1965, Rilles, Ridges, and Domes - Clues to Maria History, Icarus, 4, 374-389.

Raitala, J., 1980, Tectonic Implications of the Mare Ridge Pattern of the Central Parts of Oceanus Procellarum on the Moon, The Moon and the Planets, 23, 307-321.

Saunders, R.S. and Gregory, T.E., 1980, Tectonic Implications of Martian Ridged Plains, Repts. Planet. Geol. Prog.-1980, NASA Tech. Mem. 82385, 93-94.

Schultz, P., 1976, Moon Morphology, University of Texas Press, Austin, Texas, 626pp.

Scott, D.H., 1974, The Geologic Significance of Some Lunar Gravity Anomalies, Proc. Lunar Sci. Conf. 5th, 3025-3036.

Scott, D.H. and Carr, M.H., 1978, Geologic Map of Mars, U.S. Geol. Surv. Map I-1083.

Sharpton, V.L. and Head, J.W., 1980, Lunar Mare Arches and Ridges: Relation of Ridge Lobes to Small Pre-Existing Craters, Lunar and Planetary Science XI, Lunar and Planetary Institute, 1024-1026.

Sjogren, W.L., 1979, Mars Gravity: High-Resolution Results from Viking Orbiter 2, Science, 203, 1006-1010.

Soderblom, L.A., Condit, C.D., West, R.A., Herman, B.M., and Kreidler, T.J., 1974, Martian Planetwide Crater Distributions: Implications for Geologic History and Surface Processes, Icarus, 22, 239-263.

Strom, R.G., 1964, Analysis of Lunar Lineaments, 1: Tectonic Maps of the Moon, Comm. Lunar Planet. Lab., Univ. Arizona, 2, 205-216.

Strom, R.G., 1972, Lunar Mare Ridges, Rings and Volcanic Ring Complexes, The Moon, IAU Symposium 47, Runcorn, S.K. and Urey, H.C., eds., 187-215.

Strom, R.G., Trask, N.J., and Guest, J.E., 1975, Tectonism and Volcanism on Mercury, J. Geophys. Res., 80, 2478-2507.

Theilig, E. and Greeley, R., 1979, Plains and Channels in the Lunae Planum-Chryse Planitia Region of Mars, J. Geophys. Res., 84, 7994-8010.

Thurber, C.H. and Toksoz, M.N., 1978, Martian Lithospheric Thickness from Elastic Flexure Theory, Geophys. Res. Lett., 5, 977-980.

Tjia, H.D., 1970, Lunar Wrinkle Ridges Indicative of Strike-Slip Faulting, Geol. Soc. Am. Bull., 81, 3095-3100.

Underwood, J.R. and Trask, N.J., 1978, Geologic Map of the Mare Acidalium Quadrangle of Mars, U.S. Geol. Surv. Map I-1048.

Vening Meinesz, F., 1947, Shear Patterns of the Earth's Crust, Am. Geophys. Union Trans., 28, 1-61.

Whitaker, E.A., 1966, The Surface of the Moon, Proc. 1965 IAU-NASA Symp., 79-98.

Wilson, R.C., Harp, E.L., Picard, M.D., and Ward, S.W., 1973, Chaotic Terrain of Mars: A Tectonic Interpretation from Mariner 6 Imagery, Geol. Soc. Am. Bull, 84, 741-748.

Wise, D.U., Golombek, M.P., and McGill, G.E., 1979, Tectonic Evolution of Mars, J. Geophys. Res., 84, 7934-7939.

Page intentionally left blank

Page intentionally left blank

SECTION III

Page intentionally left blank

Page intentionally left blank

THE MORPHOLOGY AND EVOLUTION OF GANYMEDE AND CALLISTO

A Thesis

Presented to the Faculty of the Graduate School

of Cornell University

in Partial Fulfillment for the Degree of

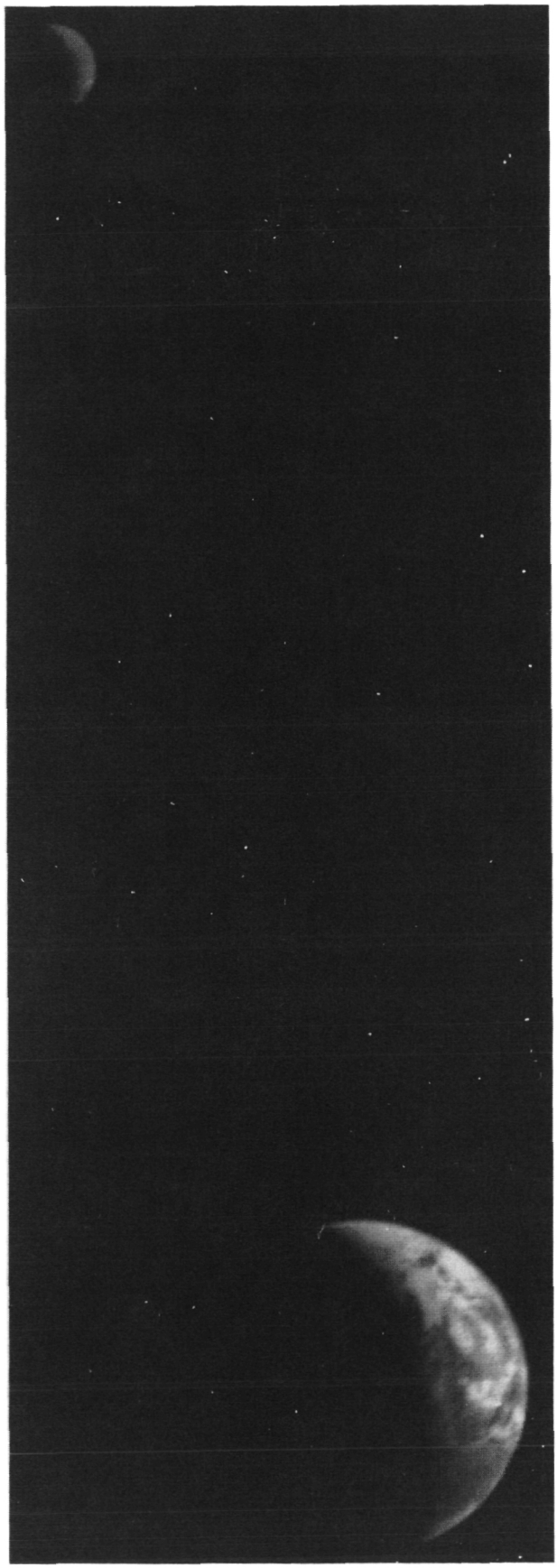
Doctor of Philosophy

by

Steven Weldon Squyres

May 1981

367



We shall not cease from exploration
And the end of all our exploring
Will be to arrive where we started
And know the place for the first time.

T. S. Eliot

THE MORPHOLOGY AND EVOLUTION OF GANYMEDE AND CALLISTO

Steven Weldon Squyres, Ph.D.
Cornell University 1981

High quality images of Ganymede and Callisto, Jupiter's two largest moons, have been obtained by the two Voyager spacecraft. These are the first predominantly icy planetary objects to be studied in detail, and are among the largest such objects known. In this thesis, Voyager images are used to investigate the surface characteristics, geologic processes, and internal evolution of Ganymede and Callisto.

Ganymede shows two principal types of terrain: one dark, old, and heavily cratered ("cratered terrain"), and another brighter, younger, and characterized by complex patterns of grooves ("grooved terrain"). The grooves are several hundred meters deep, several km wide, and spaced 3-10 km apart. Some areas of the brighter unit are smooth and free of grooves. Grooved terrain shows widespread evidence of tectonic extension, limited evidence of shear, and little or no evidence of compression. It indicates a period of tectonic activity, probably caused by global expansion, early in Ganymede's history. Ganymede also has conspicuous bright ray craters concentrated in the grooved terrain, and prominent "polar caps" poleward of about 45° latitude. The surface of Callisto is uniformly dark, heavily cratered, nearly free of bright ray

craters, and shows no evidence of tectonic activity.

Voyager images are used to determine photometric properties of surface features on both bodies at phase angles up to 120°. All terrain types, including the brightest craters, have scattering functions similar to that of the lunar surface. Mean normal reflectances in the Voyager clear filter are 0.35 for Ganymede cratered terrain, 0.44 for Ganymede grooved terrain, 0.18 for Callisto, and $\lesssim$ 0.7 for the brightest craters on both bodies. No terrain type shows significant variation of photometric properties with wavelength between 0.4 and 0.6 μm. The albedo of surface materials on Ganymede and Callisto, as well as most other planetary objects, varies substantially with solar incidence angle. This variation is important in calculating surface temperatures on many bright objects, including Ganymede.

Surface temperatures are calculated for the major terrain types. Callisto is found to be somewhat warmer than Ganymede. The temperature difference between grooved and cratered terrain on Ganymede is small. Temperature variations are insufficient to account for the uneven distribution of bright ray craters. The distribution appears to result from a higher fraction of ice in the grooved terrain. Ganymede's polar caps are apparently very thin frost deposits. Ice sublimation on both bodies may leave a deposit of silicate grains at the top of the regolith, overlain by an extremely thin transient frost layer.

Global expansion expressed in Ganymede's grooved

terrain may have resulted from internal differentiation. Heating and formation of a silicate core would displace dense ice polymorphs deep in the interior to shallower levels, forming liquid water or ices with lower densities. A surface area increase of nearly 7% is possible during differentiation. Callisto should have been heated less than Ganymede, causing slower and perhaps less complete differentiation. Slower expansion would result in lower crustal stresses, and may have prevented grooved terrain formation on Callisto.

A model for the origin of grooved terrain is considered in which extension creates broad, downdropped rift zones in the crust that are filled with water or clean ice from below. With continued extension the ice deposits fracture, forming open fractures or long, narrow grabens. Degradation by mass-wasting and/or viscous relaxation produces the observed topography. Other features that may date from this period of Ganymede's history are two broad domes about 250 km in diameter and 2-2.5 km high. They are surrounded by secondary impact craters, and may have formed when large impacts caused liquid water vulcanism or isostatic upwarping of the crust.

BIOGRAPHICAL SKETCH

Steven Weldon Squyres was born January 9th, 1956, in Woodbury, New Jersey. He graduated from Cornell University with the degree of Bachelor of Arts in Geology in 1978. After completion of the Ph.D., he will continue to conduct research in planetary science at the NASA Ames Research Center.

ACKNOWLEDGMENTS

It has been my privilege and pleasure to have Dr. Joseph Veverka as my scientific advisor and personal friend through most of my years at Cornell. I hope to someday live up to the example he has set for me.

The other faculty members who have served on my committee, Drs. Arthur Bloom, Steven Ostro, Carl Sagan, and William Travers, have provided valuable help and encouragement.

A number of scientists outside Cornell have given me both their guidance and their hospitality. Most notable among these are Drs. Eugene Shoemaker and Laurence Soderblom at the USGS office in Flagstaff, Drs. E. Marc Parmentier and James Head at Brown University, and Dr. Bradford Smith and the other members of the Voyager Imaging Team.

Many other individuals have helped me, both scientifically and personally, through the last three years. At the risk of leaving many people out, thanks are due to Tina Bochicchio, Bonnie Buratti, Pat Clark, Dennis Costello, Margaret Dermott, Jay Goguen, Jean Kolva, Steve Lee, Leslie Pieri, Mary Roth, Jody Swann, Peter Thomas, Reid Thompson, and Joy Veverka.

Financial support for my graduate study at Cornell was provided by a National Science Foundation graduate fellowship and a Cornell University Andrew Dickson White fellowship. Additional research support came from NASA grant NSG 7156 and JPL contract 953616.

Finally, very special thanks to Pam Squyres for love and support when it was needed most.

TABLE OF CONTENTS

CHAPTER		page
1.	INTRODUCTION	387
	1.1 Purpose of the Thesis	387
	1.2 Discovery and Telescopic Study of Jupiter's Satellites	388
	1.3 The Voyager Mission	391
	1.4 Organization of the Thesis	392
2.	THE GEOLOGY OF GANYMEDE AND CALLISTO	396
	2.1 Introduction	396
	2.2 The Geology of Ganymede	396
	2.3 The Geology of Callisto	429
	2.4 Conclusions	432
3.	BROADBAND PHOTOMETRY OF SURFACE FEATURES	436
	3.1 Introduction	436
	3.2 Ganymede	436
	3.3 Callisto	468
	3.4 Discussion	490
4.	COLOR PHOTOMETRY OF SURFACE FEATURES	497
	4.1 Introduction	497
	4.2 Available Data	498
	4.3 Analysis	502
	4.4 Conclusions	517
5.	VARIATION OF ALBEDO WITH INCIDENCE ANGLE	522
	5.1 Introduction	522
	5.2 A(i) for Theoretical Surfaces	523
	5.3 A(i) for Real Surfaces	533
	5.4 Temperature Effects	538
	5.5 Conclusions	542

CHAPTER		page
6.	SURFACE TEMPERATURES AND FROST RETENTION	545
	6.1 Introduction	545
	6.2 Procedure	547
	6.3 Results	551
	6.4 Discussion	556
	6.5 Other Factors Affecting the Calculations	572
	6.6 Conclusions	574
7.	GROOVED TERRAIN AND DOME TOPOGRAPHY	575
	7.1 Introduction	575
	7.2 Procedure	575
	7.3 Results	584
	7.4 Discussion	600
8.	VOLUME CHANGES AND GROOVED TERRAIN ORIGIN	605
	8.1 Introduction	605
	8.2 Volume Change During Differentiation	607
	8.3 Volume Change During Refreezing	617
	8.4 Discussion	621
9.	GROOVED TERRAIN FORMATION ON GANYMEDE	629
	9.1 Introduction	629
	9.2 The Resurfacing Process	630
	9.3 The Groove Formation Process	632
	9.4 Discussion	650
10.	DOME FORMATION ON GANYMEDE	656
	10.1 Introduction	656
	10.2 Ice Vulcanism	660
	10.3 Isostatic Upwarping	669
	10.4 Discussion	674

CHAPTER page

11. SUMMARY 679

11.1 Introduction 679
11.2 Conclusions 679
11.3 Interpretations 681
11.4 Recommendations for Future Work . . 683

APPENDICES

A. PHOTOMETRIC TERMS 690

B. DERIVATION OF PHOTOCLINOMETRIC EQUATIONS FOR GENERALIZED SCATTERING GEOMETRY . . 697

C. DERIVATION OF FAILURE CRITERIA FOR A VISCOELASTIC CRUST SUBJECTED TO EXTENSION 702

REFERENCES 707

LIST OF TABLES

Table		page
1.1	Physical Properties of Ganymede, Callisto, and the Moon	389
3.1	Voyager Images Used for Ganymede and Callisto Photometry	438
3.2	Bright Craters on Ganymede	463
3.3	Bright Craters on Callisto	489
3.4	Summary of Photometric Results	491
3.5	Summary of Phase Curve Parameters	494
4.1	Voyager Images Used for Color Photometry	499
4.2	Relative Color Reflectance of Points on Ganymede	503
4.3	Fits to Ganymede Color Phase Curves . . .	508
4.4	Relative Color Reflectance of Points on Callisto	513
4.5	Fits to Callisto Color Phase Curves . . .	516
6.1	Calculated and Observed 21 Micron Brightness Temperatures	555
8.1	The Polymorphs of Ice	609

LIST OF FIGURES

Figure		page
Frontispiece	The Earth and Moon from Voyager 1	368
2.1	U.S.G.S. Preliminary Map of Ganymede	397
2.2	Ganymede at Low Resolution	398
2.3	Ganymede's Polar Caps	399
2.4	Ganymede: Cratered Terrain	402
2.5	Ganymede: Furrows in Cratered Terrain . . .	403
2.6	Ganymede: Single Sets of Grooved Terrain . .	405
2.7	Ganymede: Crosscutting Relationships in Grooved Terrain	406
2.8	Ganymede: Irregular Smooth Regions in Grooved Terrain	408
2.9	Ganymede: Smooth Swaths of Grooved Terrain	409
2.10	Ganymede: Smooth Region with Diffuse Margin	410
2.11	Ganymede: Bright Ray Crater	412
2.12	Ganymede: Dark Ray Craters	413
2.13	Ganymede: Raised Ejecta Deposits	414
2.14	Ganymede: Crater Palimpsest	415
2.15	Ganymede: A Dome	417
2.16	Geologic Map of Part of Ganymede	419
2.17	Ganymede: Strike-Slip Faulting	421
2.18	Ganymede: Truncation of Grooves against Narrow Groove Sets	422

Figure		page
2.19	Ganymede: Grooved Band with Matching Edges	423
2.20a	Ganymede: Strike-Slip Faulting--Evidence for Extension	424
2.20b	Ganymede: Strike-Slip Faulting--Evidence for Extension	425
2.21	Ganymede: Cut and Spread Impact Crater . . .	427
2.22	Ganymede: Possible Compressive Feature . . .	428
2.23	U.S.G.S. Preliminary Map of Callisto . . .	430
2.24	Heavily Cratered Surface of Callisto . . .	431
2.25	Callisto: Valhalla Ringed Impact Structure	433
2.26	Callisto: Valhalla Outer Rings	434
3.1	Voyager Clear Filter Spectral Reflectance .	439
3.2a	Variation of Brightness with Photometric Longitude: Ganymede Surface Features, Phase Angle 20°	442
3.2b	Variation of Brightness with Photometric Longitude: Ganymede Surface Features, Phase Angle 20°	443
3.2c	Variation of Brightness with Photometric Longitude: Ganymede Surface Features, Phase Angle 30°	444
3.2d	Variation of Brightness with Photometric Longitude: Ganymede Surface Features, Phase Angle 30°	445
3.3a	Variation of Brightness with Photometric Longitude: Grooved Terrain, Phase Angle 67°	446
3.3b	Variation of Brightness with Photometric Longitude: Grooved and Cratered Terrain, Phase Angle 89°	447

Figure		page
3.4	Points Selected for Photometric Analysis on Ganymede	448
3.5	Observed Surface Phase Functions, Cratered Terrain	450
3.6	Average Surface Phase Function, Cratered Terrain	451
3.7	Normal Reflectance, Cratered and Grooved Terrain	453
3.8	Observed Surface Phase Functions, Grooved Terrain	455
3.9	Average Surface Phase Function, Grooved Terrain	456
3.10	Variation of Brightness with Photometric Longitude: Polar Cap, Phase Angle 67°	458
3.11	Observed Surface Phase Functions, Polar Cap	459
3.12	Average Surface Phase Function, Polar Cap	460
3.13	Observed Surface Phase Functions, Bright Craters	464
3.14	Average Surface Phase Function, Bright Craters	465
3.15	Disc-Integrated Phase Function, Ganymede	467
3.16	Points Selected for Photometric Analysis on Callisto	470
3.17	Observed Surface Phase Functions, Callisto	471
3.18	Observed Surface Phase Functions, Callisto	472
3.19	Average Surface Phase Function, Callisto	473
3.20	Disc-Integrated Phase Function, Callisto	476
3.21	Normal Reflectance, Callisto	478

Figure		page
3.22a	Variation of Brightness with Photometric Longitude: Callisto Surface Features, Phase Angle 10°	479
3.22b	Variation of Brightness with Photometric Longitude: Callisto Surface Features, Phase Angle 10°	480
3.23a	Variation of Brightness with Photometric Longitude: Callisto, Phase Angle 35° . . .	481
3.23b	Variation of Brightness with Photometric Longitude: Callisto, Phase Angle 49° . . .	482
3.23c	Variation of Brightness with Photometric Longitude: Callisto, Phase Angle 75° . . .	483
3.24a	Variation of Brightness with Photometric Longitude: Callisto Craters, Phase Angle 10°	485
3.24b	Variation of Brightness with Photometric Longitude: Callisto Craters, Phase Angle 10°	486
3.25	Observed Surface Phase Functions, Callisto Craters	488
3.26	Summary of Observed Phase Curves	493
4.1	Points Selected for Color Photometric Analysis on Ganymede	500
4.2	Points Selected for Color Photometric Analysis on Callisto	501
4.3	Color Phase Curves, Ganymede Cratered Terrain	504
4.4	Color Phase Curves, Ganymede Grooved Terrain	505
4.5	Color Phase Curves, Ganymede Polar Caps . .	506
4.6	Color Phase Curves, Ganymede Bright Craters	507
4.7	Color Phase Curves, Ganymede Full Disc . . .	510

Figure		page
4.8	Individual Phase Curves, Ganymede and Callisto Bright Craters	512
4.9	Color Phase Curves, Callisto Cratered Terrain	514
4.10	Color Phase Curves, Callisto Bright Craters	515
4.11	Color Phase Curves, Callisto Full Disc . . .	518
5.1	Effects of Surface Phase Function on Variation of Albedo with Incidence Angle	526
5.2	Effects of Multiple Scattering on Variation of Albedo with Incidence Angle	529
5.3	Effects of Surface Roughness on Variation of Albedo with Incidence Angle	532
5.4	Variation of Albedo with Incidence Angle: MgO + Charcoal	534
5.5	Variation of Albedo with Incidence Angle: Moon, Ganymede, and Callisto	537
5.6	Variation of Albedo with Incidence Angle: Earth	539
5.7	Effects of Albedo Variation on Maximum Surface Temperature	541
5.8	Effects of Albedo Variation on Subsurface Temperature	543
6.1	Surface Temperatures on Ganymede and Callisto	552
6.2	Subsurface Temperatures on Ganymede and Callisto	553
6.3	Sublimation Rates on Ganymede and Callisto	557
6.4	Diurnal Mean Sublimation Rates	558

Figure		page
6.5	Distribution of Bright Ray Craters on Ganymede	559
6.6	Maps of Ganymede's Polar Caps	563
7.1	Angles Used for Photoclinometry	578
7.2	Averaging Technique for Photoclinometry . .	580
7.3	Removal of Surface Curvature from Topographic Profiles	581
7.4	Topographic Profile Across an Impact Crater	585
7.5	Grooved Terrain Topographic Profiles, Image 660J2-001	587
7.6	Grooved Terrain Topographic Profiles, Image 658J2-001	589
7.7	Grooved Terrain Topographic Profile, Image 578J2-001	591
7.8	Grooved Terrain Topographic Profile, Image 572J2-001	593
7.9	Grooved Terrain Topographic Profiles, No Vertical Exaggeration	595
7.10	Topographic Profiles Across a Surface Fracture	596
7.11	Topographic Profiles Across a Dome	598
7.12	Grooved Terrain with Broad, Flat Divides	603
8.1	Pressure-Temperature Phase Diagram of H_2O	608
8.2	Mean Density of H_2O in Internally Molten Ganymede and Callisto	612
8.3	Internal Structure of Cold, Undifferentiated Ganymede and Callisto	615

Figure		page
8.4	Calculated Surface Area Changes During Thermal Evolution	616
8.5	Surface Area Changes During Refreezing . . .	620
9.1	Strain History Used in Fracturing Calculations	635
9.2	Results of Viscoelastic Crust Fracture Calculations	637
9.3	Radiative Cooling of Fracture Walls with Time	640
9.4	Radiative Cooling of Fracture Walls: Effects of Geothermal Gradient	642
9.5	Experimental Viscous Relaxation of Extension Fractures	646
9.6	Experimental Viscous Relaxation of Grabens	648
9.7	Modification of an Extension Fracture by Mass-Wasting	651
9.8	Grooved Band Showing Evidence of Reflooding	652
9.9	Summary Diagram of Inferred Grooved Terrain Formation	655
10.1	Dome in Image 967J1+000	657
10.2	Distribution of Small Craters Around the Dome	658
10.3	Impact Crater in Grooved Terrain with a Secondary Field	659
10.4	Dome in Image 124J2-001	661
10.5	Cylindrical Conduit Used in Ice Vulcanism Model	664
10.6	Effects of Parameter Variations on Model Results	668

Figure		page
10.7	Cumulative Fracture Length Required for Fissure Eruption	670
10.8	Isostatic Upwarping of a Crater	671
10.9	Time Required for Isostatic Upwarping . . .	675
A.1	Definition of Intensity	691
A.2	Definition of Incidence, Emission, and Phase Angle	691
A.3	Definition of Photometric Latitude and Longitude	694
B.1	Coordinate System Used for Photoclinometry	698
C.1	Mohr Circle and Failure Envelope	704

CHAPTER 1

INTRODUCTION

1.1 Purpose of the Thesis

The solid planets and moons that exist with such diversity in our solar system may be simply divided into two fundamental classes based on their composition. One class consists of bodies composed primarily of rock and, in some cases, metal. Bodies in this class include Mercury, Venus, the Earth, the Moon, Mars, and Jupiter's moons Io and Europa. The other class consists of bodies made up largely of ice. Important bodies in this class are Jupiter's moons Ganymede and Callisto, Saturn's moons Mimas, Enceladus, Tethys, Dione, Rhea, and Titan, and probably also the moons of Uranus and Neptune, as well as the planet Pluto and its moon Charon.

Rocky solar system objects have been investigated in some detail. The Surveyor, Lunar Orbiter, and Apollo lunar explorations, the Mariner 10 mission to Mercury, the Mariner 9 and Viking missions to Mars, and years of geologic study of the Earth have provided large amounts of information about objects in this class. Until very recently, however, almost nothing was known about the morphology or evolution of any icy objects.

In March and July of 1979 the two Voyager spacecraft passed through the Jupiter system, transforming in a few days Jupiter's four large moons from small points of light to separate worlds that can be mapped and studied in great detail. Hundreds of high resolution images were obtained of the two icy moons, Ganymede and Callisto. These moons are important not only because they are the first icy bodies to be explored, but because they are among the largest such bodies in the solar system. Both are substantially larger than the Moon, and Ganymede is actually larger than Mercury. (The physical properties of Ganymede, Callisto, and the Moon are tabulated and compared in Table 1.1.) Only cloud-covered Titan and Neptune's unexplored moon Triton are of comparable size. Ganymede and Callisto are thus the two best examples of the important and previously unexplored class of icy planetary objects presently available for study. The broad goal of this thesis is to describe their morphology and understand their evolution using Voyager images.

1.2 Discovery and Telescopic Study of Jupiter's Satellites

On the night of January 7th, 1610, Galileo Galilei focused his newly constructed telescope on the planet Jupiter. He recorded on that night that the planet was accompanied by what appeared to be several faint stars.

TABLE 1.1 Physical Properties of Ganymede, Callisto, and the Moon*

	Ganymede	Callisto	Moon
Radius, km	2640	2420	1738
Mass, g	1.49×10^{26}	1.06×10^{26}	7.35×10^{25}
Density, g cm^{-3}	1.93	1.79	3.34
Surface gravity, g/g_{earth}	0.146	0.123	0.166
Mean orbital radius, km	1.07×10^{6}	1.88×10^{6}	3.84×10^{5}
Mean orbital radius, planetary radii	15.1	20.6	60.2
Orbital period, days	7.16	16.69	27.32
Rotation state	synchronous	synchronous	synchronous
Geometric albedo	0.43	0.19	0.12
Atmosphere	none	none	none

* Radii of Ganymede and Callisto are from Smith et al. (1979a), masses from Anderson et al. (1974), geometric albedos from Chapter 3 of this thesis.

When he observed Jupiter on the following night, however, he noted to his astonishment that the positions of the stars had changed. After several nights of observation, Galileo determined that the "stars" were in fact four objects orbiting Jupiter. He realized that he had discovered a smaller version of the solar system configuration that Copernicus had proposed some 80 years earlier. His observation provided the first strong support for the theory of a sun-centered planetary system. He was later forced by the religious leaders of his day to recant his views on the Copernican theory, but the four moons he discovered have come to be called the Galilean satellites. Simon Marius named the satellites Io, Europa, Ganymede, and Callisto, after lovers of Jupiter. He independently discovered them at about the same time as Galileo, but has perhaps unfairly not been similarly honored.

Considerable effort has been devoted to Earth-based observations of the Galilean satellites since Galileo's time. Useful reviews of this work have been presented by Morrison and Cruikshank (1974), Morrison and Burns (1976), and Johnson (1978). One of the first significant observations made was that the lightcurves of all the Galilean satellites vary exactly with their orbital periods (Stebbins, 1927). This observation shows that the satellites are tidally locked, with one face always

pointing toward Jupiter. For Ganymede, the hemisphere that leads in the orbit is slightly brighter than the trailing hemisphere, while the reverse is true for Callisto (Stebbins, 1927; Morrison and Morrison, 1977). Ganymede's overall brightness is more than twice that of Callisto. Their geometric albedos calculated from Earth-based observations are 0.43 ± 0.02 and 0.17 ± 0.02, respectively (Morrison and Morrison, 1977). The infrared reflectance spectra of both bodies show H_2O frost absorption features (Clark and McCord, 1980). The features are much more pronounced for Ganymede's spectrum, indicating that there is more frost on its surface than on Callisto's. Radii determined from telescopic observations and masses determined from mutual perturbations give densities of less than 2.0 g cm^{-3} for both bodies (Johnson, 1978, Table 1.1).

1.3 The Voyager Mission

Each of the two Voyager spacecraft carries a total of eleven instruments for investigating the planets, moons, rings, magnetospheres, and plasma environments of the jovian and saturnian systems. Along with the imaging system, these include a photopolarimeter, an infrared radiometer, an ultraviolet spectrometer, and several magnetometers, radio antennas, and charged particle detectors. The imaging system on each spacecraft consists of two slow scan selenium-sulfur vidicon cameras.

The fields of view of the wide angle and narrow angle cameras are 55.6 × 55.6 and 7.5 × 7.5 milliradians, respectively. Each camera is equipped with a variety of filters: clear, violet, blue, orange, green, ultraviolet, and, for the wide angle cameras, narrowband methane and sodium-D filters. An image frame consists of 800 × 800 picture elements (pixels), each assigned an 8-bit numerical data number (DN) ranging from 0 to 255 according to its brightness. Images are available in both print and numerical form.

As each Voyager spacecraft approached the Jupiter system, low resolution narrow angle images of Ganymede and Callisto were obtained at phase angles of about 10°-30°. During the near encounter, high resolution targeted mosaics of narrow angle images were obtained, along with wide angle images covering the full disc of each object at phase angles of up to about 120°. For both Ganymede and Callisto the Voyager 1 and 2 high resolution images covered opposite sides of the bodies. Closest approach to Ganymede was 115,000 km for Voyager 1 and 62,000 km for Voyager 2, giving a maximum narrow angle resolution of 0.6 km/pixel. For Callisto, closest approach was 126,000 km for Voyager 1 and 215,000 for Voyager 2, giving a maximum resolution of 1.2 km/pixel.

1.4 Organization of the Thesis

In this study a variety of techniques are used to

investigate the surface properties and geologic evolution of Ganymede and Callisto using the Voyager images.

Chapter 2 presents an overall description of the geology of the two bodies. Voyager images are used to define the principal geologic units on Ganymede and to describe and interpret its complex tectonic patterns. The simpler geology of Callisto is also described, and the two bodies are compared.

Chapters 3 and 4 describe the photometric properties of the surfaces of Ganymede and Callisto. In Chapter 3 the Voyager cameras are used as high spatial resolution photometers to investigate the photometric functions of surface features on the two bodies. The high resolution makes it possible to determine the photometric properties of individual terrain types, and the Voyager trajectories provide data at phase angles far higher than previously attainable. Chapter 4 uses color images to determine the dependence of the photometric properties on wavelength.

Chapter 5 is a theoretical discussion of the variation of albedo of planetary surfaces with solar incidence angle. This variation, which has long been observed for the surface of the Earth, is explained as a result of the photometric properties of most particulate surfaces. The effect is important for correct calculation of the surface temperatures of many solar system objects, including Ganymede.

Chapter 6 presents calculations of surface temperatures on Ganymede and Callisto. The calculated temperatures are used to estimate ice loss rates on the two bodies and to investigate the evolution of ice in their regoliths. They are also used to show that Ganymede's more extensive surface frost deposits probably indicate a substantial enrichment of the ice content of parts of its crust.

Chapter 7 makes use of the photometric properties determined in Chapter 3 to investigate the topography of Ganymede's tectonic features. The technique of photoclinometry, in which variations in the intensity of reflected light are used to determine slope angles, is employed to calculate topographic profiles across features in the highest resolution images.

Chapter 8 presents calculations of variations that would have occurred in the volume of Ganymede and Callisto as a result of internal phase changes. The phase changes involve liquid water and the many polymorphs of ice, and may have caused a global expansion responsible for the pervasive tectonic features on Ganymede. The chapter also discusses factors that may have prevented formation of similar features on Callisto.

Chapter 9 presents a more detailed investigation of the geologic processes responsible for the formation of Ganymede's tectonic features. The observational

constraints on the processes are presented and their implications are discussed. Numerical calculations are used to investigate the nature and depth of fractures that could form in Ganymede's crust. Experiments that investigate the degradation of surface features created by fracturing are discussed.

Chapter 10 presents evidence concerning two unusual dome-shaped features on Ganymede. Models for their formation by ice vulcanism or isostatic upwarping of impact craters are presented. Calculations are performed that constrain the types of vulcanism and upwarping possible.

Chapter 11 is a summary of conclusions, interpretations and recommendations for future work.

CHAPTER 2

THE GEOLOGY OF GANYMEDE AND CALLISTO

2.1 Introduction

The detailed study of any distant solar system object begins with careful examination of spacecraft images. In this chapter the Voyager images of Ganymede and Callisto are used to describe the morphology of these bodies and to provide an overall framework for the rest of the study. The principal geologic units and complex tectonic patterns on Ganymede are shown and described. The morphology of Callisto is also discussed, and a comparison is made between the two bodies.

2.2 The Geology of Ganymede

The U.S. Geological Survey pictorial map of Ganymede is shown in Figure 2.1. Low resolution Voyager images of Ganymede show it to have two principal types of terrain, one dark and one bright (Fig. 2.2). Each covers about half of the surface. The dark terrain is in roughly polygonal regions that are divided and separated by bands of bright terrain. Superimposed on both of these units at the poles are bright polar caps apparently consisting of frost deposits (Fig. 2.3). The dark and bright terrains are

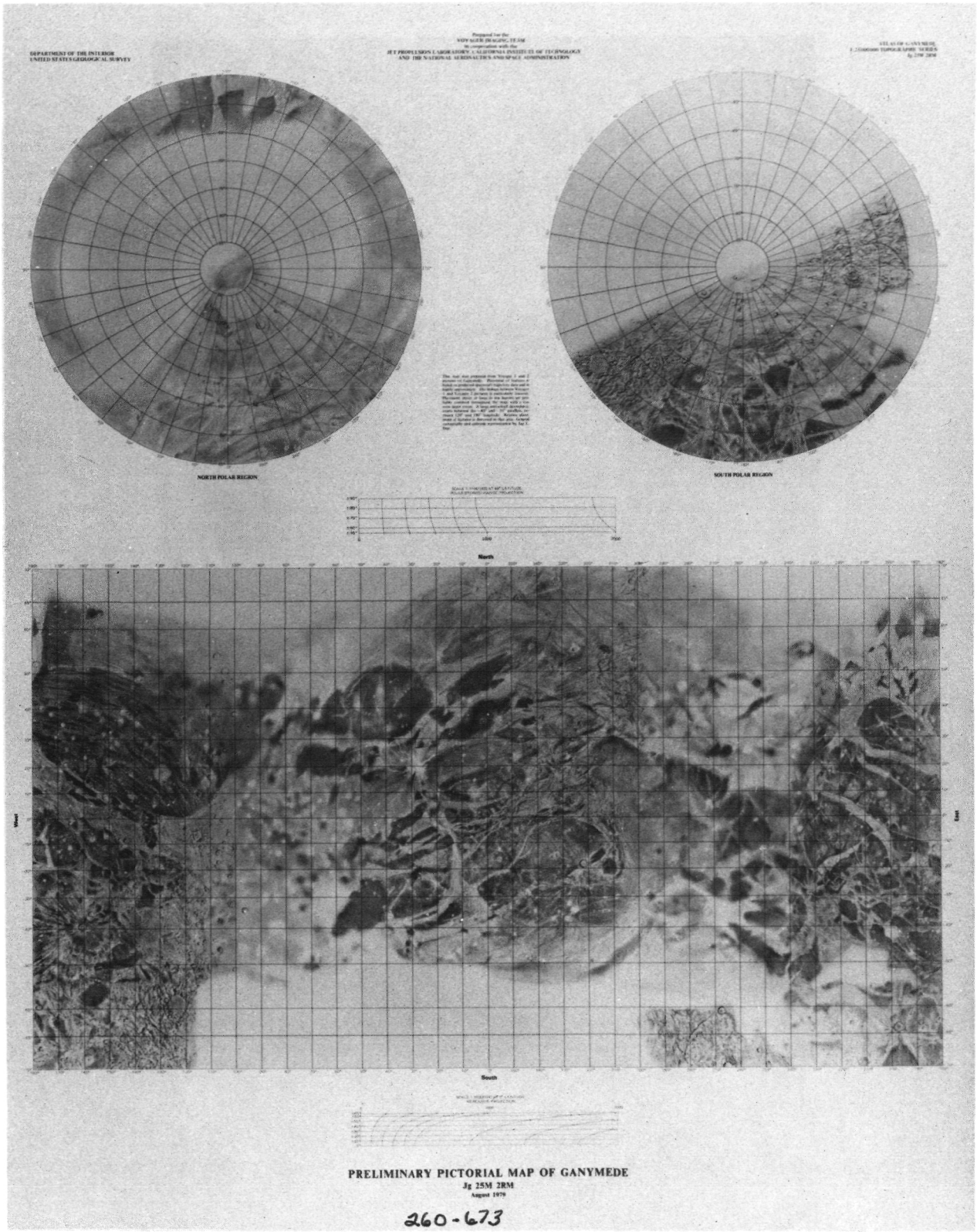


FIGURE 2.1. U.S. Geological Survey preliminary (uncontrolled) pictorial map of Ganymede (in map pocket at back of thesis).

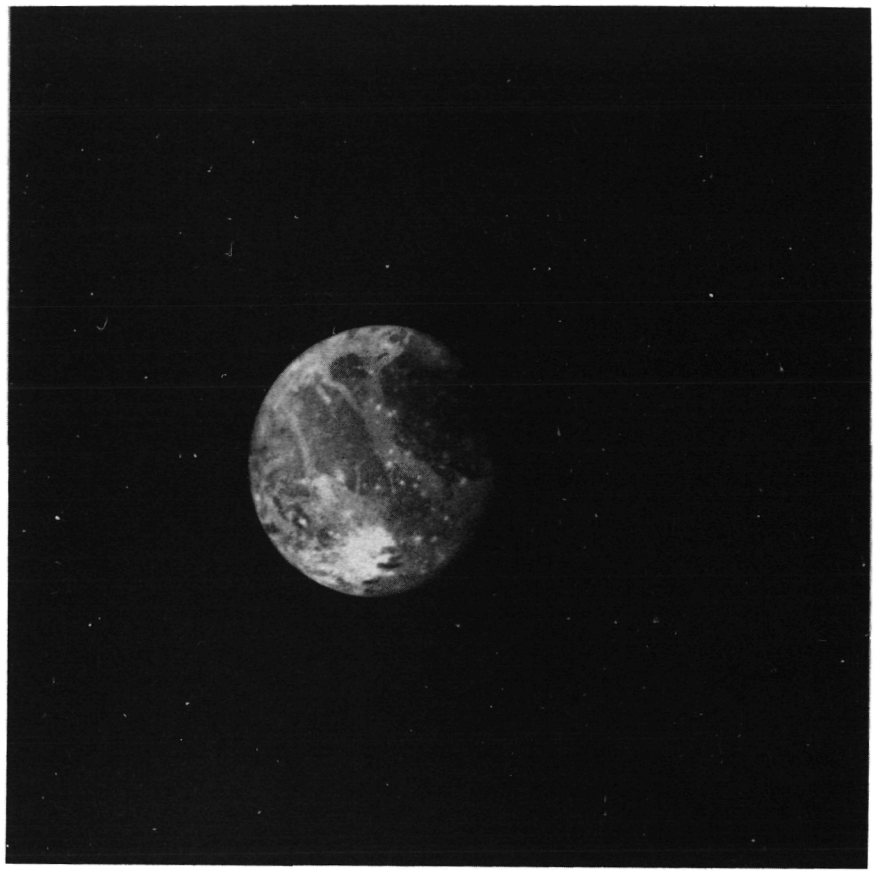


FIGURE 2.2. Ganymede at low resolution, showing polygons of dark terrain separated by brighter bands (image 109J2-001).



FIGURE 2.3. An image of Ganymede, showing bright polar frost deposits.

probably distinct lithologic units. These two units were named "cratered terrain" and "grooved terrain" respectively by Smith et al. (1979a). These names were chosen because long narrow grooves are the dominant structures in the brighter unit, while impact craters are the dominant structures in the darker unit. In keeping with normal conventions, all the units described and mapped in this thesis are lithologic rather than structural or geomorphic. The names "cratered terrain" and "grooved terrain" have been retained here for these two major units for consistency with established literature. It must be stressed, however, that these terms as used in this thesis are lithologic, not structural or geomorphic, as grooves are sometimes observed in cratered terrain, and craters are common in grooved terrain.

Parts of the grooved terrain unit possess many closely-spaced grooves, while others are free of grooves. For this reason it is sometimes convenient for descriptive purposes to divide the lithologic unit "grooved terrain" into the two morphologic types, "grooved regions" and "smooth regions." There is no evidence for any lithologic distinction between these two morphologic types, however, and they are not considered or mapped as separate units.

2.2.1 Cratered Terrain

High resolution images of the cratered terrain show

it to be dark, hummocky, and heavily cratered (Fig. 2.4). The craters show a continuum of preservation, from forms similar to fresh lunar craters to highly degraded, indistinct circular albedo markings. This continuum in part probably reflects the relaxation of crater topography with time due to cold viscous flow of the ice-rich crust (Johnson and McGetchin, 1973; Smith et al., 1979a). The principal morphologic difference between fresh craters on Ganymede and the Moon is the high incidence of central pits in craters on Ganymede larger than about 40 km (Shoemaker et al., 1981). The high crater density in the cratered terrain suggests that it dates from the heavy terminal bombardment phase of solar system evolution that ended about 4 b.y.a. (Smith et al., 1979a). A comprehensive study of impact craters on Ganymede and Callisto is currently being conducted by Passey (Passey et al., 1980, and work in progress). Detailed work on impact craters is therefore not included in this thesis.

Many regions of cratered terrain have a distinct linear texture consisting of subparallel shallow furrows (Fig. 2.5). These furrows range from distinct to barely discernible, and where well-preserved show irregular scalloped edges. Craters are often superimposed on furrows, but there are no clear instances of furrows cutting craters. The furrows are thus some of the oldest features preserved on Ganymede.

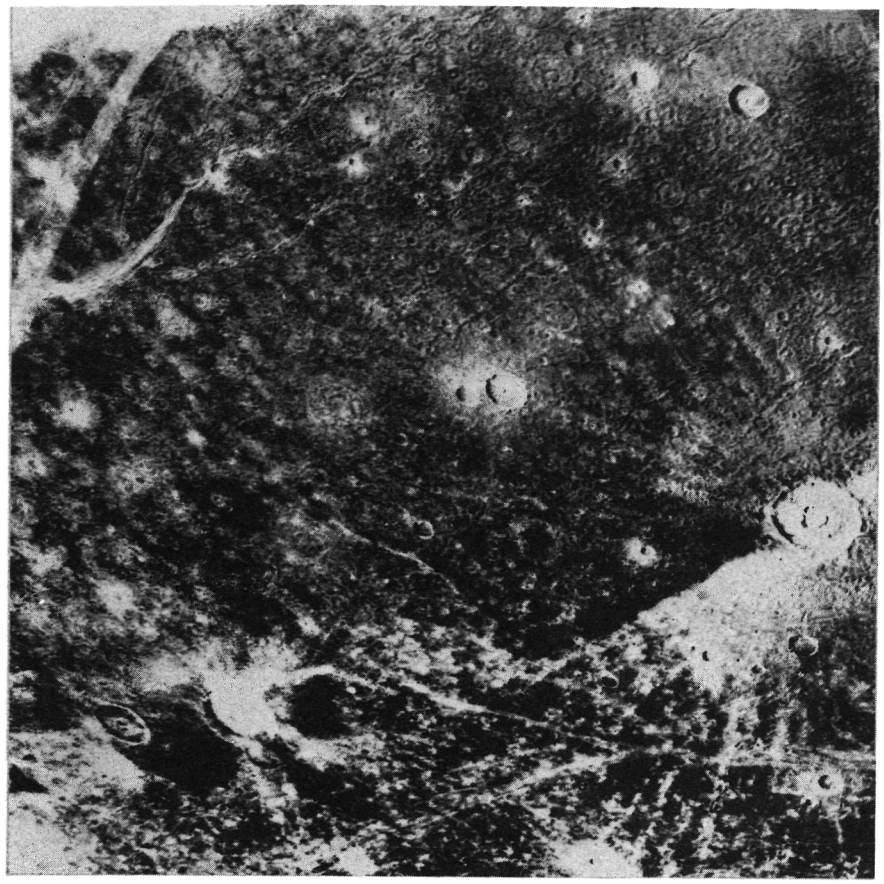


FIGURE 2.4. Nicholson Regio, a typical area of cratered terrain (scale across image = 1140 km; image centered at ∿ -15° lat., 35° long; image 939J1+000).

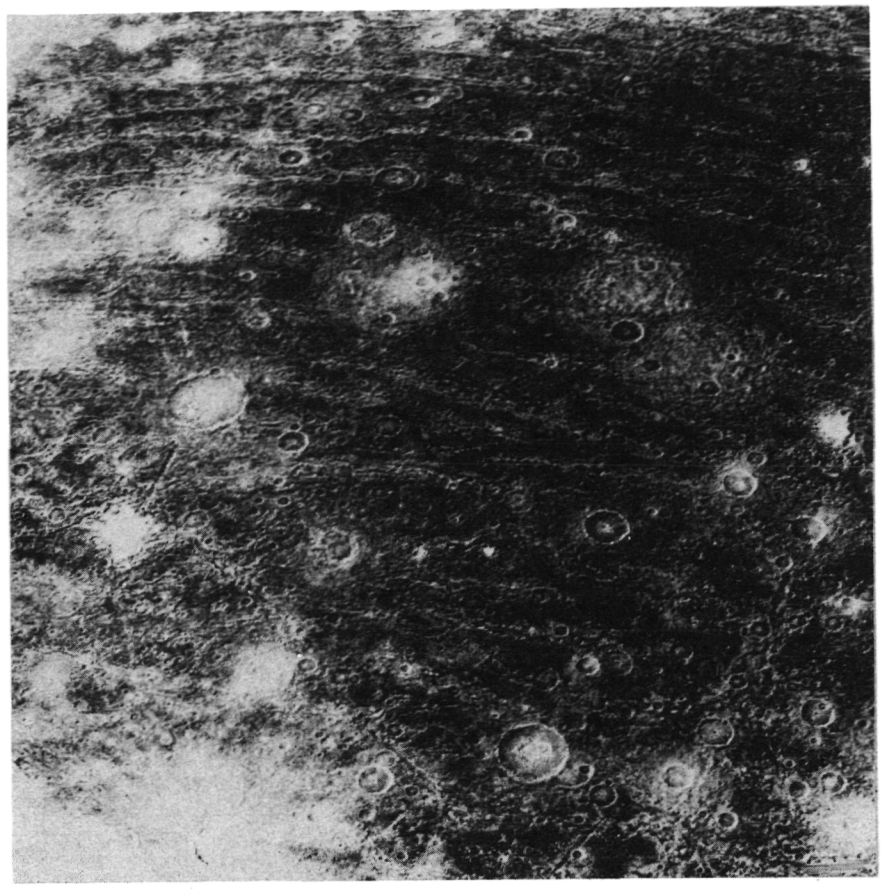


FIGURE 2.5. Furrows in the cratered terrain, Galileo Regio (scale across image = 950 km; image centered at ∿ 35° lat., 160° long; image 449J2-001).

2.2.2 Grooved Terrain

2.2.2.1 Grooved regions

Most of the surface of the grooved terrain unit is characterized by a complex pattern of long, narrow topographic depressions first called grooves by Smith et al. (1979a). They are generally a few km wide, and often hundreds of km long. Grooves terminate by merging, gradual shallowing, or abrupt truncation against other grooves or other structural features. They are often closely spaced in subparallel sets that may be up to several hundred km wide. The sets are curvilinear and may occur singly (Fig. 2.6) or in complex crosscutting relationships (Fig. 2.7). The grooves that mark set boundaries are often particularly prominent, especially where they lie at the boundary between grooved and cratered terrain. Most contacts between grooved and cratered terrain are marked by a distinct groove or groove set. Solitary grooves are also observed, and may be straight or meandering. Solitary grooves commonly extend into regions of cratered terrain (Fig. 2.6), where they may lie parallel to or merge with the ancient furrows.

2.2.2.2 Smooth regions

Some areas of the grooved terrain unit have no grooves, and at the maximum Voyager resolution of about 600 m per picture element appear quite smooth even under very low angle illumination. Smooth regions may occur as

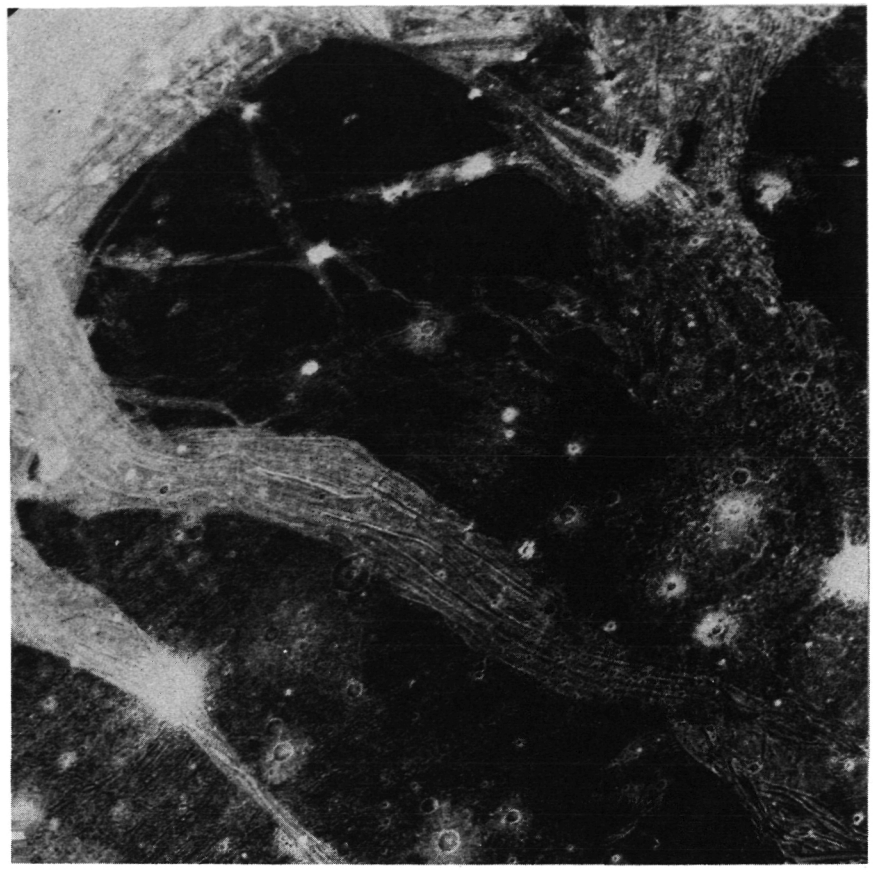


FIGURE 2.6. Single sets of grooved terrain, Anshar, Mashu, and Uruk Sulci. Also note numerous solitary grooves in the cratered terrain (scale across image = 1250 km; image centered at ∿ 25° lat., 195° long.; image 370J2-001).

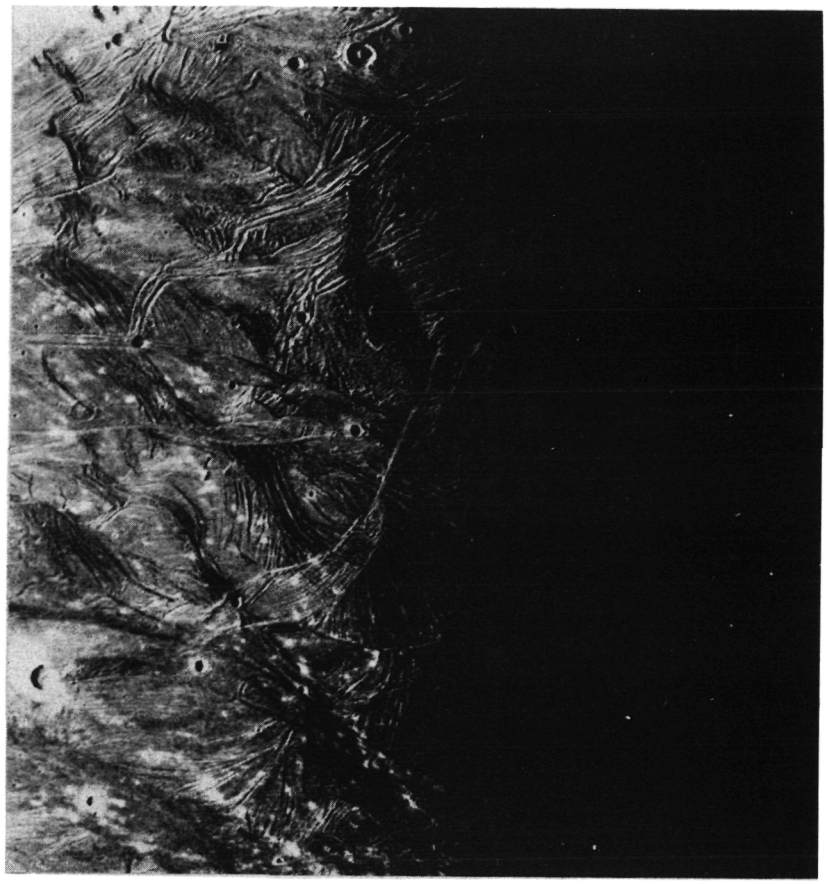


FIGURE 2.7. Complex crosscutting relationships in the grooved terrain, Nun Sulci (scale across image = 980 km; image centered at ∿ 45° lat., 300° long.; image 979J1+000).

irregularly-shaped groove-free patches in areas that are otherwise dominated by a complex pattern of grooves (Fig. 2.8). They also occur as long curvilinear swaths with geometry similar to the groove sets (Fig. 2.9). Smooth swaths and regions often have very sharp boundaries. These boundaries may be marked only by an abrupt transition to the hummocky texture and lower albedo of the cratered terrain, or may be marked by solitary grooves. A few smooth regions have very diffuse, indistinct boundaries transitional to grooved regions or cratered terrain (Fig. 2.10).

2.2.2.3 Crater densities

The density of impact craters in the grooved terrain is lower and more variable than in the cratered terrain. Preliminary crater counts suggest that grooved terrain formation began near the end of terminal bombardment and continued for one hundred to perhaps a few hundred m.y. (Smith et al., 1979b). Craters in the grooved terrain are deeper and more fresh than those in the cratered terrain, suggesting an increase in crustal viscosity at or soon after the time of grooved terrain formation (Shoemaker et al., 1981).

2.2.3 Impact Craters

Four distinct types of deposits are observed associated with craters on Ganymede: bright rays, dark rays, raised ejecta, and crater palimpsests.

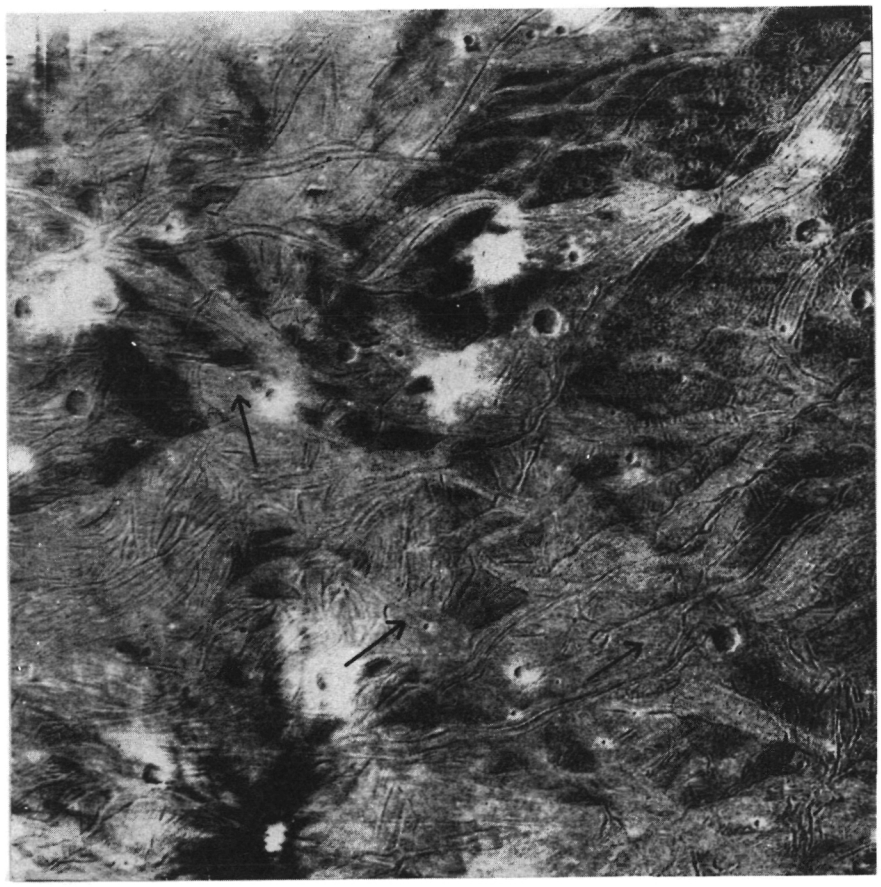


FIGURE 2.8. Irregular smooth regions in the grooved terrain, Mysia Sulci (scale across image = 1060 km; image centered at ∿ 20° lat., 330° long.; image 957J1+000).

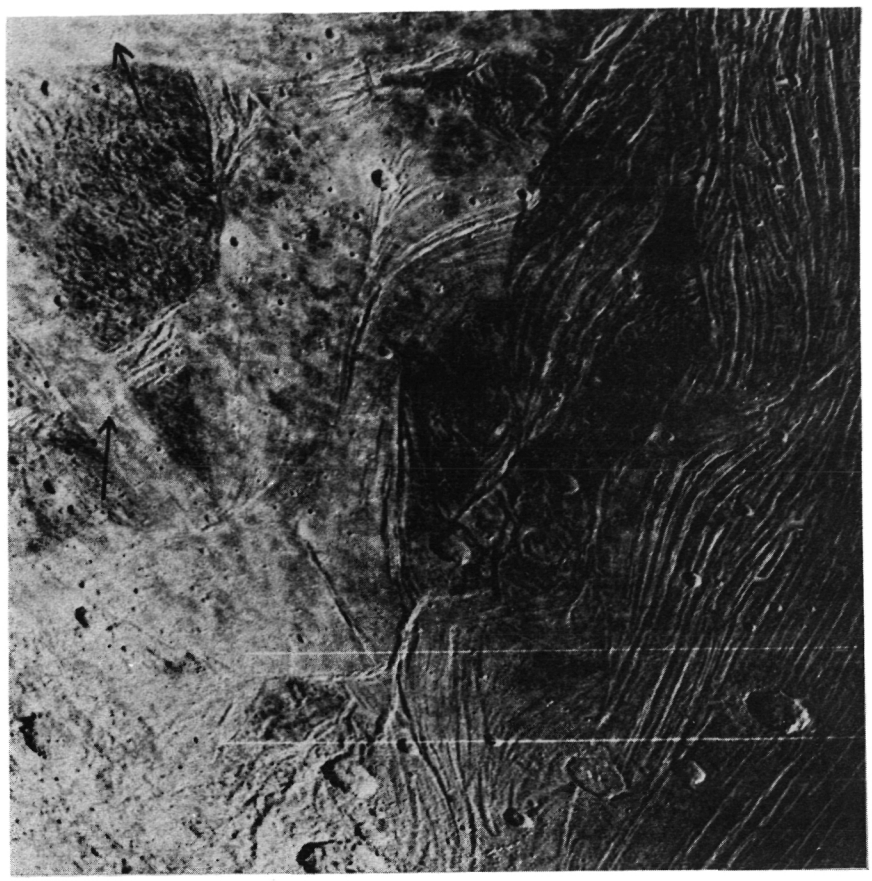


FIGURE 2.9. Curvilinear smooth swaths of grooved terrain (scale across image = 450 km; image centered at ∿ -75° lat., 200° long.; image 672J2-001).

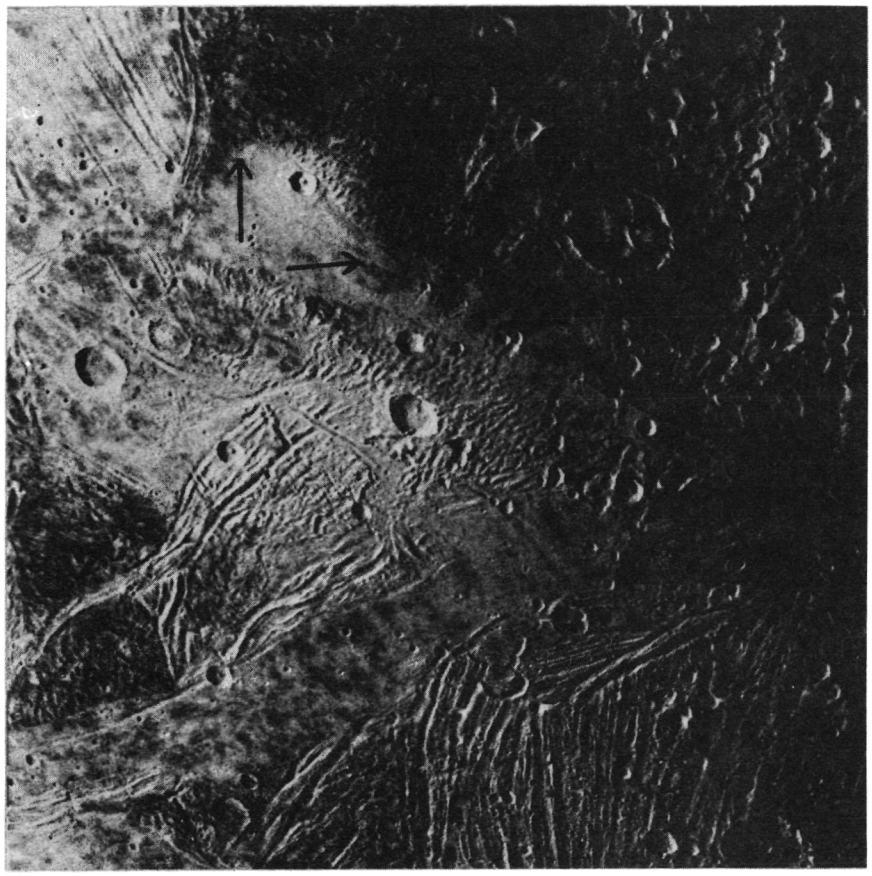


FIGURE 2.10. Smooth region with an indistinct, diffuse transition to cratered terrain (scale across image = 440 km; image centered at ∿ -75° lat., 150° long.; image 658J2-001).

High albedo rays similar to those observed with some lunar craters are common on Ganymede (Fig. 2.11). They probably are relatively thin deposits of ice excavated by impact events and deposited ballistically on the surface. Dark rays are also observed (Fig. 2.12), but are considerably less common and generally less extensive than bright rays. The dark rays may form when impacts penetrate through a thin, high albedo surface layer and excavate darker material from below.

Deposits of ejecta that are distinctly raised above the surrounding terrain are observed with some craters, particularly in the grooved terrain (Fig. 2.13). The deposits have a hummocky surface, extend about one crater radius outward from the rim, and are often bounded by a crudely lobate scarp. The raised nature of the deposits indicates a thickness of as much as a few hundred meters, though in some cases the topography of buried grooves is still apparent through the deposits.

Circular deposits of relatively high albedo material in the cratered terrain have been called crater palimpsests by Smith et al. (1979a) (Fig. 2.14). They have been interpreted as the remains of large craters that have lost their topography by viscous relaxation of the crust. In a few instances the crater rim is still barely visible, and has a diameter about one-half to one-third of that of the palimpsest. This relationship suggests that the edge of

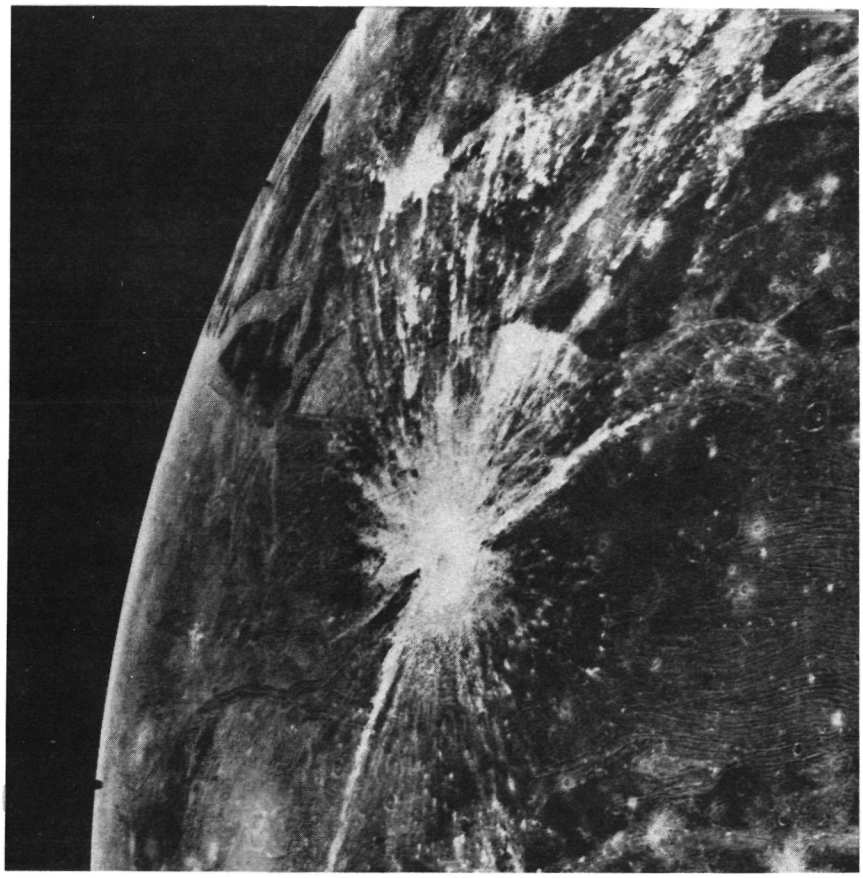


FIGURE 2.11. A large bright ray crater, Tros, in Phrygia Sulcus (scale across image = 1320 km; image centered at ∿ 25° lat., 25° long.; image 899J1+000).



FIGURE 2.12. Dark ray craters (scale across image = 1250 km; image centered at ∿ 10° lat., 230° long.; image 374J2-001).

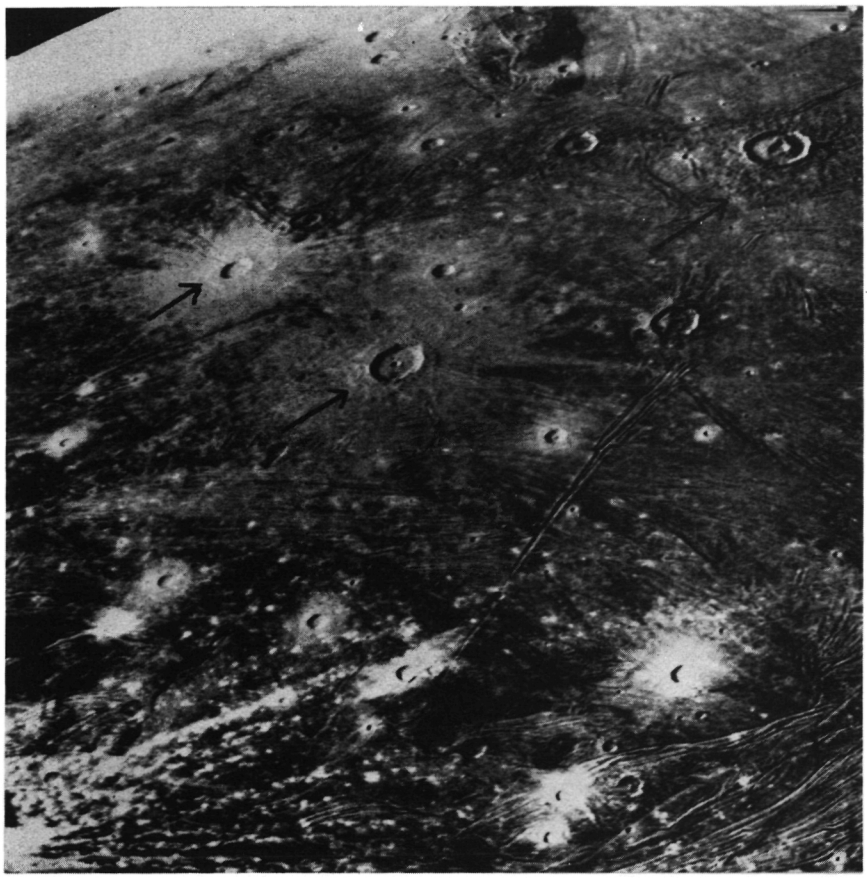


FIGURE 2.13. Craters with raised ejecta deposits, Sebek, Achelous, and Kishar (scale across image = 970 km; image centered at ∿ 65° lat., 340° long.; image 985J1+000).

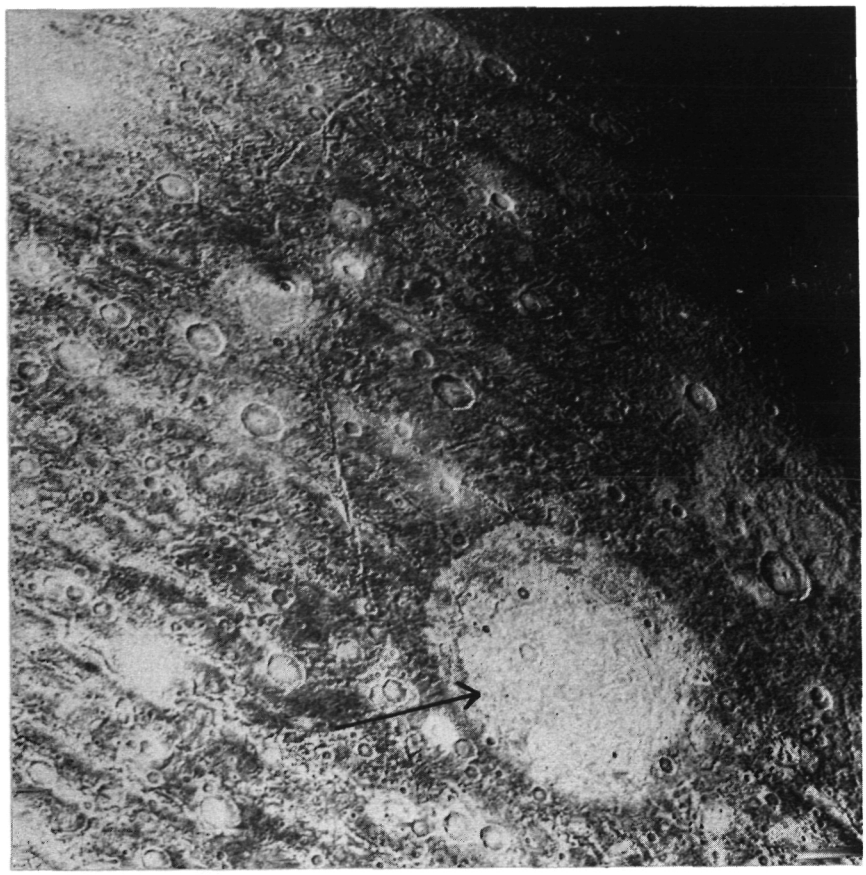


FIGURE 2.14. Crater palimpsest in Galileo Regio (scale across image = 930 km; image centered at ∿ 25° lat., 130° long.; image 455J2-001).

the observed palimpsest might mark the limit of continuous ejecta from the original crater (Shoemaker et al., 1981).

One final type of material is observed that may be associated with impact craters. It forms broad, circular, gently sloping topographic domes, and is here called dome material (Fig. 2.15). Only two domes have been positively identified in Voyager images. The one observed at high resolution is surrounded by a dense field of small pits closely resembling a secondary crater field. The circularity and apparent secondary field may indicate that emplacement of the dome material was associated with an impact event, although there is no trace of any crater structure. Domes are distinguished from palimpsests by their elevation above the surrounding topography.

2.2.4 Polar Caps

High albedo deposits that appear nearly as bright as the brightest ray craters are observed near Ganymede's poles in full-disc images (Fig. 2.3). At high resolution, however, areas within these bright regions (for example, Figs. 2.9, 2.10, and 2.13) show no morphologic characteristics that distinguish them from equatorial regions, indicating that the deposits must be fairly thin. In fact, the deposits are thin enough that the albedo contrast between the underlying grooved and cratered terrain may still be recognized in high resolution images. Because the caps



FIGURE 2.15. A dome (scale across image = 1020 km; image centered at ∿ 35° lat., 330° long.; image 967J1+000).

are very thin and are not mappable at high resolution, they are not considered distinct geologic units here. Their nature and origin are discussed more fully in Chapter 6.

2.2.5 Geologic Mapping

Figure 2.16 is a geologic map of part of Ganymede compiled from Voyager 1 images, showing the principal geologic units and the structure of the grooved terrain. The map area is the northern half of Ganymede's Jupiter-facing hemisphere. It is one section of a four-part preliminary geologic map of Ganymede to be published by Shoemaker et al. (1981). Lines in the grooved terrain show the boundaries of sets of subparallel grooves. Crater deposits (bright rays, dark rays, raised ejecta, and palimpsests) are only mapped if they exceed 100 km in diameter. The base is the U.S.G.S. preliminary mercator projection pictorial map of Ganymede. Position errors equivalent to as much as ten degrees of equatorial longitude may be present on this base.

2.2.6 Tectonic Patterns

The complex organized structure of the grooved terrain probably indicates a tectonic origin. If this interpretation is correct, there are three possible stress regimes that could account for the grooved terrain structure: shear, extension, and compression.

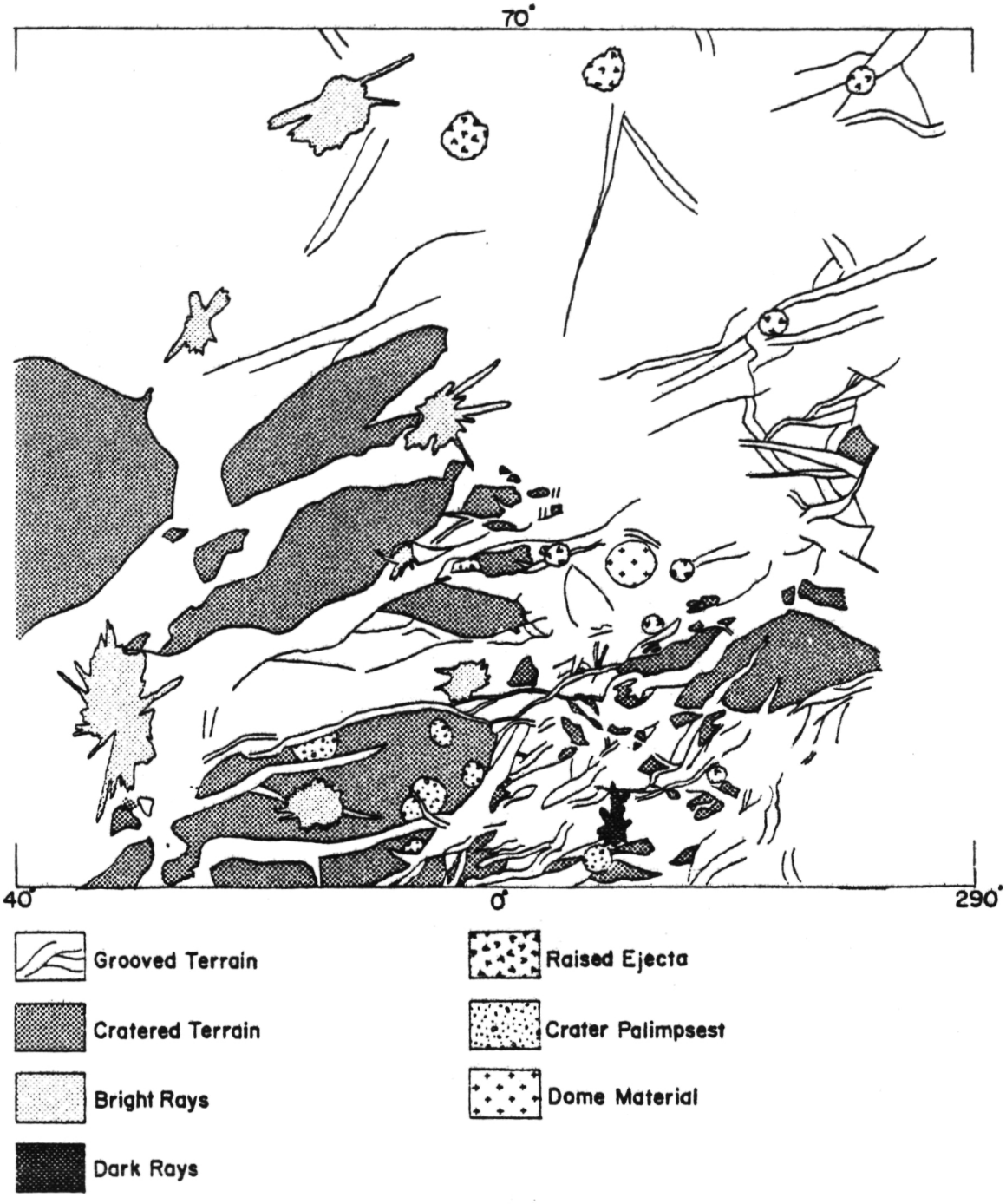


FIGURE 2.16. Geologic map of the northern part of Ganymede's Jupiter-facing hemisphere. The base is the U.S.G.S. mercator projection preliminary pictorial map (Fig. 2.1).

The clearest evidence for shear is lateral offset of recognizable features along a linear structure. Several groove sets appear offset along narrow shear zones (Fig. 2.17). In each case the offset is small, generally less than 100 km. Another observation that could perhaps be interpreted as evidence for shear is that well-developed groove sets commonly strike into and are truncated against narrow groove sets or single grooves (Fig. 2.18). While this situation could arise from large scale shear along the truncating grooves, it is always impossible in such cases to identify the "other half" of the truncated structure along the far side of the prospective shear zone. The clear evidence for shear is thus limited to a few instances of small offset.

There is considerable evidence that the grooved terrain resulted from extension perpendicular to the trend of the grooves. The opposite sides of some grooved terrain bands match closely, suggesting formation by spreading and creation of new crust (Fig. 2.19). Many grooved terrain bands have sharp terminations at one or both ends, suggesting formation as a propagating extensional fracture in the crust. In several cases, strike-slip faults cut grooved terrain obliquely (Fig. 2.20). If the stress field causing the inferred faulting had the same general orientation as that forming the grooves, the fault trends and offsets indicate a maximum extensional

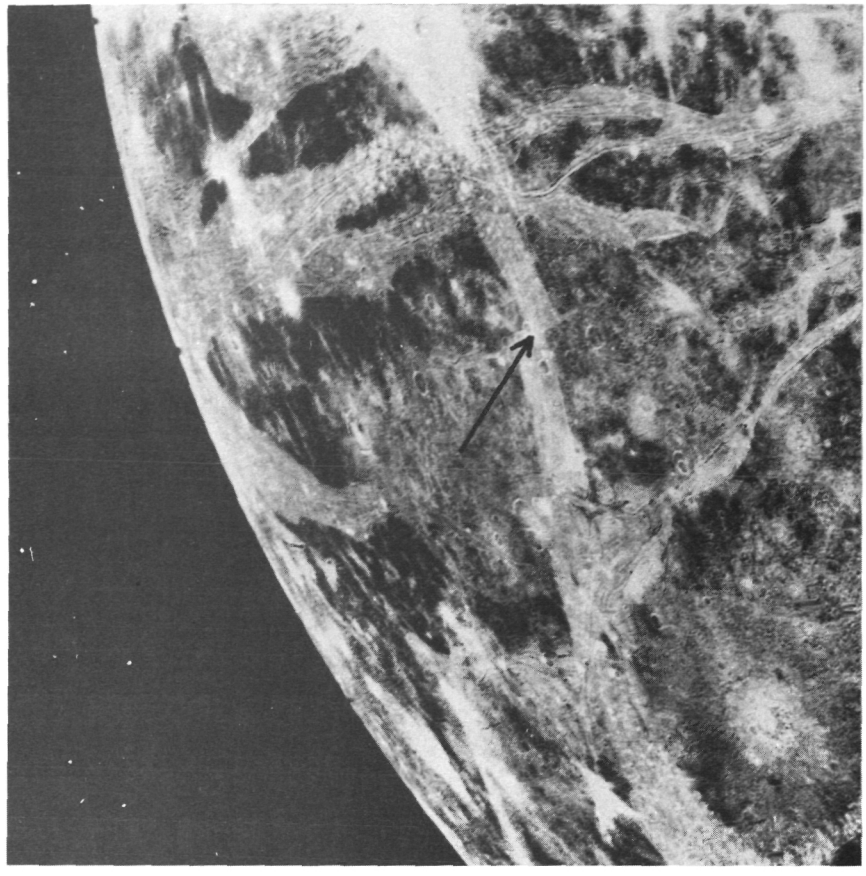


FIGURE 2.17. Lateral offset along a narrow shear zone cutting Dardanus Sulcus (scale across image = 1220 km; image centered at ∿ -15° lat., 15° long.; image 921J1+000).



FIGURE 2.18. Parallel grooves truncated against a single groove or groove set in Uruk Sulcus (scale across image = 860 km; image centered at ∿ 0° lat., 150° long.; image 473J2-001).

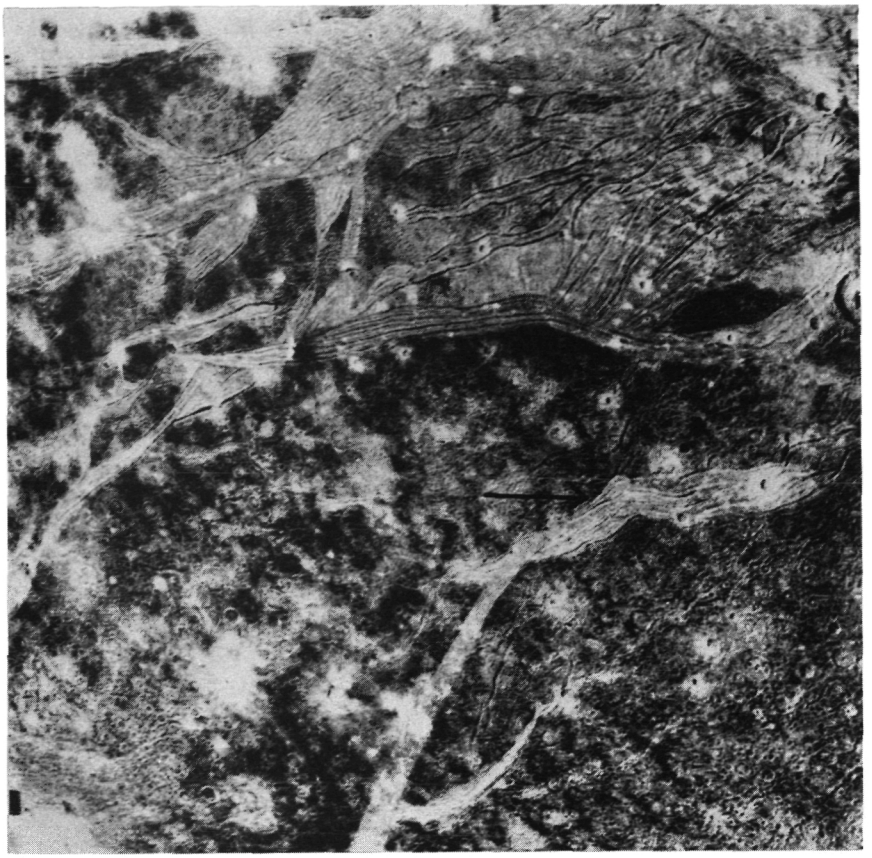


FIGURE 2.19. Opposite sides of a groove band that match closely, cutting across Nicholson Regio (scale across image = 1200 km; image centered at ∿ 0° lat., 345° long.; image 923J1+000).

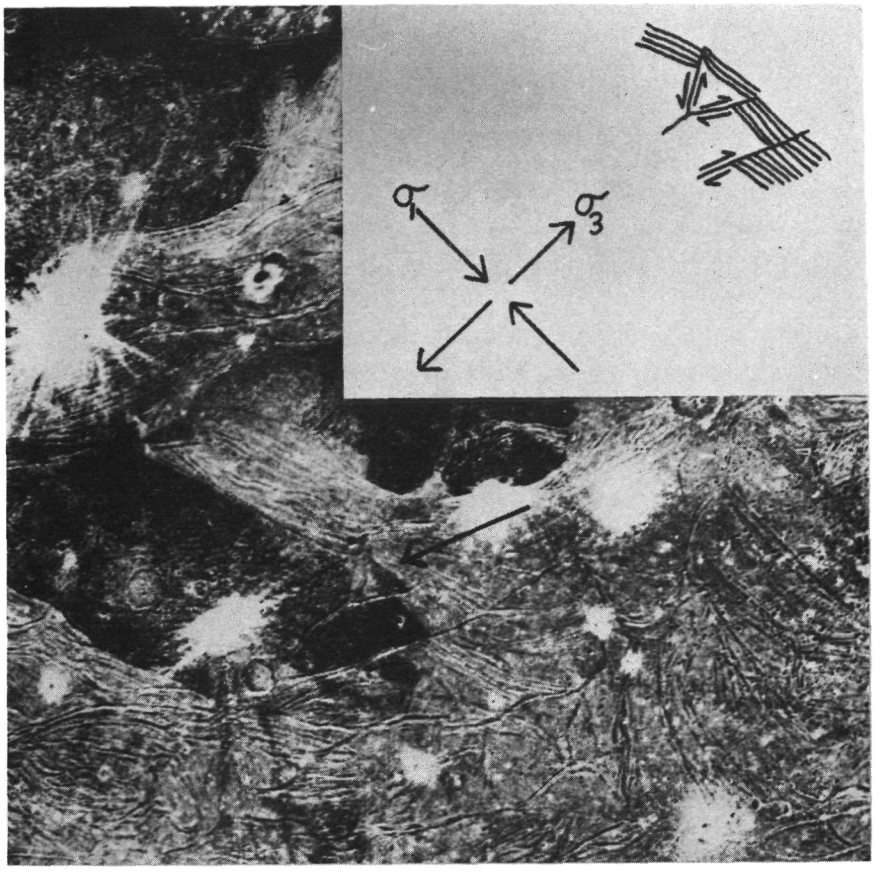


FIGURE 2.20a. Grooved terrain cut by strike-slip faults. In all cases the inferred orientation of the maximum extensional stress is perpendicular to the trend of the grooves (scale across image = 1030 km; image centered at ∿ 35° lat., 345° long.; image 965J1+000).

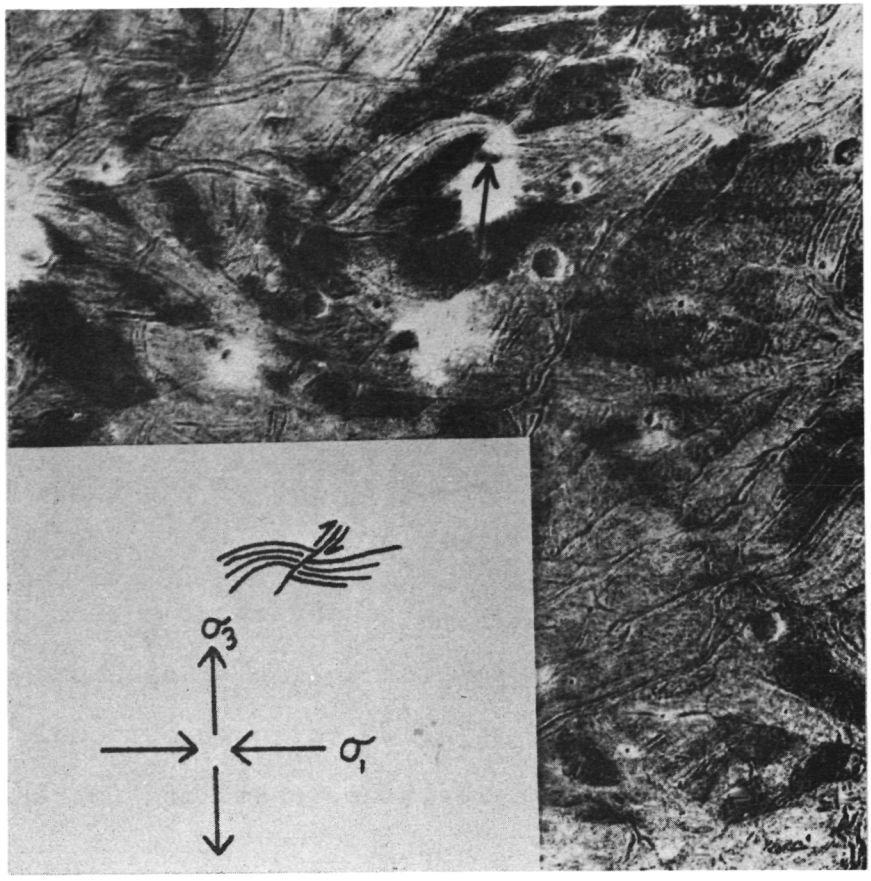


FIGURE 2.20b. Grooved terrain cut by a strike-slip fault. The inferred orientation of the maximum extensional stress is perpendicular to the trend of the grooves (scale across image = 1060 km; image centered at ∿ 20° lat., 330° long.; image 957J1+000).

stress perpendicular to the grooves. Finally, the negative relief of the grooves provides strong evidence for extension and fracture of a brittle surface layer.

The clearest evidence for extension would be the separation and spreading of surface features such as impact craters. Only one instance of clear spreading of a crater has been found (Fig. 2.21). Many craters are truncated by grooved terrain bands, but no trace of the rest of the crater is ever observed on the far side of the band. While the grooves seem to result from extension, the actual amount of spreading involved in formation of a band of grooved terrain must be a small fraction of the band width.

There is very little evidence for compressional deformation on Ganymede. No features resembling terrestrial thrust faults or subduction zones, lunar wrinkle ridges, or mercurian lobate scarps have been observed. The topographic symmetry of the grooves argues against a thrust faulting origin, and the negative relief argues against formation by folding. One feature superficially resembling a fold belt has been identified, however (Fig. 2.22). Unlike most other groove sets, it has a highly variable width. Its boundaries are marked by ridges rather than grooves, and remnants of an older grooved structure are still visible through the principal structure. It is the most likely possibility for a compressive feature on



FIGURE 2.21. An impact crater cut and spread by a narrow irregular feature (scale across image = 1150 km; image centered at ∿ -20° lat., 165° long.; image 395J2-001).

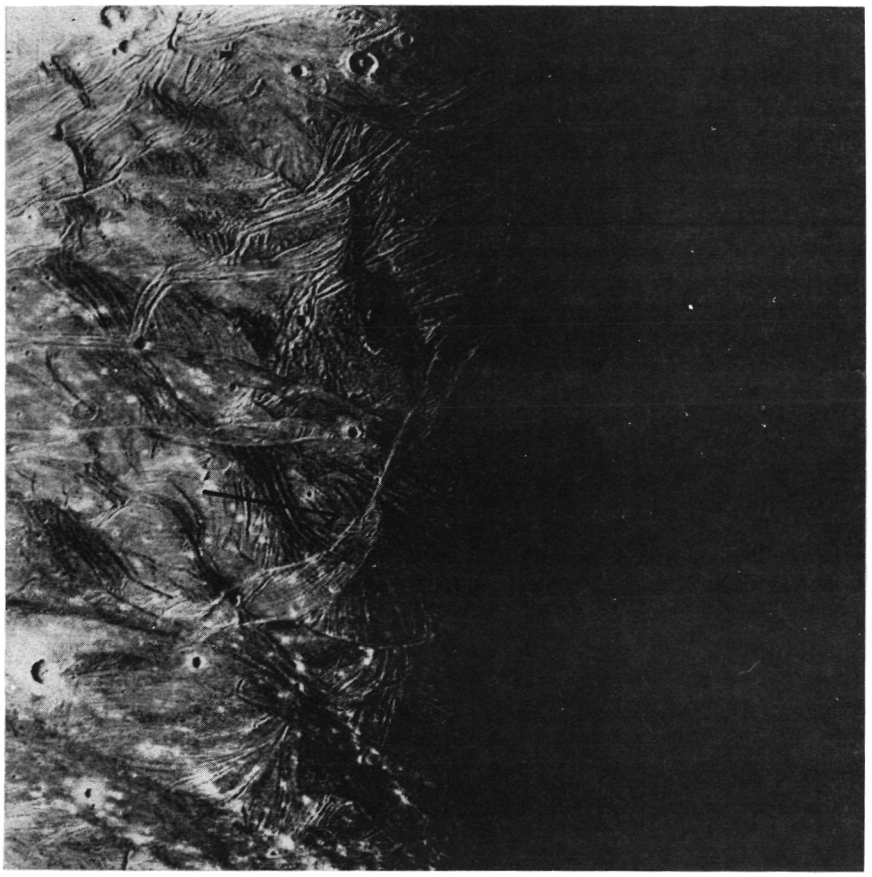


FIGURE 2.22. An unusual raised feature that superficially resembles a fold belt. This is probably the best prospect for a compressional feature on Ganymede (scale across image = 950 km; image centered at ∿ 35° lat., 300° long.; image 979J1+000).

Ganymede. In general, however, evidence for compression on Ganymede is very weak.

The interpretation of grooved terrain formation as primarily extensional deformation may lead to some interesting interpretations regarding the observed truncation relationships. Many groove sets end abruptly against a single groove or narrow groove set. The truncating groove or groove set may actually be a shear margin in these cases, with spreading only occurring on one side of the margin. This style of faulting would be unique to Ganymede in the solar system.

2.3 The Geology of Callisto

The U.S. Geological Survey pictorial map of Callisto is shown in Figure 2.23. Callisto is one of the most uniformly heavily cratered objects observed in the solar system (Fig. 2.24). The surface is dark and nearly saturated with impact craters. The craters have subdued topography and a maximum diameter of about 100 km, indicating viscous relaxation of relief as in the case of Ganymede. Many craters appear as bright spots, and only a few have extremely faint ray systems. There are no bright ray systems like those observed on Ganymede, however, and no polar caps. There is also no photogeologic evidence of tectonic activity on Callisto.

The most interesting features observed on Callisto

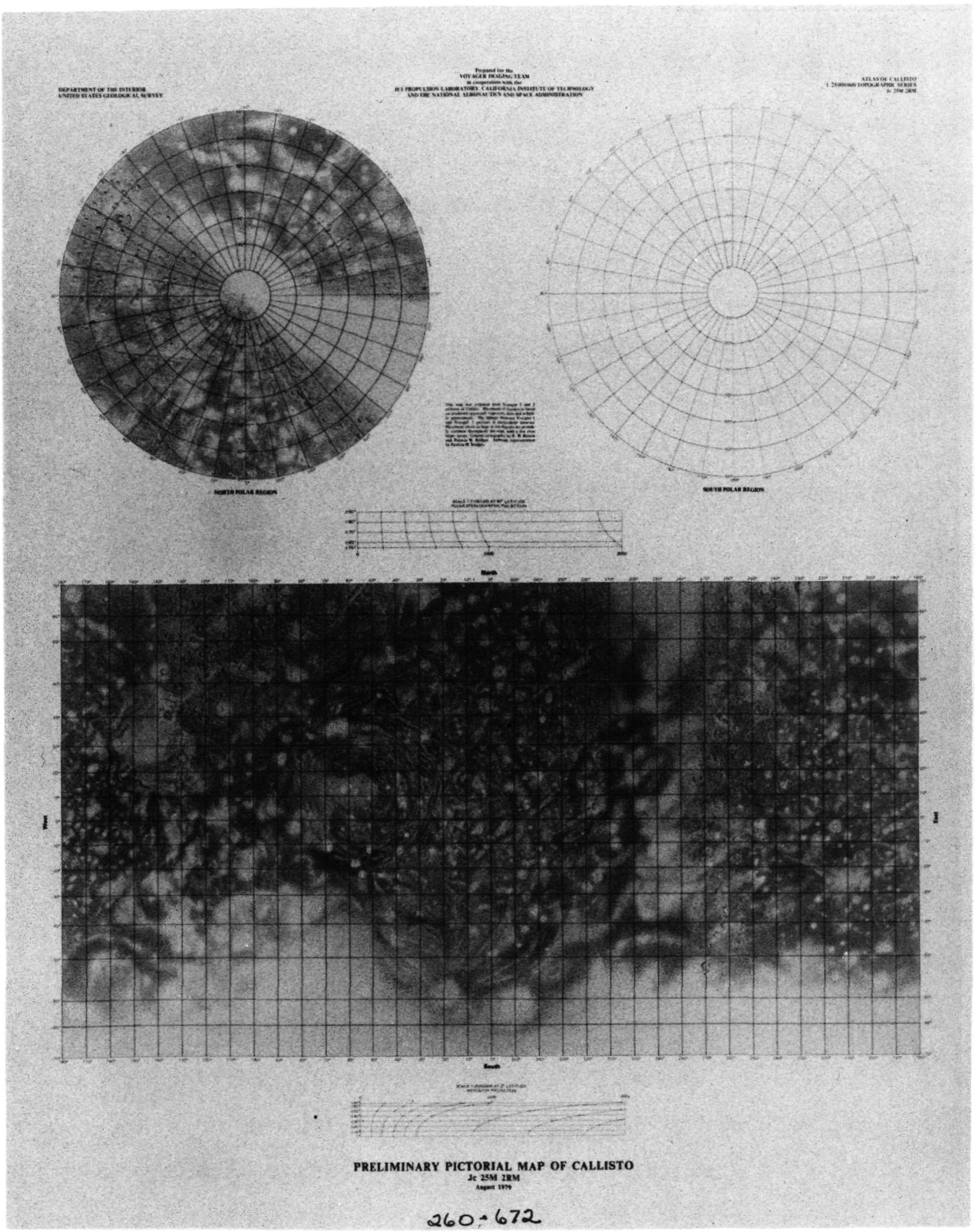


FIGURE 2.23. U.S. Geological Survey preliminary (uncontrolled) pictorial map of Callisto (in map pocket at back of thesis).

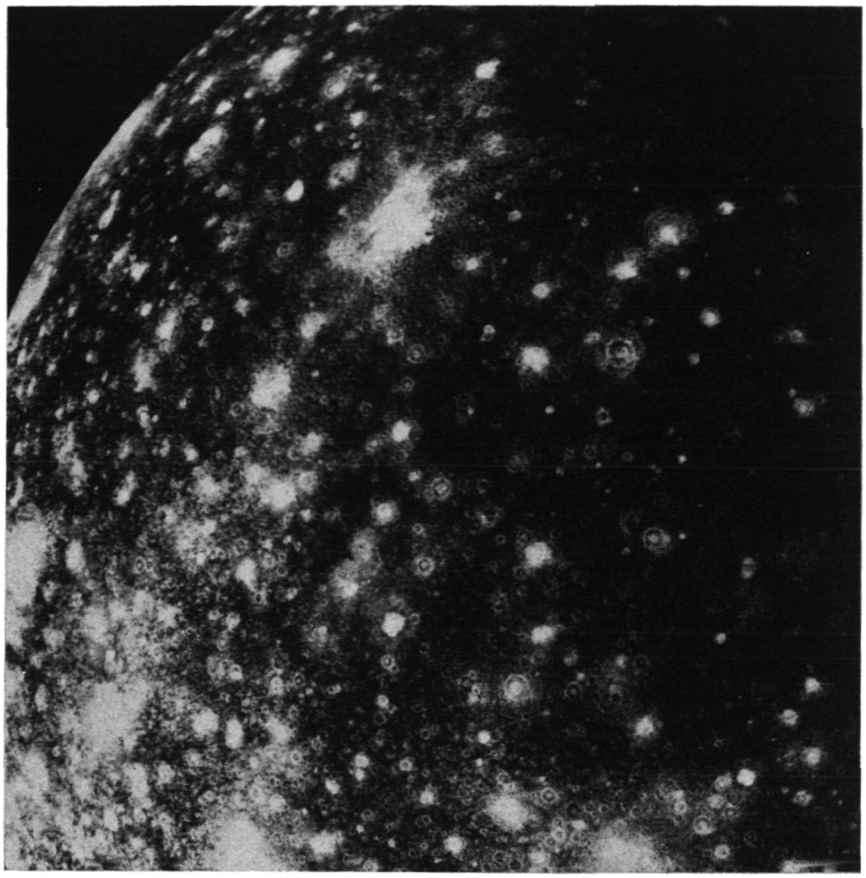


FIGURE 2.24. The heavily cratered surface of Callisto (scale across image = 2800 km; image centered at ∿ -10° lat., 200° long.; image 430J2-002).

are several large multi-ring structures apparently created by major impact events (Fig. 2.25). The largest of these consists of a circular bright region about 300 km in diameter surrounded by eight to ten roughly concentric discontinuous rings out to about 1500 km from the center. The rings appear at high resolution to be very subdued asymmetric ridges (Fig. 2.26). The ring structure is strikingly different from large ring basins on Mercury and the Moon. The rings are more numerous and more closely and evenly spaced, there are no radially lineated ejecta deposits, and the topography is much more subdued. These differences may be due to the response of a crust on Callisto that was less rigid and thinner than the lunar or mercurian crusts (Smith et al., 1979a).

2.4 Conclusions

The major geologic similarity between Ganymede and Callisto exists between Callisto's surface and Ganymede's cratered terrain. Callisto's surface is darker than Ganymede's cratered terrain and somewhat more heavily cratered (Smith et al., 1979a), but the two are otherwise very much alike. The most important difference between the two bodies is the presence of grooved terrain on Ganymede. Another important and perhaps related difference is that there appears to be more ice present at Ganymede's surface. It has bright ray craters and polar



FIGURE 2.25. The Valhalla ringed impact structure (scale across image = 1470 km; image centered at ∿ 20° lat., 55° long.; image 168J1+001).

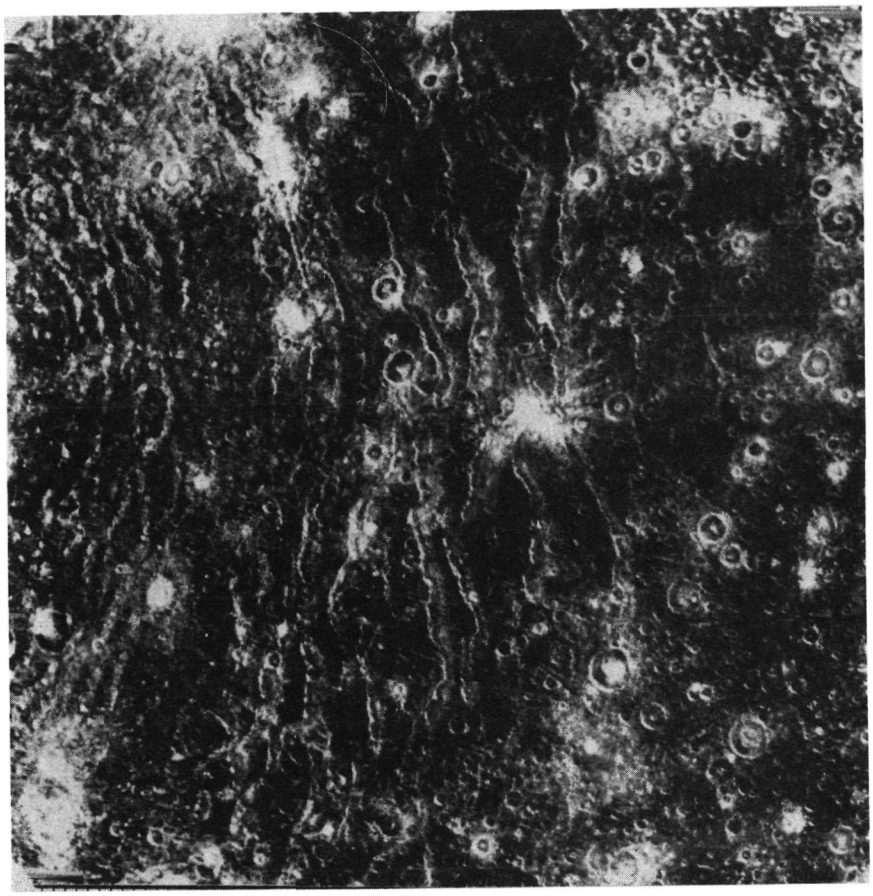


FIGURE 2.26. Outer rings of the Valhalla structure (scale across image = 1480 km; image centered at ∿ 30° lat., 30° long.; image 164J1+001).

caps, both of which are absent on Callisto, and is overall substantially brighter. These observations imply that Callisto's surface has been undisturbed by processes other than impacts since completion of accretion, but that Ganymede's surface was disrupted early in its history and largely replaced by the brighter grooved terrain. As shown in Chapter 6, grooved terrain formation may have been the process that brought more ice to the surface of Ganymede.

CHAPTER 3

BROADBAND PHOTOMETRY OF SURFACE FEATURES

3.1 Introduction

Images obtained during the Voyager flybys of Jupiter provide unique photometric data for Ganymede and Callisto over a wide range of phase angles. For the first time the photometric properties of individual terrain types and specific surface features can be determined, properties that are useful not only for investigating texture/composition differences on the surfaces, but that are essential for precise calculations of surface temperatures and for photoclinometric determination of topography (Chapters 6 and 7). In this chapter the broadband visible photometric properties of surface features on Ganymede and Callisto are examined. A preliminary photometric study of surface features on Io has been published by Clancy and Danielson (1981).

3.2 Ganymede

3.2.1 Introduction

The study of Ganymede's photometric properties is based on thirteen Voyager 1 images that cover a range of phase angles from 18° to 124°, and span subspacecraft

longitudes from 176° to 339° (Table 3.1). Four photometrically distinct terrain types are considered:

i) Cratered Terrain, making up about 38% of the satellite's projected surface area;

ii) Grooved Terrain, accounting for about 46%;

iii) Bright Polar Caps, very thin frost deposits that cover about 14% of the projected surface area;

iv) Bright Craters, commonly associated with prominent rays, which account for the remaining 2% of the projected area.

All images used were obtained through the clear filter, which has a broad passband that is centered near 0.47 microns and extends from 0.31 to 0.65 microns (Fig. 3.1). The photometric calibration of the Voyager camera systems has been described by Danielson et al. (1981). Calibration was performed prior to launch, and was checked during flight with images of a calibration plaque on board each spacecraft. The absolute accuracy of the measured intensities in the clear filter images used in this chapter is $\sim$ 10%.

3.2.2 Cratered Terrain

To begin analysis of the scattering properties of individual areas on Ganymede's surface it is best to see

TABLE 3.1 Voyager Images Used for Ganymede and Callisto Photometry*

Picture Number	α	Subspacecraft Longitude	Range (km)	Scale (km/pixel)	Camera
Ganymede:					
1510J1-005	18°	176°	4,200,000	39	NA1
0268J1-004	22°	195°	3,900,000	36	NA1
1211J1-004	28°	227°	3,600,000	33	NA1
0015J1-003	31°	247°	3,400,000	31	NA1
0539J1-003	32°	263°	3,300,000	30	NA1
0318J1-002	30°	305°	3,100,000	29	NA1
0772J1+000	49°	339°	270,000	17	WA1
0870J1+000	59°	332°	200,000	13	WA1
0918J1+000	67°	326°	170,000	11	WA1
0952J1+000	75°	320°	150,000	10	WA1
1002J1+000	89°	306°	130,000	8	WA1
1067J1+000	113°	281°	110,000	7	WA1
1095J1+000	124°	269°	110,000	7	WA1
Callisto:					
0720J2-005	10°	124°	3,500,000	32	NA2
0620J2-004	10°	142°	2,300,000	21	NA2
0828J2-003	13°	171°	1,100,000	10	NA2
0436J2-002	35°	211°	280,000	25	WA2
0849J2-002	65°	248°	240,000	16	WA2
0142J1+001	49°	3°	220,000	14	WA1
0320J1+001	75°	354°	130,000	8	WA1
0386J1+001	91°	306°	130,000	8	WA1
0487J1+001	110°	206°	150,000	10	WA1
0547J1+001	124°	201°	180,000	11	WA1

*Phase angles, subspacecraft longitude, and range are from the Voyager final SEDR document calculated from the spacecraft trajectory.

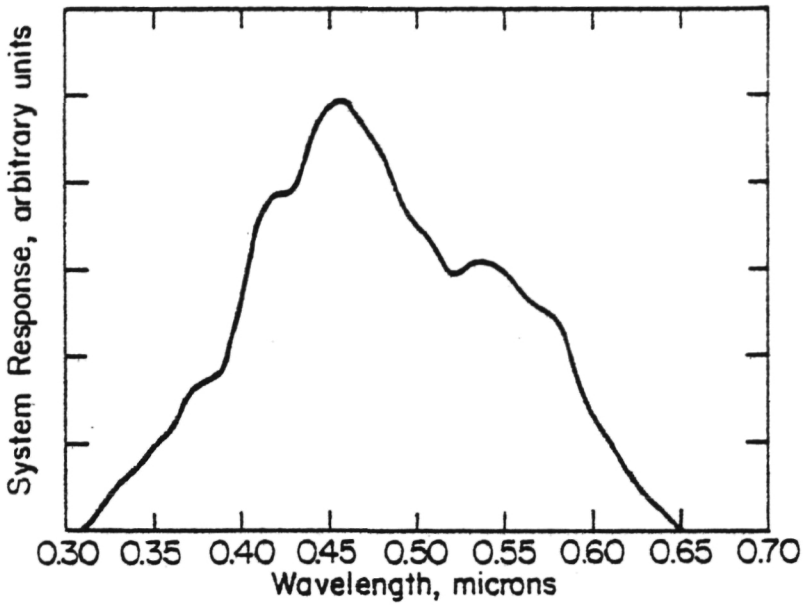


FIGURE 3.1. Typical spectral response curve for a Voyager camera through the clear filter. The system response scale is linear.

whether these can be represented in terms of one of several laws that have proven useful for studying the surfaces of other solar system objects. Foremost among these is a scattering law that fits lunar-like surfaces, of the form

$$I(i,\varepsilon,\alpha) = F[\mu_o/(\mu_o + \mu)]f(\alpha) \qquad (3.1)$$

where i = incidence angle,

ε = emission angle,

α = phase angle,

μ_o = cos i,

μ = cos ε,

I = intensity of scattered sunlight,

πF = incident solar flux, and

$f(\alpha)$ = phase function of the surface.

The various photometric quantities are defined in the sense of Harris (1961) and Veverka (1977). These quantities and a number of other photometric terms are described in detail in Appendix A. Note that when $f(\alpha)$ is defined in this way, $f(0°)$ is equal to twice the normal reflectance r_n of the surface.

For very bright surfaces one could try Lambert's law:

$$I(i,\varepsilon,\alpha) = F\, r_n\, \mu_o \qquad (3.2)$$

In view of Ganymede's relatively high reflectance ($\sim$ 0.43 according to Morrison and Morrison, 1977) one might expect

Lambert's law to approximate Ganymede's scattering properties better than equation (3.1). It is easily demonstrated that this is not the case, however.

In Figure 3.2, the brightness of individual bright craters and individual areas of cratered and grooved terrain is plotted as a function of sin ω, where ω is the photometric longitude (Harris, 1961), defined in such a way that the limb is at $\omega = +90°$, and the terminator is at $\omega = \alpha - 90°$. Curves are shown for phase angles of 20° and 30° for cratered terrain, grooved terrain, and bright craters. Equation (3.1) compares well with the data, whereas Lambert's law does not. Figure 3.3 shows that equation (3.1) also reproduces very well the observed brightness along lines of photometric latitude on Ganymede at higher phase angles for both cratered and grooved terrain. In what follows it is assumed that all terrain types on Ganymede scatter according to equation (3.1). With this assumption, the phase function $f(\alpha)$ for each terrain type may be determined from observations that span a range of phase angles.

Twenty-five areas typical of Ganymede's cratered terrain have been selected (Fig. 3.4). The areas selected typically cover 5 × 5 to 10 × 10 pixels, with their sizes scaled inversely with the spacecraft's range from one image to the next. In this way the true area sampled on Ganymede's surface remains constant as the spacecraft range

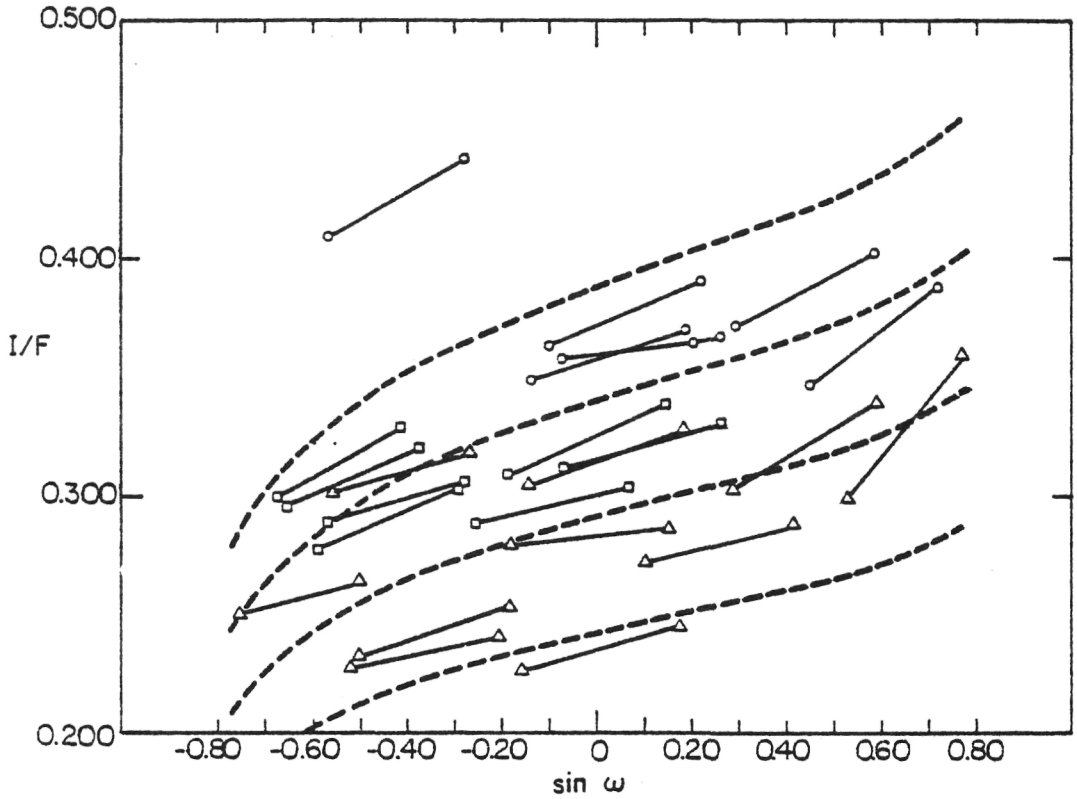


FIGURE 3.2a. Observed variation of intensity with photometric longitude for Ganymede bright craters (circles), grooved terrain (squares), and cratered terrain (triangles). For all points the phase angle is ∿ 20°. Solid lines connect observations of a single point at different photometric longitudes. Dashed curves give behavior expected for a lunar-like photometric function (equation 3.1) with f(20°) = 0.5-0.8 at intervals of 0.1.

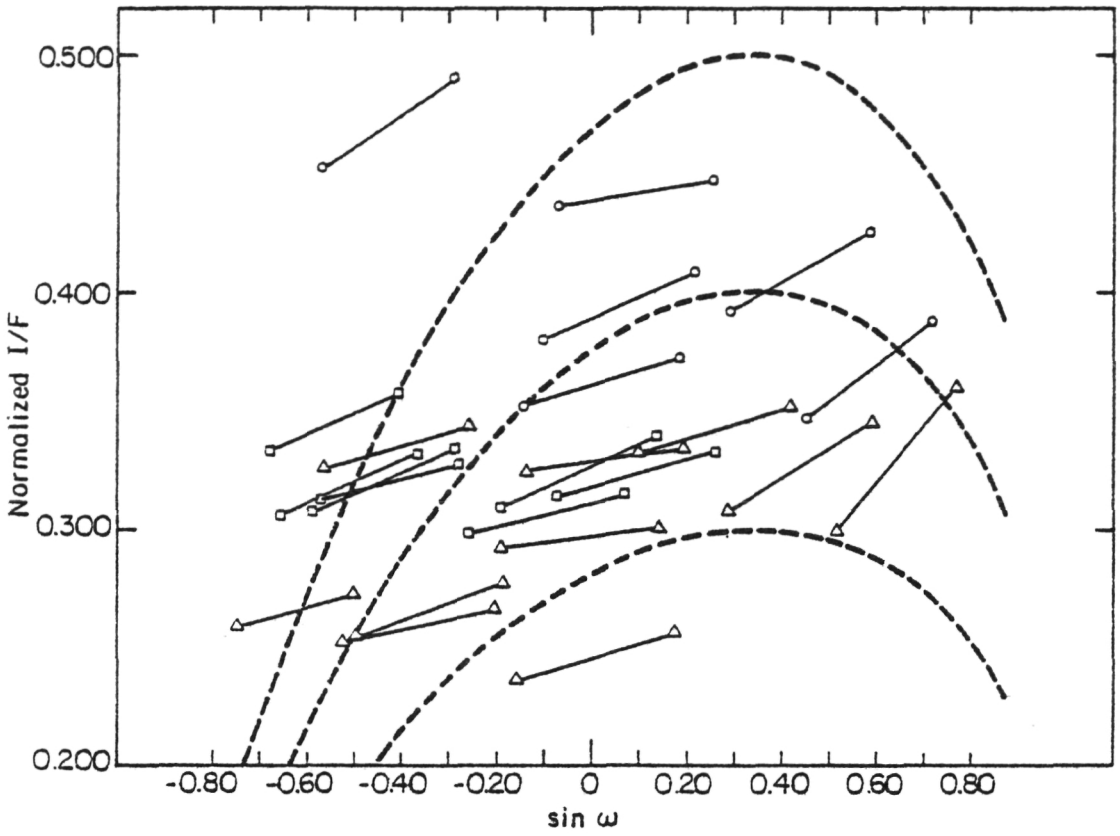


FIGURE 3.2b. Intensity variations at $\alpha \sim 20°$ compared with Lambert's law behavior (equation 3.2, dashed curves). Dashed curves are for r_n = 0.3, 0.4, and 0.5. Because the photometric latitude of individual points varies from image to image, all points have been normalized to the photometric equator according to Lambert's law, by dividing by the cosine of the photometric latitude.

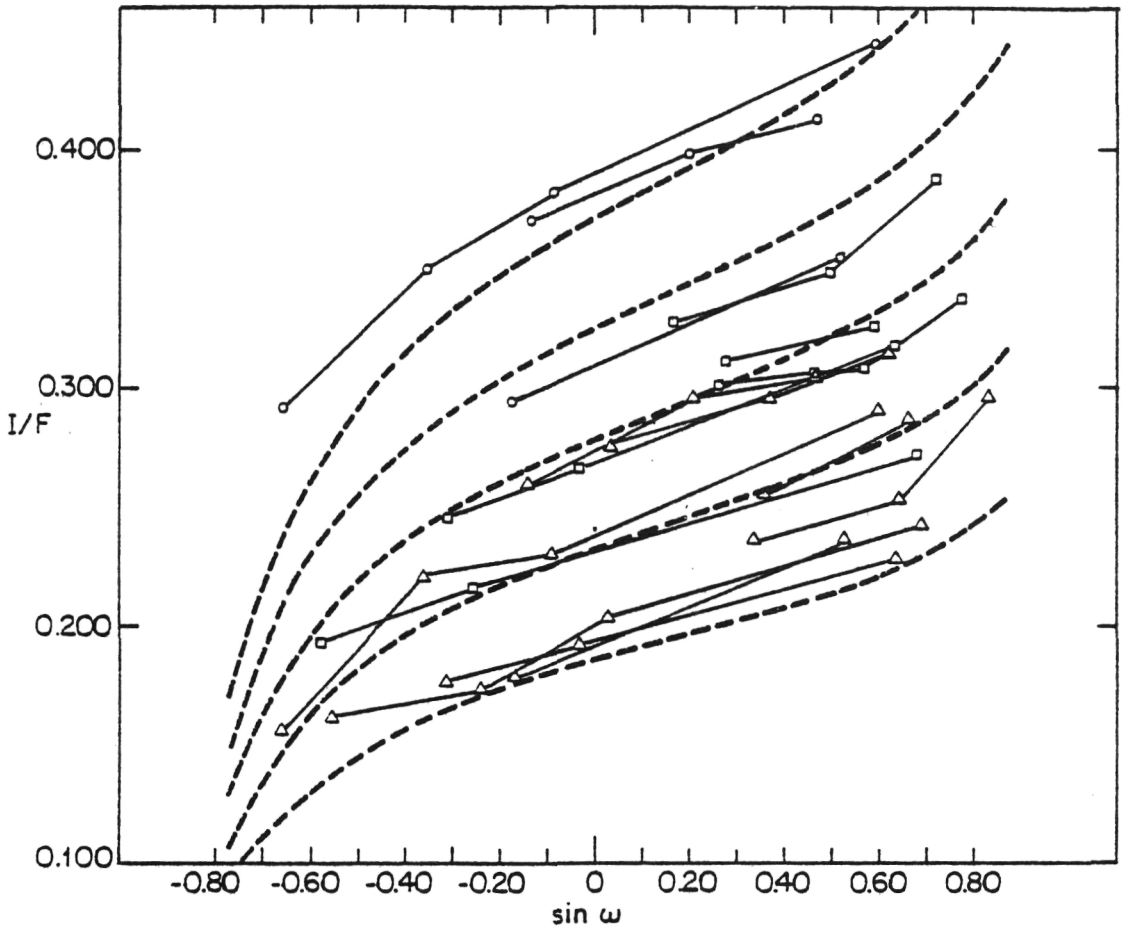


FIGURE 3.2c. Intensity variations at $\alpha \sim 30°$ compared with lunar-like behavior (equation 3.1). Dashed curves are for f(30°) = 0.4-0.8 at intervals of 0.1.

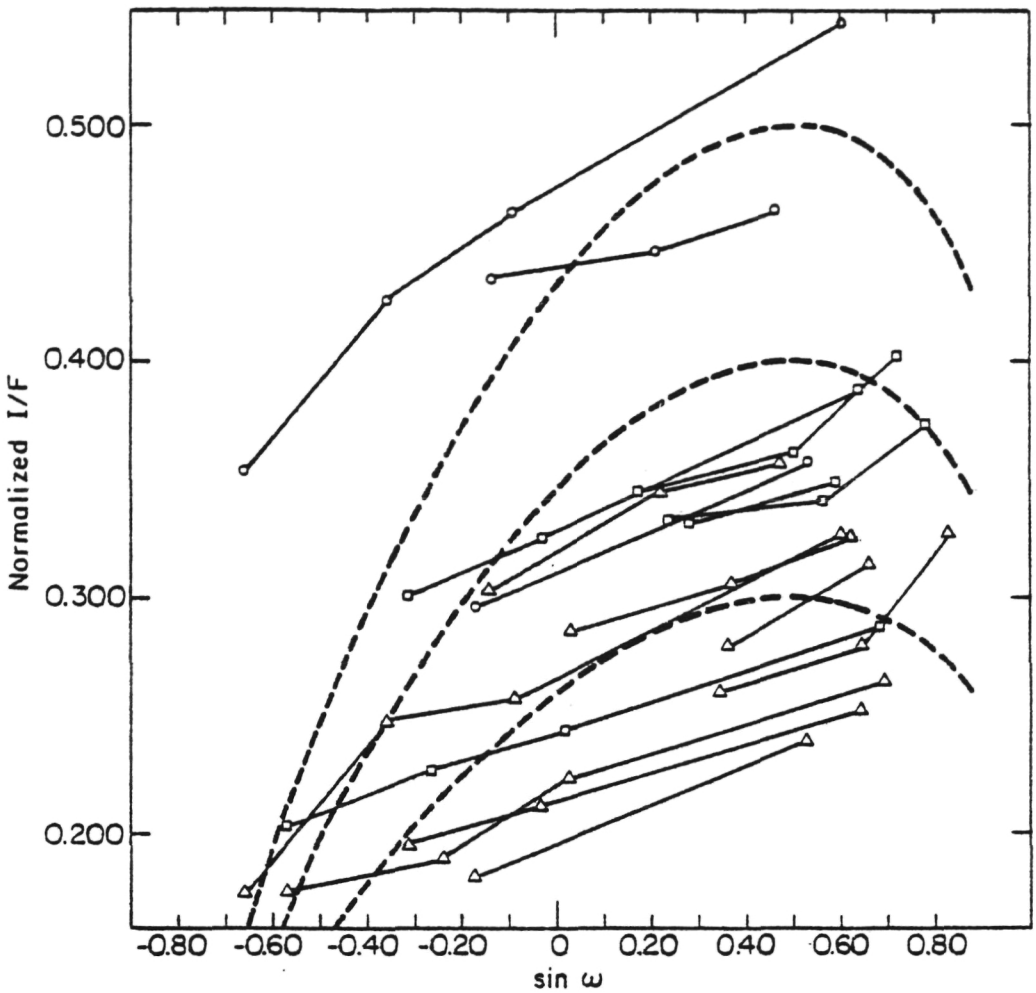


FIGURE 3.2d. Intensity variations at $\alpha \sim 30°$ compared with Lambert's law behavior. Dashed curves are for r_n = 0.3, 0.4, and 0.5.

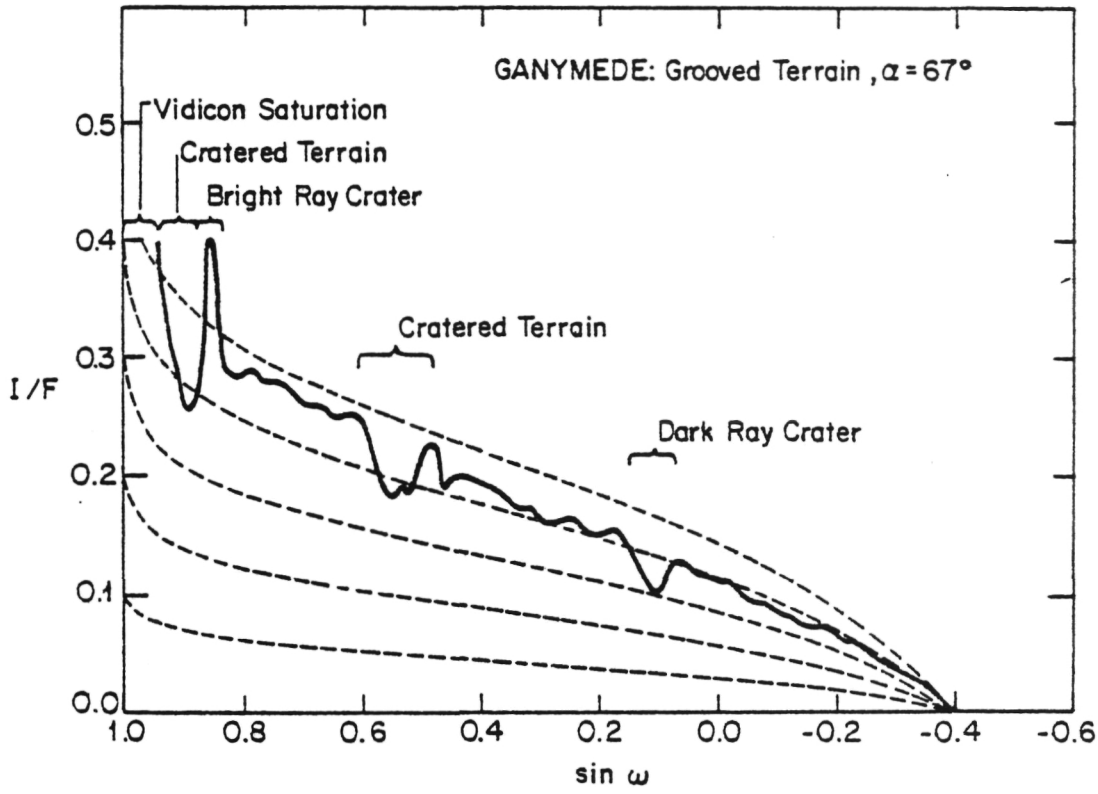


FIGURE 3.3a. Intensity scan across grooved terrain on Ganymede's disc at $\alpha = 67°$. Except for a few deviations caused by other terrain types, equation (3.1) (dashed curves) gives a good fit. Dashed curves are for $f(67°) = 0.1$-0.5 at intervals of 0.1.

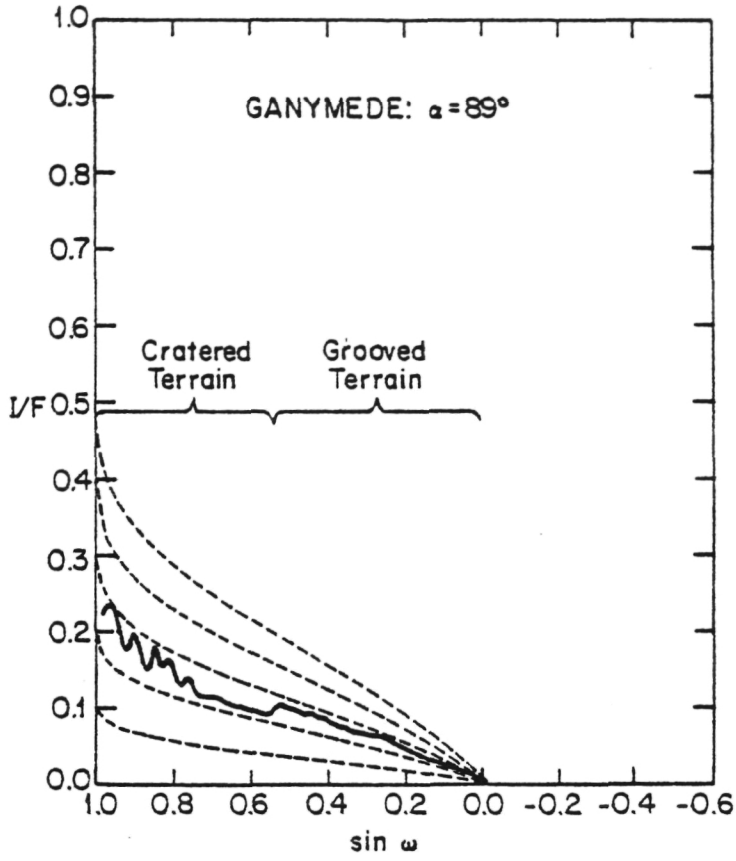


FIGURE 3.3b. Intensity scan across grooved and cratered terrain on Ganymede at $\alpha = 89°$. Dashed curves are for $f(89°) = 0.1$-0.5 at intervals of 0.1.

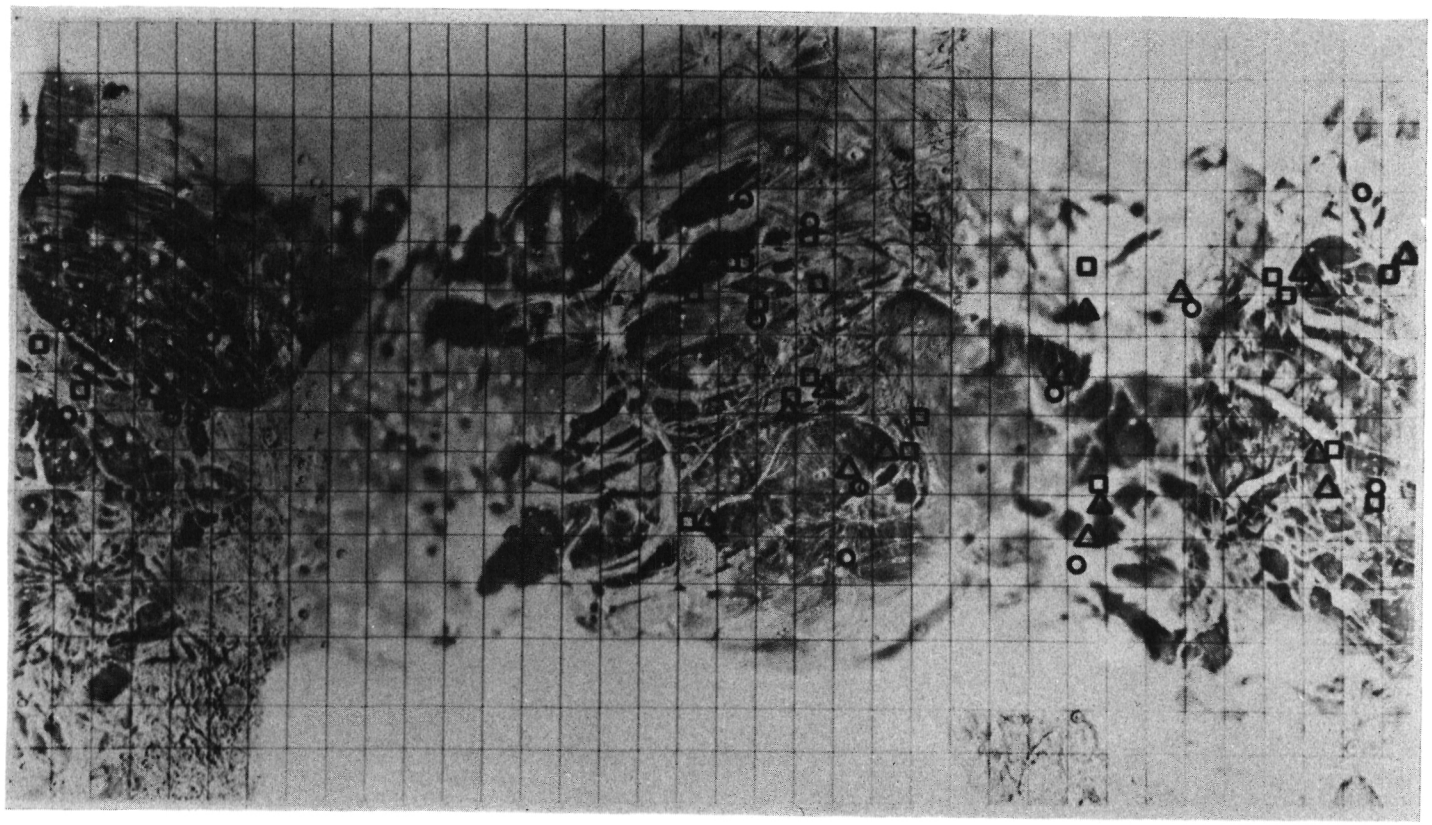


FIGURE 3.4. Points selected for photometric analysis on Ganymede: bright craters (circles), grooved terrain (squares), and cratered terrain (triangles). The base map is the U.S.G.S. preliminary pictorial map of Ganymede. Incidence and emission angles were calculated by using spacecraft trajectory information, and are unaffected by position errors that may exist in this map.

and resolution change. From the wide angle camera data individual areas may be followed over seven phase angles ranging from 49° to 124°. Additional information for different areas can be obtained with varying incidence angles from narrow angle images at two nearly constant phase angles, 20° ± 2° and 30° ± 2° (Table 3.1).

For each of these areas $f(\alpha)$ has been determined using equation (3.1). For the wide angle data, the results are shown in Figure 3.5. Averaging these yields a mean $f(\alpha)$ for the average cratered terrain on Ganymede (Fig. 3.6). Figure 3.6 also includes points at 20° and 30° determined similarly (but from different areas) from the narrow angle data. The obvious offset between the narrow and wide angle data could be due to uncertainties that may exist in the relative calibration of the two cameras on Voyager 1. Perhaps more likely, the offset indicates real differences in the cratered terrain on various parts of the satellite. In what follows the two curves are averaged to obtain a better estimate of the photometric properties of the average cratered terrain on Ganymede.

The next step is to combine the data in Figure 3.6 with Earth-based observations below $\sim$ 12°. The average $f(\alpha)$ for Ganymede can be calculated from published disc-integrated observations (Morrison and Morrison, 1977). Two assumptions are necessary. The first is that both

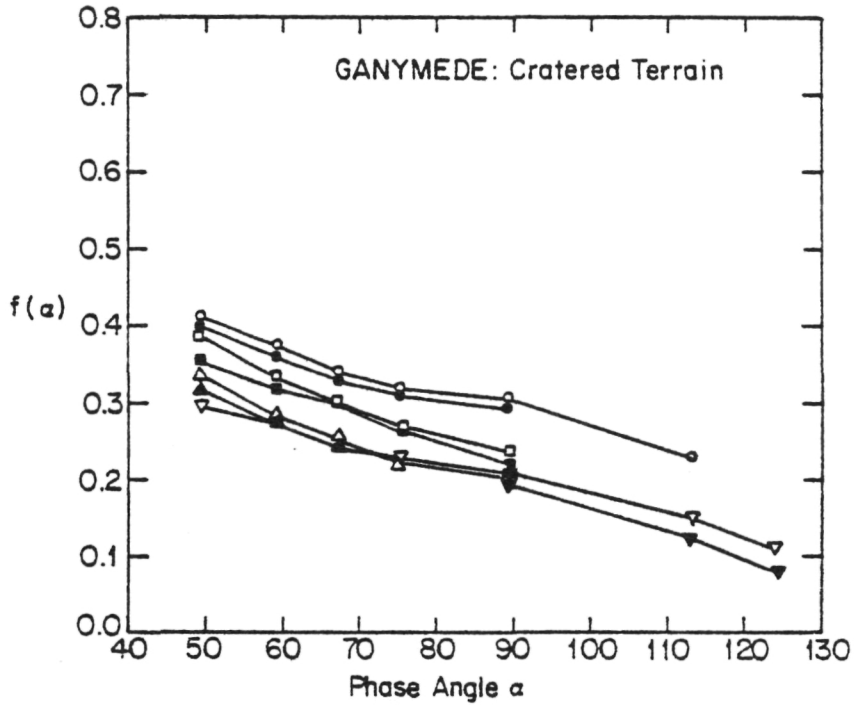


FIGURE 3.5. Curves of f(α) for regions of cratered terrain on Ganymede.

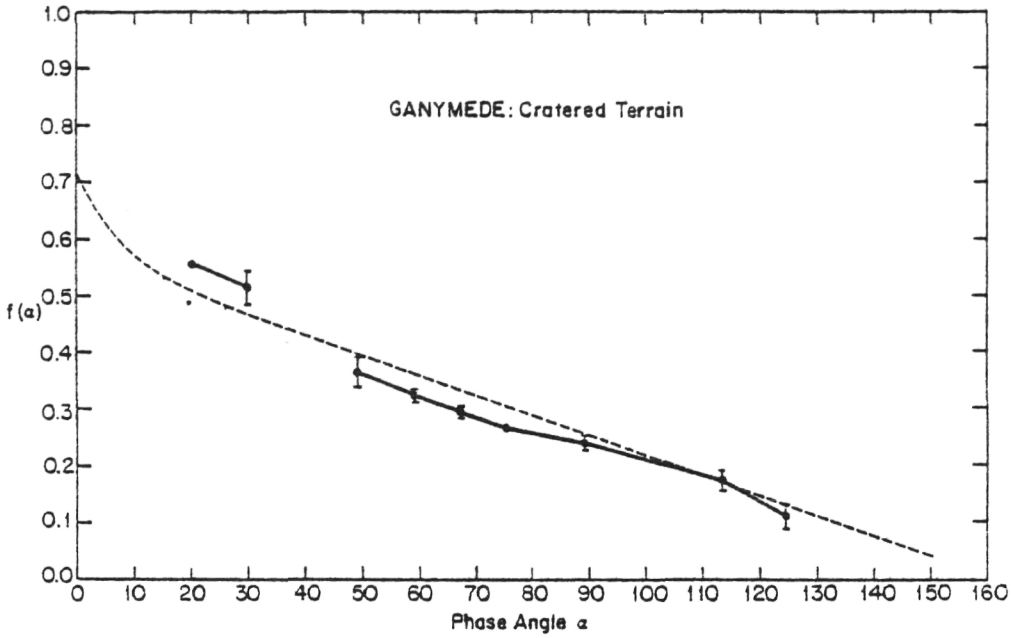


FIGURE 3.6. Averaged $f(\alpha)$ curves for Ganymede cratered terrain. Solid curves were obtained by normalizing all curves to the mean $f(\alpha)$ at a single phase angle (20° for Narrow Angle data, 75° for Wide Angle data) and averaging. Error bars are one standard deviation. Dashed curve is a best fit of the form given in equation (3.3): $f(\alpha) = 0.57 - 0.0035\alpha + 0.14e^{-0.14\alpha}$ (α in degrees). The slope from $\alpha = 0°$ to $\alpha = 12°$ is taken from Earth-based observations.

dominant terrain types on Ganymede scatter according to equation (3.1), an assumption supported by the observations mentioned previously. The second is that the shapes of the $f(\alpha)$ curves are the same below $\sim 12°$ for both grooved and cratered terrain, something about which no information is available at present. The shapes are, however, indistinguishable above $\sim 20°$.

The three data sets are combined: Earth-based, Voyager 1 narrow angle, and Voyager 1 wide angle, by fitting the following mathematically convenient form of $f(\alpha)$ to the points in Figure 3.5:

$$f(\alpha) = A + B\alpha + Ce^{-D\alpha} \qquad (3.3)$$

The result (Fig. 3.6) shows that this functional form compares with the data very well. The smooth curve in Figure 3.6 is the best estimate of the photometric properties of Ganymede's cratered terrain. The value of $f(0°)$ indicates an average normal reflectance of 0.36. To obtain an independent estimate of the range of this quantity, 32 areas have been randomly selected in image 1002J1+000 ($\alpha = 89°$). The calculated normal reflectance of these areas ranges from 0.28 to 0.42, with a mean of 0.34 (Fig. 3.7). In what follows 0.35 is adopted as the normal reflectance of the average cratered terrain on Ganymede.

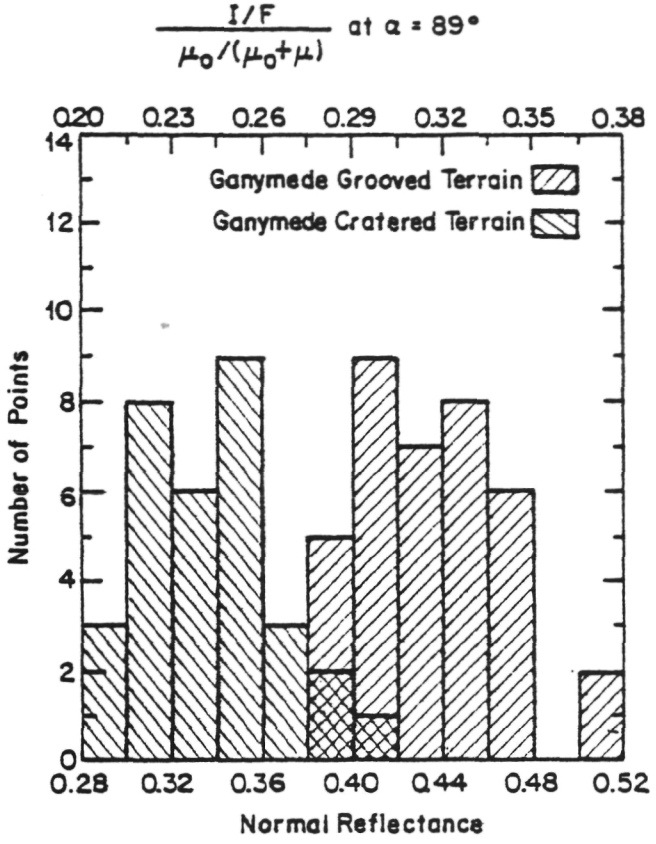


FIGURE 3.7. Histograms of extrapolated normal reflectances for 32 points in Ganymede's grooved and cratered terrains.

3.2.3 Grooved Terrain

The analysis of this terrain type follows the procedure developed in the previous section. A total of 20 areas were selected (Fig. 3.4). The conclusion that equation (3.1) represents the scattering properties of the grooved terrain has already been discussed (cf., Figs. 3.2 and 3.3). The $f(\alpha)$ curves obtained for the individual areas from the wide angle camera images are shown in Figure 3.8. The corresponding average $f(\alpha)$, as well as the 20°-30° segment obtained from the narrow angle camera images, are shown in Figure 3.9. Figure 3.9 also represents the smooth curve fitted to these data as well as to the near-opposition segment approximated from Earth-based observations as in the case of the cratered terrain (above). This smooth curve, the best estimate of the photometric properties of the average grooved terrain on Ganymede, yields a normal reflectance of 0.44.

To estimate the range in reflectance of the grooved terrain, 32 areas have been randomly selected in image 1002J1+000 (α = 89°). The result (Fig. 3.7) shows a range of normal reflectances from 0.32 to 0.52, and a mean of 0.44.

3.2.4 Polar Caps

Cap-like bright areas near the poles are evident in the Voyager images of Ganymede; these were first noticed

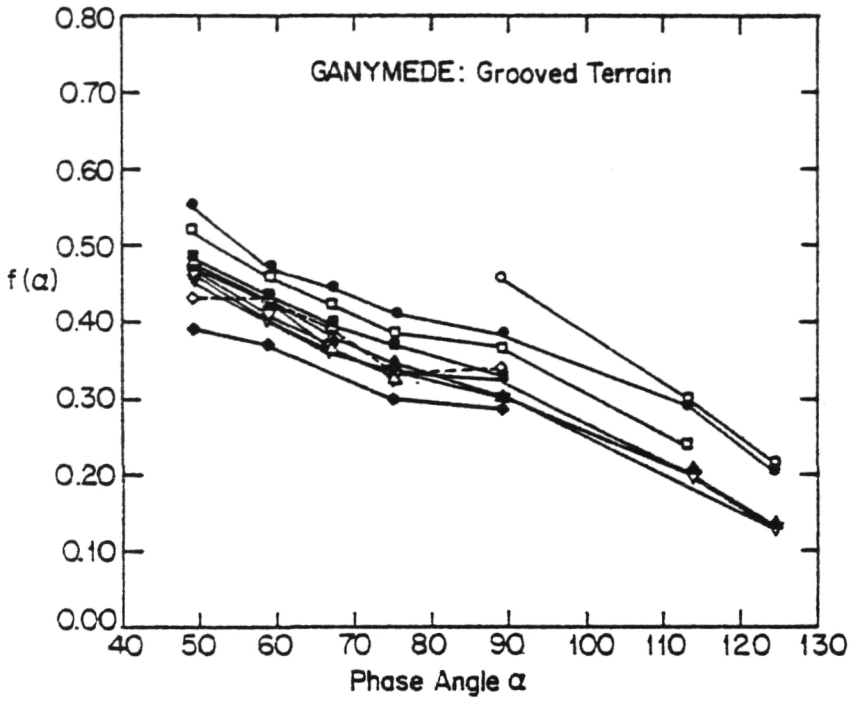


FIGURE 3.8. Curves of f(α) for regions of grooved terrain on Ganymede.

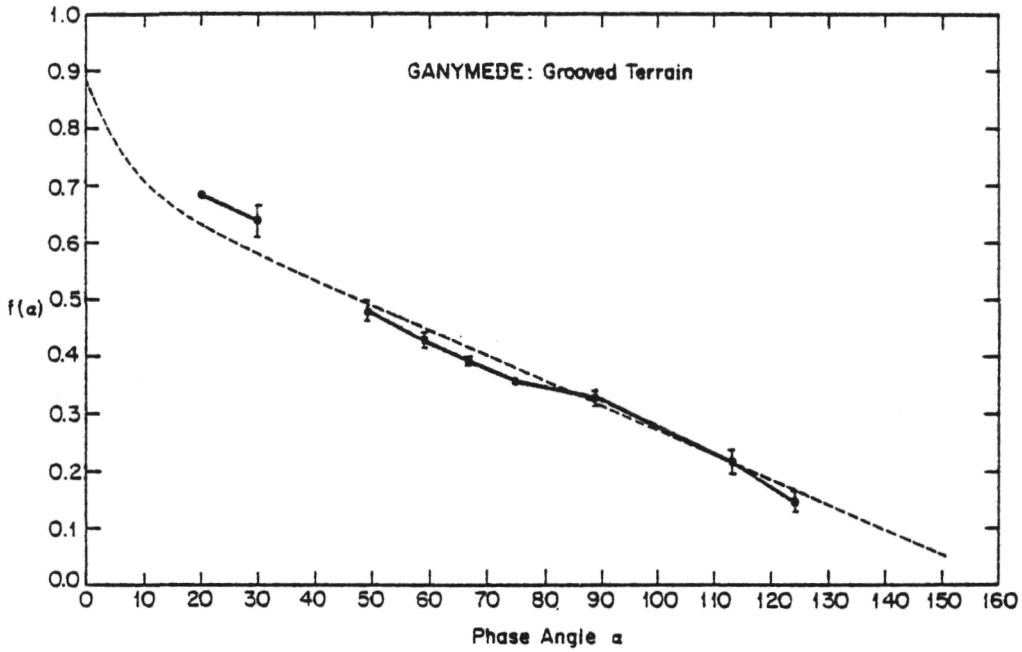


FIGURE 3.9. Curves of $f(\alpha)$ for Ganymede's grooved terrain obtained by the method of Figure 3.6. Dashed curve is a best fit of the form given in equation (3.3): $f(\alpha) = 0.71 - 0.0044\alpha + 0.18e^{-0.14\alpha}$ (α in degrees).

by telescopic observers almost a century ago (e.g., Barnard, 1897; Comas Solá , 1906). Of the two, the bright cap near the north pole is most easily observed in the images examined. Its normal reflectance is clearly higher than that of Ganymede's cratered or grooved terrain. Still, its photometric properties appear to be described satisfactorily by equation (3.1) (Fig. 3.10). The $f(\alpha)$'s derived from four individual areas are shown in Figure 3.11. In all four areas the bright frost deposits comprising the caps lie on grooved terrain. Where the caps overlie cratered terrain their reflectance seems to be lower, but there are no extensive areas of this type in the images used in this study. The mean of the curves in Figure 3.11 is adopted as the average phase function of polar cap material overlying grooved terrain (Fig. 3.12). Unlike the $f(\alpha)$'s of the cratered and grooved terrains, the mean $f(\alpha)$ of the polar caps is very slightly concave down. From Figure 3.12 the average reflectance of the polar cap is 1.7 times that of the cratered terrain at $\alpha = 50°$. Data are not available to determine the behavior of $f(\alpha)$ at lower phase angles, but if $f(0°)/f(50°)$ were taken to be the same as that for the cratered terrain, the normal reflectance of the polar cap material would be 0.58.

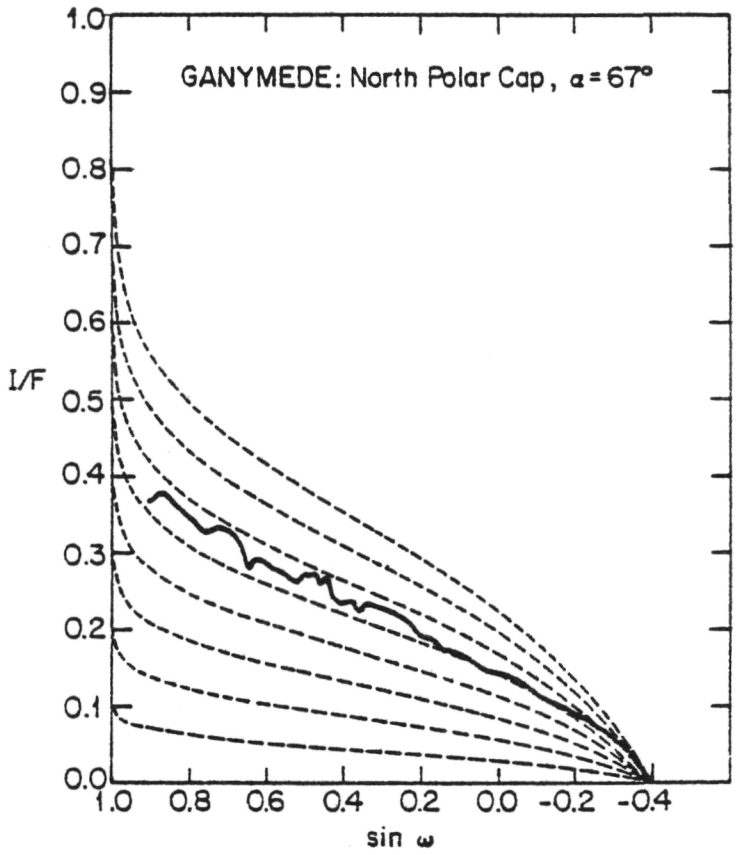


FIGURE 3.10. Intensity scan across Ganymede's north polar cap at $\alpha = 67°$. Dashed curves give behavior expected for a lunar-like photometric function (equation 3.1) with $f(67°) = 0.1$-0.8 at intervals of 0.1.

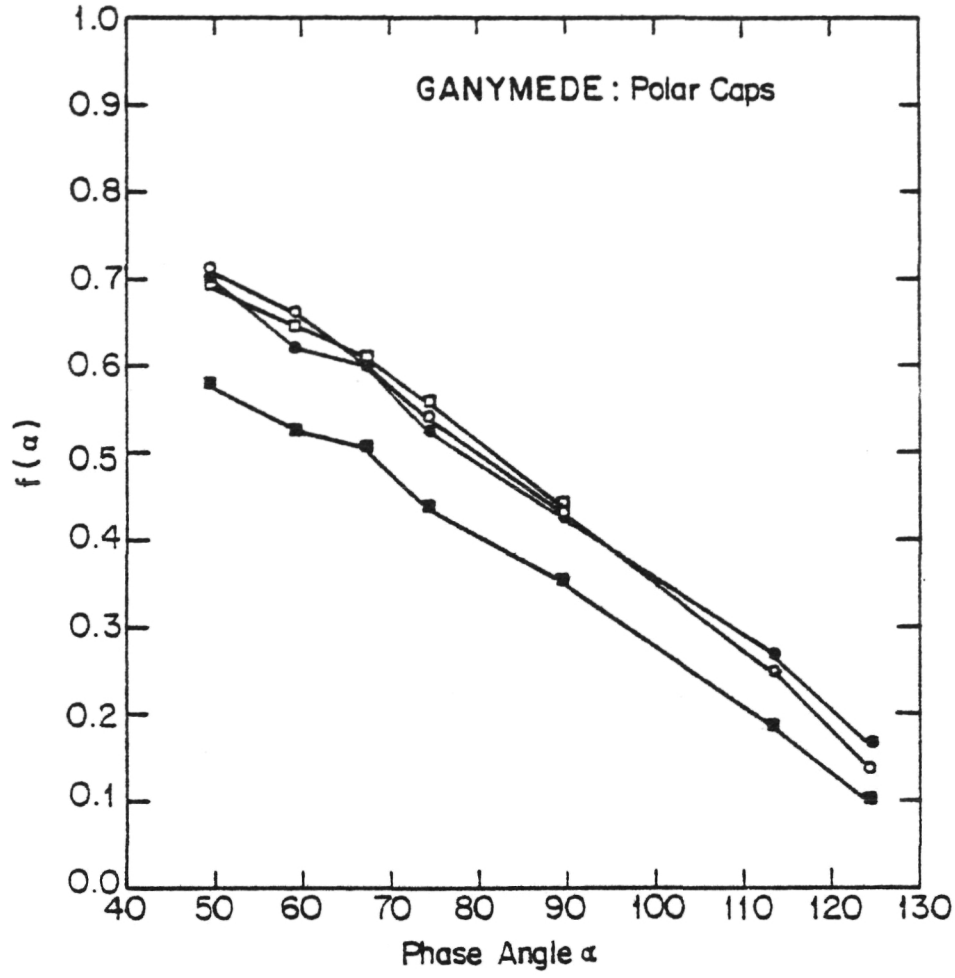


FIGURE 3.11. Curves of f(α) for regions in Ganymede's north polar cap.

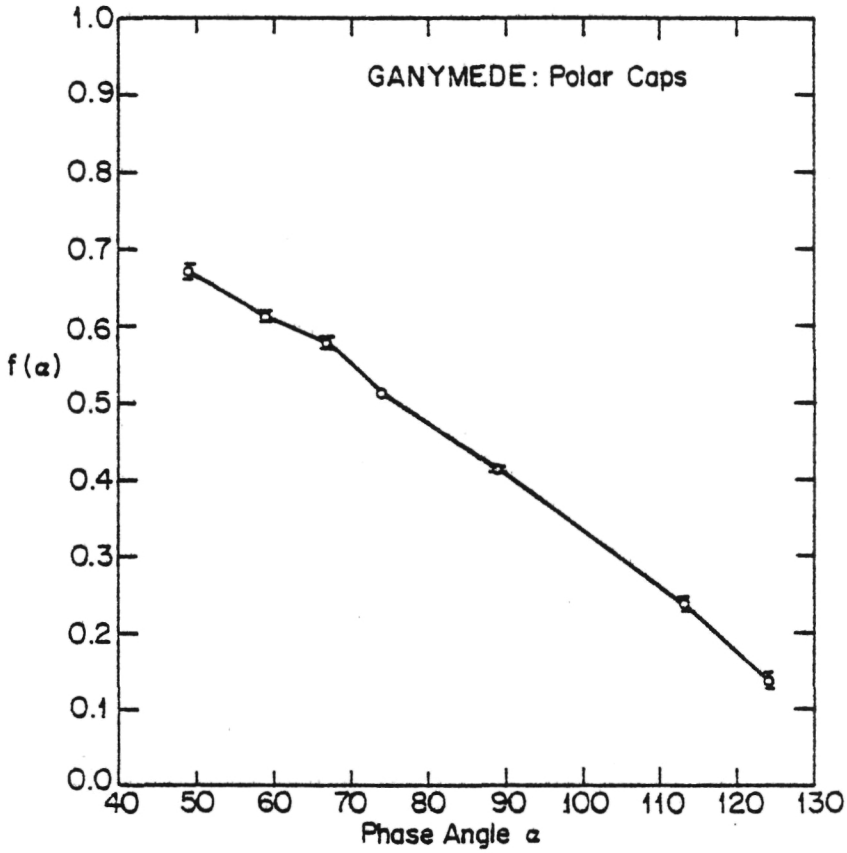


FIGURE 3.12. Curve of f(α) for Ganymede's north polar cap obtained by the method of Figure 3.6.

3.2.5 Bright Craters

Bright craters, most with conspicuous ray systems, are present in many of the Ganymede images. Fifteen, whose locations are indicated in Figure 3.4, were selected for detailed study.

As shown by Figure 3.2 (plots of I/F vs. sin ω), equation (3.1) gives a much better fit to the observed brightness dependence of the bright craters on photometric longitude than does Lambert's law. To quantify this unexpected conclusion the data for the bright craters in Figure 3.2 have been fitted to a generalized scattering law of the form

$$I(i,\varepsilon,\alpha) \propto (b - 1)[\mu_0/(\mu_0 + \mu)] + b\mu_0 . \qquad (3.4)$$

Allowing b to vary in steps of 0.05 from 0 to 1, in all but one case the best fit occurs for b = 0. In one instance a slightly better fit is obtained for b = 0.2, but in no case does b = 1 (Lambert's law) provide a good fit. The Voyager data permit longitude tests of the type shown in Figure 3.3 to be carried out only for small phase angles (20° and 30°). At large phase angles the coverage does not allow a particular crater to be followed as a function of photometric longitude, with the phase angle remaining fixed. Due to the restricted extent of bright craters, and to the diversity among these features, it is impossible to test the photometric behavior of these

features in the manner done for the cratered and grooved terrain (Figure 3.3).

For two of the craters (latitude 47°, longitude 352°; latitude 23°, longitude 348°) it is possible to check for enhanced specular reflection; none is found.

Having shown that the bright craters on Ganymede scatter light according to equation (3.1) at phase angles below $\sim$ 30°, it is assumed that they do so at all phase angles. Individual $f(\alpha)$ curves derived from the wide angle camera data for six craters (Table 3.2) are shown in Figure 3.13. In Figure 3.14 the data for these craters have been averaged, and combined with measurements derived from the narrow angle images at phase angles of 20° and 30°. As in the analysis of the polar cap, the resulting phase curve is concave down. In fact, the two curves seem to have similar shapes. Careful examination of the data shows that this concave down shape is real and is definitely not a result of vidicon saturation at low phase angles.

From Figure 3.13, the brightness of the craters relative to the cratered terrain at α = 49° ranges from 1.3 to 2.0 (Table 3.2). The corresponding normal reflectances can be estimated by extrapolating the data in Figure 3.13 below $\alpha \sim 20°$, according to the phase function of the grooved terrain. In this manner, the four brightest craters on Ganymede are estimated to have normal reflectances

TABLE 3.2 Bright Craters on Ganymede

Location	Brightness Relative to Cratered Terrain, $\alpha = 49°$	Estimated Normal Reflectance, r_n
47°N, 352°	2.00	0.70
23°N, 348°	1.90	0.67
35°N, 355°	1.75	0.61
44°N, 335°	1.70	0.59
19°S, 322°	1.40	0.49
35°S, 326°	1.30	0.46

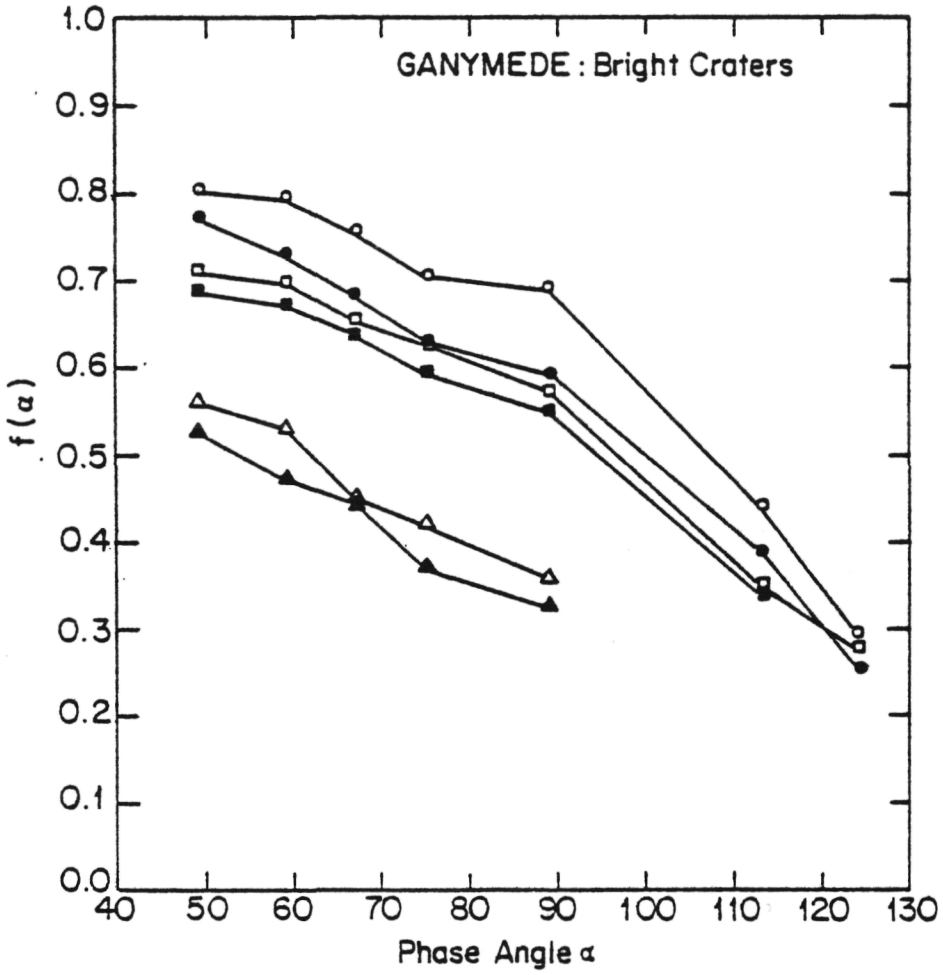


FIGURE 3.13. Curves of f(α) for bright craters on Ganymede.

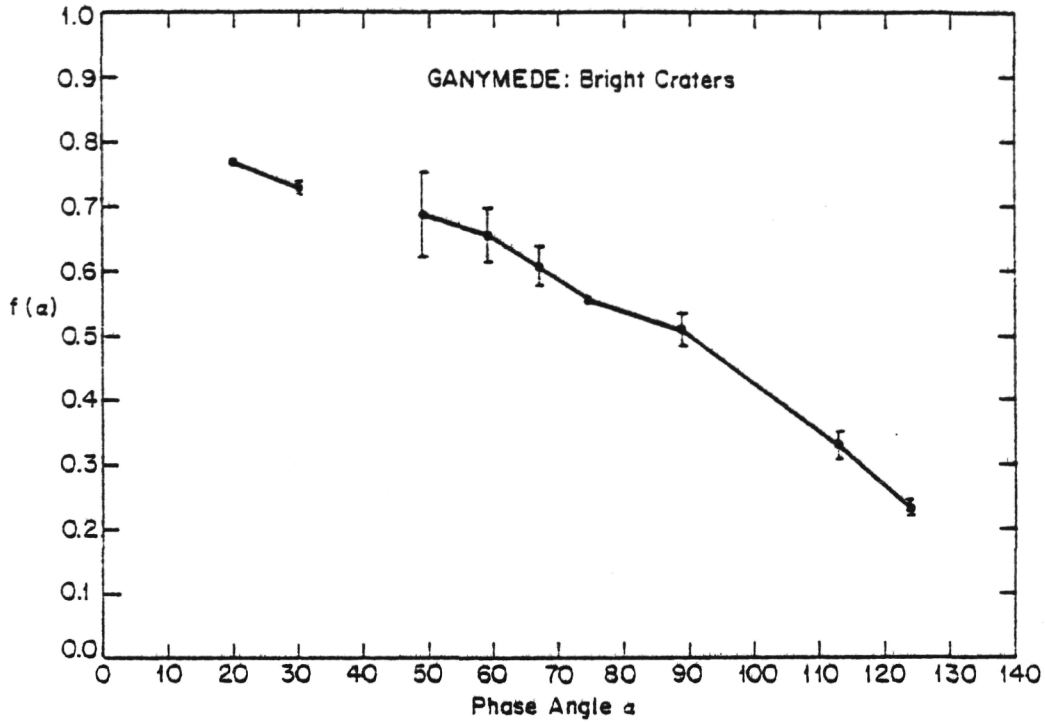


FIGURE 3.14. Curves of f(α) for Ganymede's bright craters obtained by the method of Figure 3.6.

ranging from 0.59 to 0.70 (mean = 0.64).

3.2.6 Disc-Integrated Properties

In Figure 3.15 observed values of $\Phi(\alpha)$, the disc-integrated brightness of Ganymede, are plotted at six phase angles ranging from 49° to 124°. To test the validity of the previous analysis these observed data are now compared to the derived $f(\alpha)$'s.

First, ignoring the bright craters and the polar caps, and combining the photometric functions of the cratered and grooved terrains in their appropriate relative proportions, the smooth curve in Figure 3.15 is obtained, a curve that slightly underestimates the slope of the observed $\Phi(\alpha)$ between 49° and 124°. This predicted curve is obtained by multiplying the observed surface phase function $f(\alpha)$ by the disc-integrated phase function of a Lommel-Seeliger planet:

$$\Phi(\alpha) \propto f(\alpha) \int_{-\pi/2}^{\pi/2} \int_{-\pi/2+\alpha}^{\pi/2} [\mu_o/(\mu_o + \mu)] \cos\omega \cos^2\psi \, d\omega d\psi$$

$$= f(\alpha)(1 - \sin\tfrac{\alpha}{2} \tan\tfrac{\alpha}{2} \ln \cot\tfrac{\alpha}{4}) \qquad (3.5)$$

where ψ is photometric latitude. By adding the contribution of the polar regions (which have a steeper phase dependence over this range of phase angles), the agreement becomes much better. (Note that, relative to the polar

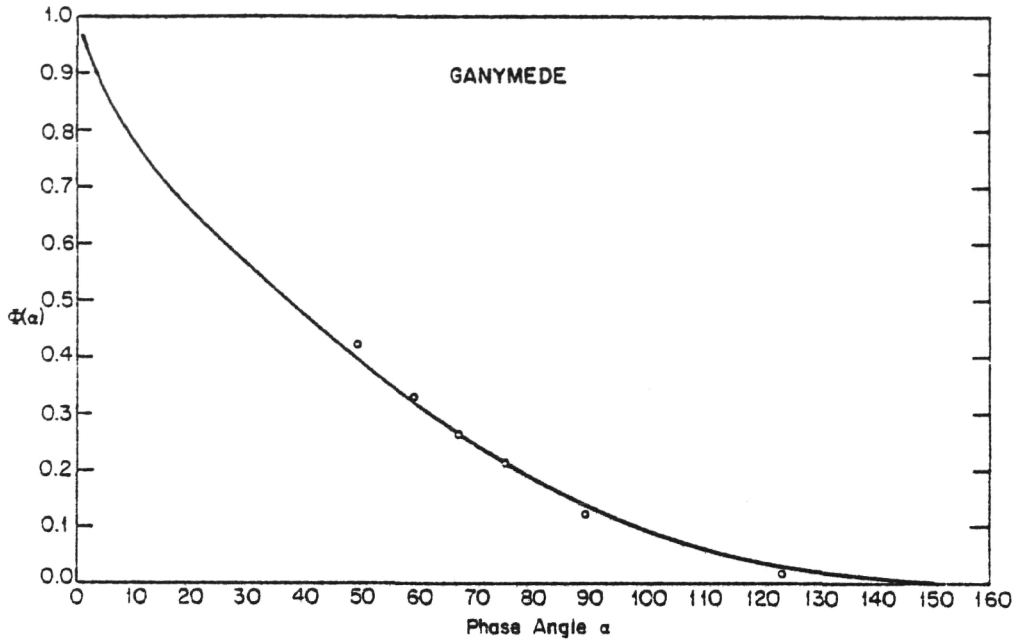


FIGURE 3.15. Observed values of disc-integrated brightness of Ganymede (circles) and curve of $\Phi(\alpha)$ predicted from the $f(\alpha)$ curves for cratered and grooved terrain (solid curve). Predicted curve is normalized to 1.0 at $\alpha = 0°$. Observations are normalized to the predicted value at $\alpha = 75°$.

caps, the contribution of the bright craters is qualitatively similar, but only 1/7 as large.)

From the observed phase curve it is possible to compute the phase integral q. Figure 3.15 yields a phase integral for the satellite of q = 0.8, consistent with the estimate of 1.0 ± 0.3 obtained by Morrison (1977) from radiometry. The derived normal reflectances in their relative proportions yield a geometric albedo in the clear filter of approximately 0.43, so that the Bond albedo in this filter is 0.35.

3.3 Callisto

3.3.1 Introduction

The analysis of Callisto is based on ten images obtained by Voyager 1 and 2 over a range of phase angles from 10° to 124° (Table 3.1). In sub-spacecraft longitude the data cover segments from 124° to 242°, and from 306° through 3° west longitude. There are no images for which the subspacecraft longitude is 90° (leading face) or 270° (trailing face).

Two photometrically distinct terrain types have been defined for the purposes of the study:

i) Cratered terrain, making up some 97% of the satellite's surface;

ii) Craters, defined as large circular features whose albedo significantly exceeds that of

the background cratered terrain. Such craters make up some 3% of the surface of Callisto.

While the reflectance of some of these craters rivals that of the "bright craters" on Ganymede, none of the Callisto craters has significant bright rays. Also, there are no bright polar caps on Callisto.

3.3.2 Cratered Terrain

To investigate the photometric properties of Callisto's cratered terrain, fourteen areas have been selected, typically 5 × 5 to 10 × 10 pixels (Fig. 3.16), and, as for Ganymede, scaled in size according to image resolution. For each area $f(\alpha)$ has been determined from equation (3.1). (It is shown below that equation (3.1) is appropriate for the analysis of the Callisto cratered terrain data.) For some areas (Fig. 3.17), data are available at five phase angles ranging from 49° to 124° from the Voyager 1 wide angle camera (Table 3.1). For others (Fig. 3.18) data are available at three phase angles between 13° and 65° from Voyager 2 (Table 3.1). Averaging all the data from Voyager 1 and Voyager 2 yields the points shown in Figure 3.19. The small systematic offset between the Voyager 1 and Voyager 2 data could be due to two major causes: (a) uncertainties in the calibration of the camera systems on the two spacecraft,

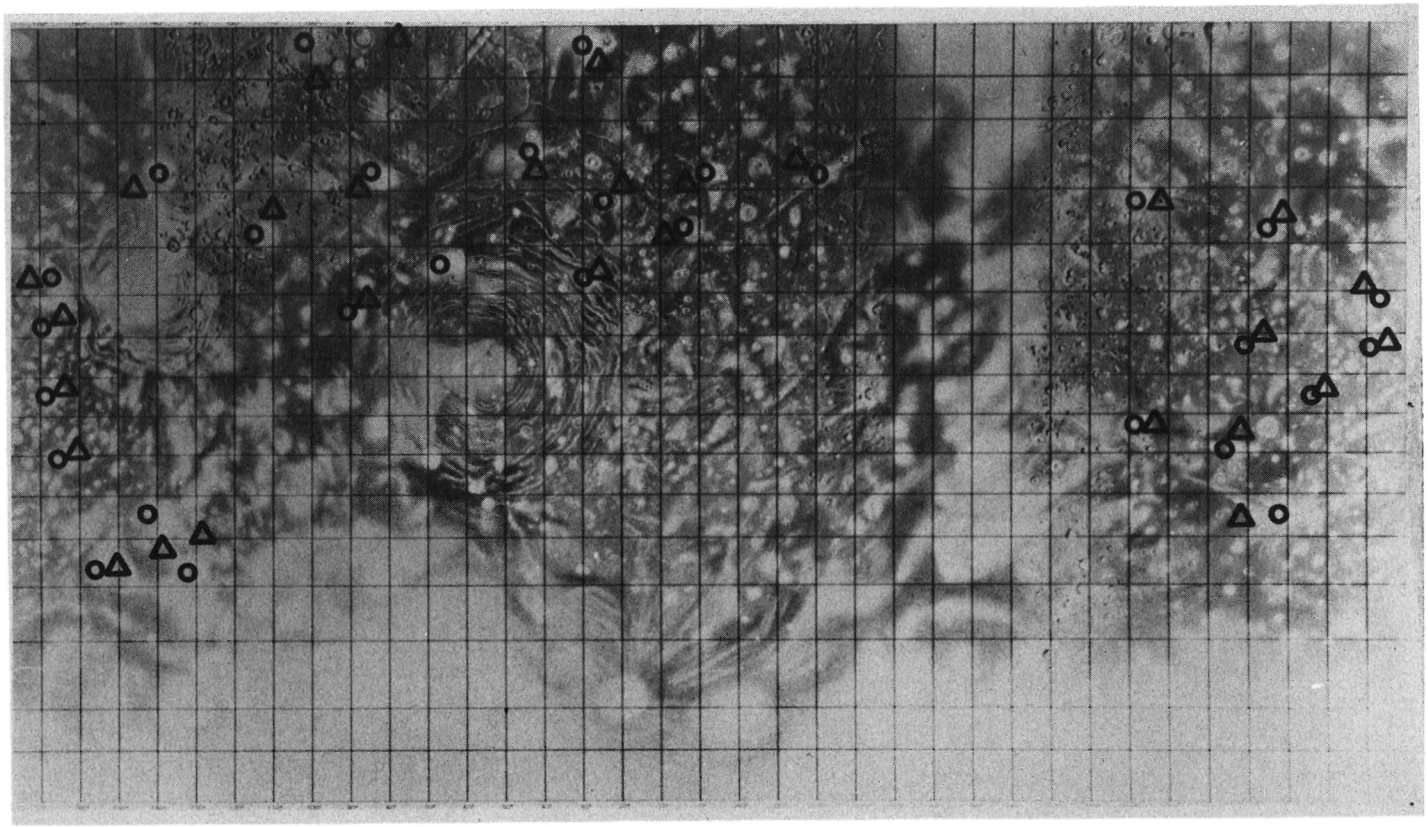


FIGURE 3.16. Points selected for photometric analysis on Callisto: craters (circles) and cratered terrain (triangles). The base map is the U.S.G.S. preliminary pictorial map of Callisto.

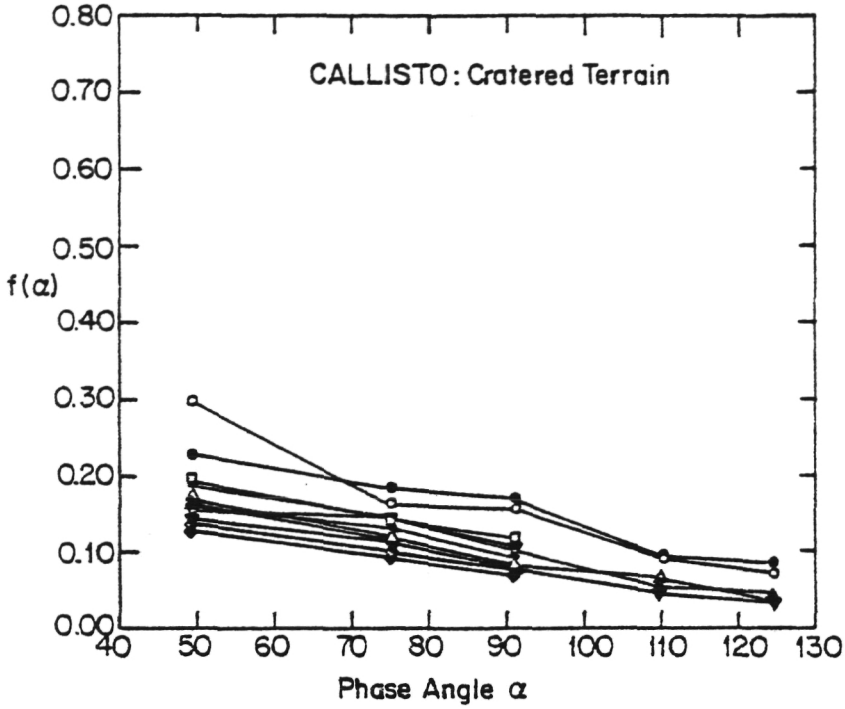


FIGURE 3.17. Curves of f(α) for regions of cratered terrain on Callisto from Voyager 1 wide angle data.

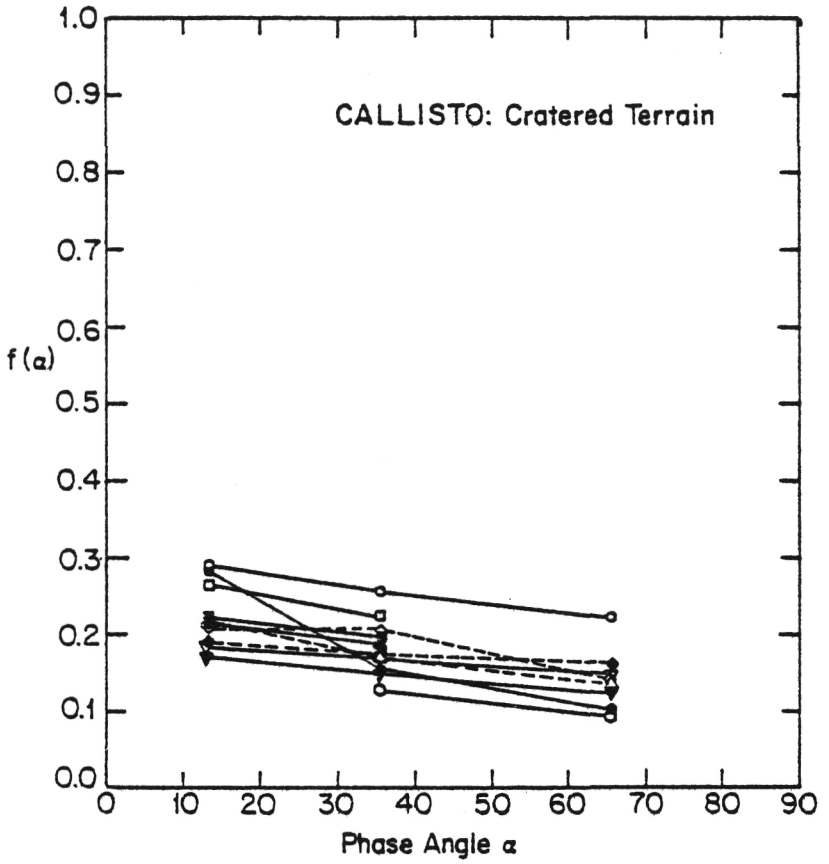


FIGURE 3.18. Curves of f(α) for regions of cratered terrain on Callisto from Voyager 2 wide angle data.

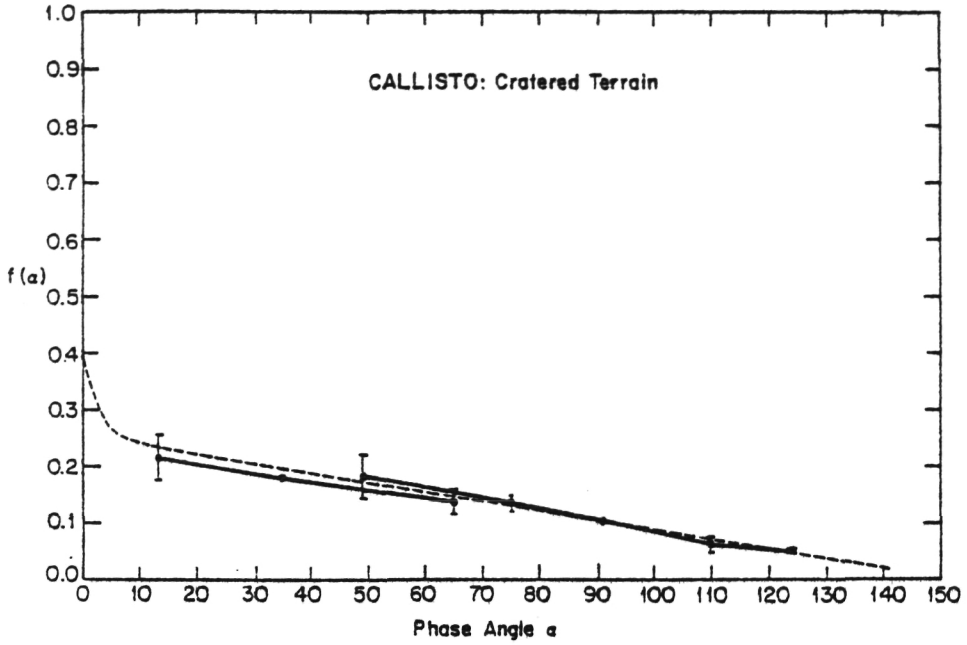


FIGURE 3.19. Curves of $f(\alpha)$ for Callisto's cratered terrain obtained by the method of Figure 3.6. Dashed curve is a best fit of the form given in equation (3.3): $f(\alpha) = 0.26 - 0.0018\alpha + 0.13e^{-0.37\alpha}$ (α in degrees).

(b) real differences on the surface of Callisto. Both effects could be involved, but the second is probably the more important since the two data sets involve different regions on Callisto. For the Voyager 1 data the range of subspacecraft longitude is from 201° through 3°, while for Voyager 2 it is from 171° to 248° (Table 3.1). Perhaps more significantly, the slightly brighter Voyager 1 data came from a pass over Callisto's north pole, while the Voyager 2 data came from a flyby at lower latitudes. The two $f(\alpha)$ segments in Fig. 3.19 match within the standard deviations of the averaged points, and averaging these two data sets should give a reliable estimate of $f(\alpha)$ for the average cratered terrain on Callisto.

The next step is to combine the data in Figure 3.19 with Earth-based observations below $\sim$ 12°. As in the case of Ganymede, $f(\alpha)$ can be calculated from the published disc-integrated observations (Morrison and Morrison, 1977); it is assumed for this purpose that Callisto is all cratered terrain. Three data sets are combined: Earth-based, Voyager 1, and Voyager 2 by again fitting to the points an $f(\alpha)$ of the form:

$$f(\alpha) = A + B\alpha + Ce^{-D\alpha} \qquad (3.3)$$

The resulting smooth curve in Figure 3.19 shows that this curve fits the Callisto observations well. The resulting $f(\alpha)$ curve is the best estimate of the photometric

properties of Callisto's cratered terrain.

As a test of the validity of reducing the Callisto data using equation (3.1), the dependence of the disc-integrated brightness of Callisto ($\Phi(\alpha)$) may be calculated from the $f(\alpha)$ shown in Figure 3.19, and compared with actual observations (Fig. 3.20). The agreement is excellent.

The average normal reflectance for the cratered terrain on Callisto is 0.19 from Figure 3.19, a value consistent with the Earth-based value for Callisto as a whole (Morrison and Morrison, 1977). In constructing the smooth curve in Figure 3.20, it has again been assumed that Callisto is all cratered terrain. It is shown below that the conspicuous craters on Callisto that cover only 3% of the surface are typically 1.5 times brighter than the cratered terrain. Thus they contribute only about 5% of the actual disc-integrated light. However, their phase curves are steeper at large phase angles, and their small contribution to the disc-integrated light may account for the slight systematic deviation of the data points in Figure 3.19 from the calculated curve.

From the data in hand it cannot be demonstrated that the scattering properties of any of Callisto's cratered terrain depart measurably from equation (3.1). As with the grooved and cratered terrain, 32 areas in image 142J1+000 (α = 49°) have been selected to determine the

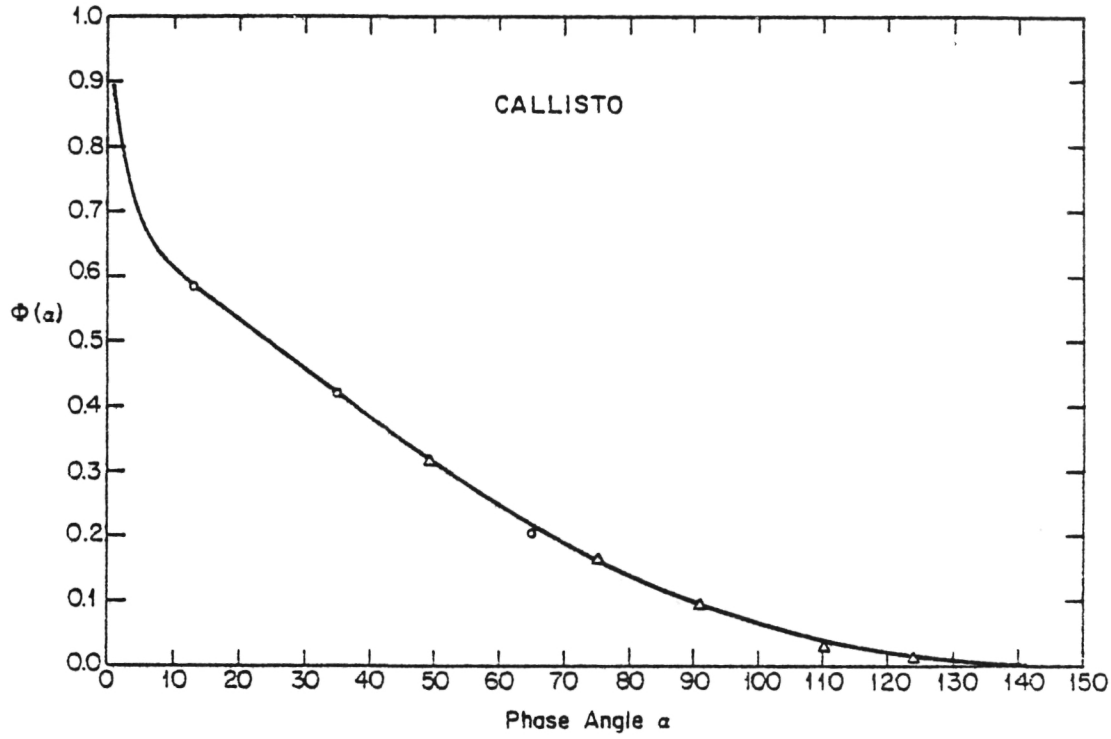


FIGURE 3.20. Observed values of disc-integrated brightness of Callisto (circles and triangles) and curve of $\Phi(\alpha)$ predicted from the $f(\alpha)$ curve of cratered terrain. Predicted curve is normalized to 1.0 at $\alpha = 0°$. Observations are normalized to the predicted values at $\alpha = 35°$ and $\alpha = 75°$.

range of reflectance. The calculated normal reflectance of these areas ranges from 0.14 to 0.22 with a mean of 0.18 (Fig. 3.21). The mean value derived in this manner is in essential agreement with the value of 0.19 derived from Figure 3.19.

It has been assumed that equation (3.1) is a valid representation of the cratered terrain's scattering properties. It has been shown that this assumption leads to the derivation of an $f(\alpha)$ that is consistent with the observed disc-integrated $\Phi(\alpha)$. Given the relatively low reflectance of the cratered terrain it is not surprising that equation (3.1) should apply (Veverka et al., 1978). Figure 3.22 demonstrates that individual areas of the cratered terrain scatter according to equation (3.1), and certainly not according to anything resembling Lambert's law at low phase angles ($\alpha \sim 10°$). Figure 3.23 shows that equation (3.1) also reproduces very well the brightness distribution along lines of photometric latitude on Callisto at phase angles of 35°, 49°, and 75°. As in the case of Ganymede, the data needed to construct curves similar to those shown in Figure 3.22 for individual areas of the cratered terrain at larger phase angles are lacking.

3.3.3 Craters

Thirty craters were selected on Callisto for individual study (Fig. 3.16). These features are

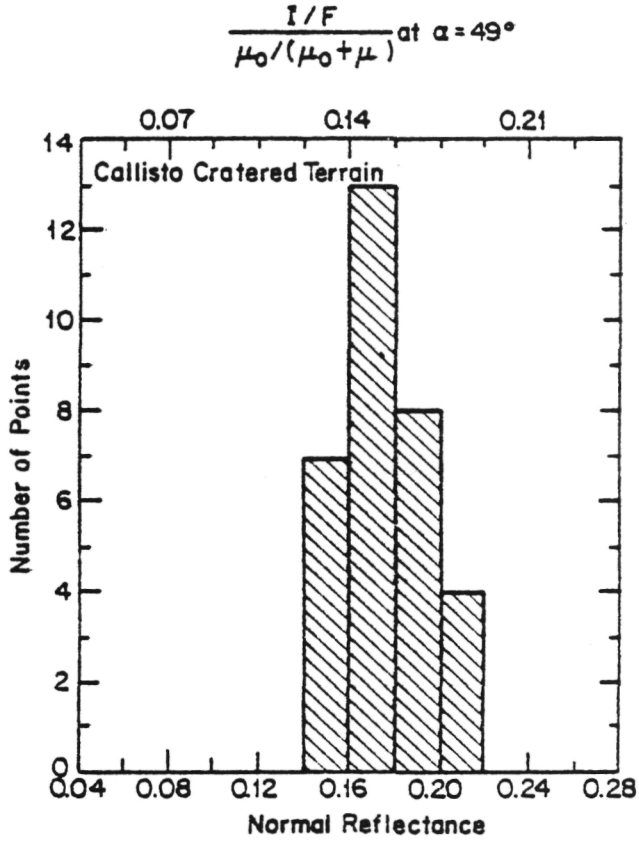


FIGURE 3.21. Histogram of extrapolated normal reflectance for 32 points in Callisto's cratered terrain.

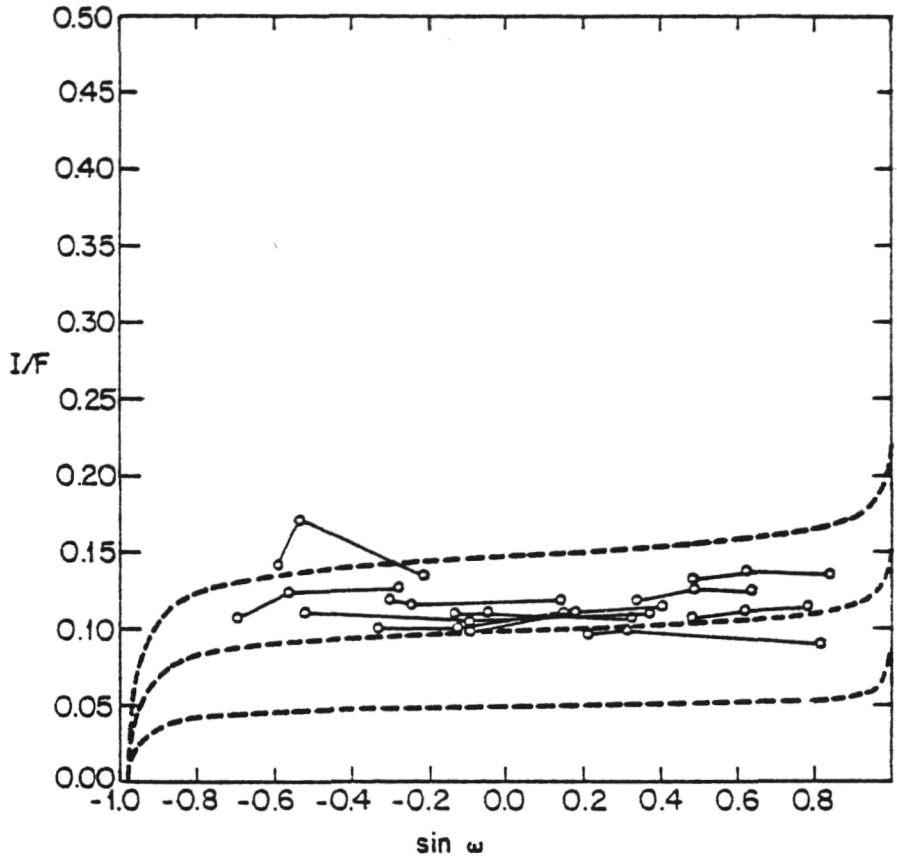


FIGURE 3.22a. Observed variation of intensity with photometric latitude for Callisto cratered terrain at $\alpha \sim 10°$. Dashed curves give behavior expected for a lunar-like photometric function (equation 3.1) with $f(10°) = 0.1$, 0.15, and 0.2.

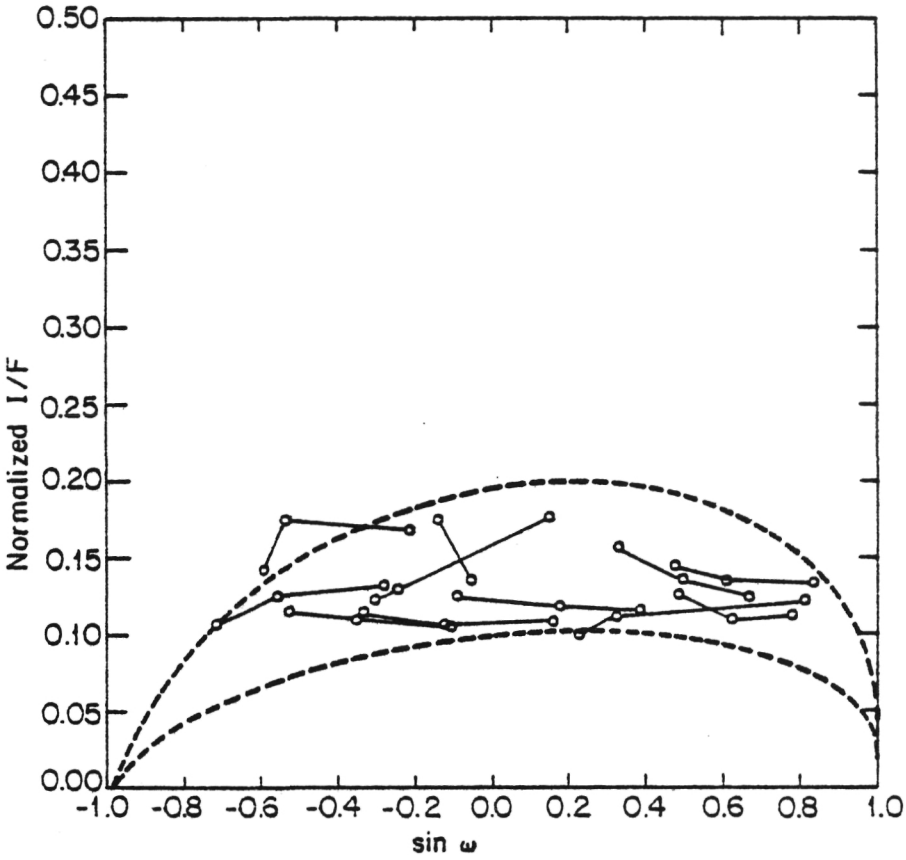


FIGURE 3.22b. Normalized intensity variations at $\alpha = 10°$ compared with Lambert's law behavior. Dashed curves are for $r_n = 0.1$ and 0.2.

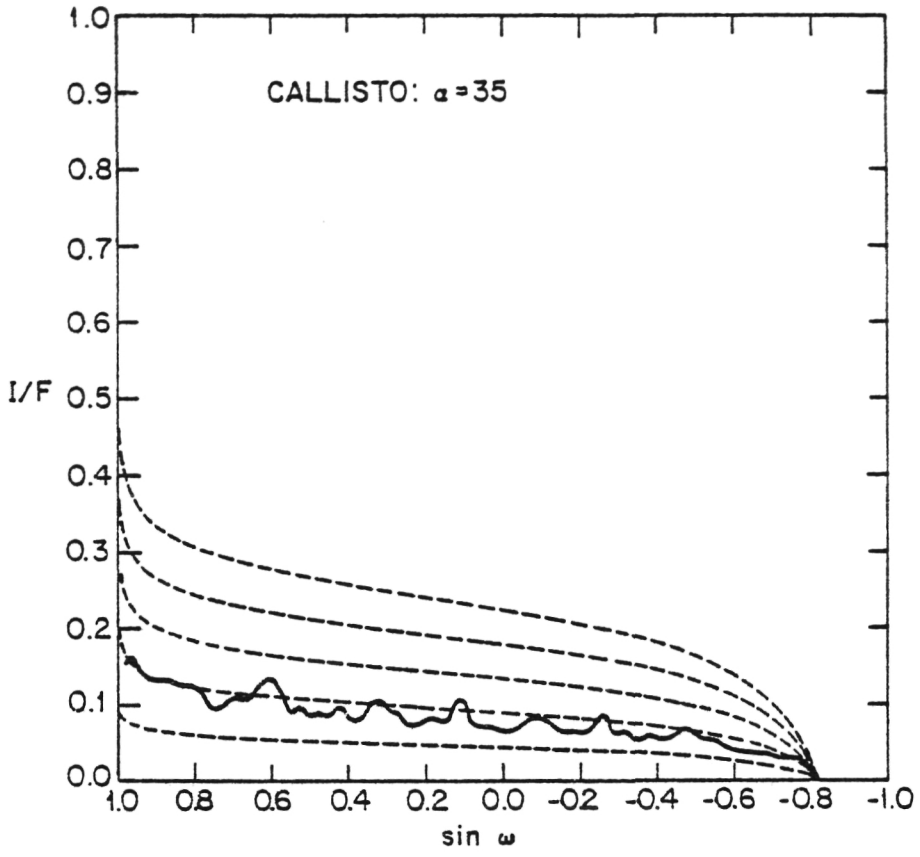


FIGURE 3.23a. Intensity scan across Callisto's disc at $\alpha = 35°$. Dashed curves give behavior predicted by equation (3.1) with $f(35°) = 0.1$-0.5 at intervals of 0.1.

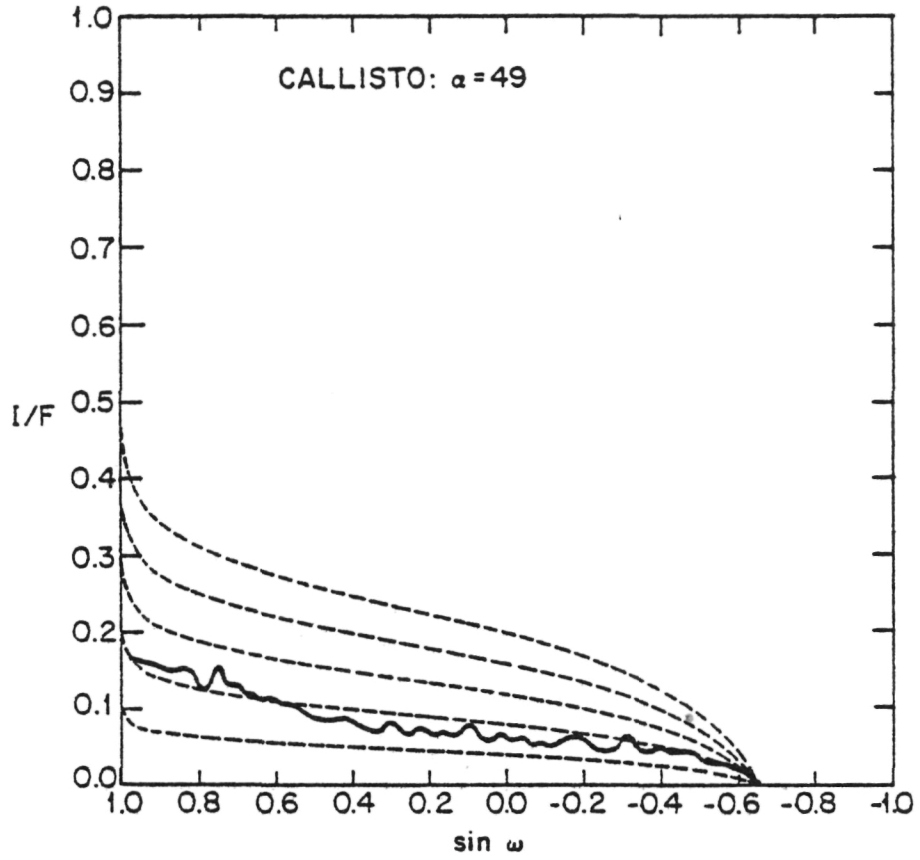


FIGURE 3.23b. Intensity scan across Callisto's disc at α = 49°. Dashed curves are for f(49°) = 0.1-0.5 at intervals of 0.1.

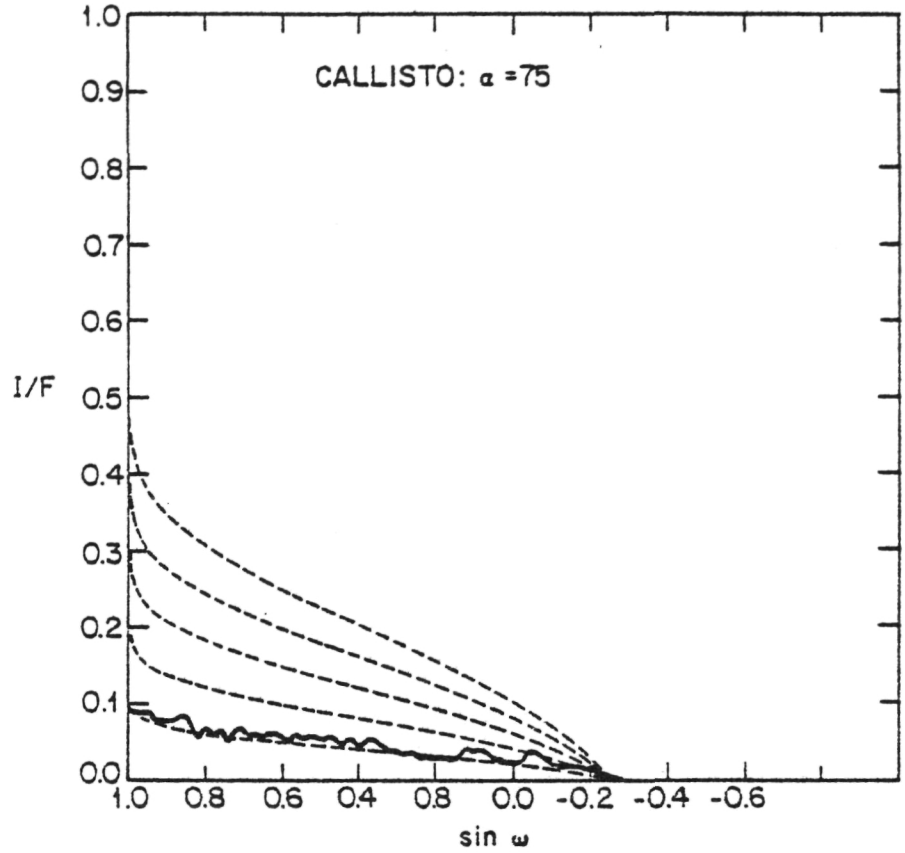


FIGURE 3.23c. Intensity scan across Callisto's disc at $\alpha = 75°$. Dashed curves are for $f(75°) = 0.1$-0.5 at intervals of 0.1.

typically $\leq$ 100 km in diameter and range in reflectance from just above that of the average cratered terrain ($\sim$ 0.2) to nearly as high as the bright craters on Ganymede ($\sim$ 0.7).

As in the case of the cratered terrain, one can demonstrate that equation (3.1) provides a good description of the scattering properties of even the brightest craters, and that Lambert's law does not fit the data well at all. Figure 3.24 compares the observed brightness variation of some of these craters as a function of sin ω (where ω = photometric longitude) against the predictions of the above two models.

Calculations of residuals confirm the visual impression that equation (3.1) provides a much better fit than Lambert's law. As in the case of Ganymede's bright craters, one may test a scattering law of the form

$$I(i,\varepsilon,\alpha) \propto (b - 1)[\mu_0/(\mu_0 + \mu)] + b\mu_0 . \quad (3.4)$$

Given the data in hand, it is only possible to carry out tests of this law at small phase angles. Tests such as those in Figure 3.23 cannot be constructed for the craters, since the craters range widely in their reflectances.

For half of the craters in Figure 3.24 (including the two brightest) the best fit of equation (3.4) occurs for b = 0. For the other half a small value of b, typically b $\sim$ 0.3, produces a slightly better fit. Due to the

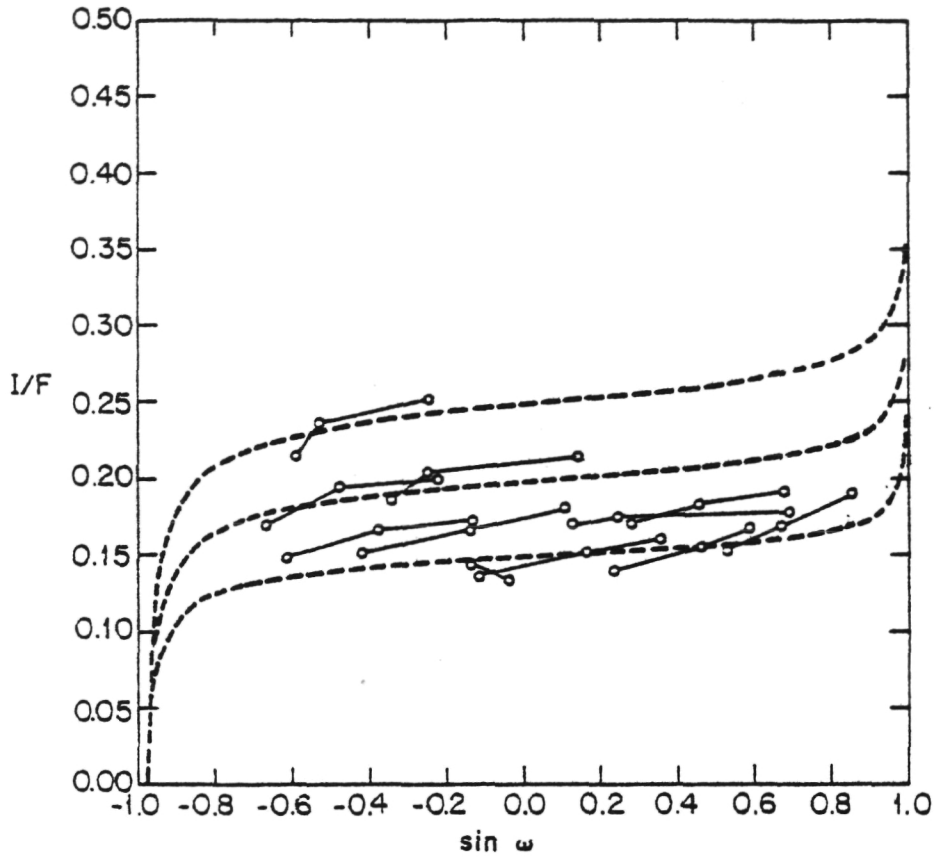


FIGURE 3.24a. Observed variation of intensity with photometric longitude for Callisto craters at $\alpha \sim 10°$. Dashed curves give behavior expected for a lunar-like photometric function (equation 3.1) with $f(10°) = 0.25$, 0.3, and 0.35.

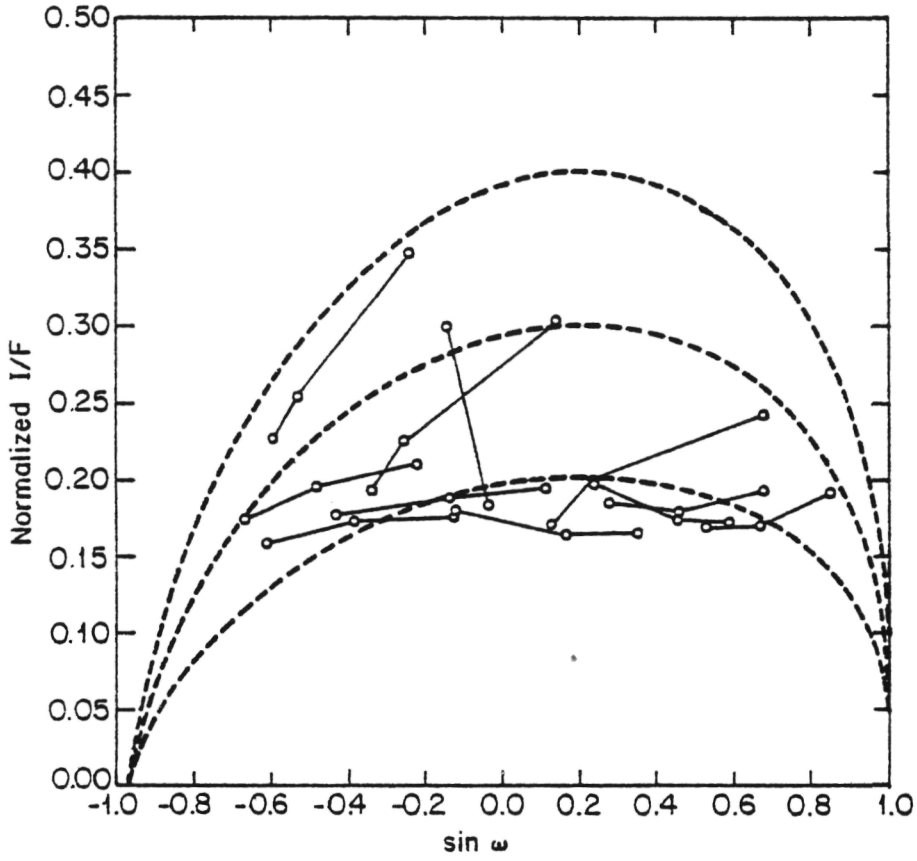


FIGURE 3.24b. Normalized intensity variations at $\alpha \sim 10°$ compared with Lambert's law behavior. Dashed curves are for r_n = 0.2, 0.3, and 0.4.

paucity of data points it is not clear that this result is significantly different from b = 0, especially since there is an anticorrelation between the reflectances and the value of b. On general physical grounds one would expect that the value of b would be largest for the brightest craters. In any case, it is clear that a value of b = 1 (Lambert's law) is inappropriate for any of the craters in the sample.

The subsequent analysis is based on the assumption that equation (3.1) provides an adequate description of the scattering properties of the craters on Callisto. The resulting $f(\alpha)$'s are shown in Figure 3.25. Note that the low latitude Voyager 2 data do not include any very bright craters, whereas the Voyager 1 polar coverage does include some craters that are as bright as some of the brighter ray craters on Ganymede. Due to the diversity among the craters, in terms of both $f(\alpha)$ and reflectance, the results shown in Figure 3.25 cannot be averaged in any meaningful way.

Table 3.3 lists the brightness of the three brightest Callisto craters relative to the average cratered terrain at the smallest phase angle for which both Voyager 1 and Voyager 2 data are available ($\alpha \sim 50°$). Also listed are normal reflectances obtained by extrapolating these data to zero phase assuming that at low phase angles

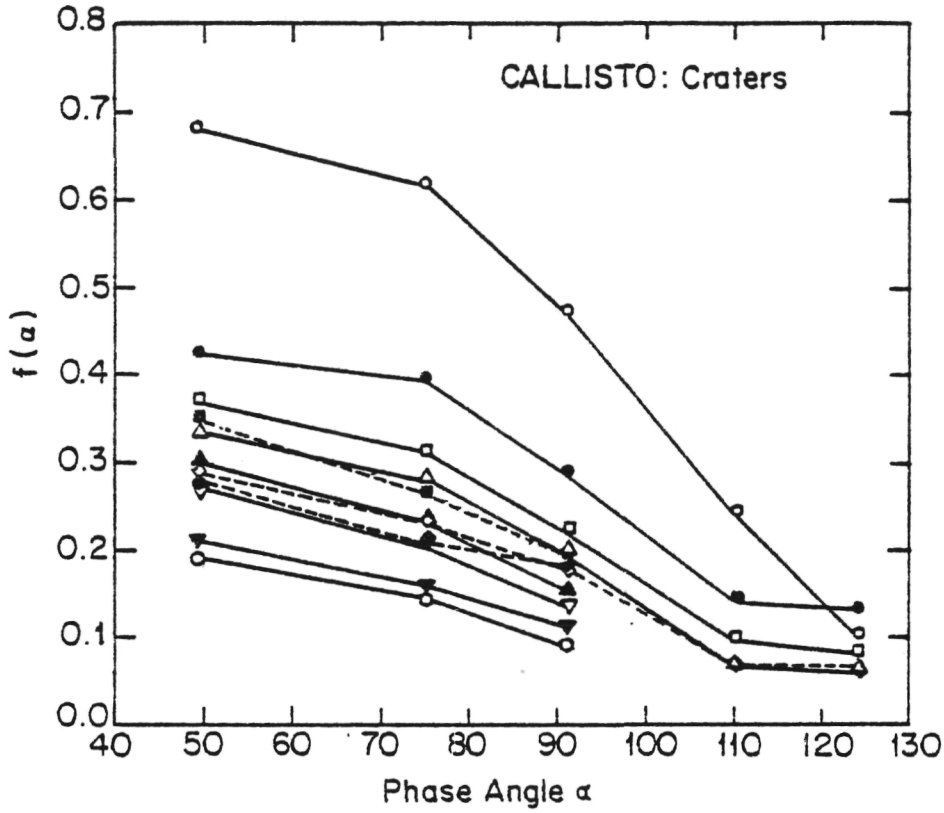


FIGURE 3.25. Curves of f(α) for craters on Callisto.

TABLE 3.3 Bright Craters on Callisto

Location	Brightness Relative to Cratered Terrain, $\alpha = 49°$	Estimated Normal Reflectance, r_n
67°N, 28°	3.80	0.72
55°N, 42°	2.35	0.45
36°N, 65°	2.10	0.40

these craters follow the phase law for the average surface of Callisto.

3.3.4 Disc-Integrated Parameters

Figure 3.19 yields a value of 0.6 for the phase integral q of Callisto in the clear filter. This value is consistent with Morrison's (1977) estimate of $q = 0.8 \pm 0.4$ for the effective radiometric phase integral of the satellite.

Since Callisto scatters light according to equation (3.1) the geometric albedo equals the normal reflectance. Taking the latter to be 0.19, the Bond albedo of Callisto in the clear filter is approximately 0.13, a value that can be considered a good approximation to the true radiometric albedo of the satellite.

3.4 Discussion

The principal results of this study are summarized in Table 3.4. The most interesting result is that the scattering properties of even the brightest surfaces observed are best matched by a lunar-like photometric function. The brightest craters on Ganymede, with normal reflectances that may reach 0.7, do not show anything like Lambertian behavior. The observed scattering function may be due to admixture of a small amount of dark, opaque silicate grains with the frost deposits. Experimental work has

TABLE 3.4 Summary of Results

	Ganymede					Callisto		
	Cratered Terrain	Grooved Terrain	Polar Caps	Bright Craters	Earth-based Estimates	Cratered Terrain	Bright Craters	Earth-based Estimates
Geometric Albedo p	0.43				0.43 ± 0.02*	0.19		0.17 ± 0.02*
Phase Integral q	0.8				1.0 ± 0.3†	0.6		0.8 ± 0.4†
Bond Albedo A_B	0.35				--	0.13		--
Normal Reflectance	0.35 ± 0.07	0.44 ± 0.10	~ 0.6	$\lesssim$ 0.7	--	0.18 ± 0.04	$\lesssim$ 0.7	--
Scattering Law	$I \propto [\mu_o/(\mu_o + \mu)]f(\alpha)$				--	$I \propto [\mu_o/(\mu_o+\mu)]f(\alpha)$		--

*from Morrison and Morrison (1977).

†from Morrison (1977).

shown that introduction of a very small percentage of dark material substantially reduces limb-darkening of bright particulate surfaces (Veverka et al., 1978). Detailed study of the photometric properties of frost/silicate mixtures is necessary to estimate the actual percentage of silicate grains present in the crater deposits.

The phase curves for most of the terrain types are summarized in Figure 3.26. Also shown for comparison are $f(\alpha)$ curves for the Moon (Shorthill et al., 1969) and Phobos (Klaasen et al., 1979). The curves for Phobos, the Moon, Callisto cratered terrain, Ganymede cratered terrain, and Ganymede grooved terrain are qualitatively similar, although the curve for Callisto cratered terrain is unusually steep at very low phase angles. All show the concave upward shape characteristic of dark particulate surfaces. In contrast, the concave downward shape shown by the Ganymede bright crater curve is characteristic of bright materials. Parameters describing all the concave upward phase curves are listed in Table 3.5. Note that $(A + C)/2$ equals the normal reflectance, and that this parameter is linearly anticorrelated with B. B describes the slope of the phase curve away from opposition. The physical significance of this anticorrelation becomes apparent when one remembers that $f(\alpha)$ approaches 0 as α approaches 180° in all cases.

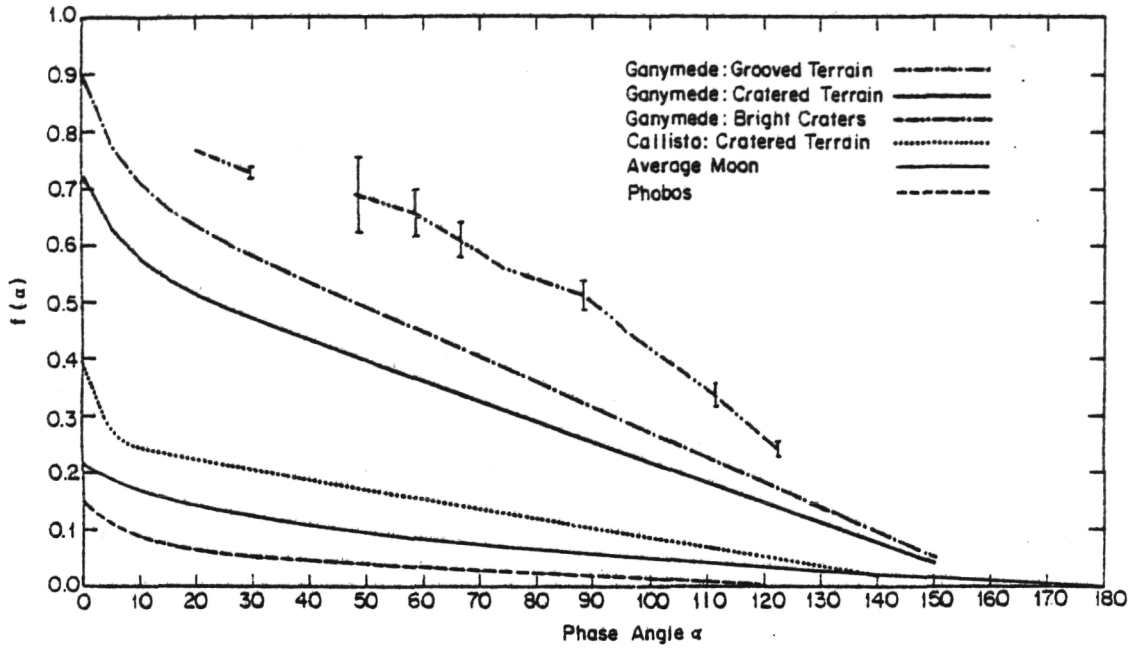


FIGURE 3.26. Summary of observed phase curves, with curves for the Moon and Phobos for comparison.

TABLE 3.5 Phase Curve Parameters:

$f(\alpha) = A + B\alpha + Ce^{-D\alpha}$ (α in degrees)

Terrain Type	A	B	C	D
Ganymede Grooved Terrain	0.71	-0.0044	0.18	0.14
Ganymede Cratered Terrain	0.57	-0.0035	0.14	0.14
Callisto Cratered Terrain	0.26	-0.0018	0.13	0.37
Moon	0.10	-0.0055	0.12	0.05
Phobos	0.04	-0.0003	0.10	0.06

The phase curves presented here appear generally consistent with results from the Voyager photopolarimeter experiment. A disc-integrated curve for Ganymede at phase angles up to 30° determined by Pang et al. (1979) is slightly less steep than the predicted curve, based on grooved and cratered terrain observations, shown in Figure 3.15. The slope of the photopolarimeter curve is, however, well within the error bars of Figures 3.6 and 3.9. The small discrepancy between the best fit prediction and the observations of Pang et al. is again probably due to the influence of the bright craters and the polar caps. If the concave downward curvature shown by the phase curves for these terrain types continues to low phase angles, their influence would make the disc-integrated curve in the range 0°-30° slightly shallower than would be predicted using only the grooved and cratered terrains.

Danielson et al. (1981) have very recently provided correction factors that adjust absolute intensities in Voyager images for some apparent inconsistencies among results obtained for different filters. For comparison with results that have been adjusted in this manner, all I/F values presented here should be multiplied by the appropriate factor: 0.931 (Voyager 1 narrow angle), 0.913 (Voyager 2 narrow angle), 0.878 (Voyager 1 wide angle), or 1.022 (Voyager 2 wide angle). Application of these

corrections to the reflectances calculated here would reduce those for Ganymede by 8% and those for Callisto by 6%.

These observations of course provide no information on any wavelength dependence of the photometric properties of Ganymede and Callisto. This problem is considered in the next chapter, using Voyager color images.

CHAPTER 4

COLOR PHOTOMETRY OF SURFACE FEATURES

4.1 Introduction

In the preceding chapter it was shown that the major photometric units on Ganymede and Callisto have scattering properties that can be described very well, within the constraints of available measurements, by a lunar-like photometric function of the form

$$I(i,\varepsilon,\alpha) = F[\mu_0/(\mu_0 + \mu)]\ f(\alpha)\ . \qquad (3.1)$$

In this chapter the extent to which the photometric phase function $f(\alpha)$ depends on wavelength between approximately 0.4 and 0.6 μm is investigated. In going from 0.4 to 0.6 μm, the disc integrated normal reflectance ($r_n = f(0°)/2$) of both Ganymede and Callisto increase by a factor of 1.4 (Johnson and Pilcher, 1977). However, it will be shown here that between phase angles of 50° and 90° the Voyager data indicate very little or no wavelength dependence of $f(\alpha)$. Thus the phase integrals of Ganymede and Callisto estimated in the preceding chapter on the basis of clear filter data alone do not require any significant adjustment for variations of photometric properties with wavelength.

4.2 Available Data

The best Voyager data set for the study of the wavelength dependence of $f(\alpha)$ consists of violet, clear, and orange triplets taken by the Voyager 1 wide angle camera between phase angles of 47° and 85° for Ganymede, and between 49° and 85° for Callisto (Table 4.1). The effective wavelength of the Voyager wide angle camera violet filter is approximately 0.4 μm; that of the orange filter about 0.6 μm (Danielson et al., 1981). The passband of the clear filter extends from about 0.3 to 0.6 μm, centered near 0.47 μm (Fig. 3.1).

The clear filter images used in this investigation are not identical with those used in the previous chapter. Therefore the clear filter information derived here is complementary to that in Chapter 3.

The color triplets analyzed cover a limited range of longitudes (Figures 4.1 and 4.2)--essentially the Jupiter-facing hemispheres of the two satellites. However, this limited longitude coverage probably does not bias the conclusions drawn here. The disc-integrated lightcurves of the two satellites are well known both as a function of wavelength and orbital phase (Morrison and Morrison, 1977). Between 0.4 and 0.6 μm these data show that, at the small phase angles observable from Earth, the trailing side of Ganymede is slightly redder than the leading

TABLE 4.1 Images Used for Color Photometry*

Picture Number	Phase Angle	Filter
Ganymede:		
740J1+000	47°	Clear
742J1+000	48°	Violet
746J1+000	48°	Orange
870J1+000	59°	Clear
872J1+000	59°	Violet
876J1+000	59°	Orange
952J1+000	75°	Clear
954J1+000	75°	Violet
958J1+000	75°	Orange
988L1+000	85°	Clear
990J1+000	85°	Violet
994J1+000	85°	Orange
Callisto:		
142J1+001	49°	Clear
166J1+001	51°	Violet
174J1+001	52°	Orange
320J1+001	75°	Clear
322J1+001	75°	Violet
326J1+001	76°	Orange
356J1+001	83°	Clear
358J1+001	84°	Violet
364J1+001	85°	Orange

*All images Voyager 1 wide angle.

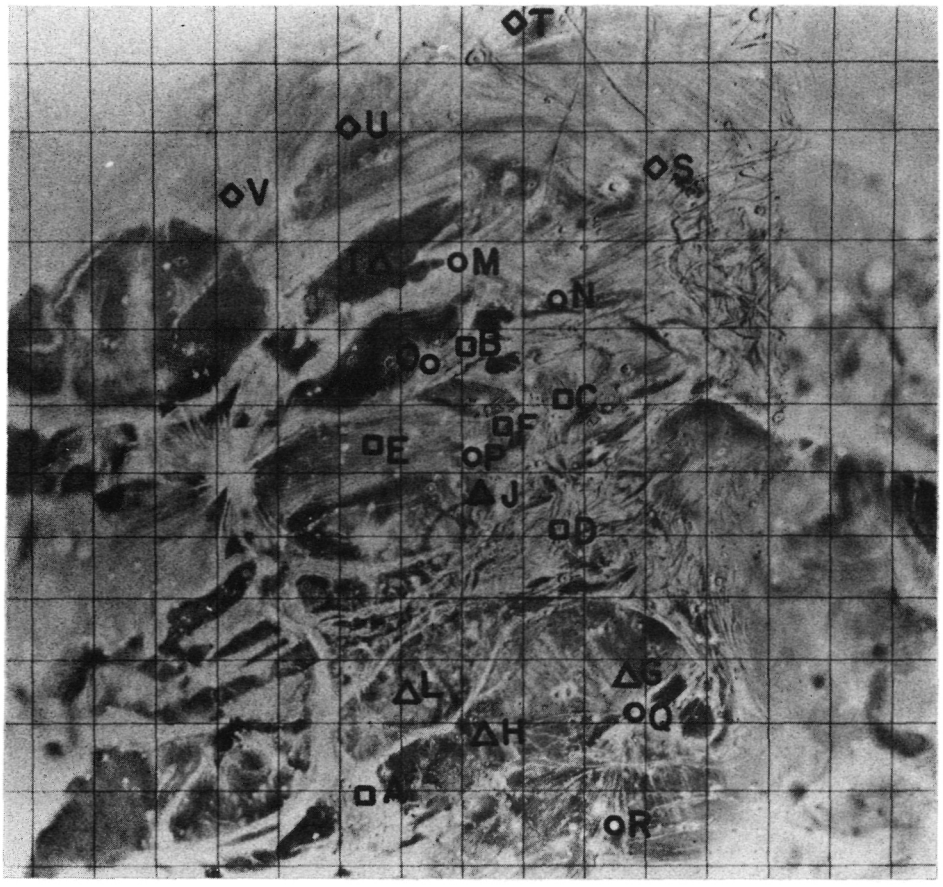


FIGURE 4.1. Points selected for color photometry on Ganymede: cratered terrain (triangles), grooved terrain (squares), polar caps (diamonds), and bright craters (circles).

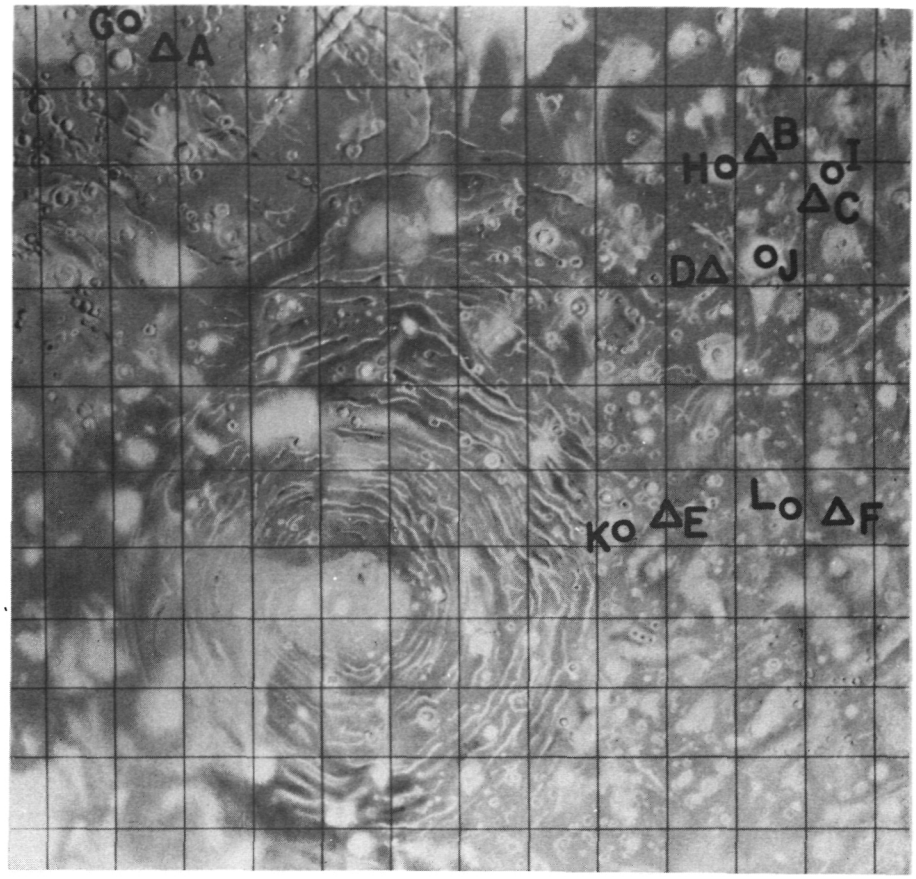


FIGURE 4.2. Points selected for color photometry of Callisto: cratered terrain (triangles), and bright craters (circles).

side (the reverse is true for Callisto). The differences are small, amounting to 5% or less.

4.3 Analysis

4.3.1 Ganymede

As in Chapter 3, four separate photometric units on this satellite are considered: cratered terrain, grooved terrain, polar caps, and bright craters. In all, 22 individual regions were studied (Fig. 4.1; Table 4.2) between phase angles of 47° and 85°. For no individual region was a significant wavelength dependence to the shape of $f(\alpha)$ observed. Therefore, to improve the signal-to-noise ratio the data were averaged for each photometric unit. The resulting averaged curves are shown in Figures 4.3-4.6. The conclusion is that the shapes of the $f(\alpha)$ curves are identical in all three filters, within the accuracy of the data and reduction technique. To quantify this assertion a quadratic polynomial of the form

$$f(\alpha) = a + b\alpha + c\alpha^2 \qquad (4.1)$$

has been fitted to the data shown in Figures 4.3 and 4.4. (It should be recalled from Chapter 3 that only for these two units is sufficient photometric coverage available to prove that the photometric function of the form given by Eqn. 3.1). The results of these fits are given in Table 4.3 and confirm this assertion. While there is a trend for

TABLE 4.2 Relative Reflectance of Points Examined on Ganymede*

Point	Terrain Type	Phase Function f(α) Violet	Clear	Orange
A	Grooved Terrain	0.563	0.589	0.577
B	" "	0.550	0.587	0.577
C	" "	0.493	0.533	0.546
D	" "	0.454	0.502	0.518
E	" "	0.609	0.628	0.661
F	" "	0.503	0.540	0.533
G	Cratered Terrain	0.359	0.384	0.393
H	" "	0.398	0.443	0.445
I	" "	0.371	0.398	0.359
J	" "	0.459	0.496	0.512
K	" "	0.498	0.535	0.530
L	" "	0.482	0.505	0.510
M	Bright Crater	0.806	0.812	0.710
N	" "	0.693	0.732	0.673
O	" "	0.620	0.661	0.644
P	" "	0.759	0.783	0.751
Q	" "	0.564	0.509	0.524
R	" "	0.593	0.600	0.553
S	Polar Cap	0.588	0.593	0.536
T	"	0.724	0.723	0.674
U	"	0.730	0.737	0.696
V	"	0.731	0.740	0.699

* All observations Voyager 1 wide angle, phase angle ≃ 47°.

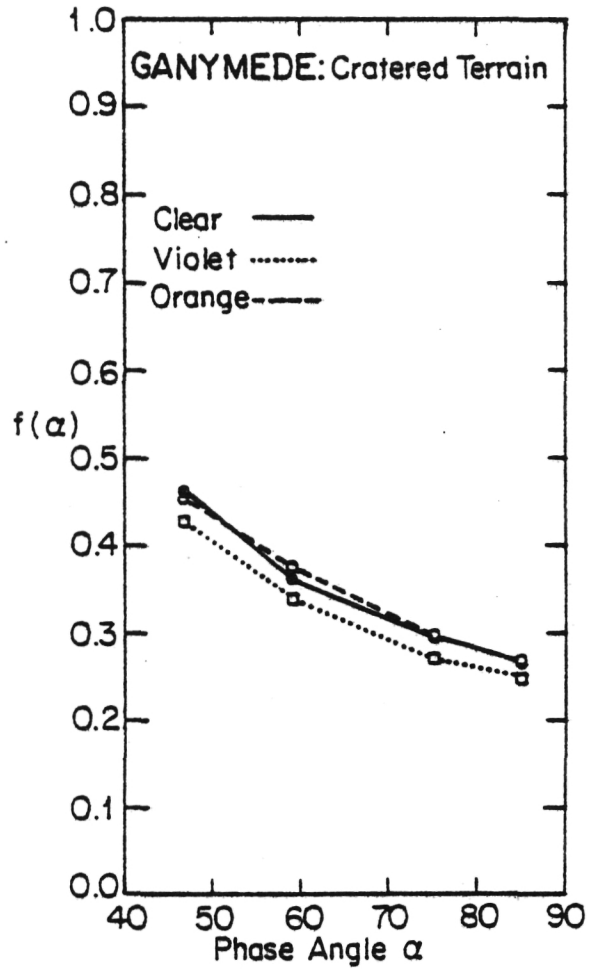


FIGURE 4.3. Average Voyager 1 wide angle color phase curves for Ganymede cratered terrain.

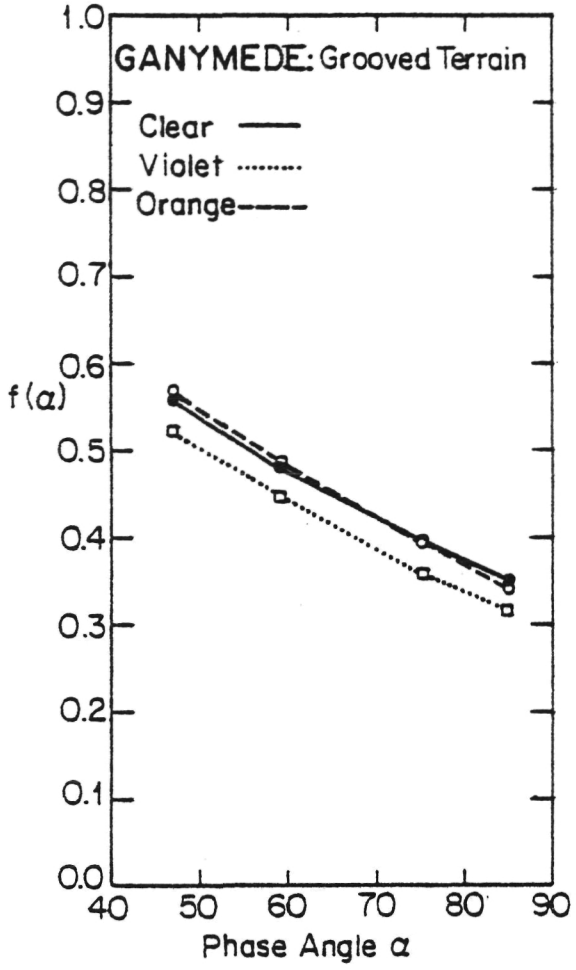


FIGURE 4.4. Average Voyager 1 wide angle color phase curves for Ganymede grooved terrain.

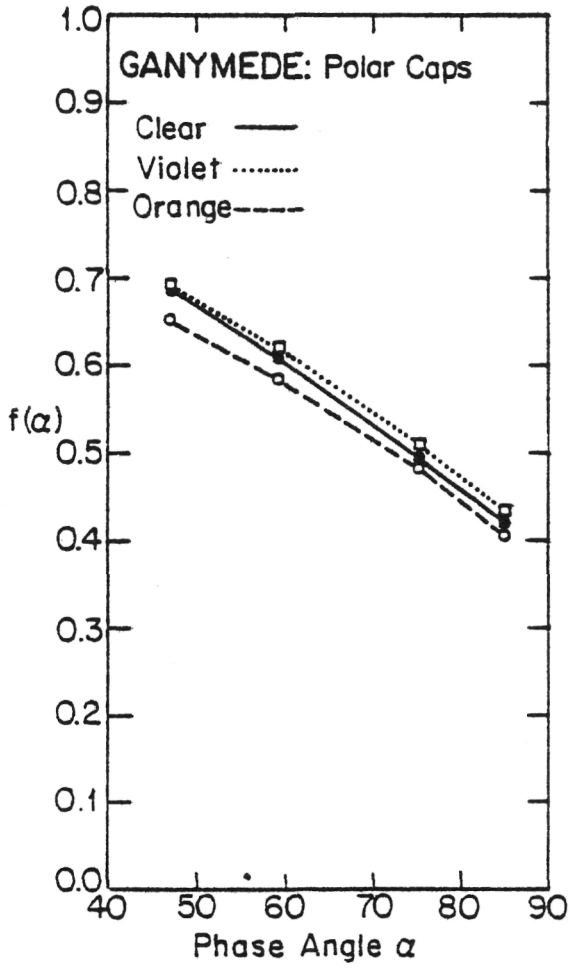


FIGURE 4.5. Average Voyager 1 wide angle color phase curves for Ganymede polar caps.

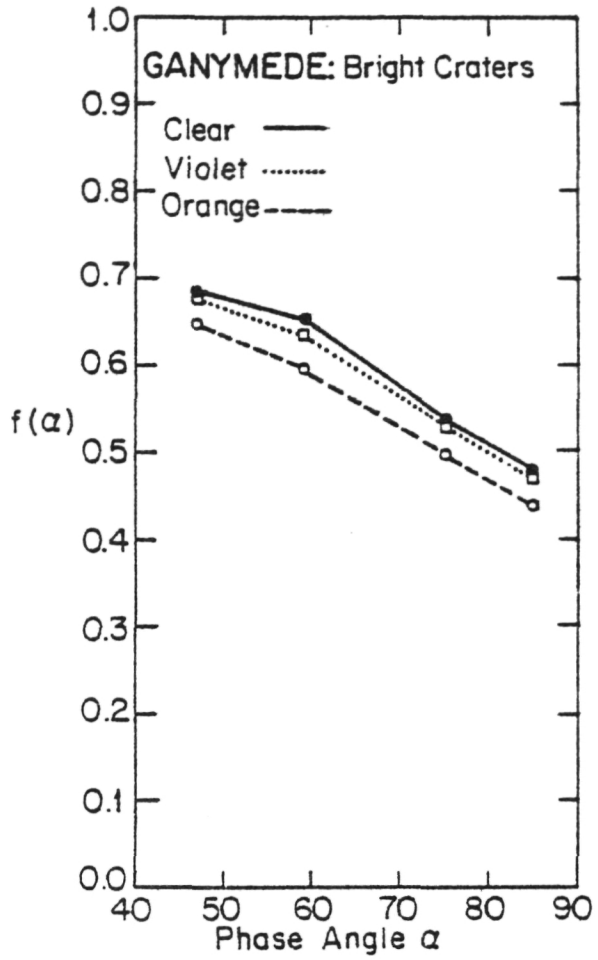


FIGURE 4.6. Average Voyager 1 wide angle color phase curves for Ganymede bright craters.

TABLE 4.3 Fits to Ganymede Color Phase Curves*

	Violet	Clear	Orange
Cratered Terrain			
$(b \pm \sigma_b) \times 10$	-0.163 ± 0.055	-0.174 ± 0.087	-0.118 ± 0.050
$(c \pm \sigma_c) \times 10^4$	0.849 ± 0.426	0.930 ± 0.646	0.509 ± 0.345
Grooved Terrain			
$(b \pm \sigma_b) \times 10$	-0.102 ± 0.041	-0.103 ± 0.028	-0.089 ± 0.047
$(c \pm \sigma_c) \times 10^4$	0.337 ± 0.291	0.367 ± 0.195	0.231 ± 0.330

* Data in Figures 4.2 and 4.3 fitted to $f(\alpha) = a + b\alpha + c\alpha^2$, α in degrees.

the curves to be slightly steeper in the violet than in the orange--consistent with the universal tendency of lower albedos being associated with larger color phase coefficients--the difference lies entirely within the error bars.

Finally, the data have also been reduced in a disc integrated form (Fig. 4.7); these data again confirm the conclusion that no wavelength dependence to the shape of $f(\alpha)$ can be demonstrated for Ganymede over this range of phase angles within the accuracy of the data.

Table 4.2 lists the absolute values of $f(\alpha)$ at $\alpha = 47°$ in the three filters for the 22 regions investigated. These values give directly the relative reflectances of these units at this phase angle. Since the major conclusion here is that $f(\alpha)$ is not measurably dependent on wavelength between 0.4 and 0.6 μm and between $\alpha = 47°$ and 85°, the best $f(\alpha)$ available--that determined in the clear filter in Chapter 3--can be used to calculate relative reflectances at other phase angles within the range in question.

It should be stressed that the $f(\alpha)$'s determined for the clear filter in this chapter agree with those of Chapter 3. However, those in Chapter 3, determined as they were from a considerably more extensive data base, should be used as the best $f(\alpha)$'s available. Since the phase curves for the bright craters show the largest diversity,

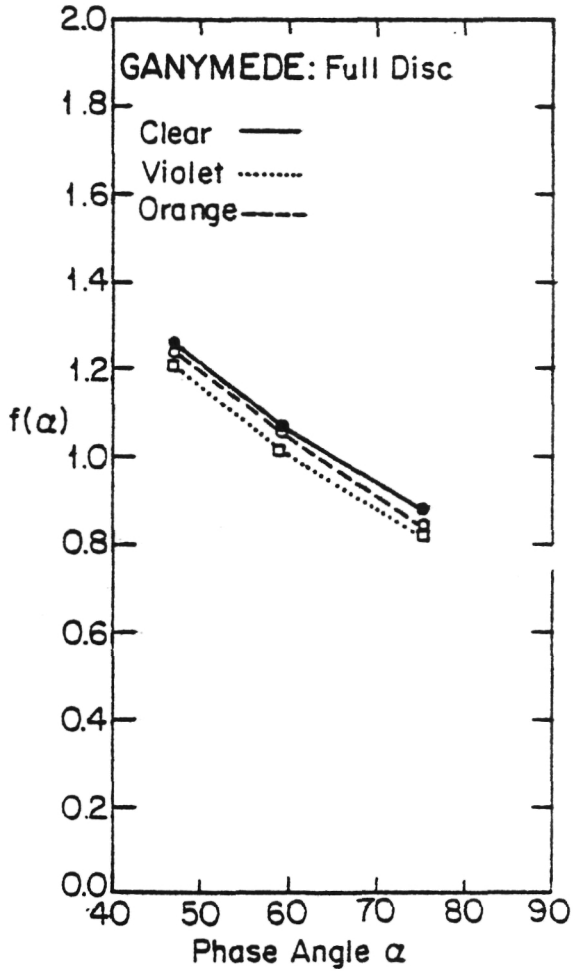


FIGURE 4.7. Disc-averaged Voyager 1 wide angle color phase curves ($f(\alpha)$) for Ganymede.

and since the craters analyzed in this chapter differ from those studied in Chapter 3, the individual clear filter phase curves for the bright craters listed in Table 4.2 are shown in Figure 4.8.

4.3.2 Callisto

On Callisto a dozen individual regions have been studied (Fig. 4.2; Table 4.4), equally divided between the two photometric units discussed in Chapter 3: cratered terrain and bright craters. Again, the individual bright craters investigated here differ from those in the previous chapter. The individual clear filter phase curves of the six bright craters listed in Table 4.4 are shown in Figure 4.8.

The Callisto color data cover a range of phase angles from $\alpha = 49°$ to $85°$. As in the case of Ganymede, no significant wavelength dependence in the shapes of the individual or average $f(\alpha)$ curves (Figs.4.9 and 4.10) is detectable. Since the phase curves are essentially linear over the phase angle range in question, a linear function of the form

$$f(\alpha) = a + b\alpha \qquad (4.2)$$

has been fitted to the data in Figures 4.9 and 4.10. The results, summarized in Table 4.5, show that while numerically the slopes are slightly higher in the violet than

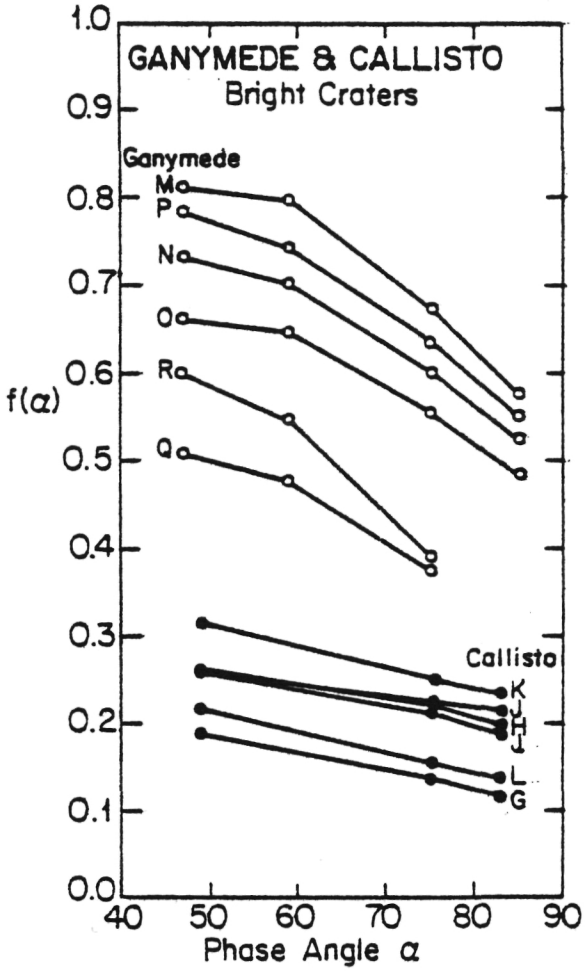


FIGURE 4.8. Voyager 1 wide angle clear phase curves for individual bright craters on Ganymede and Callisto.

TABLE 4.4 Relative Reflectance of Points Examined on Callisto*

Point	Terrain Type	Phase Function f(α) Violet	Clear	Orange
A	Cratered Terrain	0.122	0.126	0.141
B	" "	0.205	0.202	0.215
C	" "	0.171	0.172	0.217
D	" "	0.152	0.167	0.176
E	" "	0.139	0.145	0.147
F	" "	0.139	0.152	0.157
G	Bright Crater	0.180	0.188	0.193
H	" "	0.251	0.262	0.247
I	" "	0.269	0.259	0.260
J	" "	0.256	0.260	0.249
K	" "	0.311	0.315	0.296
L	" "	0.194	0.217	0.197

* All observations Voyager 1 wide angle, phase angle ≈ 50°.

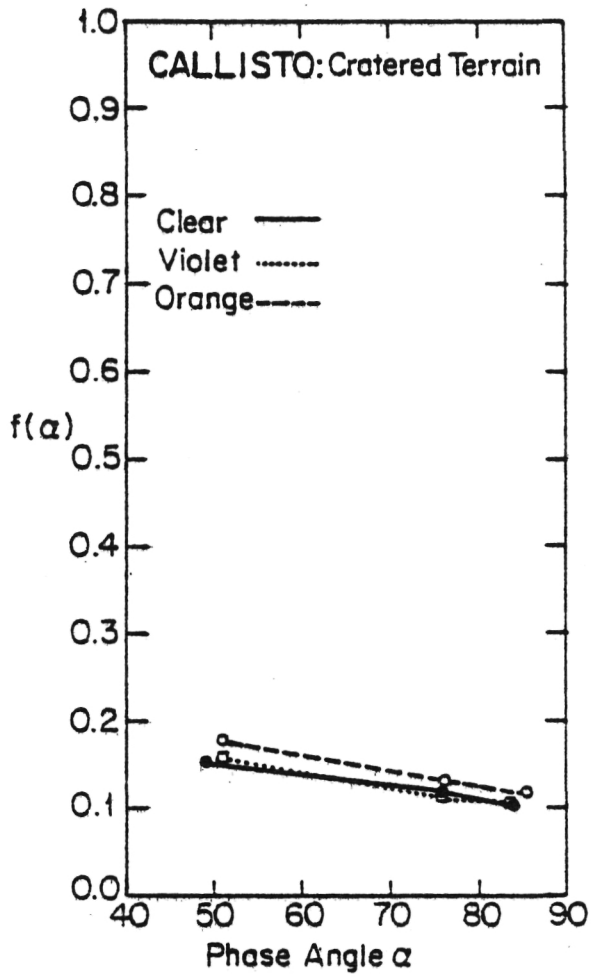


FIGURE 4.9. Average Voyager 1 wide angle color phase curves for Callisto cratered terrain.

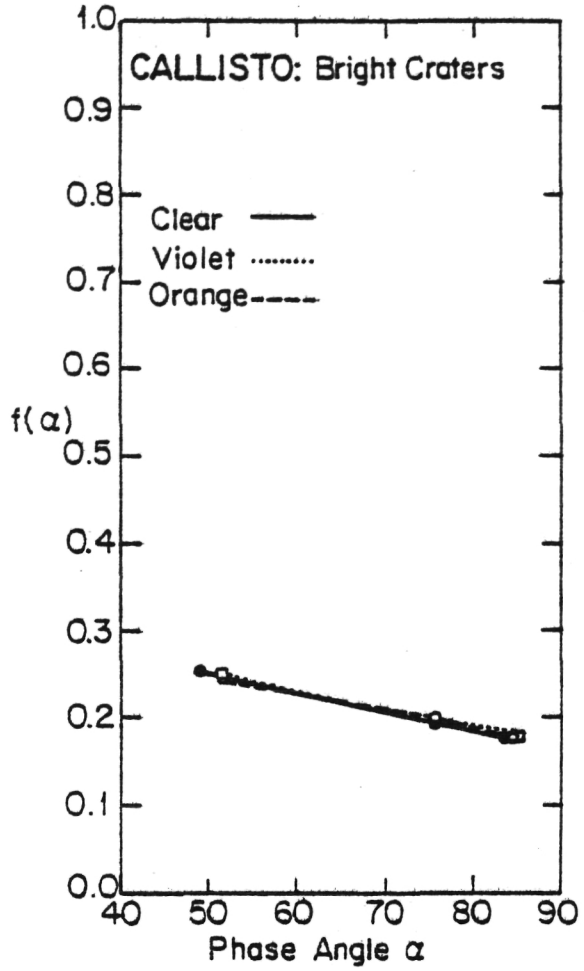


FIGURE 4.10. Average Voyager 1 wide angle color phase curves for Callisto bright craters.

TABLE 4.5 Fits to Callisto Color Phase Curves

	Violet	Clear	Orange
Cratered Terrain			
$(b \pm \sigma_b) \times 10^3$	-1.763 ± 0.460	-1.667 ± 0.483	-1.629 ± 0.551
Bright Craters			
$(b \pm \sigma_b) \times 10^3$	-2.110 ± 0.652	-2.114 ± 0.681	-2.051 ± 0.753

* Data in Figures 4.9 and 4.10 fitted to $f(\alpha) = a + b\alpha$.

in the orange, the differences lie entirely within the error bars. Similar conclusions hold for the disc-integrated data shown in Figure 4.11.

As in the case of Ganymede, the Voyager data analyzed in this chapter contain no evidence for a measurable wavelength dependence of the shape of $f(\alpha)$. Hence the results of Chapter 3 may be used over a wavelength range of at least 0.4 to 0.6 μm.

Table 4.4 lists the absolute values of $f(\alpha)$ at $\alpha \simeq 50°$, in the three filters, for the twelve Callisto regions investigated (Figure 4.2).

4.4 Conclusions

One conclusion of immediate importance is that the phase integral q (Appendix A) for both bodies is not strongly wavelength dependent between 0.4 and 0.6 μm. Since this is precisely the spectral region over which the most dramatic spectral reflectance variations occur (Johnson and Pilcher, 1977) one would expect the wavelength dependence of $f(\alpha)$, and hence of q, to be at a maximum here. Thus, the phase integrals and Bond albedos derived for Ganymede and Callisto in Chapter 3 on the basis of the clear filter phase data and the observed spectral reflectance curve at low phase angles are believed to be accurate within about ± 10%.

The negligible wavelength dependence of $f(\alpha)$ between

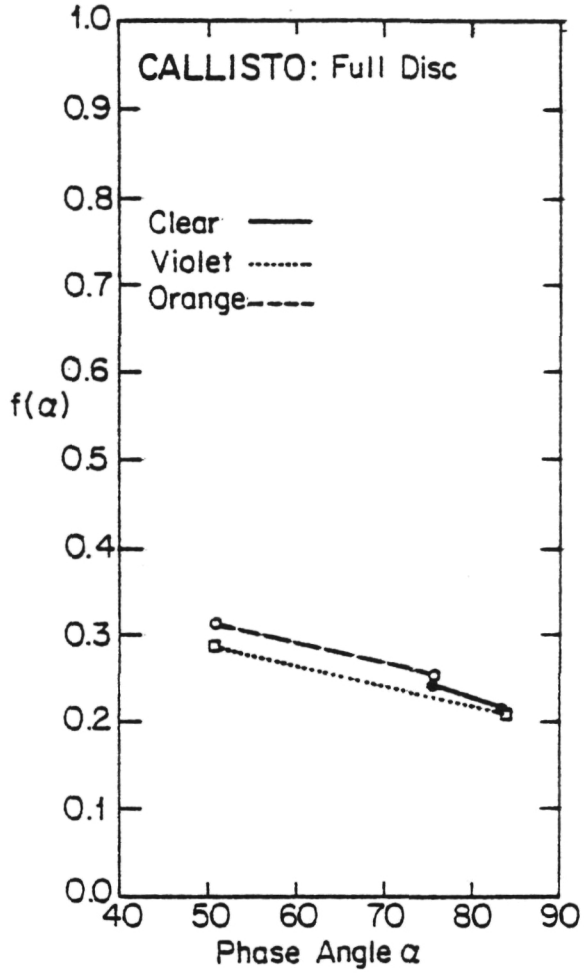


FIGURE 4.11. Disc-averaged Voyager 1 wide angle color phase curves (f(α)) for Callisto.

0.4 and 0.6 μm is consistent with available Earth-based observations between $\alpha = 0°$ and 12°. According to Veverka (1977) the color phase coefficient $d(v - y)/d\alpha$ is about 0.003 mag/deg for Ganymede and 0.004 mag/deg for Callisto. (The effective wavelengths of the Stromgren v and y filters are about 0.41 and 0.55 μm, respectively.) Thus, even if a similar color dependence held over the range of phase angles covered by the Voyager color data, one would expect to see a magnitude difference of

$$\Delta m(v - y) \simeq 40 \times 0.003 \simeq 0.1$$

between $\alpha = 50°$ and 90°, so $f(90°)/f(50°)$ might be no more than 10% lower in the violet than in the orange. Such a small possible difference is consistent with the data presented here.

The very slight color dependence of Ganymede's phase coefficient can be understood easily in terms of a naive model which considers the surface to be made up of two photometric elements: (1) clean water frost, and (2) a dark, carbonaceous material. Assuming that the frost has a reflectance of 0.8 and the dark material 0.05, the average $\sim$ 0.5 value of Ganymede means that about 20 times as much light comes from the frost as from the dark component. The clean ice, being spectrally neutral, should have a negligibly small color dependence to its phase coefficient. A typical value for the color

phase coefficient of carbonaceous chondrites is $\beta(0.4\text{-}0.6\ \mu m) \approx 0.001\text{-}0.002$ mag/deg (Gradie and Veverka, 1981). Thus, Ganymede cannot have a strongly color-dependent $f(\alpha)$.

In the case of Callisto, a similar argument indicates that about four times as much light would come from the frost and the color dependence of the phase coefficient should be only one-fourth that of pure carbonaceous materials. The model on which this discussion is based is too naive to describe the true nature of the surfaces (Chapter 6), or to reproduce accurately the observed values of $\beta(0.4\text{-}0.6\ \mu m)$ near opposition (Veverka, 1977). However, it is sufficient to rationalize why the shape of $f(\alpha)$ can only be very weakly dependent on wavelength for both Ganymede and Callisto.

As in Chapter 3, the absolute values of the $f(\alpha)$'s given in this chapter must be multiplied by the correction factors of Danielson et al. (1981) for comparison with other results corrected in this manner. These factors are 0.878 for clear images, 0.737 for violet, and 1.03 for orange.

Now that it has been demonstrated that the photometric properties of all terrain types on Ganymede and Callisto do not depend significantly on wavelength, the clear filter results of Chapter 3 will be used in the next chapter to calculate true surface albedos. These albedos

will then be used in Chapter 6 for calculation of surface temperatures.

CHAPTER 5

VARIATION OF ALBEDO WITH INCIDENCE ANGLE

5.1 Introduction

To calculate the temperature of a planet's surface one must know the "albedo" of the surface; that is, the ratio of total energy scattered by a surface element to the total energy incident on the element. It is often assumed that the albedo A does not depend on the incidence angle i of the incoming radiation, an assumption that is not generally valid. In the case of icy bodies such as Ganymede this assumption leads to significant errors in calculated temperatures. In the first part of this chapter, calculations are performed that investigate the effects on the function A(i) of variations in surface phase function, multiple scattering, and macroscopic surface roughness. In the second part, calculations of A(i) are performed for real surfaces whose photometric properties are known. Using the photometric properties determined in Chapters 3 and 4, it is found that the albedos of surface materials on Ganymede and Callisto increase significantly with increasing incidence angle. In Chapter 6 these albedos will be used to calculate surface temperatures on the two bodies.

5.2 A(i) for Theoretical Surfaces

The albedo of a surface element for radiation incident in a parallel beam at an angle i to the surface normal is

$$A(i) = \frac{\text{Energy out}}{\text{Energy in}} = \frac{\int_0^{\pi/2} \int_0^{2\pi} I(\theta,\phi) \cos\theta \sin\theta \, d\phi \, d\theta}{\pi F \cos i} \qquad (5.1)$$

where I is the scattered intensity in the direction (θ,ϕ) of a spherical coordinate system, and πF is the plane parallel incident solar flux (cf., Horak, 1950). For a Lambert surface A(i) is independent of i, since in this case $I = bF \cos i$, where $0 \leq b \leq 1$, and equation (5.1) simply reduces to $A(i) = b$. In fact, for a Lambert surface A(i) is equal to the Bond albedo. The surfaces of most planets and satellites, however, are strongly non-Lambertian.

A more appropriate expression for the photometric function of a particulate surface, neglecting multiple scattering, is

$$I(i,\varepsilon,\alpha) = bF[\mu_0/(\mu_0 + \mu)]f(\mu,\mu_0,\alpha) \qquad (5.2)$$

where ε is the emission angle, α is the phase angle, $\mu_0 = \cos i$, and $\mu = \cos \varepsilon$ (Hapke, 1963; Irvine, 1966). In many cases one can use the approximation $f(\mu,\mu_0,\alpha) = f(\alpha)$ (Veverka, 1972), so that

$$I = bF[\mu_o/(\mu_o + \mu)]f(\alpha). \qquad (5.3)$$

This equation adequately represents the photometric properties of many low albedo objects including the Moon (Hapke, 1963), Phobos and Deimos (Noland and Veverka, 1977 a,b; Klaasen et al., 1979), and Callisto (Chapter 3), and even of moderately bright bodies such as Ganymede (Chapter 3). In the special but unrealistic case $f(\alpha) = 1$, equation (5.3) reduces to the traditional Lommel-Seeliger law. Noting that $\mu = \cos\theta$ and $\cos\alpha = \cos i \cos\theta - \cos\phi \sin i \sin\theta$ (Horak, 1950), substitution of equation (5.3) into equation (5.1) gives

$$A(i) = \frac{b}{\pi}\int_0^{\pi/2}\int_0^{2\pi} \frac{f[\cos^{-1}(\cos i \cos\theta - \cos\phi \sin i \sin\theta)]\cos\theta \sin\theta \, d\phi d\theta}{\cos i + \cos\theta} \qquad (5.4)$$

and in general A(i) is no longer independent of i.

5.2.1 Effect of Surface Phase Function f(α)

First, let us investigate the effects of variations in the surface phase function f(α) on A(i). Consider a Henyey-Greenstein form for f(α):

$$f(\alpha) = \frac{1 - g^2}{(1 + g^2 + 2g\cos\alpha)^{3/2}} \qquad (5.5)$$

(Henyey and Greenstein, 1941). Here g = <cos α> and the photometric properties vary from pure forward scattering for g = 1 to pure backscattering for g = -1. If g = 0, f(α) = 1, and the behavior is that of the Lommel-Seeliger law.

Numerical solutions to equation (5.4) with a Henyey-Greenstein surface phase function are presented in Figure 5.1. The curves have been normalized by dividing by A(0°). All show an increase in albedo with increasing incidence angle. As expected, the effect is most pronounced for strongly forward scattering surfaces. For g = 0.6, the value of A at i = 80° is greater than A at i = 0° by almost a factor of six. For extremely strong backscattering, the variation of albedo with incidence angle is essentially eliminated. Note that for Lommel-Seeliger behavior, g = 0, A(80°) is more than twice A(0°).

5.2.2 Effect of Multiple Scattering

Next, let us investigate the effects of multiple scattering on A(i). Because no rigorous theoretical expression presently exists for the photometric function of a particulate surface of arbitrary albedo, consider instead the closely related problem of scattering by a cloud of suspended particles. The fundamental difference between a particulate surface and a cloud is that inter-particle shadowing does not occur to any significant

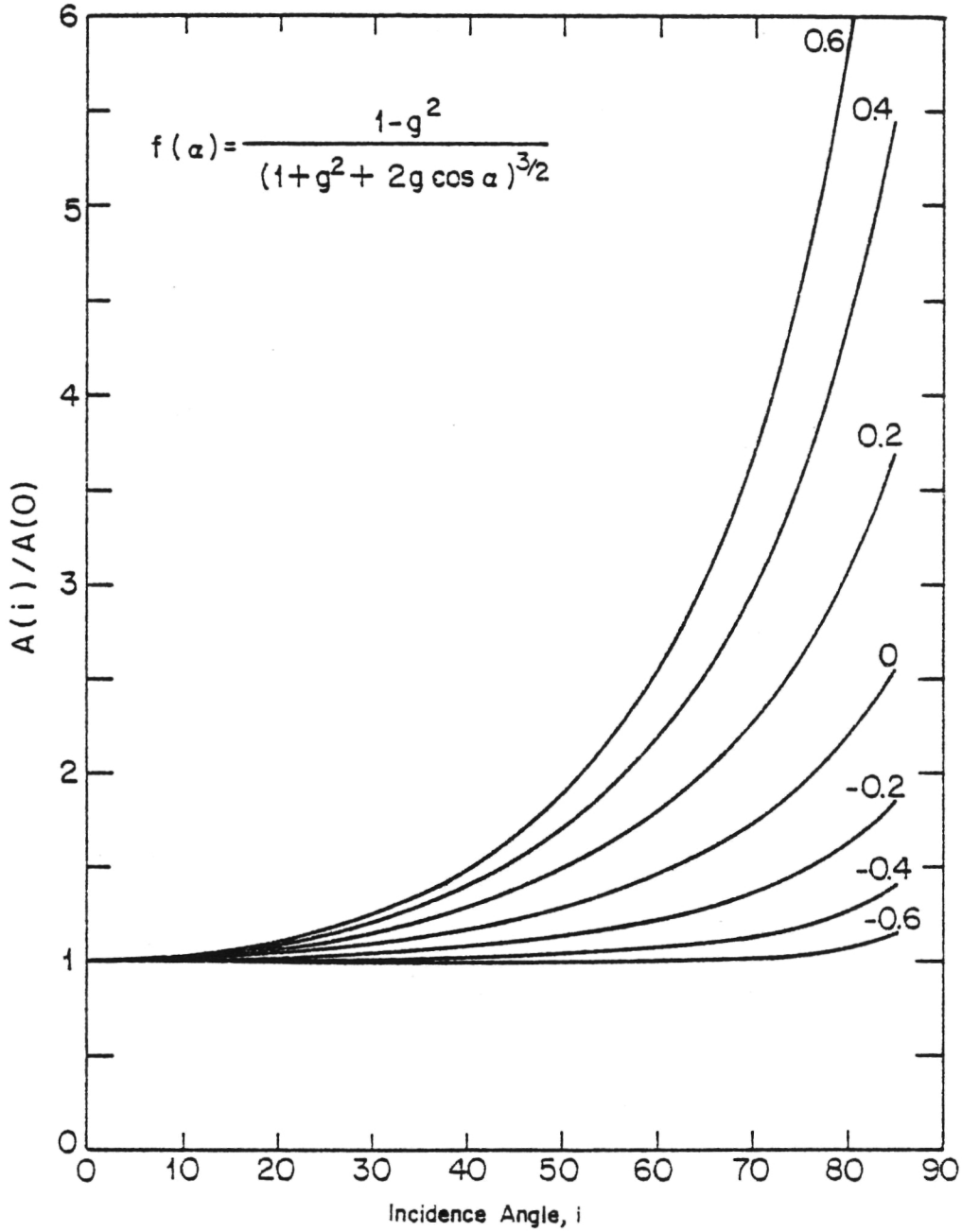


FIGURE 5.1. Variation of albedo with incidence angle for a Henyey-Greenstein surface phase function $f(\alpha)$. Curves are shown for several values of asymmetry parameter g.

degree in the latter.

For a cloud of infinite optical depth made up of suspended particles, the photometric function of light scattered from the top is given by

$$I(i,\varepsilon,\alpha) = (F/4)[\mu_0/(\mu_0 + \mu)]p(\alpha)H(\mu,\tilde{\omega}_0,p)H(\mu_0,\tilde{\omega}_0,p) \quad (5.6)$$

(Chandrasekhar, 1960). Here $\tilde{\omega}_0$ is the single scattering albedo of a particle and $p(\alpha)$ is the phase function of a single particle. The H-functions describe the contribution of multiply scattered light. These functions are relatively simple for isotropic scattering ($p = \tilde{\omega}_0$), and are tabulated by Chandrasekhar (p. 125). For non-isotropic scattering the situation is more complex, and solutions are normally calculated by numerical multiple scattering algorithms, such as the doubling method described by Hansen and Travis (1974). To investigate the effects of multiple scattering, a Henyey-Greenstein particle phase function is considered for the cases $g = -0.3$, $g = 0$ (isotropic scattering), and $g = 0.3$, with arbitrary $\tilde{\omega}_0$. The calculations were carried out using a program supplied by W. R. Thompson based on the Hansen-Travis scheme. Solutions for the case $g = 0$ are identical to those obtained using equation (5.6) and Chandrasekhar's H-functions.

The principal result of this set of calculations is that increased multiple scattering decreases the change

of A(i)/A(0°) with i (Fig. 5.2). For the case where no light is absorbed at all (i.e., $\tilde{\omega}_o = 1$, perfect scattering) A(i) is, like a Lambert surface, independent of i. As $\tilde{\omega}_o$ approaches zero the solutions approach those shown in Figure 5.1, for which no multiple scattering is assumed.

5.2.3 Effect of Macroscopic Surface Roughness

As a final theoretical calculation, consider the effects of shadowing by macroscopic roughness (boulders, crater walls, etc.) on the function A(i). A simple way of assessing the influence of such shadowing is to consider the effect of placing parabolic craters with depth-to-radius ratios Q on a surface that scatters according to equations (5.3)-(5.5) with g = -0.3. The surface is considered to be entirely covered with such craters. Results for Q = 0 (no roughness), 0.2, and 0.5 are shown in Figure 5.3. Macroscopic surface roughness diminishes the value of A(i)/A(0°) at high incidence angles. For an extremely rough surface such as Q = 0.5, A(i)/A(0°) may actually show a substantial decrease with increasing i. At high incidence angles, large areas of such a surface are shadowed, substantially reducing the amount of scattered radiation.

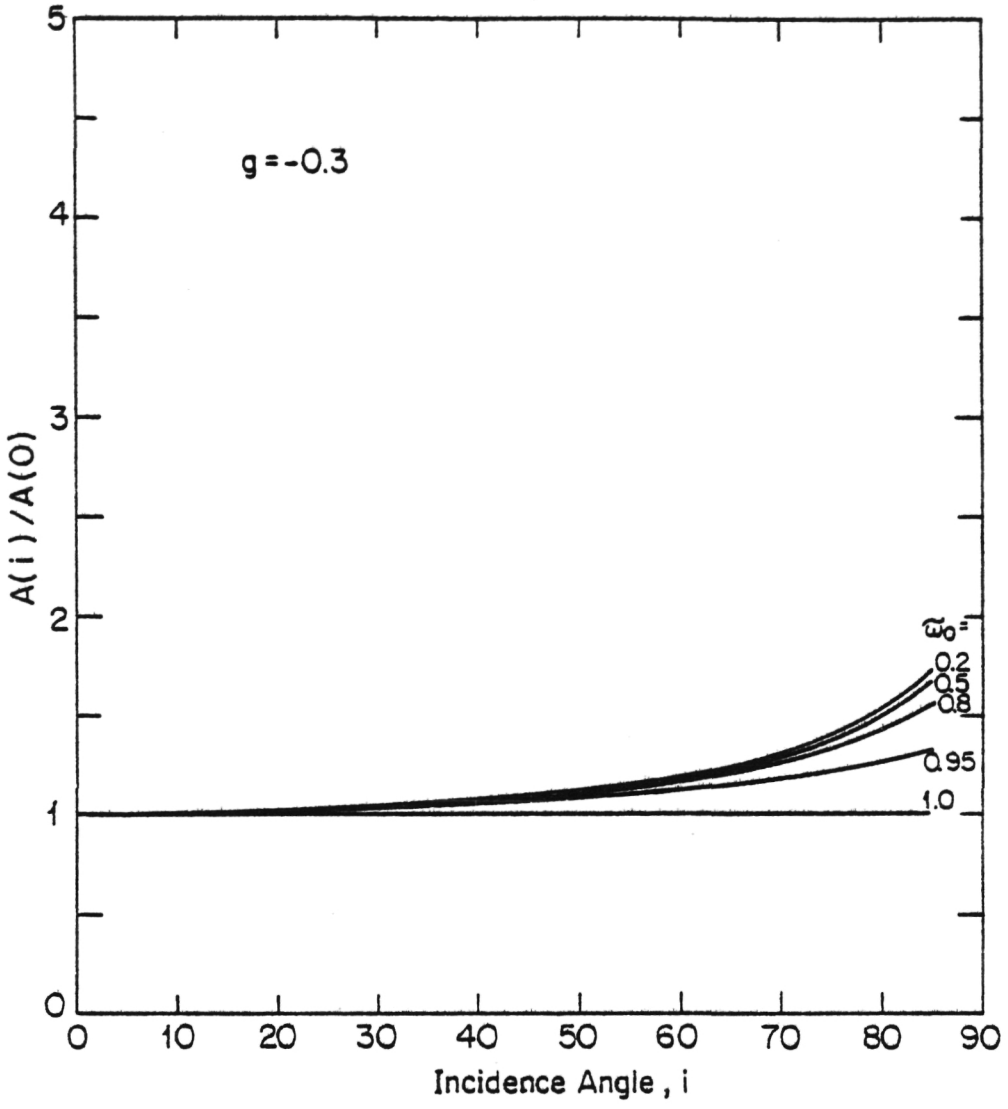


FIGURE 5.2. A(i) curves showing the effects of multiple scattering for three different Henyey-Greenstein particle phase functions $p(\alpha)$. Curves are shown for three values of the asymmetry parameter g and five values of the single scattering albedo $\tilde{\omega}_o$.

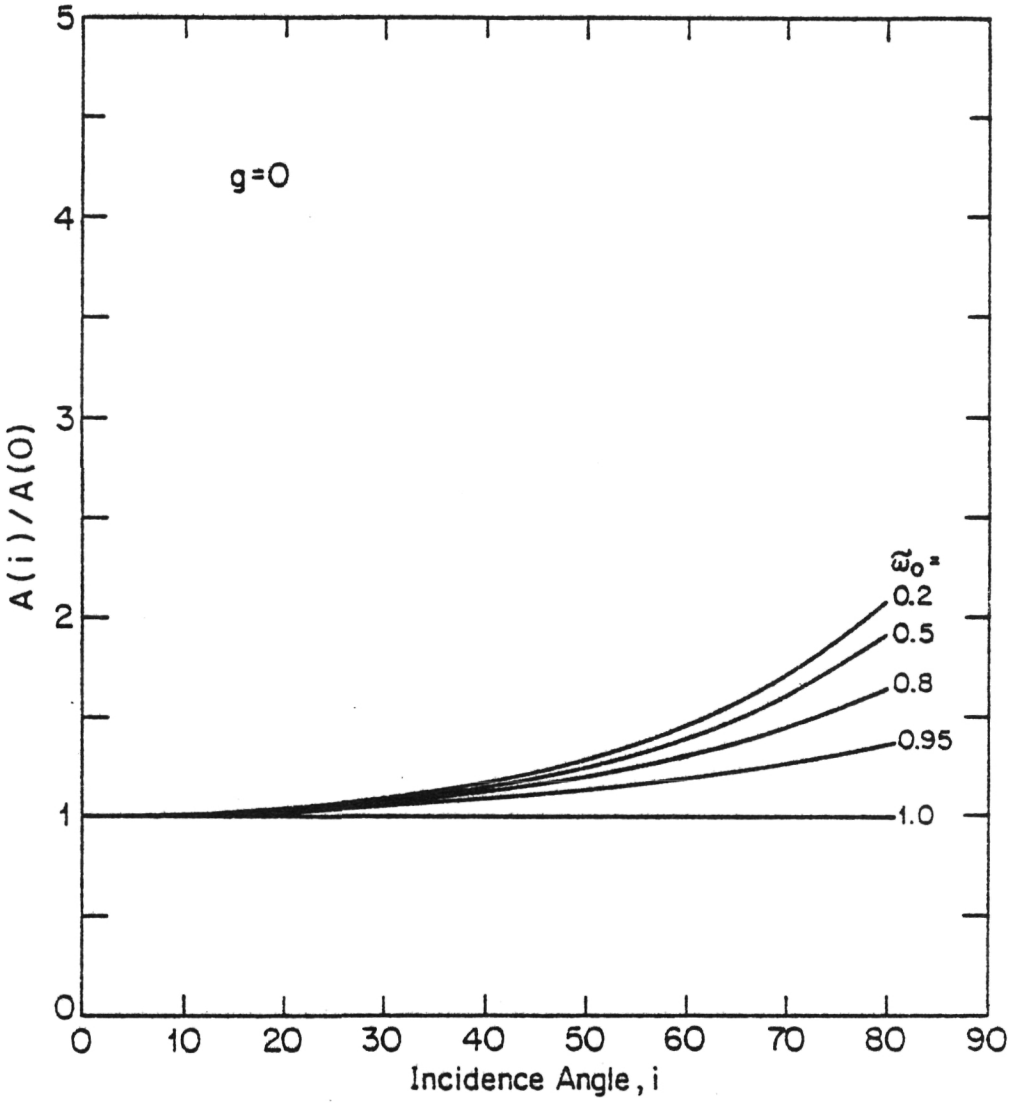


FIGURE 5.2 (continued)

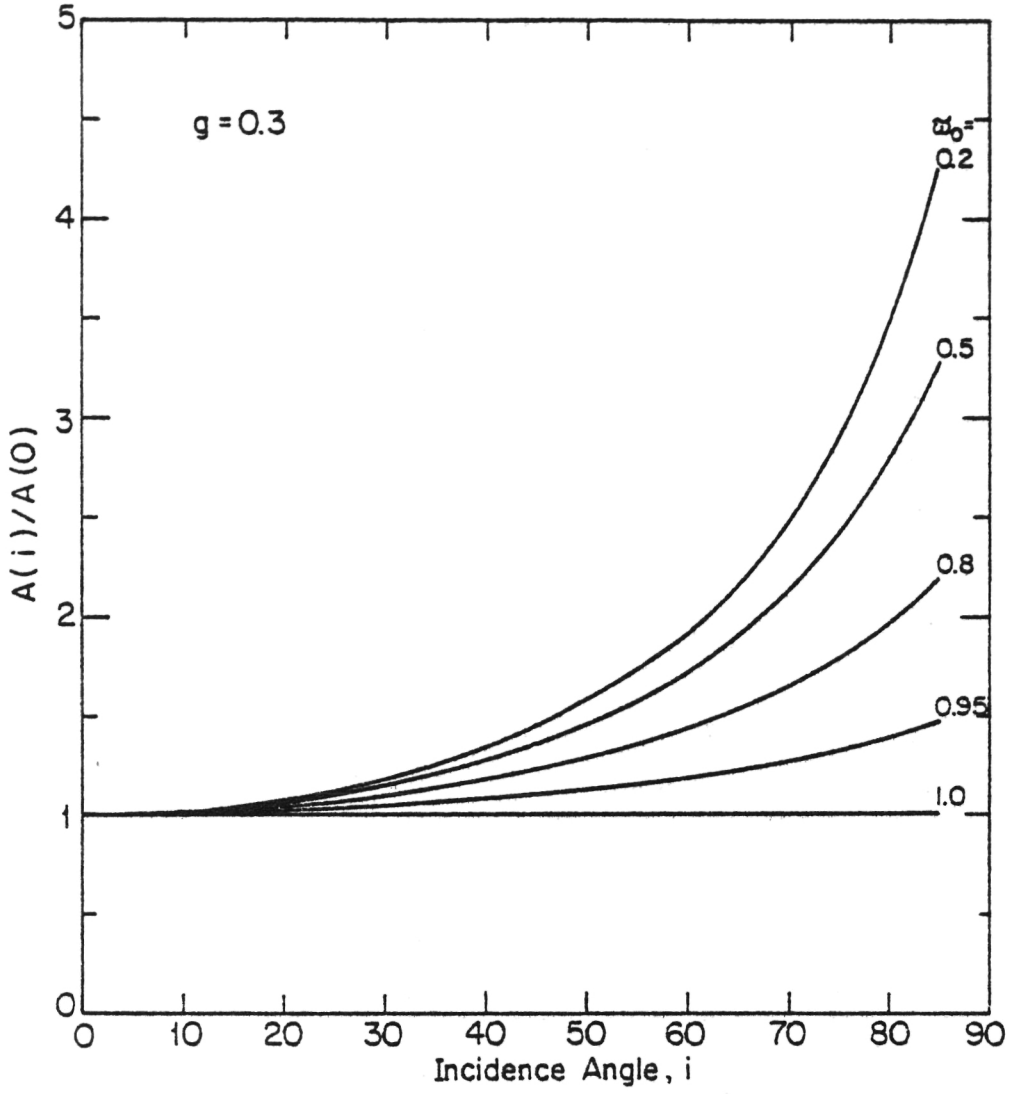


FIGURE 5.2 (continued)

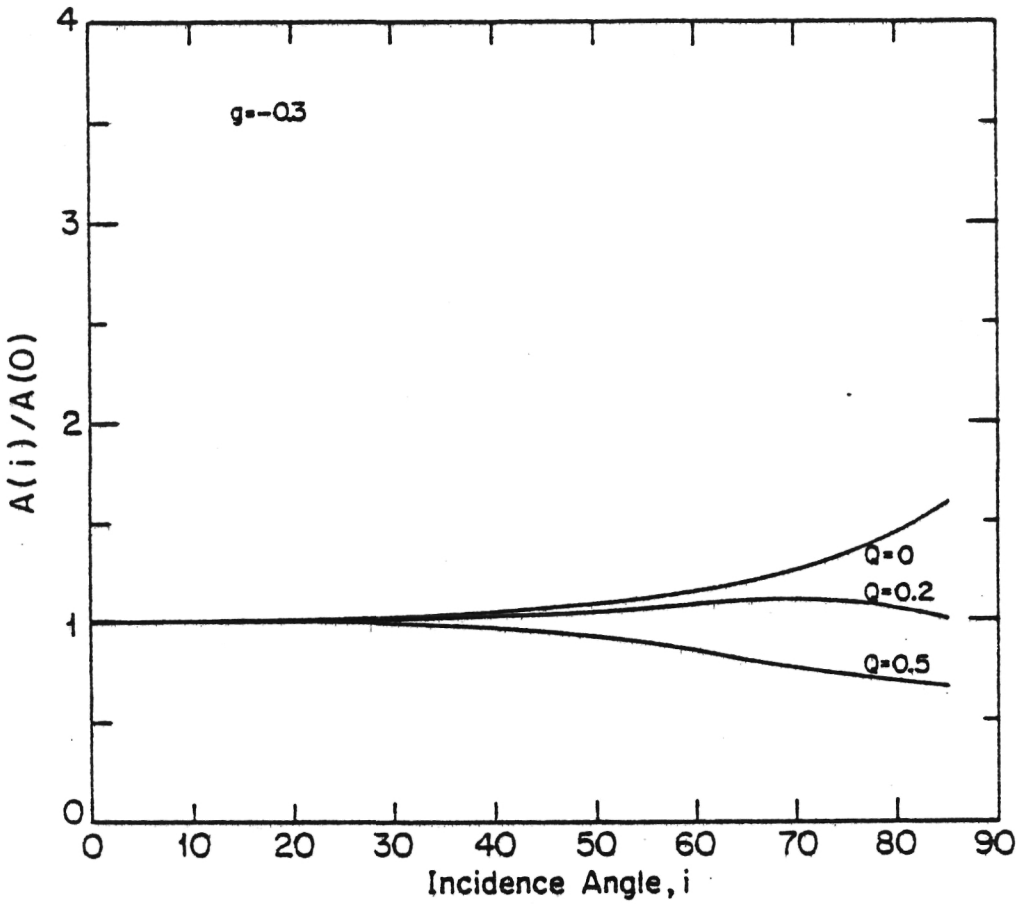


FIGURE 5.3. A(i) curves showing the effects of macroscopic surface roughness. The surface is assumed to be completely covered with parabolic craters with depth/radius ratios Q. The surface on which the craters are formed has a Henyey-Greenstein surface phase function $f(\alpha)$ with an asymmetry parameter of $g = -0.3$.

5.3 A(i) for Real Surfaces

5.3.1 Laboratory Samples

Let us now turn to calculation of A(i) for real surfaces whose photometric properties are known. Consider first a particulate surface composed of mixed MgO and charcoal powders, which has been extensively studied in the laboratory by Goguen (1981). By varying the proportions of MgO and charcoal, the photometric properties of such a mixture may be varied over a wide range. Goguen has found that the photometric function of this surface is closely matched by

$$I = (F/4)[\mu_0/(\mu_0 + \mu)][p(\alpha)S(D) + B(\mu_0 + \mu) + B^2\mu_0\mu] \qquad (5.7)$$

where D is a parameter describing the degree of compaction of the surface, S is a function that adjusts for interparticle shadowing (Irvine, 1966), and B is a parameter, derived from a linear approximation to Chandrasekhar's H-functions, that describes the contribution of multiple scattering in a simple manner. A(i) calculations using best fits to the parameters of equation (5.7) for two of Goguen's sample surfaces with normal reflectances r_n of 0.04 and 0.69 are shown in Figure 5.4. Note that the calculations do not extend beyond i = 70°, the limit of reliable measurements in this particular experiment.

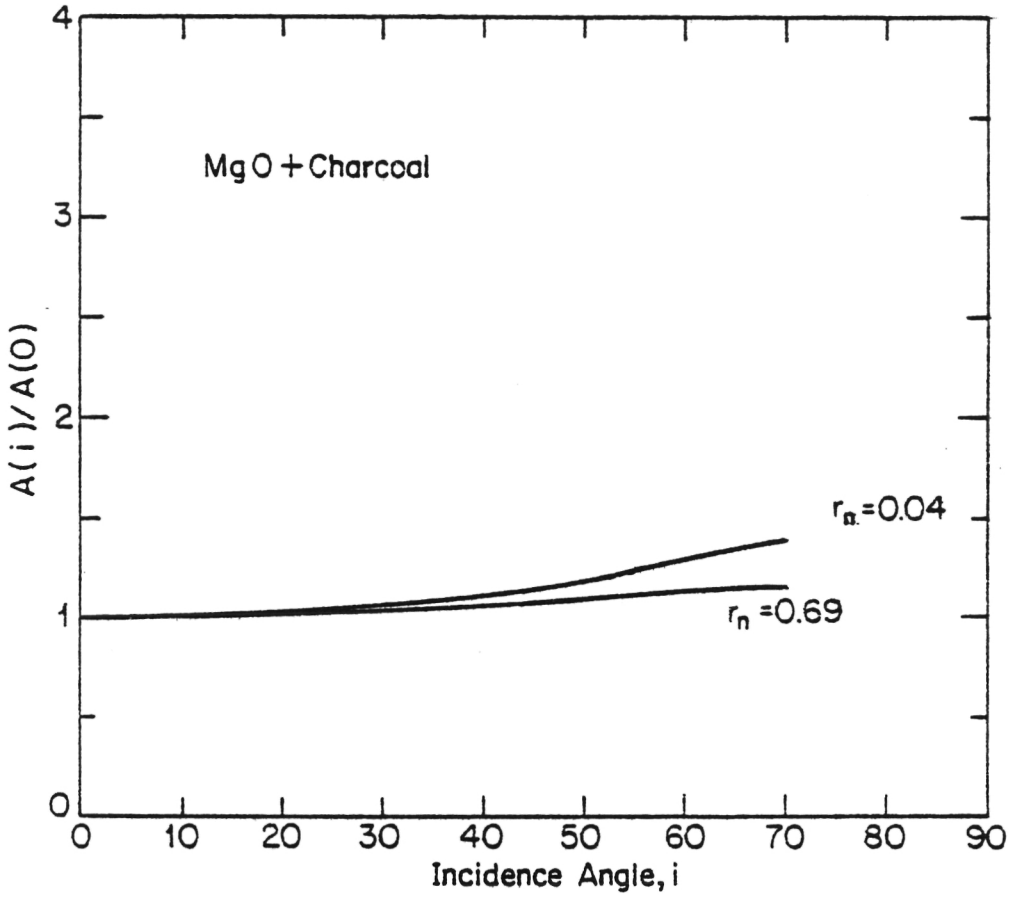


FIGURE 5.4. A(i) curves for two different mixtures of MgO and Charcoal.

In many respects, the curves of Figure 5.4 are similar to the theoretical curves of Figures 5.1 and 5.2. The variation of A(i) is less pronounced for the brighter sample (r_n = 0.69), for which multiple scattering is more important. According to Goguen, the Henyey-Greenstein asymmetry parameter g of the particles in these samples is nearly zero (-0.07 for r_n = 0.04, 0.03 for r_n = 0.69), and the values of $\tilde{\omega}_o$ are 0.55 and 0.95. Comparing Figure 5.4 to Figure 5.2 (multiple scattering, g = 0), we see that the A(i) curves for the experimental samples are similar to the theoretical calculations for equivalent $\tilde{\omega}_o$'s at low incidence angles, but fall somewhat below the theoretical curves at high incidence angles. This unpredicted dropoff in scattered intensity is the result of interparticle shadowing, which was not included in the multiple scattering calculations of Figure 5.2.

5.3.2 Solar System Objects

Bodies whose surface photometric properties are known over a wide range of phase angles include the Moon (Lane and Irvine, 1973), Phobos and Deimos (Klaasen et al., 1979), and, of course, Ganymede and Callisto. For all terrain types on these bodies the angular distribution of scattered light is represented adequately by equation (5.3).

The disc-integrated brightness Φ of the Moon has been measured at phase angles of up to 120° by Lane and Irvine (1973). The phase function $f(\alpha)$ of the lunar surface may be determined from this $\Phi(\alpha)$ by dividing by the disc-integrated brightness that would be expected for a sphere with a Lommel-Seeliger surface:

$$f(\alpha) \propto \Phi(\alpha) \Big/ \int_{-\pi/2}^{\pi/2} \int_{-\pi/2+\alpha}^{\pi/2} [\mu_o/(\mu_o + \mu)] \cos\omega \cos^2\psi \, d\omega \, d\psi \qquad (5.8)$$

where ω and ψ are photometric longitude and latitude respectively (Appendix A). The resulting $A(i)/A(0°)$ for the lunar surface is shown in Figure 5.5. The behavior is similar to that calculated in Figure 5.1 for a Henyey-Greenstein surface phase function $f(\alpha)$ with $g = -0.3$ (cf., Veverka, 1970).

The phase functions for a variety of terrain types on Ganymede and Callisto were presented in Chapter 3. As two examples, consider the grooved terrain of Ganymede and the cratered terrain of Callisto. Curves of $A(i)$ calculated using the observed surface phase functions for the two terrain types are also shown in Figure 5.5. Note that, because Callisto cratered terrain is a stronger backscatterer than Ganymede grooved terrain, its variation of albedo with incidence angle is slightly smaller, even

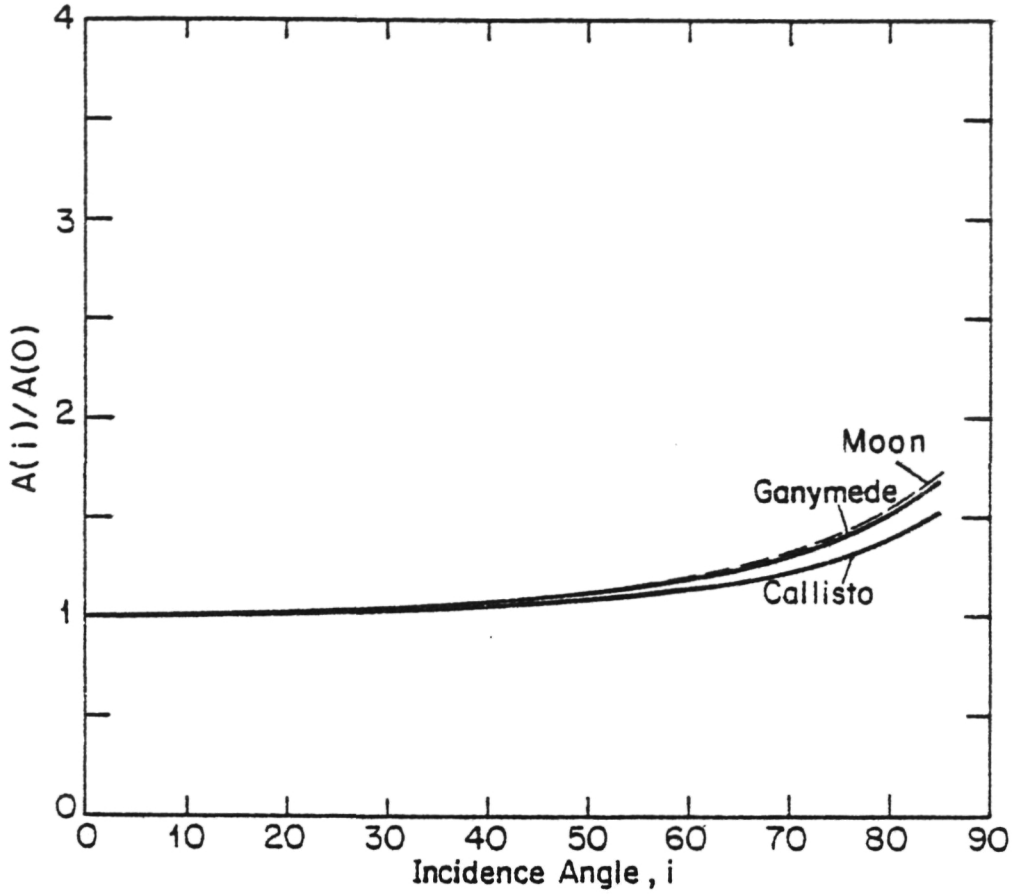


FIGURE 5.5. Variation of albedo with incidence angle for the Moon, Ganymede, and Callisto.

though the surface albedo is considerably lower. It is interesting that Ganymede's grooved terrain has a behavior very similar to that of the Moon. The flattening of the Ganymede curve that would be caused by its higher albedo is offset by its comparatively weaker backscattering.

One planet for which actual measurements of the variation of A(i) with solar incidence angle have been performed is the Earth. Such studies have generally been conducted with airborne radiometers that measure total hemisphere-integrated upward and downward radiative fluxes. Representative results from measurements at visible wavelengths over the central Australian desert are shown in Figure 5.6 (Paltridge and Platt, 1976). They show a strong dependence of albedo on incidence angle, with the albedo increasing by a factor of three as the incidence angle increases from 45° to 85°. Similar results have been reported by Kondratiev (1954, 1969) for a wide variety of surfaces, including several soil types, light and heavy vegetation, and snow.

5.4 Temperature Effects

Now that it has been demonstrated that A(i) does depend on i in actual cases, consider the effects of this variation on planetary surface temperatures. In the absence of an atmosphere, the surface temperature T at some

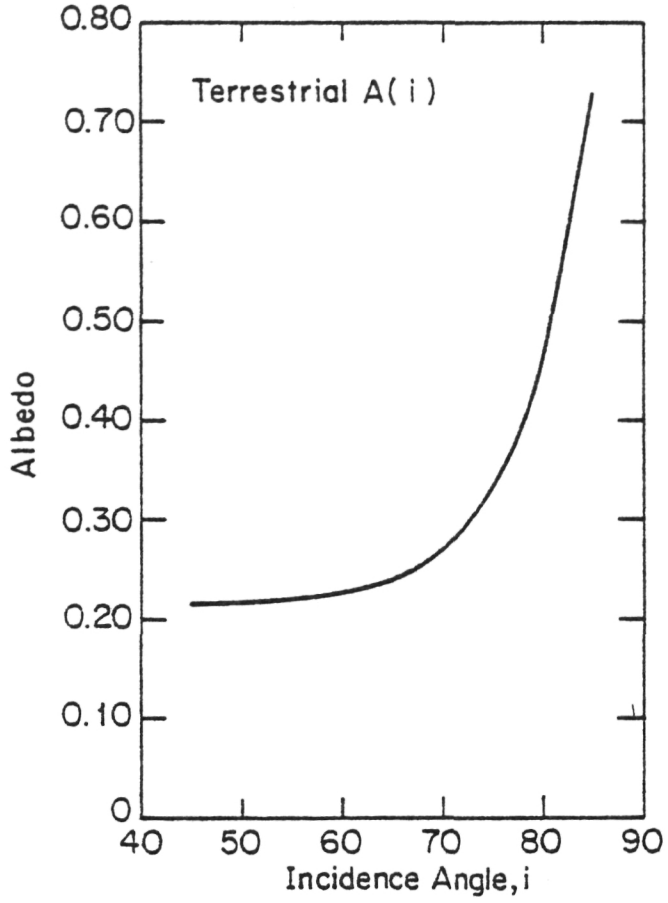


FIGURE 5.6. Observed variation of albedo with incidence angle for the Australian desert. The observations were corrected for the diffuse illumination component produced by atmospheric scattering. The latitude of the sample area prevented determination of A(i) at lower incidence angles (after Paltridge and Platt, 1976).

point on a planet is given by the energy balance equation

$$e\sigma T^4 = K\left(\frac{\partial T}{\partial x}\right)_{x=0} + (1 - A)\pi F \cos i \qquad (5.9)$$

where e is emissivity, σ is the Stefan-Boltzmann constant, K is thermal conductivity, and $\partial T/\partial x$ is the subsurface thermal gradient. While the true surface temperature depends on the subsurface thermal properties and the diurnal timescale, a useful demonstration of the effects of varying albedo on surface temperature is provided by ignoring thermal conduction. This approximation is physically realistic for many objects, such as Ganymede and Callisto, that have very low surface thermal conductivities (Morrison and Cruikshank, 1973).

Correctly calculated noontime surface temperatures as a function of latitude for Ganymede grooved terrain and Callisto are compared in Figure 5.7 with the temperatures that would be obtained by using the constant Bond albedo A_B in equation (5.9) rather than A(i). The temperature profile from the equator to 85° latitude on Ganymede is more than 10°K steeper when the variation of albedo is considered than when it is not. The effect is smaller on Callisto, primarily because for a dark object like Callisto the term $(A - 1)^{\frac{1}{4}}$ does not vary substantially even for proportionally large fluctuations

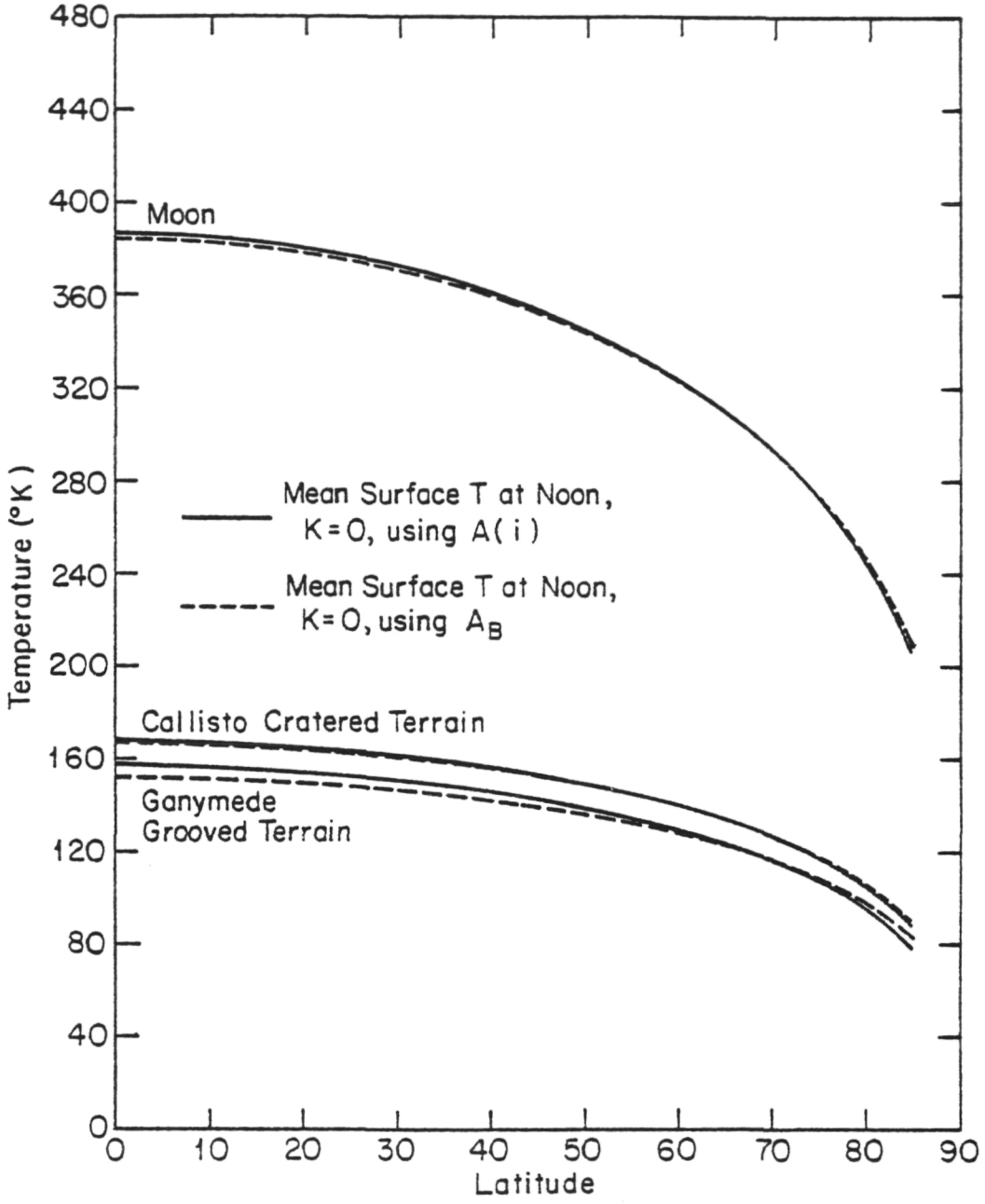


FIGURE 5.7. Latitudinal variation of surface temperature at noon for Ganymede, Callisto, and the Moon, considering the variation of albedo with incidence angle (solid curve), and neglecting it (dashed curve).

in albedo. The same is true for the Moon.

One may also readily calculate the diurnal mean subsurface temperature that will exist below the depth of propagation of the diurnal temperature wave. This is shown for Ganymede grooved terrain, Callisto, and the Moon in Figure 5.8. Again, the effect of varying albedo is important for a bright object like Ganymede, but becomes insignificant for darker objects like Callisto and the Moon.

5.5 Conclusions

For most planetary surfaces, albedo increases significantly with increasing incidence angle. This effect is enhanced for forward scattering surfaces, and is diminished for backscattering surfaces. It is also diminished in cases where multiple scattering is important. At high incidence angles the albedo of a very rough surface may be substantially reduced by shadowing.

Other factors held equal, the effect of albedo variations on surface temperatures is most pronounced for bright objects. For objects like Ganymede that have fairly high albedos but strongly non-Lambertian scattering properties, the effect should result in substantially cooler temperatures near the poles and terminators than would be calculated otherwise. Other bodies for which the effect may be significant include Io, Europa, and

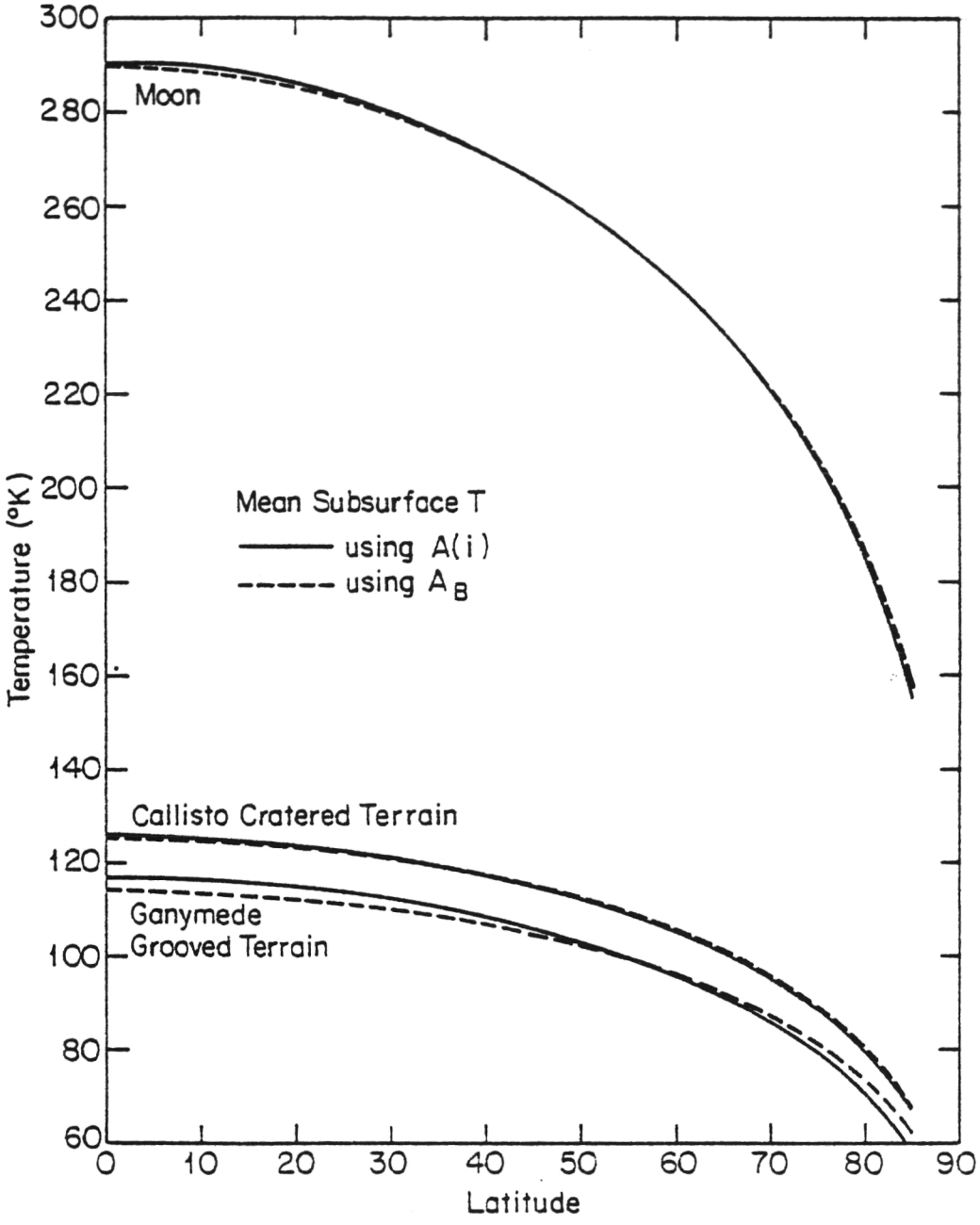


FIGURE 5.8. Latitudinal variation of mean subsurface temperature for Ganymede, Callisto, and the Moon, considering the variation of albedo with incidence angle (solid curve), and neglecting it (dashed curve).

the moons of Saturn. It is important when considering the stability of frosts, which may be very strongly dependent on temperature. One case where it may be particularly important is the problem of the stability of SO_2 frost on Io. The effect is considered in calculation of surface temperatures and ice sublimation rates on Ganymede and Callisto in the next chapter.

CHAPTER 6

SURFACE TEMPERATURES AND FROST RETENTION

6.1 Introduction

It was expected prior to the Voyager mission that the Gaillean satellites would have ice on their surfaces. Watson et al. (1963) and Lebofsky (1975) demonstrated that H_2O ice should be stable on these bodies for a geologically significant period of time. The signature of water frost has been found in the infrared spectra of Europa and Ganymede (Pilcher et al., 1972), and more weakly in the spectrum of Callisto (Clark and McCord, 1980). Voyager images agree with these findings, showing extensive bright material on Europa, polar caps and bright crater rays on Ganymede, and limited bright crater deposits on Callisto.

Disc-integrated brightness temperatures for Ganymede and Callisto have been calculated by Hansen (1972), and Morrison and Cruikshank (1973). Using temperatures calculated from disc-integrated albedos, Purves and Pilcher (1980) considered the thermal migration of water frost on the surfaces of the two bodies. With determination of albedos for the different terrain types on the bodies from spacecraft images, however, more precise calculation of temperatures is possible, as well as comparison of

temperatures for different terrain types on the same body. In this chapter, temperatures are calculated as a function of latitude, time of day, and depth in the regolith for the principal terrain types on Ganymede and Callisto. The accuracy of the calculations in this study is further increased by considering the variation of albedos with solar incidence angle discussed in the previous chapter.

The calculated temperatures are used to address three questions concerning the retention of H_2O ice on the surfaces of Ganymede and Callisto raised by the Voyager images. First, the reasons for the unusual distribution of bright ray craters are examined. Bright ray craters are common in Ganymede's grooved terrain, rare in Ganymede's cratered terrain, and almost absent on Callisto. It is found that this distribution is not simply an effect of varying temperatures and ice sublimation rates, but reflects real variations in the ice content of the cratered substrate. Second, surface temperatures and ice sublimation rates calculated as a function of latitude are used to determine the factors controlling the evolution and extent of Ganymede's polar caps and the lack of caps on Callisto. It is found that this lack, like the lack of bright ray craters, is not a simple thermal effect, but reflects a real deficiency in the amount of frost available for cap

formation relative to Ganymede. Third, diurnal temperature variations calculated for the surface and subsurface materials of both bodies are used to investigate the distribution and evolution of ice in the regolith. Ice loss by charged particle sputtering (Lanzerotti et al., 1978) is not included in the calculations, but is considered qualitatively in the discussion of results.

6.2 Procedure

In order to address these problems, it is necessary to obtain a general solution for temperature within the surface material as a function of depth x, time t, latitude ϕ, and albedo A. This is done by solving the one-dimensional heat conduction equation

$$\rho(x)c(x,T)\frac{\partial T}{\partial t} = \frac{\partial}{\partial x}\left[K(x,T)\frac{\partial T}{\partial x}\right] \qquad (6.1)$$

with the boundary condition

$$K(0,T)\left(\frac{\partial T}{\partial x}\right)_{x=0} = \varepsilon\sigma\, T^4_{x=0} - (1-A)S\,. \qquad (6.2)$$

Here ρ is density, T is temperature, c is heat capacity, K is thermal conductivity, ε is emissivity, σ is the Stefan-Boltzmann constant, and S is time-dependent insolation.

Equation (6.1) is solved numerically using a simple

finite difference technique. Replacing the partial differentials ∂T, ∂t, and ∂x with the small finite intervals ΔT, Δt, and Δx, equation (6.1) may be rewritten as

$$\rho(x)c(x,T)\frac{\Delta T}{\Delta t} = \frac{\left[K(x,T)\frac{\Delta T}{\Delta x}\right]_{x+\frac{\Delta x}{2}} - \left[K(x,T)\frac{\Delta T}{\Delta x}\right]_{x-\frac{\Delta x}{2}}}{\Delta x}. \quad (6.3)$$

Calculations are performed for a number of plane-parallel layers with independent values of K, ρ, and c. Writing the temperature at time $n(\Delta T)$ and depth $m(\Delta x)$ as T_m^n, equation (6.3) gives the temperature at a point within a layer as

$$T_m^n = T_m^{n-1} + \frac{\Delta t}{\rho c(\Delta x)^2}\left[\left(T_{m+1}^{n-1}\right)^2 - 2T_{m+1}^{n-1}\,T_{m-1}^{n-1} + \left(T_{m-1}^{n-1}\right)^2\right]. \quad (6.4)$$

At the boundary between two layers L and L + 1, the temperature is

$$T_m^n = T_m^{n-1} + \frac{4(\Delta t)}{\left(\rho_L c_L + \rho_{L+1}c_{L+1}\right)\left[(\Delta x)_L + (\Delta x)_{L+1}\right]} \times \frac{K_{L+1}\left(T_{m+1}^{n-1} - T_m^{n-1}\right)}{(\Delta x)_{L+1}} - \frac{K_L\left(T_m^{n-1} - T_{m-1}^{n-1}\right)}{(\Delta x)_L}. \quad (6.5)$$

To satisfy the surface boundary condition, the surface temperature T_o is calculated by using Newton's method to solve the equation

$$K_1 \left[\frac{-T_2^n + 4T_1^n - 3T_o^n}{2(\Delta x)_1} \right] = \varepsilon\sigma T_o^4 - (1 - A)S \ . \qquad (6.6)$$

The albedos used for the various terrain types are those calculated in Chapter 5; the variation of albedo with incidence angle is included in the calculations. In using the albedos determined from Voyager images, it is implicitly assumed that there is no significant segregation of bright and dark materials at a scale finer than that of the imaging resolution. The extreme age of all terrain types on Ganymede and Callisto indicates that substantial impact gardening of the surface has occurred, indicating that this assumption is probably valid.

It is assumed that the conductivity and heat capacity of surface materials are independent of temperature; that is, that $K(x,T) = K(x)$ and $c(x,T) = c(x)$. The justification for this assumption will be discussed later in this chapter.

The values used for $\rho(x)$, $K(x)$, and $c(x)$ are selected in accord with infrared observations of eclipses of Ganymede and Callisto. The temperature variations that take place during an eclipse may be used to place constraints

on the values of these parameters and their variation with depth. Results of eclipse radiometry are quite similar for Ganymede and Callisto. Both Hansen (1972) and Morrison and Cruikshank (1973) found that the results cannot be matched well by a surface with homogeneous thermal properties. The results can be matched very well, however, by a thin surface layer with an extremely low thermal inertia overlying a material with much higher thermal inertia. Morrison and Cruikshank suggested that the upper layer might be fluffy H_2O frost while the lower layer might be fused ice and silicates. Adopting the values for $(K\rho c)^{\frac{1}{2}}$ and surface density of the upper layer obtained by Morrison and Cruikshank, the model uses an upper layer 0.25 cm thick with $\rho = 0.6$ g cm^{-3}, $K = 10^{-6}$ cal cm^{-1} s^{-1}°K^{-1}, and $c = 0.2$ cal g^{-1}°K^{-1}. For the lower layer, the values used are $\rho = 1.5$ g cm^{-3}, $K = 10^{-3}$ cal cm^{-1} s^{-1}°K^{-1} and $c = 0.2$ cal g^{-1}°K^{-1}. The model results are quite insensitive to reasonable variations in the thermal properties of the lower layer.

A thermal emissivity of unity is used in the calculations. This value is consistent with the surface of ice and silicates expected to be present on Ganymede and Callisto (Hansen, 1972). It is also consistent with Earth-based measurements of disc-integrated thermal flux, assuming equilibrium with insolation, and with the

lack of observed spectral features in the thermal infrared (Morrison, 1977).

6.3 Results

Diagrams showing surface temperature calculated as a function of time of day and latitude are given for Ganymede grooved terrain, Ganymede cratered terrain, and Callisto in Figure 6.1. Temperatures are those at the surface of the upper layer. Maximum daytime temperatures are greater than 150°K at the equator and less than 75°K at 85° latitude on Ganymede, greater than 160°K and less than 80°K at those latitudes on Callisto. Nighttime temperatures on both bodies generally lie in the range 80°-95°K. Temperatures in the grooved terrain on Ganymede are slightly cooler than those in the cratered terrain.

Because of the insulating properties of the upper layer, the lower layer remains essentially isothermal through the diurnal cycle. The temperature of the lower layer as a function of latitude is shown for the three terrain types in Figure 6.2.

The calculated surface temperatures may be checked for consistency with Earth-based measurements of brightness temperature. The disc-averaged thermal emission at some frequency ν may be calculated from the results of Figure 6.1 by numerically integrating the expression

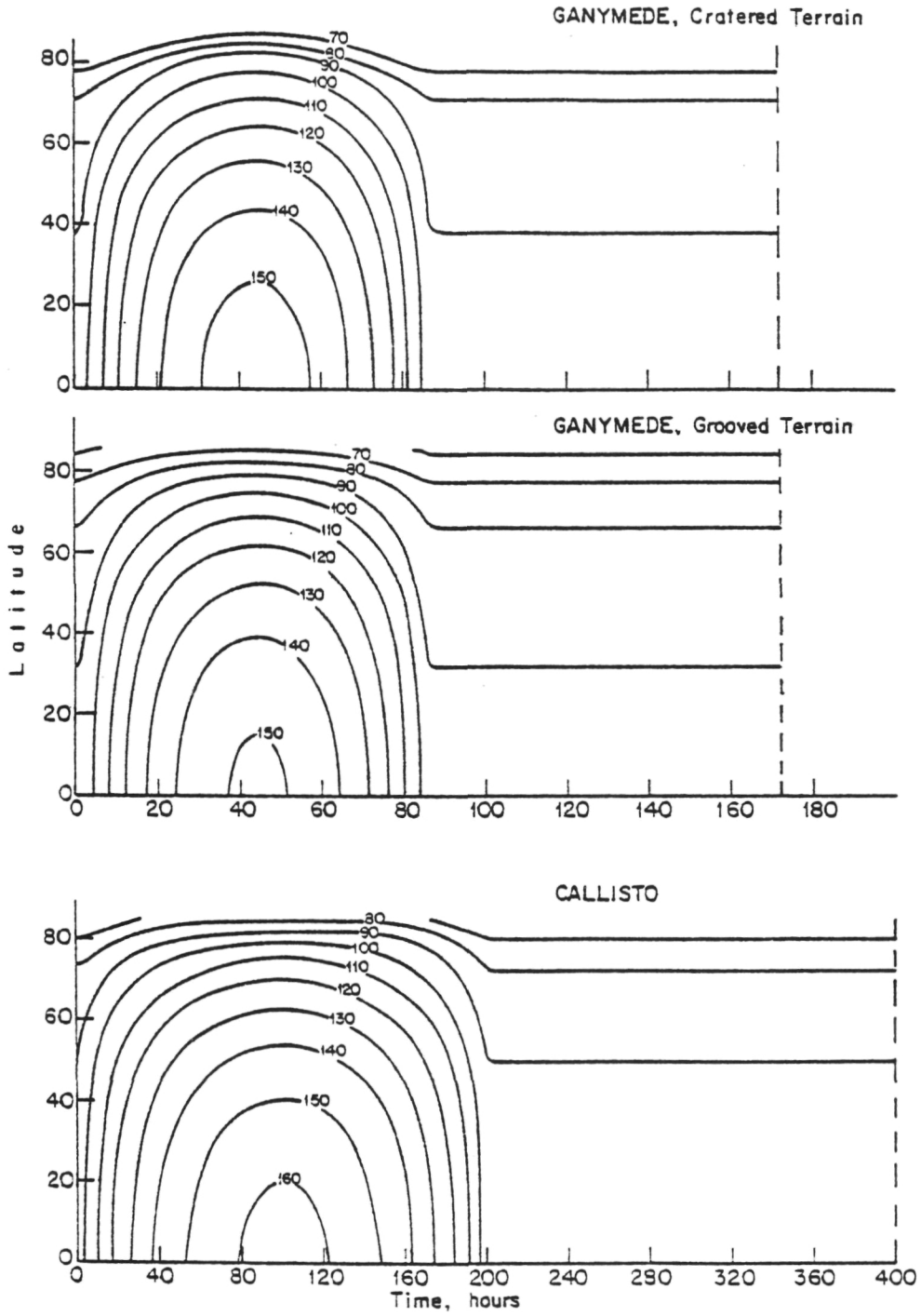


FIGURE 6.1. Surface temperatures on Ganymede and Callisto. Isothermal contours are shown for one complete diurnal cycle, with dawn at time = 0.

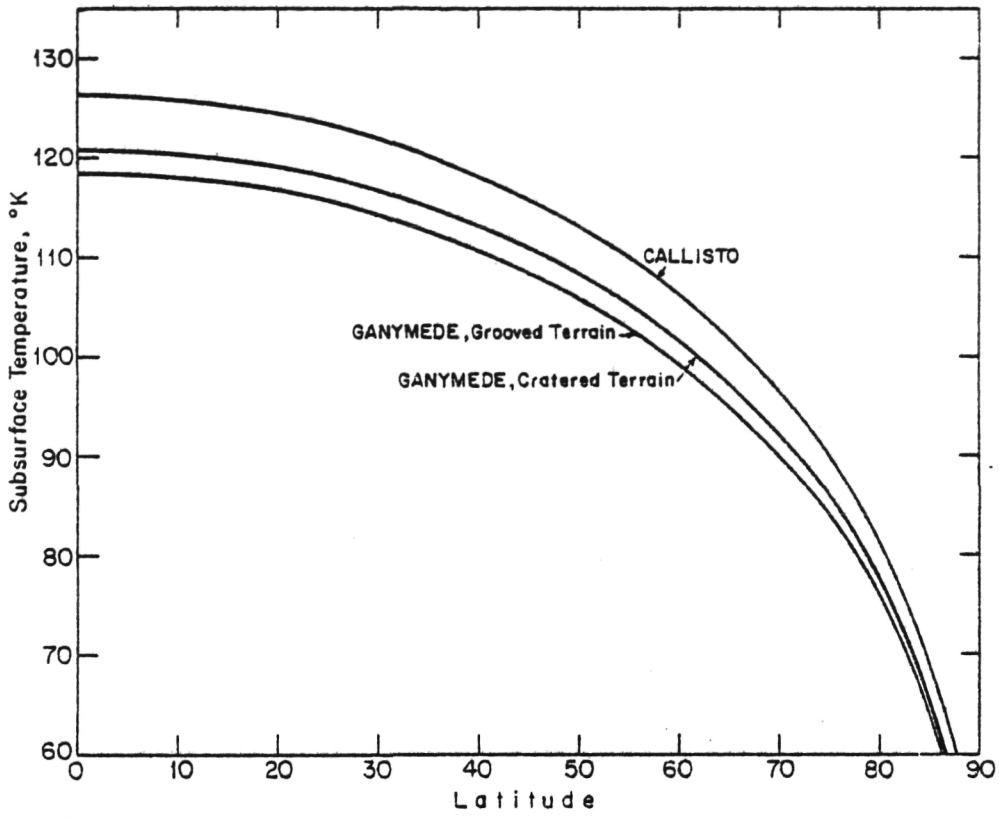


FIGURE 6.2. Temperatures in the lower, high thermal inertia layer as a function of latitude. The low conductivity of the thin surface layer results in the subsurface layer remaining essentially isothermal throughout the diurnal cycle.

$$\frac{8\nu^3 h}{C^2}\int_{-\pi/2}^{\pi/2}\int_{0}^{\pi}\frac{\sin\psi\cos^2\phi}{e^{h\nu/kT(\phi,\psi)}-1}\,d\psi d\phi \qquad (6.7)$$

where h is the Planck constant, C is the speed of light, k is the Boltzmann constant, ϕ is latitude, and ψ is rotational phase measured from the dawn terminator. This expression, like the one used in calculation of brightness temperatures, assumes black body thermal radiation. Simple trapezoidal summation was used for integration in $d\psi$. Trapezoidal integrations were performed for four latitudes, 10.6°, 31.7°, 52.8°, and 73.8°. These latitudes were selected so that the values of sin ϕ were those appropriate for integration in $d\phi$ by eight point Gaussian quadrature (Chandrasekhar, 1960). Brightness temperatures calculated from the results of this double integration are given in Table 6.1, along with actual measurements of the 21 μm brightness temperatures of Ganymede and Callisto obtained by Hansen (1972) and Morrison et al. (1972). There is good agreement between the theoretical and observed temperatures.

Another important calculation is the sublimation rate of H_2O frost. For simple sublimation into a vacuum, the loss rate $\dot{m}$ is given by

$$\dot{m} = \alpha p_{H_2O}(M/2\pi RT)^{\frac{1}{2}} \qquad (6.8)$$

TABLE 6.1 Observed and Calculated 21 μm Brightness Temperatures for Ganymede and Callisto

		Calculated	Observed	
			Hansen (1972)	Morrison et al. (1972)
Ganymede	(cratered terrain)	139°	132 ± 5°	138 ± 5°
	(grooved terrain)	136°		
Callisto		147°	142 ± 6°	151 ± 7°

(Kennard, 1938), where α is the coefficient of sublimation, p_{H_2O} is the vapor pressure of the ice, M is the molecular weight of the vapor, and R is the universal gas constant. For pure ice, a value for α of 0.94 ± 0.06 has been empirically determined by Tschudin (1946). The effects of impurities in the ice on α are not known, but are probably small as long as the amounts are small. The vapor pressure is strongly temperature dependent, and is assumed to follow the expression given by Dorsey (1940). Diagrams giving $\dot{m}$ at the surface as a function of time of day and latitude are shown for the three terrain types in Figure 6.3. Note that near the equator of both bodies the value of the calculated sublimation rate varies by at least eleven orders of magnitude during a diurnal cycle. The calculated diurnal mean sublimation rate $\bar{\dot{m}}$ is given as a function of latitude in Figure 6.4. To obtain absolute rates of ice loss, it is necessary to also consider molecules that do not reach escape velocity and reimpact the surface (Purves and Pilcher, 1980). The ideal sublimation rates shown in Figure 6.4 may be used, however, to compare relative ice loss rates for the various terrain types.

6.4 Discussion

6.4.1 Bright Ray Craters

Figure 6.5 shows the distribution of bright ray

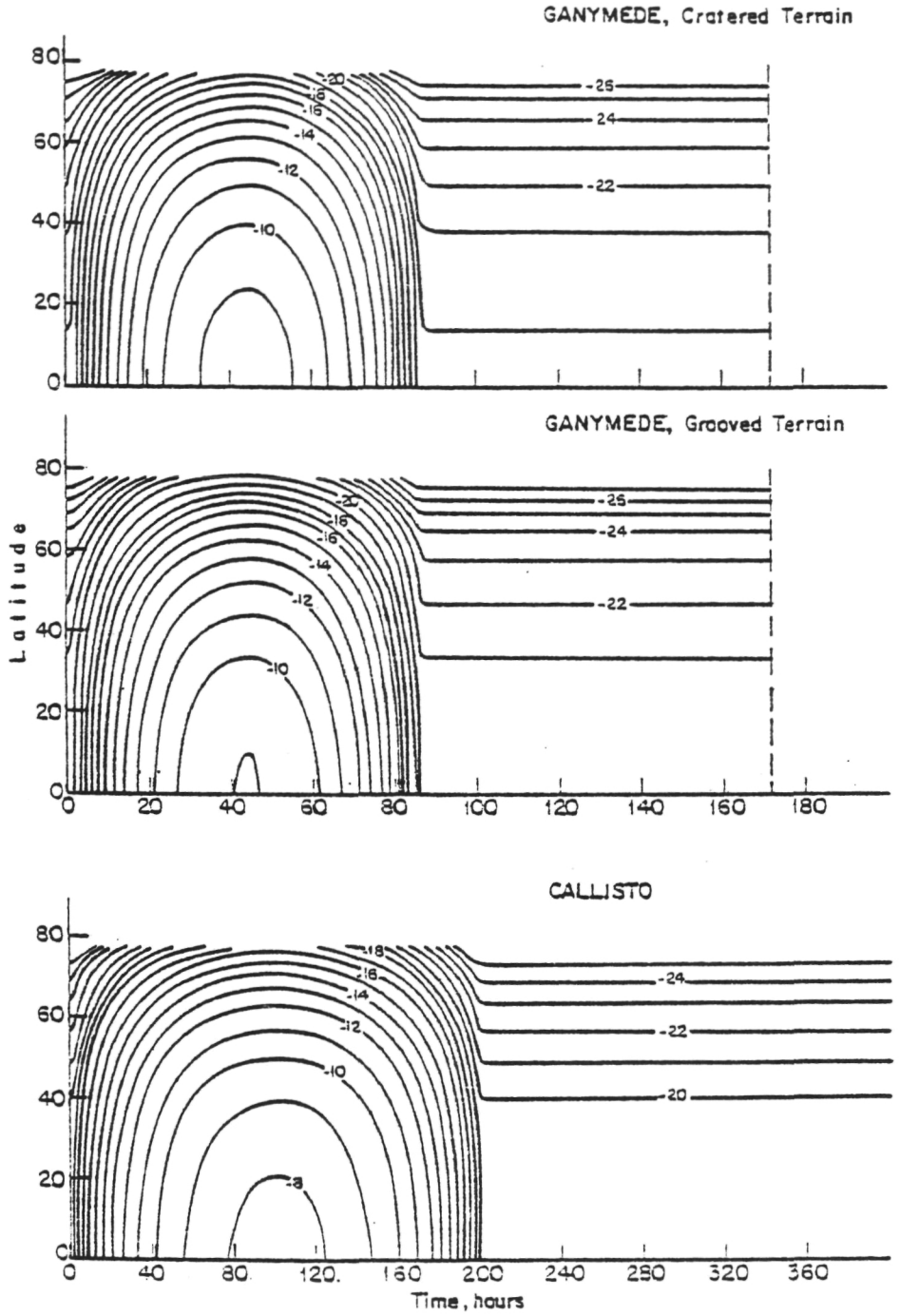


FIGURE 6.3. Ice sublimation rates on Ganymede and Callisto. Contours of constant sublimation rate ($\log_{10}\dot{m}$, g $cm^{-2}s^{-1}$) are shown for one complete diurnal cycle, with dawn at time = 0. These calculations assume sublimation into a vacuum, and neglect the effects of reimpacting H_2O molecules.

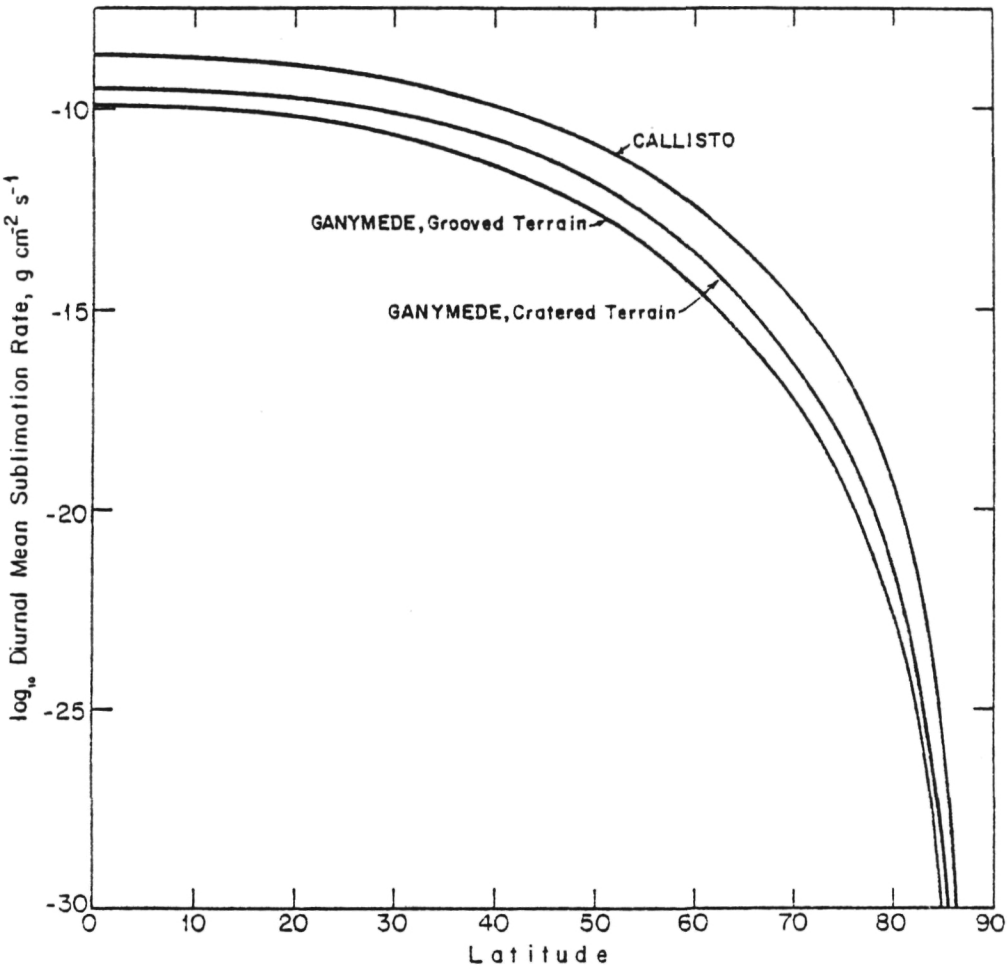


FIGURE 6.4. Diurnal mean sublimation rates, assuming irretrievable sublimation into a vacuum, as a function of latitude.

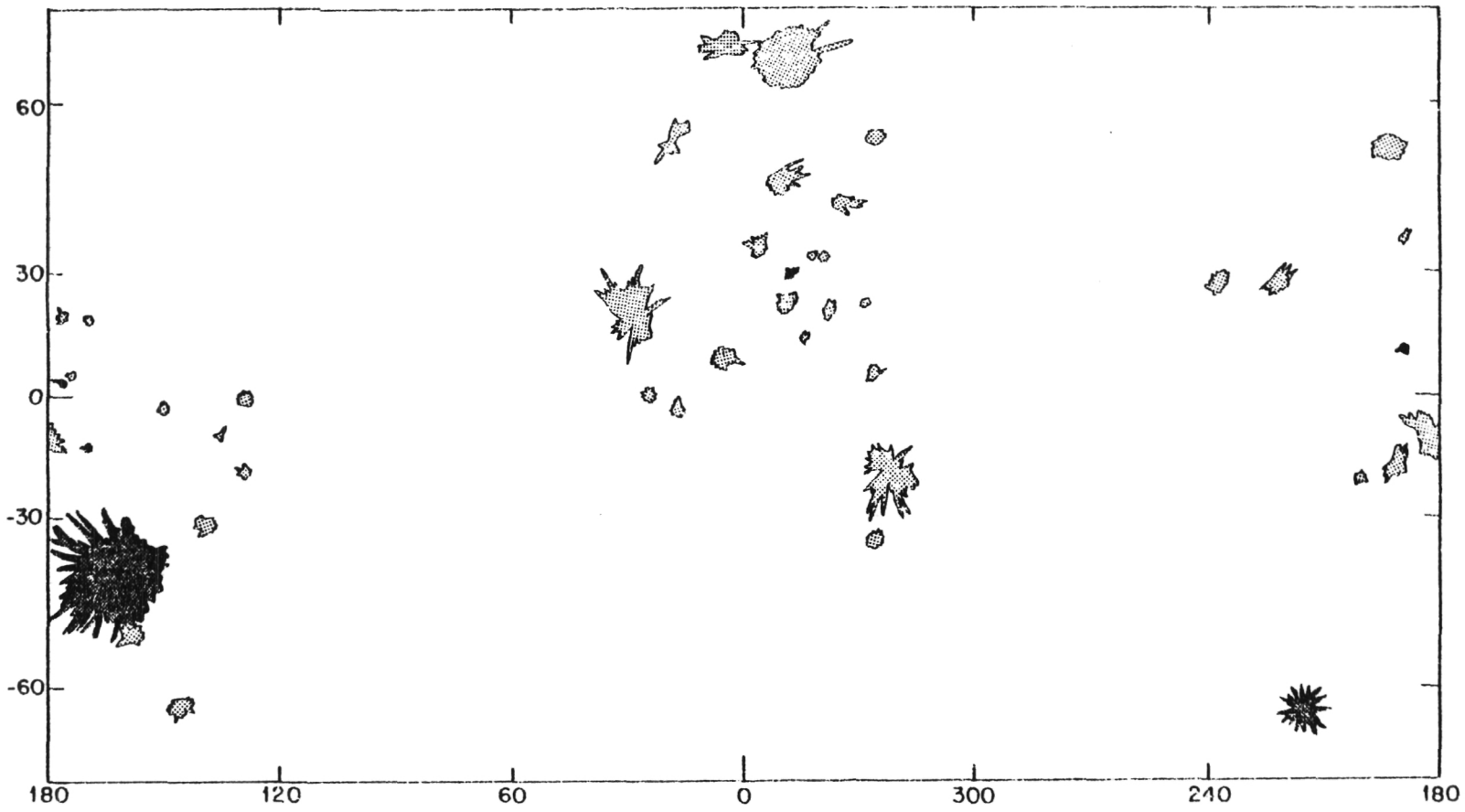


FIGURE 6.5. Bright ray craters on Ganymede formed in grooved terrain (light stipple) and cratered terrain (dark stipple). Craters are mapped only if they clearly exhibit discrete bright rays and if the terrain type of the impact point can be unambiguously determined. The uneven areal distribution is due to incomplete photographic coverage.

craters observed on Ganymede. Although the surface of Ganymede is roughly 50% grooved terrain and 50% cratered terrain, bright ray craters are formed in grooved terrain much more commonly than in cratered terrain. With only a few possible exceptions, bright ray craters are absent on Callisto.

It is important to determine whether the distribution of bright ray craters is simply a result of surface temperature differences among the three terrain types (Ganymede grooved terrain, Ganymede cratered terrain, and Callisto cratered terrain), or if it reflects real variations in crustal ice content. Bright ray craters are found in Ganymede's grooved terrain at all latitudes down to the equator, demonstrating that even the equatorial sublimation rate for that terrain type is low enough to preserve bright rays for a significant period. This calculated rate is roughly 10^{-10} g cm^{-2} sec^{-1} (Fig. 6.4). The same calculated ideal sublimation rate is found at about 20° latitude in Ganymede's cratered terrain and at about 45° latitude on Callisto. If the distribution were due to simple thermal effects, one would expect to see bright ray craters poleward of these latitudes, as temperatures would be low enough to preserve them there as well. There are very few ray craters poleward of 20° in the cratered terrain on Ganymede, however, and

virtually none poleward of 45°, or in fact anywhere else, on Callisto. The distribution therefore suggests that the grooved terrain is significantly more ice-rich than the cratered terrain, and that both contain more ice than the crust of Callisto.

This inference has important geologic implications. During grooved terrain formation, crustal material was apparently reworked or replaced with water or clean ice from lower depths. This process increased the ice/silicate ratio in the grooved terrain. The few bright ray craters in the cratered terrain may be formed in places where water or clean ice almost reached the surface. This idea is supported by the observation that most of the bright ray craters in the cratered terrain either lie directly adjacent to a grooved band, or are quite large, excavating to a substantial depth. The crust of Callisto did not undergo grooved terrain formation, and thus seems nowhere to be enriched in ice, at least not to the depths excavated by impacts.

6.4.2 Polar Caps

As discussed in Chapter 2, Ganymede's polar caps appear to be deposits of frost that overlie both grooved and cratered terrain. The deposits must be extremely thin, as their optical depth is low enough to allow albedo contrasts between underlying grooved and cratered terrain

units to be discerned despite their frost cover. Laboratory studies of the reflectance of frost deposits on silicate grains (Clark, 1981) show that a frost thickness of about 0.1 mm is sufficient to produce a visible albedo like that of Ganymede's caps. Because albedo variations beneath the caps are observable, the thickness of the caps, if they are continuous, cannot substantially exceed this value. With the data in hand, however, the possibility of somewhat thicker discontinuous polar frost deposits cannot be ruled out. The margins of the caps lie closer to the equator in grooved terrain than in cratered terrain (Fig. 6.6). In the image used to construct map A of Figure 6.6 the margin of the north polar cap is quite distinct, and lies in cratered terrain at a mean latitude of about 48°N. The margin of the southern cap is very indistinct, but appears to lie in grooved terrain at roughly 35°S. In map B both margins are fairly distinct, and lie primarily in grooved terrain at 40°N and 40°S. In general then, cap margins lie at roughly 40° latitude in grooved terrain and 50° latitude in cratered terrain.

It is perhaps significant that the diurnal mean sublimation rate calculated for grooved terrain at 40° is very close to that for cratered terrain at 50°. The rate shown in Figure 6.4 for both these latitudes is about 10^{-12} g cm^{-2} s^{-1}, which, neglecting replenishment by

FIGURE 6.6. Ganymede's bright polar caps (cross-hatched regions) from two three-color Voyager images. Note that the cap margin lies farther poleward in the cratered terrain (coarse stipple) than in the grooved terrain (fine stipple). Map A is made from the image shown in Fig. 2.3, Map B from images 1653J1-002, 1655J1-002, and 1657J1-002.

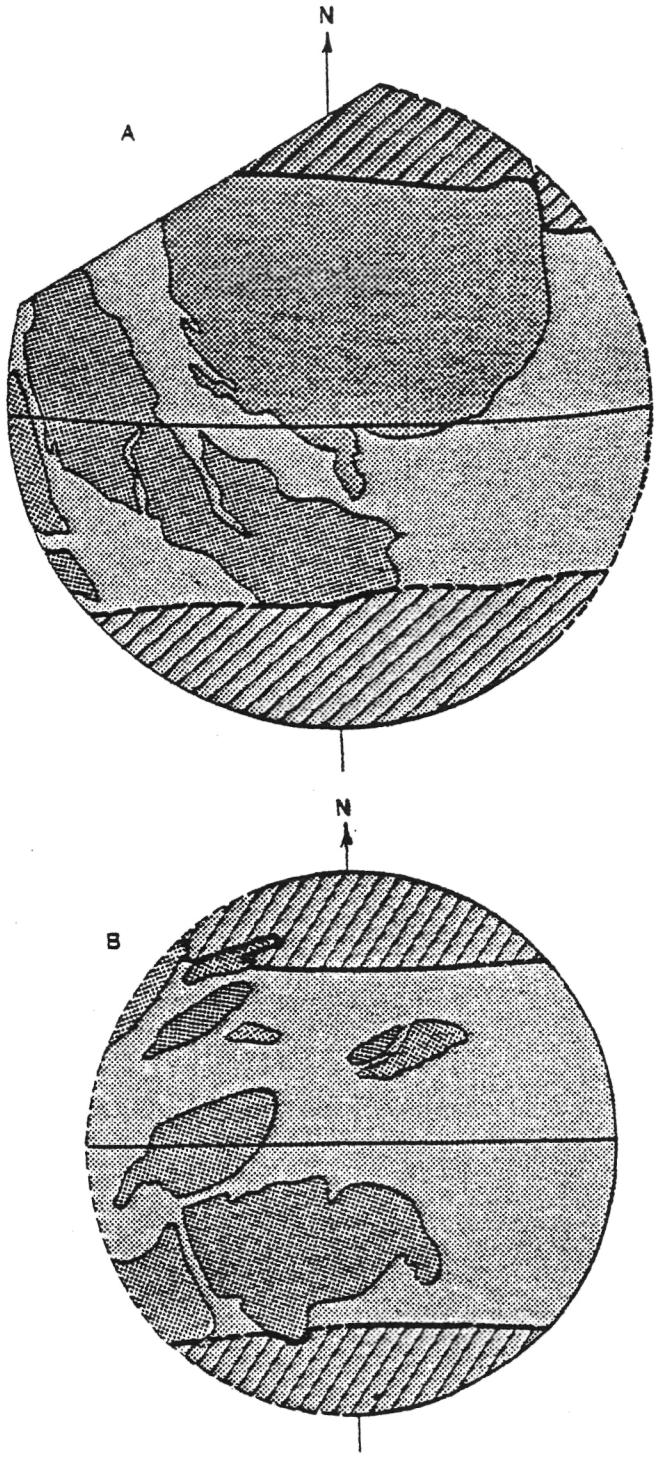


FIGURE 6.6 (continued)

reimpacting H_2O molecules, would amount to a loss of 1 g cm^{-2} in 3×10^4 years. This high loss rate suggests that the cap margin is actually controlled by an equilibrium between loss by sublimation and the replenishment by reimpacting H_2O molecules migrating from lower latitudes suggested by Purves and Pilcher (1980). As the molecules execute a two-dimensional random walk, there will be a net transport of H_2O toward the poles. These calculations suggest that the influx of water molecules at the latitudes of the cap margin is also roughly 10^{-12} g cm^{-2} s^{-1}. Poleward of these latitudes accumulation should dominate over sublimation, resulting in net accumulation of thin frost deposits. Purves and Pilcher (1980) have pointed out, however, that thermal migration is probably negligible poleward of $\sim$ 65°-70° on Ganymede. Thus, while the outer portion of Ganymede's polar cap is probably largely composed of ice that has migrated from lower latitudes, the portion nearer the pole may be composed almost entirely of frost that has been exposed locally by impact gardening and has undergone no further movement.

The same type of analysis applied to the problem of the bright ray crater distribution may be used to understand the lack of polar caps on Callisto. A calculated diurnal mean sublimation rate equal to that

found at the margin of Ganymede's cap (40° latitude in the grooved terrain and 50° latitude in the cratered terrain) is found at a latitude of about 60° on Callisto (Fig. 6.4). If the lack of caps on Callisto were simply a result of Callisto's somewhat warmer temperatures, one would still expect to see polar frost deposits poleward of 60°, as the temperatures there should be cold enough to allow them to exist. No evidence is found in the Voyager images of Callisto for such frost, however, even much farther poleward than 60°. Like the lack of bright ray craters on Callisto, then, the lack of polar caps is not simply a thermal effect, but reflects a real deficiency in the amount of frost present in the regolith and available for thermal migration and cap formation.

6.4.3 Regolith Structure and Evolution

Both Ganymede and Callisto show evidence for a long cratering history. Therefore, they should have appreciable impact-generated regoliths. The photometric functions and thermal inertias (Hansen, 1972; Morrison and Cruikshank, 1973) of both bodies are best explained by surfaces consisting of loosely-packed fine particles.

In some respects, the regoliths of Ganymede and Callisto may resemble that of the Moon. Ganymede and Callisto both have surface gravity comparable to the Moon's (Table 1.1). The amount of cratering exhibited

by Ganymede's grooved terrain is comparable to that of the lunar maria, while the amount shown by the cratered terrain on both bodies is roughly comparable to that of the lunar highlands (Smith et al., 1979a). Also, the strength of ice at very low temperatures is similar to that of silicates (Parameswaran and Jones, 1975). Ignoring the effects of sublimation, then, one might expect the regolith of Ganymede's grooved terrain to have a depth and structure similar to that of the lunar maria, while the regolith of cratered terrain on both bodies should show similarities to that of the lunar highlands.

Apollo seismic experiments showed that the lunar regolith is typically $\sim$ 5 m thick in the maria and $\sim$ 10 m thick in the highlands (Nakamura et al., 1975). The density is less than half that of the constituent grains at the surface, and increases roughly logarithmically with depth (Carrier et al., 1974). It is fine grained (mean particle size = 60 μm) and poorly sorted (Lindsay, 1973). The composition is like that of the underlying bedrock at depth, and increases in the proportion of impact products, such as meteoritic material and melts, toward the surface. Micrometeorite impacts turn over the upper 1 mm every 10^4 to 10^5 years, but the gardening rate drops off very sharply below that depth (Gault et al., 1974).

Using the Moon as analogue, one might expect a regolith thickness of roughly 5 m in Ganymede's grooved terrain, and roughly 10 m in the cratered terrain of both Ganymede and Callisto. Neglecting sublimation effects, one would also expect a density structure like that on the Moon, and a composition that reflects that of the bedrock. The "bedrock" in both bodies' cratered terrain may have a fairly high silicate content. At least in its upper part the silicate content may approach the mean silicate mass fraction of the bodies as a whole, about 50%. The bedrock of Ganymede's grooved terrain, however, is much more ice rich. In fact, geologic evidence (Chapter 9) suggests it may be nearly pure ice. As on the Moon, the proportion of impact products, largely meteoritic material, should increase toward the surface. This could create an enrichment in silicates very near the surface, as sublimation may significantly deplete the ice component of micrometeorites at the orbit of Jupiter. Also, much of the fine material impacting Ganymede and Callisto may be derived from the outer irregular satellites of Jupiter (Pollack et al., 1978), and would thus be composed of silicates.

The foregoing discussion neglects sublimation, which should have important effects on the upper part of the regolith. There is evidence that the upper regolith is very different from that on the Moon, as

the thermal inertia $(K\rho c)^{\frac{1}{2}}$ for the surface layer on Ganymede and Callisto (Hansen, 1972; Morrison and Cruikshank, 1973) is very low, typically only about one-fourth that found for the lunar surface (Wesselink, 1948; Jaeger, 1953). This difference may be largely due to creation of a highly porous silicate lag deposit at the surface by sublimation of regolith ice grains. The mean sublimation rate calculated at the equator on Ganymede is roughly 10^{-10}g cm^{-2} s^{-1}. Purves and Pilcher (1980) showed that most molecules escaping by sublimation will reimpact the surface, and that the actual net loss is about three orders of magnitude lower than that obtained by assuming irretrievable sublimation into a vacuum. Even with a loss rate of 10^{-13} g cm^{-2} s^{-1}, however, the thin, low thermal inertia upper layer of the regolith, if it were dominantly H_2O frost, could last only a few hundred thousand years. The survival time on Callisto would be about an order of magnitude shorter. Sublimation would thus be expected to rapidly deplete the upper part of the regolith of ice. With any significant amount of silicates in the regolith, this sublimation would leave behind a loosely-packed surface lag deposit composed mostly of silicate grains. The eclipse radiometry results indicate that this deposit, if present, is several mm thick (Morrison and Cruikshank, 1973). Its upper portion should be fairly well-mixed, and supplemented by addition of silicate micrometeorites.

Due to its loose packing and low thermal conductivity, it would act as an insulator, maintaining a low constant temperature in the underlying ice-silicate regolith. Sublimation rates for the lower layer temperatures of Figure 6.2 are four or five orders of magnitude lower than those at the surface. Further, sublimation of ice in the lower layer would be strongly inhibited by the necessity of diffusion of vapor through the upper layer. Thus, such a configuration would be essentially stable, with significant sublimation occurring only when impacts disrupt the surface layer. This is the justification for assuming no temperature dependence on the thermal properties in the model. Silicate powders have essentially constant K and c over the temperature range of interest. The values of K and c for ice do show some temperature variation. Because ice is probably only a major constituent of the lower, high thermal inertia layer, however, there is no significant effect on model results.

When ice from the lower part of the regolith or the bedrock is excavated by impacts, it will undergo fairly rapid sublimation. Most molecules, however, will reimpact the surface many times before either escaping or being trapped at high latitudes (Purves and Pilcher, 1980). While they are undergoing this thermal migration, they may form a very thin steady-state layer of transient ice molecules that covers the surface of the regolith nearly

uniformly. There is evidence from Earth-based observations that such a frost layer exists. Near-infrared spectra of Ganymede show strong water absorption features that imply a surface at least 90% covered by H_2O frost (Clark and McCord, 1980). Features in Callisto's spectrum show a frost cover of at least 30%, and probably closer to 60%. The features are definitely interpreted to be the result of free surface frost, not bound water. Laboratory studies of the infrared reflectance of frost-coated silicate grains show that a frost layer only a few tens of μm thick is sufficient to show strong H_2O absorption features (Clark, 1981). A layer that thin affects the visible reflectance of the substrate much less, however, as frost is very transparent at visible wavelengths. The extensive frost cover implied by the infrared spectra may thus be an extremely thin frost layer at the top of the regolith.

To summarize, the nature of the regolith on Ganymede and Callisto is inferred to consist of three principal layers: the main regolith, with a composition reflecting that of the underlying bedrock and a thickness of roughly 5-10 m, an upper layer several mm thick consisting primarily of loosely-packed silicate grains, and a steady-state surface layer of H_2O frost a few tens of μm thick. The ice content of the main regolith of Ganymede's grooved terrain should be substantially higher than that of the cratered terrain on either body. With the larger amount

of ice exposed by impacts, the steady-state surface frost layer should be thicker on Ganymede than Callisto, accounting for the stronger infrared features and perhaps for the higher albedo of Ganymede's cratered terrain than Callisto's.

This very simple model of the regolith requires some refinement to explain the anomalous polarization properties shown by radar observations of Ganymede and Callisto (Ostro et al., 1980). These must instead result from structure at scales larger than the ∿ 12 cm radar wavelength. This structure may be either rough surface topography below the Voyager resolution limit or some type of subsurface inhomogeneities. If subsurface, density inhomogeneities in the regolith (Ostro, 1980) are much more likely than open void spaces (Goldstein and Green, 1980), as void spaces could not be supported in a fine-grained, noncohesive regolith.

6.5 Other Factors Affecting the Calculations

It should be noted that other processes may also cause significant loss of ice from the surfaces of Ganymede and Callisto. In particular, sputtering by charged particles in the Jovian magnetosphere may be important (Lanzerotti et al., 1978). The effect of sputtering will not vary with terrain type, however, so the conclusions drawn here regarding bright ray crater distribution do not depend on the importance of sputtering. The influence of sputtering would not be homogeneous, however. The trajectories of charged particles, which follow the lines of

Jupiter's magnetic field, would concentrate the charged particle flux at the bodies' poles. Sputtering would also be enhanced on their trailing hemispheres, as the entire body of trapped particles corotates with Jupiter at a velocity higher than the bodies' orbital velocities. The enhancement of sputtering at the poles indicates that sputtering inhomogeneities are not responsible in controlling the distribution of visible frost deposits on Ganymede, which are concentrated at the poles. Also, because sputtering should be more pronounced on Ganymede than Callisto, it cannot be responsible for the lack of polar caps on Callisto. Enhanced sputtering of ice from Ganymede's trailing hemisphere could perhaps have decreased that hemisphere's disc-integrated visible brightness, which is slightly lower than that of the trailing hemisphere (Stebbins, 1927; Morrison and Morrison, 1977). It cannot, however, account for the observed hemispheric albedo asymmetry of Callisto, which has the opposite sense. The principal effect that sputtering should have on the results obhere is an overall enhancement of ice loss rates, resulting in more rapid development of the silicate lag deposit and depletion of the transient frost layer.

The most critical assumption used is that of unit emissivity. A lower thermal emissivity would result in

temperatures higher than those calculated. Like sputtering, the only effect that higher overall temperatures would have on the conclusions drawn here is that they would result in more rapid ice loss and lag deposit development. The 10% uncertainty in the absolute albedos used in the calculations produces very small uncertainties in the calculated temperatures, about 1% for Ganymede and less for Callisto. These uncertainties of course do not affect any conclusions regarding relative temperatures among the different terrain types.

6.6 Conclusions

The surface material of Ganymede and Callisto may consist of a regolith of ice and silicates, an overlying lag deposit that is primarily loosely-packed silicate dust, and a very thin transient surface frost layer. When impacts occur in regions, such as the grooved terrain of Ganymede, where the subsurface material has been enriched in ice, bright ray craters form. As sublimation of the ice exposed by impacts occurs, H_2O molecules that do not escape undergo thermal migration about the surface (Purves and Pilcher, 1980). Net accumulation of polar frost deposits occurs at latitudes where the influx rate exceeds the sublimation rate. With less ice in the crust, and consequently less exposed by impacts, no observable polar caps have formed on Callisto.

CHAPTER 7

GROOVED TERRAIN AND DOME TOPOGRAPHY

7.1 Introduction

In order to understand the geology of Ganymede's grooved terrain, it is necessary to obtain a clear picture of its appearance. Along with detailed mapping, accurate topographic information is needed. Unfortunately, the distant Voyager flybys did not permit acquisition of useful stereoscopic data. Some topographic information may be obtained, however, using the technique of photoclinometry. This technique has been applied to impact craters on Ganymede and Callisto (Passey et al., 1980, and work in progress), and is applied here to Ganymede's grooved terrain and one of its domes.

7.2 Procedure

If the photometric function of a surface is known completely then it is possible, knowing the lighting geometry and assuming a constant albedo, to invert the brightness variations observed in an image to determine surface topography. For grooved terrain we can use the photometric function determined in Chapter 3:

$$I(i,\varepsilon,\alpha) = C[\mu_0/(\mu_0 + \mu)]f(\alpha) \qquad (7.1)$$

where i = incidence angle, ε = emission angle, α = phase angle, $\mu = \cos \varepsilon$, $\mu_0 = \cos i$, and C = constant. The function f need not be considered here, as the phase angle remains constant in any given image. Thus

$$I = C'[\mu_0/(\mu_0 + \mu)] \qquad (7.2)$$

in a single image (α = constant) where C' is another constant.

In general, complete three-dimensional photoclinometric determination of topography is a complex mathematical problem with severe limitations on its practical application. The problem is simplified greatly, however, if the goal is to construct a two-dimensional topographic profile that lies perpendicular to topographic strike along its entire length. The unusual corrugated nature of Ganymede's grooved terrain fortunately results in topographic strike remaining nearly constant over large areas, and allows its direction to be clearly established. Profiles perpendicular to topographic strike may also be obtained across the center of radially symmetric features such as impact craters or domes. The technique used here is much more simple and straightforward than a complete three-dimensional technique, but is restricted to calculation of profiles perpendicular to topographic strike. Ganymede's grooved terrain is ideally suited to this restriction. A complete discussion

of the theory of three-dimensional photoclinometry is given by Wildey (1975).

Consider two surfaces, one horizontal and one tilted so that its normal makes an angle θ with the vertical (Fig. 7.1). The observed intensity scattered from the horizontal surface will be given by

$$I = C'[\cos i/(\cos i + \cos \varepsilon)] = C'[\mu_o/(\mu_o + \mu)] \quad (7.2)$$

while that from the tilted surface will be given by

$$I^* = C'[\cos i^*/(\cos i^* + \cos \varepsilon^*)] = C'[\mu_o^*/(\mu_o^* + \mu^*)]. \quad (7.3)$$

The slope angle of the tilted surface may be determined if i, ε, i^*, ε^*, and α are known. The values of i, ε, and α can of course be readily determined for any point on an image from the spacecraft trajectory. In the simple case where the incident ray, the emitted ray, and the vertical are coplanar (i.e., when $\alpha = i + \varepsilon$), $\theta = i^* - i = \varepsilon - \varepsilon^*$. In the more general case, unique solutions for i^* and ε^* may be obtained from the observed intensity I^* and the constant C' using equation (7.3) and geometric expressions relating i^*, ε^*, and α. The method for obtaining these solutions is given in Appendix B. Thus it is possible to determine the slope angle θ from the intensity I^* at any point if the value of C' is known.

In practice, topographic profiles are constructed in the following manner: A profile line on an image is

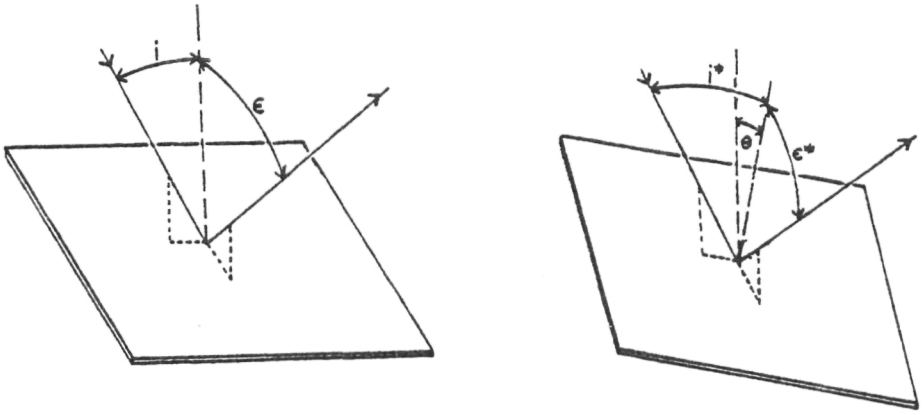


FIGURE 7.1. Horizontal surface with incidence angle i and emission angle ε. Tilted surface with incidence angle i* and emission angle ε*. In general, the two rays and the surface normal are not coplanar.

selected that lies perpendicular to topographic strike. Care is taken to avoid areas with obvious variations in surface reflectance. Intensities are sampled along the line, averaging several pixels perpendicular to the direction of the line in order to reduce noise (Fig. 7.2). The value of C' is determined by

$$C' = \bar{I}[(\mu_o + \mu)/\mu_o] \qquad (7.4)$$

where $\bar{I}$ is the mean intensity observed along the profile. This method of determining C' assumes that the mean value of θ along a profile is zero; i.e., that there is no regional slope. The slope angle for each element of the profile is then calculated from the intensity I* measured for the element. The slope calculated for a profile element is of course an average over the entire element. Slopes on scales smaller than the element size may be gentler or steeper than the average slope obtained for the element as a whole.

In any long profile the curvature of the satellite's surface becomes apparent. This curvature may be removed from the topographic profiles either by subtracting out the regional shading variation along the line prior to calculation of slopes, or by directly subtracting out the curvature after elevations have been calcualted (Fig. 7.3). Comparison of profiles corrected in each of these two manners provides a useful check on the accuracy of the

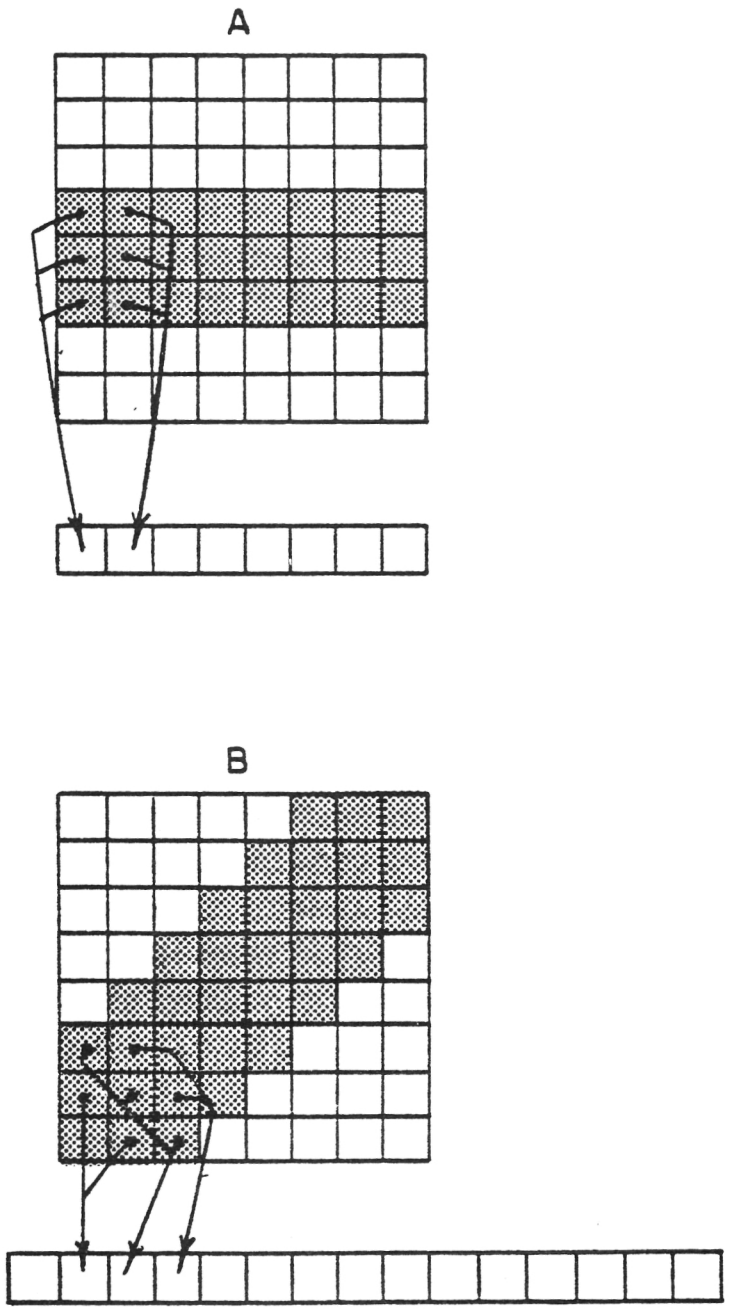


FIGURE 7.2. Averaging technique used in construction of profiles. Rather than using single pixels, several pixels perpendicular to the line of the profile are combined and averaged to yield a single profile element. Averaging is thus done parallel to topographic strike, and reduces noise in the profiles.

FIGURE 7.3. Schematic representation of the two methods for removal of Ganymede's surface curvature from profiles. A) Regional shading variation resulting from curvature across an image is removed prior to calculation of the profile. The slope of a linear least squares fit to the intensity data numbers (DN's) of each profile element (dashed line) is subtracted out, while maintaining the mean DN value along the profile. B) After calculation of a profile using uncorrected DN's, the curvature known from Ganymede's radius is subtracted directly from the profile elevations. If elevations are calculated correctly, these two different correction methods yield the same results.

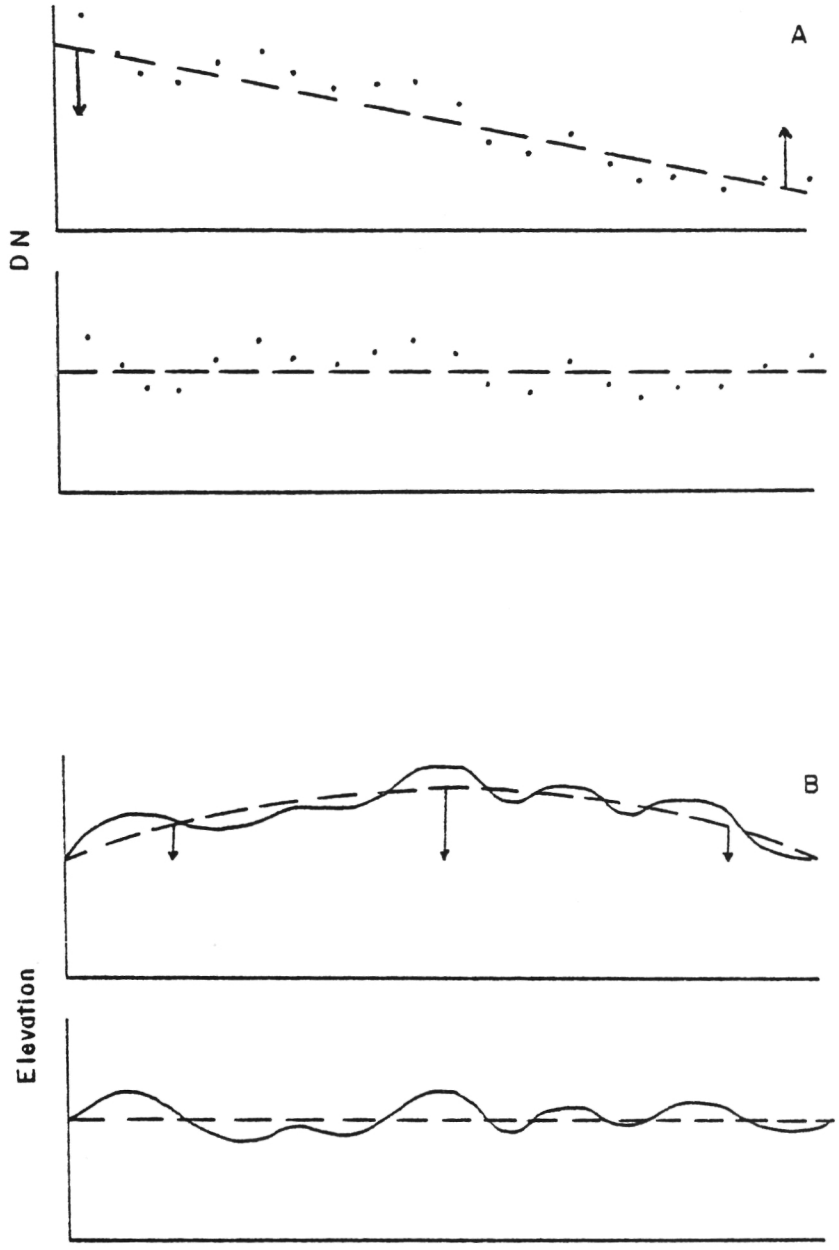


FIGURE 7.3 (continued)

slopes calculated. If the slopes calculated were consistently too steep or too gentle, simple geometric subtraction of the surface curvature would give profiles that appear respectively bowed upward or downward in the center. In all cases, the two correction methods give nearly identical results.

While most variations in surface albedo are obvious in the images and may be readily avoided, some might be more subtle. For example, a very gentle albedo gradient along a profile would be difficult to detect visually. It would appear, however, as either anomalously high or low surface curvature when the correct surface curvature was removed. A problem of this sort could be eliminated by removal of the regional shading along a profile. In none of the profiles calculated, however, did this seem to be a difficulty. A problem could also arise if sun-facing slopes were frost-free, while bright frost deposits were present on slopes facing away from the sun. This potential difficulty was dealt with by avoiding grooves that run east-west and by avoiding areas near the margins of the polar caps where uneven frost distribution might be most likely to occur.

Photoclinometry is of course impossible if shadows larger than or equal to the element size are present. All profiles were chosen far enough from the terminator that no elements were shadowed. A second check against

shadowing effects may be made by examining the profiles for any consistent topographic asymmetry; none is observed.

7.3 Results

As a test of the calculation technique, a profile was obtained across an impact crater (Fig. 7.4). The shape of the profile is plausible for a crater on Ganymede, demonstrating the general validity of the technique.

Topographic profiles of grooved terrain obtained from several Voyager 2 images are shown in Figures 7.5-7.8. All of the images are from an area in Ganymede's southern hemisphere. The resolution in these images is the highest obtained for Ganymede, about 600 m per pixel. All profiles are shown with a vertical exaggeration of 8 to 1. For comparison, several of the profiles are reproduced with no vertical exaggeration in Figure 7.9.

Profiles constructed for two other types of topographic features are shown in Figures 7.10 and 7.11. Figure 7.10 shows two representative profiles across a linear fracture observed by Voyager 1 that is quite different in appearance from ordinary grooved terrain in that it is a very straight solitary groove with distinctly raised rims. Figure 7.11 shows several profiles across the topographic dome observed by Voyager 1. The dome profiles were corrected for surface curvature by direct subtraction after elevations were calculated. For comparison, a profile of a flat area just

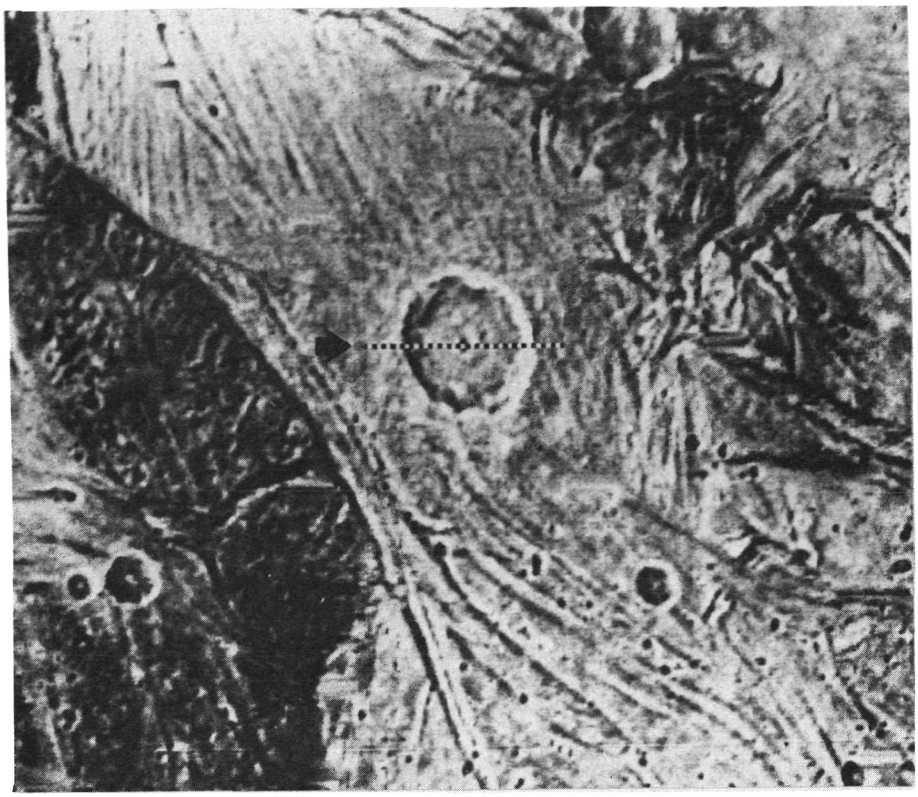


FIGURE 7.4. Sample photoclinometric profile across an impact crater in image 550J2-001. Note the central pit with its raised rim and the floor bowed up by viscous relaxation. Vertical exaggeration is 8 to 1. In this and following profiles, elevations are in relation to that at the starting point of the profile (image centered at ∿ 0° lat., 130° long.).

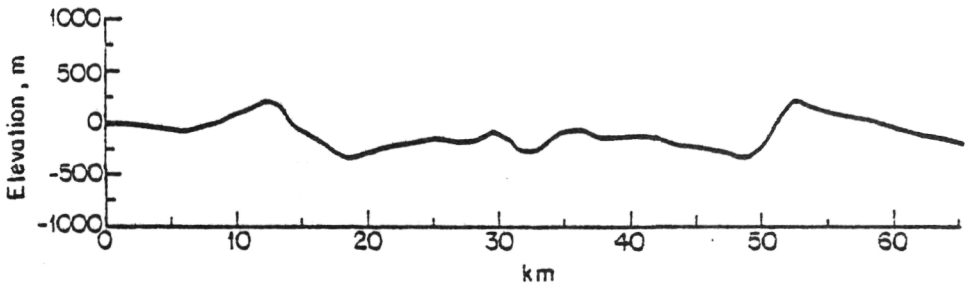


FIGURE 7.4 (continued)



FIGURE 7.5. Topographic profiles in image 660J2-001. Vertical exaggeration is 8 to 1. Arrows in 7.5c indicate secondary terraces occasionally observed on groove walls (image centered at ∿ - 80° lat., 200° long.).

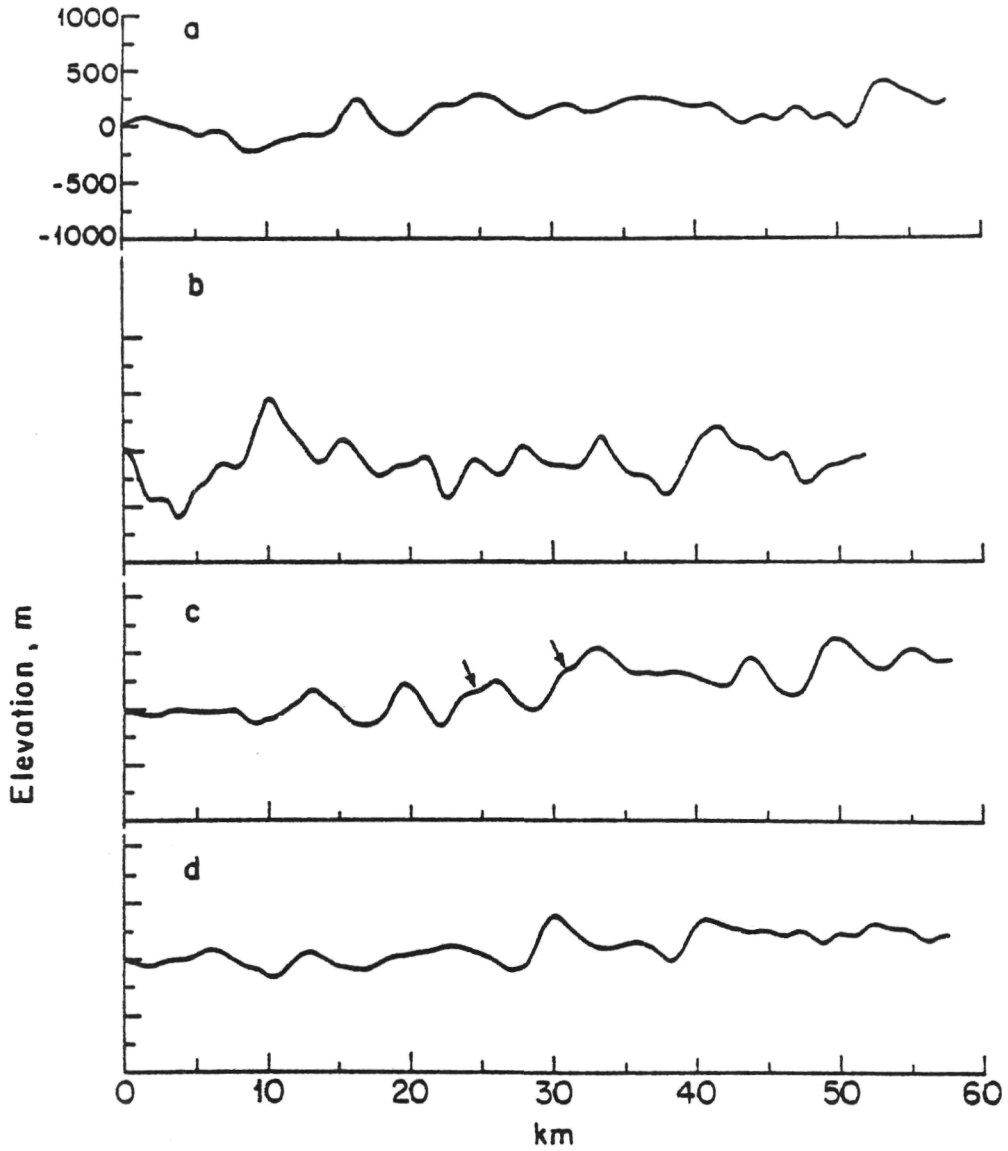


FIGURE 7.5. (continued)



FIGURE 7.6. Topographic profiles in image 658J2-001. Vertical exaggeration is 8 to 1 (image centered at ∿ -75° lat., 180° long.).

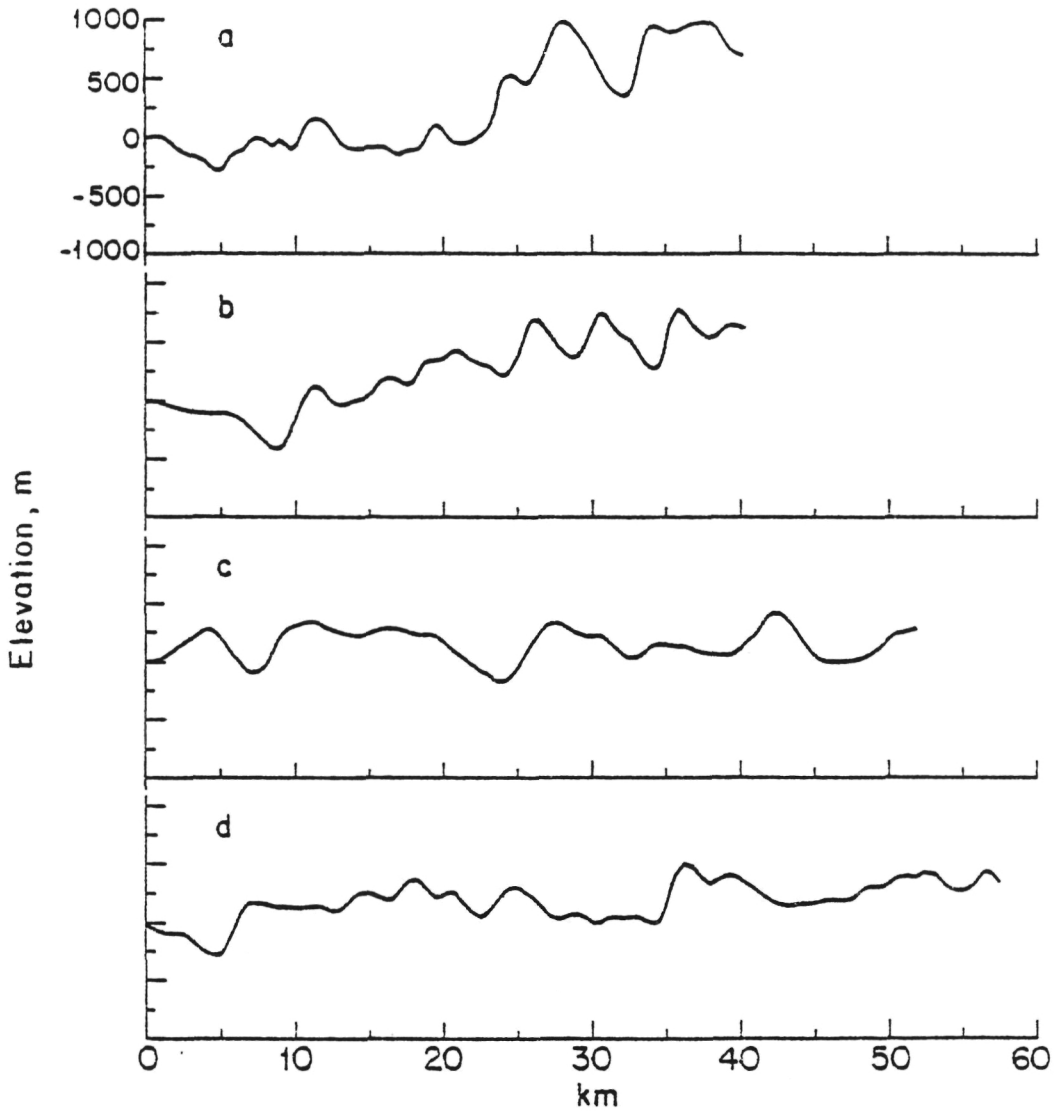


FIGURE 7.6 (continued)



FIGURE 7.7. Topographic profile in image 578J2-001. Vertical exaggeration is 8 to 1 (image centered at ∿ -40° lat., 120° long.).

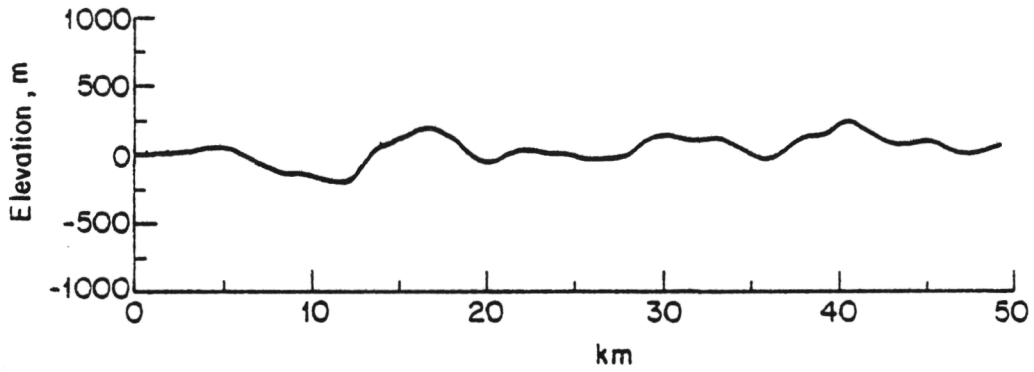


FIGURE 7.7 (continued)

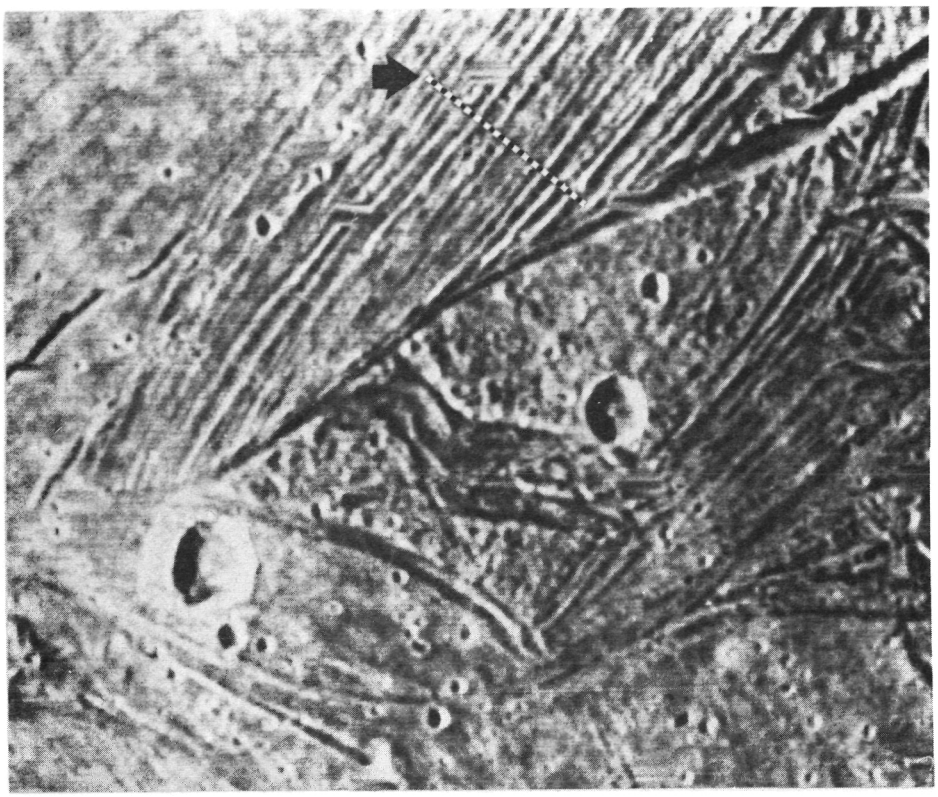


FIGURE 7.8. Topographic profile in image 572J2-001. Vertical exaggeration is 8 to 1 (image centered at ∿ -30° lat., 120° long.).

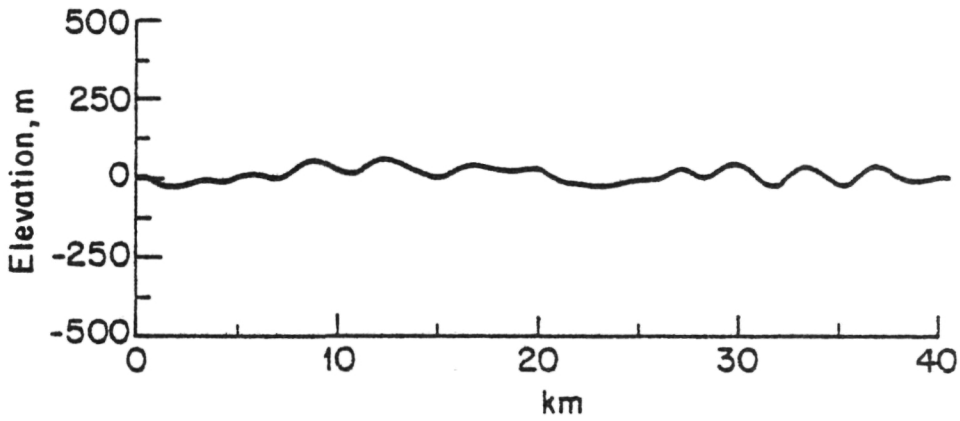


FIGURE 7.8 (continued)

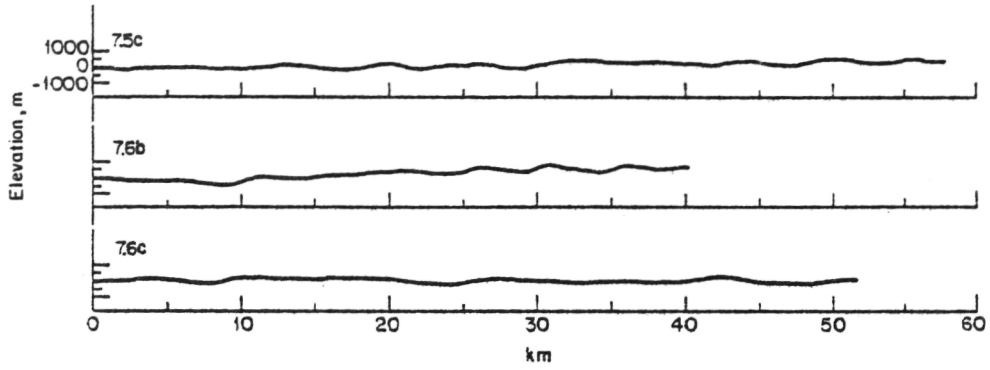


FIGURE 7.9. Three representative topographic profiles reproduced with no vertical exaggeration.

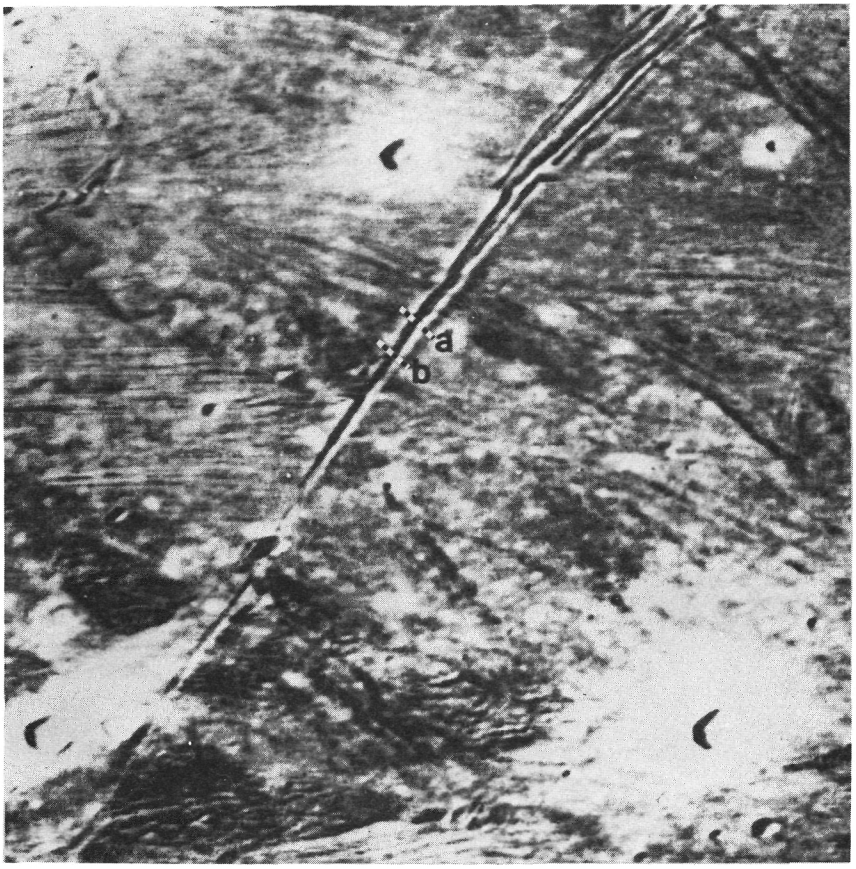


FIGURE 7.10. Topographic profiles across an unusual fracture in image 985J1+001. Vertical exaggeration is 8 to 1 (image centered at ∿ 60° lat., 335° long.).

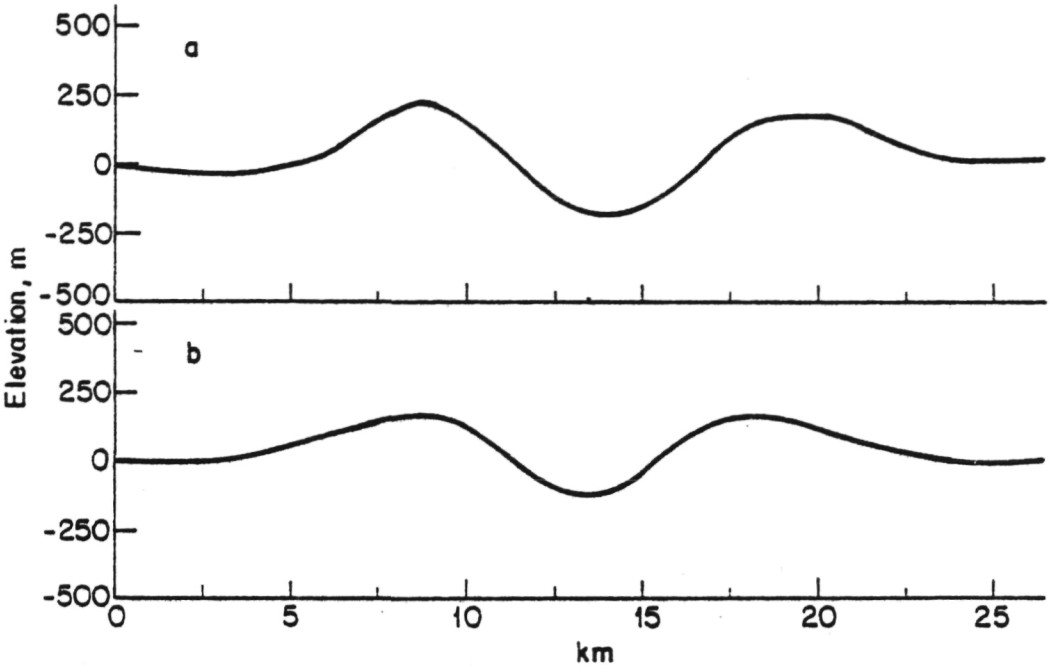


FIGURE 7.10 (continued)

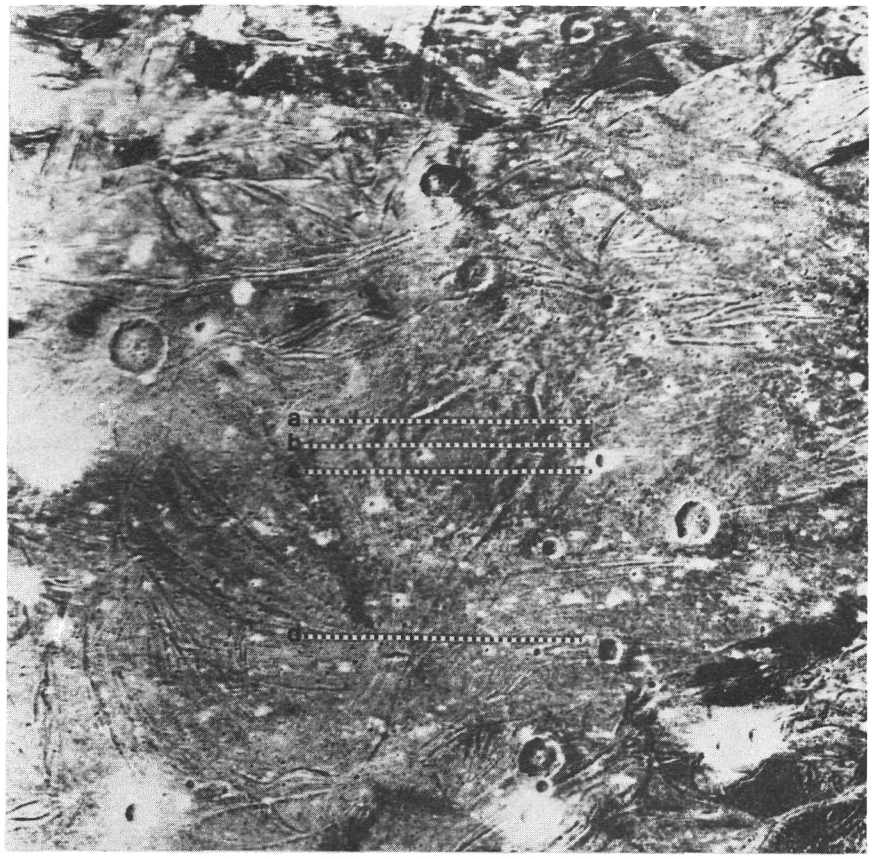


FIGURE 7.11. Topographic profiles across a dome in image 967J1+001. These profiles were corrected by direct geometric subtraction of surface curvature. Profile 7.11d shows a flat area just south of the dome corrected in the same manner for comparison (image centered at ∿ 35° lat., 330° long.).

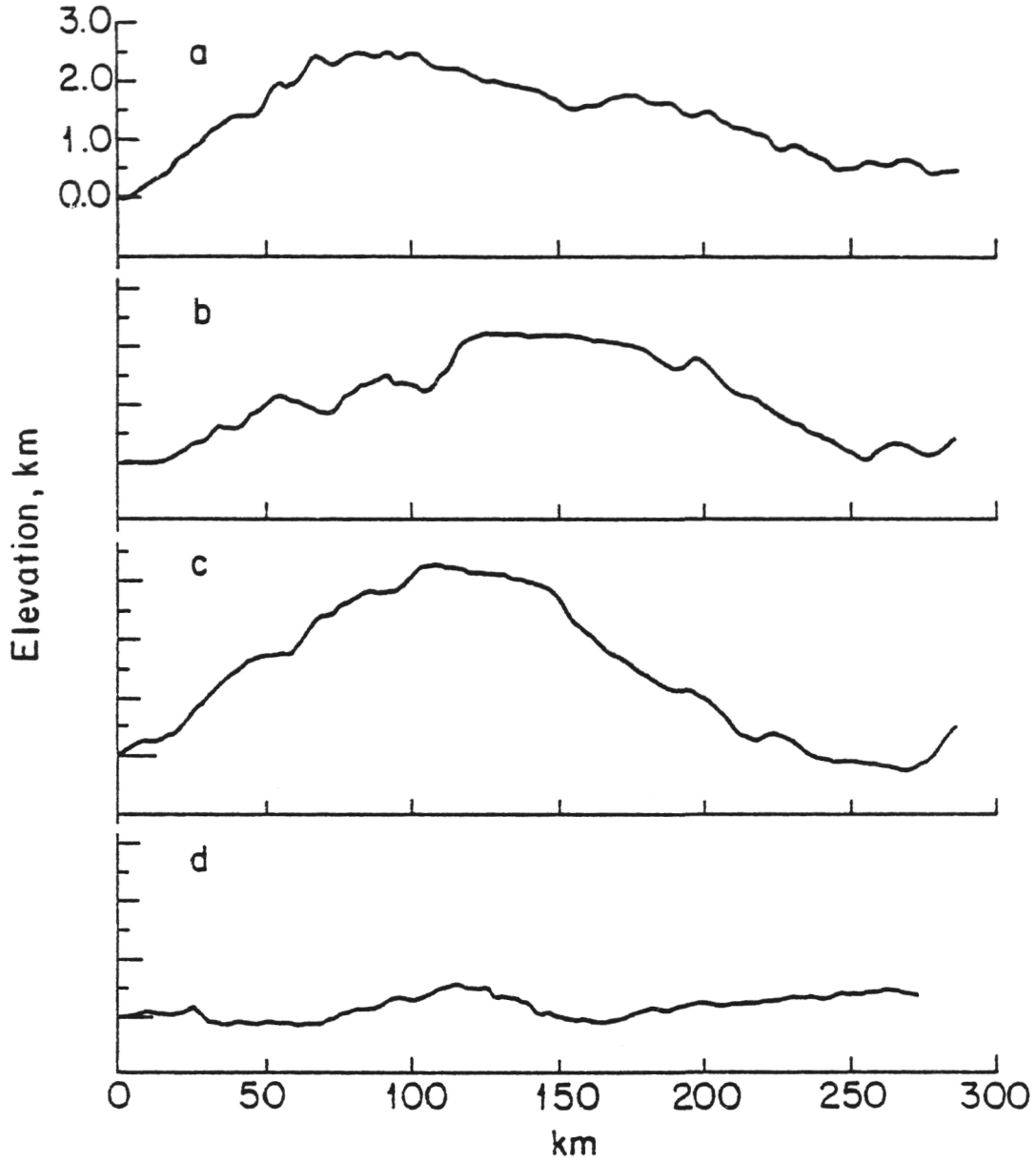


FIGURE 7.11 (continued)

south of the dome corrected in the same manner is also shown.

7.4 Discussion

The most noteworthy aspect of these profiles is that the topography of the grooved terrain is not very rugged at Voyager resolution. The steepest slopes calculated anywhere are about 20°, and the root mean square (RMS) slope at a resolution of 600 m per pixel for all the grooved terrain profiles constructed is only 5.5°. These profiles are of course a biased sample, as they were selected from areas where the grooves are well-developed. The RMS slope for all grooved terrain at this scale is probably lower than this value. Thus, it is clear that surface roughness on the scale visible in Voyager images cannot be responsible for the diffuse radar scattering law or anomalous polarization properties exhibited by Ganymede (Ostro et al., 1980). If topographic features are responsible for these unusual radar properties, they must be at scales < 1200 m.

The "wavelength" of the topography--the distance between successive groove troughs--is variable. It is typically about 5-6 km, ranging from a minimum of 3 km to a maximum of about 8 km. Within a single set of subparallel grooves, however, the spacing appears often much more constant, but may vary substantially from one groove set to another in a given area.

The amplitude of the topography is also variable, and also seems to remain fairly constant within a single set of subparallel grooves. Amplitudes range from barely perceptible undulations to a maximum crest-to-trough elevation diference of about 700 m. Typical amplitudes are 300-400 m. The variability exhibited by different sets of grooves is well illustrated by comparing profile 7.7, with low amplitude and wavelength, to profile 7.6c, with high amplitude and wavelength. Not enough high resolution areas may be sampled to determine if any correlation between amplitude and wavelength exists.

The profiles also provide information about slope shapes. The profiles of individual grooves vary considerably. Some are simple U-shapes, while others appear to have secondary terraces on their walls (for example, profile 7.5c). One consistent result is that concave-up slopes are more common than convex-up slopes. This may be shown statistically by evaluating the finite difference equivalent of the second derivative of the topography at each point. Out of nearly 2,500 points on all the grooved terrain profiles constructed, 54% have positive (concave-up) curvature and 46% have negative (convex-up) curvature, differing significantly from a distribution that is 50% positive, 50% negative with a confidence level of > 0.999. The shape of the grooved terrain is thus not roughly sinusoidal, but instead tends toward broad, U-shaped troughs

and somewhat sharper crests. As demonstrated by Figure 7.9, however, this tendency is extremely subtle.

It should be stressed here that, with the exception of large features such as the dome, photoclinometry is only useful for an area in Ganymede's southern hemisphere imaged at the highest resolution. This area may not be completely representative of the grooved terrain as a whole. Figure 7.12 shows an area observed at lower resolution in which grooves are spaced roughly 10 km apart. The grooves in this area appear to be only several km wide, and the areas separating them appear qualitatively to be quite flat. While all the images suggest fairly consistent groove morphology, the terrain separating the grooves seems to vary from the relatively sharp divides dominant in the area sampled to broader, flatter divides in some other areas.

It has already been noted that in virtually all cases a trough, not a crest, marks the boundary of a band of grooved terrain. In other words, the grooved terrain truly consists of parallel grooves depressed below their surroundings, rather than parallel elevated ridges (Smith et al., 1979a,b). The fracture in Figure 7.10 is thus unusual in that it has distinctly raised rims. Another rare positive relief feature is the possible compressional feature shown in Figure 2.22. Unfortunately, it lies too close to the terminator to obtain a photoclinometric profile. To summarize, then, the grooved terrain of Ganymede consists

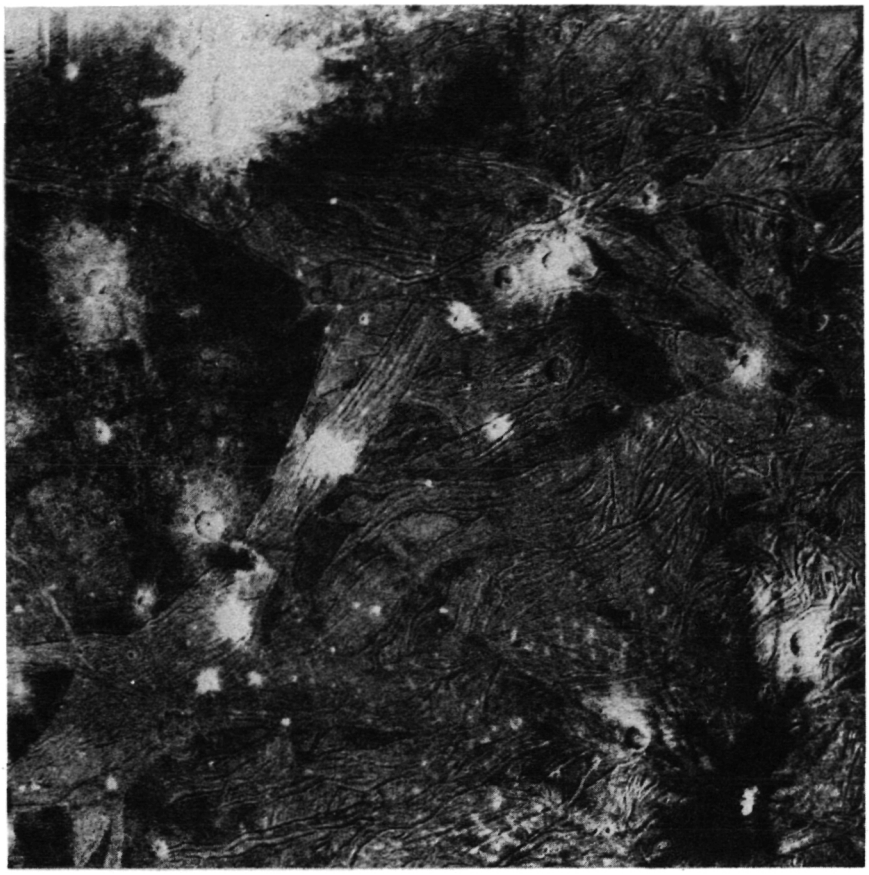


FIGURE 7.12. Grooved terrain in image 955J1+000. Many grooves in this area appear to be separated by relatively broad, flat divides, rather than the sharper divides dominant in the topographic profiles presented (image centered at ∿ 15° lat., 340° long.; scale across image = 1070 km).

of subparallel grooves several hundred meters deep and spaced 3-10 km apart. Slopes at Voyager resolution are gentle and tend to be primarily concave upward. At scales smaller than Voyager resolution, however, the topography is unknown and could be considerably more rugged.

Perhaps the most unusual feature observed by Voyager on Ganymede is the dome shown in Figure 2.15. A number of parallel profiles have been constructed across it (Fig. 7.11). It has gentle, undulating slopes and a smooth, flat central summit region. The profiles give a mean summit elevation 2.5 km above the surrounding plain. Confidence in this figure is increased by profiles across adjacent flat regions. For example, profile 7.11d is constructed across a flat area just south of the dome and is corrected for surface curvature by direct subtraction of elevations, as are the dome profiles. The total relief from the center to the edges of this profile is negligible, as it must be if elevations are being calculated correctly. The dome is thus a substantial geologic feature, and is certainly one of the highest relief features on Ganymede. A second dome (Fig. 10.4) has been identified on Ganymede, but it is too close to the terminator and at too low resolution for photoclinometry to be useful. The structure and origin of these domes are considered in detail in Chapter 10.

CHAPTER 8

VOLUME CHANGES AND GROOVED TERRAIN ORIGIN

8.1 Introduction

As discussed in Chapter 2, the surface of Ganymede is dominated by extensional tectonic features. If surface area had been conserved, tectonic compression equivalent to the extension expressed in the grooved terrain must have taken place. There is no convincing geologic evidence on Ganymede for significant compression, however. It seems, then, that surface area was not conserved, and that Ganymede expanded early in its history, creating grooved terrain. In this chapter, internal changes that may have caused variations in the mean specific volume of Ganymede and Callisto are investigated. Factors are discussed that may have led to lesser and slower expansion for Callisto than for Ganymede, preventing formation of grooved terrain there.

Consolmagno and Lewis (1976) considered the internal evolution of Ganymede and Callisto. They assumed that the chemical composition of these bodies is the result of equilibrium condensation from a nebula of solar composition. Under this assumption, bodies formed at the orbit

of Jupiter should initially consist of silicates with a bulk composition like that of C1 carbonaceous chondrites, plus large amounts of H_2O ice (Lewis, 1972). Temperatures in that part of the solar nebula were probably too high to allow significant condensation of other ices. They also assumed that the bodies accreted homogeneously; that is, that ice and silicates would be homogeneously distributed throughout the body at the end of accretion. They found that under these assumptions Ganymede and Callisto should undergo internal melting early in their histories through radiogenic heating. Differentiation should occur, with the denser silicates concentrating in a core and the water and ice forming a thick mantle and crust around it. Ganymede was found to differentiate somewhat more rapidly than Callisto due to its slightly higher density (1.93 g cm^{-3}, compared to 1.79 g cm^{-3}) and radionuclide content. They predicted that Ganymede and Callisto currently each consist of a silicate core surrounded by a thick convecting mantle of liquid water and a thin crust of solid ice.

Reynolds and Cassen (1979) considered solid state convection in the ice crust. Using conservative estimates of viscosity, they found that such a crust would be convectively unstable. Further, they found that the enhanced heat transfer rates resulting from this convection should be sufficient to refreeze the liquid water mantle

in a time that is short compared to the life of the body. They therefore predicted that Ganymede and Callisto currently each consist of a silicate core surrounded by a thick layer of solid ice that may be actively convecting.

An important factor to consider in any evolutionary model is the complex physical chemistry of water. A pressure-temperature phase diagram for water and the various ices is shown in Figure 8.1. Ice has a number of polymorphs, only one of which, ice I, has a density less than 1.0 g cm^{-3}. The higher density polymorphs have densities ranging from 1.16 to 1.66 g cm^{-3} (Table 8.1). These high pressure polymorphs are the ones that should be stable through most of a frozen, post-accretionary Ganymede or Callisto. Because they are denser than liquid water, internal melting and differentiation should lead to an increase in the volume and surface area of the body.

8.2 Volume Change During Differentiation

The maximum surface area increase possible during differentiation may be calculated using a simple quantitative model. All parameters of the model are chosen to place an upper limit on the expansion during differentiation. It is assumed that a fully differentiated body consists of a silicate core, a liquid mantle with an adiabatic temperature gradient maintained by convection, and an ice I crust arbitrarily chosen to be 100 km thick.

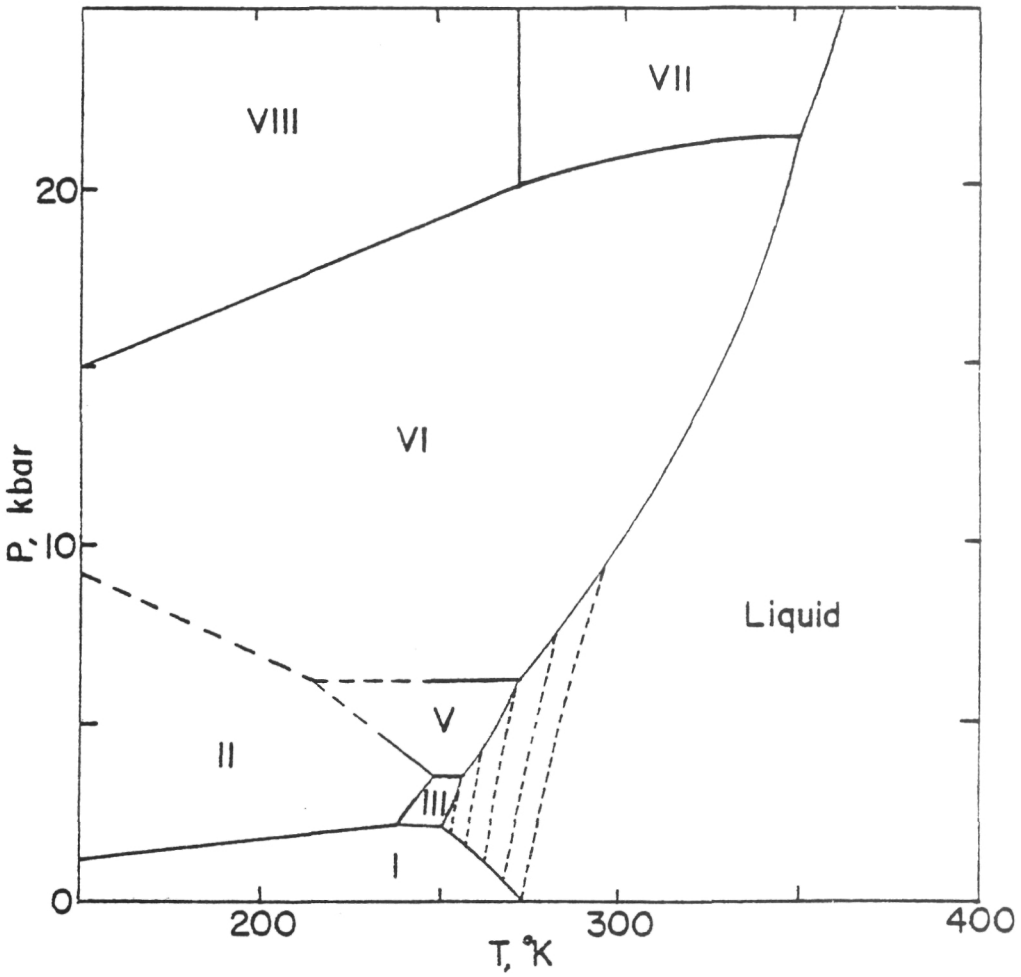


FIGURE 8.1 The pressure-temperature phase diagram for H_2O. Several adiabats are shown in the liquid field (phase diagram from Eisenberg and Kauzmann, 1969; adiabats calculated from Sharp, 1972).

TABLE 8.1 The Polymorphs of Ice

Polymorph	Density,* g cm^{-3}
I	0.92
II	1.18
III	1.15
V	1.24
VI	1.34
VII	1.66
VIII	1.66

* Mean density in stability range, after Eisenberg and Kauzmann (1969).

Variation of this crustal thickness affects the calculation results by less than 10%. The increase of liquid water density with pressure is assumed to be that calculated by Sharp (1972). The water is assumed to be pure H_2O, although it may be of future interest to consider the effects of dissolved salts or other volatiles that may be present.

Knowing the approximate mass and current radius of the body and assuming the mean density of the silicates in its interior, it is straightforward to numerically calculate the mean density of H_2O present. The calculation is performed by integrating in mass upward from the core, adding successive spherical shells of equal masses of water until the total mass of H_2O is exhausted. The pressure within a layer is given by

$$p = \frac{G(m_s + m_b + \Delta m_w/2)(m_w - m_b - \Delta m_w/2)}{4\pi(r + \Delta r/2)^4} \qquad (8.1)$$

where m_s is the total mass of silicates, m_b is the mass of H_2O below the layer, Δm_w is the mass of the layer, m_w is the total mass of H_2O, r is the radius to the base of the layer, and Δr is the estimated thickness of the layer. The density ρ of the layer is then determined from the known pressure-density relationship and an iteration is performed until consistent values of ρ and

Δr are obtained. The mean density of all the H_2O present is then readily obtained from the densities of the spherical shells.

The results of this calculation are shown in Figure 8.2. The mean density of the H_2O in a fully differentiated, internally molten body is found to vary from roughly 1.1 g cm^{-3} for a silicate density of 2.5 g cm^{-3} to about 1.25 g cm^{-3} for a silicate density of 3.7 g cm^{-3}. The variation results from the compressibility of liquid water. With a high silicate density, pressure at the bottom of the water column is increased, resulting in a higher overall mean H_2O density. Because the density of the silicates is not known, it is kept as the independent variable throughout the calculations.

These mean H_2O densities are used to calculate the maximum expansion that can take place during differentiation. For a given silicate density ρ_s and mean H_2O density ρ_w the overall mass fraction of silicates is given by

$$x_s = \left(\frac{\rho_s \rho_w}{\rho} - \rho_s\right) \Big/ (\rho_w - \rho_s) \qquad (8.2)$$

where ρ is the mean density of the body (Consolmagno and Lewis, 1976). It is assumed that this silicate mass fraction is constant through the initial undifferentiated body; that is, that ice and silicates are homogeneously mixed. Following Consolmagno and Lewis (1976), the

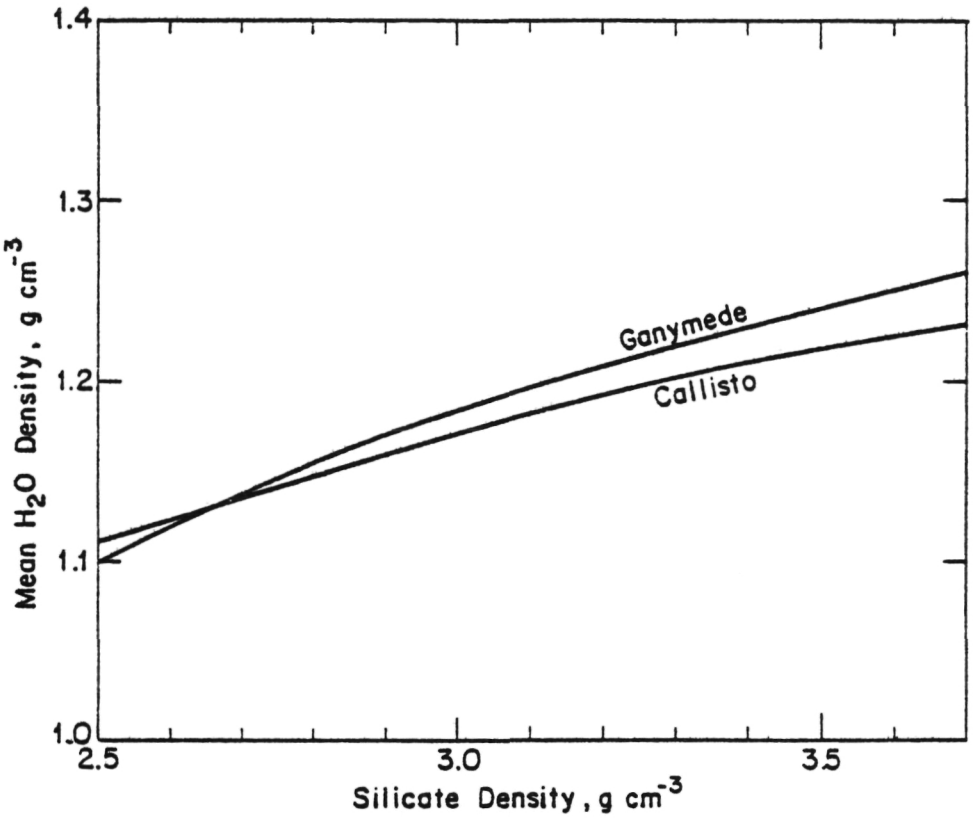


FIGURE 8.2. Mean density of H_2O in a completely differentiated body with a liquid mantle and ice I crust.

temperature through the initial body is assumed to be 100°K. The ice present will then be largely ice VIII, with succeeding layers of ice VI, ice II, and ice I. The intermixture of silicates through a layer of ice i creates an overall density within that layer of

$$\rho_{i+s} = \frac{\rho_i \rho_s}{(\rho_i - \rho_s)x_s + \rho_s} \tag{8.3}$$

From these ice + silicate densities ρ_{8+s} through ρ_{1+s}, the phase transition pressures of ice at 100°K, and the mass of the body, it is possible to calculate the positions of phase change boundaries and total radius. The calculation is performed iteratively, beginning with an initial estimate of the total body radius r_1. It is then possible to solve for the radius to each of the internal phase change boundaries. For example, the radius to the top of the ice II layer r_2 may be determined from the ice I/ice II transition pressure p_2 using the expression

$$p_2 = \int_{r_2}^{r_1} \rho_1 g dr = \int_{r_2}^{r_1} \rho_1 \frac{G}{r^2} \left[m - \rho_1 \frac{4}{3}\pi (r_1^3 - r^3) \right] dr \tag{8.4}$$

where m is the total mass of the body. The position of each phase change boundary is determined in a similar

manner. An iteration on r_1 is then performed until phase change boundary radii are found that are consistent with the known total mass. The calculated internal structures for the undifferentiated bodies are given in Figure 8.3. Comparing the calculated radii of the undifferentiated bodies to the current radii, the increase in surface area resulting from complete differentiation is obtained (Fig. 8.4.).

Complete differentiation would lead to a substantial increase in surface area. The calculated surface area increase is 5.7 to 7.4% for Ganymede and 5.2 to 7.0% for Callisto, depending on the mean silicate density assumed. The "turnover" in the curves at high silicate densities is due to the increasing importance of the compressibility of liquid water at high H_2O/silicate ratios. The similarity of the results for Ganymede and Callisto demonstrates the insensitivity of the calculations to small errors in the measured radii and masses of the bodies.

It is important to note that several other possible heat sources could affect these expansion calculations. Heat produced by accretion impacts and by decay of short-lived radionuclides such as ^{26}Al may have caused some internal melting early in the bodies' history, perhaps before the oldest parts of the present crusts were formed. Because some melting and differentiation may have taken

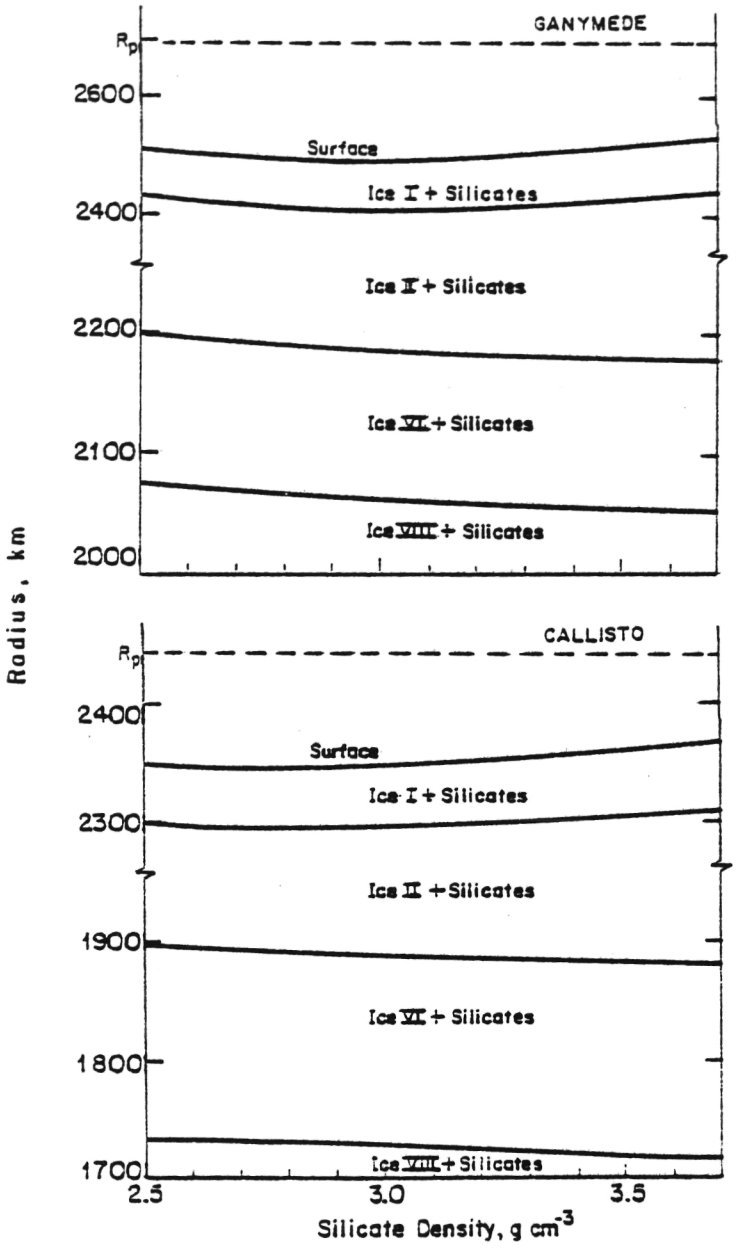


FIGURE 8.3. Internal structure of a cold (100°K) undifferentiated Ganymede and Callisto. Dashed line labeled R_p gives present radius.

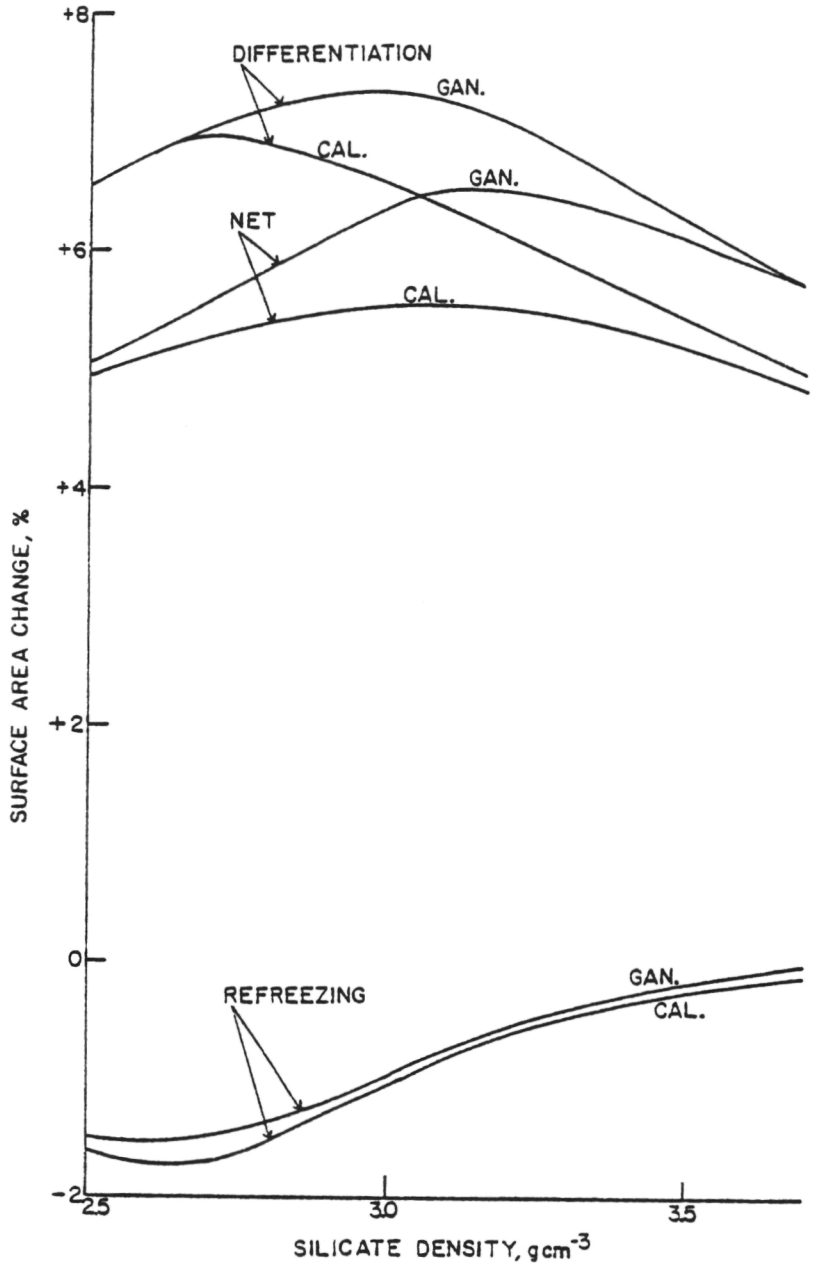


FIGURE 8.4. Calculated surface area changes for Ganymede and Callisto. Curves show the total surface area change resulting from complete melting and differentiation, the total change resulting from complete refreezing, and the net change resulting from both processes.

place before formation of the present crusts, the values for global expansion calculated here must be regarded as upper limits for geological application.

8.3 Volume Change During Refreezing

Now consider refreezing of a differentiated body, as predicted by Reynolds and Cassen (1979). The body is assumed to begin with the fully differentiated configuration described earlier, and finish as completely frozen ice around a silicate core. The temperature gradient is assumed to be linear, from 100°K at the surface to the melting point at the core/ice boundary. The pressure at the top of a layer of ice i in the refrozen body is given by

$$P_i = \frac{G[m_b + \rho_i \frac{4}{3}\pi(r_i^3 - r_b^3)][m_a - \rho_i \frac{4}{3}\pi(r_i^3 - r_b^3)]}{4\pi r_i^4} \qquad (8.5)$$

where m_b is the mass of ice and silicates below the bottom of the ice i layer, m_a is the mass of ice above the bottom of the ice i layer, r_i is the radius to the top of the ice i layer, and r_b is the radius to the bottom of the ice i layer. Beginning at the core/ice boundary, this equation is solved for each successive r_i. The calculated surface area changes resulting from refreezing are shown in Figure 8.4.

The calculations suggest that refreezing of a fully differentiated body would result in very little change in surface area. For silicate densities greater than 3.2 g cm^{-3} the change amounts to a decrease of less than 0.5% for both Ganymede and Callisto. This higher end of the silicate density range is most likely to be applicable, as radiogenic heating should cause dehydration of originally carbonaceous silicates (Fanale et al., 1976). With silicates occupying the center of the body, no ice VIII and very little ice VII form. Most of the ice is present as ice VI, II, and I, in proportions that give a mean ice density very similar to that of compressed liquid water. The net change that would take place as a result of complete differentiation followed by complete refreezing is also shown in Figure 8.4.

Because refreezing would be the most recent internal change that could influence crustal evolution, it is important to consider the refreezing process in some detail. Figure 8.1 shows several adiabats in the liquid field of the H_2O phase diagram. These give temperature gradients that will be maintained by convection in the liquid mantle. As cooling occurs, the adiabatic gradient will gradually shift toward lower temperatures. Because both ends of the adiabats intersect the solidus, cooling will result in simultaneous freezing from the core upward and

the crust downward. As freezing progresses, a layer of high density ices will develop outward from the core, and at the same time the crust will thicken by crystallization of ice I.

The incremental change in volume during refreezing is

$$dV = dT_u 4\pi r_u^2(\rho_{wu}/\rho_i - 1) + dT_\ell 4\pi r_\ell^2(\rho_{w\ell}/\rho_i - 1) \qquad (8.6)$$

where r_u is the radius to the base of the upper solid layer, r_ℓ is the radius to the top of the lower solid layer, T_u and t_ℓ are the thicknesses of the upper and lower solid layers, ρ_{wu} and $\rho_{w\ell}$ are the liquid water densities at the upper and lower water/ice interfaces, and i is the polymorph developing at the top of the lower solid layer. Using the water phase diagram, this equation may be solved for dV/dT_u (Figure 8.5). It is found that dV/dT_u remains negative (i.e., the volume decreases) during all but the very final stages of the refreezing. During most of the process the contraction caused by formation of ice VI and ice V at depth more than compensates for the expansion caused by formation of ice I. Only during the simultaneous freezing of ice I and ice II does dV/dT_u become positive, causing a surface area increase of only about 0.05%. If cooling continues, the total further expansion possible from solid state phase

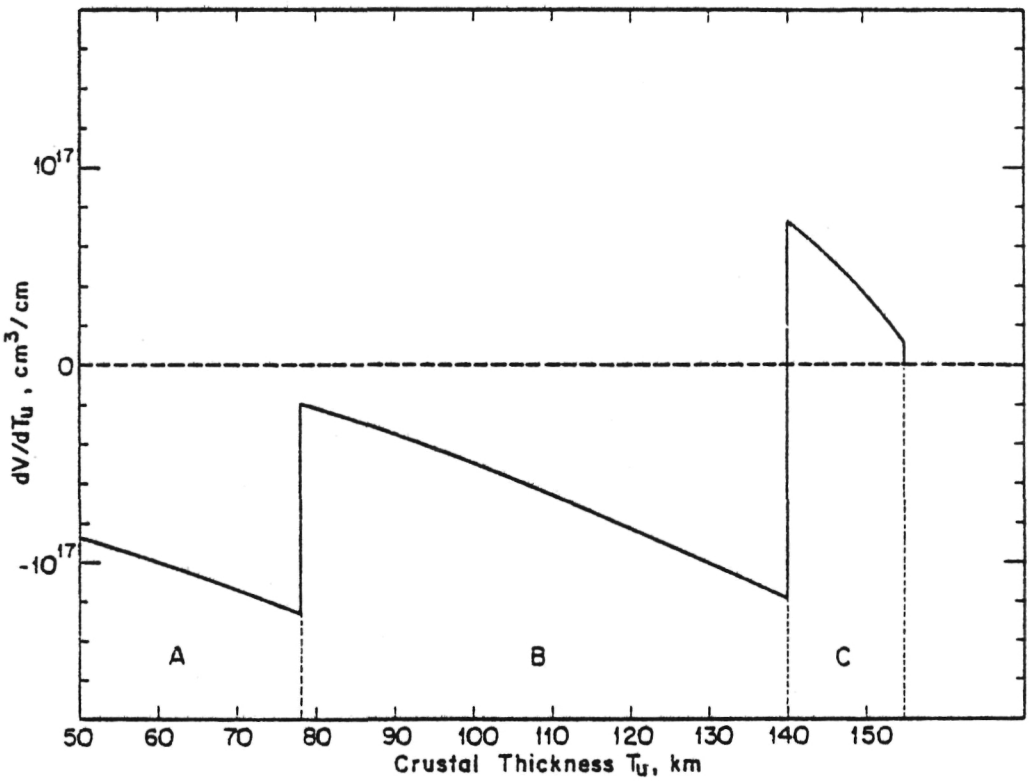


FIGURE 8.5. dV/dT_u vs. T_u during refreezing. In region A, ice VI forms at the base of the mantle while ice I forms at the top. In B, ice V and ice I form simultaneously, and in C, ice III and ice I. Calculations are for Ganymede with $\rho = 3.2$.

changes (e.g., transition of ice II to ice V) is only about 0.1%. It is probable then that the grooved terrain of Ganymede resulted from crustal extension generated during differentiation. The minor late stage expansion that would have taken place with refreezing is probably not significant, as it would be almost two orders of magnitude less than the expansion during differentiation.

8.4 Discussion

The calculations presented here do not include the effects of accretional heating. Given the uncertainties of accretion rates and impact energy partitioning, the influence that accretional heat would have is difficult to estimate. Recent work by Schubert et al. (1981) suggests that an outer layer anywhere from a few hundred km to perhaps as much as 1000 km thick would have been melted by accretion. The central portion, however, where the high density ice polymorphs are present, would not undergo accretional melting. Because it is the differentiation of this initially high density inner region that creates the increase in volume, the expansion calculated here would not be substantially affected. Accretional heat would, however, have at least one very important geologic effect: it would cause the crust to be initially very thin. An initially thin crust could perhaps delay the onset of refreezing, as a crustal thickness of

several tens of km is required for convective instability (Reynolds and Cassen, 1979). The importance of accretional heating, therefore, may have been that the crust of Ganymede was extremely thin when the expansion took place.

It is important to note that complete melting of the ice in the interior is not required for the calculated expansion to occur. All that is required is that the silicates separate from the ices to form a core. It has been suggested that rapid heat transport by solid state convection may have largely prevented radiogenic melting (Thurber et al., 1980; Schubert et al., 1981). The mobility of ice required for such convection would probably also allow considerable differentiation to occur in the solid state, however (Schubert et al., 1981). Even if no substantial radiogenic melting of the interior occurred, expansion of up to the amount shown in the net change curves of Figure 8.4 could have taken place as a result of solid state differentiation.

The surface area increase calculated here places an upper limit on the amount of "new" surface material generated in grooved terrain formation. The maximum surface area increase calculated for Ganymede is about 7.5%. The grooved terrain, where this increase is expressed, covers about 50% of Ganymede's surface. Thus the total

surface area increase involved in forming a band of grooved terrain is no more than about 15% of the area of the band. Most of the activity involved in grooved terrain formation must therefore be replacement or deformation of material already present, rather than production of new material.

Preliminary estimates of crater densities in the grooved terrain are consistent with formation during differentiation. Smith et al. (1979a) conclude that formation of grooved terrain began during the period of torrential bombardment that ended some 4.0 b.y. ago, and continued for one to a few hundred million years. This conclusion is valid for a wide range of assumed impact fluxes. The thermal models of Consolmagno and Lewis (1976) predict complete differentiation of Ganymede by 2.0 b.y. after formation, with most of the melting occurring between the time of formation and 4.0 to 3.5 b.y. ago. Keeping in mind the uncertainties in both the thermal and impact histories, these figures are in acceptable agreement with the crater densities.

Because of the small surface area change involved in refreezing a differentiated body, it is difficult to evaluate the influence that solid state convection has had from the evidence of surface area changes alone. If the zone of convection is effectively detached from the rigid upper crust, it is possible for active convection

and complete refreezing to have occurred without leaving any recognizable tectonic evidence on the surface. Comparison of crater morphologies in the grooved and cratered terrains suggests considerable thickening of the crust soon after grooved terrain development, however (Smith et al., 1979b).

An important remaining question concerns the absence of grooved terrain on Callisto. The best geologic evidence indicates that Ganymede's grooved terrain resulted from global expansion that caused widespread fracturing of the crust. It is improbable that grooved terrain formed on Callisto early in its history and has since been obliterated by impacts. Grooved terrain formation appears to enrich the crust in ice to a substantial depth, and no part of Callisto shows any evidence of such enrichment. It is inferred, then, that stress levels in Callisto's crust never became high enough to cause fracturing.

Because of their high ice content, the crusts of Ganymede and Callisto should exhibit approximately viscoelastic behavior (Chapter 9). As such, the maximum crustal stresses attained would depend strongly on the strain rate. Maximum stresses, and hence the probability of fracturing, would increase with increasing rate of global expansion. Crustal thickness might be important in governing the ease with which clean water or ice could reach the surface from below after fracturing,

but would not affect the stress levels attained during expansion. The rate of expansion during differentiation would depend on at least five factors. Four are the sources of energy that control the rate and degree of differentiation: accretional heating, radiogenic heating, gravitational energy release during core formation, and perhaps tidal heating. The fifth is the total amount of expansion possible.

Accretional heating should have been greater for Ganymede than for Callisto. First, Ganymede's gravitational potential is higher than Callisto's. This potential is given by

$$\Omega = -\int_0^{r_1} \frac{m(r)G}{r} \, 4\pi\rho(r)r^2 dr \qquad (8.7)$$

where m(r) is the mass within radius r and $\rho(r)$ is the density at radius r. For similar internal density distributions, the gravitational potential of Ganymede is about 80% larger than that of Callisto. This difference alone would lead to an 80% difference in total accretional energy input. Second, Ganymede lies deeper in Jupiter's gravitational potential well. Shoemaker and Wolfe (1981) calculate that the mean impact velocity at Ganymede is enhanced by a factor of about 25% over that at Callisto by the gravitational attraction of Jupiter. The mean energy of impacts on Ganymede is thus enhanced by more

than 50% over that for Callisto by its relative proximity to Jupiter.

Radiogenic heating is also greater for Ganymede than Callisto. At any given time the radiogenic heat production rate for each body is proportional to its silicate mass. Assuming a silicate density of 3.5 g cm^{-3}, the radiogenic heat production rate for Ganymede is about 60% larger than that for Callisto.

The greater mass of silicates in Ganymede also leads to a greater gravitational energy release during differentiation. Applying equation (8.7) to undifferentiated and fully differentiated internal structures, the energy release during core formation is about 150% higher for Ganymede than Callisto. This energy release is a fairly small fraction (roughly 10%) of the total gravitational potential of each body, however.

Cassen et al. (1980) have considered the effects of tidal heating on Ganymede and Callisto. While tidal heating has had spectacular effects on Io (Peale et al., 1979), and has perhaps been important on Europa (Cassen et al., 1979), it has probably not been a major factor for Ganymede and Callisto. For Callisto, Cassen et al. (1980) find that tidal heating would be negligible throughout its history. For Ganymede, they find that a small amount of heating is possible if its orbital eccentricity were

high early in its history, but that the lack of resonant forcing of the eccentricity would cause heating to become negligible in less than 10^8 years after formation.

Finally, the total expansion possible for Ganymede is greater than that for Callisto (Fig. 8.4). The difference is fairly small, however, about 15% of the total volume change.

The actual rate of differentiation would depend sensitively on the balance between energy input by the sources discussed above and energy loss by conduction, solid state and liquid convection, and radiation to space. Large uncertainties in the rate of satellite accretion and the rheology of high pressure ice polymorphs make precise calculation of differentiation and expansion rates impossible for the present. Note, however, that all five factors affecting expansion rates imply more rapid expansion and higher crustal stresses for Ganymede than Callisto. While no single factor may alone be responsible for the difference between the two bodies, their combined effects might have led to significantly slower and perhaps less complete differentiation for Callisto. With a sufficiently low expansion rate, stresses in Callisto's crust would never exceed the fracture strength, and all extension would take place by viscous deformation. Testing of this hypothesis will require detailed calculations

that put quantitative constraints on the relative differentiation rates and resultant crustal stresses for the two bodies.

CHAPTER 9

GROOVED TERRAIN FORMATION ON GANYMEDE

9.1 Introduction

It was shown in Chapter 2 that Ganymede's grooved terrain is probably the result of tectonic extension, and in Chapter 8 that this extension may have resulted from internal phase changes and may have taken place when the crust was very thin and underlain by a liquid water mantle. In this chapter the process of grooved terrain formation under these conditions is examined in detail.

A cursory look at Ganymede reveals two basic geologic materials: the dark cratered terrain that has undergone little other than impact cratering and crater degradation, and the brighter grooved terrain that has been geologically resurfaced. A point of critical importance to interpretation of Ganymede's geology is that there is not a one-to-one correspondence between the presence of bright, geologically resurfaced terrain and the presence of grooves. There are bands and broad regions of the brighter terrain that are quite smooth and groove-free. There are also grooves that extend for hundreds of km into the darker cratered terrain.

Again, it must be stressed that the terms "grooved terrain" and "cratered terrain" denote distinct lithologic units and are derived from the structural features that are found dominantly, but not exclusively, in the two units. There are thus two processes that must be considered in the formation of grooved terrain: one that created bands or broad regions of bright, smooth, geologically resurfaced terrain, and another that created grooves. The groove formation process worked most effectively, but certainly not exclusively, in the bright material.

9.2 The Resurfacing Process

There are a number of observations that provide evidence concerning the resurfacing process that formed the bright bands. (1) The overall geometry of the bands and their orientations with respect to adjacent shear offsets suggests tectonic extension perpendicular to the bands. (2) The lack of compressional features and the calculated maximum possible increase of Ganymede's surface area mean that the total extension involved in formation of a band of grooved terrain can be no more than $\sim$ 15% of the band width. (3) The extreme smoothness of the smooth regions at Voyager resolution, in the absence of an effective erosional process, suggests emplacement of a fairly mobile material. (4) The observation that

bright regions usually have distinct curvilinear boundaries, but that occasionally the boundaries are diffuse, suggests that emplaced material was structurally confined in most cases, but occasionally was not. (5) The higher albedo of the grooved terrain and the concentration of bright ray craters there indicate that the grooved terrain is substantially enriched in ice relative to the cratered terrain.

Taking these observations together suggests that bright bands could have formed when extension of a thin ice + silicate crust led to normal faulting and creation of a broad, downdropped rift zone. With a silicate mass fraction of more than about 15%, the crust would be slightly more dense than the liquid mantle. This density contrast would cause displaced liquid, or perhaps slush or even warm ice, to be forced upward along fault zones and flood the downdropped rift. The process is closely analogous to formation of terrestrial rift zones that are flooded with basaltic lava. The flood deposits would rapidly freeze to form bright curvilinear bands of relatively clean ice. The boundaries of the bands would be sharp as long as the flood deposits were confined within the rift zone, but would be diffuse where they overflowed onto the adjacent cratered terrain.

9.3 The Groove Formation Process

The negative relief and topographic symmetry of the grooves strongly suggests formation by extension and fracturing of a brittle near-surface layer. The grooves may have originated as either very long narrow grabens or as open extension fractures. In either case, there has been some modification of the grooves since their formation, as their present topography appears different from both fresh extension fractures and grabens. The concentration of grooves in the bright terrain indicates a response to extensional strain there that is fundamentally different from that of the cratered terrain. This is an expected result, as experimental work has shown that polycrystalline ice containing inclusions (silicate particles in the case of the cratered terrain) has a tensile strength substantially higher than that of clean polycrystalline ice (Shvaishtein, 1973; also, compare results of Haynes and Karalius (1977) with those of Hawkes and Mellor (1972)).

The low gravity and low crustal density on Ganymede favor formation of extension fractures rather than normal faults, as compressional stresses at depth are low. This may be shown by considering strain of a viscoelastic slab. The mechanical properties of ice may be approximated by those of an ideal Maxwell viscoelastic material

(Jellinek and Brill, 1956; Nevel, 1976). The stress in such a body is related to the applied strain by

$$\dot{\varepsilon} = \frac{\sigma}{\eta} + \frac{\dot{\sigma}}{E} \tag{9.1}$$

where η is viscosity and E is the elastic modulus. Taking $\sigma_{t=0} = 0$, the solution of this equation is

$$\sigma(t) = e^{\frac{-tE}{\eta}} E \int_0^t \dot{\varepsilon}(t') e^{\frac{t'E}{\eta}} dt' \tag{9.2}$$

where t' is an integration variable. Applying simple failure theory, it is possible to calculate the time and depth at which failure will occur within the slab, and whether failure will occur by extension fracture or normal faulting (Appendix C).

The parameters required for this calculation are η, E, density ρ, tensile strength σ_t, and the strain history $\dot{\varepsilon}(t)$. The viscosity of ice is given approximately by

$$\eta = \eta_o \exp\left[\beta\left(\frac{T_m}{T} - 1\right)\right] \tag{9.3}$$

where T is temperature, T_m is melting temperature, η_o is the viscosity at T_m (approximately 10^{14} poise), and the constant β is about 18 (Weertman, 1970; Reynolds and Cassen, 1979). The elastic modulus E has been experimentally determined for temperatures from 273° to 220°K

(Haynes, 1978). It has a value of about 5×10^{10} dyne cm^{-2} and shows little temperature variation in this range. Density for the calculation is taken to be that of pure ice I, 0.92 g cm^{-3}. The tensile strength of ice increases with decreasing temperature and has not been experimentally determined for very low temperatures. It is assumed here that the tensile strength at 250°K is that measured by Hawkes and Mellor (1972) (about 2.6×10^7 dyne cm^{-2}), and that it has a temperature dependence like that of the uniaxial compressive strength approximately determined to low temperatures by Parameswaran and Jones (1975). The temperature as a function of depth in the crust is thus an important unknown; a complete range of possible geothermal gradients is considered in this calculation. The other important unknown is the strain history $\dot{\varepsilon}(t)$. In order to investigate a wide variety of strain rates, a Gaussian distribution function is considered:

$$\dot{\varepsilon}(t) = \varepsilon_f \frac{h}{\sqrt{\pi}} e^{-h^2(t-m)^2} \qquad (9.4)$$

The peak of this function occurs at time m, and decreases by a factor of 1/e at times m - 1/h and m + 1/h (Fig. 9.1). The time 1/h thus characterizes the strain rate. The corresponding expression for $\varepsilon(t)$ is

$$\varepsilon(t) = \frac{\varepsilon_f}{2} \operatorname{erfc}\,[-h(t-m)] \; . \qquad (9.5)$$

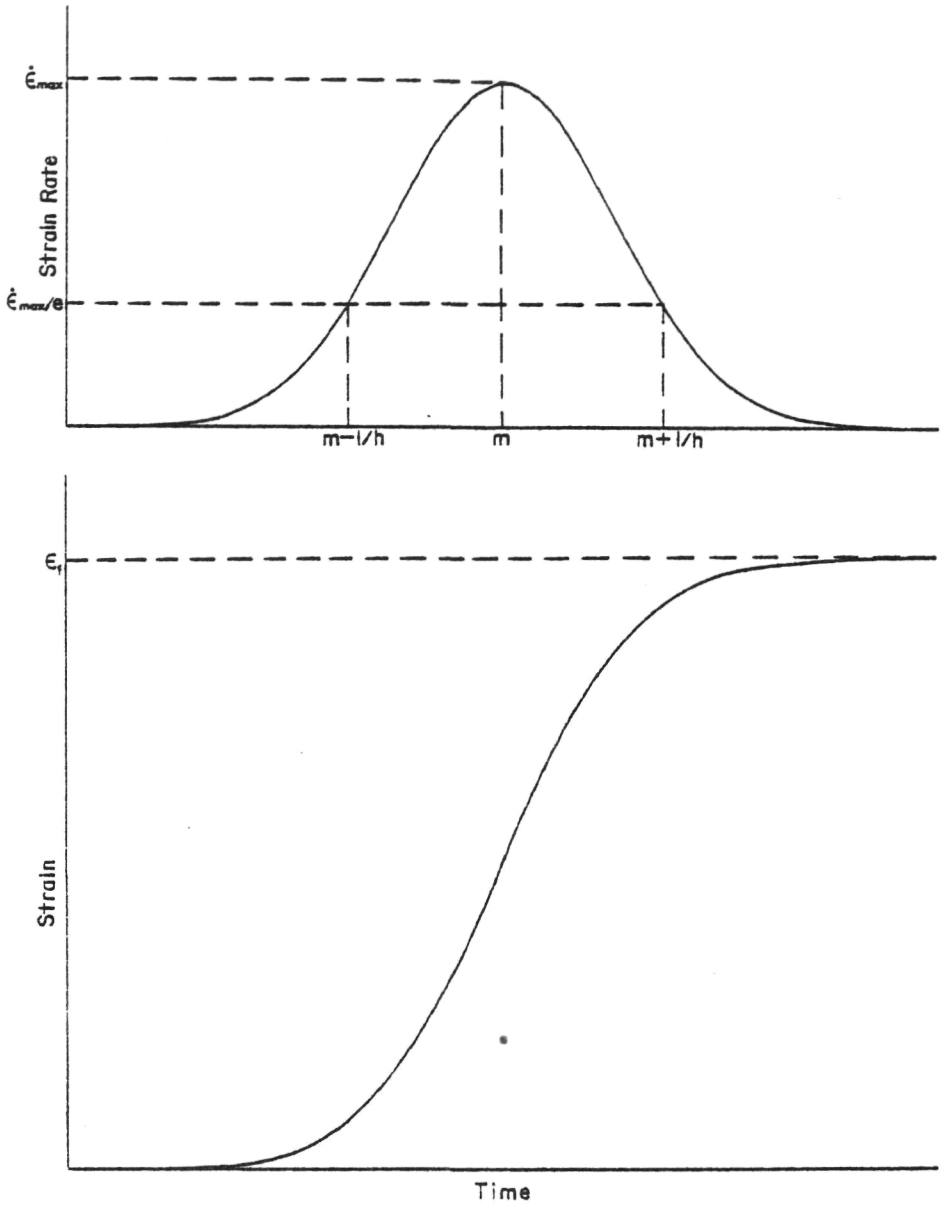


FIGURE 9.1. Strain history used in calculations.

This function has an initial value ($t = -\infty$) of zero and a final value ($t = \infty$) of ε_f. In performing the calculation, 10% was used for ε_f, while the characteristic strain time 1/h was varied over a wide range.

The results of this calculation for the full range of geothermal gradients and strain times are shown in Figure 9.2. For the entire range considered in the model, only extension fractures form. The depth of the fractures increases with decreasing geothermal gradient, and also with decreasing strain time. Decreasing geothermal gradient and decreasing strain time both increase tensional stresses at depth. Under the assumptions used, normal faulting would first become possible for a strain time 1/h of only 10^4 years at a geothermal gradient of $1°K\ km^{-1}$, and for substantially shorter times at higher geothermal gradients. There are enough uncertainties in this calculation that it cannot be considered an overwhelming argument against the grooves originating as grabens. It does show, however, that deep extension fractures may be expected to form in the ice deposits under a wide variety of conditions, while the conditions required for graben formation are much more tightly constrained.

One particularly striking feature of the grooves is their extreme parallelism and regular spacing. Although the spacing between adjacent grooves may vary

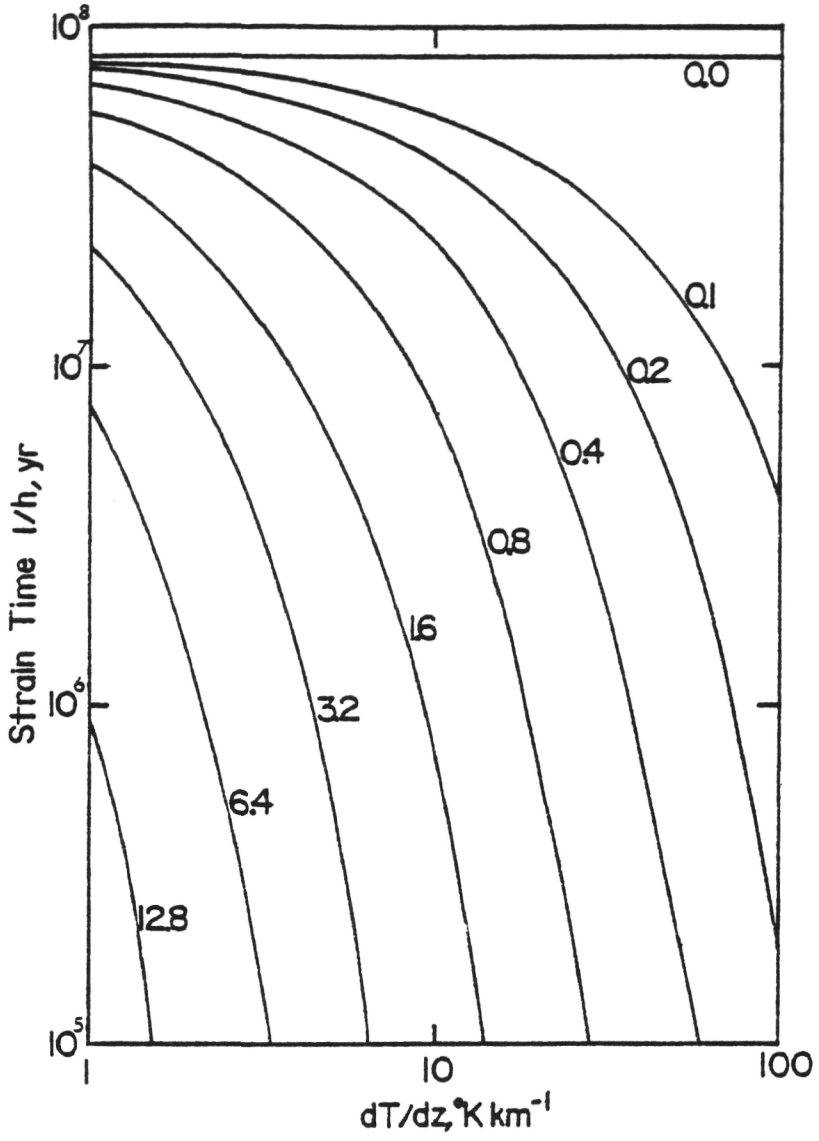


FIGURE 9.2. Results calculated for strain of a viscoelastic crust as a function of characteristic strain time 1/h and geothermal gradient dT/dz. Contours give the depth of extension fractures in km. No normal faulting occurs for the conditions considered. Calculations are for a surface temperature of 120°K.

from about 3 to 10 km, the spacing within a single set of parallel grooves is generally quite regular. If the grooves originated as extension fractures their regular geometry could perhaps be explained as a result of radiative cooling of fracture walls and rapid strengthening of the crust adjacent to a fracture. Consider again an ice slab, with some geothermal gradient, that is subjected to an extensional strain. For a given strain rate, there is a level in the crust that may be defined by a critical isotherm above which the material deforms by brittle fracture, and below which it deforms by viscous flow. Formation of an extension fracture creates vertical walls that receive negligible insolation but radiate heat, causing cooling in the vicinity of the fracture. Because the strength of ice increases substantially with decreasing temperature (Parameswaran and Jones, 1975; Haynes, 1978), cooling would result in strengthening of the area around the fracture.

Calculations have been performed that simulate thermal conduction in an ice crust and radiative cooling of fracture walls. The finite difference technique described in Chapter 6 is used for modeling thermal conduction, with terms added to expand the calculation to a two-dimensional grid. The boundary condition at the upper surface is taken to be equilibrium with insolation, while that on the vertical fracture walls is taken to be

free radiation with no solar input. Most energy radiated from the fracture walls will be retained in the fracture, with only a small fraction eventually escaping from the top. To account for this, the upper surface is assigned unit emissivity, while an effective emissivity, equal to the ratio of the open area at the top of a fracture to the total wall area, is used for the fracture walls. The width of a single fracture is the mean groove spacing (about 5 km) multiplied by the total extensional strain. The depth is that of the critical isotherm, which depends on the steepness of the geothermal gradient.

Typical results, for a geothermal gradient of 15°K km^{-1} and a total strain of 10%, are shown in Figure 9.3. Radiative cooling results in substantial cooling and strengthening of crustal material around a fracture over extremely short geologic time scales. A deep region extending several km either side of the fracture is cooled to temperatures lower than the pre-fracturing surface temperatures in less than 10^4 years. Note that the rate of growth of the strengthened zone decreases roughly exponentially, and that the extent of the region affected by the cooling is comparable to the observed spacing between grooves. Figure 9.4 shows results for two different geothermal gradients. The width of the strengthened zone is inversely related to the steepness of the geothermal gradient.

FIGURE 9.3. Calculated isotherms in an icy crust with an open extension fracture. Radiation from fracture walls results in rapid cooling of crustal material around the fracture. The critical isotherm defining the limit of brittle fracture was arbitrarily chosen to be 160°K.

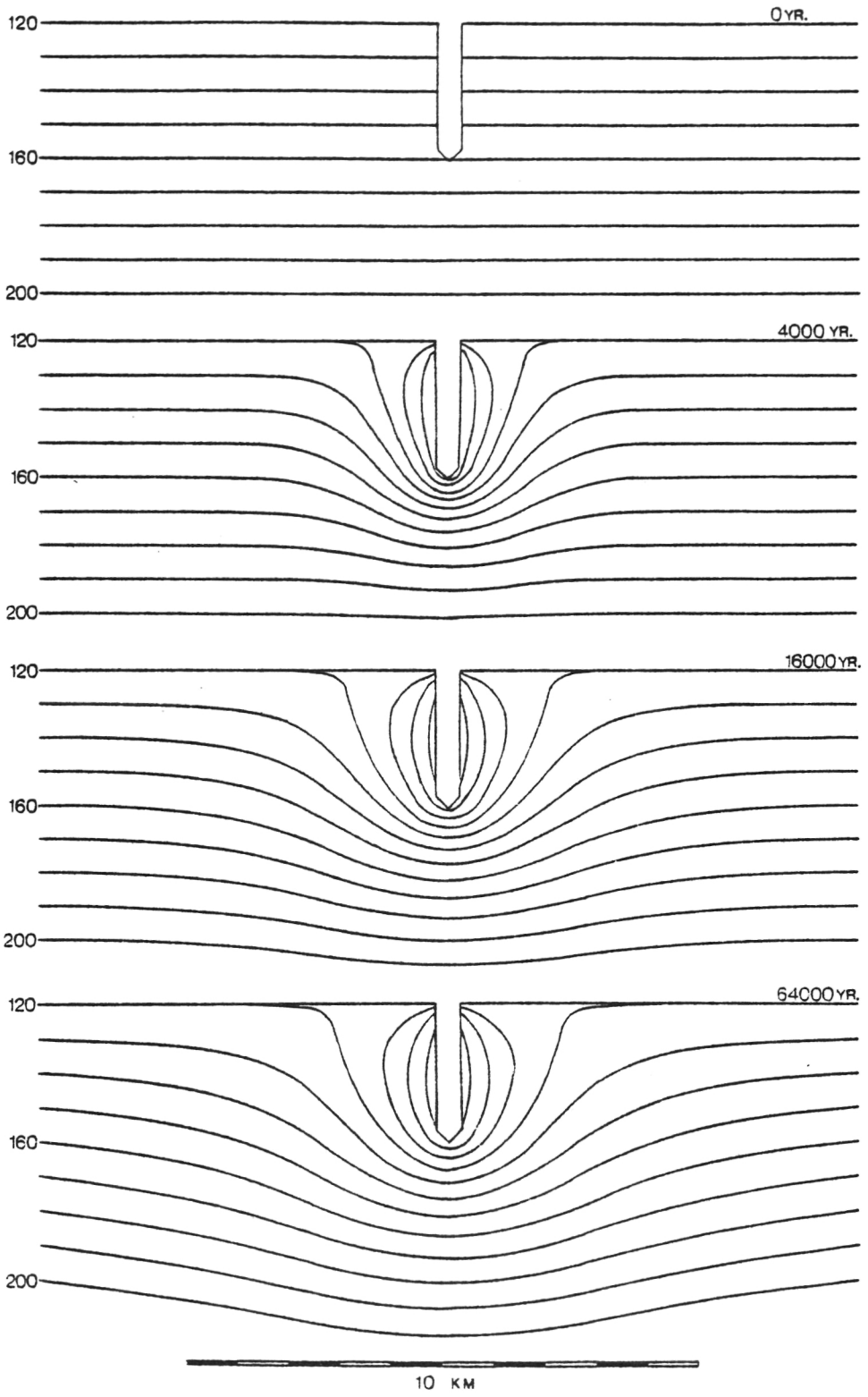


FIGURE 9.3 (continued)

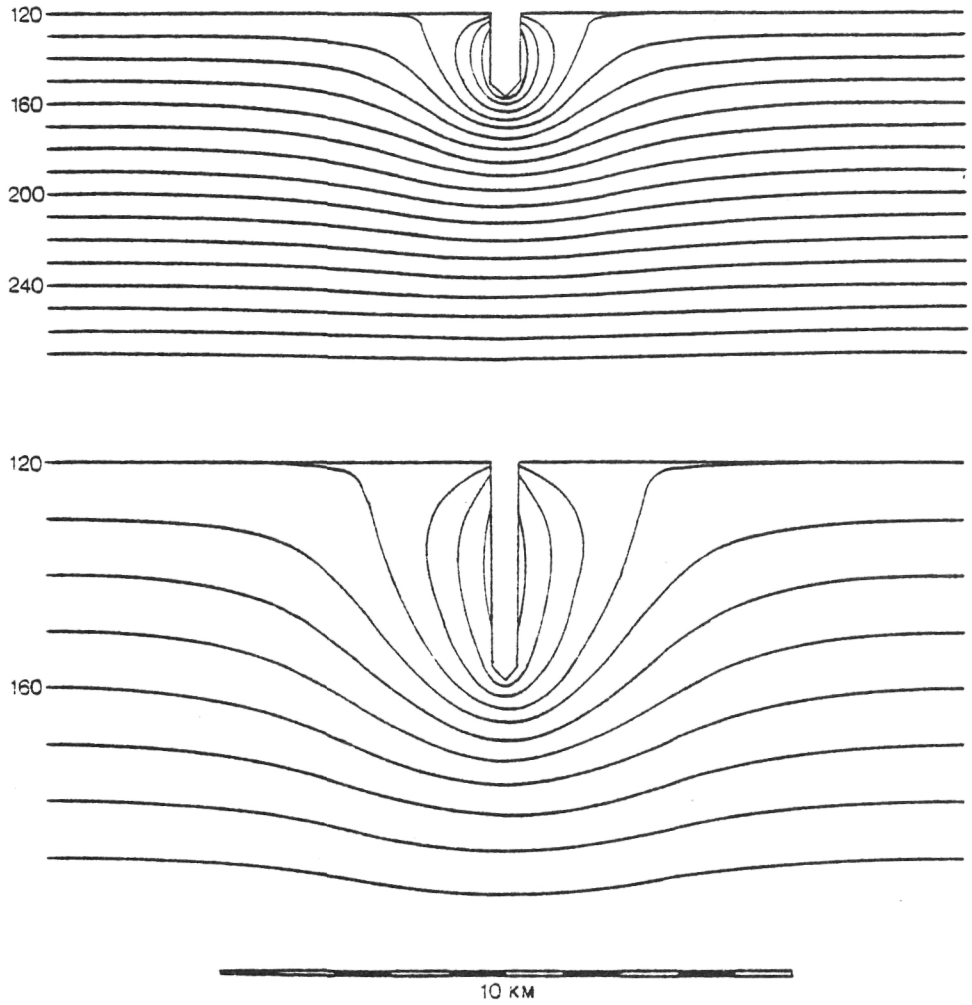


FIGURE 9.4. Calculated isotherms around a fracture after 16,000 years. Results are for an initial geothermal gradient of 25°K km^{-1} (above) and 10°K km^{-1} (below).

With rapid strengthening around a fracture, fractures caused by strain would have a regular spacing set by the width of the strengthened zone. The groove spacing in a band would reflect the geothermal gradient at the time of fracture formation, with the most closely spaced grooves forming where the gradient was steepest. Also, fractures would not form intersecting or braided patterns. A fracture propagating toward another older fracture with an oblique trend would not cross it, but would instead be deflected to a parallel adjacent trend. Because cratered terrain at the boundary of a grooved band would be relatively resistant to fracturing due to its higher tensile strength, the boundaries of a band may be important in establishing the trend of grooves in the interior of the band.

The present topography of the grooved terrain in the areas sampled in Chapter 7 does not closely resemble either extension fractures or grabens. Some modification is necessary to give either primary tectonic landform the present appearance of the grooved terrain. One process that may have been important is viscous relaxation of topography. The influence this process would have had depends strongly on the effective viscosity of the crust, a parameter that is not well known. The viscosity may be estimated from the observed degree of relaxation of impact craters. Parmentier et al. (1980) have estimated

a value of 10^{23} poise from the observed relaxation of palimpsests in the cratered terrain. This value may be too low for application to the grooved terrain, however, as the longer wavelength topography of the palimpsests would cause them to be affected by deeper, lower viscosity levels in the crust. For this reason, viscosities ranging from 10^{23} to 10^{25} poise are considered here.

To investigate the effects of viscous relaxation, experiments were conducted using models constructed of a high viscosity polymer. The substance used was polyisobutylene, a high molecular weight, straight-chain hydrocarbon polymer with a viscosity at 25°C of 7×10^5 poise. Experiments were conducted by constructing a plaster mold of the initial topography and impressing it in the surface of the polymer. A fine powder was spread over the model to improve its photographic properties and to prevent the mold from sticking to the surface of the polyisobutylene. Changes in the topography were then recorded as it evolved over a period of several hours.

A conversion from model time to true time on Ganymede may be made using the scaling relationship

$$\frac{t_m}{t_G} = \frac{\eta_m \ell_G g_G \rho_G}{\eta_G \ell_m g_m \rho_n} \qquad (9.6)$$

where ℓ is a characteristic length (for example, groove spacing), and the subscripts m and G denote model and

and Ganymede, respectively. In the experiments the spacing between initial groove forms was typically 10 cm. The depth of the viscous layer was large compared to the amplitude of the topography.

Results for viscous relaxation of extension fractures spaced 5 km apart and expressing 10% strain are shown in Fig. 9.5. The degree of relaxation is strongly dependent on the crustal viscosity. At no point during the relaxation, however, does the topography resemble that of the present grooved terrain. If given sufficient time, the fractures simply close shut without substantially affecting the surrounding topography. Relaxation of grabens does not come any closer to producing the topography calculated for the grooved terrain. Results for grabens, again spaced 5 km apart and expressing 10% strain, are shown in Figure 9.6. With enough time, graben floors warp upward and horsts warp downward, again producing topography quite different from that calculated for the grooved terrain. These results are for constant viscosity, but will be qualitatively similar for viscosity that decreases with depth (Parmentier and Head, 1981). Regardless of the original nature of the grooves, relaxation in a thick, viscous layer alone cannot account for modification to the topography calculated in Chapter 7.

Several billion years of mass-wasting might be capable of producing topography similar in form to that observed. Mass-wasting would reduce vertical walls to

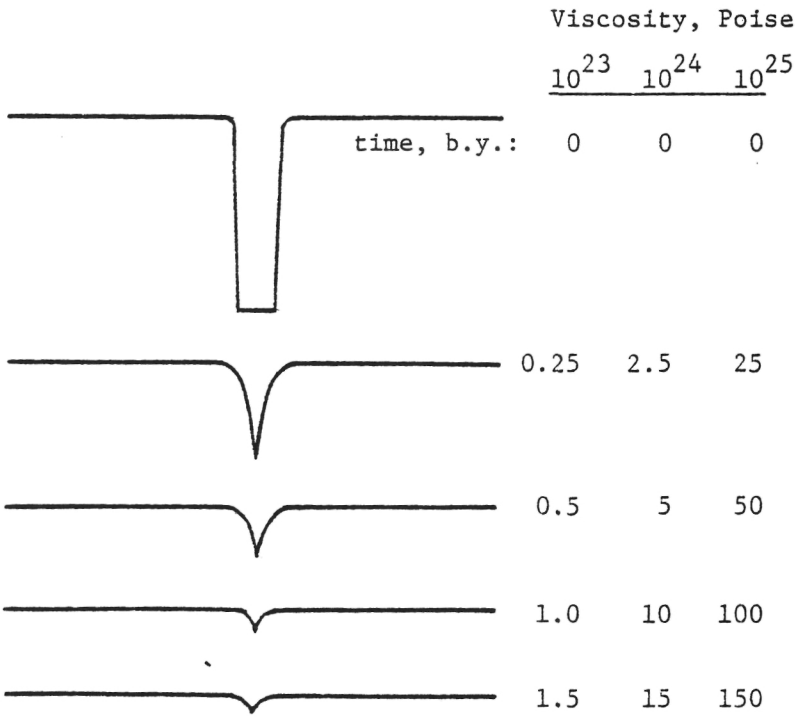


FIGURE 9.5. Experimental viscous relaxation of extension fractures. Photographs show initial and final configurations of the model.

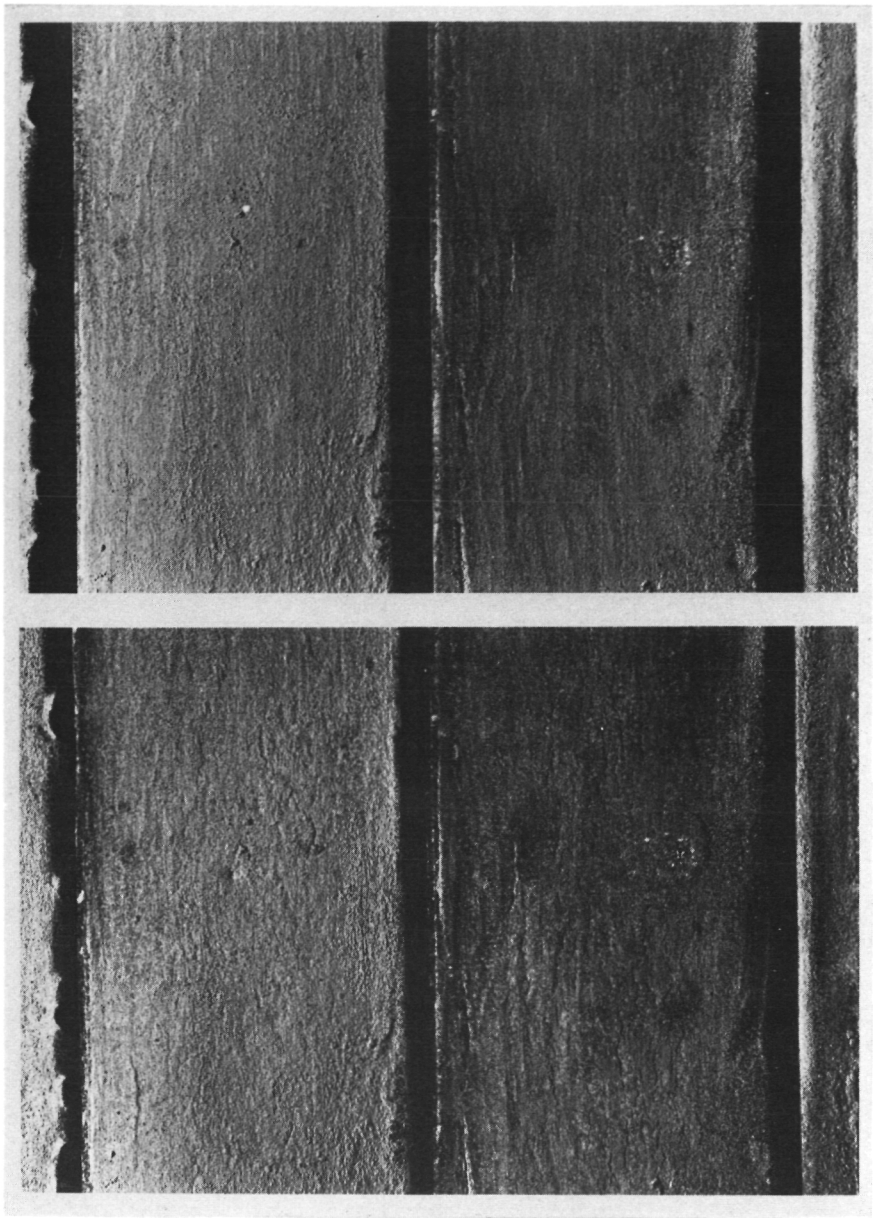


FIGURE 9.5 (continued)

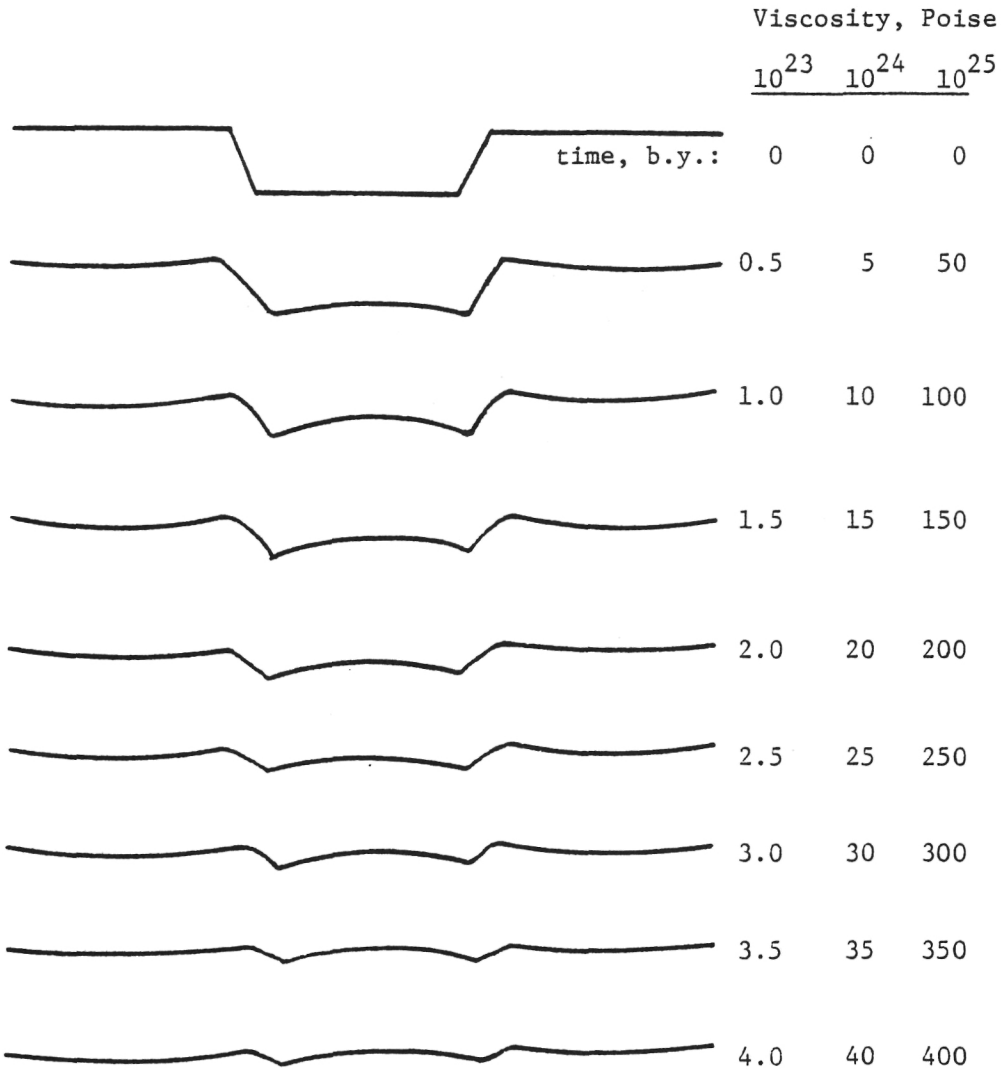


FIGURE 9.6. Experimental viscous relaxation of grabens.



FIGURE 9.6 (continued)

angle of repose, filling in and widening the original grooves (Fig. 9.7). As on other bodies without atmospheres, impacts would be a major contributor to breakup of wall material. Thermally-induced volume changes could also be important, as the volume expansion coefficient of ice is large, about 100 times that of silicates. The final topography resulting from mass-wasting of either extension fractures or grabens would be similar in form to that observed but somewhat steeper. Limited viscous relaxation, working simultaneously with mass-wasting, would be required to produce the gentle slopes observed. The images presently available are not of sufficient resolution to identify mass-wasting deposits in the grooves, however, so it is not possible now to quantitatively evaluate the influence of this process.

9.4. Discussion

Several important inferences may be drawn from geologic relationships in the grooved terrain. A particularly interesting situation is shown in Figure 9.8. Here a band of grooved terrain appears to have been downdropped at one end and partially reflooded, with the younger flood deposits lapped up against the older tilted grooved block. This is the only geologic relationship that has been observed that provides evidence regarding the question of flooding in a single event vs. many flooding events. It suggests that the downdropping and

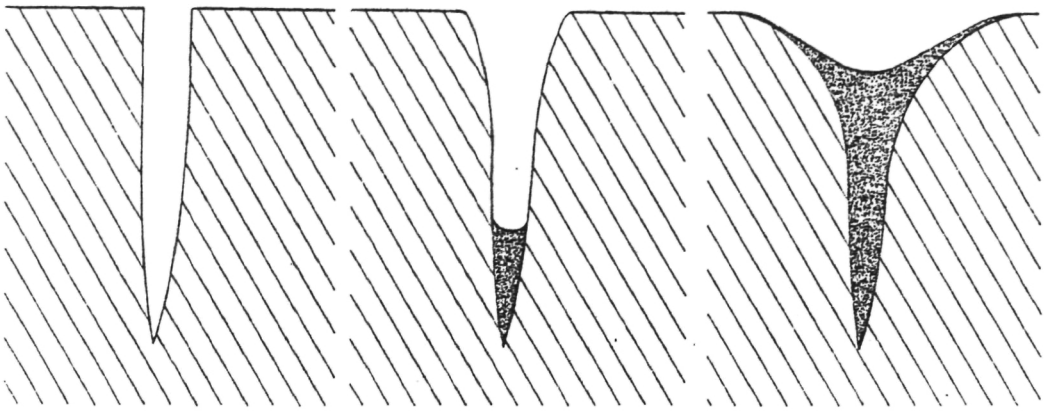


FIGURE 9.7. Schematic representation of filling of an extension fracture by mass-wasting. The final topography resulting from mass-wasting in a graben should be qualitatively similar.

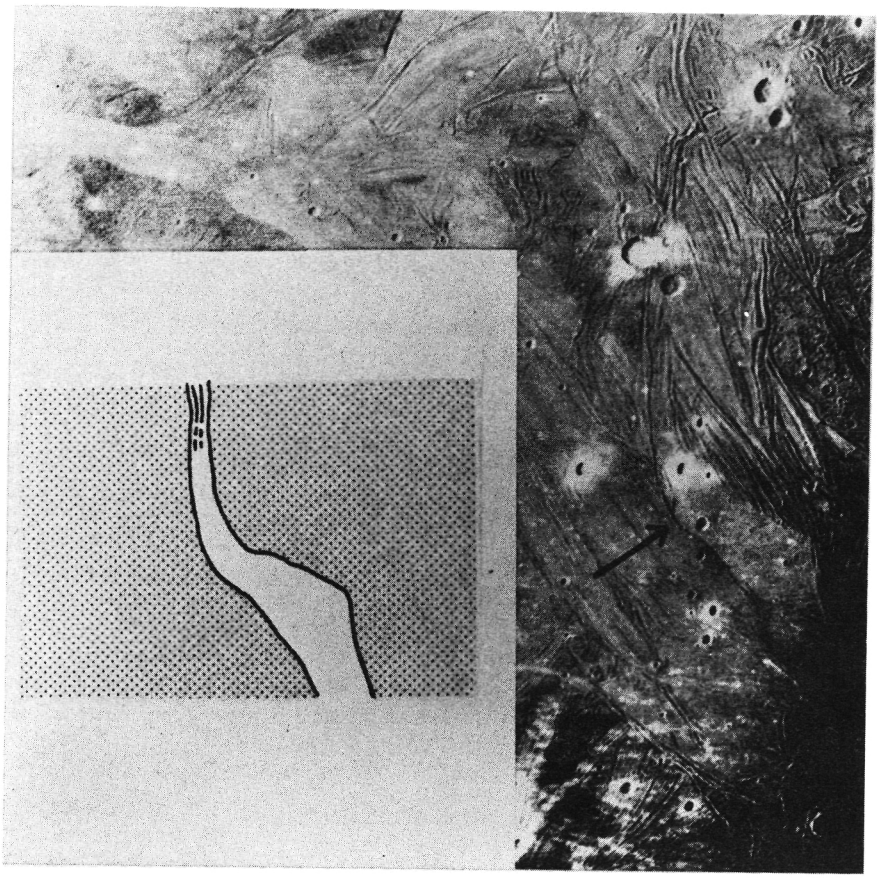


FIGURE 9.8. A band of terrain that appears to have been grooved, and then, with renewed activity on the bounding faults, downdropped at one end and partially reflooded (scale across image = 1360 km; image centered at ∿ -5° lat., 315° long.; image 891J1+000).

flooding of bright bands may take place in a number of episodes.

There is no consistent relationship observed between the time of formation of grooved bands and the time of formation of smooth bands. There are many instances of grooved bands crosscutting smooth bands and of smooth bands crosscutting grooved bands. The variety of cross-cutting relationships observed shows that there was not a global period of flooding followed by a period of groove formation, but that both processes took place intermittently and concurrently. This observation supports the idea that both processes result from the same extensional tectonic regime.

It is impossible now to confidently rule out either extension fractures or grabens as the original grooves. Available topographic information is insufficient for making this choice. Simple theoretical arguments, particularly those concerning the effects of low lithostatic stresses on Ganymede, tentatively favor extension fractures. It should be stressed again that useful photoclinometric calculation of topography is restricted to a limited region of high resolution, and that grooves in other areas appear qualitatively to show significant variations in morphology. It is possible then that both extension fractures and grabens are present in the grooved terrain.

A schematic cross section summarizing a possible formation sequence for a band of grooved terrain is shown in Figure 9.9. The process may begin with formation and flooding of a broad downdropped rift zone. With continued extension, grooves, either open fractures or grabens, form in the weaker clean ice deposits. Finally, several billion years of degradation, perhaps a combination of viscous relaxation and mass-wasting, reduce the steep walls of the grooves to the gentle topography presently observed at Voyager resolution.

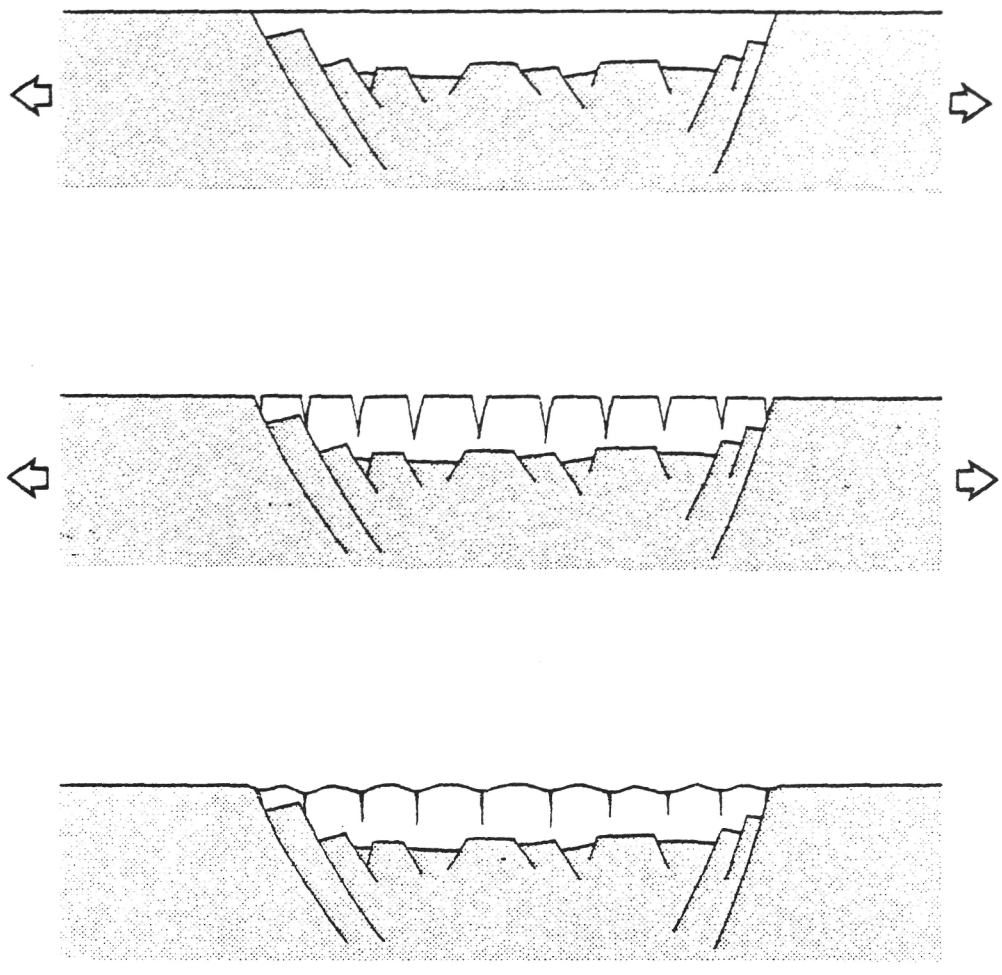


FIGURE 9.9. Schematic summary of the processes that may lead to creation of grooved terrain.

CHAPTER 10

DOME FORMATION ON GANYMEDE

10.1 Introduction

One of the most unusual landforms observed in the Voyager 1 images of Ganymede is the dome shown in Figure 10.1. It lies in a broad region of grooved terrain, and has a diameter of 260 km. Its topography is roughly concentric and gently undulating, except for a smooth central region about 60 km across. Photoclinometric profiles presented in Chapter 7 indicate a summit elevation of about 2-2.5 km (Fig. 7.11).

The dome is surrounded by a dense field of small pits or craters (Fig. 10.2). The diameters of these pits do not generally exceed 5 km. The maximum extent of the field is about 300 km from the center of the dome. The field is not radially symmetric, showing concentrations northeast and southwest of the dome. The field resembles, in form and extent, secondary crater fields associated with impact craters roughly 75 km in diameter elsewhere on Ganymede (Fig. 10.3). The double-lobed shape is probably the result of an oblique impact (Gault and Wedekind, 1978).

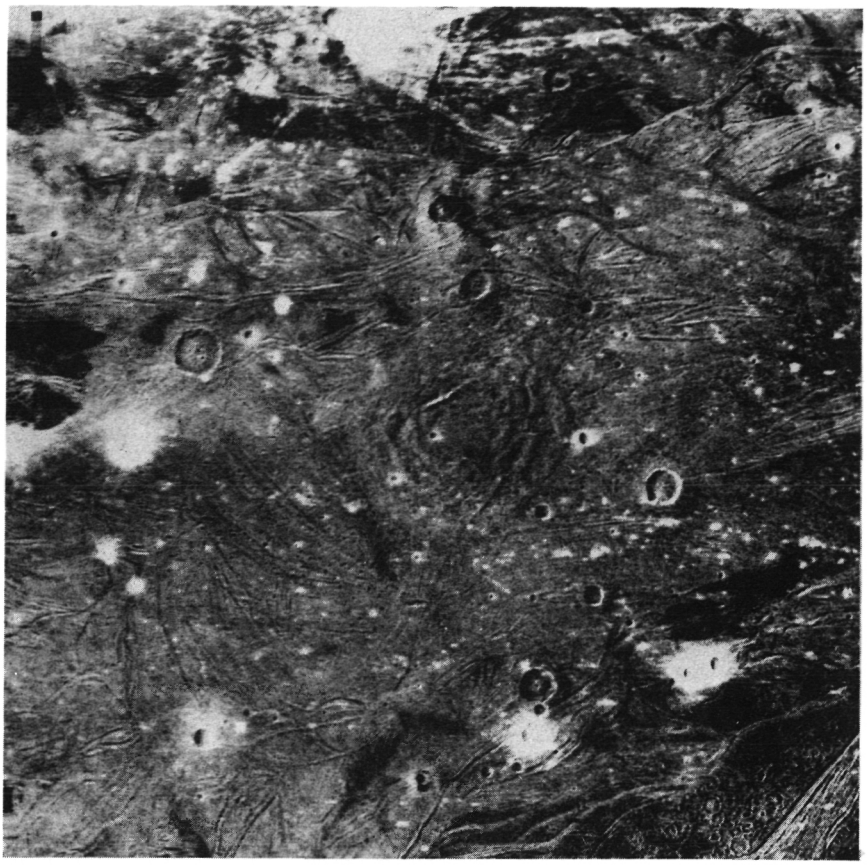


FIGURE 10.1. The dome in Voyager image 967J1+000. It lies in grooved terrain and has a diameter of about 260 km (scale across image = 1020 km; image centered at ∿ 35° lat., 330° long.).

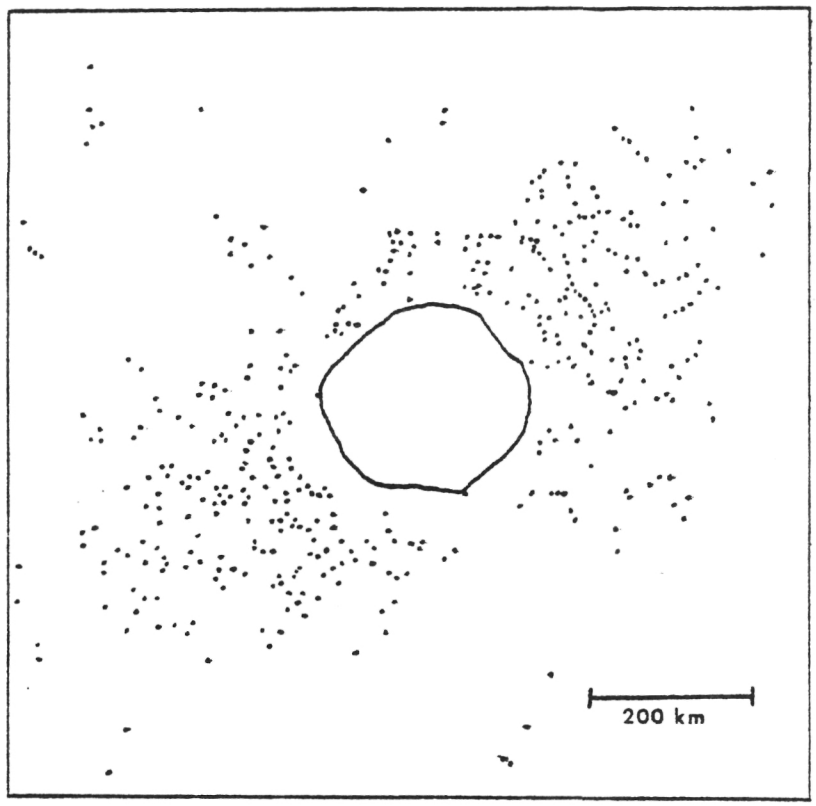


FIGURE 10.2. Distribution of small (≤ 5 km) craters around the dome in Figure 10.1. The maximum extent of the crater field is ∿ 300 km from the center of the dome.

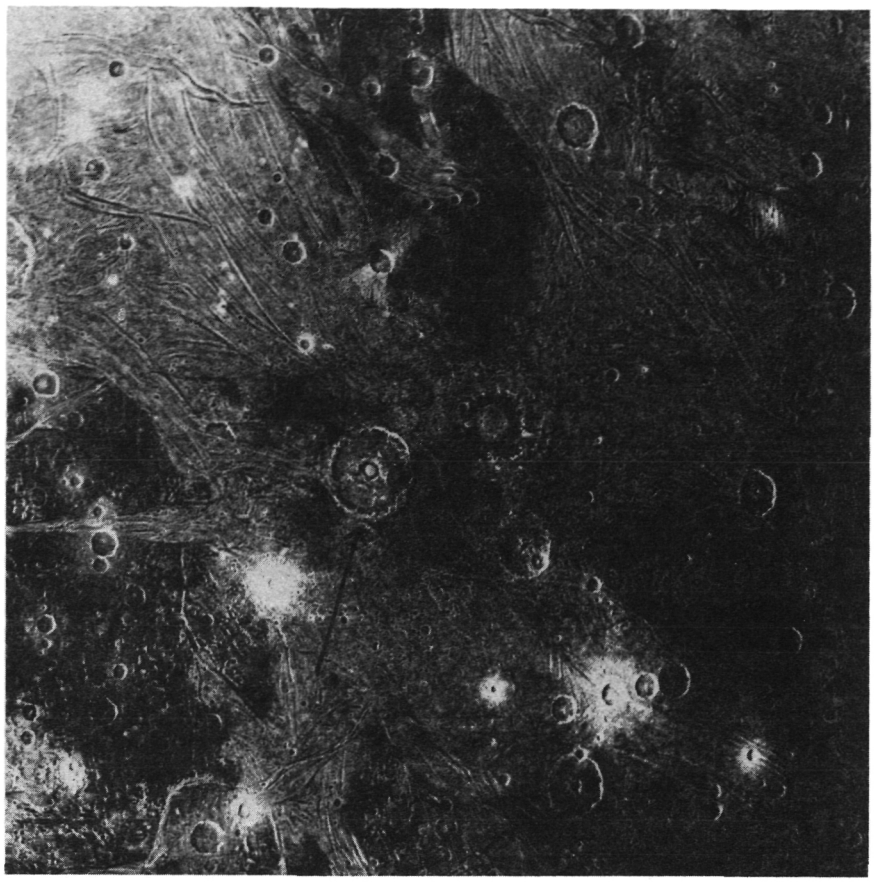


FIGURE 10.3. An impact crater in the grooved terrain with a secondary field that extends about 300 km from the point of impact. The diameter of the crater is about 75 km. The extent of the secondary field is the same as that of the crater field surrounding the dome in Figure 10.1. Note, however, that the diameter of the dome in Figure 10.1 substantially exceeds the diameter of this crater (scale across image = 850 km; image centered at -15° lat., 135° long.; image 476J2-001).

A similar dome is observed at much lower resolution in Voyager 2 images (Fig. 10.4). Its diameter is comparable to that of the Voyager 1 dome. One important morphologic difference between the two features is that the smooth central region of the Voyager 2 dome appears to be a roughly circular "plug" that is distinctly raised above the rest of the feature. The resolution for this dome is too low to determine if it has a secondary field.

The raised topography of these features and the association of at least one with a field of small craters suggest that their formation involved upward movement of material resulting from a relatively large impact event. There are at least two possible ways to produce these features, both of which involve a thin ice + silicate crust underlain by liquid water. One is ice vulcanism triggered by an impact, and the other is isostatic upwarping of an impact crater formed in a thin crust.

10.2 Ice Vulcanism

During and immediately following differentiation, Ganymede's crust may have been quite thin and underlain by a liquid water mantle. For a short period preceding refreezing of the mantle, the silicate component of the crust may have resulted in a bulk crustal density that exceeded that of the underlying water. This would have been the case if the silicate mass fraction in the crust

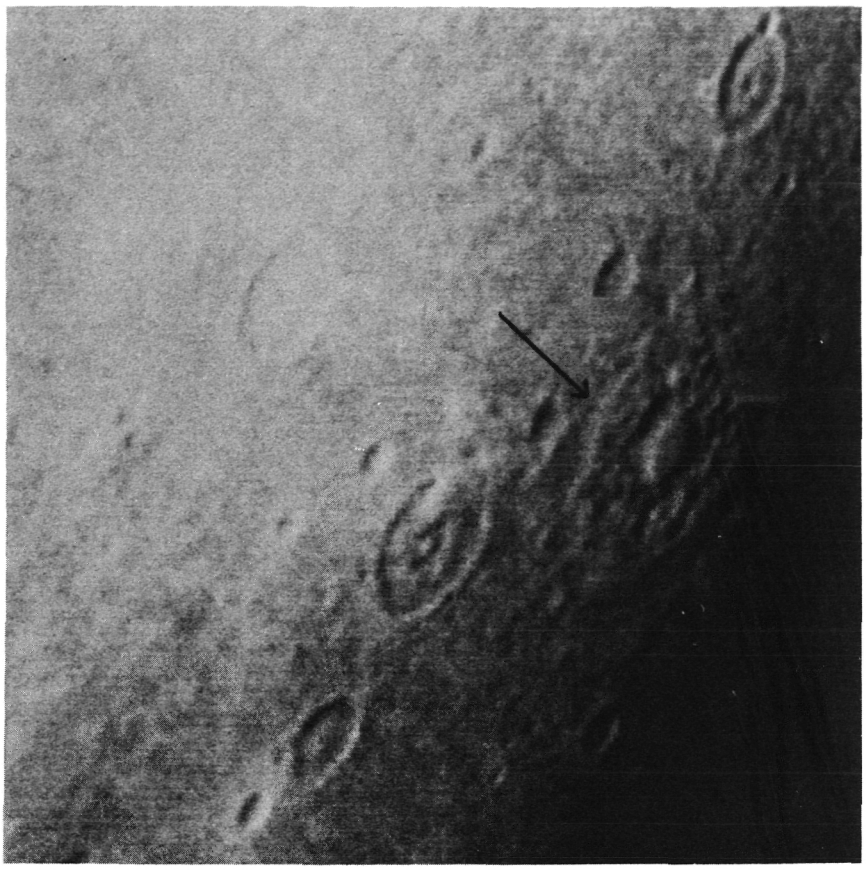


FIGURE 10.4. The dome in Voyager image 124J2-001. Note the central plug that rises above the rest of the feature. Higher resolution images are not available because the dome had rotated past the terminator by the time of the near encounter imaging sequences (scale across image = 670 km; image centered at ∿ 10° lat., 100° long.).

exceeded about 15%. Consider a column of liquid water moving upward through a conduit in this ice + silicate crust. The motion would be driven by the density contrast between the crust and the mantle. Two freezing processes would operate in the water column. First, freezing would occur as a result of the pressure drop along the conduit. For adiabatic decompression

$$\frac{dx_\ell}{dT} = -\frac{C_p}{H_f}\left(1 - \frac{\alpha\sigma T}{\rho C_p}\right) \qquad (10.1)$$

where x_ℓ is the liquid mass fraction in the conduit, H_f is the heat of fusion, C_p is the specific heat, ρ is the density, α is the coefficient of thermal expansion, and σ is dp/dT of the solidus (Parmentier and Head, 1980). The maximum possible thickness of an ice I + silicate crust on Ganymede is about 150 km. Decompression of water from this depth would only cause about 10% crystallization. A thinner crust would reduce this figure. Crystals formed by decompression would be uniformly distributed through the fluid. Because of the low concentration of cyrstals, however, their presence would not significantly affect the dynamics of the flow.

Freezing would also occur as a result of loss of heat to the conduit walls. This freezing would have an important effect on the flow, as crystallization would occur on the walls of the conduit, eventually choking it and halting

the eruption. Using a simple numerical model, it is possible to calculate this heat loss, and thus the duration and total volume of such an eruption.

The model assumes a conduit with height h and radius R (Fig. 10.5). The densities of the crust and the liquid water are ρ_c and ρ_w respectively. Fully turbulent, high Reynolds number flow is assumed. The total pressure drop along the conduit is $\rho_c gh$, which is equal to the sum of the hydrostatic pressure drop in the fluid column and the frictional pressure drop resulting from the turbulent flow:

$$\rho_c gh = \rho_w gh + \frac{\lambda \rho_w u^2 h}{4R} \qquad (10.2)$$

where u is the mean flow velocity and λ is a friction factor related to the roughness of the conduit walls (Prandtl, 1957). The value of λ is given by the empirical formula

$$1/\lambda = 2.0 \log_{10} q + 1.7 \qquad (10.3)$$

where q is defined as the ratio of the size of projections on the conduit walls to the conduit radius (Prandtl, 1957).

If R varies as a function of the depth z, the frictional pressure drop must be expressed as

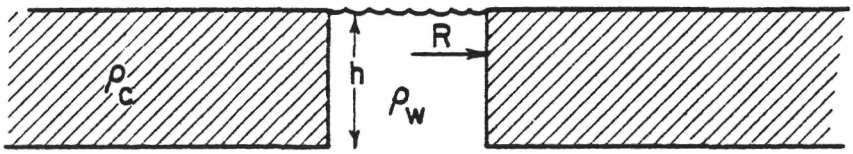


FIGURE 10.5. Configuration of the cylindrical conduit used in the model. Water will rise through the conduit if $\rho_c > \rho_w$.

$$(\rho_c - \rho_w)gh = \int_0^h \frac{\lambda\rho_w \left(u_o \frac{R_o^2}{R^2}\right) dz}{4R} \qquad (10.4)$$

where u_o and R_o are the flow velocity and radius at the surface. Thus the rate of eruption $\dot{V}$ is given by

$$\dot{V} = u_o \pi R_o^2 = \pi \left[\frac{4(\rho_c - \rho_w)gh}{\lambda\rho_w \int_0^h \frac{dz}{[R(z)]^5}} \right]^{\frac{1}{2}} . \qquad (10.5)$$

The decrease of R that occurs as a result of freezing may be readily calculated from the heat loss by conduction to the conduit walls. In time dt, a disc of water in the conduit with unit thickness will lose heat dQ. This heat loss is given by

$$dQ = 2\pi RK \left(\frac{\partial T}{\partial x}\right)_{x = 0} dt \qquad (10.6)$$

where K is the thermal conductivity of the wall material and x is the distance measured outward from the wall surface. The mass of ice formed in time dt is dQ/H_f, so that

$$\pi(R + dR)^2 = \pi R^2 - \frac{2\pi KR\left(\frac{\partial T}{\partial x}\right)_{x = 0} dt}{H_f \rho_i} \qquad (10.7)$$

where ρ_i is the density of the newly formed ice.

A numerical solution of the two-dimensional heat conduction equation is performed to find $(\partial T/\partial x)_{x=0}$ along the conduit. The calculation technique is similar to that described in Chapter 9. The thermal properties of the wall are assumed to be those of ice I. The initial temperature gradient in the crust is assumed to be linear, from temperature T_o at the surface to the ice I solidus temperature at the base of the crust. With R(z,t) obtained from equation (10.7) and $\dot{V}(t)$ obtained from equation (10.4), the model solves for the total volume and total time of the eruption. Results were also obtained for eruption through a linear fissure, which involves similar relationships.

The model results are strongly dependent on conduit size, and very weakly dependent on other parameters. Calculations were performed for a crustal thickness h of 20 km, crustal density ρ_c of 1.25 g cm^{-3}, surface temperature T of 100°K, and conduit wall roughness factor q of 0.2. The variation of total eruption volume V and eruption time t with initial conduit radius R_i for this set of parameters is found to be

$$V \simeq 3 \times 10^{-3} R_i^{4.5} \qquad (10.8)$$

and

$$t \simeq 360 R_i^2 \qquad (10.9)$$

where R_i is in m, V in km^3, and t in hr. Reasonable variation of ρ_c, T_o, and q does not affect these results by more than a factor of 2 or 3 (Fig. 10.6).

For a linear fissure eruption,

$$V_f \simeq 2 \times 10^{-1} W_i^{3.5} \qquad (10.10)$$

and

$$t \simeq 90\ W_i^2 \qquad (10.11)$$

where W_i is initial fissure width in m and V_f is volume erupted per unit of fissure length in km^2 (i.e., in $km^3\ km^{-1}$).

Using the central elevation of 2.0-2.5 km calculated in Chapter 7, the volume of the Voyager 1 dome is roughly 5×10^4 km^3. For a single cylindrical conduit, this volume corresponds to a conduit radius of only $\sim$ 40 m and an eruption time of $\sim$ 60 years. Such a conduit seems inconsistent with formation by a major impact. An impact capable of forming a 300 km secondary field and penetrating completely through the crust would create a hole in the crust very much larger than 80 m. The volume of water that could reach the surface through such a hole would far exceed the volume of the dome. In fact, the erupted volume given by equation (10.8) for a single hole in the crust 2 km in diameter exceeds the total volume of H_2O in Ganymede. Creation of such a hole would probably cause foundering of large portions of Ganymede's crust. Thus, the domes apparently cannot result

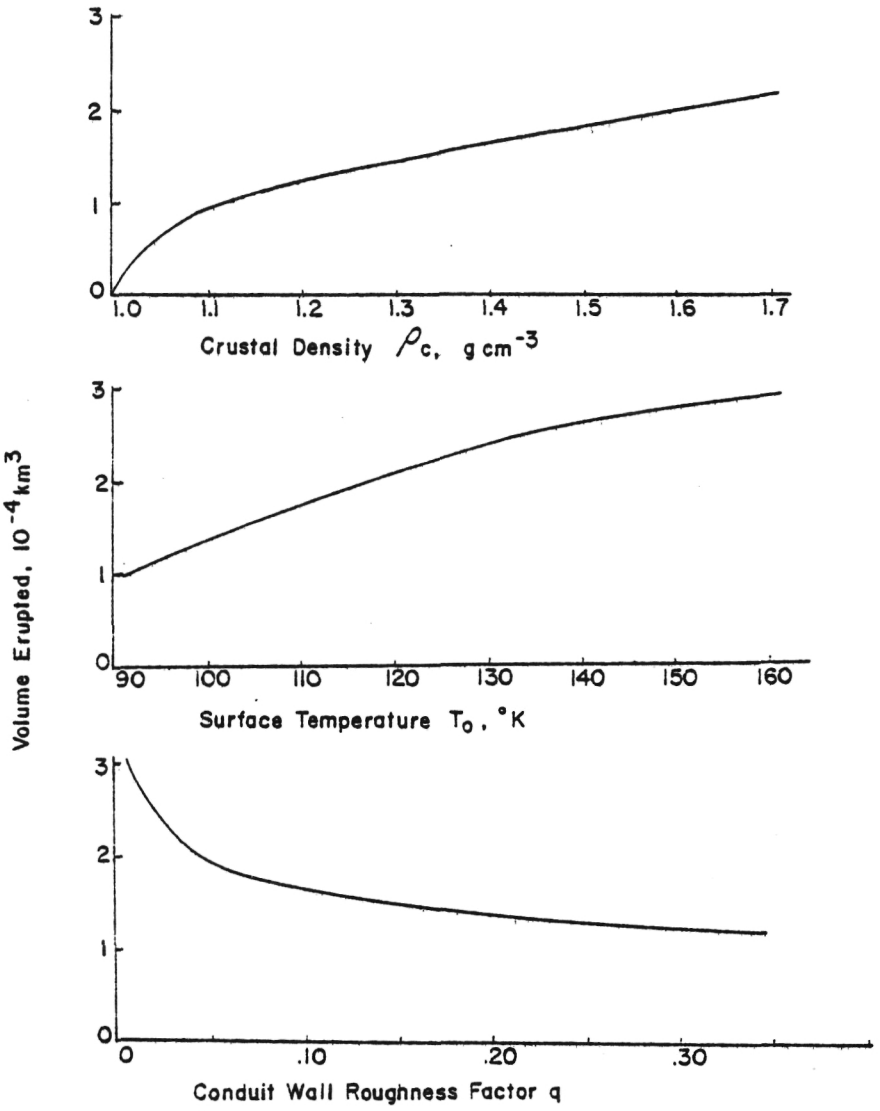


FIGURE 10.6. Effect of variations in model parameters on results. Individual parameters are varied independently, keeping others constant. Results are calculated for a conduit radius of 50 cm and a crustal thickness of 20 km in all cases. Variation of crustal thickness does not affect the results.

from complete penetration of the crust by an impacting body.

The model results are consistent, however, with eruption through fractures created by the impact. A major impact in an icy crust a few tens of km thick, while not completely excavating through the crust, could create fractures that propagate to the mantle. Liquid water would then reach the surface through this network of fractures, with water pressure from the crustal overburden maintaining the flow. Making the simplifying assumption that all fractures in the network have the same width, Figure 10.7 gives the cumulative fracture length required for formation of the dome as a function of the fracture width. The time required for such an eruption would range from several months for 5 m fractures to only a few hours for fractures tens of cm wide. If the domes are indeed ice volcanoes, eruption through an impact-created fracture network seems to be the most probable formation mechanism.

10.3 Isostatic Upwarping

Consider an impact crater of depth D formed in an ice + silicate crust (Fig. 10.8). The removal of crustal material by the impact will lead to isostatic upwarping of the crater floor if the crustal material is mobile enough for the deformation to take place. If $\rho_c > \rho_w$, and if sufficient mobility exists, the upwarping will cause the

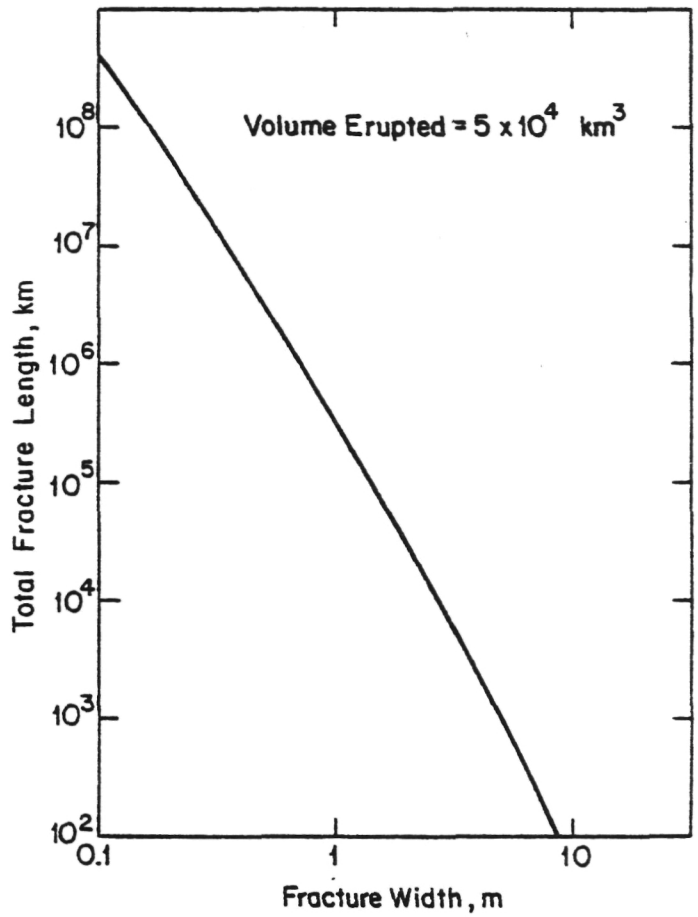


FIGURE 10.7. Cumulative fracture length required to form the Voyager 1 dome by fissure eruptions. Total fracture length required is given as a function of fracture width.

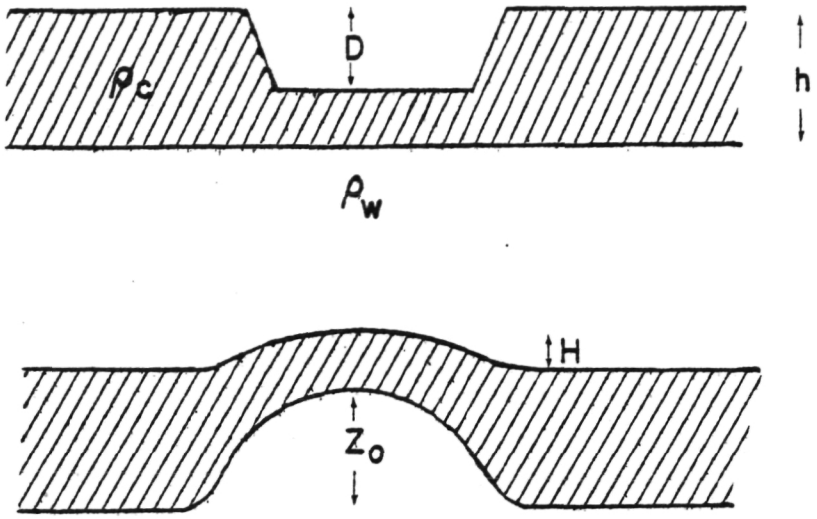


FIGURE 10.8. Isostatic upwarping of a crater formed in a thin crust. Height H will be positive if $\rho_c > \rho_w$.

crater floor to be forced above the level of the surrounding terrain. The maximum height to which it could rise is

$$H = D(\rho_c/\rho_w - 1) \quad . \tag{10.12}$$

At any point during the upwarping, the net upward force on a centered, disc-shaped segment of the crater floor with radius r is

$$F = 2\pi \int_0^r g[\rho_c D - \rho_w Z(x)]x\,dx \tag{10.13}$$

where x is distance measured outward from the crater center, and Z(x) is the vertical displacement of the crust. Because the crustal thickness beneath the crater is (h - D), the shear stress at the edge of the disc-shaped segment is

$$\tau = \frac{2\pi \int_0^r g[\rho_c D - \rho_w Z(x)]x\,dx}{2\pi r(h - D)} \quad . \tag{10.14}$$

Assuming viscous behavior of the crust,

$$\tau = \eta \frac{d}{dr}\left(\frac{dz}{dt}\right) \tag{10.15}$$

where η is the effective viscosity. Substituting in equation (10.14) and integrating, the upward velocity at the center of the upwarp is

$$\frac{dZ_o}{dt} = \frac{gR^2(\rho_c D - \rho_w z_o)}{4\eta(h - D)} \quad . \qquad (10.16)$$

Integrating equation (10.16) gives the time required for a given amount of vertical movement, Z_o:

$$t = \frac{4\eta(h - D)}{gR^2\rho_w} \ln\left(\frac{1}{1 - \frac{\rho_w Z_o}{\rho_c D}}\right) \quad . \qquad (10.17)$$

The maximum amount of upwarp possible is $D(\rho_c/\rho_w)$. Note that as Z_o approaches this maximum, $t \to \infty$.

Equation (10.17) may be used to estimate the time required for upwarping to occur. The critical parameter in this expression is the effective viscosity. Following Reynolds and Cassen (1979), the expression of Weertman (1970) is adopted:

$$\eta = \eta_o \exp\left[\beta \frac{T_m}{T} - 1\right] \qquad (9.3)$$

where T_m is the melting temperature and η_o is effective viscosity at T_m. A value of 10^{14} poise is adopted for η_o, and a value of 18 for the constant β (Reynolds and Cassen, 1979).

Consider an impact crater with a diameter of 100 km and an initial depth of 10 km, formed in a 20 km crust with a density of 1.25 g cm^{-3}. The maximum amount of upwarping that could occur would be 12.5 km, placing the summit of the dome

2.5 km above the surrounding plains. The linear relationship between upwarping time and viscosity results in a very strong dependence of upwarping time on crustal temperature. As an example, the time required to form a dome that rises 2 km above its surroundings is shown as a function of the effective crustal temperature in Figure 10.9. For an effective temperature of 240°K the upwarp time is about a week, while for 100°K it substantially exceeds the age of the solar system. The actual effective temperature will of course depend on the geothermal gradient and the depth of the crater. Neglecting heat generated by the impact and assuming a linear geothermal gradient, the effective temperature at the beginning of upwarping will be given by

$$T_{eff} \geq T_o + \frac{D}{h} (T_m - T_o) \quad . \qquad (10.18)$$

This temperature will decrease rapidly, however, as the freshly exposed crater floor material reaches thermal equilibrium. The principal conclusion to be drawn from these calculations, then, is that isostatic upwarping is a reasonable method of producing domes on Ganymede, but only if the depth of the crater is a substantial fraction of the crustal thickness.

10.4 Discussion

Both of the processes discussed here may involve formation of large impact craters in a thin crust with a

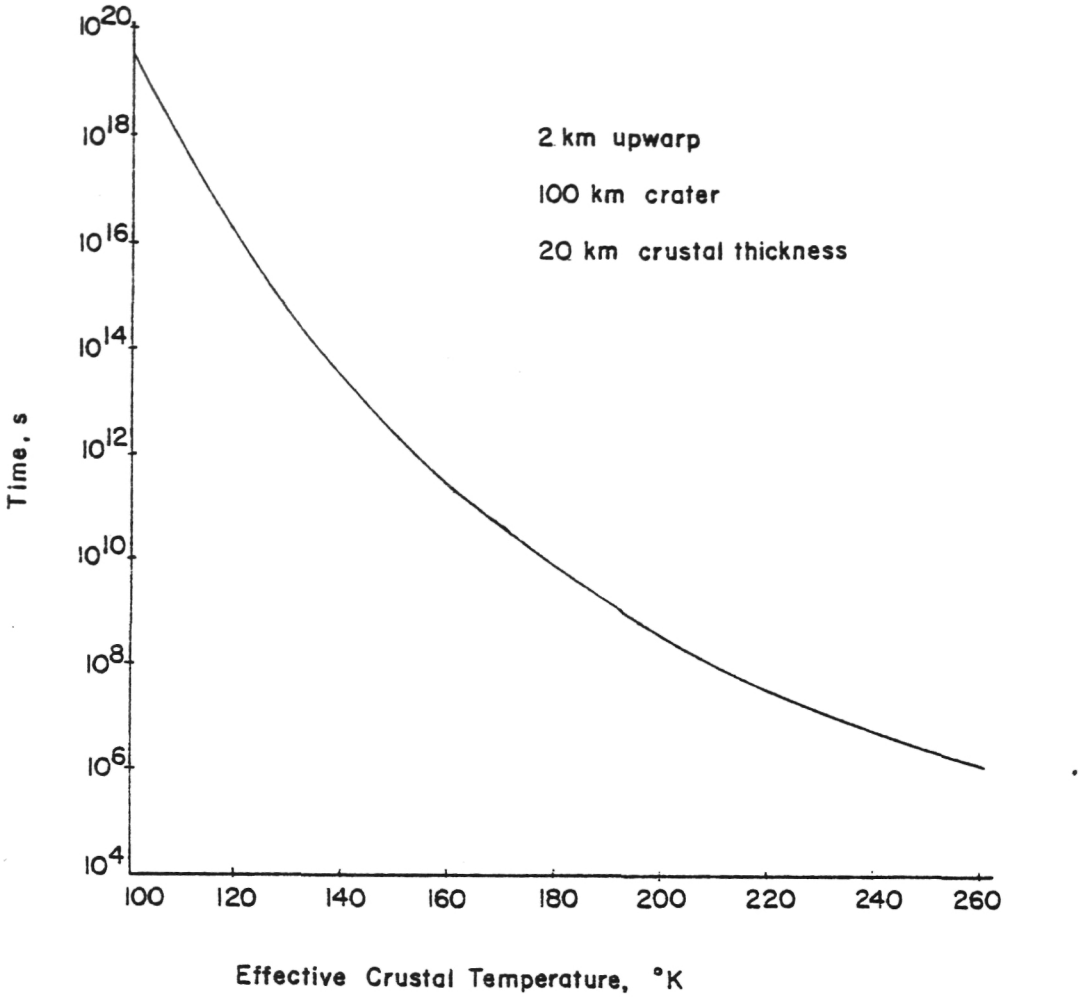


FIGURE 10.9. Time required to form a 2 km dome by isostatic upwarping as a function of effective crustal temperature. Calculations assume a crater 100 km in diameter and initially 10 km deep, a crustal density of 1.25 g cm^{-3}, a crustal thickness of 20 km, and the temperature-viscosity relationship of equation (10.18).

density slightly exceeding that of the liquid mantle. It is possible that both processes are important in dome formation. Simple effusive eruption of liquid water does not seem capable of producing the raised plug observed in the center of the Voyager 2 dome. A problem with the upwarping model is that the diameter of the upwarp should be about the same as the diameter of the initial crater. Yet the crater responsible for at least the Voyager 1 dome seems to have been significantly smaller than the dome itself, based on the extent of the secondary field. The actual formation process may then involve both vulcanism and upwarping. Upwarping may be responsible for formation of the smooth central region or plug, while volcanic eruptions around the perimeter of the upwarp may have created the irregular terrain of the rest of the dome.

One factor that must be considered in the interpretation of these features is the relaxation of topography. The very gentle slopes of the grooved terrain and the low depth/diameter ratio of craters indicate that viscous relaxation of topography in the ice-rich crust has been important on Ganymede. Deformation and radial outward creep therefore have probably occurred subsequent to dome formation. This deformation unfortunately may have destroyed surface features, such as radial fractures that might be caused by upwarping, that would be useful in evaluating

formation models. The irregular concentric topography on the dome flanks may have resulted from gravity-driven outward flow or thrust faulting.

If either of the formation mechanisms suggested here is correct, there are several important geologic implications. First, there must have been at least a short period when Ganymede's crust was very thin and when the mean density of the crust exceeded that of the underlying liquid mantle. The rapid refreezing proposed by Reynolds and Cassen (1979) would of course quickly thicken the crust and reduce the mean density to below that of water, so that this condition would exist only for a short time. The scarcity of domes is consistent with the crust being thin for a geologically brief period. While there is considerable uncertainty in the cratering history of Ganymede, it may be shown that the small number of domes is roughly consistent with the approximate duration of geologic activity in the grooved terrain ($\sim 10^8$ years). Assuming a cratering rate like the mean lunar rate for the last 3.9 b.y. (Hartmann, 1969), craters $\sim$ 75 km in diameter should form on Ganymede at a rate of $\sim 1.4/10^8$ years. If craters this large are required to create domes, the observation of only two domes in the Voyager images is consistent with the crust being sufficiently thin for only $\sim 10^8$ years.

A second important implication involves the fact that the domes lie in grooved terrain. Formation of the domes

must have coincided with or followed grooved terrain formation. If either of the models discussed here is correct, the age relationship indicates that grooved terrain formation cannot have occurred during or after thickening of the crust, but must have preceded it. The appearance of the domes therefore provides additional evidence that the grooved terrain formed when the crust was very thin.

A final implication concerns Callisto. Geologic evidence and consideration of heat sources indicate that Callisto's crust may never have become as thin as Ganymede's. If either mechanism proposed here is correct, there should therefore be no domes on Callisto. None are observed in the Voyager images.

CHAPTER 11

SUMMARY

11.1 Introduction

This chapter is divided into three sections. The first summarizes the factual conclusions of this work--conclusions that may be stated confidently based on the available data. The second summarizes the major interpretations based on these conclusions. These interpretations are hypotheses that may be tested by future work. The final section presents recommendations for future research based on the Voyager data and for future spacecraft observations of the Jupiter system.

11.2 Conclusions

1) The grooved terrain of Ganymede formed early in the satellite's history, and shows widespread evidence for tectonic extension, limited evidence for shear, and little or no evidence for tectonic compressions. There is no evidence of tectonic activity on Callisto.

2) All terrain types on Ganymede and Callisto, including the brightest craters, have light scattering properties like those of the lunar surface. The scattering properties do not show significant wavelength

dependence between 0.4 and 0.6 μm.

3) The albedo of surface materials on Ganymede and Callisto, and in fact on most other bodies, increases with increasing solar incidence angle.

4) Temperature variations among the major terrain types on Ganymede and Callisto are small, and cannot account for the concentration of bright ray craters in Ganymede's grooved terrain or for the lack of polar caps on Callisto. The crust of Ganymede's grooved terrain is enriched in ice relative to the cratered terrain on both bodies.

5) Grooves on Ganymede are typically 300-400 m deep, several km wide, and spaced 3-10 km apart. One of the domes on Ganymede has gentle slopes and a summit elevation of 2-2.5 km.

6) Internal phase changes that would occur during differentiation of Ganymede and Callisto could lead to a global expansion that would increase surface area by up to ∿7%.

7) Ganymede's low gravity and crustal density make it easier to form open fractures by extension than grabens. Relaxation of a deep viscous layer alone cannot produce the present groove topography from either extension fractures or grabens.

8) An apparent secondary crater field around one dome on Ganymede indicates that it is related to an

impact event. The domes could not result from ice vulcanism triggered by complete penetration of the crust by an impact. They could result from ice vulcanism through fractures created by an impact or by isostatic upwarping of a large crater.

11.3 Interpretations

The lunar-like photometric function of all the terrain types on Ganymede and Callisto indicates a particulate surface that, even in the brightest crater rays, probably contains some silicate grains. The mixture of ice and silicate grains at the surface is an impact-generated regolith that may be roughly 5-10 m thick. Its upper layer is probably a thin (a few mm), loosely packed deposit composed largely of silicate grains left behind by sublimation, covered by an extremely thin (a few tens of μm) transient layer of frost. Bright ray craters form when impacts occur where the subsurface material is relatively rich in ice. The most ice-rich material is the grooved terrain of Ganymede. No comparable unit exists on Callisto. With sublimation of ice exposed by impacts, H_2O molecules that do not escape migrate about the surface, forming the transient frost layer. Accumulation of polar frost deposits on Ganymede occurs at latitudes where the influx rate exceeds the sublimation rate. With less ice in the crust, and

consequently less exposed by impacts, a less extensive transient frost layer and no observable polar caps have formed on Callisto.

The tectonic extension expressed in Ganymede's grooved terrain probably reflects a brief period of global expansion early in the satellite's history. This expansion could have resulted from internal differentiation. While differentiation was occurring in the interior, the crust of Ganymede may have been fairly thin due to accretional heating, and underlain by liquid. Extension of the crust, if sufficiently rapid, could have produced broad, downdropped rift zones that were filled in with deposits of clean ice from below in a manner analogous to flooding of terrestrial rifts with basaltic lava. With continued extension, open fractures or long, narrow grabens may have formed in the weaker clean ice deposits, creating the grooves. Some degradation by viscous relaxation and mass-wasting is required to produce the groove topography presently observed. Because of its lower mass, lower density, and greater distance from Jupiter, radiogenic and accretional heating of Callisto would have been less than that of Ganymede. Lesser heating could have resulted in slower and perhaps less complete differentiation and expansion. With sufficiently slow expansion, extensional stresses on Callisto may have never become great enough to cause

fracturing and formation of grooved terrain.

11.4 Recommendations for Future Work

The questions raised by this work show a need for future research in at least four areas: the photometric properties of ice-silicate mixtures, the strength and rheology of ice at low temperatures, the contribution of accretional heating to the thermal evolution of icy bodies, and, most important, improved high resolution imaging of Ganymede and Callisto.

Using the Voyager images, it has been possible to describe the reflectance and photometric behavior of surface materials on Ganymede and Callisto. It is not presently possible, however, to fully determine the implications of these results. The albedos, phase functions, and color behavior of the various terrain types that contain a great deal of information about surface composition and texture. Detailed laboratory work on the photometric properties of ice-silicate mixtures at low temperatures is needed to interpret these data. It is necessary first to determine how visible broadband and spectral reflectance varies with ice/silicate ratio for mixtures of ice and silicates and for silicate grains coated with thin frost layers. This problem is being investigated in the near infrared by Clark (1981). It is also necessary to determine how the photometric

functions of such surfaces vary with grain size and packing. Such a study could be carried out using a facility such as the Cornell goniometer with modifications to allow measurements of low temperature samples.

For any work on the structural evolution of Ganymede's grooved terrain or the internal evolution of both bodies, a detailed understanding of the strength and rheology of ice at low temperatures is needed. It is necessary to perform tests of ice strength under triaxial stress over a wide range of temperatures down to 100°K or less. Similar work is needed on the strength of ice-silicate mixtures, introducing the added variables of silicate grain size and mass fraction. Results of such a study would enable considerable refinement of calculations, such as those of Chapter 9, of the conditions required for crustal fracturing. Work is also needed on the viscosity of ice and ice-silicate mixtures. The temperature dependence of the viscosity of pure ice I is poorly known, and that of ice-silicate mixtures and other ice polymorphs is completely unknown. These viscosities are required for calculations of the rate and extent of differentiation, which depend sensitively on the efficiency of heat transport by solid state convection (e.g., Thurber et al., 1980). Such a study may involve considerable work, requiring sophisticated equipment that allows stressing of samples at very low temperatures and high pressures. No really

firm conclusions about the internal evolution of icy bodies is possible, however, without testing of this sort.

One of the most important heat sources driving the early internal activity of these bodies, and one of the most poorly understood, is accretional heating. It should have had an important influence on the rate and extent of differentiation, and especially may have controlled the thickness of the crust at the time of differentiation. The effects of accretional heating are therefore essential for understanding the formation of grooved terrain on Ganymede and the lack of grooved terrain on Callisto. The most effective way of investigating this problem would be numerical simulation of the accretion of an icy body. Such a calculation requires knowledge of the compositions of impacting bodies, their size and velocity distributions and flux rate, and the shock heating and the partitioning of energy on impact. All of these aspects of the problem have been studied by various workers. Combining these factors into a comprehensive model of accretion, it should be possible to place some useful constraints on the contribution of accretional heating to the evolution of icy objects.

Perhaps the greatest need for better understanding of Ganymede and Callisto is improved photographic coverage. As it is currently planned, NASA's Galileo Jupiter

orbiter mission can fill this need. A spacecraft in orbit around Jupiter will be able to make a number of flybys of the satellites. The closeness of the flybys and the quality of the planned Galileo camera system will provide significantly higher resolution than was obtained by Voyager. With the present knowledge of Ganymede and Callisto, it will be possible to target imaging sequences to provide a very high scientific return from these flybys. In the planning of imaging sequences, there are a number of items that could profitably be given high priority:

1) Medium resolution global mapping (1-2 km/pixel). The Voyager coverage of both Ganymede and Callisto is incomplete. With Galileo, it should be possible to fill in the gaps in the existing coverage with images of sufficient resolution to construct complete, high quality maps of both bodies.

2) High resolution images of grooved terrain ($\lesssim$ 100 m/pixel) for relative age determinations. There is a need to understand the age relationships among crosscutting sets of parallel grooves in complex regions of grooved terrain. Voyager images do not show enough craters to allow relative dating of adjacent sets in a given area. With improved resolution, such dating may be possible. It may even be possible in some cases to look for variations in age across a single set. If present, such variations

could indicate the sequence in which the grooves that make up a set form.

3) High resolution images of grooves. The precise origin of Ganymede's grooves is uncertain, at least partly because the Voyager images do not adequately show the details of their morphology. A major goal of the Galileo mission should be to obtain the highest resolution images of the grooves possible, with a very high priority placed on obtaining useful stereo coverage. If mass-wasting deposits or evidence for viscous degradation can be observed, it may be possible to describe the original morphology of the grooves. It is especially important to be able to compare the morphology of grooves in the grooved terrain to that of grooves in the cratered terrain. The concentration of grooves in the cleaner ice deposits probably reflects a difference in physical properties (tensile strength, viscosity) between clean ice and the rest of the crust at the time of groove formation. If so, grooves in the cratered terrain may show details of morphology that reflect this difference.

4) High resolution images of smooth regions. The clean ice of the grooved terrain may have been emplaced as liquid water, slush, or warm, mobile ice. High resolution images should be acquired of smooth regions undisturbed by groove formation to look for morphologic clues to the mode of emplacement.

5) High resolution images of domes. The domes on Ganymede are very unusual features, and only one has been observed at moderately high resolution. An effort should be made to observe the Voyager 2 dome at high resolution, to obtain good stereo coverage of both domes for accurate determination of topography, and to search for additional domes on both Ganymede and Callisto.

6) Comparison of cratered terrain furrows on Ganymede and impact rings on Callisto. It has been suggested that the parallel furrows observed in Ganymede's cratered terrain may be disrupted concentric structures resulting from a major impact like the one that created the Valhalla ringed structure on Callisto (Smith et al., 1979a). If this is true, the impact must have been enormous, as the furrows are very nearly great circles. At Voyager resolution, however, the furrows appear very different from the Valhalla rings. Higher resolution images of both types of features are needed to precisely determine their differences and to provide clues concerning the origin of the furrows.

7) Stereo coverage of impact craters. Because impact craters have been extensively studied on other bodies, good estimates may be made of the original topography of craters on Ganymede and Callisto. With precise determination of their present topography, it will be possible to estimate the degree of viscous degradation that has

occurred. Measurements of a large sample of craters will allow estimation of crustal viscosity and its variation with depth and time. The viscosity history of the crust is of course related to its thermal history, and may provide useful information about the thermal evolution of the interior.

The Galileo mission is a natural extension of the reconnaissance of the Jupiter system performed so spectacularly by Voyager. It will increase tremendously our understanding of the icy objects that prevail in the outer solar system.

APPENDIX A

PHOTOMETRIC TERMS

Intensity I: Consider radiative energy flowing through some surface element dA in a direction normal to the surface (Fig. A.1). The amount of energy flowing through this area dA, within solid angle $d\Omega$, in time dt, and in frequency interval $d\nu$, is the intensity of that radiation in that direction. The units of intensity are thus, for example, erg cm^{-2} sec^{-1} $steradian^{-1}$ $(d\nu^{-1})$. In this thesis "intensity" refers to true intensity integrated over a range of wavelengths; for example, the bandpass of a Voyager camera filter.

Incidence Angle i: The incidence angle at a point P on a surface is the angle between a ray of incident radiation and the surface normal at P (Fig. A.2). The symbol μ_o is often used for cos i.

Emission Angle ε: The emission angle at point P is the angle between the surface normal and a ray of radiation scattered by the surface to the observer (in this thesis, the Voyager spacecraft). The symbol μ is often used for cos ε.

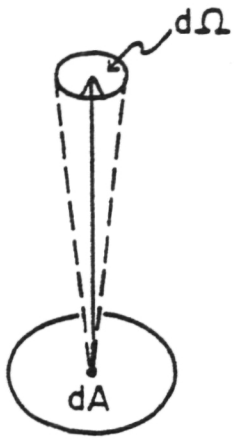


FIGURE A.1. Intensity through area dA.

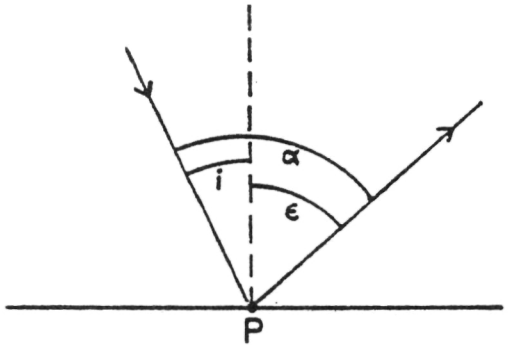


FIGURE A.2. Incidence angle i, emission angle ε, and phase angle α.

Phase Angle α: The phase angle at point P is the angle between the incident ray and the emitted ray. In the special case where the incident ray, the emitted ray, and the surface normal are coplanar, $\alpha = i + \varepsilon$ if i and ε lie on opposite sides of the normal, and $\alpha = |i - \varepsilon|$ if on the same side. In general, however, they are not coplanar. For a given image the phase angle does not vary substantially across the field of view as long as the spacecraft is not too close to the planet, since α is simply the angle subtended by the sun, a point on the planet, and the spacecraft.

Incident Solar Flux πF: The incident solar flux on a surface element dA is the solar energy striking that area in time dt and in frequency interval $d\nu$. The units of flux are thus, for example, erg cm^{-2} sec^{-1} $(d\nu^{-1})$. Like "intensity," "solar flux" as used here is the flux integrated over a filter bandpass. With an incident solar flux of πF, the intensity of light scattered by a 100% reflecting perfectly diffuse scatterer (a perfect Lambert surface) would be F; that is, $I/F = 1$. For practical purposes observed intensity I is often normalized to I/F, which lies in the range $0 < I/F < 1$ for most real surfaces.

Lambert's Law: Lambert's Law is an ideal scattering function of the form

$$I/F \propto \mu_o \ . \qquad (A.1)$$

For example, a white, non-glossy wall scatters light in approximately this fashion.

Lommel-Seeliger Law: The Lommel-Seeliger law is an ideal scattering function of the form

$$I/F \propto \frac{\mu_o}{\mu_o + \mu} \qquad (A.2)$$

No real surface scatters light in this fashion. However, it is known that many particulate surfaces do scatter light according to

$$I/F \propto \frac{\mu_o}{\mu_o + \mu} f(\alpha) \qquad (A.3)$$

where $f(\alpha)$ is the phase function of the surface. The Lommel-Seeliger law is a simplified but unrealistic version in which $f(\alpha)$ = constant.

Photometric Latitude ψ and Longitude ω: Consider a spherical planet with subsolar point Z, subspacecraft point S, and central point C (Fig. A.3). The plane containing the vectors CZ and CS defines the photometric equator for that viewing geometry. The photometric latitude and longitude (ψ,ω) of a point P are defined relative to this equator with (0,0) at point S. The photometric longitude at point z is equal to the phase angle α, while the limb and terminator lie at photometric longitudes $+\pi/2$ and $-\pi/2 + \alpha$, respectively.

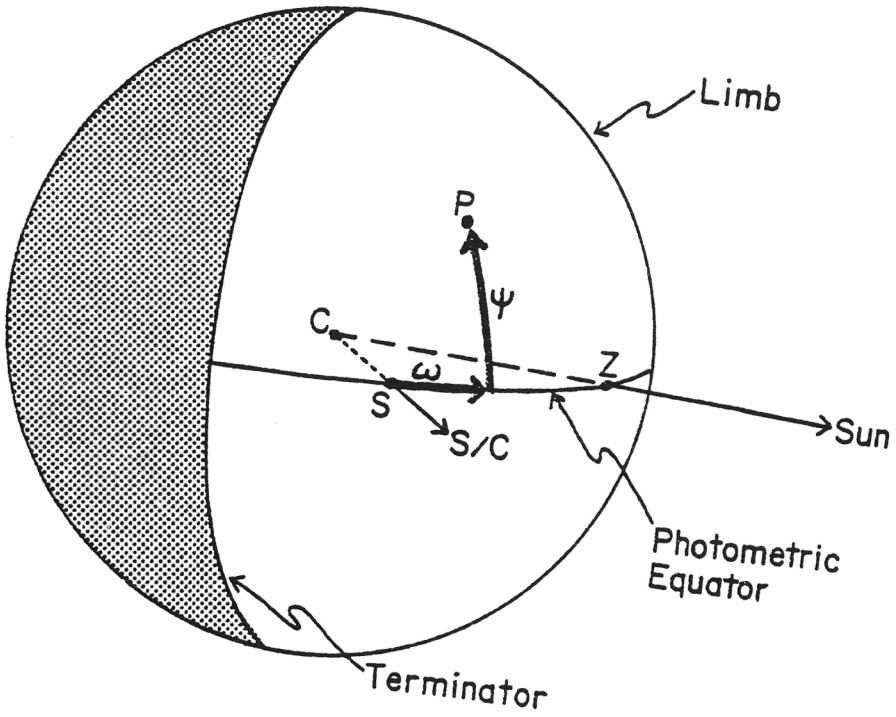


FIGURE A.3. Photometric latitude ψ and longitude ω (S/C denotes spacecraft).

Normal Reflectance r_n: The normal reflectance of a surface is the value of I/F under the conditions $i = 0$, $\varepsilon = 0$, $\alpha = 0$.

Geometric Albedo p_λ: The geometric albedo of a planet at a wavelength λ is the total scattered energy flux received by an observer (here, the Voyager spacecraft) between wavelengths λ and $\lambda + d\lambda$ from that planet at $\alpha = 0$ divided by the flux that would be received from a disc of a 100% reflecting perfectly diffuse white scatterer as big as the planet, at the same distance from the sun, and at $\alpha = 0$. The wavelength-integrated geometric albedo p is given by

$$p = \frac{\int p_\lambda \pi F(\lambda) d\lambda}{\int \pi F(\lambda) d\lambda} \qquad (A.4)$$

Bond Albedo A_B: The Bond albedo of a planet is the total radiative energy scattered in all directions by the planet divided by the total radiative energy incident on the planet.

Phase Integral q_λ: The phase integral of a planet at a wavelength λ is given by

$$q_\lambda = 2 \int_0^\pi \frac{j(\alpha)}{j(0)} \sin \alpha \, d\alpha \qquad (A.5)$$

where

$$j_\lambda(\alpha) = \int_{-\pi/2}^{\pi/2} \int_{-\pi/2+\alpha}^{\pi/2} I_\lambda \cos\omega \cos^2\psi \, d\omega d\psi \ . \qquad (A.6)$$

Note that $j_\lambda(\alpha)$ is proportional to the total scattered energy flux received from a planet at phase angle α between wavelengths λ and $\lambda + d\lambda$. The wavelength-integrated phase integral q is given by

$$q = \frac{\int q_\lambda \pi F(\lambda) d\lambda}{\int \pi F(\lambda) d\lambda} \qquad (A.7)$$

Note that $A_B = pq$.

For further details, the reader is referred to reviews by Russell (1916) and Horak (1950).

APPENDIX B

DERIVATION OF PHOTOCLINOMETRIC EQUATIONS FOR GENERALIZED SCATTERING GEOMETRY

Consider the coordinate system shown in Figure B.1. The x-axis lies along a line of photometric latitude, positive to the east. The y-axis lies along a photometric meridian, positive to the north. The z-axis is positive up. Let ψ be the rotation, positive counterclockwise, of the desired profile trace (A - A') from the x-axis. Let ϕ be the photometric latitude of a point P on the profile, i the incidence angle for a horizontal surface, ε the emission angle for a horizontal surface, and α the phase angle. Let θ be the angle, measured positive to the east, between the surface normal at P and the z-axis. Let i_x, i_y, and i_z be the x, y, and z components of an upward-directed unit vector parallel to the incident ray. Similarly define ε_x, ε_y, ε_z, θ_x, θ_y, and θ_z. Finally, let μ_o^* and μ^* be the local incidence angle and emission angle cosines at P as defined in Chapter 7. Thus:

$$\mu_o^* = i_x\theta_x + i_y\theta_y + i_z\theta_z$$

$$\mu^* = \varepsilon_x\theta_x + \varepsilon_y\theta_y + \varepsilon_z\theta_z \ .$$

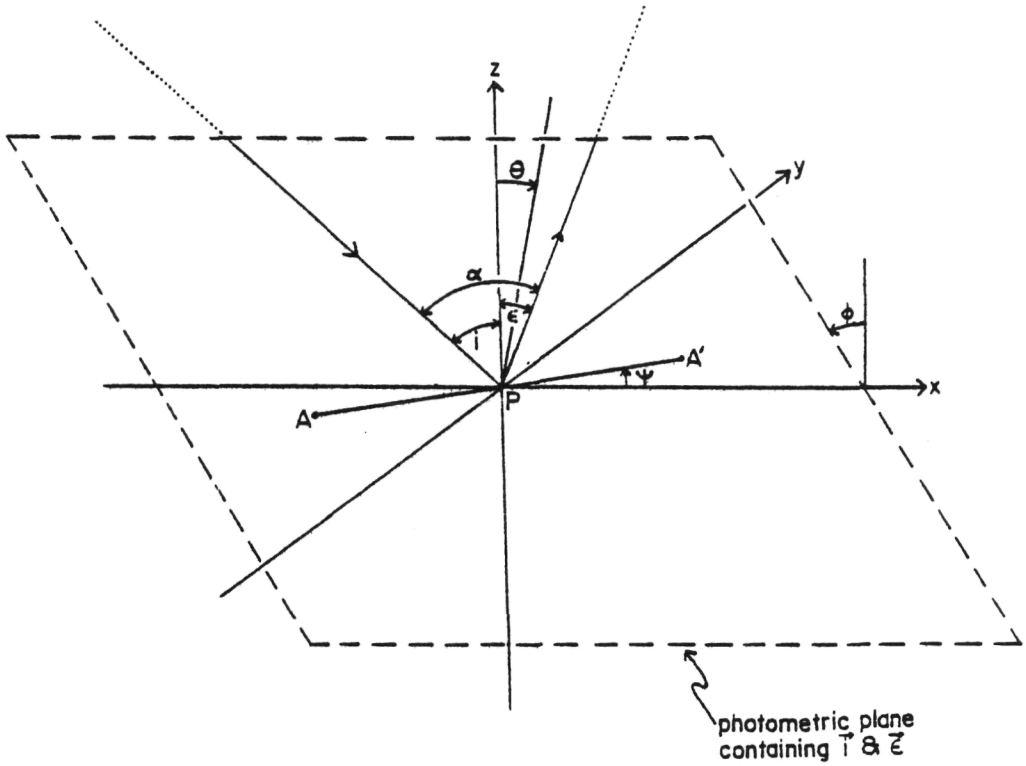


FIGURE B.1. Coordinate system used for photoclinometry.

Now, we find that:

$$i_x = -\sqrt{1 - (\cos^2 i/\cos^2\phi)}$$

$$i_y = -\tan\phi \cos i$$

$$i_z = \cos i$$

$$\varepsilon_x = \sqrt{1 - (\cos^2\varepsilon/\cos^2\phi)}$$

$$\varepsilon_y = -\tan\phi \cos\varepsilon$$

$$\varepsilon_z = \cos\varepsilon$$

$$\theta_x = \sin\theta \cos\psi$$

$$\theta_y = \sin\theta \sin\psi$$

$$\theta_z = \cos\theta$$

So,

$$\mu_o^* = -\sqrt{1 - (\cos^2 i/\cos^2\phi)} \sin\theta \cos\psi$$

$$- \tan\phi \cos i \sin\theta \sin\psi + \cos i \cos\theta$$

$$\mu^* = \sqrt{1 - (\cos^2\varepsilon/\cos^2\phi)} \sin\theta \cos\psi$$

$$- \tan\phi \cos\varepsilon \sin\theta \sin\psi + \cos\varepsilon \cos\theta$$

Or, letting

$$u = (-\sqrt{1 - (\cos^2 i/\cos^2 \phi)}\ \cos \psi - \tan \phi \cos i \sin \psi)$$

$$v = (\sqrt{1 - (\cos^2 \varepsilon/\cos^2 \phi)}\ \cos \psi - \tan \phi \cos \varepsilon \sin \psi),$$

we find that

$$\mu_o^* = u \sin \theta + \mu_o \cos \theta \qquad (B.1)$$

$$\mu^* = v \sin \theta + \mu \cos \theta \qquad (B.2)$$

Now, with the photometric function determined in Chapter 3,

$$I^* \propto \frac{\mu_o^*}{\mu^* + \mu_o^*}, \qquad (B.3)$$

where I* is the observed intensity. Substituting,

$$I^* \propto \frac{u \sin \theta + \mu_o \cos \theta}{v \sin \theta + \mu \cos \theta + u \sin \theta + \mu_o \cos \theta}.$$

Or, inserting the proportionality constant C',

$$I^* = C' \frac{u \sin \theta + \mu_o \cos \theta}{v \sin \theta + \mu \cos \theta + u \sin \theta + \mu_o \cos \theta}$$

where $C' = \bar{I}\left(\frac{\mu_o + \mu}{\mu_o}\right)$ (7.4)

($\bar{I}$ is the mean intensity along the profile). Thus:

$$\sin \theta\,(I^*v + I^*u - C'u) = \cos \theta\,(C'\mu_o - I^*\mu - I^*\mu_o)$$

So,

$$\tan \theta = \frac{C'\mu_o - I^*\mu - I^*\mu_o}{I^*v + I^*u - C'u} \qquad (B.4)$$

Using equations (B.1), (B.2), (B.3), and (B.4), it is possible to calculate θ at any point on the profile from ε, i, ψ, ϕ, I^*, and $\overline{I}$, all of which are known.

APPENDIX C

DERIVATION OF FAILURE CRITERIA FOR A VISCOELASTIC CRUST SUBJECTED TO EXTENSION

Consider a slab of Maxwell viscoelastic material with viscosity η and elastic modulus E subjected to extensional strain ε. The stress-strain relationship in such a material is given by

$$\dot{\varepsilon} = \frac{\sigma}{\eta} + \frac{\dot{\sigma}}{E} \qquad (9.1)$$

where σ is stress (Jaeger and Cook, 1969). Taking $\sigma_{t=0} = 0$ and considering $\dot{\varepsilon} = \dot{\varepsilon}(t)$, the solution of equation (9.1) is

$$\sigma(t) = e^{-\frac{tE}{\eta}} E \int_0^t \dot{\varepsilon}(t') e^{\frac{t'E}{\eta}} dt' \qquad (9.2)$$

where t' is an integration variable for the interval time = 0 to time = t.

For a material of density ρ the stress $\sigma_1 = \sigma_2$ at depth z is simply the lithostatic pressure:

$$\sigma_1 = \sigma_2 = \rho g z. \qquad (C.1)$$

The stress parallel to the applied strain is

$$\sigma_3 = \rho g z - e^{-\frac{tE}{\eta}} E \int_0^t \dot{\varepsilon}(t') e^{\frac{t'E}{\eta}} dt'. \qquad (C.2)$$

Note that compression here is positive, extension negative.

Next, consider a Mohr circle describing the stress field and a failure envelope for the material (Fig. C.1). A point on the circle given by the angle 2α gives σ and τ, the resolved normal and shear components of the stresses σ_1 and σ_3 with respect to a plane oriented at an angle α to σ_3. Define:

r the radius of the circle, $r = \frac{\sigma_1 - \sigma_3}{2}$

σ_c the center of the circle, $\sigma_c = \frac{\sigma_1 + \sigma_3}{2}$

R the distance from σ_c to the nearest point on the envelope

The failure envelope for ice at low temperatures is not known. Griffith failure theory predicts, however, an envelope described by

$$\sigma = -\frac{\tau^2}{\gamma \sigma_t} + \sigma_t \qquad (C.3)$$

where σ_t is the uniaxial tensile strength and, maintaining the sign convention, is negative. The simplest

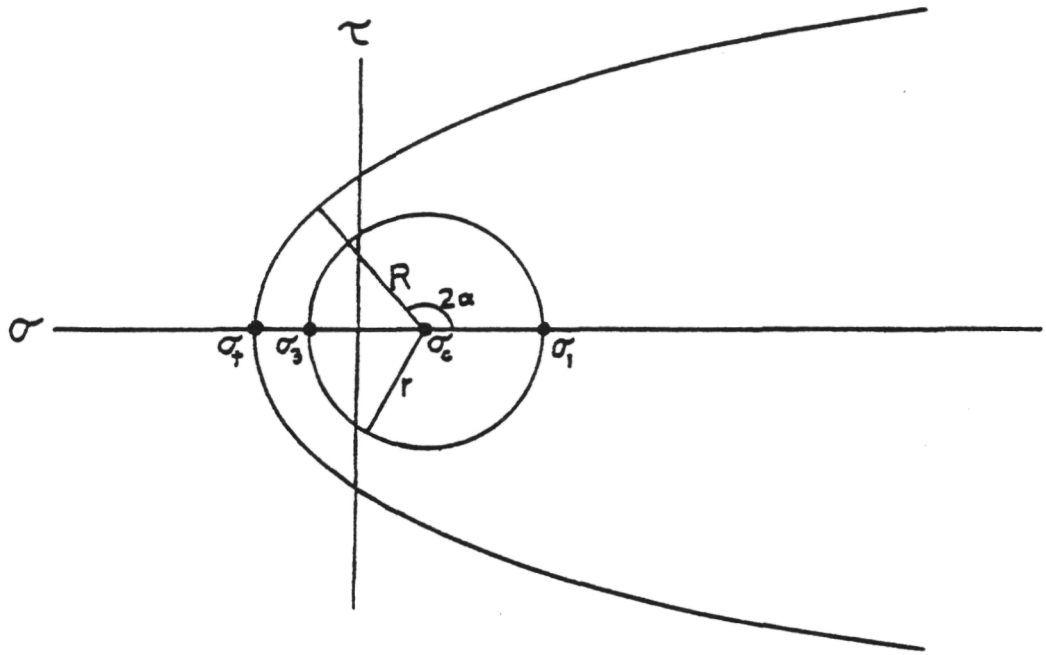


FIGURE C.1. A Mohr circle and failure envelope.

theory predicts a value of 4 for the constant γ. More complex treatments give larger values (Jaeger and Cook, 1969). Fracturing will occur when the circle describing the stress field becomes tangent to the failure envelope (i.e., when r = R). The orientation angle α of the fracture is given by the angle 2α at the point of tangency. Thus extension fracture will occur when $2\alpha = 180°$, normal faulting when $2\alpha < 180°$. For $\gamma = 4$, transition from first failure by extension to first failure by shear (i.e., from $2\alpha = 180°$ to $2\alpha < 180°$) takes place at $\sigma_c = -\sigma_t$. For larger values of γ, transition occurs at larger values of σ_c. A value of $\gamma = 4$ is used here to provide the most conservative constraints possible on the conditions required for failure by extension fracturing. Under these conditions, $R = \sigma_c - \sigma_t$ when $\sigma_c \leq -\sigma_t$, and $R = 2\sqrt{-\sigma_t \sigma_c}$ when $\sigma_c > -\sigma_t$.

For extension fracture, the condition $\sigma_c \leq -\sigma_t$ leads to

$$\rho g z = -\frac{e^{-\frac{tE}{\eta}} E}{2} \int_0^t \dot{\varepsilon}(t') e^{\frac{t'E}{\eta}} dt' \leq -\sigma_t \qquad (C.4)$$

while $r \geq R$ leads to

$$e^{-\frac{tE}{\eta}} E \int_0^t \dot{\varepsilon}(t') e^{\frac{t'E}{\eta}} dt' \geq \rho g z - \sigma_t . \qquad (C.5)$$

Equations (C.4) and (C.5) together constitute the criterion for extension fracture. For shear fracture, $\sigma_c > -\sigma_t$ gives

$$\rho g z = -\frac{e^{-\frac{tE}{\eta}} E}{2} \int_0^t \dot{\varepsilon}(t') e^{\frac{t'E}{\eta}} dt' > -\sigma_t \qquad (C.6)$$

while $r \geq R$ gives

$$\frac{e^{-\frac{tE}{\eta}} E}{2} \int_0^t \dot{\varepsilon}(t') e^{\frac{t'E}{\eta}} dt'$$

$$\geq 2 \left[-\sigma_t \left(\rho g z - \frac{e^{-\frac{tE}{\eta}} E}{2} \int_0^t \dot{\varepsilon}(t') e^{\frac{t'E}{\eta}} dt' \right) \right]^{\frac{1}{2}}. \qquad (C.7)$$

Equations (C.6) and (C.7) give the criterion for shear fracture. If the values of ρ, η, E, and σ_t within the slab are known, then the time and mode of first failure anywhere in the slab may be calculated for any strain history $\dot{\varepsilon}(t)$.

REFERENCES

Anderson, J. D., Null, G. W., and Wong, S. K. (1974). Gravity results from Pioneer 10 Doppler data. Jour. Geophys. Res. 79, 3361-3364.

Barnard, E. E. (1897). On the third and fourth satellites of Jupiter. Astronomische Nachrichten 144, 321-330.

Carrier, W. D., Mitchell, J. K., and Mahmood, A. (1974). Lunar soil density and porosity. Proc. Lunar Sci. Conf. 5th, 2361-2364.

Cassen, P. M., Reynolds, R. T., and Peale, S. J. (1979). Is there liquid water on Europa? Geophys. Res. Lett. 6, 731-734.

Cassen, P. M., Reynolds, R. T., and Peale, S. J. (1980). On the comparative evolution of Ganymede and Callisto. Icarus 41, 232-239.

Chandrasekhar, S. (1960). Radiative Transfer. Clarendon Press, Oxford.

Clancy, R. T., and Danielson, G. E. (1981). High resolution albedo measurements on Io from Voyager 1. Jour. Geophys. Res., in press.

Clark, R. N. (1981). The spectral reflectance of water-mineral mixtures at low temperatures. Submitted to Jour. Geophys. Res.

Clark, R. N., and McCord, T. B. (1980). The Galilean satellites: New near-infrared spectral reflectance measurements (0.65-2.5μm) and a 0.325-5μm summary. Icarus 41, 323-339.

Comas Solá, J. (1906). Observations d'une tache blanche sur le III satellite de Jupiter. Astronomische Nachrichten 173, 297-298.

Consolmagno, G. J., and Lewis, J. S. (1976). Structural and thermal models of icy Galilean satellites. In Jupiter (T. Gehrels, ed.). University of Arizona Press.

Danielson, G. E., Kupferman, P. N., Johnson, T. V., and Soderblom, L. A. (1981). Radiometric performance of the Voyager cameras. To be submitted to Jour. Geophys. Res.

Dorsey, N. E. (1940). Properties of Ordinary Water-substance in All its Phases: Water-vapor, Water, and All the Ices. Reinhold, New York.

Eisenberg, D., and Kauzmann, W. (1969). The Structure and Properties of Water. Oxford University Press, New York.

Fanale, F. P., Johnson, T. V., and Matson, D. L. (1977). Io's surface and the histories of the Galilean

satellites. In Planetary Satellites (J. A. Burns, ed.). University of Arizona Press.

Gault, D. E., Horz, F., Brownlee, D. E., and Hartung, J. B. (1974). Mixing of the lunar regolith. Proc. Lunar Planet Sci. Conf. 5th, 2365-2386.

Gault, D. E., and Wedekind, J. A. (1978). Experimental studies of oblique impact. Proc. Lunar Planet. Sci. Conf. 9th, 3843-3875.

Goguen, J. (1981). A Theoretical and Experimental Investigation of the Photometric Functions of Particulate Surfaces. Ph.D. dissertation, Cornell University, Ithaca, New York.

Goldstein, R. M., and Green, R. R. (1980). Ganymede's radar surface characteristics. Science 207, 179-180.

Gradie, J., and Veverka, J. (1981). The effects of photometric geometry on spectral reflectance: Color light curves of asteroids. Proc. Lunar Planet. Sci. Conf. 12th (abst.), 359-361.

Hansen, J. E., and Travis, L. D. (1974). Light scattering in planetary atmospheres. Space Sci. Rev. 16, 527-610.

Hansen, O. L. (1972). Thermal Radiation from the Galilean Satellites Measured at 10 and 20 Microns. Ph.D. dissertation, California Institute of Technology, Pasadena, California.

Hapke, B. W. (1963). A theoretical photometric function for the lunar surface. Jour. Geophys. Res. 68, 4571-4586.

Harris, D. L. (1961). Photometry and colorimetry of planets and satellites. In Planets and Satellites (G. P. Kuiper and B. M. Middlehurst, eds.). University of Chicago Press.

Hartmann, W. K. (1969). Preliminary note on lunar cratering rates and absolute timescales. Icarus 12, 131-133.

Hawkes, I., and Mellor, M. (1972). Deformation and fracture of ice under uniaxial stress. Jour. Glaciol. 11, 103-131.

Haynes, J. (1978). Effect of temperature on the strength of snow-ice. USA CRREL Report 78-27.

Haynes, J., and Karalius, F. (1977). Effect of temperature on the strength of frozen silt. USA CRREL Report 77-3.

Henyey, L. G., and Greenstein, J. L. (1941). Diffuse reflection in the galaxy. Astrophys. Jour. 93, 70-87.

Horak, H. G. (1950). Diffuse reflection by planetary atmospheres. Astrophys. Jour. 112, 445-463.

Irvine, W. M. (1966). The shadow effect in diffuse reflection. Jour. Geophys. Res. 71, 2931-2937.

Jaeger, J. C. (1953). Surface temperature of the Moon. Australian Jour. Phys. 6, 10-19.

Jaeger, J. C., and Cook, N.G.W. (1969). Fundamentals of Rock Mechanics. Methuen, London.

Jellinek, H.H.G., and Brill, R. (1956). Viscoelastic properties of ice. Jour. Appl. Phys. 27, 1198-2014.

Johnson, T. V. (1978). The Galilean satellites of Jupiter: Four worlds. Ann. Rev. Earth Planet. Sci. 6, 93-125.

Johnson, T. V., and McGetchin, T. R. (1973). Topography on satellite surfaces and the shape of asteroids. Icarus 18, 612-620.

Johnson, T. V., and Pilcher, C. B. (1977). Satellite spectrophotometry and surface compositions. In Planetary Satellites (J. Burns, ed.). University of Arizona Press.

Kennard, E. H. (1938). Kinetic Theory of Gases. McGraw-Hill, New York.

Klaasen, K. P., Duxbury, T. C., and Veverka, J. (1979). Photometry of Phobos and Deimos from Viking orbiter images. Jour. Geophys. Res. 84, 3478-3486.

Kondratiev, K. Ya. (1954). Radiant Solar Energy. Leningrad.

Kondratiev, K. Ya. (1969). Radiation in the Atmosphere. Academic Press, New York.

Lane, A. P., and Irvine, W. M. (1973). Monochromatic phase curves and albedos for the lunar disc. Astrophys. Jour. 78, 794-798.

Lanzerotti, L. J., Brown, W. L., Poate, J. M., and Augustyniak, W. M. (1978). On the contribution of water products from the Galilean satellites to the Jovian magnetosphere. Geophys. Res. Lett. 5, 155-158.

Lebofsky, L. A. (1975). Stability of frosts in the solar system. Icarus 25, 205-217.

Lewis, J. S. (1972). Low temperature condensation from the solar nebula. Icarus 16, 241-252.

Lindsay, J. F. (1973). Evolution of lunar grain-size and shape parameters. Proc. Lunar Sci. Conf. 4th, 215-224.

Morrison, D. (1977). Radiometry of satellites and of the rings of Saturn. In Planetary Satellites (J. A. Burns, ed.). University of Arizona Press.

Morrison, D., and Burns, J. A. (1976). The Jovian satellites. In Jupiter (T. Gehrels, ed.). University of Arizona Press.

Morrison, D., and Cruikshank, D. P. (1973). Thermal properties of the Galilean satellites. Icarus 18, 224-236.

Morrison, D., and Cruikshank, D. P. (1974). Physical properties of the natural satellites. Space Sci. Rev. 15, 641-739.

Morrison, D., Cruikshank, D. P., and Murphy, R. E. (1972). Temperatures of Titan and the Galilean satellites at 20 microns. Astrophys. J. 173, L143-L146.

Morrison, D., and Morrison, N. (1977). Photometry of the Galilean satellites. In Planetary Satellites (J. A. Burns, ed.). University of Arizona Press.

Nakamura, Y., Dorman, J., Duennebier, F., Lammlein, D., and Latham, G. (1975). Shallow lunar structure determined from the passive seismic experiment. The Moon 13, 57-66.

Nevel, D. E. (1976). Creep theory for a floating ice sheet. USA CRREL Research Report 76-4.

Noland, M., and Veverka, J. (1977a). The photometric functions of Phobos and Deimos. II. Surface photometry of Deimos. Icarus 30, 200-211.

Noland, M., and Veverka, J. (1977b). The photometric functions of Phobos and Deimos. III. Surface photometry of Phobos. Icarus 30, 212-223.

Ostro, S. J., Campbell, D. B., Pettengill, G. H., and Shapiro, I. I. (1980). Radar observations of the icy Galilean satellites. Icarus, in press.

Ostro, S. J. (1980). Radar properties of Europa, Ganymede, and Callisto. IAU Colloquium 57: The Satellites of Jupiter, Kailua-Kona, Hawaii.

Paltridge, G. W., and Platt, C.M.R. (1976). Radiative Processes in Meteorology and Climatology. Elsevier, Amsterdam.

Pang, K., Hord, C. W., West, R. A., Simmons, K. E., Coffeen, D. L., Bergstralh, J. T., and Lane, A. L. (1979). Voyager 1 photopolarimeter experiment and the phase curve and surface microstructure of Ganymede. Nature 280, 804-806.

Parameswaran, V. R., and Jones, S. J. (1975). Brittle fracture of ice at 77 K. Jour. Glaciol. 14, 305-315.

Parmentier, E. M., Allison, M. L., Cintala, M. J., and Head, J. W. (1980). Viscous degradation of impact

craters on icy satellite surfaces. Lunar Planet. Sci. Conf. 11th (abst.), 857-859.

Parmentier, E. M., and Head, J. W. (1980). Internal processes affecting surfaces of low density satellites: Ganymede and Callisto. Jour. Geophys. Res. 84, 6263-6276.

Parmentier, E. M., and Head, J. W. (1981). Viscous degradation of impact craters on icy surfaces: Viscosity variation with depth. Proc. Lunar Planet. Sci. Conf. 12th (abst.), 813-815.

Passey, G. R., Shoemaker, E. M., and McCauley, J. F. (1980). Craters and basins on Ganymede and Callisto. IAU Colloquium 57, Kailua-Kona, Hawaii.

Peale, S. J., Cassen, P. M., and Reynolds, R. T. (1979). Melting of Io by tidal dissipation. Science 203, 892-894.

Pilcher, C. B., Ridgway, S. T., and McCord, T. B. (1972). Galilean satellites: Identification of water frost. Science 167, 1372-1373.

Pollack, J. B., Wittenborn, F. C., Erickson, E. F., Strecker, D. W., Baldwin, B. J., and Bunch, T. E. (1978). Near-infrared spectra of the Galilean satellites: Observations and compositional differences. Icarus 36, 271-303.

Prandtl, L. (1957). Essentials of Fluid Dynamics. Blackie & Son, London.

Purves, N. G., and Pilcher, C. B. (1980). Thermal migration of water on the Galilean satellites. Icarus 43, 51-55.

Reynolds, R. T., and Cassen, P. M. (1979). On the internal structure of the major satellites of the outer planets. Geophys. Res. Lett. 6, 121-124.

Russell, H. N. (1916). On the albedo of the planets and their satellites. Astrophys. Jour. 43, 173-189.

Schubert, G., Stevenson, D. J., and Ellsworth, K. (1981). Internal structures of the Galilean satellites. Submitted to Icarus.

Sharp, W. E. (1962). Lawrence Radiation Laboratory Report UCRL-7118.

Shoemaker, E. M., Boyce, J., Lucchitta, B. K., Passey, Q. R., Squyres, S. W., and Wilhelms, D. E. (1981). The geology of Ganymede. In preparation.

Shoemaker, E. M., and Wolfe, R. (1981). Cratering time scales for the Galilean satellites. In preparation.

Shorthill, R. W., Soari, J. M., Baird, R. E., and Le Compte, J. R. (1969). Photometric properties of selected lunar areas. NASA Report CR-1429.

Shvaishtein, Z. I. (1973). Experimental studies in an ice-research laboratory. In Ice Physics and Ice Engineering (G. N. Vakovlev, ed.). Israel Program for Scientific Translations, Jerusalem.

Smith, B. A., Briggs, G. A., Cook, A. F., Danielson, G. E., Davies, M. E., Hunt, G. E., Masursky, Owen, T., Sagan, C., Soderblom, L. A., and Suomi, V. E. (1977). The Voyager imaging experiment. Space Sci. Rev. 21, 103-117.

Smith, B. A., Soderblom, L. A., Johnson, T. V., Ingersoll, A. P., Collins, S. A., Shoemaker, E. M., Hunt, G. E., Masursky, H., Carr, M. H., Davies, M. E., Cook, A. F., Boyce, J., Danielson, G. E., Owen, T., Sagan, C., Beebe, R. F., Veverka, J., Strom, R. G., McCauley, J. F. Morrison, D., Briggs, G. A., and Suomi, V. E. (1974a). The Jupiter system through the eyes of Voyager 1. Science 204, 951-972.

Smith, B. A., Soderblom, L. A., Beebe, R. F., Boyce, J., Briggs, G. A., Carr, M. H., Collins, S. A., Cook, A. F., Danielson, G. E., Ingersoll, A. P., Johnson, T. V., Masursky, H., McCauley, J. F., Morrison, D., Owen, T., Sagan, C., Shoemaker, E. M., Strom, R. G., Suomi, V. E., and Veverka, J. (1979b). The Galilean satellites and Jupiter: Voyager 2 imaging science results. Science 206, 927-950.

Stebbins, J. (1927). The light-variations of the satellites of Jupiter and their application to measures of the solar constant. Lick Obs. Bull. 13, 1-11.

Thurber, C. H., Hsui, A. T., and Toksoz, M. N. (1980). Thermal evolution of Ganymede and Callisto: Effects of solid-state convection and constraints from

Voyager imagery. Proc. Lunar Planet. Sci. Conf. 11th, 1957-1977.

Tschudin, K. (1946). Rate of vaporization of ice. Helv. Phys. Acta 19, 91-102.

Veverka, J. (1970). Photometric and Polarimetric Studies of Minor Planets and Satellites. Ph.D. dissertation, Harvard University, Cambridge, Massachusetts.

Veverka, J. (1972). The physical meaning of phase coefficients. In Physical Studies of Minor Planets (T. Gehrels, ed.). NASA SP-267.

Veverka, J. (1977). Photometry of satellite surfaces. In Planetary Satellites (J. A. Burns, ed.). University of Arizona Press.

Veverka, J., Goguen, J., Young, S., and Elliot, J. (1978). Scattering of light from particulate surfaces. I. A laboratory assessment of multiple scattering effects. Icarus 34, 406-414.

Watson, K., Murray, B. C., and Brown, H. (1963). The stability of volatiles in the solar system. Icarus 1, 317-327.

Weertman, J. (1970). The creep strength of the Earth's mantle. Rev. Geophys. Space Phys. 8, 145-168.

Wesselink, A. J. (1948). Heat conductivity and the nature of the lunar surface material. Bull. Astron. Inst. Neth. 10, 351-362.

Wildey, R. L. (1975). Generalized photoclinometry for Mariner 9. Icarus 25, 613-626.

1. Report No.	2. Government Accession No.	3. Recipient's Catalog No.
NASA TM-84412		

4. Title and Subtitle	5. Report Date
ADVANCES IN PLANETARY GEOLOGY	November 1981
	6. Performing Organization Code: SL-4
7. Author(s): Alex Woronow, Editor	8. Performing Organization Report No.
9. Performing Organization Name and Address	10. Work Unit No.
	11. Contract or Grant No.
	13. Type of Report and Period Covered: Technical Memorandum
12. Sponsoring Agency Name and Address: National Aeronautics and Space Administration, Washington, DC 20546	14. Sponsoring Agency Code

15. Supplementary Notes

16. Abstract

Advances in Planetary Geology is a new series intended to serve the planetary geology community with a form for quick and thorough communications. The previous issue in this series is NASA TM-83089.

Topics in this issue are a catalog of terrestrial craterform structures for northern Europe, abstracts of results of the Planetary Geology Intern Program, and photographic holdings of regional planetary image facilities.

17. Key Words (Suggested by Author(s))	18. Distribution Statement
Planetary geology Planetology	Unclassified—unlimited Subject Category 91

19. Security Classif. (of this report)	20. Security Classif. (of this page)	21. No. of Pages	22. Price*
Unclassified	Unclassified	724	A99

N-305

For sale by the National Technical Information Service, Springfield, Virginia 22161

*U.S. GOVERNMENT PRINTING OFFICE: 1981 539-007/25 1-3

DATE DUE

GAYLORD			PRINTED IN U.S.A.

FL2827
30SPW/XPOT TECHNICAL LIBRARY
BLDG. 7015
806 13th ST., SUITE A
VANDENBERG AFB, CA 93437-5223

U.S. AIR FORCE
VAFB TECHNICAL LIBRARY

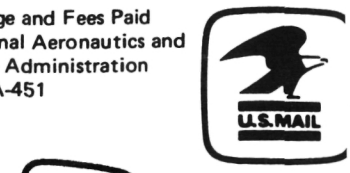
National Aeronautics and
Space Administra

Washington, D C
20546

Official Business
Penalty for Private U

SPECIAL FOURTH CLASS MAIL
BOOK

Postage and Fees Paid
National Aeronautics and
Space Administration
NASA-451







National Aeronautics and
Space Administration

Washington, D.C.
20546

SPECIAL FOURTH CLASS MAIL
BOOK

Postage and Fees Paid
National Aeronautics and
Space Administration
NASA-451

Official Business
Penalty for Private Use $300



[redacted]



POSTMASTER: ıdeliverable (Section 158
Postal Manual) Do Not Return